K. Yamanouchi
S. L. Chin
P. Agostini
G. Ferrante (Eds.)

Progress in Ultrafast Intense Laser Science II

Springer

PUILS

Springer Series in
CHEMICAL PHYSICS 85

Springer Series in
CHEMICAL PHYSICS

Series Editors: A.W. Castleman, Jr.   J. P. Toennies   K. Yamanouchi   W. Zinth

The purpose of this series is to provide comprehensive up-to-date monographs in both well established disciplines and emerging research areas within the broad fields of chemical physics and physical chemistry. The books deal with both fundamental science and applications, and may have either a theoretical or an experimental emphasis. They are aimed primarily at researchers and graduate students in chemical physics and related fields.

Kaoru Yamanouchi · See Leang Chin
Pierre Agostini · Gaetano Ferrante

Progress in Ultrafast Intense Laser Science

Volume II

With 170 Figures, 3 in Colour

Springer

Professor Kaoru Yamanouchi

University of Tokyo, Department of Chemistry
Hongo 7-3-1, 113-0033 Tokyo, Japan
e-mail: kaoru@chem.s.u-tokyo.ac.jp

Professor See Leang Chin

Laval University Quebec
Center for Optics, Photonics and Laser (COPL)
& Department of Physics, Engineering Physics
and Optics
Quebec, Qc G1K 7P4 , Canada
e-mail: slchin@phy.ulaval.ca

Professor Pierre Agostini

Ohio State University
Department of Physics
191 W Wodruff Ave Columbus OH 43210
e-mail: agostini@mps.ohio-state.edu

Professor Gaetano Ferrante

Università di Palermo
Dipto. di Fisica e Tecnologie Relative
Viale delle Scienze, 90128 Palermo, Italy
e-mail: ferrante3@unipa.it

Series Editors:

Professor A. W. Castleman, Jr.

Department of Chemistry,
The Pennsylvania State University
152 Davey Laboratory, University Park, PA 16802,
USA

Professor J. P. Toennies

Max-Planck-Institut für Strömungsforschung
Bunsenstraße 10, 37073 Göttingen, Germany

Professor K. Yamanouchi

University of Tokyo, Department of Chemistry
Hongo 7-3-1, 113-0033 Tokyo, Japan

Professor W. Zinth

Universität München,
Institut für Medizinischen Optik
Öttingerstraße 67, 80538 München, Germany

Preface

The world is filled with light, and, no doubt, we have developed our idea of nature by "seeing" matters, that is, by irradiating matters with light. When increasing the intensity of light, we realized recently that a variety of new and hitherto unimaginable phenomena emerge. In rapid succession, above-threshold ionization, Coulomb explosion, selective chemical bond breaking, high-order harmonic generation into deep XUV, generation of short-pulsed X ray, filamentation, and light-pulse shortening into the attosecond (10^{-18} s) time domain have been reported. Light has gained a new function which is to change the character of matter itself and the consequences have triggered a lot of enthusiasm, discussions and collaborations among the researchers.

A series of annual meetings, "International Symposium on Ultrafast Intense Laser Science" (http://www.isuils.jp), with which this new Springer sub-series collaborates, was designed to stimulate further interdisciplinary interactions at the forefront of research aiming at expanding the frontiers of the field. The first ISUILS was held in Tokyo in 2002, featuring the issue of control of molecules in intense laser fields, and the second ISUILS was held the next year in Quebec City. From this ISUILS2, we started honoring distinguished researchers who have contributed to the establishment of the basis of this new research field. Prof. Hiroshi Takuma (Tokyo) and Prof. Gerard Mainfray (Saclay) served as Honorary Co-chairs at ISUILS2, and Prof. Leonid Keldysh (Moscow) and Prof. Orazio Svelto (Milano) at ISUILS3 held in Palermo in 2004.

The unquestionable success of the ISUILS meetings has encouraged us to launch this series of new-style review books of PUILS, in which concise review-style articles written by researchers at the forefront of their sub-fields are compiled to address the needs of researchers with different backgrounds and graduate students. Although conference proceedings may be useful for researchers with specific interests, and long and complete review articles are necessary for researchers moving to a new theme, the PUILS reviews are fitted to the interdisciplinary interaction in UILS and the rapidly growing character of the field.

The research areas treated in this series will be: (i) atoms, molecules, and clusters in intense laser fields, (ii) control of molecules and clusters in intense laser fields, (iii) attosecond pulse generation, metrology, and applications, (iv) wavepacket control for high-order harmonics, (v) generation,

metrology and interaction of intense few-cycle pulses, (vi) non-linear dynamics in chaotic tunneling for understanding ionization in intense laser fields, (vii) non-linear propagation and fs-ablation, (viii) short-pulsed laser plasma interaction, (ix) non-linear optics in nano plasmas, (x) X ray imaging, (xi) short-pulsed electron diffraction, (xii) nuclear transitions in laser fields, (xiii) relativistic quantum dynamics, (xiv) laser pulse interaction with materials having nano structure, (xv) femtosecond biology.

Each book of the new series is a compilation of 15- to 25-page chapters; the beginning of each chapter provides clear and concise accounts of the significance of the topics, followed by a description of the authors' most recent research results. All chapters are peer-reviewed. Invitations to contribute have been extended to the invited participants of the first three ISUILS symposia. Hence, the first three or four volumes of PUILS will be on invitation only. As in the first volume, the articles of this second volume cover the diverse range of the interdisciplinary research field, reflecting the various activities in the ultrafast intense laser science. The topics may be grouped in three categories: strong-field ionization of atoms and molecules (1–4), control of molecular dynamics and harmonic generation using pulse shaping (5–8), laser-plasma interaction and X-ray emission (9–17).

The PUILS series has been edited in cooperation with the activities of MEXT Priority Area Program on Control of Molecules in Intense Laser Fields (FY2002–2005), JSPS Core-to-Core Program on Ultrafast Intense Laser Science (FY2004–) and JILS (Japan Intense Light Field Science Society). We would also like to take this opportunity to thank all the authors who have kindly contributed to the new PUILS series by describing frontiers of ultrafast intense laser science. We also thank reviewers who have served for this book project by reading carefully the submitted manuscripts. One of the co-editors (KY) thanks Ms. Miyuki Kusunoki and Ms. Chie Sakuta for their help with the editing processes. Dr. Claus Ascheron, Physics Editor of Springer Verlag at Heidelberg kindly agreed to our idea and helped us co-edit the first volumes of PUILS. We very much appreciate his kind cooperation and support.

We hope this book series of PUILS will convey the excitement of Ultrafast Intense Laser Science to the readers, and stimulate interdisciplinary interactions among researchers, thus paving the way to explorations of new frontiers.

Co-editors of PUILS II

University of Tokyo	*Kaoru Yamanouchi*
Laval University	*See Leang Chin*
Ohio State University	*Pierre Agostini*
University of Palermo	*Gaetano Ferrante*

May 25, 2006

Contents

List of Contributors

Felicie Albert
Laboratoire d'Optique Appliquée
(LOA) (ENSTA-CNRS-Ecole
Polytechnique) LOA-ENSTA
Chemin de la Hunière
91761 Palaiseau cedex, France

Wilhelm Becker
Max-Born-Institut
12489 Berlin, Germany
`wbecker@mbi-berlin.de`

Quanli Dong
Laboratory of Optical Physics
Institute of Physics
Chinese Academy of Sciences
Beijing 100080, China

**Carla Figueira
de Morisson Faria**
Centre for Mathematical Science
City University
London EC1V OHB, UK
`C.F.M.Faria@city.ac.uk`

Shinsuke Fujioka
Institute of Laser Engineering
Osaka University, 2-6 Yamada-oka
Suita, Osaka 565-0871, Japan

Yuji Fukuda
Kansai Photon Science Institute
(KPSI)
Japan Atomic Energy Agency
(JAEA)
8-1 Umemidai, Kizu-cho
Souraku-gun, Kyoto 619-0215, Japan
`fukuda.yuji@jaea.go.jp`

Masaki Hashida
Institute for Chemical Research
Kyoto University, Gokasho Uji
Kyoto 611-0011, Japan

Akiyoshi Hishikawa
Institute for Molecular Science
National Institutes
of Natural Sciences, Myodaiji
Okazaki, Aichi 444-8585, Japan

Yuichi Inubushi
Institute of Laser Engineering
Osaka University, 2-6 Yamada-oka
Suita, Osaka 565-0871, Japan

Ryuji Itakura
Department of Chemistry
School of Science
The University of Tokyo
7-3-1 Hongo, Bunkyo-ku
Tokyo 113-0033, Japan

Tomoyuki Johzaki
Institute of Laser Engineering
Osaka University, 2-6 Yamada-oka
Suita, Osaka 565-0871, Japan

Fumihiko Kannari
Department of Electronics
and Electrical Engineering
Keio University, 3-14-1 Hiysohi
Kohoku-ku, Yokohama
223-8522, Japan
`kannari@elec.keio.ac.jp`

Jérôme Kasparian
Teramobile, Laboratoire
de Spectrométrie Ionique
et Moléculaire, UMR CNRS 5579
Bâtiment Kastler
Université Claude Bernard Lyon 1
43 bd du 11 novembre
F69622 Villeurbanne Cedex France
`jkaspari@lasim.univ-lyon1.fr`

Tohru Kawamura
Tokyo Institute of Technology
4259 Nagatsuda-cho, Midori
Yokohama, Kanagawa 226-8502,
Japan

Hyung Taek Kim
Dept. of Phys. and Coherent X-ray
Research Center
Korea Advanced Institute of Science
and Technology (KAIST)
Yuseong-gu, Daejeon 305-701, Korea

Fumihiro Koike
Physics Laboratory
School of Medicine
Kitasato Unversity
Kitasato 1-15-1, Sagamihara
Kanagawa 228-8555, Japan

Miroslav Kolesik
Arizona Center
for Mathematical Sciences
and Optical Sciences Center
University of Arizona
Tucson AZ 85721

Alexey Kondorskiy
P.N. Lebedev Physical Institute
Leninsky pr., 53, Moscow, 119991
Russia
    and
Moscow Institute
of Physics and Technology,
Institutsky per., 9, Dolgoprudny
Moscow region, 141700, Russia
`kondor@sci.lebedev.ru`

Yutong Li
Laboratory of Optical Physics
Institute of Physics
Chinese Academy of Sciences
Beijing 100080, China

Xiaojun Liu
Wuhan Institute
of Physics and Mathematics
Chinese Acadamy of Sciences
Wuhan 430071, P.R. China
`xjliu@wipm.ac.cn`

Maurizio Lontano
Plasma Physics Institute
"P. Caldirola", C.N.R.
Milan, Italy
`lontano@ifp.cnr.it`

Xin Lu
Laboratory of Optical Physics
Institute of Physics
Chinese Academy of Sciences
Beijing 100080, China

Hiroki Mashiko
RIKEN, 2-1 Hirosawa, Wako-shi
Saitama 351-0198, Japan
    and
Graduate School of Science
and Engineering
Saitama University, 255 Okubo
Saitama-shi, Saitama 338-8570
Japan

Katsumi Midorikawa
RIKEN, 2-1 Hirosawa, Wako-shi
Saitama 351-0198, Japan

Gennady Mil'nikov
Division of Electrical, Electronic
and Information Engineering
Graduate School of Engineering
Osaka University 2-1 Yamada-oka
Suita City, Osaka 565-0871, Japan
`gena@e3.eei.eng.osaka-u.ac.jp`

Kunioki Mima
Institute of Laser Engineering
Osaka University, 2-6 Yamada-oka
Suita, Osaka 565-0871, Japan

Jerome V. Moloney
Arizona Center
for Mathematical Sciences
and Optical Sciences Center
University of Arizona
Tucson AZ 85721
jml@acms.arizona.edu

Hideo Nagatomo
Institute of Laser Engineering
Osaka University, 2-6 Yamada-oka
Suita, Osaka 565-0871, Japan

Hiroki Nakamura
Institute for Molecular Science
Myodaiji, Okazaki 444-8585, Japan
    and
The Graduate University
for Advanced Studies
Myodaiji, Okazaki 444-8585, Japan
nakamura@ims.ac.jp

Nobuaki Nakashima
Department of Chemistry
Graduate School of Science
Osaka City University, Sugimoto
Sumiyoshi, Osaka 558-8585, Japan
nakashim@sci.osaka-cu.ac.jp

Chang Hee Nam
Dept. of Phys. and
Coherent X-ray Research Center
Korea Advanced Institute
of Science and Technology (KAIST)
Yuseong-gu, Daejeon 305-701, Korea
Chnam55@kaist.ac.kr

Hiroaki Nishimura
Institute of Laser Engineering
Osaka University, 2-6 Yamada-oka
Suita, Osaka 565-0871, Japan
nishimu@ile.osaka-u.ac.jp

Kimihisa Ohno
Department of Electronics
and Electrical Engineering
Keio University, 3-14-1 Hiysohi
Kohoku-ku, Yokohama
223-8522, Japan

Tatsuyoshi Okamoto
Department of Electronics
and Electrical Engineering
Keio University, 3-14-1 Hiysohi
Kohoku-ku, Yokohama
223-8522, Japan

Matteo Passoni
Nuclear Engineering Dept.
Polytechnic of Milan, Milan, Italy
matteo.passoni@polimi.it

Kim Ta Phuoc
Laboratoire d'Optique Appliquée
(LOA) (ENSTA-CNRS-Ecole
Polytechnique) LOA-ENSTA
Chemin de la Hunière
91761 Palaiseau cedex, France

Antoine Rousse
Laboratoire d'Optique Appliquée
(LOA) (ENSTA-CNRS-Ecole
Polytechnique) LOA-ENSTA
Chemin de la Hunière,
91761 Palaiseau cedex, France
antoine.rousse@ensta.fr

Shuji Sakabe
Institute for Chemical Research
Kyoto University, Gokasho Uji
Kyoto 611-0011, Japan

Zhengming Sheng
Laboratory of Optical Physics
Institute of Physics
Chinese Academy of Sciences
Beijing 100080, China

Seiji Shimizu
Institute for Chemical Research
Kyoto University, Gokasho Uji
Kyoto 611-0011, Japan

Akira Suda
RIKEN, 2-1 Hirosawa, Wako-shi
Saitama 351-0198, Japan
asuda@riken.jp

Takasumi Tanabe
Department of Electronics
and Electrical Engineering
Keio University, 3-14-1 Hiysohi
Kohoku-ku, Yokohama, 223-8522,
Japan

Valer Tosa
Dept. of Phys. and Coherent
X-ray Research Center
Korea Advanced Institute
of Science and Technology (KAIST)
Yuseong-gu, Daejeon 305-701, Korea

Marc J.J. Vrakking
FOM Institute for Atomic
and Molecular Physics (AMOLF)
Kruislaan 407, 1098 SJ Amsterdam
The Netherlands
m.vrakking@amolf.nl

Zhiyi Wei
Laboratory of Optical Physics
Institute of Physics
Chinese Academy of Sciences
Beijing 100080, China

Koichi Yamakawa
Advanced Photon Research Center
Japan Atomic Energy
Research Iinstitute (JAERI)
8-1 Umemidai, Kizu-cho
Souraku-gun, Kyoto 615-0215, Japan

Kaoru Yamanouchi
Department of Chemistry
School of Science
The University of Tokyo
7-3-1 Hongo, Bunkyo-ku
Tokyo 113-0033, Japan

Tomoyuki Yatsuhashi
Department of Chemistry
Graduate School of Science
Osaka City University, Sugimoto
Sumiyoshi, Osaka 558-8585, Japan
tomo@sci.osaka-cu.ac.jp

Hiroki Yazawa
Department of Electronics
and Electrical Engineering
Keio University, 3-14-1 Hiysohi
Kohoku-ku, Yokohama
223-8522, Japan

Jie Zhang
Laboratory of Optical Physics
Institute of Physics
Chinese Academy of Sciences
Beijing 100080, China
jzhang@aphy.iphy.ac.cn

Shiyang Zou
Department of Theoretical Studies
Institute for Molecular Science
Myodaiji, Okazaki 444-8585, Japan

1 Coulomb Explosion Imaging
of Molecular Dynamics in Intense Laser Fields

Akiyoshi Hishikawa[1] and Kaoru Yamanouchi[2]

[1] Institute for Molecular Science, National Institutes of Natural Sciences,
    Myodaiji, Okazaki, Aichi 444-8585, Japan
[2] Department of Chemistry, School of Science, The University of Tokyo,
    7-3-1 Hongo, Bunkyo-ku, Tokyo 113-0033, Japan

Summary. The nuclear dynamics of polyatomic molecules in intense laser fields
($\sim 1\,\mathrm{PW/cm^2}$) is studied through the momentum imaging of the fragment ions
produced through Coulomb explosion. Characteristic nuclear dynamics that occur
on the multidimensional potential energy surfaces in intense laser fields, such as
sequential and concerted bond-breaking and hydrogen migration, are elucidated
from momentum correlations among the fragment ions.

1.1 Introduction

Molecular dynamics in an intense laser field (10^{12} to $10^{15}\,\mathrm{W/cm^2}$) has proved
to be one of the most attractive research fields in molecular science over the
last few decades. From pioneering studies [1–5], it has been revealed that
a molecule present in an intense light field exhibits a variety of character-
istic dynamical processes, such as alignment of its principal molecular axis,
ultrafast structural deformation, enhanced ionization, and bond-breaking as-
sociated with multiple ionization (known as a "Coulomb explosion").

When the intensity of a laser field reaches as high as $\sim 10^{15}\,\mathrm{W/cm^2}$, the
magnitude of the electric field of the light becomes comparable to that of the
Coulomb field within a molecule. Thus, the electrons bound in a molecule
become heavily perturbed by the external electric field and form a new class
of states, often referred to as light-dressed states, in which the molecules and
the light field are strongly coupled. Since the internuclear potential within the
molecule is deformed in response to the temporal variation of the amplitude
of the light field, it should be possible to control dynamical processes of
molecules such as vibration and chemical bond-breaking if the light field is
designed properly.

Experimentally, evidence of the potential deformation induced by an
intense laser field was first obtained from the kinetic energy spectrum
of the H^+ fragment ions produced through the bond breaking process,
$H_2^+ \rightarrow H^+ + H$ [6, 7]. The three peaks separated by the photon energy that
appear in the spectra were attributed to the bond softening and the above-
threshold dissociation that occurs via the coupling between the $1s\sigma_g$ and $2p\pi_u$

states of H_2^+. The deformations of the potential energy curves induced by the strong coupling were also identified [8] as resulting from the energy shift of the vibrational levels in the bound well, the magnitude of which increases as the field intensity increases.

How does a polyatomic molecule, with more vibrational degrees of freedom, behave in intense laser fields, and how can the phenomenon be interpreted in terms of light-dressed states? In order to answer these questions, a new experimental approach is required that can shed light on the nuclear dynamics that occur on the multidimensional potential energy surface (PES). In general, when molecules are exposed to an intense laser field whose magnitude is as great as $\sim 10^{15}\,\mathrm{W/cm^2}$, momentum vectors of the fragment ions ejected in the Coulomb explosion carry valuable information on the nuclear dynamics induced by intense laser fields, because they sensitively reflect the geometrical structure of the molecule just before the Coulomb explosion (see Fig. 1.1). That is, the evolution of the geometrical structures of molecules induced by the intense laser field is mapped onto the observed momentum distribution of the fragment ions.

In the present chapter, we describe how molecules respond to an ultrashort intense laser field by referring to our recent series of studies. In Sect. 1.2, we describe the experimental techniques – such as mass-resolved momentum imaging (MRMI) and coincidence momentum imaging (CMI) – that have been developed in order to measure the momentum distributions of fragment ions generated by the Coulomb explosions of molecules in intense laser fields. In Sect. 1.3, we show how the dynamics induced within CS_2 by ultrashort intense laser fields is elucidated by the CMI method from momentum
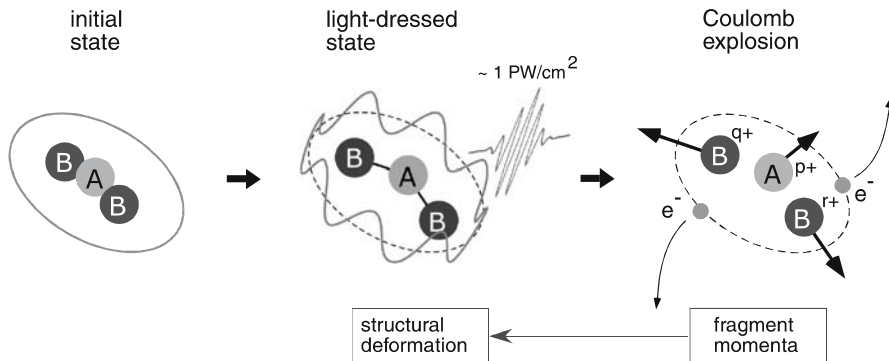
Fig. 1.1. Schematic view of the Coulomb explosion imaging of nuclear dynamics. Molecules exposed to an intense laser field undergo structural deformation in response to the formation of light-dressed potential energy surfaces, and decompose into fragment ions after multiple ionization. Since the momentum vectors of fragment ions sensitively reflect the geometrical structure just before the Coulomb explosion, the ultrafast nuclear dynamics of a molecule in an intense laser field can be elucidated through measurements of the momenta of fragment ions

correlations among the fragment ions. In Sect. 1.4, we introduce the pump-and-probe CMI method, and probe the evolution of the nuclear wavepacket of CS_2 in real time. In Sect. 1.5, we apply the CMI method to CH_3CN, and show how the hydrogen atoms migrate within a molecule.

1.2 Experimental Techniques

1.2.1 Mass-Resolved Momentum Imaging

In order to measure the momentum distributions of fragment ions produced in intense laser fields, an ion imaging technique known as mass-resolved momentum imaging (MRMI) was developed [9], and this has been applied to triatomic molecules such as SO_2 [9], CO_2 [10], NO_2 [11], H_2O [12, 13], and OCS [14]. The fragment ions produced in the extraction region of a TOF mass spectrometer have forward and backward components along the direction parallel to the axis of the TOF mass spectrometer, so these two components reach the detector at different times. The atomic or molecular fragment ions with a positive initial momentum, $p_{//}$, along the TOF axis towards the detector, reach the detector at a flight time t, which is $\Delta t = (t_0 - t)$ earlier than the central flight time t_0 obtained when $p_{//} = 0$. The momentum of the fragment ion is expressed as

$$p_{//} = qF\Delta t , \tag{1.1}$$

where q denotes the charge of the fragment ion and F is the electric-field strength in the extraction region. Thus, by using (1.1), the temporal shift of the respective ion species in the recorded time-of-flight spectrum can be converted into their momentum distribution along the flight tube axis. The two-dimensional momentum distribution of the mass-selected fragment ions can be constructed from time-of-flight spectra measured at different angles α between the detection axis and the laser polarization vector (ε), as shown in Fig. 1.2.

The two-dimensional mass-resolved momentum imaging (MRMI) maps observed for the Coulomb explosion process of CO_2 in an intense laser field $(1.1 \times 10^{15}\,\text{W/cm}^2, 100\,\text{fs}, 800\,\text{nm})$ are shown in Fig. 1.3. The MRMI map for O^{2+} in Fig. 1.3a exhibits a pair of symmetrical crescent-like distributions along the vertical axis, showing that O^{2+} ions tend to be ejected along the laser polarization vector. In contrast, C^{2+} ions exhibit a peak in the momentum distribution at the zero momentum, as shown in Fig. 1.3b. These observations show that highly charged CO_2 molecules are prepared in the intense laser field so that the molecular a-axis is distributed around the direction of the ε vector, while the average geometry is maintained around the linear configuration.

It is also apparent from Fig. 1.3b that the distribution of C^{2+} spreads along the directions perpendicular to ε to form an elliptical pattern. This
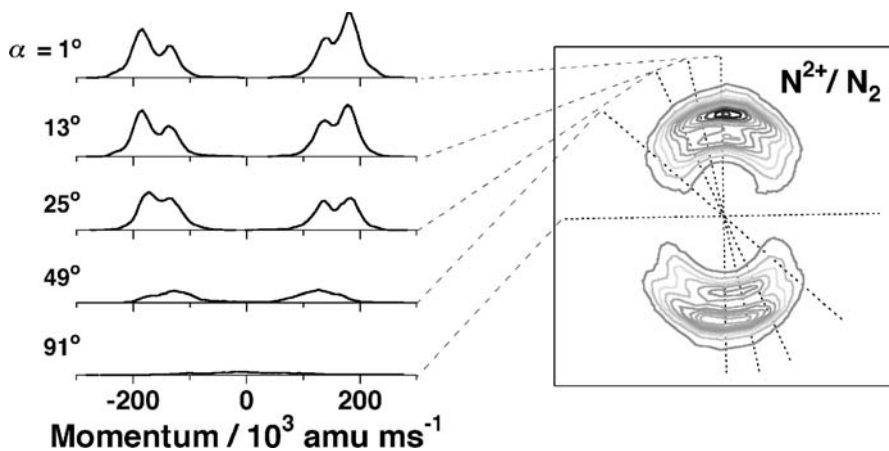
Fig. 1.2. Mass-resolved momentum imaging (MRMI) technique applied to the N^{2+} ion produced from N_2 in intense laser fields ($\sim 3.5\,PW/cm^2$). The two-dimensional momentum map is constructed from a set of time-of-flight mass spectra recorded at different angles α between the laser polarization direction and the TOF tube axis
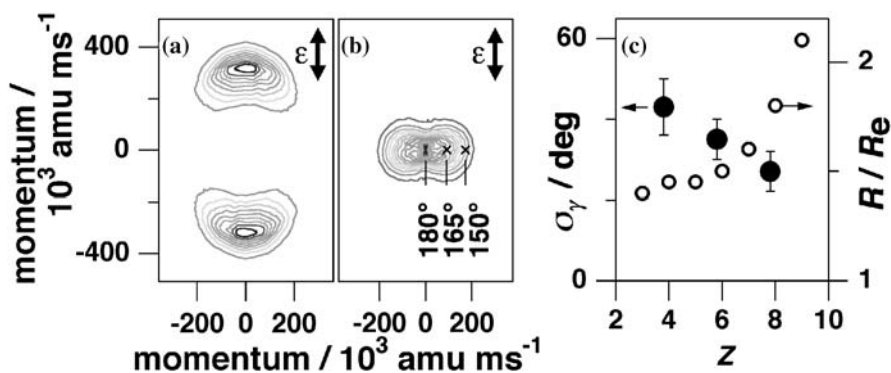
Fig. 1.3. MRMI maps for O^{2+} (**a**) and C^{2+} (**b**) produced through the Coulomb explosion of CO_2 in an intense laser field ($\sim 1.1\,PW/cm^2$). The *arrow* represents the direction of the laser polarization vector (ε). **c** The determined structural parameters R/R_e (*open circles*) and σ_γ (*solid circles*) of CO_2^{z+} just before the Coulomb explosion as a function of charge number z

indicates that the distribution of the $\angle$O–C–O bond angle distribution is substantially broadened in the intense laser field. When a C–O bond length of $R(\text{C–O}) = 1.74\,\text{Å}$ is chosen to reproduce the momentum value of O^{2+} at the peak in the momentum distribution in Fig. 1.3a, the three selected points are converted into the $\angle$O–C–O ($= \gamma$) bond angles, as shown in Fig. 1.3b. Since the mean amplitude of the bending vibration in the vibrational ground state of CO_2 $X^1\Sigma_g^+$, defined as the full width at half maximum of the proba-

bility distribution along the bending coordinate, is $\sigma_\gamma = 12.5°$, the elliptical distribution of C^{2+} extending beyond $\gamma = 150°$ (that is, the bending angle of $30°$ from the linear configuration) provides evidence that ultrafast nuclear motion is induced along the bending coordinate through exposure to the intense laser field.

More qualitative information on the nuclear dynamics can be obtained from a simulation of the MRMI maps [10,11,15,16]. Since the detector located at the end of the flight tube of the TOF mass spectrometer has a finite size with a diameter d, the fragment ions ejected along a direction slightly away (by angle $\delta\theta$) from the detection axis can also hit the detector. Since ions ejected at the ejection angle $\delta\theta$ with momentum $p_m = (\cos\delta\theta)^{-1}p_{//}$, have a momentum component $p_{//}$ along the detection axis, the finite size of the detector modifies the observed momentum and angular distributions from the original distributions in a somewhat complex manner.

When (i) the angular distribution $f(\theta)$ of the axis of the parent molecular ions in the laboratory frame and (ii) the momentum distribution of the fragment ion species $g(\theta_m, p_m)$ expressed in terms of the momentum value $p_{//}$ and the ejection angle θ_m with respect to ε are given, the momentum-scaled TOF spectrum $I^\alpha(p_{//})$, which corresponds to the shape of the cross-section when the MRMI map is cut at angle α, can be expressed [11,16] in terms of the Legendre polynomials P_{2k},

$$I^\alpha(p_{//}) = \int_{|p_{//}|}^{p_{\max}} \frac{g(\theta_m, p_m)}{2p_m} \left[\sum_{k=0}^{\infty} a_{2k} P_{2k}(\cos\theta_m) P_{2k}(\cos\alpha) P_{2k}\left(\frac{p_{//}}{p_m}\right) \right] dp_m \ ,$$

$$(1.2)$$

where $p_{\max}$, defined as $p_{\max} = [p_{//}^2 + (md/2t)^2]^{1/2}$, is the upper limit of the momentum of the fragment ion with mass m that reaches the detector at flight time t. The a_{2k} coefficients are those obtained when $f(\theta)$ is expressed by the Legendre expansion as $f(\theta) = (8\pi^2)^{-1} \sum_k a_{2k} P_{2k}(\cos\theta)$.

It should be noted that the multiply charged parent molecular ions decompose into fragment ions through a variety of pathways: through (p, q, r) three-body explosion pathways $CO_2^{z+} \rightarrow O^{p+} + C^{q+} + O^{r+}$ $(z = p + q + r)$ and (m, n) two-body pathways $CO_2^{z+} \rightarrow CO^{m+} + O^{n+}$ $(z = m + n)$. Therefore, O^{2+} fragment ions, for example, can be produced through one two-body pathway (1,2) and five different three-body pathways, (1,1,2), (1,2,2), (2,2,2), (2,2,3) and (2,3,3), together with CO^+, O^+, O^{2+}, O^{3+}, C^+, C^{2+} and C^{3+}. Thus, for quantitative analysis, the branching ratio as well as the angular distribution $f(\theta)$ and the structural parameters determining the momentum distribution $g(\theta_m, p_m)$ should be modeled for the respective explosion pathways in order to reproduce the observed MRMI maps of all the fragment ions simultaneously [10].

The C–O bond lengths $R(C–O)$ and the mean amplitudes σ of the bent angle distribution were determined from trial-and-error fits of the observed MRMI maps [10], as plotted in Fig. 1.3c. The large values of $R(C–O)$ com-

pared with the equilibrium bond length R_e of CO_2 $X^1\Sigma_g^+$, and its parabolic increase as a function of z shows that the C–O bond length rapidly increases within the ultrashort laser pulse, leading to the formation of highly charged parent ions through the enhancement of the ionization probability at large internuclear distances, the so-called *enhanced ionization effect* [1,5]. As shown in Fig. 1.3c, the bond angle distribution decreases from the full width $\sigma_\gamma = 40°$ at $z \sim 3$ as z increases. The width at $z = 8$ is $\sigma_\gamma = 26°$, which is still much larger than the σ_γ value of 12.5° for the vibrational ground state of CO_2 $X^1\Sigma_g^+$. It was clearly demonstrated that the geometrical structure of CO_2 is greatly deformed along both the stretching and bending coordinates under intense laser fields within time durations as short as ∼100 fs.

1.2.2 Covariance Mapping

As introduced in the previous section, we can extract the essential features of nuclear dynamics of molecules in intense laser fields from the momentum distributions of the respective fragment ion species. On the other hand, due to the presence of a number of different explosion pathways contributing simultaneously to the momentum distribution of fragment ions, the information for the respective fragmentation pathways can only be obtained after the simultaneous analysis of all of the observed MRMI maps of the fragment ions involved in the pathway, and a number of assumptions need to be introduced into the analysis.

In order to correlate the different ion species ejected from the same Coulomb explosion pathway, the covariance mapping technique [17] was introduced, in which correlations among the fragment ions are extracted from the fluctuation in the ion signals of a large number of TOF mass spectra recorded at respective laser shots. When the fragment ions are produced through the same explosion pathway, their covariance becomes positive.

From the covariance map, in which the covariance coefficients [17] are plotted on a two-dimensional plane, we can identify the respective explosion pathways and show how the momentum components along the TOF axis of the different ion species are correlated. The characteristic patterns appearing in the double covariance map for the ion pairs (O^+, O^+), (O^+, C^+) and (O^+, O^{2+}) ejected from CO_2 at the field intensity of 10^{15} W/cm^2 were interpreted in terms of a large amplitude bending motion [18], where the widths of the bond angle distribution were found to be constant $\sigma_\gamma = 40°$ for all of the different charge states ($z = 3$–6).

Since the covariance map is constructed based on one-dimensional TOF mass spectra, the angular distribution of fragment ions with respect to the laser polarization direction is only indirectly incorporated into the map through the momentum distribution along the TOF axis (see [19] for the extension to two-dimensional measurements). In order to derive three-dimensional momentum vector distributions of the fragment ions together

with the information on how they are correlated, it was necessary to develop a new method.

1.2.3 Coincidence Momentum Imaging

In 2001, we introduced for the first time a new experimental technique called coincidence momentum imaging (CMI) to investigate ultrafast nuclear dynamics of molecules in intense laser fields [20]. This technique, based on single-particle detection with a fast position-sensitive detector (PSD), has two major advantages over the two momentum imaging methods presented in the previous sections. First, all of the fragment ions originating from a single parent ion are detected in coincidence so that the charge number of the parent ion and the successive charge redistribution into the fragment ions can be specified definitively. Second, unlike one-dimensional momentum measurements along the TOF axis, all three components of the momentum vector for each fragment ion are simultaneously determined in every single event of the Coulomb explosion, allowing us to convert the momentum vectors from the laboratory frame to the molecular frame directly. Thus, the momentum correlation among the fragment ions can be derived in a straightforward manner without the need for any assumption about the molecular orientation with respect to the laser polarization direction.

The experimental set-up [20] for the coincidence momentum imaging is shown in Fig. 1.4. The sample gas is introduced into a vacuum chamber as an effusive beam through a skimmer. The sample gas does not need to be introduced as a cold molecular beam used in cold target recoil-ion momentum spectroscopy (COLTRIMS) [21]. The ions produced at the interaction region containing intense laser fields are guided by three equally spaced ($d = 15\,\mathrm{mm}$) parallel-plate electrodes to a detector after a field-free drift region. The velocity-mapping configuration [22] (in which the acceleration and ground electrodes have open holes) is employed to avoid the blurring effect induced by mesh grids on the ion images as well as to achieve the high transmission of ions required for multiple coincidence measurements.

Each of the fragment ions generated from a single parent ion is detected by a fast PSD (RoentDek Handels GmbH, Kelkheim-Ruppertshain, Germany) equipped with a pair of delay-line anodes positioned behind a multichannel plate (MCP) to decode the (x, y) position. The position along the x- or y-axis is determined by the corresponding delay line from the time difference between the signals at the two ends. The time of flight (t) of each fragment ion is obtained from the sum of the times of the signals at both ends of the anodes. The arrival time of a signal at the end of the delay line is recorded by a multi-hit time-to-digital converter after amplification and noise discrimination. A delayed output from a fast photodiode monitoring the laser pulse is commonly used as a stop trigger pulse during acquisition.

Coincidence detection of the fragment ions produced from a specific explosion pathway is achieved by collecting the events in which all of the frag-
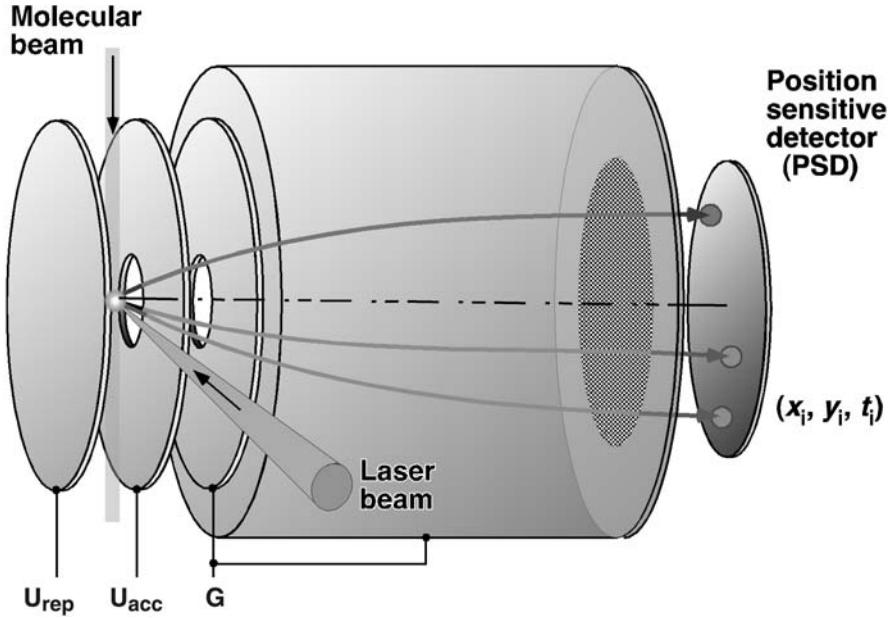
Fig. 1.4. Experimental set-up used for the coincidence momentum imaging. The laser polarization vector (ε) is set parallel to the detector plane [20]. The voltages applied to the electrodes are $U_{\mathrm{rep}} \sim 500\,\mathrm{V}$ and $U_{\mathrm{acc}} \sim 400\,\mathrm{V}$ in order to collect all of the fragment ions in the 4π solid angle with high mass resolution. The third electrode and the flight tube are connected to the ground potential (G). The flight tube is shielded from the bias potential of the detector by high-transmission ($> 90\%$) mesh. Because of the high voltages at the electrodes, the effect of the contact potential is negligibly small

ment ions are detected. In order to securely detect the coincidence events originating from a single parent ion, it is necessary to maintain the number of ion-detection events per laser shot at less than unity. This condition can be achieved by using a low number density of target molecules in an ultra-high vacuum chamber system. Typically, the residual pressure in the vacuum chamber needs to be kept below $10^{-8}\,\mathrm{Pa}$ when the laser field intensity is on the order of 10^{14} to $10^{15}\,\mathrm{W/cm^2}$.

The momentum vector, $\boldsymbol{p} = (p_x, p_y, p_z)$, of each fragment ion is determined in the laboratory frame from the (x, y) position and the time of flight (t) [20, 21] as

$$\begin{pmatrix} p_x \\ p_y \\ p_z \end{pmatrix} = \begin{pmatrix} \alpha_x m \Delta x \\ \alpha_y m \Delta y \\ \alpha_z q F \Delta t \end{pmatrix}, \tag{1.3}$$

where Δx and Δy are the shifts from the reference position in the x–y coordinate system where an ion released with $p_x = p_y = 0$ hits the detector,

Δt is the time delay with respect to the reference flight time when an ion with $p_z = 0$ reaches the detector, and $F = (U_{\mathrm{rep}} - U_{\mathrm{acc}})/d$ is the nominal electric field strength defined by the voltages on the repeller (U_{rep}) and the accelerator (U_{acc}). A set of correction factors, (α_x, α_y, α_z), is introduced to account for a weak nonuniformity in the electrostatic field in the ion extraction region of the TOF mass spectrometer used with the velocity mapping configuration [22]. Since the magnitude of the momentum carried by the emitted electrons is smaller than that of the fragment ions by more than two orders of magnitude, the momentum vector $\boldsymbol{p}_i$ of the i-th fragment ions ejected from a single parent ion should fulfill the momentum conservation rule, $\sum \boldsymbol{p}_i = 0$. Therefore, false coincidence events originating from more than two parent ions at the interaction spot can be excluded based on the momentum conservation rule.

1.3 Nuclear Dynamics of CS_2 in Intense Laser Fields

1.3.1 Identification of Coulomb Explosion Pathway

The TOF mass spectrum recorded at the laser field intensity of $0.2\,\mathrm{PW/cm^2}$ exhibits two strong peaks corresponding to CS^+ and S^+, and small features assigned to S^{2+} and C^+ [23]. These fragment ions are produced from CS_2^{z+} formed in the intense laser fields through either the three-body (p, q, r) pathway, $CS_2^{z+} \rightarrow S^{p+} + C^{q+} + S^{r+}$ $(z = p+q+r)$, or the two-body (m, n) pathway, $CS_2^{z+} \rightarrow CS^{m+} + S^{n+}$ $(z = m + n)$. For example, the S^+ fragment ions can be formed together with the CS^+, S^+, S^{2+} and C^+ fragment ions through the two kinds of two-body pathways, (0,1) and (1,1), and through the six kinds of three-body pathways, i.e., (1,0,0), (1,0,1), (1,1,0), (1,1,1), (1,1,2). Consequently, the ion image of S^+ at the detector in Fig. 1.5a is recorded as a superposition of the images of these fragmentation pathways. Using coincidence momentum imaging, the S^+ ions produced through three different pathways:

$$CS_2^{2+} \rightarrow CS^+ + S^+, (1,1) \tag{1.4}$$

$$CS_2^{3+} \rightarrow S^+ + C^+ + S^+, (1,1,1) \tag{1.5}$$

$$CS_2^{4+} \rightarrow S^+ + C^+ + S^{2+}, (1,1,2) \tag{1.6}$$
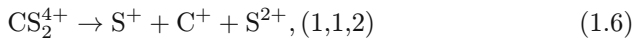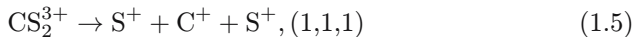
are extracted securely, as shown in Fig. 1.5b–d. The isotropic pattern observed in the central region in Fig. 1.5a is attributed to the non-Coulomb explosion type pathways, (0,1), (1,0,0), (1,0,1) and (1,1,0).

The coincidence ion images obtained exhibit a pair of crescent-like patterns, as shown in Fig. 1.5b–d. Greater momentum separation is observed when the parent ions have greater charge numbers, reflecting the release of more Coulombic energy. Since the momenta of all of the fragment ions, $\{\boldsymbol{p}_i\}$, are obtained in a straightforward manner from the coincidence measurements,
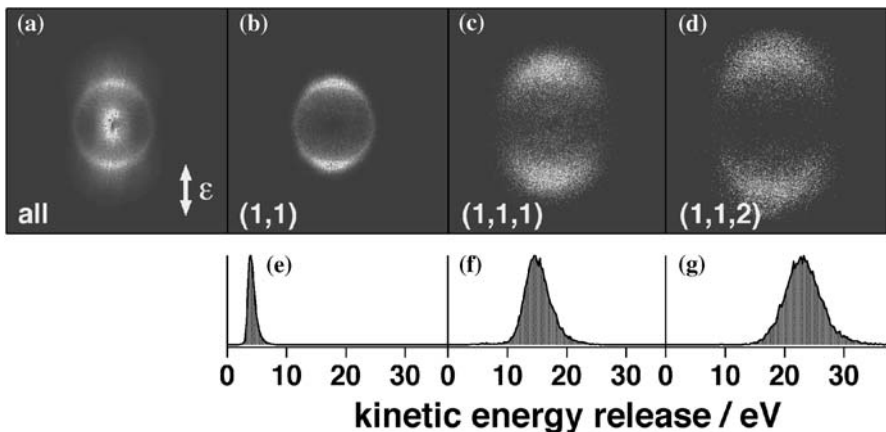
Fig. 1.5. Ion image of S^+ (**a**) produced from CS_2 in an intense laser field $(0.36\,\text{PW/cm}^2)$, recorded with a position-sensitive detector (PSD). The small hole in the central part of the accumulated image is ascribable to the degraded sensitivity of the central part of the detector. The coincidence ion images of S^+ (**b–d**), and the corresponding kinetic energy release distributions (**e–f**) obtained for the (1,1), (1,1,1) and (1,1,2) Coulomb explosion pathways, respectively

the total kinetic energy E_{kin} released in the Coulomb explosion process can be calculated as $E_{\text{kin}} = \sum |\boldsymbol{p}_i|^2/(2m_i)$, where m_i is the mass of the i-th fragment ion. The distributions of total kinetic energies obtained for the (1,1), (1,1,1) and (1,1,2) pathways are shown in Fig. 1.5e–g. The kinetic energy distribution of the (1,1) pathway exhibits a peak at $E_{\text{kin}} = 4.1(1)\,\text{eV}$, with a longer tail on the higher energy side, while the distribution peaks are observed at $E_{\text{kin}} = 14.8(5)$ and $22.8(7)\,\text{eV}$ for the (1,1,1) and (1,1,2) pathways, respectively.

1.3.2 Sequential Versus Concerted Bond-Breaking of the Two C–S Bonds in CS_2

For a three-body Coulomb explosion event, the total number of momentum components determined is nine (three for each fragment ion) in the laboratory frame. However, the number of independent momentum parameters required to describe the Coulomb explosion event in the molecular frame is reduced to three under conditions of conserved momentum. This is because three degrees of freedom in the momentum vector space are reserved to describe the translational momentum vector of the center of mass, and another three are used for the overall rotation of the system that describes the conversion from the laboratory frame to the molecular frame. In other words, the nuclear dynamics of a single Coulomb explosion event of CS_2^{3+}, $CS_2^{3+} \rightarrow S^+ + C^+ + S^+$ in the molecular frame can be fully described in the three-dimensional momentum space specified by a set of three independent momentum parameters. There

are several ways to choose this set of three momentum parameters [24]. For example, the length of the momentum vector of each of the three fragment ions may be adopted to form a set of three parameters, (p_1, p_2, p_3), where $p_1 = |\boldsymbol{p}_1(S^+)|$, $p_2 = |\boldsymbol{p}_2(S^+)|$ and $p_3 = |\boldsymbol{p}_3(C^+)|$. Alternatively, as shown in Fig. 1.6, (p_1, p_2, θ_{12}) can be adopted, where θ_{12} is the angle between the two momentum vectors, $\boldsymbol{p}_1(S^+)$ and $\boldsymbol{p}_2(S^+)$.

The three-dimensional momentum map observed exhibits a pair of wings extending from the dense distribution in the central area of the map towards the smaller p_1 (or p_2) and larger θ_{12} values. The origin of these two wings becomes clear when the three-dimensional distribution is projected onto the bottom plane spanned by the p_1 and p_2 coordinates. In this p_1–p_2 momentum plane, these wings are transformed into a pair of straight distributions running parallel to the p_1 and p_2 axes, as shown in Fig. 1.6. This is the signature of the sequential three-body explosion process, in which the fission of the two C–S bonds proceeds in a stepwise manner via the formation of metastable CS^{2+}, i.e., $CS_2^{3+} \rightarrow S^+ + CS^{2+} \rightarrow S^+ + C^+ + S^+$ [24]. The distribution parallel to the p_2 axis, for example, means that the momentum value of $p_1 \sim 170 \times 10^3$ amu m/s is realized independent of p_2; that is, one of the S^+ ions is ejected independently of the ejection process of the other S^+. Such a situation is realized when the three-body Coulomb explosion proceeds in a sequential manner and the second bond fission, $CS^{2+} \rightarrow C^+ + S^+$, occurs after S^+ and CS^{2+} are well-separated from each other.
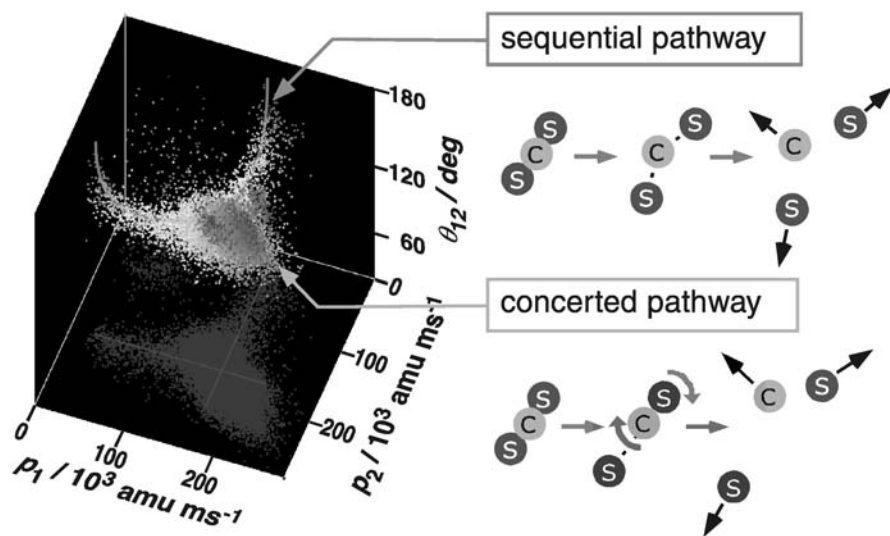
Fig. 1.6. Three-dimensional coincidence momentum imaging map obtained for the three-body Coulomb explosion of CS_2, $CS_2^{3+} \rightarrow S^+ + C^+ + S^+$, in an intense laser field ($0.2\,\text{PW/cm}^2$), expressed in the p_1–p_2–θ_{12} coordinate system. Each *dot on the map* represents a single event of Coulomb explosion

In fact, these wing-like features are well-reproduced (as shown in Fig. 1.6) by a simple free-rotor model [24], in which the metastable CS^{2+} is assumed to rotate freely with no interaction with the counterpart S^+ ion. In the simulation, the momentum vector p_{first} imposed on the S^+ and CS^{2+} fragments in the first step ($CS_2^{3+} \rightarrow S^+ + CS^{2+}$) and p_{second} to the C^+ and S^+ fragments in the second step ($CS^{2+} \rightarrow S^+ + C^+$) are treated as adjustable parameters.

The two wings observed in the three-dimensional map (Fig. 1.6) are transformed into a pair of curved arms in the two-dimensional momentum map in the $\Delta p_{12} - \theta_{12}$ plane, as shown in Fig. 1.7a, where Δp_{12} represents the difference between the momentum values of the two S^+ ions, i.e., $\Delta p_{12} = p_1 - p_2$. As shown in the two-dimensional momentum map drawn on a logarithmic intensity scale, the observed curved arms are well-reproduced by the classical free-rotor model.

The curved arm-like features are barely visible in the $\Delta p_{12} - \theta_{12}$ map plotted on a linear scale (Fig. 1.8a). This is because the number of the corresponding events shows that this sequential process forms only 17% of all the three-body explosion events. The other coincidence events forming the dense distribution in the central part correspond to the concerted or nonsequen-
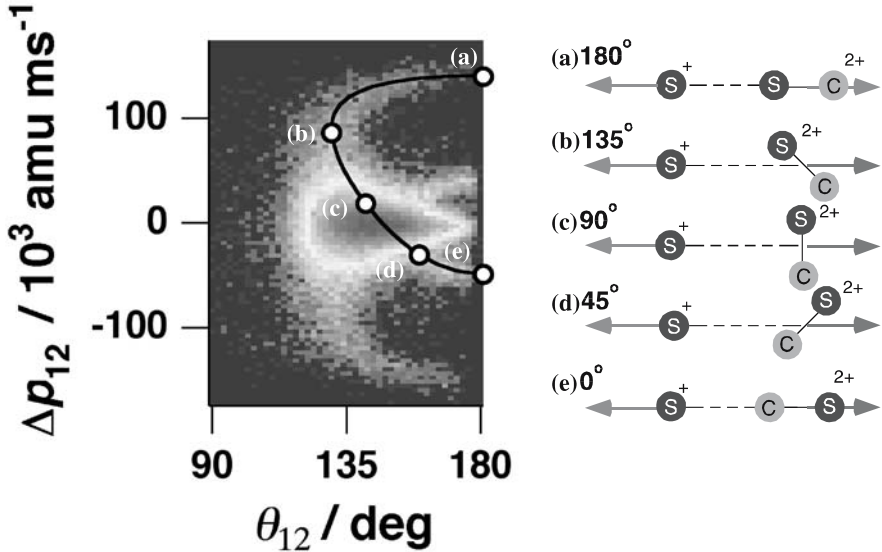
Fig. 1.7. Two-dimensional Δp_{12}–θ_{12} correlation map for the three-body Coulomb explosion of CS_2^{3+} at a field intensity of $0.2\,PW/cm^2$. A logarithmic intensity scale is used to emphasize weak features. The *solid curve* represents the trajectory obtained from classical mechanical calculations for the sequential explosion pathway. The *open circles* represent the values for five rotational angles, $\varphi = 0°, 45°, 90°, 135°$ and $180°$ of the metastable CS^{2+} moiety in the body fixed frame [24]
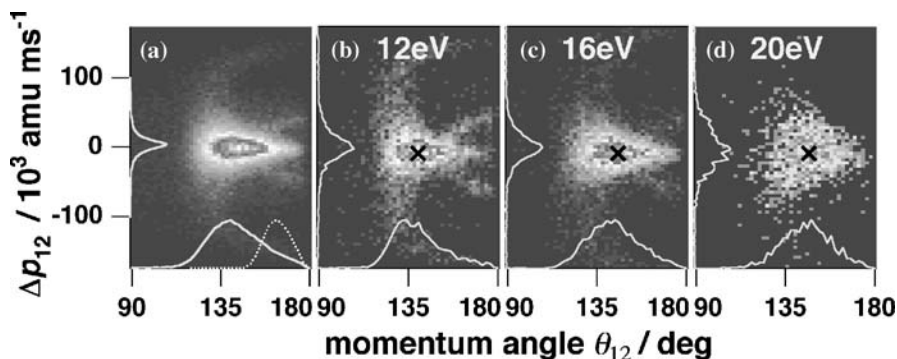
Fig. 1.8. The Δp_{12}–θ_{12} momentum correlation map for the (1,1,1) pathway of CS_2 at a field intensity of $0.2\,PW/cm^2$, obtained for **a** all of the coincidence events, **b** $E_{kin} = 20\pm1.5\,eV$, **c** $16\pm0.5\,eV$, and **d** $12.5\pm1.5\,eV$. *Solid curves* drawn along the vertical and horizontal axes in each map represent the projections of the 2D distribution onto the Δp_{12} and θ_{12} axes, respectively. The θ_{12} distribution expected from the geometry of the neutral CS_2 is shown with a *dotted line* in **a**

tial explosion process leading to the simultaneous breaking of the two C–S bonds, $CS_2^{3+} \rightarrow (S\cdots C\cdots S)^{3+} \rightarrow S^+ + C^+ + S^+$. The nuclear dynamics of a molecule in the intense laser field can be understood through the correlation between the fragment momentum vectors of the fragment ions, since the ejection of the two S^+ ions through the concerted process is determined by the nuclear dynamics in the molecular region where the bending and the two C–S stretching modes are coupled with each other.

1.3.3 From Momentum Correlation to Nuclear Dynamics

It is known that the PES of the lowest electronic state $^4\Pi_u$ of CS_2^{3+} is mostly dissociative due to the Coulombic repulsive force acting between the three atoms, with a shallow bound part in the molecular region. The energy of the metastable CS_2^{3+} trapped at the bottom of the bound well with respect to the $S^+ + C^+ + S^+$ dissociation limit is estimated to be $E_0 = 21.1\,eV$ [23]. It is found from our measurements that the total kinetic energy release, E_{kin}, is distributed in the energy region below E_0, as shown in Fig. 1.5f. This means that the triply charged CS_2^{3+} ions are prepared in the stretched geometrical configuration, in which both of the C–S bonds are greatly elongated prior to the bond fission process proceeding on the Coulombic repulsive part of the PES. It can be said that the nuclear dynamics that occur on the light-dressed PES of CS_2^{z+} in the lower charge states ($z = 0$–2) are projected onto the repulsive part of the PES of CS_2^{3+}; the momentum vectors of the fragment ions are then determined by the downhill process.

The observed distributions of the momentum parameters θ_{12} and Δp_{12} in Fig. 1.8a show the existence of two different types of the momentum cor-

relation between $\boldsymbol{p}_1$ and $\boldsymbol{p}_2$, reflecting the characteristic nuclear dynamics of CS_2 in the intense laser field. First, the momentum angle θ_{12}, representing the relative directions of the ejection of the two S^+ ions, exhibits a broad distribution ranging from $\theta_{12} = 110°$ to $180°$ with the maximum at $\theta_{12} \sim 140°$. Since the equilibrium geometrical structure of neutral CS_2 in the electronic ground state, $\tilde{X}^1\Sigma_g^+$, is linear, the small momentum angle observed indicates that the bending motion is largely induced within the ultrashort duration (60 fs) of the pulsed intense laser field.

Second, the momentum difference Δp_{12} has a sharp peak at $\Delta p_{12} = 0\,\mathrm{amu\,m/s}$, with a full-width-at-half-maximum of $19 \times 10^3\,\mathrm{amu\,m/s}$, showing that the two S^+ ions tend to be produced with almost equal momentum values, i.e., $|\boldsymbol{p}_1| \sim |\boldsymbol{p}_2|$. This finding suggests that the structural deformation of CS_2 in the intense laser field preferentially proceeds along the symmetric stretching coordinate rather than along the antisymmetric coordinate.

The three-body Coulomb explosion process of a triatomic molecule has also been observed when multiple ionization is achieved through collisional ionization processes with highly charged atomic ions or by charge stripping processes through thin carbon foil. In such cases, the momentum vector distribution of the resultant fragment ions may directly reflect the geometrical structure of the target molecule in the initial ground electronic state [25]. In fact, the distribution of the momentum angle θ_{12} of the fragment S ions from CS_2^{3+} formed by collisional ionization with Ar^{8+} [26] was explained well by the projection of the zero-point vibrational function of the neutral CS_2 onto the purely Coulombic potential of CS_2^{3+}, which gives a distribution peak at $\theta_{12} = 164°$, as represented by the dotted curve in Fig. 1.8a.

1.3.4 Deformation of the Molecular Structure in Intense Laser Fields

In order to discuss the nuclear dynamics of CS_2 in an intense laser field more quantitatively, it is necessary to specify all three momentum parameters that provide a full description of the three-body Coulomb explosion process. A series of Δp_{12}–θ_{12} maps are plotted for the three different total kinetic energies, $E_{\mathrm{kin}} = 12.5$, 16, and 20 eV (see Fig. 1.5) in Fig. 1.8b–d, where each point in each map represents a set of the three momentum parameters, (θ_{12}, Δp_{12}, E_{kin}).

It is clearly seen that the peak position in the θ_{12} distribution shifts from $\theta_{12} = 148°$ to $132°$ as E_{kin} decreases from 20 eV to 12.5 eV, though the peak position in the Δp_{12} distribution stays at $\Delta p_{12} = 0$ independent of the energy. Since the Coulomb explosion process occurring at the larger C–S bond length results in a smaller kinetic energy of the fragment ions, the observed energy dependence of θ_{12} shows that the structural deformation from linear to bent along the bending coordinate proceeds largely simultaneously with the stretching of the two C–S bonds.

This correlation can be described in terms of the geometrical structure of CS_2^{3+} just before the Coulomb explosion, which is defined as the geometrical structure that reproduces the observed momentum vectors of the three fragment ions when the internuclear potentials are assumed to be purely Coulombic. The geometrical structures of CS_2^{3+} determined from the distribution peaks (marked by a cross) in the three $\Delta p_{12} - \theta_{12}$ plots in Fig. 1.8b–d show that the S–C–S bond angle becomes smaller (dropping from $162°$ to $140°$) as the two C–S bonds stretch simultaneously from 1.8 Å to 3.0 Å [23].

According to recent theoretical studies [27, 28] of an isovalent molecule, CO_2, in an intense laser field, the light-dressed PES of CO_2^{2+} at a field intensity of 0.2 PW/cm^2 is largely deformed by the light fields due to mixing between a large number of the electronic states, and that it becomes shallower along the bending coordinate as the C–O bond length increases. This means that the nuclear wavepacket prepared on this light-dressed PES after the ejection of two electrons spreads along the bending coordinate as well as along the symmetric stretch of the two C–O bonds, which is consistent with the experimental results on CS_2 described here.

Another characteristic feature identified in the momentum maps in Fig. 1.8b–d is that the width of the Δp_{12} distribution becomes narrower as E_{kin} decreases from 20 eV to 12.5 eV. Since the decrease in E_{kin} corresponds to the stretching of the C–S bonds, the narrower distribution is also explained in terms of the evolution of the nuclear wavepacket on the light-dressed PES. That is, the longer the molecule explores the PES in the intense laser field before the formation of CS_2^{3+}, the greater the tendency towards simultaneous stretching of the two C–S distances. This interesting feature is discussed in more detail in the next section, by the real-time probing of the nuclear wavepacket evolution.

1.4 Pump-and-Probe Coincidence Momentum Imaging: Evolution of Nuclear Wavepacket in CS_2^{2+}

It has been shown theoretically [27] that the structural deformation of CO_2 most likely occurs at the doubly charged state, CO_2^{2+}, because no significant potential deformation is identified at CO_2 and CO_2^+, even when the laser field intensity within an ultrashort laser pulse becomes sufficiently large for further ionization into CO_2^+ and CO_2^{2+}, respectively. Since the adiabatic ionization potential of CS_2^{2+} to form CS_2^{3+} (~ 27 eV) is substantially larger than those of $CS_2 \rightarrow CS_2^+ + e$ (10 eV) and $CS_2^+ \rightarrow CS_2^{2+} + e$ (17 eV), the observed structural deformation in the intense laser field is considered to reflect the nuclear dynamics at the doubly charged state, CS_2^{2+}, in the same manner as predicted by the theoretical calculation on the isovalent CO_2.

When a circularly polarized probe pulse is introduced at a time delay of Δt after the pump laser pulse, new features with a pair of straight distributions running parallel to the horizontal and vertical axes emerge [29], as

shown in Fig. 1.9b–d near the original straight arms in the p_1–p_2 momentum correlation maps (Fig. 1.9a), and shift gradually toward the lower momentum side as Δt increases. These new features are again reproduced well with the classical free rotor model mentioned above [24], showing that they originate from the sequential three-body explosion process of CS_2^{3+}. It is found that the p_{first} momentum value decreases gradually as a function of Δt, reflecting the fact that the potential slope of CS_2^{3+} along the antisymmetric stretch coordinate is steeper than that of CS_2^{2+}. At large Δt, p_{first} reaches to an asymptote of 130×10^3 amu m/s, which is in good agreement with the peak value (127×10^3 amu m/s) of the momentum distribution obtained for the two-body Coulomb explosion of CS_2, $CS_2^{2+} \rightarrow S^+ + CS^+$, recorded only with the pump pulse. This agreement shows that the probe pulse traces the nuclear dynamics of the two-body Coulomb explosion into $S^+ + CS^+$ induced by the pump pulse, and that CS^+ is ionized by the probe pulse to form a metastable state of CS^{2+} with a dissociation lifetime that is sufficiently longer than the rotational period. The gradual decrease in the p_{second} momentum value indicates that the C–S bond stretches in the CS^+ moiety as the distance from S^+ becomes longer as the first step of the dissociation proceeds: $CS_2^{2+} \rightarrow S^+ + CS^+$.

In Fig. 1.9, another feature varying sensitively with Δt is identified: the dense distribution along the diagonal line in the p_1–p_2 map (marked with a broken circle). The peak centered at around 160×10^3 amu m/s at $\Delta t = 300$ fs moves along the diagonal $p_1 = p_2$ line to $\sim 110 \times 10^3$ amu m/s at $\Delta t = 1$ ps. This component is attributed to the nuclear wavepacket moving towards the symmetric stretching coordinate on the potential energy surface of CS_2^{2+}, which leads to the simultaneous breaking of the two C–S bonds. Based on the distribution function of the angle parameter χ, defined as the angle between the momentum vectors, $\boldsymbol{p}_1(S^+) - \boldsymbol{p}_2(S^+)$ and $\boldsymbol{p}_3(C^+)$ [24], it was found that about 40% of the CS_2^{2+} formed in the intense laser field undergoes dissociation along the concerted three-body dissociation pathway, while the rest ($\sim$60%) dissociates through the two-body Coulomb pathway.

The ground $X^3\Sigma_g^-$ state of CS_2^{2+} has a quasi-bound well separated by a potential barrier from a Coulomb-type repulsive potential along the dissociation coordinates into both $CS^+(X^2\Sigma^+) + S^+(^4S)$ and $S^+(^4S) + C(^3P) + S^+(^4S)$. According to an ab initio molecular orbital calculation [30] the height of the barrier along the two-body explosion pathway is 1.9 eV measured from the bottom of the quasi-bound well, while the dissociation energy to the three-body pathway is substantially higher (5.6 eV) [29]. Thus, the large yield of the concerted pathway observed shows that the nuclear motion in the intense laser field does not necessarily follow the minimum energy path and can be regarded as a characteristic feature in an intense laser field, where the shape of the light-dressed potentials is significantly deformed. In fact, the wavepacket calculation on the light-dressed PES [28] showed that in an intense laser field CO_2^{2+} undergoes three-body dissociation along the
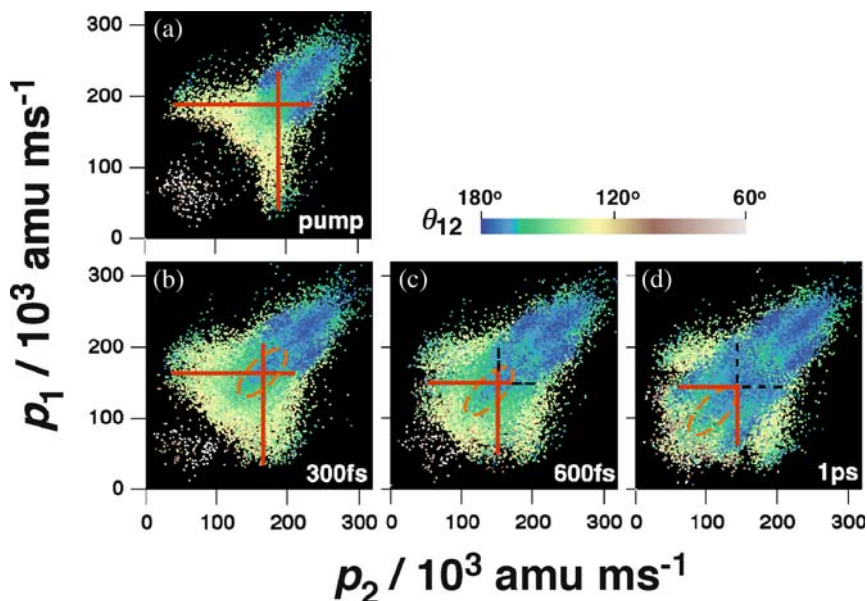
Fig. 1.9a–d. The p_1–p_2 correlation maps obtained with a pump pulse only (**a**), and with $\Delta t = 300$ fs (**b**), 600 fs (**c**) and 1 ps (**d**). *Red solid lines* indicate results from the free-rotor simulation for the sequential process via the formation of metastable CS^{2+}. The component corresponding to the nuclear wavepacket of CS_2^{2+} dissociating towards the symmetric stretching coordinate is visible along the diagonal $p_1 = p_2$ line (*orange broken circle*)

symmetric stretching coordinate ($\sim$85%) rather than two-body dissociation along the antisymmetric coordinate ($\sim$15%). This indicates that the simultaneous breaking of the two C–O bonds is preferred to the breaking of either one of the two C–O bonds.

The temporal evolution of the nuclear motion along the symmetric stretching coordinate is more clearly seen in Fig. 1.10, where the total kinetic energy released into all three fragment ions, E_{kin}, during the events of symmetric bond breaking satisfies $|p_1-p_2| \leq 20 \times 10^3$ amu m/s. In addition to the strong peak at 17 eV, corresponding to Coulomb explosion by either the pump pulse or the probe pulse, a new component emerges in the lower energy range below $\sim$12 eV. The low-energy component shifts to lower energy as Δt increases and converges at $\Delta t = 1$ ps. The convergence of the E_{kin} distribution shows that the three-body dissociation in CS_2^{2+} reaches the asymptotic limit by $\Delta t = 1$ ps, so that no additional kinetic energy is imposed by ionization to the triply charged state. In other words, the asymptotic distribution of the lower energy component at $\Delta t \geq 1$ ps represents the kinetic energy distribution for the three-body dissociation of CS_2^{2+}.

At $\Delta t \geq 1$ ps, a series of small peaks separated by $\sim$1.4 eV become apparent on the broad E_{kin} distribution below 12 eV, which may represent the com-
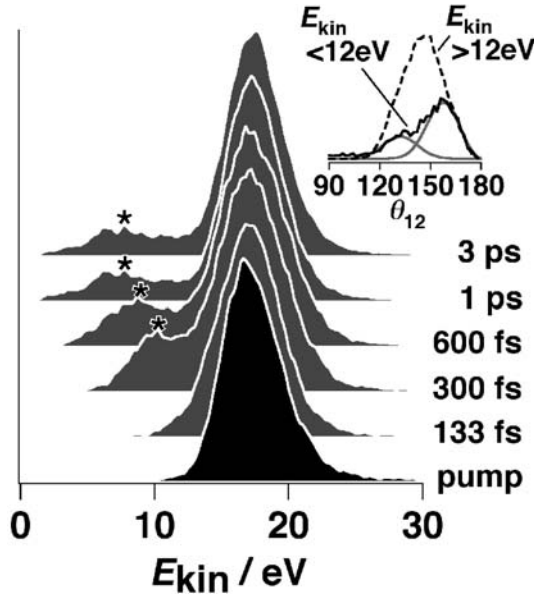
Fig. 1.10. Time evolution of the total kinetic energy distribution of $CS_2^{3+} \rightarrow S^+ + C^+ + S^+$ for the symmetric events ($|p_1-p_2| < 20 \times 10^3$ amu m/s). The *inset* shows the θ_{12} distribution for the symmetric events at $\Delta t = 1$ ps for $E_{kin} > 12$ eV (*dotted line*) and $E_{kin} < 12$ eV (*solid line*)

ponents that appear after coupling with different numbers of photons, as observed for H_2^+ [1,2]. It seems that the most prominent peak at $E_{kin} = 10.2$ eV for $\Delta t = 300$ fs evolves smoothly to the peak at $E_{kin} = 8.8$ eV for $\Delta t = 600$ fs and then to that at $E_{kin} = 7.8$ eV for $\Delta t = 1$ ps. The C–S distances at different time delays Δt can be estimated from the increase in the kinetic energy ΔE_{kin} from the asymptotic value ($E_{kin} = 7.8$ eV), since ΔE_{kin} is given as $\Delta E_{kin} = \Delta V_3(R) - \Delta V_2(R)$, where $\Delta V_2(R)$ and $\Delta V_3(R)$ represent the differences in the potential energies at the distances R and $R = \infty$ for CS_2^{2+} and CS_2^{3+}, respectively. When Coulomb potentials are assumed for CS_2^{3+} and for CS_2^{2+} dissociating into $S^+ + C + S^+$ at large internuclear distances, the internuclear distances are $R = 12$ and 29 Å at $\Delta t = 300$ and 600 fs, respectively, for linear geometrical structures [29].

Since the angle between the momentum vectors of the two S^+ ions has a straightforward correspondence with the ∠S–C–S bent angle [23], the information on the structural deformation along the bending coordinate in CS_2^{2+} can be extracted from the distribution of the momentum angle θ_{12}. The inset in Fig. 1.10 shows the θ_{12} distribution obtained for $\Delta t = 1$ ps, when the three-body dissociation in CS_2^{2+} reaches its asymptote. For $E_{kin} > 12$ eV, that is, when the explosion process proceeds either by the pump pulse or by the probe pulse, the θ_{12} distribution (dotted line) peaks at $\theta_{12} \sim 140°$, covering the broad range of $\theta_{12} = 100° \sim 180°$ (see Sect. 1.3.4). On the other

hand, when all the events with $E_{kin} < 12\,eV$ are collected, that only appear when both pump and probe pulses are introduced, the θ_{12} distribution (solid line) exhibits two different components peaked at $\theta_{12} = 158°$ and $135°$. The angle $\theta_{12} = 158°$ is close to the angle $\theta_{12} = 164°$ expected when neutral CS_2 in the ground $X^1\Sigma_g^+$ state is projected onto the purely Coulombic potential of CS_2^{3+} [23]. Therefore, the component at $\theta_{12} = 158°$ is considered to represent the contribution from a quasi-linear geometrical configuration. This means that these two components peaked at $\theta_{12} = 158°$ and $135°$ represent, respectively, the contributions to the bending process from the two different electronic states with linear and bent-type geometries in the nuclear dynamics of CS_2^{2+} in the intense laser field. This is consistent with theoretical results on CO_2^{2+} showing that the nonadiabatic transition between the linear and bent light-dressed states induces bending motion [28]. According to the ab initio calculation of CS_2^{2+} [30], the lowest excited $^3\Delta_u$ state is located $2.78\,eV$ above the ground $X^3\Sigma_g^-$ state in the linear geometry. The lower component of the Renner–Teller pair for the $^3\Delta_u$ state may be the electronic state that contributes to the bending process [28].

1.5 Hydrogen Migration in Acetonitrile in Intense Laser Fields

When hydrocarbon molecules are exposed to intense laser fields, hydrogen atom migration proceeds at the same time as the skeletal structural deformation. In order to investigate how this rapid migration of hydrogen atoms from one site to another is induced by intense laser fields, we have applied, for the first time, coincidence momentum imaging to the Coulomb explosion processes of hydrocarbon molecules; that is, two-body Coulomb explosion of acetonitrile, CH_3CN, in intense laser fields [31, 32]. Since all three hydrogen atoms initially belong to the terminal carbon atom, their migration to the CN moiety can be readily identified by detecting HCN^+ or H_2CN^+ fragment ions.

At a field intensity of $0.15\,PW/cm^2$, three different two-body Coulomb explosion pathways,

$$CH_3CN^{2+} \rightarrow CH_{3-n}^+ + H_nCN^+ (n = \text{0-2}) \,, \qquad (1.7)$$

are identified: the direct C–C bond-breaking without the migration of a hydrogen atom ($n = 0$) and C–C bond-breaking after single ($n = 1$) and double ($n = 2$) hydrogen migration. The coincidence ion images for the $n = 0$ pathway exhibit a pair of clear crescent-like features, showing that most of the fragment ions tend to be ejected along the direction of laser polarization. On the other hand, the anisotropy in the $n = 1$ pathway is less pronounced, and an almost isotropic distribution is observed for the $n = 2$ pathway.

The relative yields of the respective explosion pathways can be derived from the number of coincidence events. For CH_3CN, the relative yields for the $n = 1$ and 2 pathways with respect to the $n = 0$ pathway are 1.3(1) and 1.0(1), respectively. The comparable yields for the three explosion pathways show that the migration of hydrogen atoms competes with the two-body Coulomb explosion of acetonitrile in the intense laser field $(0.15\,PW/cm^2)$.

In the CMI measurements, the momentum distribution of the fragment ions is determined in three-dimensional momentum space, so that their angular distribution, $I(\theta)$, with respect to the laser polarization direction can be derived in a straightforward manner without the need for a complicated mathematical procedure such as an inverse Abel transformation. The angular distribution can be derived from a thin slice of the three-dimensional momentum distribution at $p_z \sim 0$, as shown in Fig. 1.11 for the three explosion pathways $(n = 0–2)$ of CH_3CN.

It can be seen in these figures that the fragment ions tend to be ejected more isotropically as the hydrogen migration from the terminal carbon to the nitrile group proceeds. The extent of the anisotropy in the explosion pathways can be evaluated quantitatively from the expectation value of the squared cosine, $\langle \cos^2 \theta \rangle = \int I(\theta) \cos^2 \theta \sin \theta d\theta / \int I(\theta) \sin \theta d\theta$. For the $n = 0$ pathway
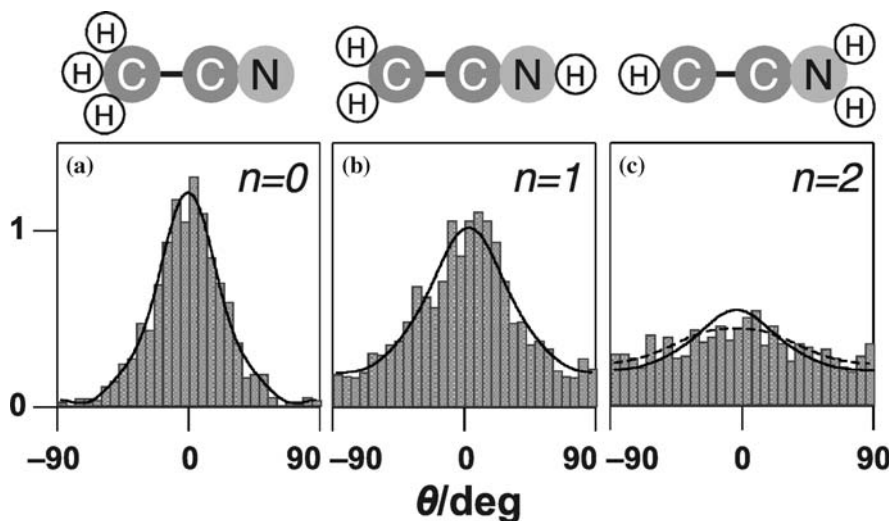
Fig. 1.11. Angular distributions of the fragment ions for the two-body Coulomb explosion of CH_3CN^{2+} through the **a** $n = 0$, **b** $n = 1$, **c** $n = 2$ pathways derived from a thin slice ($\delta p_z = \pm 16 \times 10^3$ amu m/s) of the momentum vector distribution at $p_z \sim 0$. The results from the least-squares fit [32] in which the effect of molecular rotation is taken into account are shown for comparison (*solid lines*). The fit was improved for the $n = 2$ pathways (**c**) when the effect of fragment ejection along the tilted direction with respect to the molecular axis is included (*dashed lines*)

$\langle \cos^2 \theta \rangle = 0.68$, while the angular distribution becomes more isotropic as n increases, i.e., $\langle \cos^2 \theta \rangle = 0.49$ and 0.37 for $n = 1$ and 2, respectively.

Information on both the distribution of the principal molecular axes of doubly charged acetonitrile ions prepared by the polarized laser field and their lifetimes are encoded in the fragment anisotropy observed. As the lifetime becomes longer, the angular distribution of the fragment ions tends to become more isotropic due to the overall rotational motion of the parent molecular ions. It should also be noted that the extent of fragment anisotropy can decrease depending on the direction of the fragment recoil in the molecular frame. This is because, unlike diatomic molecules, the recoil direction of the fragment ions from a polyatomic molecule does not always correspond to the principal molecular axis.

The angular distribution of the fragment ion was analyzed using a least-squares fit to an analytical model in which the following three factors are incorporated: (i) the distribution of the principal molecular axis, (ii) the lifetime of the parent ion, and (iii) the direction of fragment recoil in the molecular frame. In the analysis, it was assumed that the explosion for the $n = 0$ pathway occurs immediately after the formation of the doubly charged acetonitrile, and that the fragments are ejected exclusively along the molecular axis. This means that the sharp angular distribution observed for the $n = 0$ pathway represents the angular distribution of the molecular axis of the parent molecules in the laboratory frame. Under this assumption the angular distributions for the $n = 1$ pathway observed for CH_3CN are well-reproduced when $\tau\omega = 0.78(1)$, as shown in Fig. 1.11, where τ and ω $(= 2\pi/\tau_{rot})$ represent, respectively, the dissociation lifetime of a molecule and its rotational frequency. The rotational period of CH_3CN, $\tau_{rot} = [2B_0(\langle J \rangle + 1)]^{-1}$, is calculated to be $\tau_{rot} = 2.4\,ps$ at room temperature $(300\,K)$ using the rotational constants of the ground vibrational state of B_0 $(CH_3CN) = 0.3068422247\,cm^{-1}$ [33] and the expectation value of the rotational quantum number J, $\langle J \rangle = 22.5$. From the values of $\tau\omega$ and τ_{rot}, the dissociation lifetime for the $n = 1$ pathway is calculated to be $\tau = 2\pi/\omega = 0.30\,ps$.

On the other hand, for the $n = 2$ pathway, it was found that the observed angular distributions shown in Fig. 1.11c could not be described well by the simple model introduced above; even the broadest distribution achieved by the model realized at the limit of $\tau\omega \gg 1$ was found to be substantially narrower than the distributions actually observed, suggesting that the structural deformation of the C–C–N skeleton causes an off-axis ejection of the fragments at a nonzero angle θ_m^0 $(\neq 0)$ in the molecular frame. When both $\tau\omega$ and θ_m^0 were adopted as variable parameters, the observed distributions were well-fitted by $\tau\omega > 10$ and $\theta_m^0 = 29(4)°$. From the lower limit values for $\tau\omega$, $\tau > 3.8\,ps$ was obtained for CH_3CN. This large offset angle, θ_m^0, suggests that substantial skeletal structural deformation occurs for the $n = 2$ pathway associated with hydrogen migration at the doubly charged stage. Since an off-axis ejection of fragments is also expected to occur for the $n = 1$ pathway,

the dissociation lifetime determined above for $n = 1$ may be regarded as the lower limit value.

As described above, the three two-body pathways ($n = 0, 1, 2$) have comparable yields. The relative yields for the $n = 1$ and 2 pathways with respect to the $n = 0$ pathway, $\Phi_1 = 1.3(1)$ and $\Phi_2 = 1.0(1)$, respectively, may reflect the ratio of the number of doubly charged parent molecules prepared in the three different states from which dissociation proceeds along the $n = 0, 1, 2$ pathways, respectively. Alternatively, the branching ratios may reflect the competition between hydrogen migration and Coulomb explosion, which occur after the doubly charged parent molecules are prepared in the common state. In the latter case, the migration of the first hydrogen atom from the methyl group to the nitrile group is considered to proceed about twice as fast as the direct Coulomb explosion process in the $n = 0$ pathway, which accounts for the sum of the relative yields, $\Phi_1 + \Phi_2 = 2.3$, for the $n = 1$ and 2 explosion pathways occurring after hydrogen migration. The branching ratio, $\Phi_1/\Phi_2 = 1.3$, may suggest that the migration of the second hydrogen atom proceeds on a timescale comparable with or slightly shorter than the dissociation lifetime of the $n = 1$ pathway, $\tau \sim 0.30\,\mathrm{ps}$.

The migration of hydrogen atoms from the methyl group to the nitrile group and C–C–N skeletal deformation may also occur in the singly charged stage of acetonitrile prior to the formation of the doubly charged acetonitrile if these processes are able to proceed within the timescale of the laser pulse duration. The contributions from these processes in the singly charged stage to the fragment anisotropy could be investigated by a pump-and-probe scheme with a probe laser whose pulse duration is much shorter than the pump laser pulse.

1.6 Summary and Outlook

When molecules are exposed to intense laser fields, they exhibit characteristic dynamical processes that are not observed in weak light fields in the perturbative regime. Rich information on ultrafast skeletal structural deformation, concerted bond-breaking, sequential bond-breaking, and hydrogen atom migration, has been extracted from momentum maps in a straightforward manner. The introduction of the coincidence momentum imaging (CMI) method afforded us a deeper understanding of the dynamics of these processes based on the correlations among the momentum vectors of the fragment ions.

As demonstrated for CS_2, the pump-and-probe technique with CMI is a promising tool for investigating how a nuclear wavepacket evolves in real time. Considering that few-cycle laser pulses are now becoming available, we are now entering into a new era when it will be possible to "see" molecules in intense laser fields in real time with highest temporal resolution [34,35].

References

1. K. Codling and L.J. Frasinski: J. Phys. B **26**, 783 (1993).
2. B. Sheehy and L.F. DiMauro: Annu. Rev. Phys. Chem. **47**, 463 (1996).
3. P.B. Corkum, C. Ellert, M. Mehendale, P. Dietrich, S. Hankin, S. Aseyev, D. Rayner and D. Villeneuve: Farad. Discuss. **113**, 47 (1999).
4. K. Yamanouchi: Science **295**, 1659 (2002).
5. J.H. Posthumus: Rep. Prog. Phys. **67**, 623 (2004).
6. P.H. Bucksbaum, A. Zavriyev, H.G. Muller and D.W. Schumacher: Phys. Rev. Lett. **64**, 1883 (1990).
7. A. Giusti-Suzor, F.H. Mies, L.F. DiMauro, E. Charron and B. Yang: J. Phys. B **28**, 309 (1995).
8. K. Sandig, H. Figger and T.W. Hansch: Phys. Rev. Lett. **85**, 4876 (2000).
9. A. Hishikawa, A. Iwamae, K. Hoshina, M. Kono and K. Yamanouchi: Chem. Phys. Lett. **282**, 283 (1998).
10. A. Hishikawa, A. Iwamae and K. Yamanouchi: Phys. Rev. Lett. **83**, 1127 (1999).
11. A. Hishikawa, A. Iwamae and K. Yamanouchi: J. Chem. Phys. **111**, 8871 (1999).
12. S. Liu, A. Hishikawa, A. Iwamae and K. Yamanouchi, in *Advances in Multiphoton Processes and Spectroscopy*, edited by Y. Fujimura and R. J. Gordon (World Scientific, Singapore, 2001), Vol. 13, pp. 182.
13. J.H. Sanderson, A. El-Zein, W.A. Bryan, W.R. Newell, A.J. Langley and P.F. Taday: Phys. Rev. A **59**, R2567 (1999).
14. J.H. Sanderson, T.R.J. Goodworth, A. El-Zein, W.A. Bryan, W.R. Newell, A.J. Langley and P.F. Taday: Phys. Rev. A **65**, 043403 (2002).
15. A. Hishikawa, A. Iwamae, K. Hoshina, M. Kono and K. Yamanouchi: Chem. Phys. **231**, 315 (1998).
16. A. Iwamae, A. Hishikawa and K. Yamanouchi: J. Phys. B **33**, 223 (2000).
17. L.J. Frasinski, K. Codling and P.A. Hatherly: Science **46**, 1029 (1989).
18. C. Cornaggia: Phys. Rev. A **54**, R2555 (1996).
19. K. Zhao, G. Zhang and W.T. Hill III: Opt. Express **9**, 42 (2001).
20. H. Hasegawa, A. Hishikawa and K. Yamanouchi: Chem. Phys. Lett. **349**, 57 (2001).
21. J. Ullrich, R. Moshammer, A. Dorn, R. Dörner, L.P.H. Schmidt and H. Schmidt-Böcking: Rep. Prog. Phys. **66**, 1463 (2003).
22. A.T.J.B. Eppink and D.H. Parker: Rev. Sci. Instrum. **68**, 3477 (1997).
23. A. Hishikawa, H. Hasegawa and K. Yamanouchi: Chem. Phys. Lett. **388**, 1 (2004).
24. A. Hishikawa, H. Hasegawa and K. Yamanouchi: Chem. Phys. Lett. **361**, 245 (2002).
25. Z. Vager: Adv. At. Mol. Opt. Phys. **45**, 203 (2001).
26. F.A. Rajgara, M. Krishnamurthy, D. Mathur, T. Nishide, T. Kitamura, H. Shiromaru, Y. Achiba and N. Kobayashi: Phys. Rev. A **64**, 032712 (2001).
27. H. Kono, S. Koseki, M. Shiota and Y. Fujimura: J. Phys. Chem. A **105**, 5627 (2001).
28. Y. Sato, H. Kono, S. Koseki and Y. Fujimura: J. Am. Chem. Soc. **125**, 8019 (2003).
29. A. Hishikawa, M. Ueyama and K. Yamanouchi: J. Chem. Phys. **122**, 151104 (2005).
30. M. Hochlaf, G. Chambaud and P. Rosmus: J. Chem. Phys. **108**, 4047 (1998).

31. A. Hishikawa, H. Hasegawa and K. Yamanouchi: Phys. Scr. **T110**, 108 (2004).
32. A. Hishikawa, H. Hasegawa and K. Yamanouchi: J. Electron Spectrosc. **141**, 195 (2004).
33. M. Koivusaari, V.-M. Horneman and R. Anttila: J. Mol. Spec. **152**, 377 (1992).
34. F. Légaré, K.F. Lee, I.V. Litvinyuk, P.W. Dooley, S.S. Wesolowski, P.R. Bunker, P. Dombi, F. Krausz, A.D. Bandrauk, D.M. Villeneuve and P.B. Corkum: Phys. Rev. Lett. **71**, 013415 (2005).
35. E. Baldit, S. Saugout and C. Cornaggia: Phys. Rev. A **71**, 021403 (2005).

2 Intact Molecular Ion Formation of Some Organic Molecules by Femtosecond Lasers

Nobuaki Nakashima and Tomoyuki Yatsuhashi

Department of Chemistry, Graduate School of Science, Osaka City University, Sugimoto, Sumiyoshi, Osaka 558-8585, Japan
nakashim@sci.osaka-cu.ac.jp and tomo@sci.osaka-cu.ac.jp

Summary. Ionization of organic molecules irradiated with intense infrared femtosecond pulses is explained from the perspective of intact molecular ion formation. Although fragmentation is more suppressed in general by femtosecond pulse excitation than pico- and nanosecond pulse excitations, molecules are still often heavily fragmented. Among the excitation parameters affecting ionization and fragmentation processes, excitation wavelengths and pulse durations at a fixed laser intensity have been found to drastically change ionization patterns. Intact molecular ions are produced when the wavelengths are non-resonant with the electronic levels of cations, whereas fragmentation proceeds to a large extent when the wave length is resonant with the electronic transitions. An ultimately short pulse presumably leads to the formation of fragment-free ions. Time-of-flight spectra of femtosecond pulse ionization of cyclohexadiene isomers, 2,3-dimethyl-1,3-butadiene, naphthalene, anthracene, and dioxin are presented. The great advantage of femtosecond laser mass spectrometry (FLMS) for the intact molecular ion formation is shown by referring briefly to the results obtained for dioxin. Some details of the experimental methods, such as a method of estimating irradiation intensity, are described.

2.1 Introduction

Intact molecular ion formation has been observed in cyclic aromatic hydrocarbons including benzene upon irradiation with a femtosecond laser using 170 fs, 0.78 μm pulses at an intensity of $3.8 \times 10^{13}\,\mathrm{W\,cm^{-2}}$ [1]. In contrast, nanosecond and picosecond pulse excitations give numerous fragments. Another representative large molecule, C_{60}, has a similar behavior. Multiply charged C_{60}^{z+} ($z = 1$–12) ions have been observed by femtosecond pulse excitation. To date, Bhardwaj et al. have reported the highest charged C_{60}, i.e., C_{60}^{12+}, which was detected with a 70 fs pulse at a central wavelength of 1.8 μm [2]. Femtosecond excitation can bypass dissociation channels and molecules can behave like atoms [1–4]. However, the formation of molecular ions is not always observed. For example, anthracene is considerably fragmentated at a wavelength of 0.8 μm [5,6].

The mechanisms of intact molecular ion formation or fragmentation in intense femtosecond fields are interesting and an important subject to be clari-

fied in complex systems. Furthermore, the molecular ion formation is of great advantage for femtosecond laser mass spectrometry (FLMS). The Ledingham group has measured the molecular ions from aromatic hydrocarbons [5] and nitro compounds [7], and the present authors have ionized some halogenated compounds and dioxins [8,9]. In this article we intend to discuss the role of the parameters that have been revealed to be significant for the formation of molecular ions. They are; besides the molecules themselves, the irradiation parameters which can be varied rather widely: intensity, wavelength, polarization, pulse width, and even focal geometry. We then outline our own results. Irradiating cyclohexadiene isomers with different cation absorption spectra, an importance of non-resonance with the cation electronic levels in molecular ion formation has been successfully demonstrated [10]. Clear wavelength effects have been observed for 2,3-dimethyl-1,3-butadiene [4] and anthracene [11] in related to resonance or non-resonance with the cation electronic levels. Electron-rescattering has been found not to enhance fragmentation using different polarised lights in the case of napthalene [12]. An example is shown that short pulse excitation is better to produce molecular ions [4,13].

The paper is organized as follows: Section 2.2 briefly reviews the effect of the laser parameters. Section 2.3 describes the experimental methods and setups used in our group. Section 2.4 outlines our results regarding isomer ionization, wavelength effects, resonance mechanism, electron recollision, and excitation pulse width dependence. Section 2.5 describes FLMS including our recent application to dioxins and femtosecond time-of-flight (TOF) mass spectra are compared with those by electron impact excitation. Finally the contents of the paper are summarized in Sect. 2.6.

2.2 Irradiation Parameters

2.2.1 Intensity

Figure 2.1 shows the ionization mechanisms for atoms in high intensity laser fields. Non-resonant multiphoton ionization (NRMPI) is expected at an irradiation intensity of around $10^{13}\,\mathrm{W\,cm^{-2}}$. Optical field ionization (OFI), which comprises tunneling ionization (TI) and barrier suppression ionization (BSI), occurs at an intensity above $10^{14}\,\mathrm{W\,cm^{-2}}$. The original Coulomb potential is distorted enough for the electron to either tunnel out through or escape over the barrier. The threshold intensity of BSI for atoms can be estimated by (2.1) [14]:

$$I_{\mathrm{BS}} = \frac{cI_{\mathrm{p}}^4}{128\pi Z^2 e^6} = 4.00 \times 10^9 \frac{I_{\mathrm{p}}^4}{Z^2}\,[\mathrm{W\,cm^{-2}}]\,, \qquad (2.1)$$

where Z is the charge number of the produced ion and I_{p} (eV) is the ionization potential. Thus I_{BS} is $2.9\times10^{13}\,\mathrm{W\,cm^{-2}}$ for $I_{\mathrm{p}} = 9.25\,\mathrm{eV}$ of benzene ionization
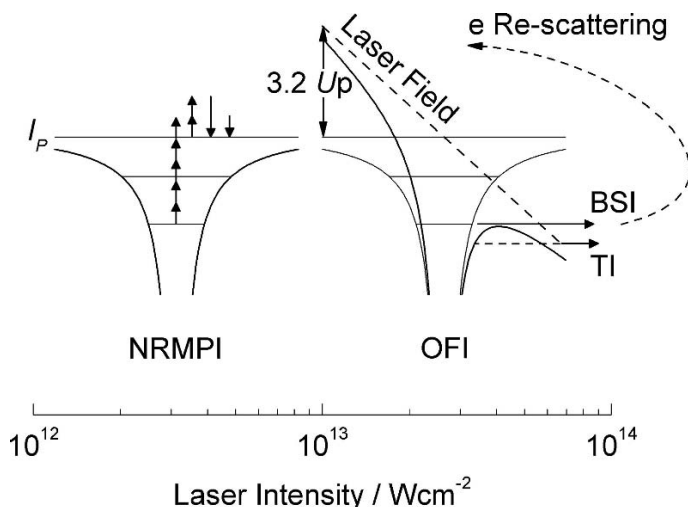
Fig. 2.1. Ionization mechanisms at different irradiation intensities are non-resonant multi-photon ionization (NRMPI); intensity $\sim 10^{13}$ W cm^{-2}, and optical field ionization (OFI), including tunnel (TI) and barrier suppression ionization (BSI); intensity $10^{13} \sim 10^{14}$ W cm^{-2}

potential and $Z = 1$. Many organic molecules have an ionization potential of 6–10 eV. Equation (2.1) is derived for atoms but it yields reasonable estimates for molecules. Also the saturation intensity for organic molecules is expected at an intensity around 10^{14} W cm^{-2}. An irradiation intensity higher than 5×10^{14} W cm^{-2} induces highly charged ions eventually leading to Coulomb explosion; in other words, fragmentation is then considerably enhanced.

2.2.2 Wavelength

Excitation wavelength effects on molecular ion formation have been observed for polyenes [15], metal CO complexes [16], C_{60} [2], and anthracene [11]. The different fragmentation patterns were observed at different excitation wavelengths at a constant intensity for each system. They can be attributed to whether or not the wavelength is resonant with the electronic levels of the cation. However, the case of polyene ionization was explained in terms of nonadiabatic multi-electron dynamics [15]. If the excitation wavelength is not resonant with the electronic levels of the cation, then fragmentation is suppressed and the molecular ions are observed. The resonance *vs.* non-resonance of excitation wavelength has been discussed by Fuß et al. [17] in a study of hexatriene ionization and by Itakura et al. [18] for the case of benzene ionization. Using isomers with different cation absorption spectra, author's group successfully demonstrated clear examples of non-resonance in molecular ion formation [10].

2.2.3 Polarization

According to Corkum's model, the ejected electron recollides with the parent molecule and may induce doubly charged molecular ions and fragment ions [19] if the recollision energy is sufficient. Formation of doubly charged ions was enhanced for the case of naphthalene by linearly polarized light [12] (with respect to the circularly polarized light as explained in the Sect. 2.4.4). The maximum recollision energy is $3.17 \times U_{\mathrm{p}}$, where U_{p} is the average kinetic energy of a free electron in the laser field, called the ponderomotive potential, and is given by (2.2):

$$U_{\mathrm{p}} = \frac{e^2 E_0^2}{4m\omega^2} = 9.33 \times 10^{-14} I_0 \lambda^2 \, [\mathrm{eV}] \, , \tag{2.2}$$

where I_0 $(\mathrm{W\,cm^{-2}})$ is the laser intensity and λ $(\mathrm{\mu m})$ is the wavelength. The maximum recollision energy reaches $58\,\mathrm{eV}$ at $1.4\,\mathrm{\mu m}$ and at $10^{14}\,\mathrm{W\,cm^{-2}}$. According to electron recollision model [19], the doubly charged molecular ion formation with circularly polarized light is suppressed compared to linearly polarrized light, because the ejected electron may avoid the recollision with the parent molecular ion. It should be noted that the the ionization potential (I_{p}) is shifted to $\sim I_{\mathrm{p}} + U_{\mathrm{p}}$.

2.2.4 Shorter Pulse

Shorter pulse excitation has been shown to be more efficient for producing a molecular ion for the case of C_{60} [20, 21]. C_{60} was ionized by pulses from $5\,\mathrm{ps}$ to $9\,\mathrm{fs}$. The shortest pulse of $9\,\mathrm{fs}$ has been shown to produce C_{60}^{z+} $(z = 1)$ without fragmentation. Metal CO complexes also showed smaller yields of fragmentation by shorter pulase excitation in two different pulse widths of 50 and $110\,\mathrm{fs}$ [16]. The same tendency has been observed in ionization of 2,3-dimethyl-1,3-butadiene. The relative molecular ion intensity increased as the decrease in the pulse width in a range from 1000 to $15\,\mathrm{fs}$ [4, 13].

2.2.5 Irradiation Geometry and Aperture

Different fragmentation patterns have been reported from different irradiation geometries. White light can be generated from an entrance window of the TOF mass chamber with a long focusing lens ($1000\,\mathrm{mm}$) more efficiently than with a short one ($300\,\mathrm{mm}$). The fragmentation of toluene was explained in terms of excitation by stimulated Raman scattering [22]. Recently Tang et al. have indicated that the fragmentation is enhanced by linear and nonlinear increases of the focal area and that the Raman mechanism is ruled out as the dominant effect [23].

An aperture is mounted in front of the flight tube of a TOF spectrometer. The size of the aperture would be significantly affect the intensity distributions of any observed species. Molecules are ionized using a focused beam

then, Coulomb explosion may be observed in the highest region of intensity, while at the periphery a singly charged molecular ion may be observed. Robson et al. have pointed out the inherent difficulty of organic molecule ionization [24].

In order to get molecular ion, the above experiments strongly suggests that a short focusing lens and an small size of aperture are recommended, and a great care has to be taken for the intensity evaluation. Examples are shown in the next section.

2.3 Experimental Methods

2.3.1 TOF Spectrometer and Femtosecond Laser

A brief outline of a time-of-flight mass spectrometer (TOF mass) and a femtosecond laser system are described. Figure 2.2 shows a TOF system with a mass resolution of $m/\Delta m = 2000$. Vaporized samples are introduced at a pressure of 10^{-5} Pa under a background pressure of 10^{-7} Pa. The aperture size of the slit of extraction plate was $1\,\text{mm}\,\phi$ or $0.5\,\text{mm}$.

Our laser system was a typical one; it consists of a Ti:sapphire femtosecond laser (Alpha 100/XS, Thales Laser) and an optical parametric amplifier (TOPAS femtosecond version, Quantronix). The laser system delivers a pulse
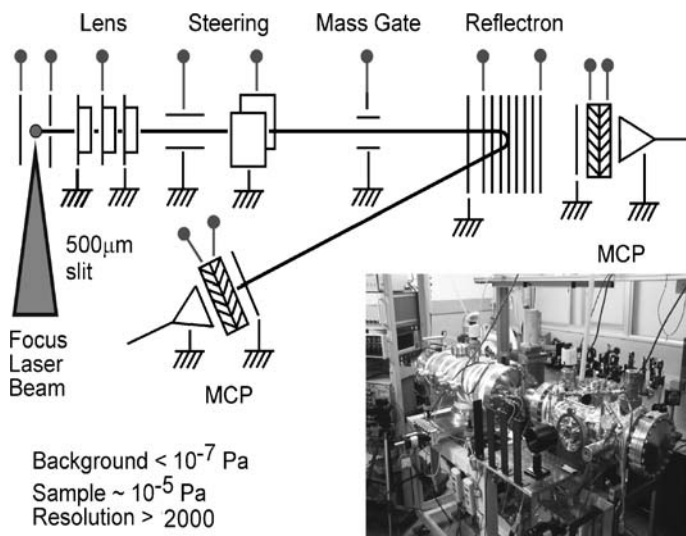

Fig. 2.2. Schematic diagram of a reflectron-type time-of-flight mass spectrometer and the look. The polarization of the fundamental pulse of $0.8\,\mu\text{m}$ was parallel to the flight axis. Typical applied voltages for ion extraction and the microchannel plate (MCP) were $3\,\text{kV}$ and $-2.1\,\text{kV}$, respectively

width of 30 fs at the center wavelength of 0.8 μm. The contrast ratios between the femtosecond pulse and amplified spontaneous emission were less than 10^{-6} for the 10-ps range pre- and post-pulses. The pulse width was variable up to a few picoseconds with the use of an acousto-optic programmable dispersive filter (Dazzler, FASTLITE). The pulse widths were monitored with a single-shot autocorrelator.

2.3.2 Intensity Evaluation

The laser intensity can be evaluated by the following (2.3):

$$P = \frac{E}{\pi r^2 \tau} ,$$
(2.3)

where E is the energy of the incident pulse and r is the radius of the beam at the focus. If $r = 15$ μm for a pulse width (τ) of 30 fs and a laser pulse energy (E) of 0.074 mJ, the average laser intensity (P) can be calculated to be 3.5×10^{14} W cm^{-2} (0.01 in atomic unit and field intensity of 5.1×10^8 V/cm). Wavelength tunable pulses are available. The typical
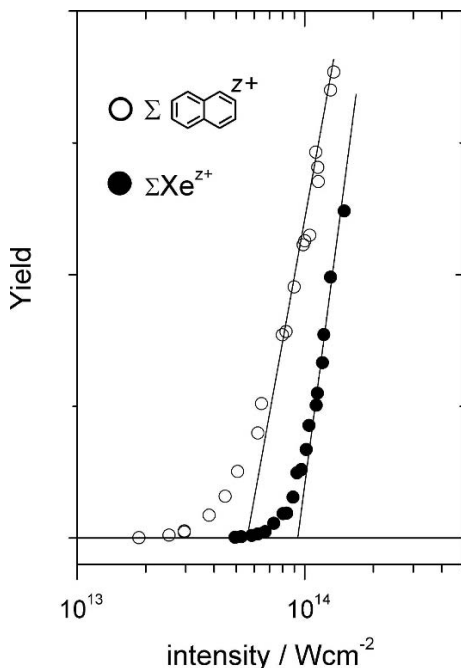

Fig. 2.3. Comparison with a standard intensity enable us to evaluate the laser intensity. The horizontal scale is corrected by the I_{sat} of a standard sample of Xe of 0.93×10^{14} W cm^{-2} for a pulse width of 130 fs at a wavelength of 1.4 μm. Then, naphthalene I_{sat} was determined to be 0.55×10^{14} W cm^{-2}

output energy of the tunable infrared pulse by optical parametric conversion was $0.4\,\mathrm{mJ}$ as the sum of signal and idler (from 1.2 to $2.4\,\mu m$) with an input laser energy of $1.2\,\mathrm{mJ/pulse}$ at the fundamental wavelength of $0.8\,\mu m$.

A conventional method of intensity evaluation is described below. Although the direct method is to mesure the spot size and the pulse width, the contrast ratios between the femtosecond pulse and the amplified spontaneous emission could vary day by day. Comparison with a standard intensity under the same conditions is much more convenient. If the ion yields and laser intensity are plotted on a semi-logarithmic chart, the result will be a straight line as an asymptote of the curve extrapolated back from the high intensity. The crossing point of the straight line with the horizontal axis is called a saturation intensity, I_{sat}. The I_{sat} value corresponds to the extrapolated back from a high intensity, where BSI occurs under intensities associated with the straight line. Hankin et al. [25] defined this value and determined the I_{sat} of Xe to be $1.12 \times 10^{14}\,\mathrm{W\,cm^{-2}}$ for a 44-fs pulse (which corresponds to $0.93 \times 10^{14}\,\mathrm{W\,cm^{-2}}$ for a pulse width of 130 fs) at $0.8\,\mu m$. The I_{sat} is well reproduced by the ADK theory. As Fig. 2.3 shows, I_{sat} for naphthalene can be determined to be $0.55 \times 10^{14}\,\mathrm{W\,cm^{-2}}$ for a 130-fs pulse at $1.4\,\mu m$ [12].

2.4 Molecular Ion Formation and Fragmentation

2.4.1 Isomer Dependent Fragmentation and Molecular Ion Fromation

With the same excitation wavelength and intensity, one of the cyclohexadiene isomers gave molecular ions and the other was heavily fragmented, as shown in Fig. 2.4. The cation of 1,3-cyclohexadiene has an absorption spectrum in the region much shorter than the excitation wavelength of $0.8\,\mu m$. In this case non-resonance holds with the cation electronic levels and intense molecular ion signals were detected. On the other hand, the absorption spectrum of 1,4-cyclohexadiene cation overlaps with the excitation wavelength of $0.8\,\mu m$ and many fragments were seen along with molecular ions of weak intensity [10]. Cation absorption spectra were taken from literature [26], though it should be noted that they were measured in the low temperature matrix.

2.4.2 Wavelength Dependence

A molecular ion-dominant spectrum has been observed for 2,3-dimethyl-1,3-butadiene (DB) excited with a 1.4-μm and 130 fs pulse, as shown in Fig. 2.5a, whereas many fragment ions were produced with a 0.8-μm femtosecond pulse of the same pulse width and intensity as shown in Fig. 2.5b. The cation absorption spectrum shown in Fig. 2.5c revealed that the non-resonant conditions hold with an excitation wavelength of $1.4\,\mu m$ [4].
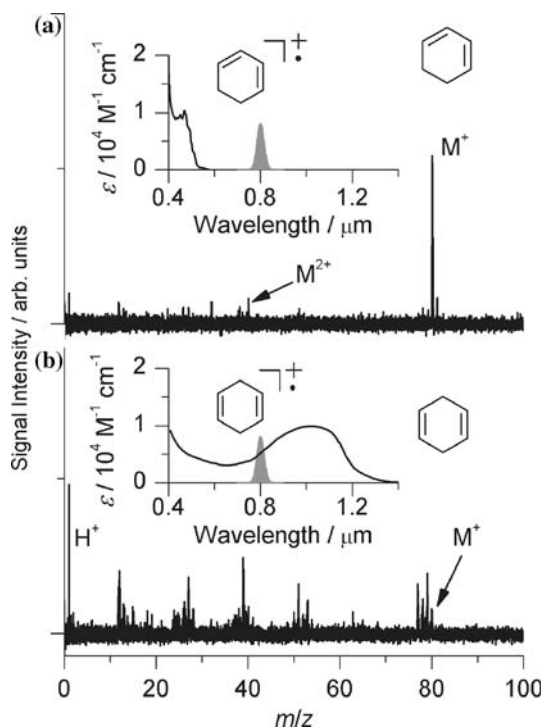
Fig. 2.4. a TOF mass spectra are shown for 1,3-cyclohexadiene (1,3-CHD) and **b** 1,4-cyclohexadiene (1,4-CHD) at $0.8\,\mu m$ with a 120-fs pulse width at an irradiation intensity of $0.6 \times 10^{14}\,W\,cm^{-2}$. The molecular ions are indicated by M^+ and the candidate for the doubly charged molecular ions is indicated by M^{2+}. The excitation laser spectrum is indicated in the inserted Figs. 1,3-CHD$^+$ is not in resonance with the laser wavelength, which resulted in a high yield of molecular ions, whereas 1,4-CHD$^+$ is resonant and gave many fragments

Anthracene was irradiated with femtosecond pulses and heavy fragmentation was observed at $0.8\,\mu m$ [5,6]; however, singly, doubly, and triply charged molecular ions were dominant at $1.4\,\mu m$ [11]. The cation absorption of anthracene indicates that $0.8\,\mu m$ is resonant and $1.4\,\mu m$ is non-resonant with the electronic levels as shown in Fig. 2.6.

2.4.3 Mechanism of Wavelength Dependence

Mechanisms of molecular ion formation and fragmentation applicable to organic molecules is shown in Fig. 2.7. a) Molecular-ion formation will be dominant, provided the excitation wavelength is non-resonant with the electronic absorption of the molecular cation. Multiply charged ions are produced, and eventually lead to a Coulomb explosion even with an intensity level of $10^{14}\,W\,cm^{-2}$. On the other way (Fig. 2.7b), fragmentation is vigor-
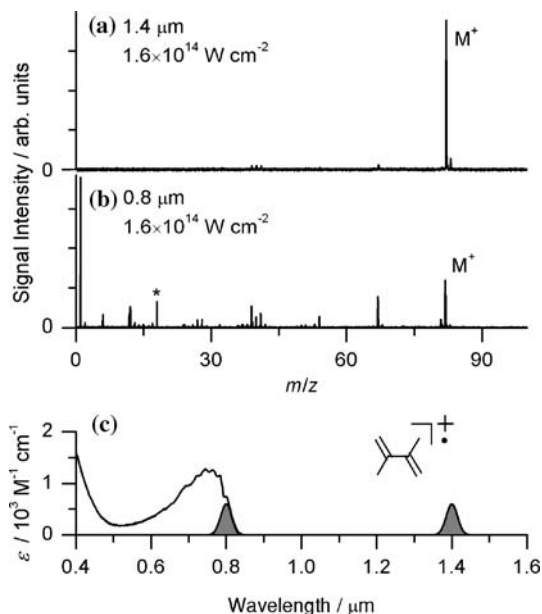
Fig. 2.5. TOF mass spectra of 2,3-dimethyl-1,3-butadiene (DB) are shown by **a** 1.4-µm excitation at an irradiation intensity of $1.6 \times 10^{14}\,\mathrm{W\,cm^{-2}}$ and **b** 0.8 µm excitation at an irradiation intensity of $1.6 \times 10^{14}\,\mathrm{W\,cm^{-2}}$. Molecular ions are indicated by M^+. The *asterisk* (*) indicates H_2O^+ signal. **c** The absorption spectrum of DB cation radical in a low-temperature matrix. The two shaded Gaussian shapes indicate the spectra of the excitation pulses

ous if the excitation wavelength is resonant with the electronic absorption of the molecular cation. Some dissociation mechanisms are conceivable. The first one involves direct and/or pre-dissociation: if there is a low-lying dissociation channel, the ions will dissociate. The second dissociation mechanism would be explained with a statistical model. Efficient non-radiative transition to the electronic ground state of the cation is expected to occur in the laser fields. The internal energy eventually increases far above the dissociation energy. The vibrationally excited ions undergo dissociation with a statistical rate. Fragmentations of some of the organic molecules shown here in the Figs. and metal CO complexes [16] can be explained in terms of the above mentioned model. The model depicted in Fig. 2.7 is practically useful for in estimating whether the fragment ions are predominant.

A high-intensity pulse induces dynamic broadening of the molecular electronic levels. The Stark broadening of the molecular eigenstates could reach several eV. The excitation and fragmentation mechanisms of some polyenes and aromatic molecules were analyzed by considering the broadening of electronic levels. This can not be described by a single electron picture; therefore, it is called nonadiabatic multi-electron (NME) dynamics [6, 15].
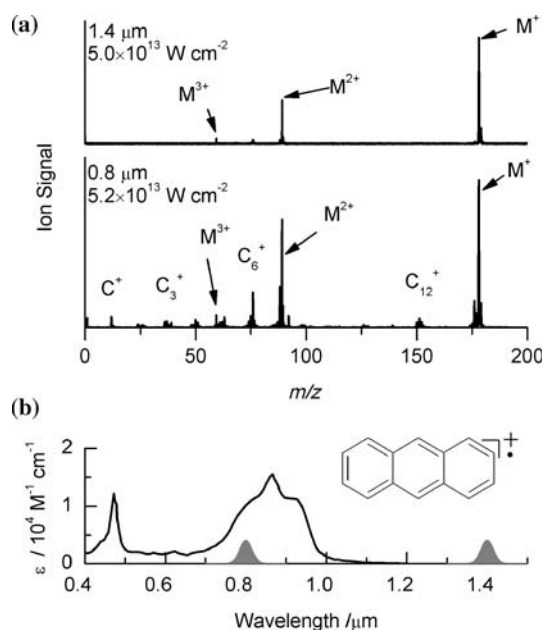
Fig. 2.6. a TOF mass spectra of anthracene at 1.4- and 0.8-μm excitations, and **b** the cation absorption spectrum in a low-temperature matrix with two spectra of the excitation pulses
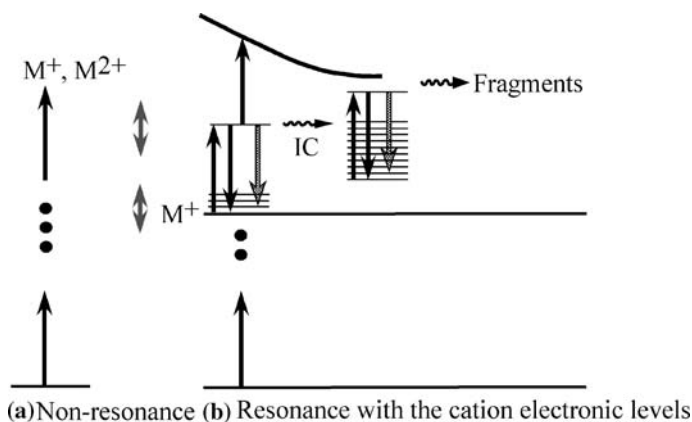
Fig. 2.7. Mechanisms of ionization and fragmentation of organic molecules: **a** Intact molecular ions are produced when the laser wavelength is non-resonant with the electronic level of the molecular cation, **b** while fragmentation occurs when the excitation wavelength is resonant. IC is internal conversion. The *both side arrows* indicate possible level shifts in the laser fields

2.4.4 Electron Recolision

A ponderomotive energy is proportional to the square of the laser wavelength λ, as shown in (2.2). The maximum electron recollision energy reaches 58 eV at 1.4 μm and 10^{14} W cm^{-2}. In fact, the recollision has been found to enhance the formation of multiply charged ions and fragmentation of benzene [19]. In the case of naphthalene, enhancement of doubly charged ions was observed but there was no significant enhancement of fragmentation. Only discernible amounts of fragment ions were detected; however, their origin could be assigned to the highly charged molecular ions themselves. These results can be explained in terms of the onset of the Coulomb explosion [12].

Naphthalene was irradiated by laser pulses of 130 fs at 1.4 μm, which is an isolated wavelength from the naphthalene cation absorption. M^{Z+} ($Z = 1$–3) were predominant at an irradiation intensity around 10^{14} W cm^{-2}. The molecular ion yields were compared for linearly and circularly polarized light against the effective laser intensity, as described below. Figure 2.8 left graph shows the clear enhancement of M^{2+} formation for linearly polarlized light excitation against circularly polarized light. As it has been explained with the electron recollision model, the recollision may be avoidable for circularly polarrized light. It is concluded that the enhancement is caused by the electron recollision excitation.

The ratios of molecular ions to total ions are plotted in Fig. 2.8 right graph. The total ions include the molecular ions and fragment ions. The ratios were about 1.0 until 0.8×10^{14} W cm^{-2}; in other words, the yields of the

effective laser intensity / Wcm^{-2}
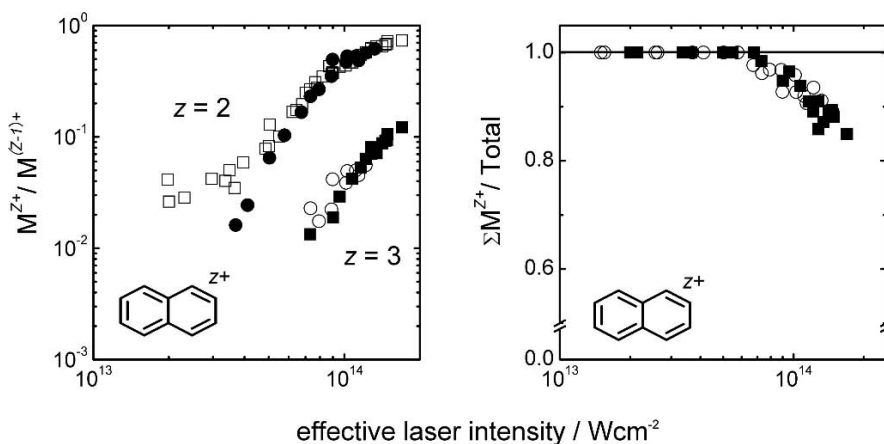
Fig. 2.8. *Left*: Ratio of doubly to singly charged ($Z = 2$, •, □) and triply to doubly charged ($Z = 3$, ○, ■) molecular ions are plotted as a function of effective laser intensity. *Circles* and *squares* indicate them by circularly and linearly polarized lights, respectively. *Right figure*: Ratio of the sum of molecular ions of all charge states ($\sum M^{z+}$) to the total ions (Total). Signals by circularly polarized light are indicated by (○) and for linearly polarized light by (■)

M^+ and M^{2+} molecular ions are 100%. Fragments appeared at a higher intensity; therefore, the ratios decreased with an increase in the intensity. The important observation is that there is no distinct difference in the ion yields with linearly and circularly polarized light excitations. It can be concluded that there is no enhancement of fragmentation by linearly polarized light, i.e., by electron recollision for this molecule. Fragments observed with small intensities were composed of acetylene$^+$ and (naphthalene minus acetylene)$^{2+}$. These ions are ascribed to the products of the Coulomb explosion of triply charged molecular ion.

The peak of the intensity of the circularly polarized light is half of that of the linearly polarized light. But this is not sufficient for the effective laser intensity in the ionization experiments. A factor of 0.65 has been estimated on the basis of the ADK calculation of Xe ionization rates [27]. The factor, 0.75 was experimentally obtained here by comparing the I_{sat} of Xe for linearly polarized light to that for circularly polarized light [12].

2.4.5 Short Pulse Excitation

Pulse-width dependent molecular ion formation was examined down to 35 fs at 0.8 μm. Femtosecond ionization of 2,3-dimethyl-1,3-dutadiene (DB) using 130-fs pulses has been shown in Fig. 2.5. Fragments along with molecular ions were observed as the excitation wavelength, 0.8 μm is resonant with the cation electronic levels. DB was irradiated with pulses of three different durations, i.e., 35 fs, 300 fs, and 1 ps at 0.8 μm. The spectrum at 130 fs has been shown in Fig. 2.5b. The relative intensities of molecular ions increased with a decrease in the pulse width from 1 ps to 35 fs, as shown Fig. 2.9 [13]. The laser peak intensity was kept at $0.22 \times 10^{14}\,\mathrm{W\,cm^{-2}}$, and negatively chirped pulses were used for pulses other than the transformed limitted 35-fs pulse. The molecular ions practically disappeared at the longest pulse duration, 1 ps excitation and the molecular ion intensity was the highest at the shortest pulse excitation. This tendency has been confirmed down to 15-fs pulse excitation [4].

C_{60} has been ionized by pulses from 5 ps to 25 fs; the shortest pulse of 25 fs produced C_{60}^{z+} $(z = 1, 2)$ without heavy fragmentation [20] at 0.79 μm. Very recently, Hertel and coworkers detected a single peak of the singly charged ions [21], where they irradiated C_{60} with a 9-fs pulse at 0.8 μm. It should be noted that this wavelength is resonant with the cation electronic level. From the above results, it may be considered that with sub ten fs pulse, intact molecular ion formation is possible for any molecule, even if the excitation wavelength is resonant with the cation absorption levels.

2.5 Femtosecond Laser Mass Spectrometry

Intact molecular ion formation has a great advantage for application to femtosecond laser mass spectrometry (FLMS). The Ledingham group has used
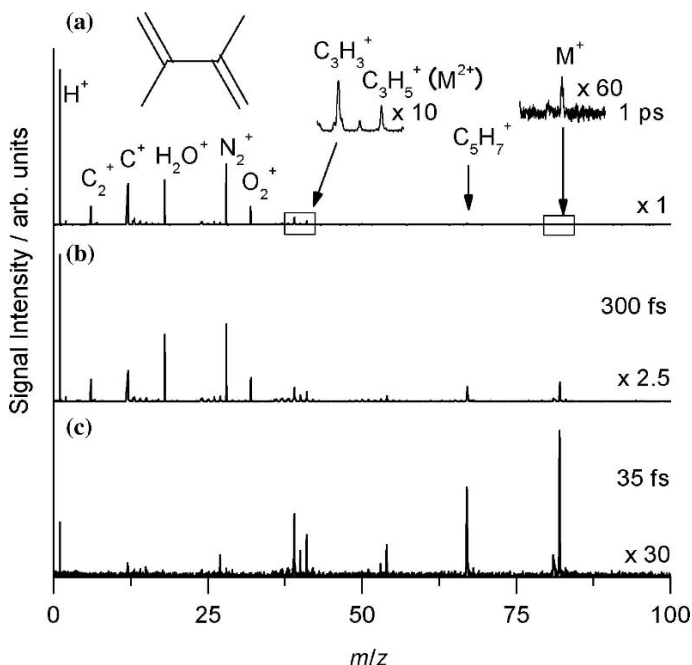
Fig. 2.9. The molecular ion signal of 2,3-dimethyl-1,3-butadiene was relatively strengthened with a decrease in pulse width at **a** 1 ps, **b** 300 fs, and **c** 35 fs. Magnified signals are shown in the *inserts*. The signal intensities in **b** and **c** were magnified by 2.5 and 30 times, respectively. The signals of N_2^+, O_2^+, and H_2O^+ were from contaminants in the chamber

the word of FLMS since 1998 [28] and ionized nitro compounds [7]. Shimada et al. ionized dioxins by femtosecond pulse excitation and the important results are summarised below [9].

The TOF mass spectra of dibenzo-*p*-dioxin consists of singly and doubly charged molecular ions with a small amount of fragments at 1.4 μm excitation at 130 fs, while many fragment ions were observed at 0.8 μm with the same pulse width. The absorption spectrum of this cation is not available, but the photoelectron spectrum gives us information on the electronic levels of the cation. The wavelength of 1.4 μm does not correspond to any peak of the spectrum and can be considered non-resonant. On the other hand 0.8 μm can be regarded as resonant with the energy level at 9 eV from the ground state, since I_p of this molecule is 7.6 eV.

The ratios of the molecular ion intensities of all charge states ($\sum M^{z+}$) to the total ions (Total) are plotted in Fig. 2.10. The total ions are the sum of molecular and fragment ions. The open circles indicate the results at 1.4 μm and the squares represent those observed at 0.8 μm. The ratio is 1.0 at 0.2–$0.3 \times 10^{14}\,\mathrm{W\,cm^{-2}}$; in other words, the molecular ions that consist of singly and doubly charged ions account for 100% of the ions for the case

of $1.4\,\mu$m excitation. The ratio of 0.6 was observed at the I_{sat} of $0.86 \times 10^{14}\,$W cm^{-2} at $1.4\,\mu$m, whereas heavy fragmentation with a ratio of 0.05 was observed with 0.8-μm excitation.

Some chlorinated dioxins are extremely toxic. One of the chlorinated dioxins was ionized and the corresponding TOF spectrum is shown in Fig. 2.11. Dominant ions are singly and doubly charged molecular ions, although there were some fragment ions.

There are several methods to produce molecular ions. Excitation sources can be VUV light, electrons, and other high energy particles. The femtosec-
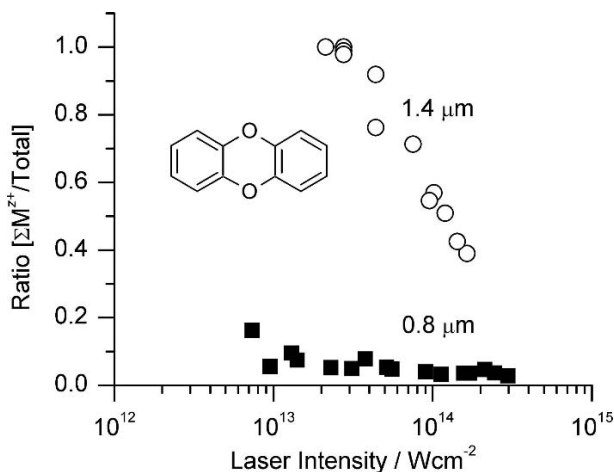
Fig. 2.10. The ratio of the molecular ion intensities to the total ions of dibenzo-*p*-dioxin *vs.* laser intensity at two excitation wavelengths: *filled squares* (■); 0.8-μm excitation. *Open circles* (○); 1.4-μm excitation
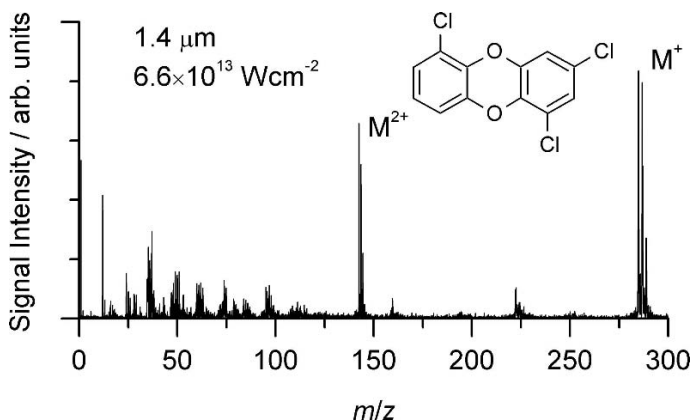
Fig. 2.11. 1,3,6-Trichlorodibenzo-*p*-dioxin was ionized by 130-fs pulses at $1.4\,\mu$m The molecular ion intensity, M$^+$, was the highest. M^{2+} indicates the doubly charged molecular ion
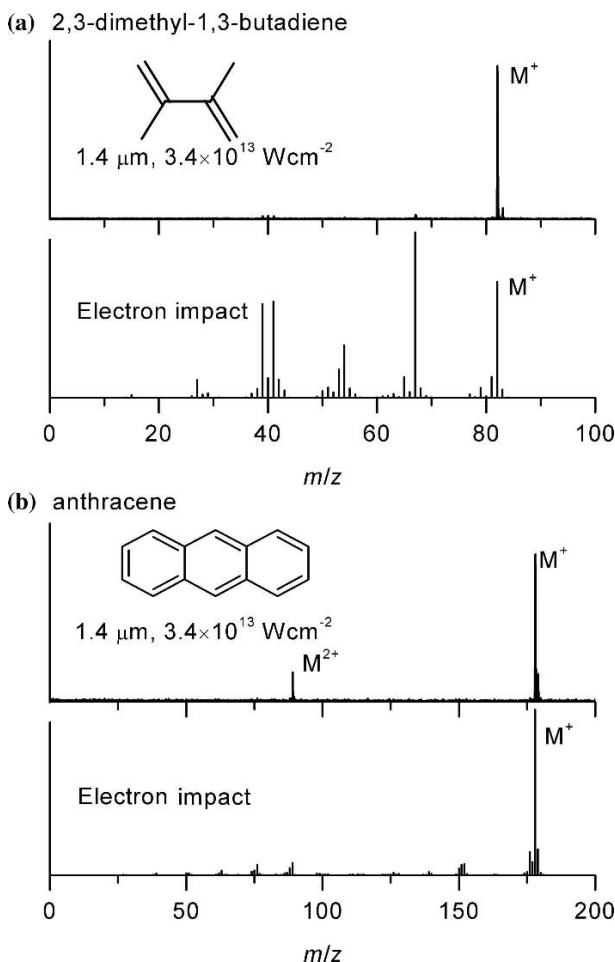
Fig. 2.12. Comparison of the mass spectra obtained by femtosecond ionization and electron impact ionization of **a** 2,3-dimethyl-1,3-butadiene, and **b** anthracene at 1.4-μm excitation of 130-fs pulses (The EI spectra are taken from NIST Standard Reference Database [29].)

ond results are compared with those by electron impact excitation at 70 eV. The femtosecond laser excitation gave simpler spectra compared to EI ionization for anthracene and 2,3-dimethyl-1,3-butadiene at 1.4 μm, as shown in Fig. 2.12.

2.6 Conclusions

Intact molecular ion formation of organic compounds is a distinct feature of femtosecond laser excitation, although some molecules show heavy fragmen-

tation even under ultrashort pulse irradiation. The effects of wavelength, electron recollision (polarization effects), and pulse width have been discussed. We have found the heavy fragmentation often occurs when the excitation wavelength is resonant with the cation electronic levels. Furthermore, we have found that shorter pulse excitation leads to less fragmentation. Therefore, excitation at a non-resonant wavelength and/or with an ultimate short pulse could generate molecular ions as a dominant product from any type of molecules around the intensity of I_{sat}. This phenomenon is therefore particularly useful for analytical purposes, as for example in dioxin detection.

Fragmentation in a high intensity laser field is complicated if it occurs. The mechanism has not been fully analyzed [3] at the present stage. A tailored shaping pulse [30–32] would be helpful to analyze these mechanisms.

References

1. M.J. DeWitt, R.J. Levis: J. Chem. Phys. **102**, 8670 (1995)
2. V.R. Bhardwaj, P.B. Corkum, D.M. Rayner: Phys. Rev. Lett. **91**, 203004 (2003)
3. I.V. Hertel, T. Laarmann, C.P. Schultz: Adv. Atom. Mol. Opt. Phy. **50**, 219 (2005)
4. M. Tanaka, S. Panja, M. Murakami, T. Yatsuhashi, N. Nakashima: Chem. Phys. Lett. **427**, 255 (2006)
5. L. Robson, A.D. Tasker, K.W.D. Ledingham, P. McKenna, T. McCanny, C. Kosmidis, P. Tzallas, D.A. Jaroszynski, D.R. Jones: Int. J. Mass Spectrometry, **220**, 69 (2002)
6. A.N. Markevitch, D.A. Romanov, S.M. Smith, H.B. Schlegel, M.Yu. Ivanov, R.J. Levis: Phys. Rev. A **69**, 013401 (2004)
7. A.D. Tasker, L. Robson, K.W.D. Ledingham, T. McCanny, C. Kosmidis, D.A. Jaroszynski: Int. J. Mass Spectrometry **225**, 53 (2003)
8. H. Harada, M. Tanaka, M. Murakami, S. Shimizu, T. Yatsuhashi, N. Nakashima, S. Sakabe Y. Izawa, S. Tojo, T. Majima: J. Phys. Chem. A **107**, 6580 (2003)
9. Y. Shimada, R. Mizoguchi, H. Shinohara, T. Yatsuhashi, N. Nakashima: Bunseki Kagaku **54**, 127 (2005) (in Japanese)
10. H. Harada, S. Shimizu, T. Yatsuhashi, S. Sakabe, Y. Izawa, N. Nakashima: Chem. Phys. Lett. **342**, 563 (2001)
11. M. Murakami, R. Mizoguchi, Y. Shimada, T. Yatsuhashi, N. Nakashima: Chem. Phys. Lett. **403**, 238 (2005)
12. T. Yatsuhashi, N. Nakashima: J. Phys. Chem. A **109**, 9414(2005)
13. R. Mizoguchi, Y. Shimada, H. Shinohara, T. Yatsuhashi, N. Nakashima: Rev. Laser Eng. **32**, 717 (2004) (in Japanese)
14. S. Augst, D. Strickland, D.D. Meyerhofer, S.L. Chin, J.H. Eberly: Phys. Rev. Lett. **63**, 2212(1989)
15. M. Lezius, V. Blanchet, M.Yu. Ivanov, A. Stolow: J. Chem. Phys. **117**, 1575 (2002)
16. S.A. Trushin, W. Fuß, W.E. Schmid: J. Phys. B: At. Mol. Opt. Phys. **37**, 3987 (2004)

17. W. Fuß, W.E. Schmid, S.A. Trushin: J. Chem. Phys. **112**, 8347 (2000)
18. R. Itakura, J. Watanabe, A. Hishikawa, K. Yamanouchi: J. Chem. Phys. **114**, 5598 (2001)
19. V.R. Bhardwaj, D.M. Rayner, D.M. Villeneuve, P.B. Corkum: Phys. Rev. Lett. **87**, 253003 (2001)
20. E.E.B. Campbell, K. Hansen, K. Hoffmann, G. Korn, M. Tchaplyguine, M. Wittmann, I.V. Hertel: Phys. Rev. Lett. **84**, 2128 (2000)
21. I. Shchatsinin, T. Laarmann, G. Stibenz, G. Steinmeyer, A. Stalmashonak, N. Zhavoronkov, C.P. Schulz, I.V. Hertel: J. Chem. Phys. **125**, 194320 (2006)
22. A.M. Müller, B. Witzel, C.J.G.J. Uiterwaal, J. Wanner, K.-L. Kompa: Phys. Rev. Lett. **88**, 023001 (2002)
23. X.P. Tang, A. Becker, W. Liu, M. Sharifi, O. Kosareva, V.P. Kandidov, P. Agostini, S.L. Chin: Phys. Rev. A **71**, 045401 (2005)
24. L. Robson, K.W.D. Ledingham, P. McKenna, T. McCanny, S. Shimizu, J.M. Yang, C.-G. Wahlström, R. Lopez-Martens, K. Varju, P. Johnsson, J. Mauritsson, J. Am. Soc. Mass Spectrom. **16**, 82 (2005)
25. S.M. Hankin, D.M. Villeneuve, P.B. Corkum, D.M. Rayner: Phys. Rev. A **64**, 013405 (2001)
26. T. Shida, *Electronic Absorption Spectra of Radical Ions* (Elsevier, New York, 1988)
27. M. Suresh, J. McKenna, B. Srigengan, I.D. Williams, E.M.L. English, S.L. Stebbings, W.A. Bryan, W.R. Newell, E.J. Divall, C.J. Hooker, A.J. Langley: Nucl. Instru. Methods Phys. Res. Sect. B **235**, 216 (2005)
28. D.J. Smith, K.W.D. Ledingham, R.P. Singhal, H.S. Kilic, T. McCanny, A.J. Langley, P.F. Taday, C. Kosmidis: Rapid Commun. Mass Spectrom, **12**, 813 (1998)
29. NIST Standard Reference Database No. 69 – June 2003 Release, WebBook http://webbook.nist.gov/chemistry
30. M. Boyle, T. Laarmann, I. Shchatsinin, C.P. Schulz, I.V. Hertel: J. Chem. Phys. **122**, 181103 (2005)
31. A. Assion, T. Baumert, M. Bergt, T. Brixner, B. Kiefer, V. Seyfried, M. Strehle, G. Gerber: Science **282**, 919 (1998)
32. R.J. Levis, G.M. Menkir, H. Rabitz: Science **292**, 709 (2001)
33. R. Itakura, K. Yamanouchi, T. Tanabe, T. Okamoto, F. Kannari: J. Chem. Phys. **119**, 4179 (2003)

3 Ultrafast Electron Dynamics

M.J.J. Vrakking

FOM Institute for Atomic and Molecular Physics (AMOLF)
Kruislaan 407, 1098 SJ Amsterdam, The Netherlands
m.vrakking@amolf.nl

Summary. We discuss the role of strongly driven electrons in the generation of attosecond laser pulses and in time-resolved experiments that can be performed using attosecond lasers. We show that the formation of attosecond laser pulses in high harmonic generation is an inevitable consequency of the physics of atoms in strong laser fields, combining the sub-cycle dependence of atomic ionization rates with controlled acceleration of the ionized electrons in the oscillatory field of the laser. Molecules undergoing dynamic alignment and/or enhanced ionization, and explosions of large rare gas clusters in an intense laser field are discussed in the context of attosecond electron dynamics.

3.1 Introduction

In ultrafast laser science the emergence of attosecond laser pulses raises the prospect of studying electronic wavepacket motion on the natural timescales of this motion in nature, namely the atomic unit of time (1 a.u. = 24 attoseconds = 0.024 femtoseconds) [1, 2]. Attosecond science may have a profound impact on the way we understand photo-induced physical and chemical processes.

Attosecond pulses are formed by high harmonic generation (HHG) [3]. When a gaseous atomic medium is exposed to an intense laser pulse, radiation is formed at soft X-ray wavelengths through a three-step mechanism, consisting of (1) ionization, (2) acceleration of the electron in the oscillatory field of the laser and (3) re-collision with the parent ion accompanied by the emission of a photon with an energy that is the sum of the parent ionization energy and the kinetic energy of the re-collision electron [4]. Both the ionized electrons and the soft X-ray photons come in bunches with a duration in the attosecond domain.

In the last few years, first measurements have been performed determining the length of the attosecond soft X-ray bunches. Paul et al. measured 250 attosecond pulses in a two-color photoionization experiment [5]. Making use of the fact that in a train of soft X-ray bunches the frequency spectrum consists of odd multiples ('harmonics') of the frequency of the driver laser, they studied the ionization of Ar atoms by simultaneous photo-absorption from the soft X-ray bunch and the fundamental color of the femtosecond laser. Measured

photoelectron spectra then contain sidebands resulting from 1 ± 1 XUV+IR two-color ionization where ionization pathways involving neighbouring harmonics interfere and carry information about their relative phase, allowing for a reconstruction of the time profile of the attosecond pulses. Similar experiments have since provided information on the frequency chirp of the pulses (the "attochirp") and the variation of the soft X-ray bunches within the train (the "femtochirp") [6–8]. The generation of *isolated* attosecond pulses was reported by Krausz et al. [9]. Key to obtaining this result was the use of an ultrashort ($\sim$5 femtosecond) driver laser. This ensured that the three-step mechanism outlined above could only occur once during the entire femtosecond laser pulse. The same team has since reported the production of isolated 250 attosecond pulses [10], has succesfully implemented the use of an amplified carrier envelope phase-stabilized laser in the production of isolated attosecond laser pulses [11] and has given the first demonstration of the use of isolated attosecond laser pulses in a time-resolved experiment where the time scale for Auger decay in Kr was measured [12]. Thus we may conclude that the field of generating and characterizing attosecond laser pulses is very rapidly reaching a mature state, where the attention is shifting from generation and characterization to possible applications.

The application of attosecond techniques to study electron dynamics poses several important challenges. First of all, the observation of electronic wavepacket motion requires that electronic states are coherently excited with a pulse that is comparable to or shorter than the characteristic timescale of the electronic motion. In many systems of interest this is a considerable challenge, since the excitation energies of the states of interest are frequently in the ultra-violet (UV) or vacuum ultra-violet (VUV) range, whereas all attosecond pulses that have been generated and characterized sofar operate in the extreme ultra-violet (XUV) or soft X-ray range. Solutions may be the application of UV/VUV attosecond pulses created via the generation of Raman sidebands [13] or the coherent excitation of the electron wavepacket itself via a Raman transition [14]. A second challenge is the current lack of available spectroscopies that relate the time-dependent dynamics of an electron wavepacket to measurable observables. Many femtosecond experiments aimed at studying the motion of atomic wavepackets have succeeded because changes in the position of atoms were accompanied by changes in the electronic absorption spectrum of the system [15]. In the case of electronic wavepackets under investigation by an attosecond laser pulse, no such spectroscopy is so far available. The fate of an atom or molecule that is exposed to an attosecond pulse is almost inevitably ionization. Therefore, it seems that information on the time-dependent electron dynamics will almost certainly have to be extracted from the imprint of this dynamics on the final properties of the photoelectrons (or photo-ions) that are formed in the photoionization event [16]. In fact, the majority of the techniques that have thus far been used to characterize attosecond laser pulses have already made use of this fact. In techniques that have derived their inspiration from well-established pulse

characterization techniques like SPIDER [17] and FROG [18], measurements of the final state kinetic and/or angular distributions of photoelectrons have given insight into the duration of the attosecond pulses that were responsible for their production [5–9, 19, 20].

Two photoelectron spectroscopic techniques have sofar predominantly been used on the basis their high collection efficiencies. In a magnetic bottle spectrometer [21] the ionization takes place in a strong, spatially varying magnetic field, that parallelizes the electron trajectories. The photoelectron kinetic energy distribution is obtained by measuring the time-of-flight of the electron towards a detector that is put at a considerable distance (typ. $\geq 1\,\mathrm{m}$). In photoelectron imaging experiments, the ionization takes place in a DC electric field that accelerates the photoelectrons towards a two-dimensional detector where the position of their impact is recorded [22]. If the time-of-flight is measured with sufficient accuracy using a delay-line detector [23], then the three velocity components of the initial electron ejection can immediately be determined, whereas an inverse Abel-transformation is needed if this timing information is lost. Imaging methods give both angular and kinetic energy information. Conversely, magnetic bottle spectrometers can be operated with retarding fields, which allows them to achieve a somewhat better resolution at high photoelectron kinetic energies.

When considering the application of attosecond pulses, we may distinguish photo-induced electron dynamics in the perturbative and in the non-perturbative regime. The former constitutes the regime of single- and few-photon absorption and includes what will hopefully turn out to be the main application area of attosecond laser pulses. The latter constitutes a regime that is often encountered in intense femtosecond laser laboratories [24], where processes like high-harmonic generation [1] and above-threshold ionization in atoms [25], dynamic alignment [26] and Coulomb explosion in molecules [27] and X-ray generation in clusters [28] are studied. In all these cases the dynamics of the system is highly non-perturbative, involves the absorption and stimulated emission of many laser photons and is determined by the interactions of the electrons in the system with the classical electric field of the laser.

In our current research, we use strongly driven electrons as model systems for developing attosecond spectroscopy [29]. Since the motion of the electron is driven by the classical field of an intense infrared laser, we may expect that this motion is relatively simple compared to the electronic rearrangement that occurs in chemical processes like intersystem crossing or the making and breaking of chemical bonds. Furthermore, since the motion is driven by the same laser that is also used in the generation of the attosecond laser pulses, there is an intrinsic synchronization, where the delay between the attosecond pulse and the field oscillations of the intense driving laser can be controlled with a precision of just a few attoseconds. If the electronic motion is periodic, then the motion can be probed both by an isolated attosecond laser pulse and by an attosecond pulse train, the latter being much easier to generate.

At the moment that this chapter is being written, our experimental program is just getting under way, and some very encouraging initial results have already been obtained [30]. In the remainder of this chapter we will discuss the role of strongly driven electrons in the generation of attosecond laser pulses, as well as how strongly-driven electrons may be studied in attosecond experiments. Sections 3.2–3.4 deal with the role of strongly-driven electrons in photoionization and high harmonic generation. We start with a discussion of experiments on ionization in the presence of a strong DC electric field, emphasizing the importance of the trajectory of the electron (Sect. 3.2). Next, we present experiments on photoionization by strong low-frequency (RF) radiation fields, emphasizing the importance of the instantaneous electric field (Sect. 3.3). These concepts come together in our description of high harmonic generation (Sect. 3.4). We argue that the generation of attosecond laser pulses is an inevitable consequence of the physics of strong field ionization and discuss the use of angle-resolved photoelectron imaging to the experimental characterization of a train of attosecond laser pulses.

In the second part, we discuss possible applications of attosecond laser pulses to future studies of time-resolved electron dynamics in strongly driven systems. We discuss our current understanding of the time-dependent behaviour of non-perturbatively driven electrons in atoms, molecules and clusters. In Sect. 3.4 we discuss differences that arise when the generation of attosecond pulses is performed in different atomic media. This is followed in Sect. 3.5 by a description of the role of electron dynamics in dynamical alignment and enhanced ionization of molecules. Finally, in Sect. 3.6 the role of electron dynamics in laser heating of large clusters is discussed.

3.2 Photoionization in DC Electric Fields

When an atom is placed in a DC electric field, ionization becomes possible as soon as the atom is excited above the saddlepoint in the Coulomb + DC field potential, which lies at an energy $\Delta E = -2\sqrt{F_{\mathrm{dc}}}$. Here, both the lowering of the ionization potential ΔE and the strength of the DC electric field F_{dc} are given in atomic units (1 a.u. = 27.2 eV). We experimentally investigated the ionization of atoms in a DC electric field by exciting Xe atoms starting from the metastable $6s[3/2]_{J=2}$ state using a tunable dye laser [31]. The atoms were ionized using either 1-photon excitation at wavelengths $\lambda < 326$ nm or 2-photon excitation at wavelengths $\lambda < 652$ nm. The photoelectrons were accelerated towards a two-dimensional (2D) detector, consisting of two microchannel plates followed by a phosphorscreen and a camera system that recorded the positions of the electron impact. The image on the detector reflects the 2D velocity distribution of the photoelectrons perpendicular to the detector axis (from here on called the x-axis). When the polarization of the light source (from here on called the z-axis) in a 2D imaging experiment is chosen parallel to the plane of the detector, then in the dipole approximation

the three-dimensional (3D) velocity distribution is cylindrically symmetric around the z-axis. In this case, as mentioned in the introduction, the 3D velocity distribution can be recovered from the 2D projection using an inverse Abel-transformation.

In the present experiment, all photoelectrons are formed with a well-defined kinetic energy, since both the initial state energy, the photon energy and the location of the saddlepoint in the Coulomb + DC field potential are known with sub-wavenumber accuracy. Nevertheless, as shown in Fig. 3.1, the experimental images reveal a number of rings, *as if* the photoelectrons are formed with several distinct kinetic energies. The reason for this is the presence of the DC electric field which breaks the cylindrical symmetry in the 3D velocity distribution, since electrons emitted in the xz-plane at angles $\pm\alpha$ with respect to the polarization axis follow very different trajectories on the way to the detector. Following the initial photoelectron ejection, which is cylindrically symmetric with respect to the polarization axis, electrons that are emitted in the direction of the detector follow a relatively simple trajectory where they do not approach the parent ion anymore. On the other hand, electrons that are emitted away from the detector tend to follow a more complicated trajectory, where they interact one or more times with the parent ion before moving downstream towards the detector. Consequently, the radius on

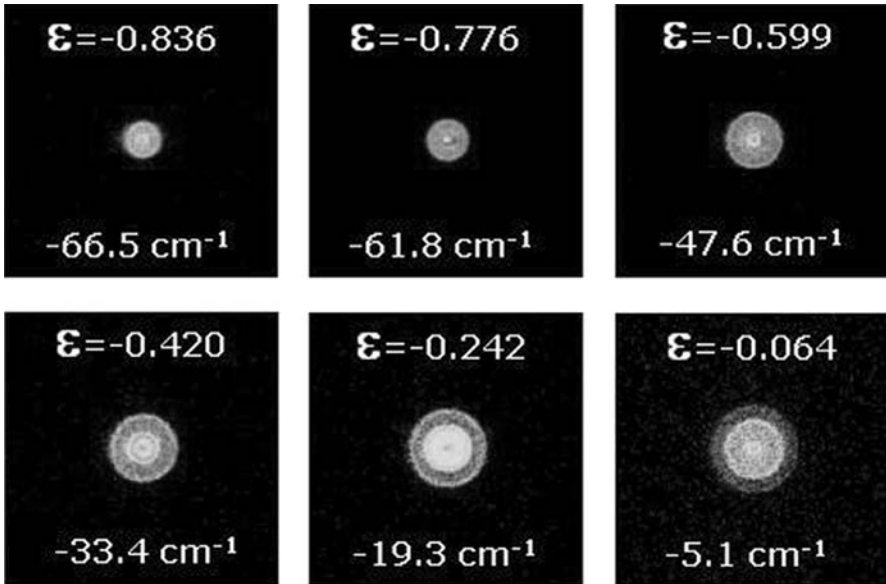**Fig. 3.1.** Six images recorded in a DC field of 170 V/cm with the laser polarization along the detector axis, for different values of the scaled energy $\varepsilon = E_{\text{electron}}/\Delta E_{\text{sp}}$. The images show the transition from predominantly indirect ionization close to the saddlepoint ($\varepsilon = -1$) to direct ionization close to the field-free ionization limit ($\varepsilon = 0$)

the detector where the electrons are detected is a non-trivial function of the strength of the DC field, the photoelectron kinetic energy and the emission angle with respect to the DC electric field axis, and contains a number of maxima [32]. At energies just above the saddlepoint, most trajectories involve interactions with the parent ion, whereas at higher energies an increasing fraction of the trajectories are direct. Significantly above the field-free ionization limit, the importance of the indirect trajectories becomes negligible, and one enters the regime where photoelectron imaging experiments are typically carried out to measure kinetic energy and angular distributions of emitted electrons [22].

Sofar the imaging results of Fig. 3.1 were discussed in very classical terms, using the notion of a set of trajectories that take the electron from the atom to the detector. However, this description does not do justice to the fact that atomic photoionization is a quantum mechanical proces. Similar to the interference between light beams that is observed in Young's double slit experiment, we may expect to see the effects of interference if many different quantum paths exist that connect the atom to a particular point on the detector. Indeed this interference was previously observed in photodetachment experiments by Blondel and co-workers, which revealed the interference between two trajectories by means of which a photo-detached electron can be transported between the atom and the detector [33]. The current case of atomic photoionization is more complicated, since classical theory predicts that there are an infinite number of trajectories along which the electron can move from the atom to a particular point on the detector [32, 34]. Nevertheless, as Fig. 3.2 shows, the interference between trajectories is observable [35] when the resolution of the experiment is improved [36]. The number of interference fringes smoothly increases with the photoelectron energy.

We have performed a semiclassical analysis of the electron trajectories and found very satisfactory agreement between experimental and simulated interference patterns, indicating that the interferences can be understood purely on the basis of semiclassical path integral arguments [37]. Just above the saddle-point, when the dynamics is dominated by indirect trajectories, the images reveal the interference between indirect trajectories, whereas higher up, when the indirect trajectories compete with direct trajectories, a more complicated interference pattern is observed, involving beats between the interference patterns resulting from indirect and direct photoionization.

While the distinction of the electron trajectories as being either 'direct' or 'indirect' and the observation of quantum mechanical interferences among the trajectories can be understood in terms of the DC electric field strength and the photoelectron kinetic energy with respect to the saddlepoint in the Coulomb + DC electric field potential, this is not the only quantity that characterizes the photoelectrons that are emitted. Above the saddlepoint in the Coulomb + DC potential there exists a continuation of the Stark manifold. This Stark manifold manifests itself in the excitation spectrum of the atom, which shows pronounced peaks in the photoionization efficiency as a func-
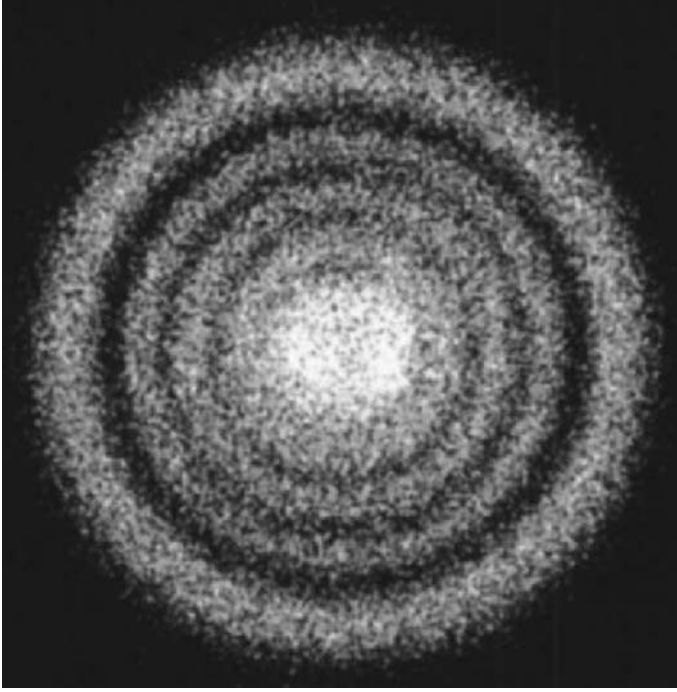
Fig. 3.2. High-resolution photoelectron image recorded in a DC field of 615 V/cm, with the laser polarization perpendicular to the detector axis, and parallel to the plane of the detector. The image shows an interference structure that can be understood in terms of the pathlength differences between classical trajectories that carry the electron from the atom to the detector

tion of wavelength [38]. In principle we might expect the choice of a particular Stark resonance to affect the interference patterns that are recorded on our 2D detector. Experimentally, however, this is not observed. When the laser is scanned over a sequence of resonances, significant modulations are observed in the ratio of direct-to-indirect ionization, reflecting the fact that the electronic wavepacket can be preferentially launched on the uphill or downhill part of the potential. However, no clear differences are observed in the interference patterns. This is most likely due to the fact that the quantum defects in Xe differ considerably from zero, inducing considerable mixing between the various Stark states. In the future we hope to perform similar experiments in atomic hydrogen. Since the one-electron Stark problem is fully separable in parabolic coordinates the nodal structure of the Stark wavefunction does not change with fieldstrength, and therefore it may be possible to record images on the two-dimensional detector that carry the signature of the Stark state that is excited.

It is interesting to develop the connection between the experiments discussed above and experiments in the optical domain, in particular those re-

lated to high harmonic generation and the formation of attosecond laser pulses. In strong laser fields, there exist three ionization regimes, namely (1) multi-photon ionization, (2) tunnel ionization and (3) over-the-barrier ionization [25]. When the ionization occurs by means of multi-photon ionization, the ionization rate is given by a perturbative expression $S \sim I^N$, where N is the number of photons that are required to ionize, satisfying the relation $N * \omega_{\text{laser}} > I_p$. Multi-photon ionization is the dominant ionization mechanism when the laser intensity is low and/or the photon frequency is high enough for the ionization to be a low-order proces. Tunnel ionization occurs when the electric field strength of the laser is so high that the electron can tunnel through the barrier in the Coulomb + laser field potential in a time that is comparable to the optical period of the laser. The related proces of over-the-barrier ionization occurs at slightly higher intensities when the electric field strength of the laser is so high that the saddlepoint in the Coulomb + laser field potential is pushed below the initial state energy of the electron. The border between the multi-photon ionization and tunneling/over-the-barrier ionization regimes is usually expressed in terms of the Keldysh parameter $\gamma = \sqrt{(I_p/2U_p)}$, where I_p is the ionization potential and $U_p = F_{\text{laser}}^2/4\omega^2 = I_{\text{laser}}/4\omega^2$ is the ponderomotive energy, corresponding to the kinetic energy of a free electron in a laser field with an electric field strength F_{laser} and a laser frequency ω. For $\gamma > 1$ the ionization is in the multi-photon regime, while for $\gamma < 1$ the ionization is in the tunneling/over-the-barrier regime. The photoionization that we have studied in DC electric fields can be viewed as an over-the-barrier ionization process, where, unlike the case of a strong laser field, the Coulomb + electric field potential is time-independent. The results of our experiments first of all suggest that in over-the-barrier and tunnel-ionization one needs to consider the action of the electric field on the motion of the electron. In the strong field laser physics community this has of course fully been recognized and has led to the development of the so-called 'strong field approximation' (SFA) [39], where the motion of the electron in the continuum is viewed as being completely governed by the laser field, neglecting any residual influence of the Coulomb interaction. Secondly, the experiments presented above suggest that in strong fields careful attention has to be paid to the role of different trajectories that the ionizing electrons can follow. We will return to this point in our discussion of the generation and characterization of attosecond pulses using high harmonic generation.

3.3 Photoionization in RF and THz Fields

Interactions of atoms with short and intense laser pulses have traditionally been discussed in terms of the intensity and pulse duration of the laser system being used. However, in recent years a number of light sources have been developed where this description is no longer appropriate. In the optical domain,

few-cycle laser pulses have been generated with a full-width-at-half-maximum (FWHM) of two cycles or less [40, 41]. In order to adequately describe these pulses, one not only has to specify the peak intensity and the pulse duration, but also the carrier-envelope offset phase (CEP), which describes the phase of the oscillation of the electric field underneath the envelope of the pulse. Similarly, in the THz domain, so-called 'half-cycle' pulses have been developed [42], consisting of a single large excursion of the electric field along one direction of the polarization axis, followed by a substantially longer tail of the opposite polarity.

Coherent light sources are characterized by a spectral intensity distribution $|E(\omega)|$ and a frequency-dependent phase $\Phi(\omega)$. According to first-order perturbation theory, linear absorption probabilities are given by the overlap between the spectrum of the light source $|E(\omega)|$ and the optical transition, and are independent of the phase function $\Phi(\omega)$. In non-linear processes (2nd order perturbation theory or non-perturbative interactions) excitation probabilities are determined by both the spectral intensity distribution $|E(\omega)|$ *and* the frequency-dependent phase $\Phi(\omega)$. If one makes a Taylor expansion of the frequency-dependent phase as $\Phi(\omega) = \Phi(\omega_0) + \Phi'(\omega_0)(\omega - \omega_0) + \Phi''(\omega_0)(\omega - \omega_0)^2 + \Phi'''(\omega_0)(\omega - \omega_0)^3 \ldots$ then the quadratic and higher order terms determine the shape of the pulse envelope, the linear term determines the delay of the pulse with respect to the origin of time and $\Phi(\omega_0)$ determines the carrier envelope phase. Unless a system has already coherently been prepared by an earlier laser pulse, excitation probabilities do not depend on the pulse delay. However, they can depend on both the laser pulse envelope and the carrier envelope phase. The former is extensively used in optimal control experiments, where manipulation of the relative phase of the frequency components in a laser pulse using a pulse shaping device permits non-linear control over the dynamics of a system [43–45]. Dependencies of excitation probabilities on the carrier-envelope phase have only been observed in the last few years, following the development of few-cycle laser systems [46]. Carrier envelope phase effects are generally restricted to pulses with a duration of 2–3 optical cycles, although there exists an experiment where CEP effects have been observed for laser pulses with a duration of 10 optical cycles [47].

In high harmonic generation and the formation of attosecond laser pulses the carrier envelope phase is very important [10]. This importance arises through the non-linear dependence of atomic ionization rates on the electric field of the driving laser. The ionization that launches the electron into the continuum is a tunnelling or over-the-barrier process that depends on the instantaneous strength of the electric field of the laser in a highly non-linear fashion. We have investigated the consequences of this non-linearity in a series of experiments where we have probed the ionization of high-lying Rydberg states by low-frequency radiation fields [48]. The advantage of using a low-frequency field is that the ionization is sufficiently slow to be directly observable using analog detectors. Specifically, in experiments using radio-frequency irradiation of 90d rubidium Rydberg states, the atomic ionization could be

recorded in *real-time* by measuring the arrival of ionized electrons at a microchannel plate detector that was positioned at some distance from the ionization region. As shown in Fig. 3.3a, the ionization yield is not determined by the envelope of the radio-frequency pulse but is directly related to the oscillations of the electric field. A small fraction of the atoms ionize at the peak of every sufficiently intense half-cycle and are released into the continuum. In high harmonic generation, these electrons are subsequently accelerated by the intense laser field, and give rise to the formation of a train of attosecond pulses, with one attosecond pulse appearing every half-cycle of the driving laser.

The extremely non-linear dependence of the ionization rates on the instantaneous electric field strength suggests possibilities for control of the ionization and – possibly – the formation of isolated attosecond pulses in high harmonic generation. We have studied ionization of rubidium Rydberg states in two-color radio-frequency fields [49], where a second color was admitted to the experiment at a reduced intensity. Using a second color that was a harmonic of the frequency of the first color, the length of the electron bursts could be reduced and one of the two ionization bursts that occur every cycle could be made to disappear. And, as shown in Fig. 3.3b, using a second color that was incommensurate with the frequency of the first color, the number of ionization bursts within the pulse could be considerably limited. In the example shown in Fig. 3.3b, the fundamental pulse was a 250 nsec long 16-cycle (17.69 MHz) pulse. Upon addition of a second pulse with a carrier
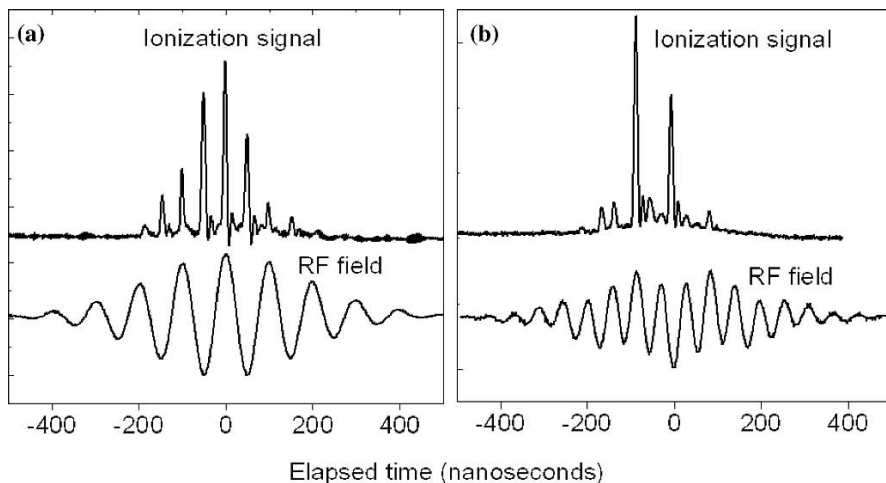

Fig. 3.3. a Ionization of 90d Rubidium Rydberg states by a 5 MHz RF field, showing that the ionization is governed by the real-time oscillations of the electric field and **b** by the superposition of a 17.69 MHz RF field (91% by energy) and a 5.14 MHz RF field (9% by energy), showing that the ionization during a significant number of half-cycles can be suppressed by using a second color with a frequency that is incommensurate with the fundamental

frequency of 5.14 MHz (at an intensity that was only 9% of the intensity of the first pulse), the ionization could be limited to two dominant bursts that were separated by 2 optical cycles. This last result is especially interesting, since it suggests that two-color high harmonic generation may be used to generate isolated attosecond laser pulses, either directly, or in combination with a time-dependent ellipticity of the driver laser [50, 51].

Recently we have performed calculations solving the time-dependent Schrödinger equation to assess the feasibility of isolated attosecond pulse formation in a two-color laser field [52]. Using a scaling of the wavelengths of the radio-frequency experiments, high harmonic generation in Ar was calculated in a two-color laser field, consisting of a 780 nm laser field that carried 91% of the intensity and a 2.68 μm laser field that carried 9% of the intensity. Isolated attosecond laser pulses could be generated starting from driver pulses that were as long as 19 femtoseconds (7 optical cycles). Interestingly, the mechanism for the formation of the isolated attosecond laser pulses not only involved two-color control over the ionization rates, but also over the electron trajectories in the continuum.

3.4 Photoionization in Optical Fields: The Generation and Characterization of Attosecond Laser Pulses

The generation of attosecond laser pulses in high-harmonic generation is a natural consequence of the physics discussed in Sects. 3.2 and 3.3. As discussed in Sect. 3.3, the ionization that launches the electron into the continuum is a highly non-linear phenomenon that will favor field maxima in the femtosecond driver laser. Following this ionization step, and in the spirit of the results presented in Sect. 3.2, the electrons will be accelerated by the oscillatory field of the laser and move along relatively well-defined trajectories that carry the electron back to the parent ion at well-defined times. Consequently, we expect the electron-parent ion recombination and the XUV production to occur only during a small portion of the optical cycle.

The frequency spectrum that is produced in high-harmonic generation is compatible with this expectation. Harmonics are formed over a broad frequency range, extending up to a cut-off that is given by $E_{\text{cut-off}} = I_{\text{p}} + 3.17 U_{\text{p}}$. As a result, there is sufficient bandwidth to support the formation of attosecond laser pulses. However, a characterization of the pulse duration requires both a knowledge of the harmonic spectral intensity distribution $|E(\omega)|$ and the frequency-dependent phase $\Phi(\omega)$ of the harmonics. We have performed an experiment characterizing the pulse duration of the harmonic emission using two-dimensional photoelectron imaging [6]. Two-color sidebands were generated in the photoionization of Ar by a combination of the harmonics and the fundamental color of the Ti:Sapphire laser. Both the strength and the angular distribution of the sidebands showed that in Ar 250 attosecond pulses were formed from the superposition of harmonics 11–21. Similar pulse durations

were obtained using Kr and Xe in the harmonic generation, although in the latter case the timing of the attosecond pulses with respect to the optical period of the driver was very different.

The observed differences for Ar and Xe as harmonic generation gas show that the experiment can not only be viewed as an experiment that characterizes the attosecond laser pulses, but is itself also an example of an experiment providing insight into strongly driven electron dynamics on sub-cycle timescales. According to the semi-classical description of harmonic generation that was sketched in the introduction and in agreement with our results on RF ionization in Sect. 3.3, ionization is predominately expected in the vicinity of field maxima of the driver laser. Integration of the classical equations of motion of the electron suggests that the attosecond pulses are then predominantly formed near zero crossings of the field of the driver laser [53]. Indeed, this is what we observed in our experiments for Ar and Kr. However, in the case of Xe the attosecond pulses show an offset of about one-quarter of a period compared to the anticipated generation time. There are two pos-
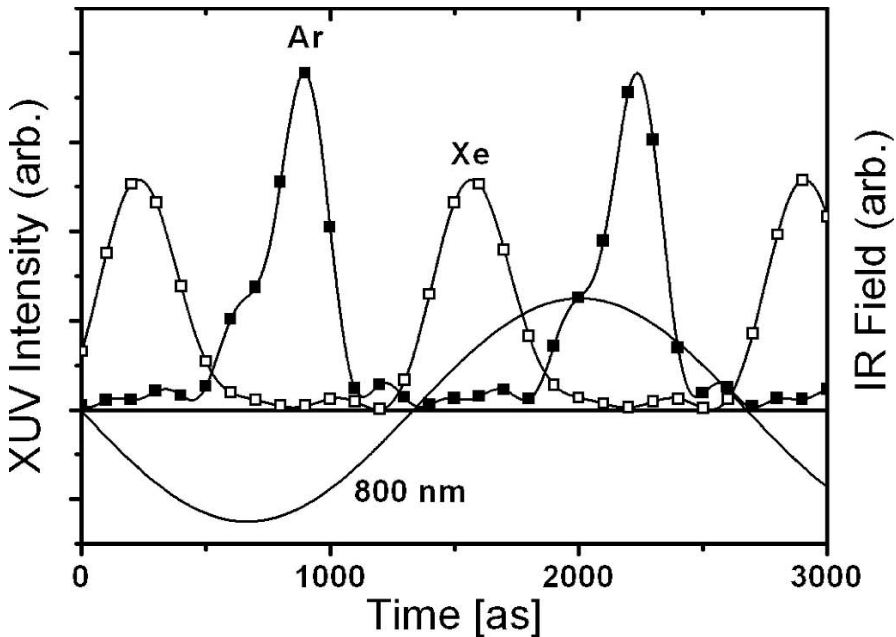

Fig. 3.4. Reconstructed attosecond XUV bursts for experiments where Ar and Xe were used as harmonic generation gas. The reconstruction of the XUV bursts was performed on the basis of harmonic phase differences that were determined by monitoring the yield of sideband photoelectrons as a function of XUV-IR time delay and harmonic amplitudes that were obtained from photoelectron spectra recorded in the absence of the IR dressing beam. Experiments that were performed using Kr gave results similar to the Ar results

sible explanations for this. First, the ionization process may not occur via the tunneling but via multi-photon ionization. Indeed, photoelectron kinetic energy measurements of Xe at 800 nm (using pulse durations and intensities similar to the ones used in our experiments) have revealed the importance of intermediate Rydberg states in the ionization process [54]. Secondly, there is more than one trajectory by means of which the acceleration and subsequent re-collision of the electron with the parent ion can occur. In HHG, the maximum re-collision energy $E_{\max}$ is obtained when the electron is ionized shortly after a field maximum of the generating laser at a delay $T_{\max} = 0.047\,T$, where T is the period of the driver laser [55]. If the electron is launched later than $T_{\max}$, the re-collision will occur slightly earlier with an energy $E_{\mathrm{short}} < E_{\max}$ (hence, the common designation of this trajectory as the "short trajectory"). By contrast, if ionization takes place before $T_{\max}$ then the electron moves along a so-called "long trajectory". Depending on the experimental conditions, either the short or long trajectory may dominate in an experiment.

3.5 Strongly Driven Electrons in Molecules

The dynamics of strongly-driven electrons on ultrafast timescales also lies at the basis of several phenomena in molecules. Among these, we have investigated dynamic alignment [26] and enhanced ionization in Coulomb explosions [27].

When molecules are placed at the focus of an intense laser field, they undergo so-called dynamic alignment. In this proces the most polarizable axis of a molecule aligns itself to the polarization axis of the laser. If the laser field is turned on and off very slowly, then the molecular axes slowly adapt to the laser field, and the alignment that occurs during the pulse disappears when the pulse is over [56]. However, if the laser pulse is turned on and off very quickly (on a timescale that is a small fraction of the rotational period of the molecule), then the laser excitation leads to the formation of a rotational wavepacket, and the molecule displays alignment both during and after the laser excitation pulse. In the latter case the alignment reoccurs under field-free conditions at revival times that are determined by the rotational constant(s) of the molecule. A few years ago evidence for this field-free alignment was obtained in our laboratory [57]. Iodine molecules were excited by pump laser pulses from a Ti:Sapphire femtosecond amplifier system that were stretched to durations of 2–10 picoseconds and focussed to an intensity high enough to induce a polarization in the molecule, yet low enough not to ionize it. At a variable time delay the molecules were furthermore exposed to a Fourier-Transform limited ($\sim$50 femtoseconds) probe laser pulse that was intense enough to (multiply) ionize the molecules, but too short to exert a substantial torque over the molecule. Fragments resulting from Coulomb explosion of the molecule were projected onto a two-dimensional velocity-map ion imaging detector [58]. As Fig. 3.5 shows, there is no preferential alignment of the

molecules along the pump laser polarization axis before the interaction of the molecule with the pump laser pulse (negative delays). Alignment sets in when the pump and probe laser pulses overlap near $\Delta t = 0$. The alignment reaches a maximum towards the end of the pump laser pulse and then disappears, due to a dephasing of the rotational wavepacket that is formed as a result of the pump laser interaction. However, at well-defined times given by the rotational constants of the molecule, the rotational wavepacket rephases, and a re-occurrence of the alignment is observed.

While the possibility to dynamically align molecules has become firmly established in the last few years, the electronic origin of the alignment force has not been directly observed yet. Quantum mechanically we understand the
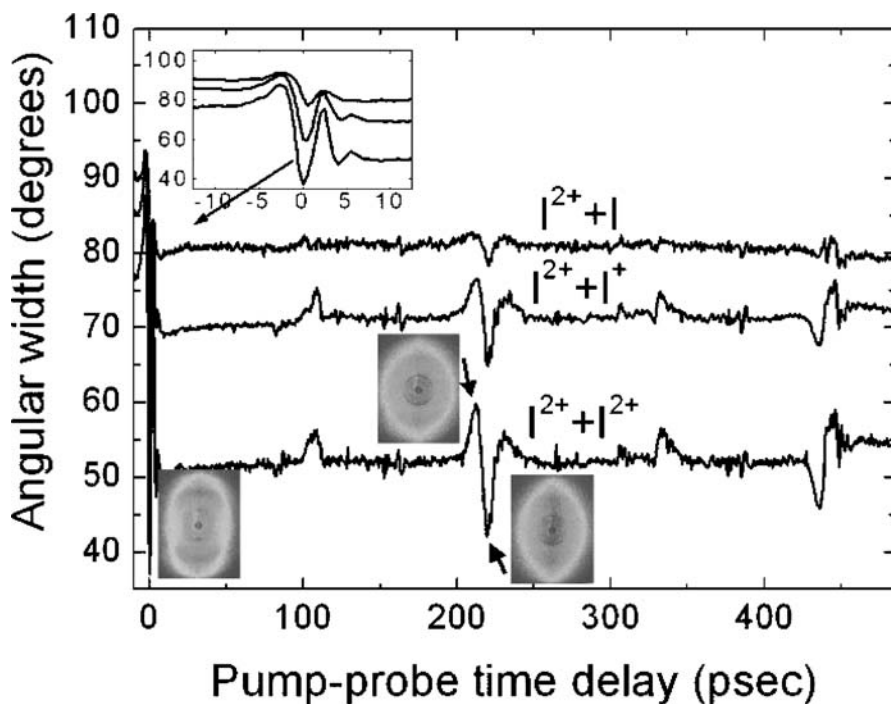

Fig. 3.5. Pump-probe time delay scan, showing the angular width of I^{2+} fragments belonging to the $I^{2+} + I$, the $I^{2+} + I^{+}$ and the $I^{2+} + I^{2+}$ Coulomb explosion channels, recorded using a 3.8 mJ 2.8 psec pump pulse to align the molecule and a 1.2 mJ 100 fsec probe pulse for the Coulomb explosion. The measurements show how the molecule becomes aligned of the molecule during the pump pulse (see *inset*) and how, following dephasing of the rotational wavepacket, the alignment re-occurs under field-free conditions at revival times that are determined by the rotational constant of I_2. Both the full revival after 440 psec, the half-revival after 220 psec and quarter-revivals after 110 and 330 psec can be distinguished. The images that are shown as insets show the raw data around zero pump-probe time delay and around the half-revival

occurrence of dynamic alignment in terms of the formation of a rotational wavepacket by means of a sequence of Raman transitions that couple different rotational energy levels of the ground state molecule. The Raman transitions represent a coupling of the ground electronic state of the molecule to one or more electronically excited states. The total electronic wavefunction of the molecule therefore transiently becomes a coherent superposition of ground and electronically excited states. This transient formation of an electronic wavepacket leads to a polarization of the molecule and the interaction of this polarization with the electric field of the laser generates the torque that forces the molecule to align along the polarization axis of the laser. Using an attosecond probe we may hope in the future to observe the motion of the electronic wavepacket directly. The motion of the electronic wavepacket may lead to time-dependent changes in the photoionization probability and in the kinetic and angular distribution of the photoelectron that can be measured once it is ionized. Furthermore, if the molecule becomes unstable upon ionization and dissociates into fragments, then the kinetic energy and angular distribution of these fragments may also depend on the location of the electron wavepacket at the time of ionization.

As mentioned above, intense femtosecond laser pulses can multiply ionize molecules. When this happens, the molecule usually becomes unstable and dissociates into two or more fragments, that repel eachother under the influence of Coulombic forces. Recently, we have performed an experiment comparing the Coulomb explosion of uracyl molecules ($C_4H_4N_2O_2$) following (1) the interaction of the molecule with an intense laser pulse or (2) a collision with energetic and highly-charged Xe-ions [59]. Remarkably, both experiments displayed very similar charge-state distributions for the various atomic and molecular fragments produced. However, the fragments that resulted from the laser-induced Coulomb explosion were formed with a fragment kinetic energy that was only about half of the kinetic energy that these fragments obtained following ion impact. The reason is that in a laser-induced Coulomb explosion a significant part of the molecular ionization occurs as the molecule is dissociating, around a time that the average internuclear distance has increased by approximately a factor 2. The so-called 'enhanced ionization' that occurs at this point is related to the localization of the electrons [27]. When the atoms in a molecule are close together (i.e. around the equilibrium geometry of the molecule), then the electrons occupy molecular orbitals. Later on, when the molecule disintegrates, the outer electrons localize on just one of the fragments. In the future, using an attosecond probe, we may be able to investigate this electron localization in real time.

3.6 Strongly Driven Electrons in Clusters

Interactions of clusters with intense laser fields have attracted considerable attention in the past few years. Clusters represent an interesting intermedi-

ate between gas phase and condensed phase research. The high local density of clusters allows for strong – bulk-like – energy absorption from an irradiating laser field, while the finite size of clusters eliminates relaxation of the deposited heat into bulk surrounding material. The efficient energy absorption leads to the production of highly charged and energetic ions [60], electrons with keV energies [61, 62] and soft X-ray radiation [28] with suitable wavelengths for applications in extreme-ultraviolet (EUV) lithography and microscopy [63].

We have performed optimal control [43] experiments and calculations, where the laser pulse shapes that lead to a maximization of the inner and outer ionization of the clusters have been determined. Here outer ionization refers to the number of electrons that leave the cluster, while inner ionization refers to the total number of electrons that are liberated from their parent atoms (taking into account that some of these electrons will remain bound by the positive charge that is left behind when electrons leave the cluster). In the experiment, the production of highly-charged ions resulting from the interaction of large Xe clusters ($N = 10^4$–10^6 atoms per cluster) with an intense laser field was monitored using detection of these ions with a time-of-flight mass spectrometer [64]. Adaptive pulse shaping under the control of a Genetic Algorithm (GA) [65] was used to optimize the production of Xe^{+M} ions ($M > 12$). As shown in Fig. 3.6, a dramatic increase in the production of these ions was obtained by using an optimized pulse shape, that consisted of a sequence of two pulses separated by a time delay that depended on the average cluster size and the peak laser intensity. Similar results were recently obtained by another group optimizing X-ray emission from Ar clusters [66].

In order to interpret the results of our experiments, optimal-control calculations were performed where a GA controlled 40 independent degrees of freedom in the laser pulses that were used in a molecular dynamics simulation of the laser-cluster interactions for Xe_N clusters with sizes ranging from 108 to 5056 atoms/cluster. These calculations, which are reported in detail elsewhere [67], showed optimization of the laser-cluster interactions by a sequence of as many as three laser pulses. Detailed inspection of the simulations revealed that the first pulse in this sequence initiates the cluster ionization and starts the expansion of the cluster, while the second and third pulse optimize two mechanisms that are directly related to the behaviour of the electrons in the cluster. We consistently observe that the second pulse in the three-pulse sequence arrives a time delay where the conditions for enhanced ionization are met. In other words, the second pulse arrives at a time where the ionization of atoms is assisted by the proximity of surrounding ions. The third peak is consistently observed at a delay where the collective oscillation of the quasi-free electrons in the cluster is $\pi/2$ out of phase with respect to the driving laser field. For a driven and damped oscillator this phase-delay represents an optimum for the energy transfer from the driving force to the oscillator.
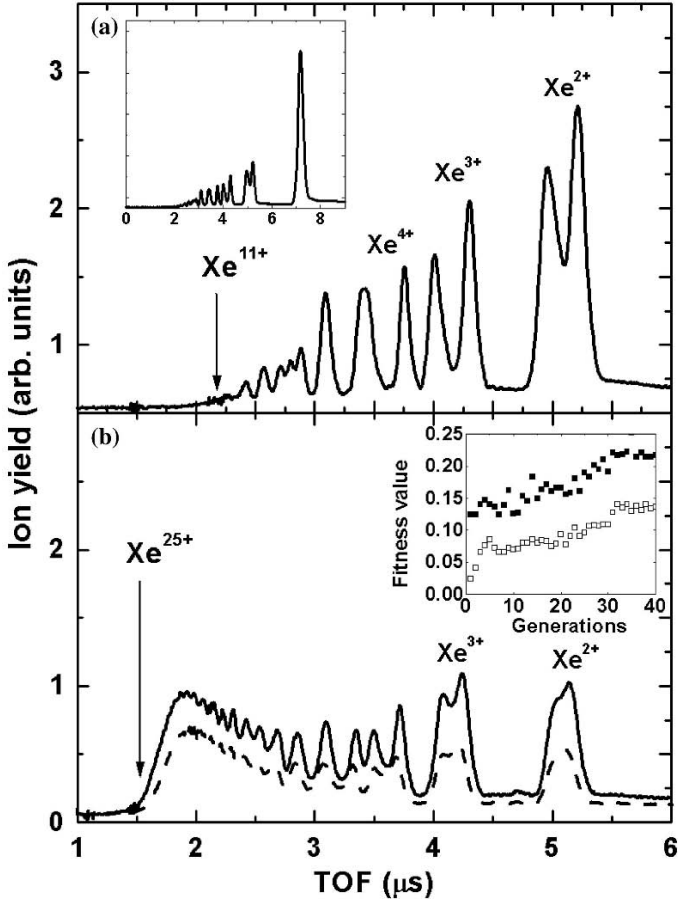
Fig. 3.6. Time-of-flight (TOF) traces for the interaction of Xe clusters ($N_{avg} = 1.6\ 10^4$) with a Fourier-Transform-limited 100 fs, 800 nm, $10^{15}\,\mathrm{W\,cm^{-2}}$ laser pulse **a**, the best pulse found by a Genetic Algorithm (GA) in an 80-parameter unrestricted optimization (**b**, *dashed line*) and the best pulse found in a restricted 3-parameter optimization (**b**, *solid line*). The best pulse found by the GA consists of a sequence of two 120 fs pulses, separated by 500 fs

3.7 Conclusions and Outlook

After several decades of highly succesful experimentation with femtosecond lasers that has allowed unravelling of atomic motion on femtosecond timescales, the recent development of attosecond techniques represents the starting point for efforts to study the motion of electrons in real time. The outcome of this effort will not be known for a number of years, but the astonishing progress that has been made in the last few years suggests that we may be very optimistic about the rewards from attosecond experiments yet

to come. In a matter of just a few years, the generation and characterization of attosecond pulses has gone from merely a concept to a stage where attosecond pulses can now almost routinely be generated and made available in experiments. As a result, the challenges facing attosecond science are shifting to practical issues like the availability of suitable beam delivery optics and conceptual questions, such as the choice of a suitable spectroscopy that relates the electron dynamics that one wishes to study to experimental observables that can be accessed in the laboratory.

In the present chapter we have emphasized the role of strongly driven electrons in the development of attosecond research. Along with the role of strongly driven electrons in high harmonic generation in atoms, we have discussed a number of phenomena that occur in molecules and clusters in strong laser fields where strongly driven electrons explain many of the observations that are made in experiments. Consequently, strongly driven electrons in atoms, molecules and clusters can be regarded as a collection of model systems that can be used in the next few years to develop attosecond science. As a result, the day may not be far, when attosecond pulses can be used to study what happens when an atom or a molecule absorbs just a single photon.

References

1. P. Agostini and L.F. DiMauro, Rep. Prog. Phys. **67**, 813 (2004). A. L'Huillier, L.-A. Lompré, G. Mainfray and C. Manus, in *Atoms in Intense Laser Fields* (edited by M. Gavrila and H.G. Muller, Academic Press, 1992), p. 139.
2. T. Brabec and F. Krausz, Rev. Mod. Phys. **72**, 545–591 (2000).
3. A. L'Huillier, L.-A. Lompré, G. Mainfray and C. Manus, in *Atoms in Intense Laser Fields* (edited by M. Gavrila and H.G. Muller, Academic Press, 1992), p. 139.
4. P.B. Corkum, Phys. Rev. Lett. **71**, 1994 (1993).
5. P.M. Paul, E.S. Toma, P. Breger, G. Mullot, F. Augé, Ph. Balcou, H.G. Muller and P. Agostini, Science **292**, 1689 (2001).

6. S.A. Aseyev, Y. Ni, L.J. Frasinski, H.G. Muller and M.J.J. Vrakking, Phys. Rev. Lett. **91**, 223902 (2003).
7. K. Varjú, Y. Mairesse, B. Carré, M.B. Gaarde, P. Johnsson, S. Kazamias, R. López-Martens, J. Mauritsson, K.J. Schafer, Ph. Balcou, A. L'Huillier and P. Salières, J. Mod. Opt. **52**, 379 (2005).
8. R.L. López-Martens, K. Varjú, P. Johnsson, J. Mauritsson, Y. Mairesse, P. Salières, M.B. Gaarde, K.J. Schafer, A. Persson, S. Svanberg, C.-G. Wahlström and A. L'Huillier, Phys. Rev. Lett. **94**, 033001 (2005).
9. M. Hentschel, R. Kienberger, Ch. Spielmann, G. A. Reider, N. Milosevic, T. Brabec, P.B. Corkum, U. Heinzmann, M. Drescher and F. Krausz, Nature **414**, 509 (2001).
10. R. Kienberger, E. Goulielmakis, M. Uiberacker, A. Baltuska, V. Yakovlev, F. Bammer, A. Scrinzi, Th. Westerwalbesloh, U. Kleineberg, U. Heinzmann, M. Drescher and F. Krausz, Nature **427**, 817 (2004).
11. A. Baltuska, Th. Udem, M. Uiberacker, M. Hentschel, E. Goulielmakis, Ch. Gohle, R. Holzwarth, V.S. Yakovlev, A. Scrinzi, T.W. Hänsch and F. Krausz, Nature **421**, 621 (2003).
12. M. Drescher, M. Hentschel, R. Kienberger, M. Uiberacker, V. Yakovlev, A. Scrinzi, T. Westerwalbesloh, U. Kleineberg, U. Heinzmann and F. Krausz, Nature **419**, 803 (2002).
13. A.V. Sokolov, D.R. Walker, D.D. Yavuz, G.Y. Yin and S.E. Harris. Phys. Rev. Lett. **87**, 033402 (2001).
14. S. Tanaka and Sh. Mukamel, Phys. Rev. Lett. **89**, 043001 (2002).
15. A.H. Zewail, J. Phys. Chem. **104**, 5660 (2000).
16. M. Wickenhauser, J. Burgdörfer, F. Krausz and M. Drescher, Phys. Rev. Lett. **94**, 023002 (2005).
17. C. Iaconis and I.A. Walmsley, Opt. Lett. **23**, 792 (1998).
18. R. Trebino, K.W. DeLong, D.N. Fittinghoff, J.N. Sweetser, M.A. Krumbügel, B.A. Richman and D.J. Kane, Rev. Sci. Instrum. **68**, 3277 (1997).
19. F. Quéré, J. Itatani, G.L. Yudin and P.B. Corkum, Phys. Rev. Lett. **90**, 073902 (2003).
20. T. Sekikawa, T. Kanai and S. Watanabe, Phys. Rev. Lett. **91**, 103902 (2003).
21. P. Kruit and F.H. Read, J. Phys. E **16**, 313 (1983).
22. A.J. Heck and D.W. Chandler, Annu. Rev. in Phys. Chem. **46** 335 (1995).
23. J. Ullrich, R. Moshammer, A. Dorn, R. Dörner, I. Ph.H. Schmidt and H. Schmidt-Böcking, Rep. Prog. Phys. **66**, 1463 (2003).
24. B. Sheehy and L.F. DiMauro, Annu. Rev. Phys. Chem. **47**, 465 (1996).
25. For a recent review, see W. Becker, F. Grasbon, R. Kopold, D.B. Miloševi, G.G. Paulus, and H. Walther, Adv. At., Mol., Opt. Phys. **48**, 35–98 (2002).
26. For a recent review, see H. Stapelfeldt and T. Seideman, Rev. Mod. Phys. **75**, 543 (2003).
27. J. Posthumus, Rep. Prog. Phys. **67**, 623 (2004).
28. T. Ditmire, T. Donnelly, A.M. Rubenchik, R.W. Falcone, and M.D. Perry, Phys. Rev. A **53**, 3379 (1996).
29. M.F. Kling, Ch. Siedschlag, A.J. Verhof, J.I. Khan, M. Schultze, Th. Uphues, Y. Ni, M. Uiberacker, M. Drescher, F. Krausz, and M.J.J. Vrakking, Science **312**, 246 (2006).
30. T. Remetter, P. Johnsson, K. Varju, Y. Ni, F. Lépine, E. Gustafsson, M. Kling, J. Khan, R. López-Martens, J. Mauritsson, M.B. Gaarde, K.J. Schafer, M.J.J. Vrakking, and A. L'Huillier, Nature Phys. **2**, 353 (2006).

31. C. Nicole, I. Sluimer, F. Rosca, M. Warntjes, F. Texier, F. Robicheaux, C. Bordas, and M.J.J. Vrakking, Phys. Rev. Lett. **85**, 4024 (2000).
32. Ch. Bordas, Phys. Rev. A **58**, 400 (1998).
33. C. Blondel, C. Delsart, and F. Dulieu, Phys. Rev. Lett. **77**, 3755 (1996).
34. V.D. Kondratovich and V.N. Ostrovsky, J. Phys.B: At. Mol. Phys. **17**, 1981 (1984); J. Phys. B: At. Mol. Phys. **17**, 2011 (1984), J. Phys. B: At. Mol. Phys. **23**, 21 (1990) and J. Phys. B: At. Mol. Phys. **23**, 3785 (1990).
35. C. Nicole, H.L. Offerhaus, M.J.J. Vrakking, F. Lépine and Ch. Bordas, Phys. Rev. Lett. **88**, 133001 (2002).
36. H.L. Offerhaus, C. Nicole, F. Lepine, C. Bordas, F. Rosca-Pruna and M.J.J. Vrakking, Rev. Sci. Instrum. **72**, 3245 (2001).
37. Ch. Bordas, F. Lépine, C. Nicole and M.J.J. Vrakking, Phys. Rev. A **68**, 012709 (2003).
38. F. Lépine, C. Bordas, C. Nicole and M.J.J. Vrakking, Phys. Rev. A **70**, 033417 (2004).
39. H.R. Reiss, Phys. Rev. A **22**, 1786 (1980).
40. M. Nisoli, S. De Silvestri, O. Svelto, R. Szipöcs, K. Ferenz, Ch. Spielmann, S. Sartania and F. Krausz, Opt. Lett. **22**, 522 (1997).
41. B. Schenkel, J. Biegert, U. Keller, C. Vozzi, M. Nisoli, G. Sansone, S. Stagira, S. De Silvestri and O. Svelto, Opt. Lett. **28**, 1987 (2003).
42. D. You, R.R. Jones, P.H. Bucksbaum and D.R. Dykaar, Opt. Lett. **18**, 290 (1993).
43. R.S. Judson and H. Rabitz, Phys. Rev. Lett. **68**, 1500 (1992).
44. C. Bardeen, V. Yakovlev, K. Wilson, S. Carpenter, P. Weber and W. Warren, Chem. Phys. Lett. **280**, 151 (1997).
45. A. Assian, T. Baumert, M. Bergt, T. Brixner, B. Kiefer, V. Seyfried, M. Strehle and G. Gerber, Science **282**, 919 (1998).
46. G.G. Paulus, F. Grasbon, H. Walther, P. Villoresi, M. Nisoli, S. Stagira, E. Priori and S. De Silvestri, Nature **414**, 182 (2001).
47. G. Sansone, C. Vozzi, S. Stagira, M. Pascolini, L. Poletto, P. Villoresi, G. Tondello, S. De Silvestri and M. Nisoli, Phys. Rev. Lett. **92**, 113904 (2004).
48. A. Gürtler, F. Robicheaux, M.J.J. Vrakking, W.J. van der Zande and L.D. Noordam, Phys. Rev. Lett. **92**, 063901 (2004).
49. S. Zamith, Y. Ni, A. Guertler, L.D. Noordam, H.G. Muller and M.J.J. Vrakking, Opt. Lett. **29**, 2303 (2004).
50. P.B. Corkum, N.H. Burnett and M.Y. Ivanov, Opt.Lett. **19**, 1870(1994).
51. R. López-Martens, J. Mauritsson, P. Johnsson, A. L'Huillier, O. Tcherbakoff, A. Zaïr, E. Mével and E. Constant, Phys. Rev. A **69**, 053811 (2004).
52. Ch. Siedschlag, H.G. Muller and M.J.J. Vrakking, Laser Physics **15**, 916 (2005).
53. Ph. Antoine, A. L'Huillier and M. Lewenstein, Phys. Rev. Lett. **77**, 1234 (1996).
54. V. Schyja, T. Lang and H. Helm, Phys. Rev. A **57**, 3692 (1998).
55. P.B. Corkum, Phys. Rev. Lett. **71**, 1994 (1993).
56. J.J. Larsen, H. Sakai, C.P. Safvan, I. Wendt-Larsen and H. Stapelfeldt, J. Chem. Phys. **111**, 7774 (1999).
57. F. Rosca-Pruna and M.J.J. Vrakking, Phys. Rev. Lett. **87**, 153902 (2001).
58. A.T.J.B. Eppink and D.H. Parker, Rev. Sci. Instrum. **68**, 3477 (1997).
59. T. Schlathölter, R. Hoekstra, S. Zamith, Y. Ni, H.G. Muller and M.J.J. Vrakking, Phys. Rev. Lett. **94**, 233001 (2005).
60. T. Ditmire, J.W.G. Tisch, E. Springate, M.B. Mason, N. Hay, R.A. Smith, J. Marangos and M.H.R. Hutchinson, Nature **386**, 54 (1997).

61. Y.L. Shao, T. Ditmire, J.W.G. Tisch, E. Springate, J.P. Marangos and M.H.R. Hutchinson, Phys. Rev. Lett. **77**, 3343 (1996).
62. E. Springate, S.A. Aseyev, S. Zamith and M.J.J. Vrakking, Phys. Rev. A **68**, 053201 (2003).
63. D. Attwood, *Soft X-rays and extreme ultraviolet radiation,* Cambridge University Press (1999).
64. S. Zamith, T. Martchenko, Y. Ni, S.A. Aseyev, H.G. Muller and M.J.J. Vrakking, Phys. Rev. A **70**, 011201 (2004).
65. The genetic algorithm used in these calculations was the micro-GA, published by D.L. Carroll and is available at http://cuaerospace.com/carroll/ga.html
66. A.S. Moore, K.J. Mendham, D.R. Symes, J.S. Robinson, E. Springate, M.B. Mason, R.A. Smith, J.W.G. Tisch, J.P. Marangos, Appl. Phys. B **80**, 101 (2005)
67. T. Martchenko, S. Zamith, Ch. Siedschlag, H.G. Muller, and M.J.J. Vrakking, Phys. Rev. A **72**, 053202 (2005).

4 *S*-Matrix Theory
of Nonsequential Double Ionization

C. Figueira de Morisson Faria[1], X. Liu[2], and W. Becker[3]

[1] Centre for Mathematical Science, City University, London EC1V OHB, UK
    C.F.M.Faria@city.ac.uk
[2] Wuhan Institute of Physics and Mathematics,
    Chinese Academy of Sciences, Wuhan 430071, P.R. China
    xjliu@wipm.ac.cn
[3] Max-Born-Institut, 12489 Berlin, Germany
    wbecker@mbi-berlin.de

Summary. Laser-induced double and multiple ionization of atoms may proceed either sequentially or nonsequentially in one coherent process. For near-infrared lasers of moderate intensity (10^{14} to 10^{15} W/cm^2), the physical mechanism of the coherent process is inelastic rescattering of a first-ionized electron off its parent ion. The quantum-mechanical S-matrix description of this process is reviewed. Momentum distributions of the ejected electrons and the doubly charged ion are calculated and compared with the experimental data. Their shape is found to be determined by the effective electron-electron interaction, by which the recolliding first electron ejects the up to this time bound second electron. The significance of the final-state electron-electron interaction is assessed. The underlying classical dynamics are elucidated. Recent experiments with ultra-short phase-stabilized laser pulses are discussed. Nonsequential multiple ionization is modeled by assuming that the returning electron thermalizes with a certain number of bound electrons, and the corresponding thermalization time is estimated.

4.1 Introduction

Atoms exposed to intense laser fields may be multiply ionized. Along the simplest pathway, this happens step by step. However, already more than twenty years ago, evidence was mounting for the contribution of a different pathway whereby two electrons are freed in one coherent process [1]. Clearly, this requires that the participating two electrons be correlated. Regardless of the detailed mechanism, this process is referred to as nonsequential double ionization (NSDI); for reviews, see [2].

The information provided by the highly differential cross sections that have been obtained with the help of the reaction-microscope technique [3–5] has largely terminated the debate about the physical mechanism responsible for NDSI: For the situation explored in most experiments, that is, high-intensity low-frequency lasers typified by the titanium-sapphire laser ($\lambda \approx 800$ nm) at 10^{14} to 10^{15} W cm^{-2}, consensus has developed that NSDI is caused by the rescattering mechanism: an electron that is freed by tunneling

ionization is driven by the laser field into a recollision with its parent ion. This is the same mechanism that is responsible, for example, for high-order harmonic generation and high-order above-threshold ionization [6]. Exactly how the up to the recollision inactive electron is freed is less clear and appears to depend, moreover, on the specific atom: the rare gases neon on the one hand and helium and argon on the other display distinctly different behavior [2].

The fact that the recollision pathway appears to be the first stage of NSDI will make possible future investigations that will explore the temporal evolution of the ionization dynamics. These rely on the fact that the time interval within the laser cycle during which the first electron is driven into the recollision is rather narrow. It is revealed by the momentum of the doubly charged ion, which is measured by the reaction microscope [7]. This technique, referred to as "streaking", has already been employed to elucidate various features of the single-ionization dynamics [8].

Various theoretical approaches have tried to advance the understanding of NSDI. The solution of the time-dependent Schrödinger equation in one spatial dimension has provided a great deal of insight [9], but in three spatial dimensions it is extremely demanding and, in any event, its applicability is restricted to the simplest rare-gas atom, viz. helium [10]. Classical-trajectory methods that pursue electrons injected into the continuum by tunneling ionization have successfully reproduced many features of the data [11]. It is also possible, for a given scenario of how NSDI evolves, to identify the leading Feynman diagrams that contribute to the transition amplitude [12] (this work is reviewed in [13]) and to compute them by various methods [14–17]. This review is concerned with the latter approach, which is fully quantum mechanical from the outset, but suggests a straightforward classical limit, which is very easy to compute. The latter has been shown to reproduce the quantum results with high accuracy provided the laser intensity is high enough [18].

In Sect. 4.2 we introduce the basic rescattering–impact-ionization S-matrix element whose detailed investigation is at the focus of this review. In Sect. 4.2.1 we sketch its evaluation with saddle-point methods. This leads to a discussion of the classical kinematics underlying the S-matrix description. Various classical concepts related to the "simple-man model" are also briefly reviewed in this section. We also draw attention to the fact that the S-matrix element depends on the gauge used in coupling the charged particles to the laser field. In Sects. 4.2.3 and 4.2.4 we briefly discuss other scenarios for NSDI. The consequences of the choice of the crucial electron–electron interaction by which the returning electron ejects the bound electron is reviewed in Sect. 4.3. Further possible refinements of the theory include the exact introduction of electron–electron repulsion in the final state (Sect. 4.4) and the detailed consideration of the initial bound states (Sect. 4.5). The classical limit of the S-matrix element considered is discussed and compared with the fully quantum-mechanical results in Sect. 4.6. We then make use of the classical description in the discussion of NSDI by few-cycle pulses (Sect. 4.7)

and nonsequential *multiple* ionization (Sect. 4.8). Throughout the paper, we make frequent contact with experimental results.

4.2 The *S*-Matrix Element
of the Rescattering–Impact-Ionization Scenario

In the rescattering scenario, NSDI is initiated by one electron tunneling to freedom through the barrier created by the binding potential and the scalar potential of the intense laser field. When the electron is driven back to its parent ion by the oscillating laser field, it may in the recollision process dislodge another electron (or several electrons). The Feynman diagram that describes the simplest such mechanism is shown in panel (a) of Fig. 4.1: the returning electron frees the bound electron through a single interaction mediated by the potential V_{12}. The corresponding transition amplitude is

$$M_{\boldsymbol{p_1 p_2}} = -\int_{-\infty}^{\infty} \mathrm{d}t \int_{-\infty}^{t} \mathrm{d}t' \langle \psi_{\boldsymbol{p_1 p_2}}^{(\mathrm{V})}(t) | V_{12} U_1^{(\mathrm{V})}(t,t') V_1 U_2^{(0)}(t,t') | \psi_0(t') \rangle \,,$$

(4.1)

where V_1 and $U_1^{(\mathrm{V})}(t,t')$ denote the atomic binding potential and the Volkov time-evolution operator acting on the first electron, $U_2^{(0)}(t,t')$ is the field-free propagator acting on the second electron, and V_{12} is the electron–electron interaction through which the second electron is freed by the first. For the initial bound state $|\psi_0(t')\rangle$, a product of one-electron states $|\psi_0^{(n)}(t')\rangle = \mathrm{e}^{\mathrm{i}|E_{0n}|t'}|\psi_0^{(n)}\rangle$ with ionization potentials $|E_{0n}|$ is adopted. In this section, the final electron state with asymptotic momenta $\boldsymbol{p}_1$ and $\boldsymbol{p}_2$ is taken as the symmetrized[4] product state of one-electron Volkov states[5],

$$\langle \boldsymbol{r} | \psi_{\boldsymbol{p}}^{(\mathrm{V})}(t) \rangle = (2\pi)^{-3/2} \exp\{\mathrm{i}[\boldsymbol{p} + \boldsymbol{A}(t)] \cdot \boldsymbol{r}\} \exp\left(\frac{-\mathrm{i}}{2} \int^{t} \mathrm{d}\tau [\boldsymbol{p} + \boldsymbol{A}(\tau)]^2\right).$$

(4.2)

We use the length gauge and employ atomic units throughout. Below, we will also consider a two-electron Volkov state, which exactly incorporates the Coulomb repulsion between the two electrons [22]. The physical assumptions underlying the amplitude (4.1) correspond to the so-called strong-field approximation (SFA), which was developed for strong-field ionization [23, 24] and high-order harmonic generation [25]. Briefly, for atomic bound states their interaction with the laser field is neglected, and for continuum states their interaction with the atomic (or ionic) binding potential. A systematic derivation of the amplitude (4.1) can be found in [12].

---

[4] For a discussion of symmetry vs. antisymmetry if spin is included, see [19, 20].

[5] A Volkov state is obtained from the solution of the time-dependent Schrödinger equation for a free particle in an external plane-wave laser field. Such states were first derived by Volkov, in a relativistic context [21].
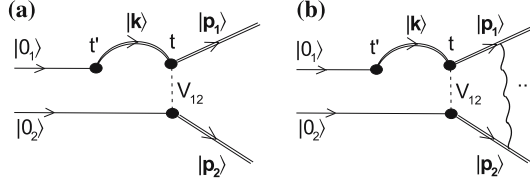
Fig. 4.1. Feynman diagrams corresponding to the transition amplitude (4.1), **a** without and **b** with electron–electron repulsion between the two electrons in the final state. The *vertical wavy line* and the *dots* in **b** indicate the Coulomb interaction, which is exactly accounted for by the two-electron Volkov solution. The *dashed vertical line* represents the electron–electron interaction V_{12} by which the second electron is set free

For the computation of the amplitude (4.1), the Volkov time-evolution operator is usually expanded in terms of the Volkov states (4.2),

$$U^{(V)}(t,t') = \int d^3k |\psi_{\boldsymbol{k}}^{(V)}(t)\rangle\langle\psi_{\boldsymbol{k}}^{(V)}(t')\,|\,. \tag{4.3}$$

As a result, the amplitude (4.1) has the form

$$M_{\boldsymbol{p}} = -\int_{-\infty}^{\infty} dt \int_{-\infty}^{t} dt' \int d^3k\, V_{\boldsymbol{pk}} V_{\boldsymbol{k}0} \exp[iS_{\boldsymbol{p}}(t,t',\boldsymbol{k})]\,, \tag{4.4}$$

with the action

$$S_{\boldsymbol{p}}(t,t',\boldsymbol{k}) = -\frac{1}{2}\left[\sum_{n=1}^{2}\int_{t}^{\infty} d\tau[\boldsymbol{p}_n + \boldsymbol{A}(\tau)]^2 + \int_{t'}^{t} d\tau[\boldsymbol{k} + \boldsymbol{A}(\tau)]^2\right] + |E_{01}|t' + |E_{02}|t\,. \tag{4.5}$$

Here $\boldsymbol{A}(t)$ denotes the vector potential of the laser field, $\boldsymbol{p} \equiv (\boldsymbol{p}_1, \boldsymbol{p}_2)$ the final electron momenta, and $\boldsymbol{k}$ the drift momentum of the first electron in between ionization and recollision. The binding potential V_1 of the first electron and the electron–electron interaction V_{12} enter (4.4) through their form factors

$$V_{\boldsymbol{pk}} = \langle\boldsymbol{p}_2 + \boldsymbol{A}(t), \boldsymbol{p}_1 + \boldsymbol{A}(t)|V_{12}|\boldsymbol{k} + \boldsymbol{A}(t), \psi_0^{(2)}\rangle \tag{4.6}$$

and

$$V_{\boldsymbol{k}0} = \langle\boldsymbol{k} + \boldsymbol{A}(t')|V_1|\psi_0^{(1)}\rangle\,. \tag{4.7}$$

Various choices have been made for the binding potential V_1 (and the corresponding wave functions) and the interaction V_{12}, which will be discussed below. If the former is described by a regularized zero-range potential so that $V_1(\boldsymbol{r}) \sim \delta(\boldsymbol{r})(\partial/\partial r)r$ and the latter by a three-body contact potential $V(\boldsymbol{r}_1, \boldsymbol{r}_2) \sim \delta(\boldsymbol{r}_1 - \boldsymbol{r}_2)\delta(\boldsymbol{r}_2)$, then the amplitude (4.1) can be reduced

to a one-dimensional quadrature involving Bessel functions [26]. Most of the time, for the binding potential V_1 a Coulomb potential and for the wave functions $\psi_0^{(i)}(\boldsymbol{r})$ ($i = 1, 2$) ground-state hydrogenic wave functions have been adopted, while different forms of the interaction V_{12} have been investigated. This will be discussed in Sect. 4.3.

4.2.1 Saddle-Point Approximations and Basic Concepts

For arbitrary potentials, given the low frequencies and high intensities employed in current experiments, for the numerical evaluation of the amplitude (4.1) in the form (4.4) the method of steepest descent [also known as the saddle-point approximation (SPA)] is the method of choice. Thus, we must determine the values of $\boldsymbol{k}$, t', and t for which the action $S_{\boldsymbol{p}}(t, t', \boldsymbol{k})$ is stationary, so that its partial derivatives with respect to these variables vanish. This condition gives the equations

$$[\boldsymbol{k} + \boldsymbol{A}(t')]^2 = -2|E_{01}| \ , \tag{4.8a}$$

$$\sum_{n=1}^{2} [\boldsymbol{p}_n + \boldsymbol{A}(t)]^2 = [\boldsymbol{k} + \boldsymbol{A}(t)]^2 - 2|E_{02}| \ , \tag{4.8b}$$

$$\int_{t'}^{t} \mathrm{d}\tau \, [\boldsymbol{k} + \boldsymbol{A}(\tau)] = 0 \ . \tag{4.8c}$$

Equations (4.8a) and (4.8b) express energy conservation at the ionization and rescattering times, respectively, while (4.8c) determines the intermediate momentum of the first electron so that it returns to the ion. Obviously, the solutions t'_s ($s = 1, 2, \dots$) of (4.8a) cannot be real. Hence, t_s and $\boldsymbol{k}_s$ are complex, too.

In the standard SPA, the action (4.5) in the matrix element (4.4) is expanded to second order about the solutions to the saddle-point equations (4.8), whereupon the integrations can be carried out with the result

$$M^{(\mathrm{SPA})} = \sum_s A_s \exp(\mathrm{i}S_s) \ , \tag{4.9a}$$

$$S_s = S_{\boldsymbol{p}}(t_s, t'_s, \boldsymbol{k}_s) \ , \tag{4.9b}$$

$$A_s = (2\pi\mathrm{i})^{5/2} \frac{V_{\boldsymbol{p}\boldsymbol{k}_s} V_{\boldsymbol{k}_s 0}}{\sqrt{\det S_{\boldsymbol{p}}''(t, t', \boldsymbol{k})|_s}} \ . \tag{4.9c}$$

Here the index s runs over the *relevant* saddle points, those that are visited by an appropriate deformation of the real integration contour, which is the real five-dimensional $(t, t', \boldsymbol{k})$ space, to complex values, and $S_{\boldsymbol{p}}''(t, t', \boldsymbol{k})|_s$ denotes the five-dimensional matrix of the second derivatives of the action (4.5) with respect to t, t' and $\boldsymbol{k}$, evaluated at the saddle points. The time dependence of the form factors (4.6) and (4.7) is considered as slow, unless stated otherwise (see Sect. 4.5 and [27]).

The SPA requires that the various saddle points be well separated. This is not always satisfied in the present case nor in intense-laser atom problems, in general. In order to see this, we must have a closer look at the solutions of the saddle-point equations (4.8).

The Classically Allowed Regime

Equation (4.8b) describes energy conservation in the rescattering process. From the point of view of the first electron, rescattering is inelastic, since it donates energy to the second electron. Let us ignore, for the moment, the ionization potential $|E_{01}|$ and consider linear polarization. Then, $\boldsymbol{k} = -\boldsymbol{A}(t')$, and $\boldsymbol{k}$ and t' are real. For given t', (4.8a) and (4.8c) then yield the rescattering time t and the momentum $\boldsymbol{k}$. In the space of the final momenta $\boldsymbol{p} = (\boldsymbol{p}_1, \boldsymbol{p}_2)$, (4.8b) is the equation of the surface of a six-dimensional sphere with its center at $(-\boldsymbol{A}(t), -\boldsymbol{A}(t))$ and its squared radius given by $[\boldsymbol{k} + \boldsymbol{A}(t)]^2 - 2|E_{02}|$. We only consider times t' such that the latter is positive. Then all possible electron momenta $\boldsymbol{p}$ that are classically accessible in the process where the first electron is ionized at the time t' are located on the surface of this sphere.

The union of all these spheres upon variation of the ionization time t' contains all final electron momenta that are in this sense classically accessible. Below, we will frequently refer to it as the "classically allowed region". Leaving this region along any path in the $(\boldsymbol{p}_1, \boldsymbol{p}_2)$ space, the NSDI yield experiences a sharp "cutoff". Outside the classically allowed region, quantum mechanics allows a nonzero yield which, however, decreases exponentially with increasing distance from its boundary. Formally, this is accomplished by the fact that the exact solutions of the saddle-point equations (4.8), which are always complex, exhibit rapidly increasing imaginary parts [28].

Saddle-Point Solutions Come in Pairs

Since the saddle-point equations (4.8) are real, for any given solution its complex conjugate is a solution as well. Let us consider a laser field represented by an infinitely extended monochromatic plane wave with period T. For given $\boldsymbol{p}_1$ and $\boldsymbol{p}_2$ and for the rescattering time $\operatorname{Re} t$ restricted to some period of the field, say $nT < \operatorname{Re} t \le (n+1)T$, there are infinitely many solutions whose ionization times $\operatorname{Re} t'$ extend further and further into the past $(\operatorname{Re} t' < \operatorname{Re} t)$. A general classification of these solutions and their significance for ATI and NSDI can be found in [29]. The solutions generally come in pairs (plus their complex conjugates); for a general discussion of this issue, see [30]. Here, we will consider the pair of solutions $t_s, t'_s, \boldsymbol{k}_s$ $(s = i, j)$ having the shortest "travel times" $\operatorname{Re}(t_s - t'_s)$. Let us suppose that inside the classical region the solutions $s = i, j$ (rather than their complex conjugates) are the relevant solutions as defined above so that they have to be included into the sum (4.9a). Usually (but not always [29]), the contributions of the other pairs can be neglected. Outside the classical region,

with increasing distance from its boundary both solutions of the pair develop quickly increasing imaginary parts, and one or the other must be discarded from the sum lest it explode exponentially [30]. This transition occurs very rapidly. It is illustrated in Fig. 4.2, which shows that the two saddle points approach each other very closely near the classical cutoff. Actually, Fig. 4.2 is for the closely related but simpler case of ATI. Corresponding illustrations for NSDI are discussed in [28]. The procedure of discarding one solution at some point is to some extent arbitrary and may lead to the artifact of a spike in the yield. This is due to the fact that the SPA is not applicable when two solutions approach each other too closely.

A convenient solution to this problem is provided by a certain uniform approximation [30], which is built on pairs of solutions and automatically takes care of the "discarding". The result requires the same input as (4.9), namely the action and its second derivatives at the saddle points, and is hardly more complicated. Within the classically allowed region, it is

$$M_{i+j} = \sqrt{2\pi\Delta S/3} \exp(\mathrm{i}\bar{S} + \mathrm{i}\pi/4) \left\{ \bar{A}[J_{1/3}(\Delta S) + J_{-1/3}(\Delta S)] \right.$$
$$\left. + \Delta A[J_{2/3}(\Delta S) - J_{-2/3}(\Delta S)] \right\}, \qquad (4.10)$$
$$\Delta S = (S_i - S_j)/2, \qquad \bar{S} = (S_i + S_j)/2 ,$$
$$\Delta A = (A_i - \mathrm{i}A_j)/2, \qquad \bar{A} = (\mathrm{i}A_i - A_j)/2 .$$

The noninteger Bessel functions have to be analytically continued when the parameters move into the nonclassical region. For details we refer to [30].
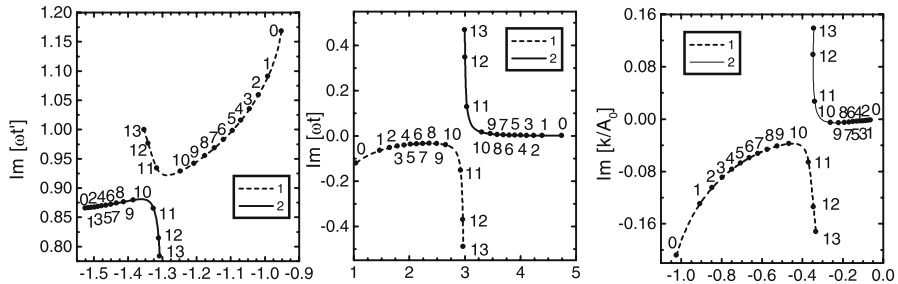

Fig. 4.2. Complex saddle points t'_s (*left panel*), t_s (*middle panel*), and k_{xs} ($s = i, j$) (*right panel*) for the pair of solutions having the shortest travel times as discussed in the text. The figure is for ATI, for a Keldysh parameter of $\gamma = 0.975$, and emission parallel to the laser field. The panels present the paths in the complex plane that are followed by the saddle points as a function of the final energy of the electron at the detector, which is indicated by the numbers (in multiples of U_p). The figure shows how the saddle points of a pair approach each other very closely near the classical cutoff at $10\,U_p$, which is the classical cutoff of the ATI energy spectrum. The contribution of the orbit that is *drawn dashed* has to be dropped after the cutoff. From [30]

Classical Cutoffs

If in (4.8a) the first ionization potential E_{01} is neglected, the electron starts its orbit in the continuum with an initial velocity $\boldsymbol{v}(t') \equiv \boldsymbol{k} + \boldsymbol{A}(t') = \boldsymbol{0}$ and t, t', and $\boldsymbol{k}$ are all real inside the classically allowed region. The classical boundary then is characterized by the fact that the two solutions of the afore-mentioned pair merge. (There are no such real solutions outside the classically allowed region.) This can be exploited to obtain (approximate) closed formulas for the cutoffs (corresponding to the well known cutoff $|E_0| + 3.17 U_p$ for high-order harmonic generation); see [31].

Electron Kinematics in the Laser Field: The "Simple-Man Model"

An electron released at the time t with zero velocity in a laser field with vector potential $\boldsymbol{A}(t)$, such that outside the laser pulse $\boldsymbol{A}(-\infty) = \boldsymbol{A}(\infty) = \boldsymbol{0}$, will reach the detector (outside the pulse) with momentum

$$\boldsymbol{p} = -\boldsymbol{A}(t) \ . \tag{4.11}$$

This simple relation follows from the fact that in a laser field that only depends on time the electron velocity is given by $\boldsymbol{v}(t) \equiv \boldsymbol{p} + \boldsymbol{A}(t)$ with constant $\boldsymbol{p}$. If the temporal average of the vector potential vanishes, $\langle \boldsymbol{A} \rangle_t = \boldsymbol{0}$, then $\boldsymbol{p}$ is the drift momentum of the electron, which is conserved when the laser pulse leaves the electron behind. The relation (4.11) sets the benchmarks for the electron and ion spectra observed in NSDI. For tunneling ionization, it implies that the electron's momentum at the detector is bound by $|\boldsymbol{p}| \leq \max_t |\boldsymbol{A}(t)| = 2\sqrt{U_p}$. For NSDI, higher momenta are classically possible, since the returning electron generally has some energy left after it dislodged the bound electron and may share it with the latter. The situation easiest to analyze is when the energy of the returning electron is just sufficient to remove the bound electron. In this case, both electrons will be released into the continuum with zero kinetic energy near a zero crossing of the electric field (since an electron returning around this time has maximal energy). Both electrons then will reach the detector with momenta near $2\sqrt{U_p}$. If the momentum of the laser photons is small enough that it can be ignored, momentum conservation implies

$$P_{\max} = 4\sqrt{U_p} \tag{4.12}$$

for the momentum of the doubly ionized ion. For higher intensities, such that the energy of the returning electron is amply sufficient to accomplish the second ionization, the above values roughly predict the *centers* of the electron and the ion momentum distributions, as will be seen below.

The Choice of Gauge

The strong-field approximation, on which the present formalism relies, is not gauge invariant; see. e.g. [32]. This problem has been present not only for

NSDI, but for all strong-field phenomena, such as above-threshold ionization and high-order harmonic generation, when they are treated via the SFA. In the nonrelativistic regime where the long-wavelength approximation can be used, the laser-matter interaction operator is $\boldsymbol{r} \cdot \boldsymbol{E}(t)$ in length gauge and $\hat{\boldsymbol{p}} \cdot \boldsymbol{A}(t) + \frac{1}{2}\boldsymbol{A}^2(t)$ in velocity gauge. Of the seminal papers, [23] employed length gauge while [24] used velocity gauge. In NSDI *S*-matrix calculations, references [14] rely on velocity gauge and [16, 17] on length gauge. Only for contact potentials are identical results obtained in different gauges. For an electron bound by a short-range potential (as is the case for a negative ion), comparison of the SFA with the numerical solution of the time-dependent Schrödinger equation has shown that in this case the length gauge yields superior results [32, 33].

For the *S*-matrix calculations of NSDI, the question of which gauge to use within the SFA is open. The difference between the two gauges enters via the spatial part of the Volkov solution (4.2), which is $\exp\{i[\boldsymbol{p} + \boldsymbol{A}(t)] \cdot \boldsymbol{r}\}$ in length gauge versus $\exp\{i\boldsymbol{p} \cdot \boldsymbol{r}\}$ in velocity gauge. Thus, in length gauge, the form factors (4.6) and (4.7) depend on the *instantaneous momenta* the time of rescattering and ionization while in velocity gauge they depend on the *drift momenta*. Specifically, in (4.6), the $\boldsymbol{A}(t)$'s are absent in velocity gauge, which invalidates the mechanism described below equation (4.21). This leads to momentum distributions that, in comparison with length gauge, are more concentrated near the diagonal $p_{1\parallel} = p_{2\parallel}$ and the origin $p_{1\parallel} = p_{2\parallel} = 0$ [14].

4.2.2 Ion-Momentum Distributions

The reaction-microscope technique is capable of measuring a fully (sixfold) differential cross section, by detecting the three-dimensional momenta of two particles of opposite charge, viz. the ion and one electron. Such a fully differential measurement was recently accomplished [7]. However, the very first experiments were content with recording the NSDI yield as a function of two momentum components of the ion, one parallel ($P_\parallel$) and one transverse ($P_\perp$) to the linearly polarized laser field, while the second transverse component ($P_{\perp,2}$) was integrated over. In terms of the amplitude (4.1), this corresponds to the momentum distribution

$$F(P_\parallel, P_\perp) = \int dP_{\perp,2} \int d^3\boldsymbol{p}_1 d^3\boldsymbol{p}_2 \delta(\boldsymbol{P} - \boldsymbol{p}_1 - \boldsymbol{p}_2)|M_{\boldsymbol{p}_1 \boldsymbol{p}_2}|^2 . \qquad (4.13)$$

Figure 4.3 shows such a distribution evaluated for the conditions of [4]. In the calculation, all potentials were taken as contact potentials. As expected from (4.12), the ion-momentum distribution peaks near $P_{\max} = 5.3$ a.u., $P_\perp = 0$. Electrons can acquire momenta higher than allowed by (4.11) for two reasons: (i) they can start with a nonzero velocity, and (ii) quantum mechanics allows momenta in excess of (4.11). By overall momentum con-

servation, the ion momentum then may also exceed the bound (4.12) and, indeed, Fig. 4.3 shows that it does.

Figure 4.4 exhibits distributions of the longitudinal component of the ion momentum for argon, helium, and neon, calculated under the same conditions as Fig. 4.3 for various laser intensities. It illustrates a general tendency of the
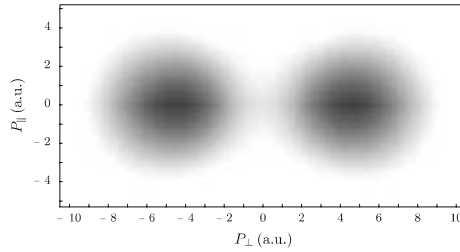

Fig. 4.3. Linear-scale density plot of the distribution of the ion momentum $P = (P_\parallel, P_\perp)$ in nonsequential double ionization of neon at $8 \times 10^{14}\,\mathrm{W/cm^2}$ and $\hbar\omega = 1.55\,\mathrm{eV}$. From [26]
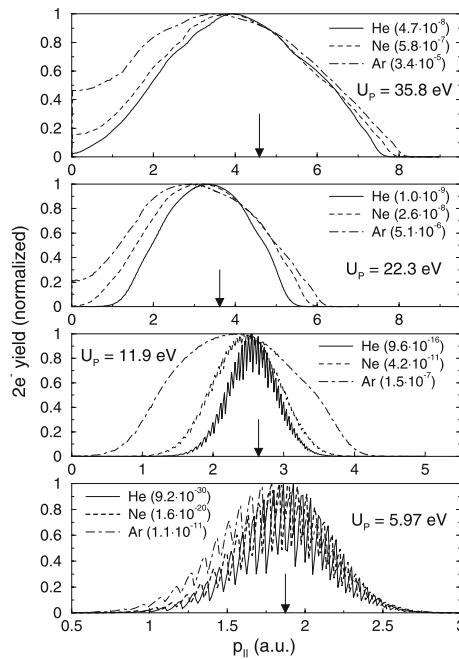
Fig. 4.4. Distribution of $P_\parallel$ for $P_\perp = 0$ for He, Ne, and Ar, $\hbar\omega = 1.55\,\mathrm{eV}$, and various intensities characterized by the corresponding ponderomotive potential U_p. Because of symmetry, the distribution is only shown for $P_\parallel > 0$. Each curve has been normalized to a maximum of unity; the *number given in parentheses* for each curve specifies the respective normalization factor. The *vertical arrows* mark the position of $4\sqrt{U_p}$; cf. (4.12). From [15]

amplitude (4.1), namely, for decreasing intensity and increasing ionization potential (that means, towards the classical boundary and beyond) the ion-momentum distribution concentrates more and more near the value (4.12). At the same time, the yield drops steeply. Both features, the narrowing and the steeply decreasing yield, are present in the data, but to a lesser degree. Indeed, the widths of the two humps stay almost the same when due to decreasing intensity the process moves out of the classical region [34].

4.2.3 Rescattering-Excitation Scenario

The measured ion-momentum distributions of neon on the one hand and helium and argon on the other [and also the electron momentum correlations to be considered below, cf. (4.20)] are very different. For neon, in contrast to helium and argon, the region about $P_{\parallel} = 0$ is largely depopulated. This becomes even more pronounced when the distribution of the electron momenta $p_{i\parallel}$ ($i = 1, 2$) parallel to the laser-field polarization is plotted [cf. (4.20) below]. For neon, it concentrates in the first and third quadrant [4, 35]. This is
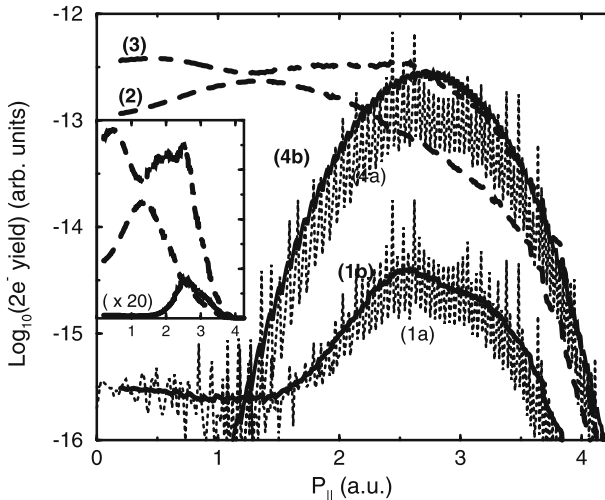

Fig. 4.5. Log-scale distribution of the total momentum in double ionization of helium for $U_p = 14\,\mathrm{eV}$ based on the assumption that the returning electron promotes the bound electron into an excited state with energy $E_{02}^* = -0.5, -0.22, -0.125$ a.u., for *curves* (*1*), (*2*), and (*3*), respectively. The calculation is in one dimension only. The *curves* (*4*) display, for comparison, the distribution generated by the direct rescattering scenario of (4.1) for contact interactions; (*4b*) was calculated in three dimensions and (*4a*) in one. The spiky structures of *curves* (*4a*) and (*1a*) are due to channel closings, which have a more pronounced effect in one than in three dimensions. *Curves* (*1b*), (*2*), and (*3*) are smoothed so as to suppress these effects, *curve* (*1a*) is not. The *inset redraws curves* (*1b*), (*2*), and (*3*) on a linear scale for easier comparison with the data [3]. From [15]

not observed for helium and argon, which exhibit a sizable population in the second and fourth quadrant [3]. Consensus has developed that for the latter rare gases another mechanism significantly contributes [5]: the recolliding electron promotes the bound electron to some excited state from which it tunnels out at a later time, usually near a maximum of the laser field so that its drift momentum will be low [cf. (4.11)].

In fact, this mechanism has been confirmed by a calculation of the cross sections for impact ionization and impact excitation in electron–ion collisions [36]. The latter was found to be exceptionally low for neon. The basic features of recollision excitation follow from an amplitude such as (4.1) with, however, integration over one additional time: the first electron tunnels out at the time t'', recollides, promotes the bound electron into an excited state with energy $E_{02}^* > E_{02}$, and leaves the interaction region at the time $t' > t''$, while the bound electron only becomes free at the later time $t > t'$. Figure 4.5 exhibits the results of such a model. Indeed, for a sufficiently high-lying excited state, the region around zero ion momentum is filled in.

4.2.4 Other Scenarios

Before the advent of the reaction microscope established the strong dominance of the recollision pathway, various other scenarios had been discussed. While none of them seems to be relevant for the recent experiments with rare gases and high-intensity Ti:Sa lasers, they might well turn out to contribute in other regimes, such as provided by high-frequency free-electron lasers. One mechanism that originally was expected to contribute is the so-called shake-off where the ion rearranges itself after one electron has been suddenly removed and ejects a second electron in the process; see, e.g., [2]. This is closely related to the so-called two-step-one process where the first electron on its way out shares energy with a second still bound electron enabling the latter to become free as well. Finally, double tunneling is a fascinating scenario [37], which is all but certain to play a role in systems such as H^- where a very large disparity exists between the detachment energy of 0.75 eV of the first electron and the binding energy of 13.6 eV of the subsequent hydrogen atom. Simple estimates using the quasistatic tunneling rate (4.26) show that it is much more favorable for the two electrons to tunnel out in one joint effort than sequentially one at a time, and this is confirmed by more elaborate calculations [38]. The big impediment for an experimental verification is the fact that laser pulses with extremely high contrast are required in order that a sufficient number of H^- ions survive into the peak of the pulse.

4.3 The Electron–Electron Interaction V_{12}

More recent experiments have recorded the distribution of the longitudinal momenta $p_{1\parallel}$ and $p_{2\parallel}$ of the two electrons, with the remaining transverse

components either entirely integrated over or restricted to certain intervals [35, 39]. These "correlation" distributions carry much more information about the NSDI dynamics than the ion-momentum distributions discussed above. For example, it is easy to envision *identical* ion-momentum distributions that correspond to very *different* correlations. In particular, the correlations very clearly display the consequences of the choice of the crucial electron–electron interaction V_{12} in the transition amplitude (4.1). We will review the effects of four different choices of this interaction, namely

$$V(\boldsymbol{r}_1, \boldsymbol{r}_2) \sim |\boldsymbol{r}_1 - \boldsymbol{r}_2|^{-1} , \tag{4.14a}$$

$$V(\boldsymbol{r}_1, \boldsymbol{r}_2) \sim \delta(\boldsymbol{r}_1 - \boldsymbol{r}_2)\delta(\boldsymbol{r}_2) , \tag{4.14b}$$

$$V(\boldsymbol{r}_1, \boldsymbol{r}_2) \sim |\boldsymbol{r}_1 - \boldsymbol{r}_2|^{-1}\delta(\boldsymbol{r}_2) , \tag{4.14c}$$

$$V(\boldsymbol{r}_1, \boldsymbol{r}_2) \sim \delta(\boldsymbol{r}_1 - \boldsymbol{r}_2) . \tag{4.14d}$$

Of these, the pure electron–electron Coulomb interaction (4.14a) appears to be the obvious choice and, indeed, has been widely used [12, 14, 16]. The electron–electron contact interaction (4.14b), which only acts if both electrons are at the position of the ion (in effect, a three-body contact interaction), has also been frequently employed [15]. Both interactions have been compared in various regards in [17, 18, 40]. More recently, the Coulomb interaction (4.14c), which is only effective if the second (bound) electron is located at the position of the ion, and the electron–electron contact interaction (4.14d), which is not restricted to the position of the ion, have also been studied [27]. The interactions (4.14b) and (4.14c) are *effective* three-body interactions, which attempt to take into account that the effective electron–electron interaction will depend on the positions of the electrons relative to the ion. An alternative interpretation, which formally leads to the same results, is to consider a two-body interaction V_{12} in (4.17) and a wave function $\langle \boldsymbol{r}|\psi_0^{(2)}\rangle$ in (4.18) that is extremely strongly localized at the position of the ion; for details, see [27].

We may write

$$V(\boldsymbol{r}_1, \boldsymbol{r}_2) = V_{\mathrm{rel}}(\boldsymbol{r}_1 - \boldsymbol{r}_2)U(\boldsymbol{r}_2) , \tag{4.15}$$

where $U(\boldsymbol{r})$ is constant unless we allow for an effective interaction. The form factor (4.6) then is the product of two Fourier transforms:

$$V_{\boldsymbol{p}\boldsymbol{k}} = [v(\boldsymbol{p}_1 - \boldsymbol{k}) + v(\boldsymbol{p}_2 - \boldsymbol{k})]u(\tilde{\boldsymbol{p}}) , \tag{4.16}$$

where

$$v(\boldsymbol{p}_1 - \boldsymbol{k}) = \int \mathrm{d}^3 r \mathrm{e}^{\mathrm{i}(\boldsymbol{p}_1 - \boldsymbol{k}) \cdot \boldsymbol{r}} V_{\mathrm{rel}}(\boldsymbol{r}) , \tag{4.17}$$

$$u(\tilde{\boldsymbol{p}}) = \int \mathrm{d}^3 r \mathrm{e}^{\mathrm{i}\tilde{\boldsymbol{p}} \cdot \boldsymbol{r}} U(\boldsymbol{r})\psi_0^{(2)}(\boldsymbol{r}) , \tag{4.18}$$

and $\tilde{\boldsymbol{p}} = \boldsymbol{p}_1 + \boldsymbol{p}_2 - \boldsymbol{k} + \boldsymbol{A}(t)$ as above. Unless $U(\boldsymbol{r})$ is a contact interaction [as it is for (4.14b) and (4.14c)], the form factor will depend via (4.18) on the initial state of the second electron; see Sect. 4.5. The Fourier transform (4.17) of

the relative interaction between the two electrons depends on the momentum transfer $\boldsymbol{k} + \boldsymbol{A}(t) - [\boldsymbol{p}_1 + \boldsymbol{A}(t)] = \boldsymbol{k} - \boldsymbol{p}_1$ from the returning electron to the bound electron. If this interaction has Coulomb form, then

$$v(\boldsymbol{p}_1 - \boldsymbol{k}) \sim (\boldsymbol{p}_1 - \boldsymbol{k})^{-2} \ , \tag{4.19}$$

is the well-known Coulomb form factor. If, on the other hand, it has contact form, then $v(\boldsymbol{p}_1 - \boldsymbol{k}) = \text{const.}$

We shall calculate and discuss integrals of the type

$$D(p_{1\|}, p_{2\|}) = \int \mathrm{d}^2 \boldsymbol{p}_{1\perp} \mathrm{d}^2 \boldsymbol{p}_{2\perp} |M_{i+j}|^2 \ , \tag{4.20}$$

where the integration extends over a certain range of the final transverse momenta, i.e. of their magnitudes and/or their relative orientation, and M_{i+j} is computed by the uniform approximation (4.10).
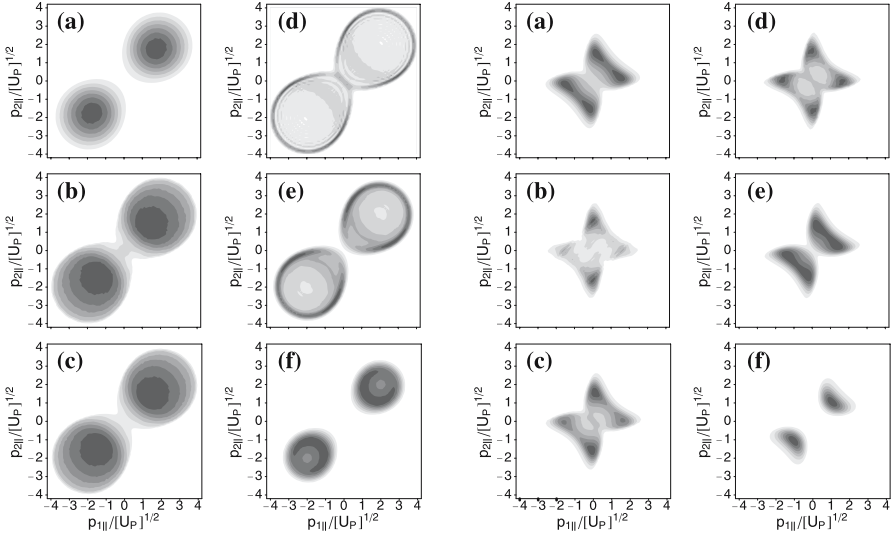
Fig. 4.6. *Left-hand panels*: Momentum correlation function (4.20) of the electron momenta parallel to the laser field for nonsequential double ionization computed with the uniform approximation using the contact interaction (4.14b). The field frequency is $\omega = 0.0551$ a.u. and the ponderomotive energy $U_p = 1.2$ a.u., which corresponds to an intensity of 5.5×10^{14} W/cm². The first two ionization potentials are $|E_{01}| = 0.79$ a.u. and $|E_{02}| = 1.51$ a.u. corresponding to neon. *Panel* (a) shows the yield for the case where the transverse momenta $\boldsymbol{p}_{n\perp}$ $(n = 1, 2)$ are completely integrated over, whereas in the remaining panels they are restricted to certain intervals. In *panels* (b) and (c), $\boldsymbol{p}_{2\perp}$ is integrated, while $0 < p_{1\perp}/[U_p]^{1/2} < 0.1$ and $0.4 < p_{1\perp}/[U_p]^{1/2} < 0.5$, respectively. In *panels* (d), (e), and (f), both transverse momenta are confined to the intervals $0 < p_{n\perp}/[U_p]^{1/2} < 0.5$, $0.5 < p_{n\perp}/[U_p]^{1/2} < 1$, and $1 < p_{n\perp}/[U_p]^{1/2} < 1.5$, respectively. *Right-hand panels*: same as left panels, but for the Coulomb interaction (4.14a). From [17]

Figure 4.6 exhibits some representative results. The two left-hand panels are for the three-body contact interaction (4.14b), the two right-hand panels for the Coulomb interaction (4.14a). A detailed discussion of the results can be found in [17, 18]. In panels (a) the transverse momenta are entirely integrated over, in the remaining panels only partly as specified in the caption. For the Coulomb interaction, we observe its characteristic footprint: one momentum is large while the other one is small. This is a consequence of the form factor of the Coulomb interaction, which is

$$V_{pk} \sim \frac{1}{(\boldsymbol{p}_1 - \boldsymbol{k})^2 [2|E_{02}| + (\boldsymbol{p}_1 + \boldsymbol{p}_2 - \boldsymbol{k} + \boldsymbol{A}(t))^2]^2} + (\boldsymbol{p}_1 \leftrightarrow \boldsymbol{p}_2) \ . \quad (4.21)$$

Physically, recall that the drift momentum $\boldsymbol{k}$ of the first electron is small [cf. (4.11)]. In most cases, since the Coulomb interaction is of long range, it will interact with the bound electron at large distance, so that it will transfer as little momentum as possible to the bound electron. Therefore, its drift momentum, which agrees with the momentum outside the field, will remain low. The second electron, on the other hand, is dislodged into the continuum near a zero of the electric field with low initial momentum. Hence, it will undergo maximal acceleration to a momentum near $2\sqrt{U_p}$. This physical argument is reflected in the form factor (4.21). In passing, we mention that the left-hand panel (d) rather well delineates the classically allowed regime discussed above.

4.4 Final-State Interaction

The Coulomb attraction of the electrons in the intermediate state and in the final Volkov states by the ion, as well as the Coulomb repulsion between the two final electrons are missing from the theory developed thus far. A rigorous treatment of the first issue has so far resisted any efforts. It is much easier to deal with the Coulomb repulsion of the two electrons in the final state, depicted in the right-hand panel of Fig. 4.1, since the product of two Volkov states (4.2) can be extended exactly to incorporate the Coulomb repulsion [22]. This is possible because in the long-wavelength approximation the laser couples to the sum $\boldsymbol{r}_1 + \boldsymbol{r}_2$ of the two electron coordinates while the Coulomb repulsion affects their difference $\boldsymbol{r} = \boldsymbol{r}_1 - \boldsymbol{r}_2$ just like in the absence of the laser field. The state reads [22]

$$\begin{aligned} \big|\psi_{\boldsymbol{p}_1 \boldsymbol{p}_2}^{(\mathrm{V})}(t)\big\rangle = \big|\psi_{\boldsymbol{p}_1}^{(\mathrm{V})}(t)\big\rangle \otimes \big|\psi_{\boldsymbol{p}_2}^{(\mathrm{V})}(t)\big\rangle \\ \times \ {}_1F_1(-\mathrm{i}\zeta, 1; \mathrm{i}(|\boldsymbol{p}||\boldsymbol{r}| - \boldsymbol{p} \cdot \boldsymbol{r})) \mathrm{e}^{-\pi\zeta/2} \Gamma(1 + \mathrm{i}\zeta) \ , \end{aligned} \quad (4.22)$$

where $\boldsymbol{p} = (\boldsymbol{p}_1 - \boldsymbol{p}_2)/2$, $\zeta = |\boldsymbol{p}_1 - \boldsymbol{p}_2|^{-1}$ and ${}_1F_1(a; b; z)$ denotes the confluent hypergeometric function.

Typical results obtained with this state are reproduced in Fig. 4.7, where the parameters have been chosen so as to allow comparison with published experimental data. As expected, the final-state repulsion causes a suppression of
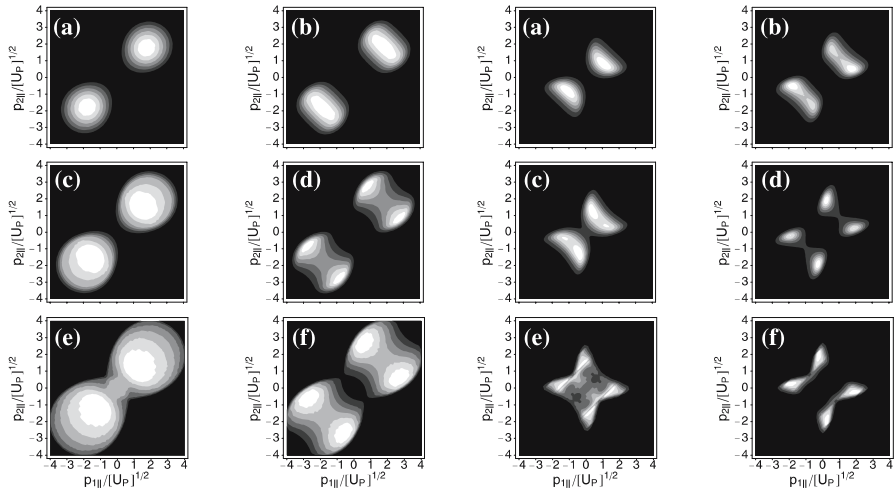
Fig. 4.7. *The two left-hand panels*: Comparison of the double-ionization correlation densities (4.20) without (*left-hand column*: panels (*a*), (*c*), and (*e*)) and with (*right-hand column*: panels (*b*), (*d*), and (*f*)) electron–electron repulsion in the final state. The interaction V_{12} is specified by the three-body contact interaction (4.14b). Parameters are for argon ($E_{01} = 0.58$ a.u., $E_{02} = 1.015$ a.u.), the laser frequency is $\omega = 0.057$ a.u. (Ti:Sa). Panels (*a*) and (*b*): $I = 2.5 \times 10^{14}$ W cm^{-2} ($U_p = 0.54$ a.u.), $|\boldsymbol{p}_{1\perp}| \geq 0.5$ a.u.; [35]; (*c*) and (*d*): as before, but with $|\boldsymbol{p}_{1\perp}| \leq 0.5$ a.u.; (*e*) and (*f*): $I = 4.7 \times 10^{14}$ W cm^{-2} ($U_p = 1.0$ a.u.), $|\boldsymbol{p}_{1\perp}|$ or $|\boldsymbol{p}_{2\perp}| \leq 0.1$ a.u. [39]. *The two right-hand panels*: same as the left-hand panels, but with V_{12} specified by the Coulomb interaction (4.14a). From [18]

the yield along the diagonal $p_{1\|} = p_{2\|}$. Remarkably, the very simplest model, the three-body contact interaction (4.14b) without final-state Coulomb repulsion (leftmost column), yields the best description of the data [18].

The correlation of the *transverse momenta* including or not including the final-state repulsion is investigated theoretically and compared with data for argon in [41]. Including the final-state repulsion yields a good description of the electron–electron correlation, but the electron–ion correlation is outside of the model.

4.5 Effect of the Initial Electron Bound States

Another ingredient that can be taken into account in our S-matrix theory are the initial states in which both electrons are bound. If the electron–electron interaction V_{12} is a pure two-body interaction as in (4.14a) or in (4.14d), then the initial bound state $|\psi_0^{(2)}\rangle$ of the second electron will enter the form factor $V_{\boldsymbol{pk}}$ via its Fourier transform, cf. (4.18). If, on the other hand, we adopt an effective three-body interaction as in (4.14b) or (4.14d),

then $V_{\boldsymbol{pk}}$ is independent of the form of the bound state $|\psi_0^{(2)}\rangle$. The bound state $|\psi_0^{(1)}\rangle$ enters via the form factor (4.7), but its effect is generally small. Since most experiments employ neon and argon as targets, whose outer-shell electrons are bound in $2p$ or $3p$ states, respectively, one would expect that p states yield a more realistic description of the two active electrons for these atoms.

Initial bound states $|\psi_0^{(2)}\rangle$ given by hydrogenic states with quantum numbers n and l affect the form factor $V_{\boldsymbol{pk}}$ via the function [cf. (4.18)]

$$u^{(nl)}(\tilde{\boldsymbol{p}}) \sim \frac{\rho_{nl}(\boldsymbol{p},\boldsymbol{k})}{\left[2|E_{02}|+\tilde{\boldsymbol{p}}^2\right]^{n+1}} + (\boldsymbol{p}_1 \leftrightarrow \boldsymbol{p}_2) , \qquad (4.23)$$

where $\rho_{1s}=1$, $\rho_{2p}=\tilde{\boldsymbol{p}}$, and $\rho_{3p}=\tilde{\boldsymbol{p}}(\tilde{\boldsymbol{p}}^2-2|E_{02}|)$, with $\tilde{\boldsymbol{p}}=\boldsymbol{p}_1+\boldsymbol{p}_2-\boldsymbol{k}+\boldsymbol{A}(t)$.

In Fig. 4.8 the effect of the initial-state wave functions is explored, for the case where the crucial electron–electron interaction is the two-body Coulomb interaction (4.14a) and for the case where this interaction is the two-body contact interaction (4.14d), which is not restricted to the position of the ion. In both cases, the form factor includes the function (4.23), which favors momenta such that $p_{1\|} + p_{2\|}$ is large. This is clearly visible for the contact interaction (4.14d) and less so for the Coulomb interaction (4.14a) whose form factor also includes the factor (4.19), which favors $p_{1\|} = 0$ (or $p_{2\|} = 0$). We conclude that (i) the effect of the specific bound state of the second electron is marginal and (ii) that a pure two-body interaction, be it of Coulomb type as in (4.14a) or contact type as in (4.14d), yields a rather poor description of the data. A three-body effective interaction, which only acts if the second electron is positioned at the ion, provides superior results, notably the three-body contact interaction (4.14b), cf. the left-hand panel (d). This points to the significance of the interaction of the electrons with the ion, which so far has not been incorporated into the S-matrix theory beyond the very approximate description via effective three-body interactions such as (4.14b) or (4.14c).

The alternative interpretation [27] mentioned above in Sect. 4.3 assumes that the wave function of the second bound electron is extremely localized near the position of the ion. The labels "localized" in Figs. 4.8 and 4.10 are motivated by this interpretation.

For exponentially decaying bound states, the form factors $V_{\boldsymbol{k}0}$ are of the form

$$V_{\boldsymbol{k}0} \sim \frac{f(\boldsymbol{k}+\boldsymbol{A}(t'))}{\left([\boldsymbol{k}+\boldsymbol{A}(t')]^2 + 2|E_{01}|\right)^n} , \qquad (4.24)$$

where n is an integer. According to the saddle-point equation (4.8a), the denominator vanishes, so that such form factors are singular. In order to overcome the problem with the bound-state singularity, we take the modified action

$$\tilde{S}(t,t',\boldsymbol{p}_j,\boldsymbol{k}) = S(t,t',\boldsymbol{p}_j,\boldsymbol{k}) - \mathrm{i}\ln V_{\boldsymbol{k}0} \qquad (4.25)$$
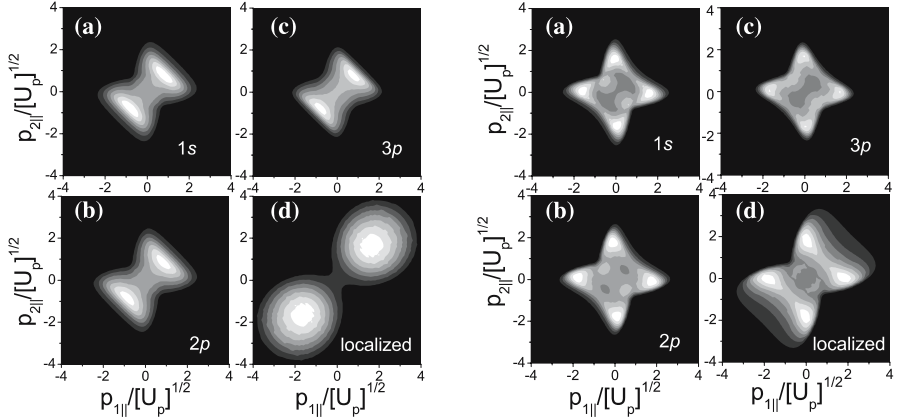
Fig. 4.8. Electron momentum-correlation distributions (4.20) and their dependence on the initial bound state. The *left-hand panels* (*a*)–(*c*) are for the interaction (4.14d) and the *right-hand panels* (*a*)–(*c*) for the interaction (4.14a), for initial 1*s*, 2*p*, and 3*p* states for both electrons. *Panels* (*d*) are for the three-body effective interactions (4.14b) (*left*) and (4.14c) (*right*) with the first electron in a 1*s* state. In all situations (even for the 3*p* - state case), the atomic species was taken to be neon ($|E_{01}| = 0.79$ a.u. and $|E_{02}| = 1.51$ a.u.), in order to facilitate a clear assessment of the effects caused by the different initial states. From [27]

in the transition amplitude (4.4). This leads to modifications in the saddle-point equations (4.8a), and (4.8c) which, physically, determine the tunneling and the return condition. Such modifications depend on the initial bound state of the first electron. We found, however, that they only lead to a minor suppression in the yield, in the region of small parallel momenta (for details cf. [27]).

4.6 The Classical Limit

The model investigated so far is a *coherent* three-step model, which comprises field-induced tunneling of the first electron out of its binding potential, propagation of this electron in the presence of the laser field, and recollision with the ion leading to second ionization. Of these, only the first step is genuinely quantum mechanical, while the other two proceed largely classically. The tunneling process is governed by a tunneling rate that is well approximated by the quasi-static limit [42]

$$R(t') \sim |E(t')|^{-1} \exp\left[-2(2|E_{01}|)^{3/2}/(3|E(t')|)\right]. \qquad (4.26)$$

Ignoring quantum-mechanical features such as spreading and interference, the essential classical physics then are described by the electron-momentum distribution function [17]

$$F(\boldsymbol{p}_1, \boldsymbol{p}_2) = \int dt' R(t') \delta \left(\frac{1}{2} \sum_{i=1}^{2} [\boldsymbol{p}_i + \boldsymbol{A}(t)]^2 + |E_{02}| - E_{\mathrm{ret}}(t) \right) |V_{\boldsymbol{pk}}|^2$$

$$= \int dt' R(t') \delta \left(\frac{1}{2} \left(\boldsymbol{p}_{1\perp}^2 + \boldsymbol{p}_{2\perp}^2 \right) - \Delta E \right) |V_{\boldsymbol{pk}}|^2 \qquad (4.27)$$

with

$$\Delta E \equiv \Delta E(p_{1\parallel}, p_{2\parallel}, t) \equiv E_{\mathrm{ret}}(t) - |E_{02}| - \frac{1}{2} \sum_{i=1}^{2} [p_{i\parallel} + A(t)]^2 . \qquad (4.28)$$

This is an integral over the ionization time t'. The rescattering time t, which is a function of t', must be calculated via classical mechanics assuming that the first electron is set free with zero velocity at the time t'. The distribution function (4.27) corresponds to a *rate* (not an amplitude), which incorporates the three steps incoherently (multiplicatively): Tunneling is specified by the rate (4.26), and propagation from the ionization time t' to the rescattering time t determines the kinetic energy $E_{\mathrm{ret}}(t)$. Finally, inelastic rescattering is subject to energy conservation (expressed by the δ function) and the momenta are distributed according to the square of the form factor (4.6).

Usually, not all six momentum components $\boldsymbol{p}_1$ and $\boldsymbol{p}_2$ are observed. Those that are not can be integrated over. This is very easily carried out analytically [17] provided the form factor is constant as it is for the three-body contact interaction (4.14b). For example, if only the longitudinal components are observed, the pertinent distribution with the transverse components completely integrated over is

$$\int d^2 \boldsymbol{p}_{1\perp} d^2 \boldsymbol{p}_{2\perp} F(\boldsymbol{p}_1, \boldsymbol{p}_2) = 4\pi^2 \int dt' R(t') (\Delta E)_+ \qquad (4.29)$$

where $x_+ = x\theta(x)$ with $\theta(x)$ the unit step function, and

$$\Delta E \equiv \Delta E(p_{1\parallel}, p_{2\parallel}, t) \equiv E_{\mathrm{ret}}(t) - |E_{02}| - \frac{1}{2} \sum_{i=1}^{2} [p_{i\parallel} + A(t)]^2. \qquad (4.30)$$

The outcome of (4.29) along with its quantum-mechanical counterpart are displayed in panels (a) of Fig. 4.9 for the three-body contact interaction (4.14b). Both distributions are very similar, apart from minor differences near the boundary of the classically allowed region. This is also true for other forms of the electron–electron interaction V_{12} and initial bound states. In the other panels (b)–(f), the transverse momenta are restricted to certain intervals. Formulas analogous to (4.29) for these situations can be found in [17].

As the intensity decreases, the classical version (4.27) becomes an increasingly poor approximation. Ultimately, at and below the "threshold intensity", when the kinetic energy of the returning electron no longer suffices to free the second electron (i.e., the argument of the δ function never vanishes), the classical distribution becomes identically zero. Figure 4.10 shows an example, for an intensity of roughly 30% above the threshold. Already in this case, the
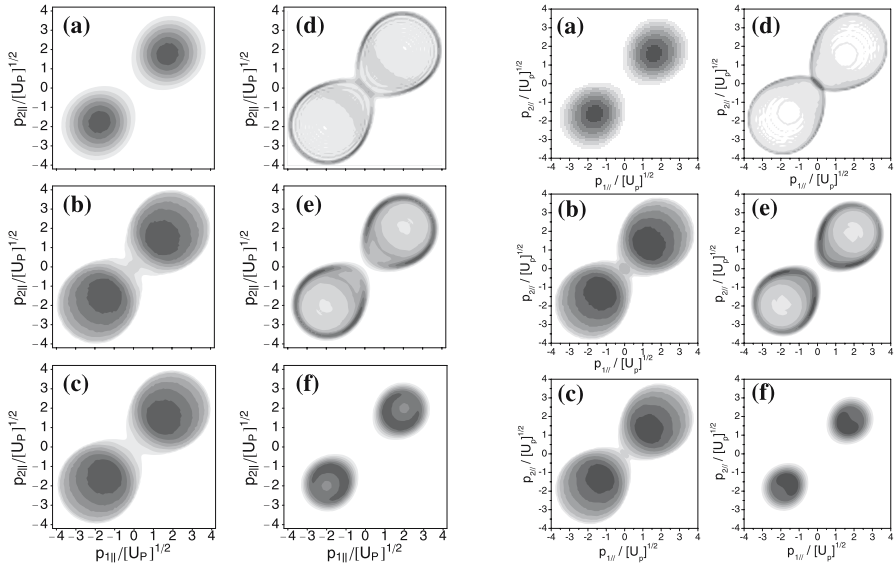
Fig. 4.9. The *left-hand panels* are identical with the left-hand panels of Fig. 4.6 where the pertinent parameters are given. They are to be compared with the right-hand panels, which were calculated under the same conditions but from the classical model (4.27) for the contact interaction. Equation (4.29) underlies panel (a)
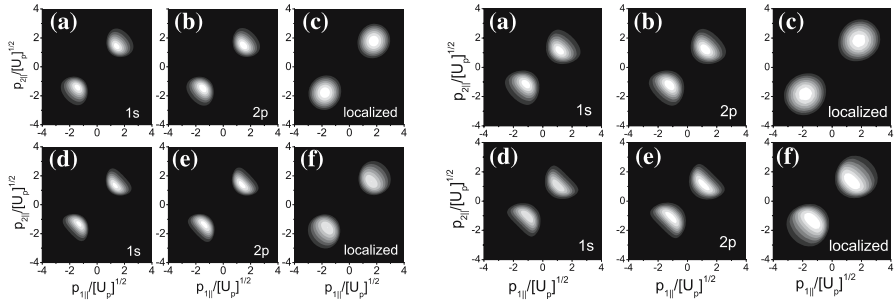

Fig. 4.10. Electron momentum distributions for neon ($|E_{01}| = 0.79$ a.u. and $|E_{02}| = 1.51$ a.u.) subject to a linearly polarized monochromatic field with frequency $\omega = 0.057$ a.u. and intensity $I = 3.0 \times 10^{14}\,\mathrm{W/cm}^2$, as functions of the electron momentum components parallel to the laser-field polarization. The *left and the right panels* correspond to the classical and to the quantum-mechanical model, respectively. The *upper and lower panels* have been computed for a contact and Coulomb-type interaction V_{12}, respectively. In *panels* (*a*) and (*d*), and (*b*) and (*e*), the second electron is taken to be initially in a $1s$, and in a $2p$ state, respectively, whereas in *panels* (*c*) and (*f*) the spatial extension of the bound-state wave function has been neglected. The transverse momenta have been integrated over

quantum-mechanical distributions are far broader than their classical coun-
terparts. This is due to the fact that the classical model underestimates the
yield already near the boundary (and, of course, outside) of the classically
allowed regime, which was defined in Sect. 4.2.1. Experiments in this in-
tensity region [34] do not exhibit any significant qualitative change in the
ion-momentum distributions when the intensity approaches and passes the
threshold intensity. In contrast, the quantum-mechanical ion-momentum dis-
tributions decrease quickly in magnitude and become narrowly concentrated
about the value (4.12); see Fig. 4.4.

The S-matrix element (4.1) does not take into account the fact that owing
to the presence of the field $E(t)$ the second electron can escape over the
saddle formed by the Coulomb field and the scalar potential $zE(t)$ of the
laser field [20]. In effect, this lowers the binding energy of the second electron
to the value $E_{02}(t) = |E_{02}| - 2\sqrt{2|E(t)|}$. This value can be introduced by
hand into the classical distribution (4.27), which thereupon becomes again
applicable down to a much lower intensity. This way, fair agreement with the
data has been reached [34]. Further discussion of this issue is given in [43].

So long as, however, the driving-field intensity is far above the threshold,
the S-matrix amplitude (4.1) and its classical limit (4.27) yield practically
identical results. This shows that, in this regime, NSDI is (apart from its
initiation via tunneling) an essentially classical phenomenon. This provides
a physical justification for extending the classical model to more complex
scenarios, such as, for instance, more than two electrons (Sect. 4.8).

The classical model can also be employed to derive one-electron spectra
in coincidence with NSDI. For constant form factors (three-body contact
interaction), the corresponding expression is [43]

$$\int \mathrm{d}^3\boldsymbol{p}_2 F(\boldsymbol{p}_1, \boldsymbol{p}_2) = 4\pi\sqrt{2} \int \mathrm{d}t' R(t') \, (\Delta E_1)_+^{1/2} \tag{4.31}$$

with $\Delta E_1 \equiv E_{\mathrm{ret}}(t) - |E_{02}| - \frac{1}{2}[\boldsymbol{p}_1 + \boldsymbol{A}(t)]^2$. An example is presented in Fig. 4.11.
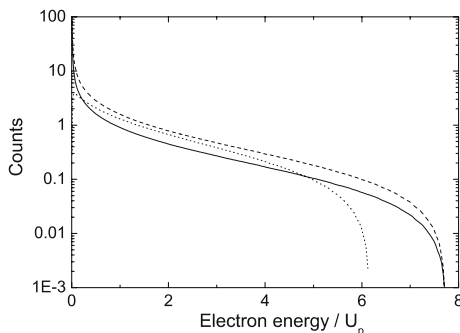
Fig. 4.11. One-electron energy spectra derived in coincidence with double ioniza-
tion derived from (4.31) for various noble gases. *Solid line*: He at laser intensity
$I = 8 \times 10^{14} \, \mathrm{W/cm}^2$, *dashed line*: Ne at $I = 6 \times 10^{14} \, \mathrm{W/cm}^2$, *dotted line*: Ar at
$I = 2.5 \times 10^{14} \, \mathrm{W/cm}^2$. The parameters correspond to the experimental data of [51]

4.7 NSDI by Few-Cycle Laser Pulses

In the results discussed so far, the external laser field has been approximated by a monochromatic plane wave. This is a reasonable approximation for pulses with a length down to, say, eight cycles which covers most NSDI experiments. Recently, however, laser pulses of only a few cycles' length have become the tools of choice in laser-atom physics [44].

A few-cycle (n-cycle) pulse can be described by the vector potential

$$\boldsymbol{A}(t) = A_0 F(t) \sin(\omega t + \phi)\boldsymbol{e}_x , \qquad (4.32)$$

where the positive-definite envelope $F(t)$ ($0 \leq F(t) \leq 1$) is zero outside the interval $0 \leq t \leq nT$ ($T = 2\pi/\omega$) and assumes its maximum at $t = nT/2$. The specific pulse shape is determined by the carrier-envelope (CE) phase ϕ, which specifies the offset between the envelope of the pulse and its "carrier wave" with frequency ω. Below, for the explicit results, we will use $F(t) = \exp[-4(\omega t - \pi n)^2/(\pi n)^2]$.

When a few-cycle pulse interacts with matter, the resulting effects strongly depend on the value of the CE phase. For example, above-threshold ionization spectra lose the backward-forward symmetry ($\boldsymbol{p} \rightarrow -\boldsymbol{p}$), which they obey for monochromatic fields. This is particularly pronounced in their high-energy part, which is caused by rescattering [45]. This effect has been used for the measurement of the CE phase. NSDI, to the extent that it is due to rescattering, can be expected also to react very sensitively to any change in the CE phase. Indeed, it has been shown that the momentum correlation distribution of NSDI can exhibit dramatic changes upon a small variation of the CE phase [46,47].

Figure 4.12 exhibits NSDI electron-momentum-correlation distributions calculated for a 4-cycle pulse having the shape (4.32). Unlike the corresponding distributions for a long pulse shown in Figs. 4.6–4.10, which are symmetric with respect to the antidiagonal $[(p_{1\parallel}, p_{2\parallel}) \rightarrow -(p_{1\parallel}, p_{2\parallel})]$, the distributions of Fig. 4.12 are, in general, unequally concentrated in the regions of either positive or negative momenta. Upon a critical value of the CE phase ($\phi \approx 1.1\pi$ at 4×10^{14} Wcm^{-2}), the distribution shifts from the first into the third quadrant. For increasing intensity, this critical value of the CE phase moves to smaller values. This behavior is obtained both from the quantum-mechanical S-matrix amplitude (4.1) (left-hand panels), and from its classical limit (4.27) (right-hand panels). (Due to its very good agreement with the experiments in the long-pulse case, we employed the three-body-contact interaction (4.14b) in both calculations.) Minor differences are only observed at the boundary of the classically allowed region, or around the critical CE phases, for which the momenta start to change sign. As observed before, the agreement between the quantum-mechanical and the classical calculations improves for increasing intensity.

The dependence of the yields on the absolute phase can be explained by a change in the dominant set of orbits of the first-ionized electron rescat-
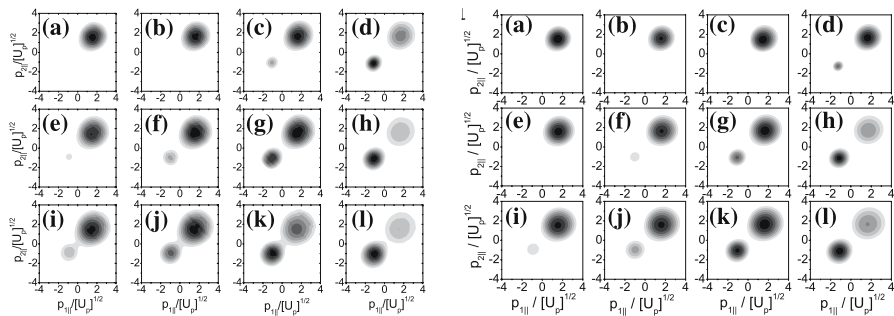
Fig. 4.12. Electron momentum distributions computed for neon ($|E_{01}| = 0.79$ a.u. and $|E_{02}| = 1.51$ a.u.) subject to a four-cycle pulse ($n = 4$) of frequency $\omega = 0.057$ a.u., for various intensities and CE phases. The *left-hand* and the *right-hand part* of the figure correspond to the quantum-mechanical and to the classical computation, respectively. The *upper*, *middle*, and *lower rows* are for $I = 4 \times 10^{14}$ W/cm^2 ($U_p = 0.879$ a.u.), $I = 5.5 \times 10^{14}$ W/cm^2 ($U_p = 1.2$ a.u.), and $I = 8 \times 10^{14}$ W/cm^2 ($U_p = 1.758$ a.u.), respectively. The CE phases are for panels (a), (e) and (i): $\phi = 0.8\pi$; for panels (b), (f) and (j): $\phi = 0.9\pi$; for panels (c), (g) and (k): $\phi = 1.0\pi$; and for panels (d), (h) and (l): $\phi = 1.1\pi$. From [47]

tering inelastically off its parent ion. For an orbit to make an important contribution, two conditions must be satisfied: first, the probability that the electron tunnel out at a time t' must not be too small[6] and, second, the subsequent acceleration must be strong enough that the electron return to the ion (at the time t) with sufficient kinetic energy $E_{\mathrm{ret}}(t)$. These two conditions reduce the significance of start times within the trailing part of the pulse ($t' \geq nT/2$).

Both in the quantum-mechanical and in the classical calculations, only the first return of the electron to the ion has been considered. Due to wave function spreading, the contributions of the longer orbits are suppressed. The most remarkable result of these investigations is the surprisingly high sensitivity of the $(p_{1\|}, p_{2\|})$-momentum distribution to variations of the CE phase. In principle, this lends itself to a very precise determination and control of this parameter.

The features discussed above have been observed in recent NSDI experiments, for argon irradiated by few-cycle pulses. The experimental findings exhibit very good agreement with the theory. In particular, the shift of the $(p_{1\|}, p_{2\|})$ distribution from the first to the third quadrant takes place around the predicted critical phases [48].

---

[6] In the classical and quantum-mechanical frameworks, this probability is related to the quasi-static rate $R(t')$ or to the imaginary part $\mathrm{Im}\, t'$, respectively. For details cf. [47].

4.8 Nonsequential Multiple Ionization

If the kinetic energy $E_{\mathrm{ret}}(t)$ of the returning electron is sufficiently high, it may as well free more than one bound electron in a single nonsequential coherent process. The signature of such a recollision-impact nonsequential multiple ionization (NSMI) process will be a large momentum of the multiply charged ion, around the value (4.12) with the factor of 4 replaced by $2N$ for N-fold NSMI. The underlying argument is in complete analogy with the one given above in connection with (4.12). Indeed, NS3I of neon was observed several years ago [4], and extensive measurements of NS3I and NS4I of neon and argon were published recently [49]. The data for neon do display the characteristic hump in the distribution of the ion-momentum component parallel to the laser field at a value compatible with the afore-mentioned estimate.

An ab-initio description of NSMI appears to be all but impossible. In the S-matrix context, the single Feynman diagram of Fig. 4.1(a) is replaced by a large number of more complicated diagrams: to establish contact between N electrons requires a minimum of $N-1$ two-particle interactions, and this entails $N-2$ internal electron propagators (for NSDI there was none). Moreover, based on the experience gained from NSDI, it appears likely that some interaction with the ion has to be included for a realistic description, which increases the number of diagrams as well as their complexity. Hence, while an extension of the quantum-mechanical amplitude (4.1) to triple and higher nonsequential ionization, maintaining two-body electron–electron interactions to be responsible for the energy exchange, appears not to be practically feasible, an extension of the classical distribution function (4.27) is near at hand. We consider a statistical description where the first-ionized electron returning to its parent ion at time t shares its energy with $N-1$ up to this time bound and inactive electrons merely according to the available phase space, without any dynamical bias. We do not attempt to model *how* this is accomplished (presumably through many repeated electron–electron and electron–ion interactions). We do assume, however, that this energy-sharing process requires some time so that the electrons are freed at the time $t + \Delta t$ rather than the return time t. Comparable statistical models have been used in many areas of physics whenever the detailed dynamics were unknown or too complicated; see, e.g. [50].

Then, the distribution of the final electron momenta $\boldsymbol{p}_n$ $(n = 1, \ldots, N)$ is given by [52] (see also [53])

$$F(\boldsymbol{p}_1, \ldots, \boldsymbol{p}_N) = \int \mathrm{d}t' R(t') \delta \left(E_0^{(N)} - E_{\mathrm{ret}}(t) + \frac{1}{2} \sum_{n=1}^{N} [\boldsymbol{p}_n + \boldsymbol{A}(t + \Delta t)]^2 \right) ,$$

$$(4.33)$$

where $E_0^{(N)} = \sum_{n=2}^{N} |E_{0n}|$ is the total energy necessary to remove the $N-1$ bound electrons. Compared with (4.27), the time delay Δt is a new feature. It

is the sum of a "thermalization time" – the time it takes for the N electrons to reach an energy distribution governed only by phase space, without any memory of the distribution at the time t when the returning electron had all the energy – and a possible additional "dwell time" before all electrons start leaving the vicinity of the ion. The corresponding distribution for the parallel ion momentum $P_\parallel$ can be obtained from (4.33) in analogy with (4.13), cf. also [52]. It is

$$F_{\text{ion}}(P_\parallel) \equiv \int \mathrm{d}^2\boldsymbol{p}_\perp F_{\text{ion}}(\boldsymbol{p}) \sim \int \mathrm{d}t' R(t') \left(\Delta E_{\text{ion}\parallel}\right)_+^{\frac{3N}{2}-\frac{3}{2}}, \qquad (4.34)$$

where $\Delta E_{\text{ion}\parallel} \equiv E_{\text{ret}}(t) - E_0^{(N)} - \frac{1}{2N}[P_\parallel - NA(t+\Delta t)]^2$.

In Fig. 4.13, we display such distributions for Ne^{3+} and Ne^{4+} and compare with the experimental data [49]. The time delay Δt between the recollision of the first electron and the time when all N electrons leave the ion influences both the width and the peaks of the momentum distributions. This is ex-
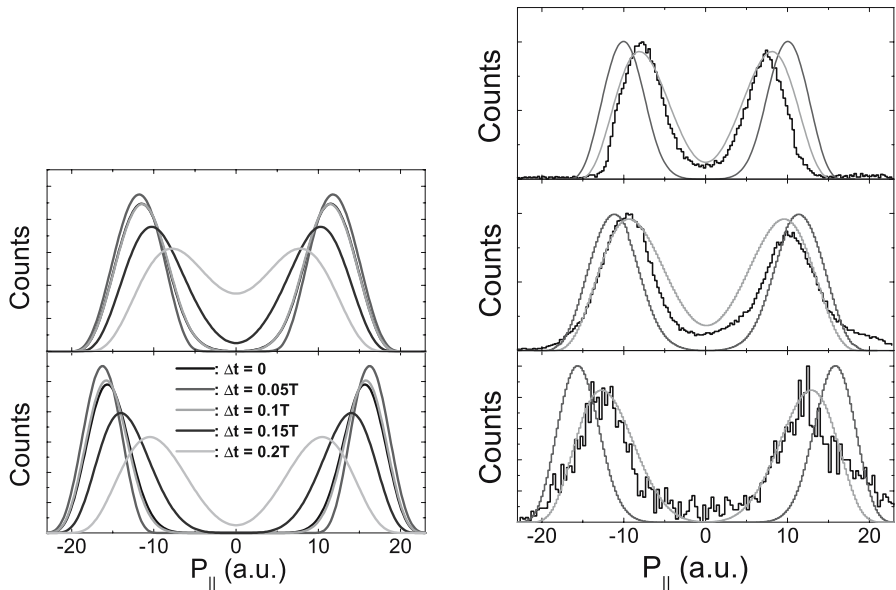
Fig. 4.13. *Left Panels*: Distribution of the longitudinal ion momentum for triple (*upper panel*) and quadruple (*lower panel*) nonsequential ionization of neon at $2\,\mathrm{PWcm}^{-2}$ calculated from (4.34) for various delays Δt as indicated in the lower panel. Note that in the *upper panel* the curves for $\Delta t = 0$ and $\Delta t = 0.1T$ almost completely overlap. *Right panels*: Distribution of the longitudinal momentum of nonsequential triple ionization of neon at $1.5\,\mathrm{PW\,cm}^{-2}$ (*upper panel*), $2.0\,\mathrm{PW\,cm}^{-2}$ (*middle panel*), and of nonsequential quadruple ionization of Ne at $2.0\,\mathrm{PW\,cm}^{-2}$ (*lower panel*). The *rugged* (*black*) *curves* represent the data of Fig. 4.2 of [49]. The *outermost smooth* (*red*) *curve* and the *innermost smooth* (*green*) *curve* are calculated from (4.34) for $\Delta t = 0$ and $\Delta t = 0.17T$. From [52]

pected since, by introducing a time delay, one is shifting the center of the hypersphere in the $(\boldsymbol{p}_1, \ldots, \boldsymbol{p}_N)$ space, which delimits the region for which nonsequential multiple ionization is energetically allowed. Specifically, for longer delays, the distributions broaden considerably, and the peak momenta are displaced towards lower values. Optimal results regarding the widths and centers of the momentum distributions are obtained if the time delay is $\Delta t \simeq 0.17T$, where T is the driving-field cycle. For a Ti:Sa laser with $T \approx 2.7\,\mathrm{fs}$, this yields an upper bound for the thermalization time of roughly 460 attoseconds.

This simple statistical model is compatible, for the case of neon, with the data available thus far. Moreover, it allows one to infer a value of the thermalization time. This value comes out to be in the attosecond regime. In principle, such bounds can be made even tighter by reducing the widths of the electron-momentum distributions. This can be done by limiting the temporal range of return times for the first electron using, for instance, an additional perpendicularly polarized driving wave at twice the frequency.

4.9 Conclusions

The fully differential cross sections currently recorded with the help of the reaction microscope pose an enormous challenge to theory. Calculations from first principles are only possible for helium, if at all. In this paper, we have surveyed S-matrix methods that implement the rescattering-impact-ionization scenario in the two-electron context, strictly speaking for helium only. Even in this simplest case, the electron interaction with the ion is neglected. We have then discussed attempts, making a virtue out of necessity, at re-interpreting the two-particle electron–electron interaction as an effective interaction that includes the presence of the ion. The fact that, at least in the case of neon, a three-body contact interaction yields a fair description of the existing data (and also agrees well with classical-trajectory simulations [11]) remains a puzzle that calls for an explanation.

Nonsequential double and multiple ionization are to a large part classical phenomena. Indeed, the S-matrix approach suggests a pertinent classical limit. We have summarized evidence that the latter reproduces the fully quantum-mechanical results very well in parameter regions where this can be expected. Finally, we have extended such classical avenues to a statistical description of nonsequential triple and quadruple ionization. For neon, such a classical statistical model yields a fair description of the available data. While a more microscopic description of these extremely involved phenomena lies in the future, we believe that the simple models summarized in this paper will remain valuable as benchmark results.

References

1. A. l'Huillier, L.A. Lompré, G. Mainfray, C. Manus: Phys. Rev. A **27**, 2503 (1983)
2. R. Dörner, Th. Weber, M. Weckenbrock, A. Staudte, M. Hattas, H. Schmidt-Böcking, R. Moshammer, J. Ullrich: Adv. At., Mol., Opt. Phys. **48**, 1 (2002); A. Becker, R. Dörner, R. Moshammer: J. Phys. B **38**, S753 (2005)
3. Th. Weber, M. Weckenbrock, A. Staudte, L. Spielberger, O. Jagutzki, V. Mergel, F. Afaneh, G. Urbasch, M. Vollmer, H. Giessen, R. Dörner: Phys. Rev. Lett. **84**, 443 (2000); Th. Weber, H. Giessen, M. Weckenbrock, G. Urbasch, A. Staudte, L. Spielberger, O. Jagutzki, V. Mergel, M. Vollmer, and R. Dörner: Nature (London) **405**, 658 (2000)
4. R. Moshammer, B. Feuerstein, W. Schmitt, A. Dorn, C.D. Schröter, J. Ullrich, H. Rottke, C. Trump, M. Wittmann, G. Korn, K. Hoffmann, W. Sandner: Phys. Rev. Lett. **84**, 447 (2000)
5. B. Feuerstein, R. Moshammer, D. Fischer, A. Dorn, C.D. Schröter, J. Deipenwisch, J.R Crespo Lopez-Urrutia, C. Höhr, P. Neumayer, J. Ullrich, H. Rottke, C. Trump, M. Wittmann, G. Korn and W. Sandner: Phys. Rev. Lett. **87**, 043003 (2001)
6. P.B. Corkum: Phys. Rev. Lett. **71**, 1994 (1993)
7. M. Weckenbrock, D. Zeidler, A. Staudte, Th. Weber, M. Schöffler, M. Meckel, S. Kammer, M. Smolarski, O. Jagutzki, V.R. Bhardwaj, D.M. Rayner, D.M. Villeneuve, P.B. Corkum, R. Dörner: Phys. Rev. Lett. **92**, 213002 (2004)
8. H. Niikura, F. Légaré, R. Hasbani, M.Yu. Ivanov, D.M. Villeneuve, P.B. Corkum: Nature (London) **417**, 917 (2002)
9. R. Panfili, S.L. Haan, J.H. Eberly: Phys. Rev. Lett. **89**, 113001 (2002); S.L. Haan, P.S. Wheeler, R. Panfili, J.H. Eberly: Phys. Rev. A **66**, 061402(R) (2002); M. Lein, E.K.U. Gross, V. Engel: Phys. Rev. Lett. **85**, 4707 (2000)
10. D. Dundas, K.T. Taylor, J.S. Parker, E.S. Smyth: J. Phys. B **32**, L231 (1999); J.S. Parker, L.R. Moore, K.J. Meharg, D. Dundas, K.T. Taylor: J. Phys. B **34**, L69 (2001); H.G. Muller: Opt. Express **8**, 425 (2001)
11. J. Chen, J. Liu, L.B. Fu, W.M. Zheng: Phys. Rev. A **63**, 011404(R) (2000); J. Chen, C.H. Nam: Phys. Rev. A **66**, 053415 (2002)
12. A. Becker, F.H.M. Faisal: J. Phys. B **29**, L197 (1996)
13. A. Becker, F.H.M. Faisal: J. Phys. B **38**, R1 (2005)
14. A. Becker, F.H.M. Faisal: Phys. Rev. Lett. **84**, 3546 (2000); *ibid* **89**, 193003 (2002)
15. R. Kopold, W. Becker, H. Rottke, W. Sandner: Phys. Rev. Lett. **85**, 3781 (2000)
16. S.V. Popruzhenko, S.P. Goreslavskii: J. Phys. B **34**, L239 (2001); S.P. Goreslavski, S.V. Popruzhenko: Opt. Express **8**, 395 (2001)
17. C. Figueira de Morisson Faria, H. Schomerus, X. Liu, W. Becker: Phys. Rev. A **69**, 043405 (2004)
18. C. Figueira de Morisson Faria, X. Liu, W. Becker, H. Schomerus: Phys. Rev. A **69**, 021402(R)(2004)
19. C. Ruiz, L. Plaja, L. Roso: Phys. Rev. Lett. **94**, 063002 (2005)
20. H.W. van der Hart, K. Burnett: Phys. Rev. A **62** 013407 (2000)
21. D.M. Volkov: Zs. Phys. **94**, 250 (1935)
22. F.H.M. Faisal: Phys. Lett. A **187**, 189 (1994); A. Becker, F.H.M. Faisal: Phys. Rev. A **50**, 3256 (1994)

23. L.V. Keldysh: Zh. Eksp. Teor. Fiz. **47**, 1945 (1964) [Sov. Phys. JETP **20**, 1307 (1965)]
24. F.H.M. Faisal: J. Phys. B **6**, L89 (1973); H.R. Reiss: Phys. Rev. A **22**, 1786 (1980)
25. M. Lewenstein, Ph. Balcou, M.Yu. Ivanov, A. l'Huillier, P.B. Corkum: Phys. Rev. A **49**, 2117 (1994)
26. S.P. Goreslavskii, Ph.A. Korneev, S.V. Popruzhenko, R. Kopold, W. Becker: J. Mod. Opt. **50**, 423 (2003)
27. C. Figueira de Morisson Faria, M. Lewenstein: J. Phys. B **38**, 3251 (2005)
28. C. Figueira de Morisson Faria, W. Becker: Laser Phys. **13**, 1196 (2003)
29. S.V. Popruzhenko, Ph.A. Korneev, S.P. Goreslavskii, W. Becker: Phys. Rev. Lett. **89**, 023001 (2002)
30. C. Figueira de Morisson Faria, H. Schomerus, W. Becker: Phys. Rev. A **66**, 043413 (2002)
31. D.B. Milošević, W. Becker: Phys. Rev. A **68**, 065401 (2003)
32. D. Bauer, D.B. Milošević, W. Becker: Phys. Rev. A **72**, 023415 (2005)
33. M.V. Frolov, N.L. Manakov, E.A. Pronin, A.F. Starace: Phys. Rev. Lett. **91**, 053003 (2003)
34. E. Eremina, X. Liu, H. Rottke, W. Sandner, A. Dreischuh, F. Lindner, F. Grasbon, G.G. Paulus, H. Walther, R. Moshammer, B. Feuerstein, J. Ullrich: J. Phys. B **36** 3269 (2003)
35. R. Moshammer, B. Feuerstein, J. Crespo López-Urrutia, J. Deipenwisch, A. Dorn, D. Fischer, C. Höhr, P. Neumayer, C.D. Schröter, J. Ullrich, H. Rottke, C. Trump, M. Wittmann, G. Korn, W. Sandner: Phys. Rev. A **65**, 035401 (2002)
36. V.L.B. de Jesus, B. Feuerstein, K. Zrost, D. Fischer, A. Rudenko, F. Afaneh, C.D. Schröter, R. Moshammer, J. Ullrich: J. Phys. B **37**, L161 (2004)
37. U. Eichmann, M. Dörr, H. Maeda, W. Becker, W. Sandner: Phys. Rev. Lett. **84**, 3550 (2000)
38. B.A. Zon: JETP **89**, 219 (1999)
39. M. Weckenbrock, M. Hattass, A. Czasch, O. Jagutzki, L. Schmidt, T. Weber, H. Roskos, T. Löffler, M. Thomson and R. Dörner: J. Phys. B **34**, L449 (2001)
40. S.P. Goreslavskii, S.V. Popruzhenko, R. Kopold, W. Becker: Phys. Rev. A **64**, 053402 (2001)
41. M. Weckenbrock, A. Becker, A. Staudte, S. Kammer, M. Smolarski, V.R. Bhardwaj, D.M. Rayner, D.M. Villeneuve, P.B. Corkum, R. Dörner: Phys. Rev. Lett. **91**, 123004 (2003)
42. L.D. Landau and E.M. Lifshitz, *Quantum Mechanics* (Pergamon Press, 1977)
43. C. Figueira de Morisson Faria, X. Liu, W. Becker: J. Mod. Opt. **53**, 193 (2006)
44. T. Brabec, F. Krausz: Rev. Mod. Phys. **72**, 545 (2000)
45. G.G. Paulus, F. Lindner, H. Walther, A. Baltuška, E. Goulielmakis, M. Lezius, F. Krausz: Phys. Rev. Lett. **91**, 253004 (2003)
46. X. Liu, C. Figueira de Morisson Faria: Phys. Rev. Lett. **92**, 133006 (2004)
47. C. Figueira de Morisson Faria, X. Liu, A. Sanpera, M. Lewenstein: Phys. Rev. A **70**, 043406 (2004)
48. X. Liu, H. Rottke, E. Eremina, W. Sandner, E. Goulielmakis, K.O. Keeffe, M. Lezius, F. Krausz, F. Lindner, M.G. Schätzel, G.G. Paulus, H. Walther: Phys. Rev. Lett. **93**, 263001 (2004)
49. A. Rudenko, K. Zrost, B. Feuerstein, V.L.B. de Jesus, C.D. Schröter, R. Moshammer, J. Ullrich: Phys. Rev. Lett. **93**, 253001 (2004)

50. See, e.g., W. Forst: *Theory of Unimolecular Reactions* (Academic Press, New York, 1973); P.J. Robinson and K.A. Holbrook: *Unimolecular Reactions* (Wiley-Interscience, New York, 1972); R. Hagedorn: Nuovo Cimento Suppl. **3**, 147 (1965)
51. J.L. Chaloupka, R. Lafon, L.F. DiMauro, P. Agostini, K.C. Kulander: Opt. Express **8**, 352 (2001)
52. X. Liu, C. Figueira de Morisson Faria, W. Becker, P.B. Corkum: J. Phys. B **39**, L305 (2006)
53. C. Figueira de Morisson Faria and X. Liu: J. Mod. Opt. (in press)

5 Laser Control of Chemical Dynamics.
I. Control of Electronic Transitions
by Quadratic Chirping

S. Zou[1], A. Kondorskiy[2], G. Mil'nikov[3], and H. Nakamura[3]

[1] Department of Theoretical Studies, Institute for Molecular Science, Myodaiji,
     Okazaki 444-8585, Japan
     E-Mail: nakamura@ims.ac.jp
[2] Lebedev Physical Institute, Leninsky pr., 53, Moscow, 119991, Russia
[3] The Graduate University for Advanced Studies, Myodaiji, Okazaki 444-8585,
     Japan

Summary. An effective scheme for the laser control of wavepacket dynamics applicable to systems with many degrees of freedom is discussed. It is demonstrated that specially designed quadratically chirped pulses can be used to achieve fast and near-complete excitation of the wavepacket without significantly distorting its shape. The parameters of the laser pulse can be estimated analytically from the Zhu–Nakamura (ZN) theory of nonadiabatic transitions. The scheme is applicable to various processes, such as simple electronic excitations, pump-dumps, and selective bond-breaking, and, taking diatomic and triatomic molecules as examples, it is actually shown to work well.

5.1 Introduction

Laser control of molecular processes is a subject that has been the focus of much recent research in chemical physics. Various approaches have been suggested in this area, including coherent phase control in competing excitation pathways [1], control by pump-dump laser fields [2], optimal control theory [3–13], self-learning algorithms [14], linear chirping and adiabatic rapid passage [15–23], and quadratic chirping [24–29]. The reader can find a comprehensive review of various schemes that have been employed in [3, 24, 28, 30, 31]. Each of these methods has its own advantages and shortcomings.

Our basic strategy for controlling chemical dynamics is based on the idea that there are two basic elements of wavepacket motion in chemical dynamics: (i) electronic nonadiabatic transitions between adiabatic potential energy surfaces and (ii) wavepacket motion on a single adiabatic potential energy surface. If we could control these two basic motions of wavepackets, it would become possible to control various kinds of realistic chemical dynamics.

An effective scheme for controlling elementary process (i) has been proposed, which is based on the idea of quadratic chirping [24–29]. It is now well-established that laser field-induced transitions among energy levels can

be regarded as nonadiabatic transitions among dressed states in the Floquet representation, and these can be nicely treated by a theory of nonadiabatic transition, such as the Zhu–Nakamura (ZN) theory [32, 33]. Here, we demonstrate that this idea can be applied to process (i) and that fast and near-complete selective excitation of the wavepacket can be achieved without significantly distorting its shape if specially designed quadratically chirped pulses are employed. This method is discussed in the first part of this review. An efficient semiclassical optimal control theory applicable to multidimensional systems has formulated in order to control elementary process (ii) [34, 35]. This approach combines the advantages of different formulations of the optimal control theory (OCT): quantum and classical on the one hand and global and local on the other. Quantum mechanical OCT is not feasible for multidimensional systems higher than 3-D and classical OCT is not reliable in this case due to the importance of phases in laser–molecule interactions. The semiclassical theory is expected to provide a framework that should allow us to circumvent these difficulties. This will be discussed in the second part of this review.

Selective excitation of wavepackets with ultrashort broadband laser pulses is of fundamental importance for a variety of processes, such as the coherent control of photochemical reactions [36–39] or isotope separation [40–42]. It can also be used to actively control the molecular dynamics in a dissipative environment if the excitation process is much faster than relaxation. For practical applications it is desirable to establish an efficient method that allows one to increase the target product yield by using short laser pulses of moderate intensity before relaxation occurs [38].

As the excitation process in an external field can be regarded as being a nonadiabatic transition between dressed adiabatic states [32], effective laser control can be achieved by manipulating the parameters of these nonadiabatic transitions directly. Based on this idea, two control schemes have been proposed. The first one is a control scheme for the branching ratio during the molecular photodissociation, achieved by utilizing the phenomenon of complete reflection [24, 43, 44]. The second is to control the population transfer by using a laser pulse with periodically swept parameters [24–29]. In both cases the best parameters of the laser pulse can be easily estimated from the ZN theory of nonadiabatic transitions.

These methods have been developed to control the transitions among quantum energy levels. However, selective excitation using a short quadratically chirped pulse of moderate intensity enjoys the advantages of control via periodically swept parameters along with relative stability against variations in pulse parameters. This provides an effective scheme for the laser control of nonadiabatic wavepacket dynamics [45]. The quadratically chirped pulse satisfies the resonance condition twice between the two Born–Oppenheimer potential energy surfaces at the position of wavepacket transition. The corresponding nonadiabatic transition matrix is directly related to the intensity and the chirping rate of the pulse by means of the ZN theory [33]. In the

case of a quadratically chirped pulse, total population transfer can be effectively controlled by adjusting the relative phase between the two transitions. The nuclear configuration of the wavepacket is assumed to remain the same during the electronic transition, and the system is regarded as a coordinate-dependent level problem with the effect of the kinetic energy operator taken into account as a perturbation. The proper parameters of the pulse can then be found analytically from the ZN theory [33]. The validity of this approximation is also analyzed.

Note the essential difference between the present approach and the methods based on linear chirping and the adiabatic passage [15–23]. In the latter case, the laser parameter, frequency or intensity, is slowly modulated so that the system evolves adiabatically along one of the adiabatic dressed states. In contrast, the key to the present method is the direct control of the nonadiabatic transitions and the interference between them. For this reason, the near-complete excitation of wavepackets can be achieved within much shorter time frames and with much lower intensity laser fields in comparison with the adiabatic passage methods. It is also worth mentioning the works of Amstrup and Henriksen [46, 47] and Elghobashi et al. [48]. They applied ultrashort few-cycle pulses to study selective bond-breaking in both asymmetric and symmetric molecules. In spite of rather good selectivity, they could not achieve a target product yield of greater than 25%, even for intensities as high as $300\,\mathrm{TW/cm^2}$ [48]. With the present method, the yield of the target product can be increased up to $70\% \sim 90\%$ for laser fields that are ten times weaker.

The remainder of this paper is organized as follows: In Sect. 5.2, we present the basic theory of the present control scheme. The validity of the theoretical method and the choice of optimal pulse parameters are discussed in Sect. 5.3. In Sect. 5.4 we provide several numerical examples: i) complete electronic excitation of the wavepacket from a nonequilibrium displaced position, taking LiH and NaK as examples; ii) pump-dump and creation of localized target wavepackets on the ground electronic state potential, using NaK as an example, and; iii) bond-selective photodissociation in the two-dimensional model of H_2O. A localized wavepacket is made to jump to the excited-state potential in a desirable force-selective region so that it can be dissociated into the desirable channel. Future perspectives from the author's point of view are summarized in Sect. 5.5.

5.2 Formulation Based on the Zhu–Nakamura Theory

We consider a molecular system composed of ground g and excited e electronic states coupled by the radiation field,

$$E(t) = \varepsilon(t)\cos\Phi(t) , \qquad (5.1)$$

which interacts with the transition dipole moment μ. The time-dependent Schrödinger equation reads

$$i\hbar\frac{\partial\Psi}{\partial t} = \hat{H}\Psi\ ,\tag{5.2}$$

where

$$\Psi = \begin{pmatrix}\Psi_{\mathrm{g}}\\ \Psi_{\mathrm{e}}\end{pmatrix}\tag{5.3}$$

is the wavefunction of the system. The total Hamiltonian is represented in the form

$$\hat{H} = \begin{pmatrix}\hat{H}_{\mathrm{g}} & -\mu E(t)\\ -\mu E(t) & \hat{H}_{\mathrm{e}}\end{pmatrix}\ ,\tag{5.4}$$

where $\hat{H}_{\mathrm{g/e}} = \hat{P}^2/2m + V_{\mathrm{g/e}}$ are the adiabatic potential energy surface Hamiltonians for the ground g and excited e electronic state, respectively. Our goal is to design an optimal pulse with a simple shape and with a few control parameters that are to be estimated from our physical intuition and the analytical theory of nonadiabatic transition. The numerical solutions of (5.2) are used to check its validity, meaning that we can confirm the usefulness of the scheme and comprehend the mechanism.

From now on we consider the quadratically chirped pulse

$$\omega(t) = \alpha_\omega(t - t_{\mathrm{p}})^2 + \beta_\omega\ ,\tag{5.5}$$

where α_ω is the chirping rate, β_ω is the carrier frequency of the laser and t_{p} represents the pulse center. If the laser frequency is not too low (like for infrared lasers) and the time dependences of ω and the laser intensity ε are relatively weak,

$$\left|\frac{\mathrm{d}\omega}{\mathrm{d}t}\right|T \ll \omega,\quad\text{and}\quad\left|\frac{\mathrm{d}\varepsilon}{\mathrm{d}t}\right|T \ll \varepsilon,\quad\text{with}\quad T = 2\pi/\omega\ ,$$

we can use the Floquet theorem [49]. In the case of one-photon excitation (within the rotating wave approximation), we can recast (5.2) in the form

$$i\hbar\frac{\partial\Psi_{\mathrm{F}}}{\partial t} = \hat{H}_{\mathrm{F}}\Psi_{\mathrm{F}}\tag{5.6}$$

with the Floquet Hamiltonian H_{F}

$$\hat{H}_{\mathrm{F}} = \begin{pmatrix}\hat{H}_{\mathrm{g}} + \hbar\omega(t)/2 & -\mu\varepsilon(t)/2\\ -\mu\varepsilon(t)/2 & \hat{H}_{\mathrm{e}} - \hbar\omega(t)/2\end{pmatrix}.\tag{5.7}$$

In order to simplify the analysis, we assume that the transition is fast enough that the nuclear configuration does not change within the excitation process

and that one can neglect the motion of the wavepacket. Then, for the transition from the ground electronic state, the total excitation probability $\mathcal{P}$ can be expressed as

$$\mathcal{P} = \int P_{12}(x)|\Psi_{\mathrm{g}}(x, t = 0)|^2 \mathrm{d}x , \tag{5.8}$$

where $\Psi_{\mathrm{g}}(x, t = 0)$ is the initial wavepacket and the nonadiabatic transition probability $P_{12}(x)$ can be found from the corresponding two-level problem which depends on x parametrically. The crudest approximation would be to neglect the kinetic energy operator in (5.7) and consider the two-level problem with the Hamiltonian

$$\tilde{H}_0(t) = \frac{1}{2} \begin{pmatrix} \hbar\omega(t) - \Delta(x) & -\mu\varepsilon(t) \\ -\mu\varepsilon(t) & \Delta(x) - \hbar\omega(t) \end{pmatrix}, \tag{5.9}$$

where

$$\Delta(x) = V_{\mathrm{e}}(x) - V_{\mathrm{g}}(x). \tag{5.10}$$

The better approximation is obtained by taking into consideration the kinetic energy operator in the scope of the perturbation theory. To the first order, the wavepacket motion results in a correction to $\Delta(x)$. The derivation is similar to the one in [50, 51].

The formal solutions of (5.6) can be written in terms of the evolution operator as

$$\Psi_{\mathrm{F}}(t) = U(t)\Psi_{\mathrm{F}}(0), \tag{5.11}$$

where $U(t)$ satisfies the equation

$$i\hbar\frac{\partial}{\partial t}U(t) = \hat{H}_{\mathrm{F}}U(t) \tag{5.12}$$

with the initial condition

$$U(0) = \mathbf{1}. \tag{5.13}$$

The Hamiltonian $\hat{H}_{\mathrm{F}}$ can be decomposed as

$$\hat{H}_{\mathrm{F}} = H_0 + \tilde{H}_0 , \tag{5.14}$$

where

$$H_0 = \left(\frac{\hat{P}^2}{2m} + \bar{V}\right)\mathbf{1} \tag{5.15}$$

is the purely adiabatic part and $\tilde{H}_0$ is given by (5.9). Equation (5.15) also introduced the average potential

$$\bar{V} \equiv \frac{V_{\mathrm{e}} + V_{\mathrm{g}}}{2}. \tag{5.16}$$

In the interaction picture, the propagator

$$U_{\text{int}}(t) = \exp(iH_0 t)U(t) \tag{5.17}$$

satisfies the equation

$$i\dot{U}_{\text{int}} = \tilde{H}(t)U_{\text{int}} \tag{5.18}$$

with the effective Hamiltonian

$$\tilde{H}(t) = \exp(iH_0 t)\tilde{H}_0(t)\exp(-iH_0 t) . \tag{5.19}$$

The difference between $\tilde{H}(t)$ and $\tilde{H}_0(t)$ stems from the kinetic energy operator in the adiabatic Hamiltonian H_0, which can be treated as a perturbation. Using the Cambell–Baker–Hausdorff expansion, to the first order we have

$$
\begin{aligned}
\tilde{H} &\approx \tilde{H}_0 + \frac{it}{\hbar}\left[H_0, \tilde{H}_0\right] \\
&= \tilde{H}_0 - \frac{t}{4m}\begin{pmatrix} \boldsymbol{\nabla}\Delta \cdot \boldsymbol{P} + \boldsymbol{P} \cdot \boldsymbol{\nabla}\Delta & E(t)\left(\boldsymbol{\nabla}\mu \cdot \boldsymbol{P} + \boldsymbol{P} \cdot \boldsymbol{\nabla}\mu\right) \\ E(t)\left(\boldsymbol{\nabla}\mu \cdot \boldsymbol{P} + \boldsymbol{P} \cdot \boldsymbol{\nabla}\mu\right) & -\boldsymbol{\nabla}\Delta \cdot \boldsymbol{P} - \boldsymbol{P} \cdot \boldsymbol{\nabla}\Delta \end{pmatrix} .
\end{aligned} \tag{5.20}
$$

The second-order term in (5.20) reads $-t^2\left[H_0, [H_0, V]\right]/\hbar^2$, which can be calculated as

$$-t^2\left[H_0, [H_0, V]\right]/\hbar^2 = -\frac{t^2}{4m}(\boldsymbol{\nabla}\Delta) \cdot (\boldsymbol{\nabla}\bar{V})\sigma_z$$

under the assumptions of a linear difference potential Δ and a constant dipole moment μ, where σ_z is the z-component of the Pauli matrix. Note that the higher order terms are exactly equal to zero with these assumptions of linear Δ and constant μ. If we keep this quadratic correction, (5.8) remains the same with the redefined α given by

$$\alpha = \alpha^{(0)} + \alpha^{(1)}, \quad \alpha^{(0)} = \frac{\hbar^3 \alpha_\omega}{(\mu\varepsilon)^3}, \quad \alpha^{(1)} = \frac{\hbar^2(\boldsymbol{\nabla}\Delta) \cdot (\boldsymbol{\nabla}\bar{V})}{2m(\mu\varepsilon)^3},$$

where $\alpha^{(1)}$ is the quadratic correction, which is found to be negligibly small in our calculations. When it is omitted the necessary condition reads

$$\alpha^{(1)} \ll 1 \quad \text{or} \quad \alpha^{(1)} \ll \alpha^{(0)} .$$

The coordinate-dependent level model is obtained if one replaces the momentum operator $\boldsymbol{P}$ by its mean value $m\boldsymbol{v}$. This substitution is warranted for short transition times τ_{tr} and a weak coordinate dependence of Δ and μ. Our calculations show that the terms related to $\boldsymbol{\nabla}\mu$ are negligible and can

be omitted. In this case, the necessary condition that the present formulation holds for can be expressed as

$$\frac{\tau_{\mathrm{tr}}\hbar\boldsymbol{\nabla}\Delta}{2m\sigma_{xx}} \ll \mu\varepsilon \,, \tag{5.21}$$

where σ_{xx} is the variance of the wavepacket.

Under this condition, the effective Hamiltonian assumes the final form

$$\tilde{H} = \tilde{H}_0 + \begin{pmatrix} -\boldsymbol{\nabla}\Delta \cdot (t - t_p)\boldsymbol{v}/2 & 0 \\ 0 & \boldsymbol{\nabla}\Delta \cdot (t - t_p)\boldsymbol{v}/2 \end{pmatrix} \,. \tag{5.22}$$

Thus, to the first order $\Delta(x)$ in (5.9) must be replaced by $\Delta(x) + t\boldsymbol{v} \cdot \boldsymbol{\nabla}\Delta(x)$, where $\boldsymbol{v}$ is the mean velocity of the wavepacket and Δt is the time delay measured from the pulse center.

At the resonance $\omega(t) = \Delta(x)$, the adiabatic potentials i.e. the eigenvalues of (5.9) show avoided crossing and the population splits into the two adiabatic Floquet states. In the case of quadratically chirped pulses, the instantaneous frequency meets the resonance condition twice and near-complete excitation can be achieved due to the constructive interference. The nonadiabatic transition matrix $U_{\tilde{H}}$ for the two-level problem of (5.9) is given by the ZN theory [33] as

$$U_{\tilde{H}} = \begin{pmatrix} T_{11}^R e^{+i(t_f - t_i)\Delta/2\hbar} & T_{12}^R \\ T_{21}^R & T_{22}^R e^{-i(t_f - t_i)\Delta/2\hbar} \end{pmatrix} , \tag{5.23}$$

where

$$T_{11}^R = \left(T_{22}^R\right)^* , \quad T_{21}^R = T_{12}^R \tag{5.24}$$

with

$$T_{11}^R = \left(1 + 2i\sqrt{p_{\mathrm{ZN}}(1 - p_{\mathrm{ZN}})}\sin\Psi_{\mathrm{ZN}}e^{i\Psi_{ZN}}\right)e^{-2i\sigma_{ZN}} \tag{5.25}$$

and

$$T_{21}^R = -2i\sqrt{p_{\mathrm{ZN}}(1 - p_{\mathrm{ZN}})}\sin\Psi_{\mathrm{ZN}} \,. \tag{5.26}$$

The one-passage nonadiabatic transition probability p_{ZN} and the phases in (5.25) and (5.26) are explicitly given by

$$p_{\mathrm{ZN}} = \exp\left[-\frac{\pi}{4\sqrt{\alpha\beta}}\left(\frac{2}{1 + \sqrt{1 + \beta^{-2}(0.4\alpha + 0.7)}}\right)^{1/2}\right]$$

$$\Psi_{\mathrm{ZN}} = \sigma_{\mathrm{ZN}} + \phi_S$$

$$\phi_S = -\frac{\delta_{\mathrm{ZN}}}{\pi} + \frac{\delta_{\mathrm{ZN}}}{\pi}\ln\left(\frac{\delta_{\mathrm{ZN}}}{\pi}\right) - \arg\Gamma\left(\frac{\delta_{\mathrm{ZN}}}{\pi}\right) - \frac{\pi}{4}$$

$$\sigma_{\mathrm{ZN}} + i\delta_{\mathrm{ZN}} = \frac{1}{2\sqrt{\alpha}}\int_{-\beta}^{i}\left(\frac{1 + \zeta^2}{\zeta + \beta}\right)^{1/2}d\zeta \,, \tag{5.27}$$

where the two basic parameters of the nonadiabatic transition, α and β, are defined as

$$\alpha(x) = \frac{\hbar^3 \alpha_\omega}{(\mu\varepsilon)^3} \quad \text{and} \quad \beta(x) = \frac{\Delta(x) - \hbar\beta_\omega + \frac{(\boldsymbol{v}\cdot\boldsymbol{\nabla}\Delta)^2}{4\hbar\alpha_\omega}}{\mu\varepsilon}. \tag{5.28}$$

In particular, the transition probability from the ground electronic state reads

$$P_{12}(x) = |T_{21}^R|^2 = 4p_{\mathrm{ZN}}(1 - p_{\mathrm{ZN}})\sin^2\Psi_{\mathrm{ZN}}. \tag{5.29}$$

$P_{12}(x)$ depends on the nuclear configuration x parametrically through $\{\alpha(x), \beta(x)\}$. With appropriate choices of $\alpha_\omega, \beta_\omega$ and ε, $P_{12}(x)$ can be made to be unity at any fixed x, but complete excitation of the wavepacket is generally impossible, of course, due to the coordinate dependence of the potential difference $\Delta(x)$ and the transition dipole moment μ.

5.3 Optimal Choice of Pulse Parameters

In this section, we will explain some basic features of excitation by quadratically chirped pulses and illustrate which areas of the (α, β) parameter space are appropriate for the scheme.

The nonadiabatic transition probability P_{12} given by (5.29) is plotted in Fig. 5.1 as a function of α and β. Complete excitation for any fixed position x can be achieved by a single quadratically chirped pulse with the appropriate values of α and β in parameter space, such as ($\alpha = 1.20$, $\beta = 0.85$), ($\alpha = 0.53$, $\beta = 2.40$), ($\alpha = 0.38$, $\beta = 3.31$), and so on. Several "islands" are
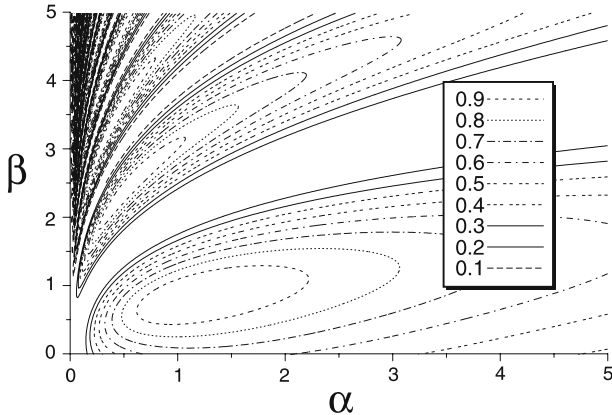
Fig. 5.1. Contour map of the nonadiabatic transition probability $P_{12} = 4p_{\mathrm{ZN}}(1 - p_{\mathrm{ZN}})\sin^2\Psi_{\mathrm{ZN}}$ induced by a quadratically chirped pulse as a function of the two basic parameters α and β

found around these complete excitation points, inside which the transition probability is close to unity (see Fig. 5.1) and decays slowly with changes in α and β. Due to the coordinate dependence of the potential difference $\Delta(x)$ and transition dipole moment $\mu(x)$, it is generally impossible to completely excite the whole wavepacket by a single quadratically chirped pulse. However, we can still achieve a very high efficiency of population transfer without significant distortion of the shape of the wavepacket. This becomes possible if we can find the wavepacket parameters inside one of these "islands" (see Fig. 5.1). Among these, the biggest one is around ($\alpha = 1.20$, $\beta = 0.85$), where the transition probability is higher than 90% in the region $\alpha \in (0.62, 2.21)$ and $\beta \in (0.45, 1.30)$. It turns out that the most efficient and robust excitation of the wavepacket is realized by a pulse which corresponds to $\alpha(x_0) = 1.20$ and $\beta(x_0) = 0.85$ at the wavepacket center x_0.

From the observation of Fig. 5.1, we are able to approximately express the "complete" excitation condition as

$$0.70 \lesssim \alpha = \frac{\hbar^3 \alpha_\omega}{(\mu\varepsilon)^3} \lesssim 2.0 \tag{5.30}$$

and

$$0.50 \lesssim \beta = \frac{\Delta(x) - \hbar\beta_\omega + \frac{(\boldsymbol{v} \cdot \boldsymbol{\nabla} \Delta)^2}{4\hbar\alpha_\omega}}{\mu\varepsilon} \lesssim 1.20 \,. \tag{5.31}$$

Hereafter, we use "complete" to mean this kind of near-complete transition. It was found in our calculation that the condition related to α is easily satisfied, because the transition dipole moment μ only weakly depends on the nuclear coordinates in many systems. The crucial limitation arises from the variation of β through the coordinate dependence of the potential difference $\Delta(x)$. If $\Delta(x)$ can be approximated by a linear function of x within the range of the wavepacket, the range of the parameter β can be roughly estimated as

$$\beta(x_0) - \frac{\sigma_{xx}|\boldsymbol{\nabla}\Delta|}{\mu\varepsilon} \lesssim \beta \lesssim \beta(x_0) + \frac{\sigma_{xx}|\boldsymbol{\nabla}\Delta|}{\mu\varepsilon} \,,$$

according to (5.28), where x_0 is the wavepacket center and σ_{xx} is the variance of the wavepacket in position space. With the optimal choice of parameters, $\beta(x_0) \sim 0.85$, so we have

$$\mu\varepsilon \gtrsim 2.86\sigma_{xx}|\boldsymbol{\nabla}\Delta| \,. \tag{5.32}$$

This single inequality is used, since we want to reduce the laser intensity as much as possible. We denote this condition (5.32) as the complete excitation criterion in the following discussions.

For excitation by quadratically chirped pulses, the transition timescale $2\tau_{tr}$ is slightly longer than the time interval $2\tau_X$ between the two crossings,

given by

$$\tau_X = \sqrt{\frac{\beta}{\alpha}} \frac{\hbar}{\mu\varepsilon}. \tag{5.33}$$

On the other hand, τ_{tr} has to satisfy (5.21) for the validity of our coordinate-dependent level approximation (5.8) to hold. If we take $\tau_{\text{tr}} = 2\tau_X$ (to ensure that no transition occurs before $t = -\tau_{tr}$ and after $t = \tau_{\text{tr}}$) and use (5.33) with (5.21), the following equation can be obtained:

$$\tau_X \le 0.65\sqrt{m\sigma_{xx}/\boldsymbol{\nabla}\varDelta} \tag{5.34}$$

or:

$$\mu\varepsilon \ge 1.30\hbar\sqrt{\boldsymbol{\nabla}\varDelta/m\sigma_{xx}} \tag{5.35}$$

with the optimal choice of $\alpha = 1.20$ and $\beta = 0.85$. Equations (5.34) or (5.35) provide the validity condition of our coordinate-dependent level approximation. We have tested (5.34) and (5.35) on several models. It is found that the total transition probability $\mathcal{P}$ given by 5.8 agrees well with the results obtained from the numerical solution of 5.2 within a few percent for all of the models when criterion (5.34) holds. It turns out that the pulse can be well-designed based on the present coordinate-dependent level approximation. Heavy numerical solutions of (5.2) are not necessary. Thus the method is expected to be applicable to high-dimensional systems.

According to (5.35), the most fortunate circumstance for the present scheme is a system with heavy mass and parallel potential energy surfaces ($\varDelta(x) \simeq$ const.). The steepness of the potential difference $\varDelta(x)$ is the most crucial parameter; it not only affects the validity of this level approximation (5.8) but it also changes the efficiency of excitation according to (5.32). It is obvious that a narrow wavepacket can be relatively easily excited by a quadratically chirped pulse (cf. 5.32). However, a narrow one can easily break the level approximation (5.35) because of the broad distribution in momentum space. The optimal width of a wavepacket can be roughly estimated as

$$\sigma_{xx} \approx 0.59\left(\frac{\hbar^2}{m\boldsymbol{\nabla}\varDelta}\right)^{1/3} \tag{5.36}$$

by making the right-hand sides of (5.35) and (5.32) equal to each other.

We would like to emphasize that the excitation process basically depends on the three parameters α_ω, β_ω and ε, but only one of them turns out to be independent if the complete excitation is taken into account. With the optimal choice of α and β (i.e., $\alpha = 1.20$ and $\beta = 0.85$), we have two (5.30) and (5.31) for the three variables α_ω, β_ω and ε, so only one of them can be independent.

5.4 Numerical Examples

In order to demonstrate the efficiency and robustness of the formulations presented in Sect. 5.2 and 5.3, three practical applications are considered here. In the first part of this section, we consider the "complete" excitation of a wavepacket from a nonequilibrium displaced position, which is directly related to the idea of bond-selective breaking, as explained in the "Introduction". This is demonstrated numerically by taking diatomic molecules LiH and NaK as examples. In the second part, we consider the complete pump-dump control and creation of a localized wavepacket using quadratic chirping within the pump-dump mechanism. The bond-selective photodissociation of the H_2O molecule is discussed in the third part of this subsection as an example of a multidimensional system.

In the present work, we monitor the laser-driven dynamics designed by the present formulation by numerically solving the time-dependent Schrödinger (5.2). It is solved by the split operator method [52] with the fast Fourier transform technique [53]. In order to prevent artificial reflections of the wavepacket at the edges, a negative imaginary absorption potential is placed at the ends of the grid [54]. The envelope of the pulses employed is taken as

$$\varepsilon(t) = \frac{\varepsilon_0}{2} \left\{ \tanh \left[\frac{t - t_c + \tau/2}{s} \right] - \tanh \left[\frac{t - t_c - \tau/2}{s} \right] \right\} \qquad (5.37)$$

where t_c, s, τ and ε_0 are the center time, the switching time, the duration, and the maximum amplitude, respectively. In addition, we take the envelope center time to coincide with the frequency center time, i.e., $t_c = t_p$ (see (5.5)).

5.4.1 Electronic Excitation
from a Nonequilibrium Displaced Position

First of all we consider the "complete" excitation of a displaced LiH wavepacket from the $X\,^1\Sigma^+$ state to the $B\,^1\Pi$ state. The initial state is taken to be a displaced ground vibrational eigenfunction of LiH on the electronic ground state potential V_g. The center of the wavepacket is located at $R = 6.0\,a_0$ and is about $3\,a_0$ away from the equilibrium position. It is not simply put at $R = 6\,a_0$ at $t = 0$, but is actually prepared by moving the ground vibrational state by a sequence of quadratically chirped IR pulses. This constitutes the second important elementary process we want to control, as explained in the "Introduction." As an illustration, the potential energy curves and the transition dipole moment μ_{BX} are plotted in Fig. 5.2, together with the initial wavepacket. The potential energy curves and the transition dipole moment of LiH molecule are taken from the work of Partridge and Langhoff [55].

The time dependence of the wavepacket population on the X and B states are plotted in Fig. 5.3 for the case of a quadratically chirped pulse centered at $t_p = 0$ fs with a full temporal duration $\tau = 20$ fs. More than 86% of the initial state is excited to the B state within a few femtoseconds (see Fig. 5.3). After the excitation, Ψ_e on the B state potential spreads rapidly due to the very light mass of LiH and the flatness of the potential. Finally, however,
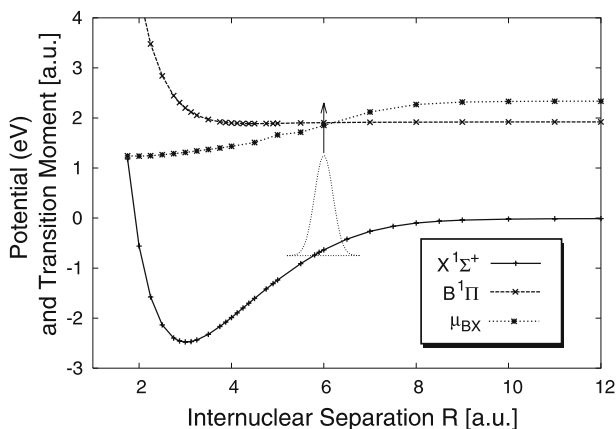
Fig. 5.2. Electronic excitation of LiH wavepacket from the outer classical turning point ($\sim 6\,a_0$) of the ground $X^1\Sigma^+$ state. The $B^1\Pi \leftarrow X^1\Sigma^+$ transition is considered and the initial wavepacket is a $3\,a_0$ shifted ground vibrational eigenfunction of LiH. The potential energy curves and the transition dipole moment of LiH are taken from the ab initio work of Partridge and Langhoff [55]
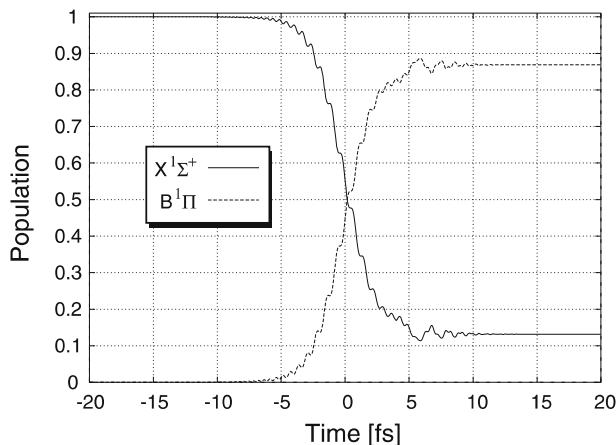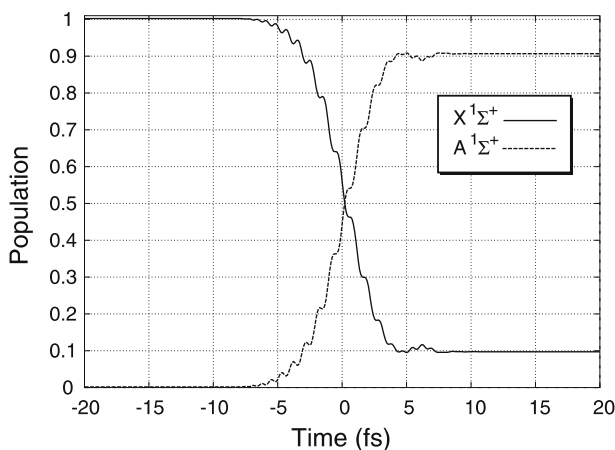

Fig. 5.3. Time variation of the wavepacket population on the $X^1\Sigma^+$ and $B^1\Pi$ states of LiH. The system is excited by a single quadratically chirped pulse with parameters: $\alpha_\omega = 5.840 \times 10^{-2}\,\mathrm{eV/fs^2}$, $\beta_\omega = 2.319\,\mathrm{eV}$ and $I = 1.00\,\mathrm{TW/cm^2}$. The pulse is centered at $t = 0$ and has a temporal width $\tau = 20$ fs

Ψ_e moves out to the asymptotic region and a high dissociation efficiency is attained.

Note that the deviation of the transformed population from 100% should not be understood as the error in our approximation (5.8). The integrated total transition probability according to (5.8) is $\mathcal{P} = 0.879$, which is in excellent agreement with the value $\mathcal{P} = 0.864$ obtained by numerical solution of (1.2). This deviation from 100% efficiency is intrinsic, i.e., it derives from the spread of the wavepacket. The total transition probability can be improved by increasing the laser intensity. This is because the range of Δ increases, as can be seen from (5.28). For instance, if we use $I = 4.0\,\text{TW/cm}^2$, then the total transition probability reaches $93 \sim 94\%$. Since we have to be careful about multiphon processes, it is better not to use very high intensities.

We should note that there is no significant distortion of the shape of the wavepacket during the transition for both $I = 1.0\,\text{TW/cm}^2$ (see Fig. 5.4) and for $I = 4.0\,\text{TW/cm}^2$. In order to eliminate adiabatic propagation effects, we have propagated the ground and excited wavepackets Ψ_g and Ψ_e forward and backward, respectively (i.e., to the same time $t = t_p$ according to the adiabatic surface Hamiltonians H_g and H_e). It can be seen that the shapes of the initial and final wavepackets are almost identical to each other, indicating that the nuclear momentum is almost conserved during the electronic transition. The excited wavepacket is only slightly to the right. During this transition period, the wavepacket moves a little bit. The present technique
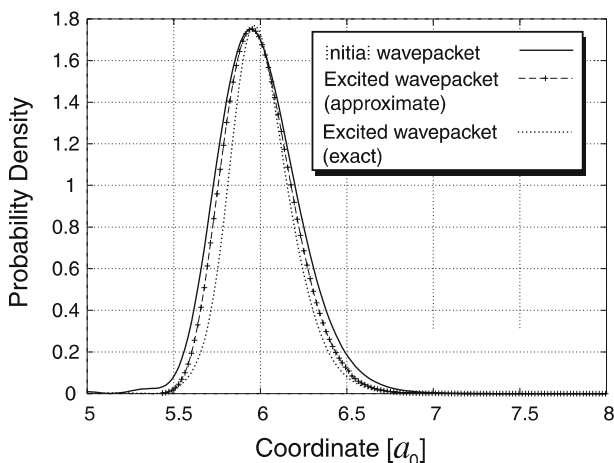
Fig. 5.4. Initial and final wavepackets of LiH excited by the same quadratically chirped pulse as that in Fig. 5.3. *Initial wavepacket* refers to the wavepacket propagated up to the pulse center according to the ground surface Hamiltonian H_g; *excited wavepacket (approximate)* refers to the result obtained using the level approximation as $P_{12}(x)|\Psi_g(x,0)|^2$; and *excited wavepacket (exact)* refers to the numerical solution of (5.1). The latter two are backward-propagated to the pulse center at time $t = t_p$ according to the excited state Hamiltonian H_e

can thus be used to rapidly create a localized wavepacket on the excited state potential energy surface, even in the case of large molecules that usually suffer from fast decoherence effects.

It should also be noted that the LiH molecule is one of the most difficult systems to apply the present method to, because the mass of LiH is very light at 0.875 amu and the gradient of potential difference is relatively large ($\boldsymbol{\nabla}\Delta \simeq -0.473\,\mathrm{eV}/a_0$) at the center of the wavepacket. All of these difficulties have been nicely overcome by employing fast quadratic chirping. This fact guarantees the usefulness of the present method.

As a second example, another extreme case of NaK was investigated. The initial wavepacket was prepared at the inner turning point on the ground state X by two quadratically chirped pulses starting from the ground vibrational state using the pump-dump mechanism discussed in the next section. Another quadratically chirped pulse is applied to excite this wavepacket to the excited state A and this leads to "complete" dissociation. The whole scheme is shown in Fig. 5.5. The potential energy curves and the transition dipole moment are taken from the work of Magnier et al. [56]. The total excitation probability $\mathcal{P}$ was found to be as high as $\mathcal{P} = 0.905$, even for the less localized initial wavepacket at $R = 5.1a_0$ with a laser intensity of only $0.2\,\mathrm{TW/cm}^2$. If we can prepare a wavepacket that is more localized initially, then much higher excitation probability can be achieved. For instance, $\mathcal{P} = 0.994$ is obtained with the same laser field when a narrow Gaussian wavepacket with variance $\sigma_{xx} = 0.075\,a_0$ is prepared at position $R = 5.0\,a_0$. The high excitation efficiency in the case of NaK in comparison to LiH is
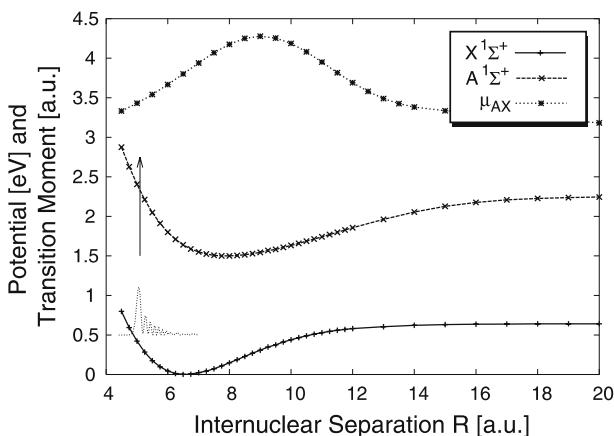
Fig. 5.5. Electronic excitation of a NaK wavepacket from the inner turning point of the ground $X^1\Sigma^+$ state. The $A^1\Sigma^+ \leftarrow X^1\Sigma^+$ transition is considered and the initial wavepacket is prepared by two quadratically chirped pulse within the pump-dump mechanism explained in the next section. The potential energy curves and the transition dipole moment are taken from the ab initio work of S. Magnier, M. Aubert-Frecon and Ph. Millie [56]

Fig. 5.6. Time variations of the wavepacket populations in the $X^1\Sigma^+$ and $A^1\Sigma^+$ states of NaK. The system is excited by a quadratically chirped pulse with parameters: $\alpha_\omega = 3.13 \times 10^2 \,\mathrm{eV/fs^2}$, $\beta_\omega = 1.76 \,\mathrm{eV}$ and $I = 0.20 \,\mathrm{TW/cm^2}$. The pulse is centered at $t = 0$ and has a temporal width $\tau = 20 \,\mathrm{fs}$

due to the relatively small potential difference gradient $\boldsymbol{\nabla}\Delta \simeq 0.208 \,\mathrm{eV}/a_0$, the large transition dipole moment $\mu = 3.43 \, ea_0$ and the large reduced mass. These conditions can also reduce the laser intensity required. The time variations of the populations in the electronic ground and excited states X and A are shown in Fig. 5.6.

The method of electronic excitation by a quadratically chirped pulse mentioned above can be applied to a wavepacket moving away from the turning point, so this technique can be applied to various processes such as pump-dump, wavepacket localization and selective bond-breaking, as we will discuss in the rest of this section.

5.4.2 "Complete" Pump-Dump Control

Since the pioneering work of Tannor and Rice [2], the pump-dump method has been widely used to control various processes (see [3, 22, 30, 31] and references therein). However, the efficiency of this is not high, simply because the ordinary transform-limited or linear chirped pulses cannot transfer a wavepacket from one potential energy surface to other "completely." Here we propose to use the quadratically chirped pulse to enhance the efficiency. "Complete" pump-dump control can then be achieved. This is demonstrated by preparing the localized wavepacket at the inner turning point on the ground state X of NaK as an example (see the previous section). We take the ground ($v = 0$) vibrational eigenfunction of the electronic ground (X) state potential V_g and excite it by a quadratically chirped pulse to the first electronic excited (A) state potential V_e. The excited

wavepacket then evolves to the right according to the excited state Hamiltonian H_e. When the wavepacket arrives at the outer turning point of V_e, it is dumped by another quadratically chirped pulse back to the ground electronic X state. The time variations of the populations of the ground X and excited A states are plotted in Fig. 5.7. Both the pump and the dump transitions are very efficient, and the overall pump-dump transition probability is found to be better than 0.981. This means that the efficiency of any pump-dump procedure can be enhanced greatly by using our quadratic chirping scheme. The dumped wavepacket Ψ_g then evolves to the left according to the ground state Hamiltonian H_g and arrives at the inner turning point at $t = 440.2\,$fs. This is the one used as the initial wavepacket in Fig. 5.5.

Finally, we demonstrated that a well-designed quadratically chirped pulse can excite or deexcite the wavepacket while it is moving in-between the turning points if the velocity of the wavepacket is not too high. As an illustration, we tried to dump the excited-state wavepacket prepared by the previous pump pulse at the minimum position of the excited A state. The time variations of the populations in the X and A states are shown in Fig. 5.8. A high dumping efficiency can still be achieved, and the overall pump-dump transition probability is about 0.958, which is only slightly lower than that of the previous case dumped at the outer turning point.
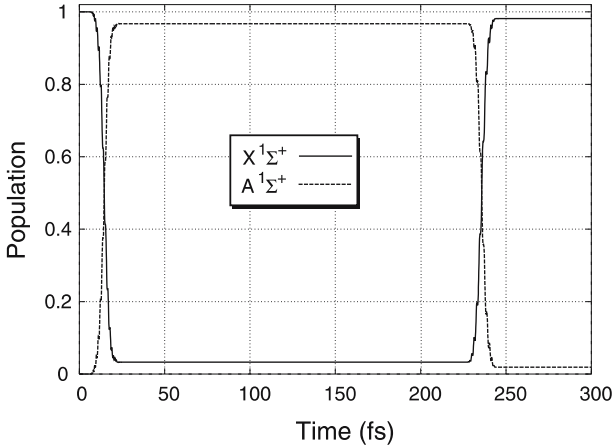
Fig. 5.7. Pump-dump control of NaK molecule using two quadratically chirped pulses. The initial state is taken as the ground vibrational eigenfunction of the ground state $X^{\,1}\Sigma^+$ and this is excited by a quadratically chirped pulse to the excited state $A^{\,1}\Sigma^+$. The excited wavepacket is dumped at the outer turning point $t \simeq 230\,$fs by the second quadratically chirped pulse. The laser parameters used are (1) first pulse: $\alpha_\omega = 2.750 \times 10^{-2}\,\mathrm{eV/fs}^2$, $\beta_\omega = 1.441\,$eV and $I = 0.15\,\mathrm{TW/cm}^2$ and (2) second pulse: $\alpha_\omega = 1.972 \times 10^{-2}\,\mathrm{eV/fs}^2$, $\beta_\omega = 1.031\,$eV and $I = 0.10\,\mathrm{TW/cm}^2$. The two pulses are centered at $t_1 = 14.5\,$fs and $t_2 = 235.8\,$fs, respectively. Both of them have a temporal width $\tau = 20\,$fs
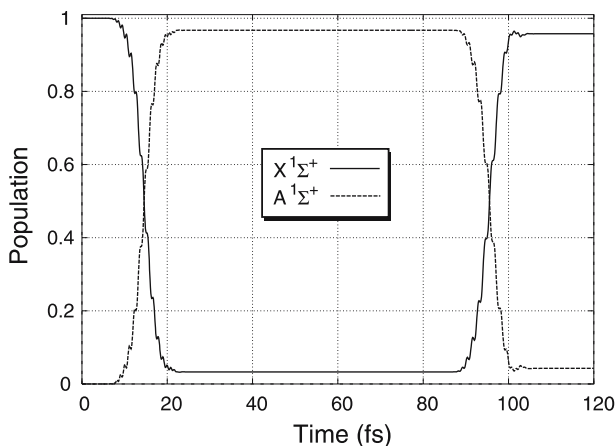
Fig. 5.8. Pump-dump control of NaK using two quadratically chirped pulses. The initial state and the first pump step are the same as in Fig. 5.7. The excited wavepacket is now dumped at $R \simeq 6.5 \, a_0$ on the way to the outer turning point. The first pulse is the same as that in Fig. 5.7, but the second one is different: $\alpha_\omega = 1.929 \times 10^{-2} \, \mathrm{eV/fs^2}$, $\beta_\omega = 1.224 \, \mathrm{eV}$ and $I = 0.10 \, \mathrm{TW/cm^2}$. The second pulse is centered at $t = 95.5 \, \mathrm{fs}$ and has a temporal width $\tau = 20 \, \mathrm{fs}$

By manipulating the timing of the pump and/or dump pulses as demonstrated above, a target wavepacket with the central momentum and position desired can be generated by appropriately designed quadratic chirping. These wavepackets can serve as initial states for other processes.

5.4.3 Selective Bond-Breaking

Since the present quadratic chirping excitation scheme works for any fixed nuclear configuration, the scheme can easily be applied to multidimensional systems. As an example, we consider here the bond-selective photodissociation of H_2O on the excited $\tilde{A}$ potential energy surface. The 2-D model of H_2O is adapted from [57, 58], with the angle ∠HOH fixed at 104.5°.

In the following calculations, the laser field is assumed to be linearly polarized parallel to the transition dipole moment μ, which is almost perpendicular to the molecular plane. The initial wavepacket is a two-dimensional symmetrical Gaussian wavepacket of form

$$\Phi = \phi_1 \phi_2 \tag{5.38}$$

with

$$\phi_i = \left(\pi \sigma_i^2\right)^{-1/4} \exp\left[-\frac{(R_i - \bar{R}_1)^2}{2\sigma_i^2} + \frac{\mathrm{i}}{\hbar} \bar{P}_i (R_i - \bar{R}_i) \right] , \tag{5.39}$$

where $i = 1, 2$ is the index of the particular OH bond (there are two). The parameters are given in Table 5.1, where $\bar{R}_i$ and $\bar{P}_i$ refer to the central position

and momentum of the i-th OH bond. It should be noted that case b represents the initial state shifted from the equilibrium position and case c corresponds to the wavepacket with finite initial momentum in the direction of R_1.

The laser parameters used for the "complete" excitation of the three initial wavepackets a, b and c are listed in Table 5.2, where the intensities of the pulses are taken to be the lowest corresponding to (5.35). The total transition probability $\mathcal{P}$ in the worst case is 73%, which corresponds to the shifted wavepacket (case b). The values of $\mathcal{P}$ obtained from the coordinate-dependent level approximation (5.8) are again in very good agreement with those obtained from the numerical solutions of (5.2). This indicates that the level approximation (5.8) gives a reasonably accurate description, even for multidimensional systems. The laser parameters of the pulses a and c are almost the same, except that the carrier frequency of the pulse c is 0.24 eV higher than that of a. This is due to the kinetic energy correction $(\boldsymbol{v} \cdot \nabla \Delta)^2 / 4\hbar\alpha_\omega$ in (5.28). It should be noted that pulse b is nearly three times more intense than the other two cases because of the exponential decay of the transition dipole moment μ and the increase of the potential energy difference $\nabla\Delta$.

In order to measure the selectivity, we define the target yield Y_e as the population density of the excited wavepacket Ψ_e integrated over the target region,

$$Y_e(t) = \int_{\mathcal{D}} |\Psi_e(t)|^2 \mathrm{d}R_1 \mathrm{d}R_2. \tag{5.40}$$

Table 5.1. Parameters of the three types of initial wavepackets considered for bond-selective photodissociation of H_2O. Allof the quantities are measured in atomic units

	$\bar{R}_1$	$\bar{R}_2$	$\bar{P}_1$	$\bar{P}_2$	σ_{xx}
a	1.82	1.82	0.0	0.0	0.20
b	2.32	1.82	0.0	0.0	0.20
c	1.82	1.82	12.0	0.0	0.20

Table 5.2. Quadratically chirped pulses for the bond-selective photodissociation of H_2O

Pulse	α_ω (eV/fs^2)	β_ω (eV)	I (TW/cm^2)	$\mathcal{P}^1$	$\mathcal{P}^2$
a	1.34	6.17	20.0	81.7%	80.2%
b	2.89	4.34	57.8	74.4%	73.0%
c	1.34	6.61	20.0	81.5%	78.8%

[1] Total excitation probability from the analytical approximation shown in (5.8).
[2] Total excitation probability obtained by the numerical solution of (5.2).

Here, the channel with $R_1 \to \infty$ is assumed to be the target channel and the actual integration domain $\mathcal{D}$ is taken to be $R_1 \in (2.5, 7.5)$ and $R_2 \in (1.0, 3.0)$.

First, we present the dynamics of the initial wavepacket a. Initially the system stands at the equilibrium position of the electronic ground $\tilde{X}$. The temporal evolution of the wavepacket Ψ_e generated in the electronic excited state is shown in the left-hand column of Fig. 5.9. Apparently, Ψ_e originates in the Frank–Condon (FC) region, which is located at the steep inner wall of the electronically excited $\tilde{A}$ state. The repulsive force of the potential V_e the drives $\Psi_e(t)$ downhill toward the saddle point and then up the potential ridge, where $\Psi_e(t)$ bifurcates into two asymptotic valleys, with $Y_e = 0.495$ in channel 1. The excitation achieved using this simple quadratically chirped pulse is not naturally bond-selective because of the symmetry of the system. The role played by our quadratically chirped pulse is similar to that of the ordinary photodissociation process, except that it can cause near-complete excitation (see Table 5.1 for the efficiency). This is not very exciting, however, because we would like to break the bond selectively.

There are two ways to achieve selective bond-breaking: (1) move the initial wavepacket to another FC region located in the target dissociative channel (bond-selective force case [46,47]); and (2) prepare the initial wavepacket with a finite momentum directed to the desired channel (bond-directed momentum case in [48]). These two methods may be combined to improve the efficiency, but on the other hand, appropriate FC regions may not be easy to find in general. In the case of H_2O, for instance, it is found that the required laser is rather intense over a broad region of the system except for a small domain near the equilibrium position of V_g. This is due to the very steep potential energy surfaces of both the $\tilde{X}$ and the $\tilde{A}$ states and the exponential decay of the transition dipole moment away from the equilibrium position.We hope, however, that this does not represent a very common case.

Following idea (1) stated above, we used the wavepacket b in Table 5.1 as a second example. The average energy measured from the bottom of V_g of Fig. 5.9 (see Table 5.2 for the laser pulse). The excited wavepacket $\Psi_e$originally appears at about $0.5a_0$ from that of wavepacket a. Since Ψ_e stands on the slope of the valley with $R_1 > R_2$, where the force is directed, resulting in a great deal of dissociation in channel 1. However, due to the light mass of H_2O, the spread of Ψ_e is quite rapid and a small (but not negligible) amount of Ψ_e gets beyond the potential barrier and appears on the other side, leading to dissociation in channel 2. Finally, a target yield Y_e of 0.72 is achieved in the selected channel (1). Although it is already about twice as high as that of the competing channel, we want an even higher yield.

Lastly, let us consider wavepacket c in Table 5.1, which has a bond-directed initial momentum $\bar{P}_1 = 12\hbar/a_0$ along the R_1 direction. Its average energy measured from the bottom of V_g is about $1.1\,\mathrm{eV}$, and the temporal evolution of Ψ_e is shown in the right-hand column of Fig. 5.9. Ψ_e is created on the excited state in the same domain as that of the wavepacket a, which is located on the steep inner wall of V_e. It moves rapidly downhill along the
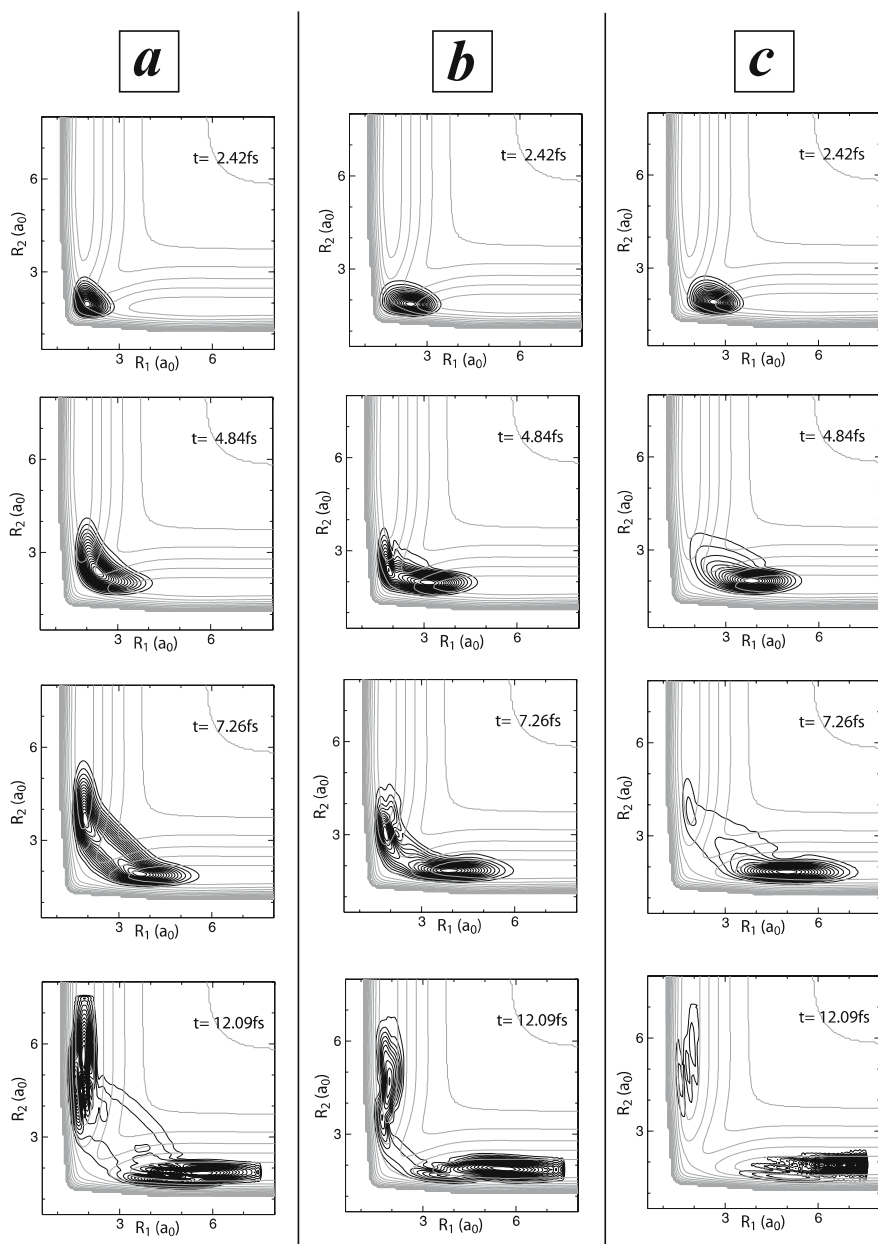
Fig. 5.9. Selective bond-breaking of H_2O by means of the quadratically chirped pulses with initial wavepackets a, b and c, as described in Table 5.1. The *left-hand*, *middle* and *right-hand columns* correspond to the cases for the initial wavepackets a, b and c, respectively. The laser-driven dynamics of the wavepackets moving on the excited potential energy surface V_e are illustrated by the density. The time is taken from the center of the pulse (i.e., $t_p = 0$)

valley in the R_1 direction due to the bond-directed momenta $\bar{P}_1$ Only a very small amount of Ψ_e can get beyond the barrier of V_e due to the spreading effect and appear in the region where the force is directed to $R_2 \to \infty$. The dissociation in channel 2 is found to be less than 5%. This high selectivity is guaranteed by the rapid motion of Ψ_e on the excited potential energy surface V_e within a very short period ($\sim$ 2 fs). The target yield Y_e achieved is as high as 0.95 in this case.

As demonstrated above, bond-selective dissociation can be achieved with high efficiency by using an initial displaced-position and/or a directed-momentum wavepacket. The latter wavepacket can be prepared via the sequence of quadratically chirped pulses or by using semiclassical optimal control theory [34, 35].

5.5 Future Perspectives

The control of molecular processes and chemical reactions by laser fields has become an area of active research in recent times due to remarkable progress in laser technology, and it is expected to be an important scientific topic in years to come. Needless to say, the control of systems with many degrees of freedom is very important for practical applications and it is a challenging aim for theoretical studies. The main difficulties involved with controlling multidimensional systems are the formidable numerical cost of quantum wavepacket propagation and the significant effects of energy exchange between different molecular modes. The latter causes extra wavepacket broadening and can dramatically reduce control efficiency.

In this sense, the control of electronic transitions of wavepackets using short quadratically chirped laser pulses of moderate intensity is a very promising method, for two reasons. First, only information about the local properties of the potential energy surface and the dipole moment is required to calculate the laser pulse parameters. Second, this method has been demonstrated to be quite stable against variations in pulse parameters and wavepacket broadening. However, controlling of some types of excitation processes, such as bond-selective photodissociation and chemical reaction, requires the control of wavepacket motion on adiabatic potential surfaces before and/or after the localized wavepacket is made to jump between the two adiabatic potential energy surfaces.

By combining the control of electronic transitions of wavepackets using quadratically chirped laser pulses with semiclassical optimal control [34, 35] on a single adiabatic surface, we should be able to establish an effective methodology for controlling the dynamics of large-dimensional chemical and biological systems.

References

1. P. Brumer and M. Shapiro, Chem. Phys. Lett. **126**, 541 (1986)
2. D. J. Tannor and S. A. Rice, J. Chem. Phys. **83**, 5013 (1985)
3. S. A. Rice and M. Zhao, *Optical Control of Molecular Dynamics* (Wiley, New York, 2000)
4. S. M. Hurley and A. W. Castleman, Science **292**, 648 (2001)
5. A. Peirce, M. Dahleh and H. Rabitz, Phys. Rev. A **37**, 4950 (1988)
6. S. Shi, A. Woody and H. Rabitz, J. Chem. Phys. **88**, 6870 (1988)
7. C. Schwieters and H. Rabitz, Phys. Rev. A **44**, 5224 (1991); *ibid.* **48**, 2549 (1993)
8. J. Botina, H. Rabitz and N. Rahman, J. Chem. Phys. **102**, 226 (1995)
9. R. Kosloff, S. Rice, P. Gaspard, S. Tersigni and D. Tannor, Chem. Phys. **139**, 201 (1989)
10. J. Somlói, V. Kazakov and D. Tannor, Chem. Phys. **172**, 85 (1993)
11. M. Sugawara, Y. Fujimura, J. Chem. Phys. **100**, 5646 (1994)
12. Y. Ohtsuki, H. Kono, Y. Fujimura, J. Chem. Phys. **109**, 9318 (1998)
13. W. Zhu, J. Botina and H. Rabitz, J. Chem. Phys. **108**, 1953 (1998)
14. R. S. Judson and H. Rabitz, Phys. Rev. Lett. **68**, 1500 (1992)
15. S. Chelkowski and G. N. Gibson, Phys. Rev. A. **52**, R3417 (1995)
16. N. V. Vitanov, T. Halfmann, B. W. Shore, and K. Bergmann, Annu. Rev. Phys. Chem. **52**, 763 (2001)
17. B. M. Garraway and K. A. Suominen, Phys. Rev. Lett. **80**, 932 (1998)
18. C. J. Bardeen, Q. Wang and C. V. Shank, J. Phys. Chem. A. **102**, 2759 (1998)
19. J. Cao, C. J. Bardeen and K. R. Wilson, Phys. Rev. Lett. **80**, 1406(1998)
20. T. Rickes L. P. Yatsenko, S. Steuerwald, T. Halfmann, B. W. Shore, N. V. Vitanov and K. Bergmann, J. Chem. Phys. **113**, 534 (2000)
21. B. Y. Chang, I. R. Solá , V. S. Malinovsky, and J. Santamariá, J. Chem. Phys. **113**, 4901 (2000)
22. B. Y. Chang, I. R. Sola, V. S. Malinovsky and J. Santamaria, Phys. Rev. A. **64**, 033420 (2001)
23. F. Legare, S. Chelkowski, and A. D. Bandrauk, J. Raman. Spectrosc. **31**, 15 (2000)
24. Y. Teranishi, K. Nagaya and H. Nakamura, *Advances in Multiphoton Processes and Spectroscopy* (World Scientific, Singapore, 2001), Vol. **14**
25. Y. Teranishi and H. Nakamura, J. Chem. Phys. **109**, 1904 (1997)
26. Y. Teranishi and H. Nakamura, Phys. Rev. Lett. **81**, 2031 (1998)
27. Y. Teranishi and H. Nakamura, J. Chem. Phys. **111**, 1415 (1999)
28. K. Nagaya, Y. Teranishi and H. Nakamura, in: *Laser Control and Manipulation of Molecules*, edited by A. D. Bandrauk, R. J. Gordon and Y. Fujimura (American Chemical Society, Washington, DC, 2001)
29. K. Nagaya, Y. Teranishi and H. Nakamura, J. Chem. Phys. **117**, 9588 (2002)
30. R. J. Gordon and S. A. Rice, Annu. Rev. Phys. Chem. **48**, 601 (1997)
31. P. Brumer, M. Shapiro, *Coherent Control of Atomic and Molecular Processes* (Wiley, New York, 2003)
32. H. Nakamura, *Nonadiabatic Transition: Concepts, Basic Theories, and Applications* (World Scientific, Singapore, 2002)

33. C. Zhu, G. Mil'nikov and H. Nakamura, *Semiclassical Theory of Nonadiabatic Transition and Tunneling*. In: *Modern Trends in Chemical Reactions Dynamics—Part I.*, edited by K. P. Liu and X. M. Yang (World Scientific, Singapore, 2003)
34. A. Kondorskiy and H. Nakamura, J. Theor. Comp. Chem. **4**, 72 (2005)
35. A. Kondorskiy, G. Mil'nikov and H. Nakamura, Phys. Rev. A **72**, 041401 (2005)
36. R. Zare, Science **279**, 1875 (1998)
37. H. Rabitz, R. D. Vivie-Riedle, M. Motzkus, and K. Kompa, Science **288**, 824 (2000)
38. A. H. Zewail, Angew. Chem. Int. Ed. **39**, 2586 (2000) (Nobel Lecture)
39. S. A. Rice, Nature (London) **409**, 422 (2001).
40. I. Sh. Averbukh, M. J. J. Vrakking, D. M. Villeneuve, and A. Stolow, Phys. Rev. Lett. **77**, 3518 (1996)
41. M. Leibscher and I. Sh. Averbukh, Phys. Rev. A **63**, 043407 (2001)
42. J. R. R. Verlet, V. G. Stavros, and H. H. Fielding, Phys. Rev. A **65**, 032504 (2002)
43. K. Nagaya, Y. Teranishi and H. Nakamura, J. Chem. Phys. **113**, 6197 (2000)
44. H. Fujisaki, Y. Teranishi and H. Nakamura, J. Theor. Comp. Chem. **1**, 245 (2002)
45. S. Zou, A. Kondorskiy, G. Mil'nikov and H. Nakamura, J. Chem. Phys. **122**, 084112 (2005)
46. B. Amstrup and N. E. Henriksen, J. Chem. Phys. **97**, 8285 (1992)
47. B. Amstrup and N. E. Henriksen, J. Chem. Phys. **105**, 9115 (1996)
48. N. Elghobashi, P. Krause, J. Manz, and M. Oppel, Phys. Chem. Chem. Phys. **5**, 4806 (2003)
49. S. I. Chu, *Advances in Multiphoton Processes and Spectroscopy*, Vol. 2 (World Scientific, Singapore, 1986).
50. T.J. Smith and J.A. Cina. J. Chem. Phys. **104**, 1272 (1996).
51. N.E. Henriksen, Chem. Phys. Lett. **312**, 196 (1999).
52. M.D. Feit and J.A. Fleck, Jr. J. Chem. Phys. **78**, 301 (1983).
53. C. Leforestier, R.H. Besseling, C. Cerjan et al., J. Comput. Phys. **94**, 59 (1991).
54. Á. Vibók and G.G. Balint-Kurti, J. Chem. Phys. **96**, 7615 (1992).
55. H. Partridge and S.R. Langhoff, J. Chem. Phys. **74**, 2361 (1981).
56. S. Magnier, M. Aubert-Frecon and Ph. Millie, J. Molec. Spec. **200**, 86 (2000).
57. S. Meyer and V. Engel, J. Phys. Chem. A **101**, 7749 (1997).
58. D.G. Imre and J. Zhang, Chem. Phys. **139**, 89 (1989).

6 Laser Control of Chemical Dynamics.
II. Control of Wavepacket Motion

A. Kondorskiy[1], G. Mil'nikov[2], and H. Nakamura[3]

[1] Department of Theoretical Studies, Institute for Molecular Science, Myodaiji, Okazaki 444-8585, Japan
e-mail: nakamura@ims.ac.jp
[2] Lebedev Physical Institute, Leninsky pr., 53, Moscow, 119991, Russia
[3] The Graduate University for Advanced Studies, Myodaiji, Okazaki 444-8585, Japan

Summary. An efficient semiclassical optimal control theory for controlling wavepacket dynamics on a single adiabatic potential energy surface applicable to systems with many degrees of freedom is discussed in detail. The approach combines the advantages of various formulations of the optimal control theory: quantum and classical on the one hand and global and local on the other. The efficiency and reliability of the method are demonstrated, using systems with two and four dimensions as examples.

6.1 Introduction

The laser control of molecular processes is a research area in chemical physics that is currently very active. One of the most natural and flexible approaches in this area is the optimal control theory (OCT) [1, 2]. This is based on the idea that the controlling laser pulse should optimize a certain functional so that the variational principle can be used to design the pulse [1–11]. An early version of the theory for classical [3–6] and quantum [7, 8] systems employed the well-established numerical conjugate gradient search method to solve the system of equations iteratively and maximize the particular functional. More effective numerical schemes for solving this system of optimal control equations were then introduced [8–11]. These iterative algorithms converge faster than those based on the gradient method.

Our strategy for controlling chemical dynamics is based on the idea that there are two basic elements of wavepacket motion in chemical dynamics: (i) electronically nonadiabatic transitions between adiabatic potential energy surfaces and (ii) wavepacket motion on a single adiabatic potential energy surface. If we could fully control these two basic motions of wavepackets, it would become possible to control various kinds of realistic chemical dynamics.

In order to control elementary process (i), an effective scheme based on the concept of quadratic chirping has been proposed [12–17]. It has been demonstrated that this idea can be applied to process (i) and that fast and near-complete selective excitation of a wavepacket can be achieved without significant distortion of its shape through the utilization of specially designed quadratically chirped pulses [18,19]. This method is discussed in the first part

of this review [19]. In order to control elementary process (ii), an efficient semiclassical optimal control theory applicable to multidimensional systems has been formulated. The approach combines the advantages of various formulations of the optimal control theory (OCT): quantum and classical on the one hand, and global and local on the other. The quantum mechanical OCT is not feasible for multidimensional systems higher than 3-D and the classical OCT is not reliable in this case due to the importance of phases in laser–molecule interactions. Therefore, the semiclassical theory is expected to provide a framework that will allow these difficulties to be circumvented. This theory is discussed in the this (second) part of the review.

Within the quantum formulation of OCT, the basic variational procedure leads to a set of equations for the optimal laser field, which include *two* Schrödinger equations to describe the dynamics starting from the initial and the target state wavepackets. The optimal laser field is given by the imaginary part of the correlation function for these two wavepackets. This system of equations of optimal control must generally be solved iteratively, making it an extremely computationally expensive approach for multidimensional systems.

In addition to the quantum approaches mentioned above, classical optimal control theories based on classical mechanics have also been developed [3–6]. These methods control certain classical parameters of the system like the average nuclear coordinates and the momentum. The optimal laser field is given as an average of particular classical values with respect to the set of trajectories. The system of equations is solved iteratively using the gradient method. The classical OCT deals only with classical trajectories and thus incurs much lower computational costs compared to the quantum OCT. However, the effects of phase are not treated properly and the quantum mechanical states cannot be controlled appropriately. For instance, the selective excitation of coupled states cannot be controlled via the classical OCT and the spectrum of the controlling field does not contain the peaks that arise from one- and multiphoton transitions between quantum discrete states.

Since the classical treatment has its restrictions and the applicability of the quantum OCT is limited to low-dimensional systems due to its formidable computational cost, it would be very desirable to incorporate the semiclassical method of wavepacket propagation like the Herman–Kluk method [20, 21] into the OCT. Recently, semiclassical bichromatic coherent control has been demonstrated for a large molecule [22] by directly calculating the percent reactant as a function of laser parameters. This approach, however, is not an optimal control.

Within the semiclassical approach, each wavepacket is propagated by running a large number of classical trajectories. In order to calculate the correlation function, a double summation with respect to these large number of trajectories should be performed at each time step, which is, unfortunately, also very demanding computationally.

Recently, a semiclassical formulation of the optimal control theory has been derived [23, 24] by combining the conjugate gradient search method

with a semiclassical expression for the correlation function. This requires only a single summation with respect to the number of trajectories. Two approximate semiclassical expressions for the correlation function, each of which contain only one summation with respect to the trajectories, are obtained [23]. The simpler one only requires the coordinates and momenta of classical trajectories to be calculated. The other one requires extra calculations of common semiclassical quantities; as a result, additional quantum effects can be taken into account. This formulation was further simplified in [24].

As this approach deals with a set of classical trajectories, its numerical cost remains reasonable for multidimensional systems. Contrary to the classical approach, which controls only the averaged classical quantities, the present semiclassical method can control the quantum motion itself. This makes it possible to reproduce almost all quantum effects at a computational cost that does not grow too rapidly as the dimensionality of the system increases. The new approach therefore combines the advantages of the quantum and classical formulations of the optimal control theory.

In general, if the initial guess field is not good enough, the overlap between the target state and the propagated initial wavepacket may be very small in the first few iterations, and a huge number of trajectories should be used to achieve reasonable accuracy. To overcome this difficulty, the idea of *guided* control has been introduced [24]. The whole process is divided into a sequence of steps with the optimization procedure used to control each step. Control is performed by setting appropriate intermediate target states, and the wavepacket obtained as a result of the previous step is set to be an initial state for the next. This approach can be regarded as an intermediate one between the global [1–8, 11] and the local [9, 10] formulations of the OCT.

The approach has been tested by controlling nuclear wavepacket motion in a two-dimensional model system [23]. The relative simplicity of the system makes it possible to compare the semiclassical results with exact quantum ones. Numerical applications to the control of HCN–CNH isomerization [24] demonstrates that the new semiclassical formulation of optimal control theory provides an effective and powerful tool for controlling molecular dynamics with many degrees of freedom.

The remainder of this paper is organized as follows: the global optimization procedure used in the formulation is discussed in Sect. 6.2. The semiclassical expression of the correlation function is derived in Sect. 6.3, and the properties of the semiclassical correlation function are discussed in Sect. 6.4. In Sect. 6.5 we introduce the idea of *guided* optimal control. The full control algorithm is provided. In Sect. 6.6 we provide three numerical examples: i) the control of wavepacket motion where a two-dimensional model of H_2O is used as an example, ii) the control of the $H + OD \rightarrow HO + D$ reaction using a two-dimensional model of HOD, and iii) the control of the 4-D model of HCN–CNH isomerization (i.e., isomerization in a plane). Future perspectives from the authors' point of view are summarized in Sect. 6.7.

6.2 Global Optimization Procedure
and Conjugate Gradient Search Method

The time-dependent Schrödinger equation for a nuclear wavepacket on a single potential energy surface in a laser field is written as

$$\left[i\hbar\frac{\partial}{\partial t} + \sum_{j=0}^{N}\frac{\hbar^2}{2m_j}\frac{\partial^2}{\partial r_j^2} - V(\boldsymbol{r}) + \sum_{k=1}^{3}\mu_k(\boldsymbol{r})E_k(t)\right]|\phi(t)\rangle = 0 , \qquad (6.1)$$

where N stands for the number of degrees of freedom in the system. The *initial* state wavepacket $|\Phi_i(t)\rangle$ is specified at time $t = 0$. The goal of control is to design an external field $E_k(t)$ such that the wavepacket calculated with (6.1) up to time $t = T$ is close enough to the desired *target* state wavepacket $|\Phi_t(t)\rangle$ [1, 2].

To find the optimal field, we employ the simplest form of global optimization procedure with the iterational conjugate gradient search method [7, 8]. At each iteration of this algorithm, the correction to the optimized laser field is determined from the following equations:

$$\delta E_k(t) \sim \hbar^{-1}\langle\Phi_t|\phi(T)\rangle\mathrm{Im}\left[\Theta_k(t)\right], \quad \Theta_k(t) = \langle\phi(t)|\mu_k(r)|\chi(t)\rangle , \qquad (6.2)$$

where $|\phi(t)\rangle$ and $|\chi(t)\rangle$ are the wavepackets determined by the previous iteration of the optimized field $E_k(t)$ starting from the initial and target states, respectively,

$$\left[i\hbar\frac{\partial}{\partial t} + \sum_{j=0}^{N}\frac{\hbar^2}{2m_j}\frac{\partial^2}{\partial r_j^2} - V(\boldsymbol{r}) + \sum_{k=1}^{3}\mu_k E_k(t)\right]|\phi(t)\rangle = 0, |\phi(0)\rangle = |\Phi_i\rangle ,$$
$$(6.3)$$

and

$$\left[i\hbar\frac{\partial}{\partial t} + \sum_{j=0}^{N}\frac{\hbar^2}{2m_j}\frac{\partial^2}{\partial r_j^2} - V(\boldsymbol{r}) + \sum_{k=1}^{3}\mu_k E_k(t)\right]|\chi(t)\rangle = 0, |\chi(T)\rangle = |\Phi_t\rangle .$$
$$(6.4)$$

The actual procedure can be summarized as follows:

1. Assume an initial guess for the controlling field $E_k(t) = E_k^{(0)}(t)$ (typically zero).
2. Integrate (6.3) forward in time from $t = 0$ to $t = T$, starting from the initial wavefunction $|\phi(0)\rangle = |\Phi_i\rangle$. Calculate the overlap between the target state and the propagated initial state as $\langle\Phi_t|\phi(T)\rangle$.
3. Simultaneously integrate (6.3) backward in time from $t = T$ to $t = 0$ starting from the target wavefunction $|\chi(T)\rangle = |\Phi_t\rangle$, and calculate the correlation function $\Theta_k(t)$ using (6.2).

4. Calculate the corrected optimized field as $E_k^{(j+1)}(t) = E_k^{(j)}(t) + a\,\delta E_k^{(j)}(t)$, with the parameter a adjusted to maximize the absolute value of the overlap between the controlled wavepacket and the target state. To do so, (6.3) should be integrated forward in time from $t = 0$ to $t = T$, starting from the initial wavefunction $|\phi(0)\rangle = |\Phi_i\rangle$, several times for different values of a.

5. Iterate the steps 2–4 until the required convergence is achieved.

Since wavepackets should be propagated at each iteration, the computational cost of the quantum calculations becomes huge for multidimensional systems. To overcome this difficulty, one should incorporate a particular semiclassical approach to wavepacket propagation, like the Herman–Kluk approach [20,21], into this algorithm. Within the semiclassical approach, each wavepacket is propagated by running a large number of classical trajectories. In order to calculate the correlation function, a double summation with respect to this large number of trajectories should be performed at each time step, which is, unfortunately, still computationally very demanding. The obvious way to avoid this double summation is to recognize that the main contribution to the correlation function comes from those trajectories that run close to each other. Recently, this idea was applied to the calculation of time correlation functions using the classical Wigner approximation [25–27]. In [23] a more accurate approach is introduced. An approximate analytical evaluation of one of the sums is achieved by direct linearization of the semiclassical Herman–Kluk propagator.

6.3 Semiclassical Expression of the Correlation Function

To propagate $|\phi(t)\rangle$ and $|\chi(t)\rangle$ semiclassically, we use the Herman–Kluk frozen Gaussian approximation [20, 21]:

$$|\phi(t)\rangle = \int \frac{\mathrm{d}\boldsymbol{q}_0 \mathrm{d}\boldsymbol{p}_0}{(2\pi\hbar)^N} |g_{\boldsymbol{\gamma},\boldsymbol{q}_0,\boldsymbol{p}_0}\rangle\, C_{\boldsymbol{\gamma q}_0\boldsymbol{p}_0,t}\mathrm{e}^{\frac{\mathrm{i}}{\hbar}S_{\boldsymbol{q}_0\boldsymbol{p}_0,t}} \langle g_{\boldsymbol{\gamma},\boldsymbol{q}_0,\boldsymbol{p}_0}|\phi(0)\rangle\,, \qquad (6.5)$$

$$|\chi(t)\rangle = \int \frac{\mathrm{d}\boldsymbol{q}_0'\mathrm{d}\boldsymbol{p}_0'}{(2\pi\hbar)^N} |g_{\boldsymbol{\gamma}',\boldsymbol{q}_t',\boldsymbol{p}_t'}\rangle\, C_{\boldsymbol{\gamma q}_0'\boldsymbol{p}_0',t}\mathrm{e}^{\frac{\mathrm{i}}{\hbar}S_{\boldsymbol{q}_0'\boldsymbol{p}_0',t}} \langle g_{\boldsymbol{\gamma}',\boldsymbol{q}_0',\boldsymbol{p}_0'}|\chi(0)\rangle\,. \qquad (6.6)$$

Here the frozen Gaussian wavepackets are

$$|g_{\boldsymbol{\gamma},\boldsymbol{q},\boldsymbol{p}}\rangle = \prod_{j=1}^{N} \left(\frac{2\gamma_j}{\pi}\right)^{\frac{1}{4}} \mathrm{e}^{-\gamma_j(r_j-q_j)^2 + \frac{i}{\hbar}p_j(r_j-q_j)}\,. \qquad (6.7)$$

The Gaussian parameters γ_j are constant in time and they are common to all of the trajectories in the set. The actions $S_{\boldsymbol{q}_0\boldsymbol{p}_0,t}$ and $S_{\boldsymbol{q}_0'\boldsymbol{p}_0',t}$ as well as the Herman–Kluk pre-exponential factors $C_{\boldsymbol{\gamma q}_0\boldsymbol{p}_0,t}$ and $C_{\boldsymbol{\gamma}'\boldsymbol{q}_0'\boldsymbol{p}_0',t}$ are functions of

the parameters of the trajectories $(\boldsymbol{q}_t, \boldsymbol{p}_t)$ and $(\boldsymbol{q}'_t, \boldsymbol{p}'_t)$ used for semiclassical propagation of $|\phi(t)\rangle$ and $|\chi(t)\rangle$ respectively, i.e.,

$$S_{\boldsymbol{q}_0\boldsymbol{p}_0,t} = \int\limits_0^t \left[\sum_{j=1}^N \frac{p_{j,\tau}^2}{2m_j} - V(\boldsymbol{q}_\tau) \right] d\tau \,, \tag{6.8}$$

$$C_{\boldsymbol{\gamma}\boldsymbol{q}_0\boldsymbol{p}_0,t} = \pm\sqrt{\frac{1}{2}\det\left[\frac{\partial \boldsymbol{q}_t}{\partial \boldsymbol{q}_0} + \boldsymbol{\gamma}^{-1}\frac{\partial \boldsymbol{p}_t}{\partial \boldsymbol{p}_0}\boldsymbol{\gamma} + \frac{i}{2\hbar}\boldsymbol{\gamma}^{-1}\frac{\partial \boldsymbol{p}_t}{\partial \boldsymbol{q}_0} - 2i\hbar\frac{\partial \boldsymbol{q}_t}{\partial \boldsymbol{p}_0}\boldsymbol{\gamma} \right]}\,, \tag{6.9}$$

where $\boldsymbol{\gamma}$ is the diagonal matrix of the frozen Gaussian parameters (see (6.7)).

The semiclassical expression of the correlation function (6.2) becomes:

$$\Theta_k(t) = \int \frac{d\boldsymbol{q}_0 d\boldsymbol{p}_0}{(2\pi\hbar)^N} C^*_{\boldsymbol{\gamma}\boldsymbol{q}_0\boldsymbol{p}_0,t} e^{-\frac{i}{\hbar}S_{\boldsymbol{q}_0\boldsymbol{p}_0,t}} \langle \phi(0)| g_{\boldsymbol{\gamma},\boldsymbol{q}_0,\boldsymbol{p}_0}\rangle \Omega_k(\boldsymbol{\gamma}, \boldsymbol{q}_t, \boldsymbol{p}_t) \,, \tag{6.10}$$

where

$$\Omega_k(\boldsymbol{\gamma}, \boldsymbol{q}_t, \boldsymbol{p}_t) = \int \frac{d\boldsymbol{q}'_0 d\boldsymbol{p}'_0}{(2\pi\hbar)^N} \langle g_{\boldsymbol{\gamma},\boldsymbol{q}_t,\boldsymbol{p}_t}| \mu_k(\boldsymbol{r}) |g_{\boldsymbol{\gamma}',\boldsymbol{q}'_t,\boldsymbol{p}'_t}\rangle$$

$$\times\, C_{\boldsymbol{\gamma}\boldsymbol{q}'_0\boldsymbol{p}'_0,t} e^{\frac{i}{\hbar}S_{\boldsymbol{q}'_0\boldsymbol{p}'_0,t}} \langle g_{\boldsymbol{\gamma}',\boldsymbol{q}'_0,\boldsymbol{p}'_0}| \chi(0)\rangle \,. \tag{6.11}$$

Without losing generality, $\boldsymbol{\gamma} = \boldsymbol{\gamma}'$ is assumed. Since $|g_{\boldsymbol{\gamma},\boldsymbol{q},\boldsymbol{p}}\rangle$ and $|g_{\boldsymbol{\gamma},\boldsymbol{q}',\boldsymbol{p}'}\rangle$ are localized Gaussian functions, the matrix element $\langle g_{\boldsymbol{\gamma},\boldsymbol{q},\boldsymbol{p}}| \mu_k(\boldsymbol{r}) |g_{\boldsymbol{\gamma},\boldsymbol{q}',\boldsymbol{p}'}\rangle$ can be calculated analytically by approximating the dipole moment as a linear function within the spread of the wavepacket, i.e.,

$$\mu_k(\boldsymbol{r}) = \mu_k(\boldsymbol{r}_0) + \sum_{j=1}^N \frac{\partial \mu_k(\boldsymbol{r}_0)}{\partial r_j}(r_j - r_{0j}) \,. \tag{6.12}$$

The matrix element becomes

$$\langle g_{\boldsymbol{\gamma},\boldsymbol{q},\boldsymbol{p}}| \mu_k(\boldsymbol{r}) |g_{\boldsymbol{\gamma},\boldsymbol{q}',\boldsymbol{p}'}\rangle = \left(\mu_k(\overline{\boldsymbol{q}}) - \frac{i}{\hbar}\sum_{j=1}^N \frac{\partial \mu_k(\overline{\boldsymbol{q}})}{\partial r_j}\frac{(p_j - p'_j)}{4\gamma_j} \right)$$

$$\times \prod_{j=1}^N e^{-\frac{\gamma_j}{2}(q_j - q'_j)^2 - \frac{(p_j - p'_j)^2}{8\gamma_j\hbar^2} + \frac{i}{\hbar}\overline{p}_j(q_j - q'_j)} \tag{6.13}$$

with $\overline{\boldsymbol{q}} = \frac{1}{2}(\boldsymbol{q} + \boldsymbol{q}')$.

Function (6.13) has a distinct maximum at $\boldsymbol{q} = \boldsymbol{q}'$ and $\boldsymbol{p} = \boldsymbol{p}'$, so the integration in (6.11) can be performed analytically by linearizing the classical dynamics around the trajectory $(\boldsymbol{q}_t, \boldsymbol{p}_t)$, since the linearization leads to an approximate Taylor series expansion in variables $\delta\boldsymbol{q}_0 = \boldsymbol{q}'_0 - \boldsymbol{q}_0$ and $\delta\boldsymbol{p}_0 = \boldsymbol{p}'_0 - \boldsymbol{p}_0$. The approximations used are the same as those used in

the cellularization procedure [28, 29]. Namely, the classical action $S_{\boldsymbol{q}_0'\boldsymbol{p}_0',t}$ is expanded to the second order,

$$
S_{\boldsymbol{q}_0'\boldsymbol{p}_0',t} \approx S_{\boldsymbol{q}_0\boldsymbol{p}_0,t} + \left(\boldsymbol{p}_t^T \frac{\partial \boldsymbol{q}_t}{\partial \boldsymbol{q}_0} - \boldsymbol{p}_0^T \right) \delta \boldsymbol{q}_0
$$
$$
+ \boldsymbol{p}_t^T \frac{\partial \boldsymbol{q}_t}{\partial \boldsymbol{p}_0} \delta \boldsymbol{p}_0 + \frac{1}{2} \delta \boldsymbol{q}_0^T \left(\frac{\partial \boldsymbol{p}_t}{\partial \boldsymbol{q}_0} \right)^T \frac{\partial \boldsymbol{q}_t}{\partial \boldsymbol{q}_0} \delta \boldsymbol{q}_0
$$
$$
+ \delta \boldsymbol{q}_0^T \left(\frac{\partial \boldsymbol{p}_t}{\partial \boldsymbol{q}_0} \right)^T \frac{\partial \boldsymbol{q}_t}{\partial \boldsymbol{p}_0} \delta \boldsymbol{p}_0 + \frac{1}{2} \delta \boldsymbol{p}_0^T \left(\frac{\partial \boldsymbol{q}_t}{\partial \boldsymbol{p}_0} \right)^T \frac{\partial \boldsymbol{p}_t}{\partial \boldsymbol{p}_0} \delta \boldsymbol{p}_0 , \qquad (6.14)
$$

the final phase space point $(\boldsymbol{q}_t', \boldsymbol{p}_t')$ to the first order,

$$
\boldsymbol{q}_t' \approx \boldsymbol{q}_t + \frac{\partial \boldsymbol{q}_t}{\partial \boldsymbol{q}_0} \delta \boldsymbol{q}_0 + \frac{\partial \boldsymbol{p}_t}{\partial \boldsymbol{p}_0} \delta \boldsymbol{p}_0 , \quad \boldsymbol{p}_t' \approx \boldsymbol{p}_t + \frac{\partial \boldsymbol{p}_t}{\partial \boldsymbol{q}_0} \delta \boldsymbol{q}_0 + \frac{\partial \boldsymbol{p}_t}{\partial \boldsymbol{p}_0} \delta \boldsymbol{p}_0 , \qquad (6.15)
$$

and the Herman–Kluk factor $C_{\gamma \boldsymbol{q}_0'\boldsymbol{p}_0',t}$ to the zeroth order, i.e., $C_{\gamma \boldsymbol{q}_0'\boldsymbol{p}_0',t} \approx C_{\gamma \boldsymbol{q}_0\boldsymbol{p}_0,t}$.

In practical calculations it is always possible to take the wavepacket $|\chi(0)\rangle$ as a Gaussian function

$$
|\chi(0)\rangle = \prod_{j=1}^{N} \left(\frac{2\alpha_j}{\pi} \right)^{\frac{1}{4}} \exp \left[-\alpha_j \left(r_j - Q_j \right)^2 + \frac{i}{\hbar} P_j \left(r_j - Q_j \right) \right] , \qquad (6.16)
$$

In this case the factor $\langle g_{\gamma,\boldsymbol{q}_0',\boldsymbol{p}_0'} | \chi(0)\rangle$ can also be evaluated to be a Gaussian function

$$
\langle g_{\gamma,\boldsymbol{q}_0',\boldsymbol{p}_0'} | \chi(0)\rangle = \langle g_{\gamma,\boldsymbol{q}_0,\boldsymbol{p}_0} | \chi(0)\rangle
$$
$$
\times e^{-\boldsymbol{w}_q \delta \boldsymbol{q}_0 - \boldsymbol{w}_p \delta \boldsymbol{p}_0 - \delta \boldsymbol{q}_0^T \boldsymbol{W}_{qq} \delta \boldsymbol{q}_0 - \delta \boldsymbol{q}_0^T \boldsymbol{W}_{qp} \delta \boldsymbol{p}_0 - \delta \boldsymbol{p}_0^T \boldsymbol{W}_{pp} \delta \boldsymbol{p}_0}
$$
$$
(6.17)
$$

with expansion coefficients given by

$$
\langle g_{\gamma,\boldsymbol{q}_0,\boldsymbol{p}_0} | \chi(0)\rangle = \prod_{j=1}^{N} \sqrt{\frac{2\sqrt{\alpha_j \gamma_j}}{\alpha_j + \gamma_j}}
$$
$$
\times e^{-\frac{\alpha_j \gamma_j}{\alpha_j + \gamma_j}(q_{0,j} - Q_j)^2 - \frac{(p_{0,j} - P_j)^2}{4\hbar^2(\alpha_j + \gamma_j)} + i \frac{(\alpha_j p_{0,j} - \gamma_j P_j)(q_{0,j} - Q_j)}{\hbar(\alpha_j + \gamma_j)}} \qquad (6.18)
$$

and

$$
w_{q,j} = \frac{2\alpha_j \gamma_j(q_{0,j} - Q_j) - i\hbar^{-1}(\alpha_j p_{0,j} + \gamma_j P_j)}{\alpha_j + \gamma_j} ,
$$
$$
w_{p,j} = \frac{\hbar^{-1}(p_{0,j} - P_j) - 2i\alpha_j(q_{0,j} - Q_j)}{2\hbar(\alpha_j + \gamma_j)} , \qquad (6.19)
$$

$$
W_{qq,jl} = \delta_{jl} \frac{\alpha_j \gamma_j}{\alpha_j + \gamma_j}, W_{qp,jl} = -\delta_{jl} \frac{i}{\hbar} \frac{\alpha_j}{\alpha_j + \gamma_j}, W_{pp,jl} = \delta_{jl} \frac{1}{4\hbar^2(\alpha_j + \gamma_j)} .
$$
$$
(6.20)
$$

In general, the target wavepacket can be expanded in terms of the frozen Gaussians as

$$|\chi(0)\rangle = \sum_n \lambda_n g(\boldsymbol{\gamma}, \boldsymbol{q}_n, \boldsymbol{p}_n) \, , \tag{6.21}$$

where index n is used to enumerate the trajectories. In this case, the coefficients in (6.17) are given by:

$$\langle g_{\boldsymbol{\gamma}, \boldsymbol{q}, \boldsymbol{p}} | \chi(0)\rangle = \sum_n \lambda_n f_n(\boldsymbol{q}, \boldsymbol{p}) \, , \tag{6.22}$$

$$w_{q,j} = -\sum_n \frac{\lambda_n}{f_n(\boldsymbol{q}, \boldsymbol{p})} \frac{\partial f_n(\boldsymbol{q}, \boldsymbol{p})}{\partial q_j}, \; w_{p,j} = -\sum_n \frac{\lambda_n}{f_n(\boldsymbol{q}, \boldsymbol{p})} \frac{\partial f_n(\boldsymbol{q}, \boldsymbol{p})}{\partial p_j} \, , \tag{6.23}$$

$$W_{qq,jl} = -\sum_n \lambda_n \frac{\frac{\partial f_n(\boldsymbol{q}, \boldsymbol{p})}{\partial q_j} \frac{\partial f_n(\boldsymbol{q}, \boldsymbol{p})}{\partial q_l} - f_n(\boldsymbol{q}, \boldsymbol{p}) \frac{\partial^2 f_n(\boldsymbol{q}, \boldsymbol{p})}{\partial q_j \partial q_l}}{(f_n(\boldsymbol{q}, \boldsymbol{p}))^2} \, ,$$

$$W_{qp,jl} = -\sum_n \lambda_n \frac{\frac{\partial f_n(\boldsymbol{q}, \boldsymbol{p})}{\partial q_j} \frac{\partial f_n(\boldsymbol{q}, \boldsymbol{p})}{\partial p_l} - f_n(\boldsymbol{q}, \boldsymbol{p}) \frac{\partial^2 f_n(\boldsymbol{q}, \boldsymbol{p})}{\partial q_j \partial p_l}}{(f_n(\boldsymbol{q}, \boldsymbol{p}))^2} \, ,$$

$$W_{pp,jl} = -\sum_n \lambda_n \frac{\frac{\partial f_n(\boldsymbol{q}, \boldsymbol{p})}{\partial p_j} \frac{\partial f_n(\boldsymbol{q}, \boldsymbol{p})}{\partial p_l} - f_n(\boldsymbol{q}, \boldsymbol{p}) \frac{\partial^2 f_n(\boldsymbol{q}, \boldsymbol{p})}{\partial p_j \partial p_l}}{(f_n(\boldsymbol{q}, \boldsymbol{p}))^2} \, , \tag{6.24}$$

where

$$f_n(\boldsymbol{q}, \boldsymbol{p}) = \langle g_{\boldsymbol{\gamma}, \boldsymbol{q}, \boldsymbol{p}} | g_{\boldsymbol{\gamma}, \boldsymbol{q}_n, \boldsymbol{p}_n}\rangle$$
$$= \prod_{j=1}^N e^{-\frac{\gamma_j}{2}(q_j - q_{n,j})^2 - \frac{(p_j - p_{n,j})^2}{8\gamma_j \hbar^2} + \frac{i}{2\hbar}(p_j + p_{n,j})(q_j - q_{n,j})} \, . \tag{6.25}$$

Under the above assumptions, (6.11) can be rewritten in the form:

$$\Omega_k(\boldsymbol{\gamma}, \boldsymbol{q}_t, \boldsymbol{p}_t) = C_{\boldsymbol{\gamma} \boldsymbol{q}_0 \boldsymbol{p}_0, t} e^{\frac{i}{\hbar} S_{\boldsymbol{q}_0 \boldsymbol{p}_0, t}} \langle g_{\boldsymbol{\gamma}, \boldsymbol{q}_0 \boldsymbol{p}_0} | \chi(0)\rangle$$
$$\times \int d\boldsymbol{z} \left(\mu_k(\boldsymbol{q}_t) + \boldsymbol{z}^T \boldsymbol{b}_{\boldsymbol{q}_0 \boldsymbol{p}_0, t}^{(k)} \right) e^{-\boldsymbol{a}_{\boldsymbol{q}_0 \boldsymbol{p}_0}^T \boldsymbol{z} - \boldsymbol{z}^T \boldsymbol{A}_{\boldsymbol{q}_0 \boldsymbol{p}_0, t} \boldsymbol{z}} \, , \tag{6.26}$$

with $\boldsymbol{z} = (\delta \boldsymbol{q}_0, \delta \boldsymbol{p}_0)^T$ and

$$\boldsymbol{a}_{\boldsymbol{q}_0 \boldsymbol{p}_0} = \left(\boldsymbol{a}_q \boldsymbol{a}_p \right), \boldsymbol{b}_{\boldsymbol{q}_0 \boldsymbol{p}_0, t}^{(k)} = \left(\boldsymbol{b}_q^{(k)} \boldsymbol{b}_p^{(k)} \right), \boldsymbol{A}_{\boldsymbol{q}_0 \boldsymbol{p}_0, t} = \left(\boldsymbol{A}_{qq} \boldsymbol{A}_{qp} \boldsymbol{A}_{pq} \boldsymbol{A}_{pp} \right) \, , \tag{6.27}$$

where

$$a_q = w_q + \frac{i}{\hbar} p_0, \, a_p = w_p \, , \tag{6.28}$$

$$b_q^{(k)} = \frac{i}{4\hbar} \left(\frac{\partial \mu_k (q_t)}{\partial r} \right)^T \gamma^{-1} \frac{\partial p_t}{\partial q_0}, \quad b_p^{(k)} = \frac{i}{4\hbar} \left(\frac{\partial \mu_k (q_t)}{\partial r} \right)^T \gamma^{-1} \frac{\partial p_t}{\partial p_0} \, , \tag{6.29}$$

$$A_{qq} = W_{qq} + \frac{1}{2} \left(\frac{\partial q_t}{\partial q_0} \right)^T \gamma \frac{\partial q_t}{\partial q_0} + \frac{1}{8\hbar^2} \left(\frac{\partial p_t}{\partial q_0} \right)^T \gamma^{-1} \frac{\partial p_t}{\partial q_0} \, ,$$

$$A_{qp} = \frac{1}{2} \left(W_{qp} + \frac{i}{2\hbar} I \right) + \frac{1}{2} \left(\frac{\partial q_t}{\partial q_0} \right)^T \gamma \frac{\partial q_t}{\partial p_0} + \frac{1}{8\hbar^2} \left(\frac{\partial p_t}{\partial q_0} \right)^T \gamma^{-1} \frac{\partial p_t}{\partial p_0} \, ,$$

$$A_{pq} = \frac{1}{2} \left(W_{pq} + \frac{i}{2\hbar} I \right) + \frac{1}{2} \left(\frac{\partial q_t}{\partial p_0} \right)^T \gamma \frac{\partial q_t}{\partial q_0} + \frac{1}{8\hbar^2} \left(\frac{\partial p_t}{\partial p_0} \right)^T \gamma^{-1} \frac{\partial p_t}{\partial q_0} \, ,$$

$$A_{pp} = W_{pp} + \frac{1}{2} \left(\frac{\partial q_t}{\partial p_0} \right)^T \gamma \frac{\partial q_t}{\partial p_0} + \frac{1}{8\hbar^2} \left(\frac{\partial p_t}{\partial p_0} \right)^T \gamma^{-1} \frac{\partial p_t}{\partial p_0} \, . \tag{6.30}$$

Here I stands for unit matrix. The following properties of this matrix are used in the derivations above:

$$\left(\frac{\partial q_t}{\partial q_0} \right)^T \frac{\partial p_t}{\partial p_0} - \left(\frac{\partial p_t}{\partial q_0} \right)^T \frac{\partial q_t}{\partial p_0} = I, \quad \left(\frac{\partial p_t}{\partial p_0} \right)^T \frac{\partial q_t}{\partial q_0} - \left(\frac{\partial q_t}{\partial p_0} \right)^T \frac{\partial p_t}{\partial q_0} = I \, . \tag{6.31}$$

After performing the integrations in (6.26) analytically, we obtain the following approximate expression for the correlation function:

$$\Theta_k(t) = \int \frac{dq_0 dp_0}{(2\pi\hbar)^N} \langle \phi(0)| \, g_{\gamma, q_0, p_0} \rangle \langle g_{\gamma, q_0, p_0} | \chi(0) \rangle$$

$$\times \left(\mu_k(q_t) - \frac{1}{2} a_{q_0 p_0}^T A_{q_0 p_0, t}^{-1} b_{q_0 p_0, t}^{(k)} \right)$$

$$\times \frac{|C_{\gamma q_0 p_0, t}|^2}{2^N \sqrt{\det (A_{q_0 p_0, t})}} e^{\frac{1}{4} a_{q_0 p_0}^T A_{q_0 p_0, t}^{-1} a_{q_0 p_0}} \, . \tag{6.32}$$

Further simplification of (6.32) can be obtained by analyzing the last term (third line) [23, 24].

Consider the special case of $\mu_k(r) \equiv 1$. The correlation function (6.2) becomes equal to the simple overlap $\langle \phi(t)| \chi(t) \rangle$ and remains constant in

time. On the other hand, this overlap can be expressed directly by using the orthogonality and completeness of the frozen Gaussian basis as

$$\langle \phi(t) | \chi(t) \rangle \equiv \langle \phi(0) | \chi(0) \rangle \equiv$$
$$\equiv \int \frac{\mathrm{d}\boldsymbol{q}_0 \mathrm{d}\boldsymbol{p}_0}{(2\pi\hbar)^N} \langle \phi(0) | g_{\gamma, \boldsymbol{q}_0, \boldsymbol{p}_0} \rangle \langle g_{\gamma, \boldsymbol{q}_0, \boldsymbol{p}_0} | \chi(0) \rangle . \tag{6.33}$$

Equation (6.32) and (6.33) should be equal for any pair of initial and target wavepackets $|\phi(0)\rangle$ and $|\chi(0)\rangle$, which is possible if and only if the third line in (6.32) equals unity. Thus, the correlation function simply takes the form

$$\Theta_k(t) = \int \frac{\mathrm{d}\boldsymbol{q}_0 \mathrm{d}\boldsymbol{p}_0}{(2\pi\hbar)^N} \langle \phi(0) | g_{\gamma, \boldsymbol{q}_0, \boldsymbol{p}_0} \rangle \langle g_{\gamma, \boldsymbol{q}_0, \boldsymbol{p}_0} | \chi(0) \rangle$$
$$\times \left(\mu_k(\boldsymbol{q}_t) - \frac{1}{2} \boldsymbol{a}_{\boldsymbol{q}_0 \boldsymbol{p}_0}^T \boldsymbol{A}_{\boldsymbol{q}_0 \boldsymbol{p}_0, t}^{-1} \boldsymbol{b}_{\boldsymbol{q}_0 \boldsymbol{p}_0, t}^{(k)} \right) . \tag{6.34}$$

In the case where the dipole moment does not significantly change within the width of the frozen Gaussian, the second term in the bracket of (6.34) is negligible and the correlation function takes the simplest form

$$\Theta_k(t) = \int \frac{\mathrm{d}\boldsymbol{q}_0 \mathrm{d}\boldsymbol{p}_0}{(2\pi\hbar)^N} \langle \phi(0) | g_{\gamma, \boldsymbol{q}_0, \boldsymbol{p}_0} \rangle \mu_k(\boldsymbol{q}_t) \langle g_{\gamma, \boldsymbol{q}_0, \boldsymbol{p}_0} | \chi(0) \rangle . \tag{6.35}$$

Only the propagation of classical trajectories is required to calculate this correlation function. On the other hand, (6.34) requires extra calculations of ordinary semiclassical quantities.

6.4 Improvement for Long Propagation Time

The accuracy of the present semiclassical method naturally deteriorates at long time durations. This is basically because of the use of the single sum approximation with respect to the trajectories instead of the double sum, which is itself an approximation for short propagation times. An improvement can be made by recalculating the frozen Gaussian expansion coefficients from time to time. This is explained here using the two-dimensional model of H_2O as an example. Bending and rotational motions are neglected for simplicity, with the bending angle fixed at the equilibrium structure of the ground electronic state $\theta = 104.52°$. The potentials and dipole moments used are taken from [30,31]. The wavepackets $|\phi(0)\rangle = |\Phi_i\rangle$ and $|\chi(0)\rangle = |\Phi_t\rangle$ are set at $t = 0$ to be symmetric Gaussians with full widths at half maximum (FWHM) equal to 0.5 a.u. and zero central momenta. The wavepacket Φ_i is put at the equilibrium position at $\mathbf{R} = (1.81 \text{ a.u.}, 1.81 \text{ a.u.})^T$ and the wavepacket Φ_t is put at $\mathbf{R} = (2.50 \text{ a.u}, 1.81 \text{ a.u.})^T$. The ground potential energy surface and the wavepackets Φ_i and Φ_t are presented in Fig. 6.1.
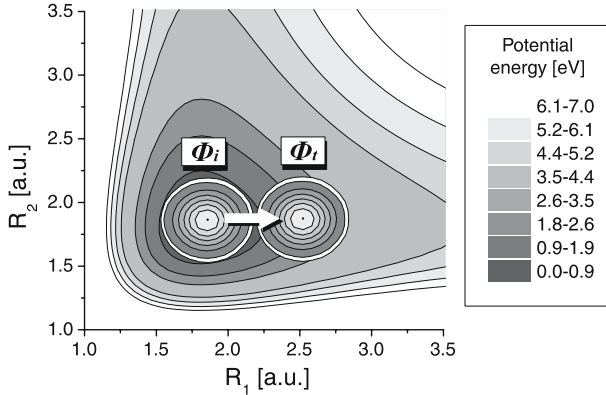
Fig. 6.1. Ground state of the two-dimensional H_2O model system. *White circles* contain the wave packets Φ_i and Φ_t

Figure 6.2 presents the time variations for the correlation function (6.2) calculated semiclassically (thin and dashed lines) compared with the exact quantum result (bold lines). Semiclassical results are presented for two approximations: the dashed line indicates the result obtained with the simple formula (6.35) and the thin line shows the result obtained with the full equation (6.34). The number of trajectories used for propagation is 5000, which is enough to achieve convergence of the correlation function as well as to perform the semiclassical propagation of the $|\phi(t)\rangle$ and $|\chi(t)\rangle$ wavepackets. Both semiclassical results are found to be in good agreement with the exact quantum one for about 5–6 oscillations of the real and imaginary parts of correlation function or for about 200 time integration steps (one step is 0.1 fs).

Comparisons of the correlation functions calculated quantum mechanically and semiclassically, like those presented in Fig. 6.2, show that the correction due to the dipole moment gradient included in (6.34) sometimes improves the accuracy especially for short propagation times. This correction affects not only the amplitude of the correlation function oscillation, but also its frequency and distortions due to the presence of high harmonics in the spectrum. An analysis of the spectrum of the correlation function indicates that including this correction in the formula enables additional quantum effects to be taken into account.

In order to improve the accuracy for long propagation times, we recalculate the frozen Gaussian expansion coefficients $\langle\phi|\, g_{\gamma,q_0,p_0}\rangle$ and $\langle g_{\gamma,q_0,p_0}|\chi\rangle$ used in (6.34) and (6.35) from time to time. To do so, two sets of trajectories should be propagated simultaneously to represent $|\phi(t)\rangle$ and $|\chi(t)\rangle$ at any time. Although the correlation function is calculated semiclassically using only one set of trajectories, the other trajectories are required to preserve information about the dynamics. Thus, if the required level of accuracy of the correlation function is lost, the coefficients $\langle\phi|\, g_{\gamma,q_0,p_0}\rangle$ and $\langle g_{\gamma,q_0,p_0}|\chi\rangle$
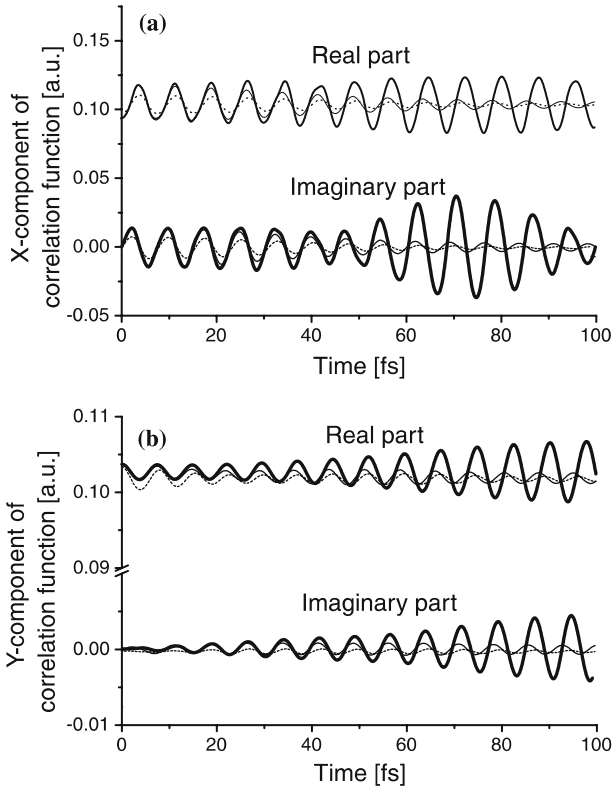
Fig. 6.2. Time variations of the x-component (**a**) and the y-component (**b**) of the correlation function (6.2). The *bold line* shows the exact quantum result. Semiclassical results: *thin line*: results obtained with full formula (6.34); *dashed line*: results obtained with the simple formula (6.35)

in (6.34) and (6.35) are recalculated for the propagated wavepackets $|\phi(t)\rangle$ and $|\chi(t)\rangle$ using similar equations to (6.22)–(6.24). This procedure can restore the accuracy.

Figure 6.3 presents the time variations for the same correlation function as in Fig. 6.2, but those obtained from the abovementioned recalculation procedure are performed at 250 time integration steps. It is clear that this recalculation procedure extends the applicability of the present semiclassical method to an arbitrarily long propagation duration.

The computational cost of this recalculation procedure is roughly the same as that of the direct double summation with respect to the trajectories. If the propagation duration is long, the re-expansion should be performed every $200 \sim 300$ time integration step. This means that this new algorithm can reduce the computational cost of semiclassical calculations by more than two orders of magnitude in comparison with the direct implementation of semiclassical methods into the OCT.
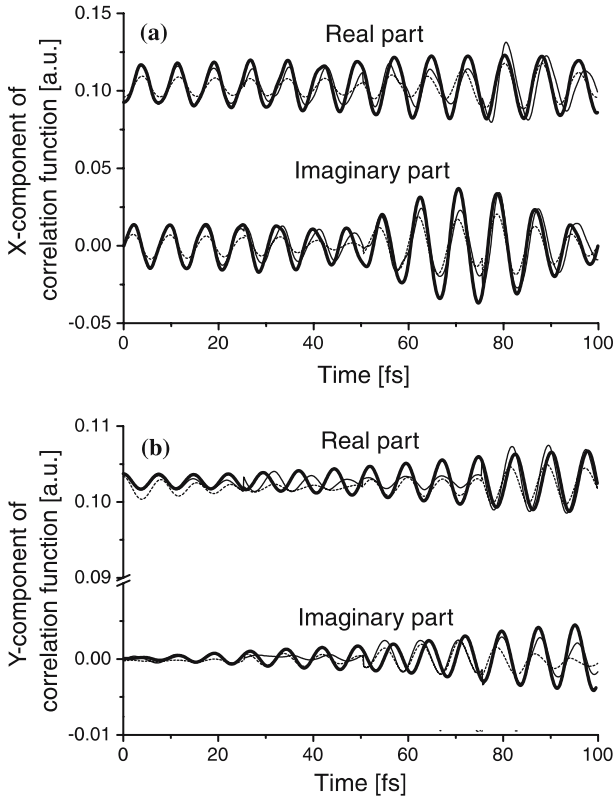
Fig. 6.3. Time variations of the x-component (**a**) and the y-component (**b**) of the correlation function (6.2). Three coefficient re-expansions are performed. The *bold line* shows the exact quantum result. Semiclassical results: *thin line*: results obtained with the full formula (6.34); *dashed line*: results obtained with the simple formula (6.35)

Unfortunately, however, when the correction due to the dipole moment gradient included in (6.34) is necessary, some additional parameters need to be calculated at the beginning. If one of the wavepackets $|\phi(0)\rangle$ or $|\chi(0)\rangle$ is a Gaussian function (6.16), these parameters are given analytically by (6.18)–(6.20). In the case of coefficient recalculation, both wavepackets take the form of frozen Gaussian expansions (6.21), and the calculation of (6.22)–(6.24) requires $3N^2 + 2N + 1$ double summations with respect to the trajectories (N is the number of degrees of freedom in the system). This makes the approximation of (6.34) ineffective for long propagation times in systems with many degrees of freedom, and the simple formula (6.35) should be used instead. However, if one of the wavepackets is a Gaussian function, correlation function calculations for short durations can be easily performed using formula (6.34), even for systems with many degrees of freedom.

6.5 Guided Semiclassical Optimal Control

During the optimization procedure, the overlap between the target state and the propagated initial wavepacket $\langle \Phi_t | \phi(T) \rangle$ should be calculated accurately at each iteration (see (6.2)). If the initial guess field is not good enough, this value may be very small in the first few iterations and a huge number of trajectories should be used to finally achieve reasonable accuracy. The direct use of the optimization procedure therefore becomes very inefficient.

To overcome this difficulty, we divide the whole process into a sequence of steps with the optimization procedure used to control each step. The control is performed by setting appropriate intermediate target states, and the wavepacket obtained as a result of the previous step is set to be an initial state for the next.

Two types of intermediate target states can be considered. The first one is a single Gaussian wavepacket with appropriately chosen central coordinate, momentum and width parameters. If the motion is complicated, however, this is not effective. The following general scheme is used in this case: the initial wavepacket is propagated first without the field and the target state is formed by shifting and stretching (or shrinking) the phase space volume occupied by the propagated wavepacket. By adjusting the parameters of this transformation, we can change the overlap of the propagated initial wavepacket with the target and improve the convergence of the optimization procedure. Although the wavepacket achieved at each control step may have a different shape to the corresponding intermediate target state, the overall control efficiency can be high. This approach can be regarded as an intermediate one between the global [1–8,11] and local [9,10] formulations of the OCT, and is termed *guided optimal control*.

6.6 Numerical Examples

6.6.1 Control of Wave Packet Motion

In order to demonstrate the efficiency and accuracy of the semiclassical formulation of optimal control theory, let us consider the control of two elementary types of motion: (a) a shift of the position of the ground-state wavepacket in the two-dimensional model system of H_2O and (b) an acceleration of the ground-state wavepacket at the same position in the same model.

a) Shift of the Position of the Ground-State Wavepacket of H_2O

The initial and target wavepackets $|\phi(0)\rangle = |\Phi_i\rangle$ and $|\chi(0)\rangle = |\Phi_t\rangle$ are specified in Sect. 6.3 (see Fig. 6.1). The optimization procedure runs for the duration of 50 fs with a zero initial guess field. The number of trajectories
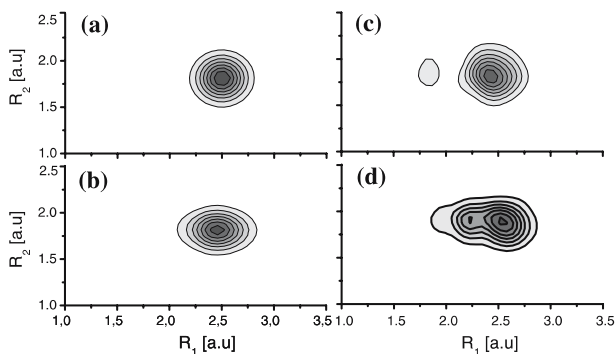
Fig. 6.4. Final wavepackets driven by the optimal field calculated quantum mechanically and semiclassically after ten iterations of the optimization algorithm. **a** Target state wave packet. **b** Quantum result. Semiclassical results: **c** correlation functions are obtained with (6.34); **d** correlation functions are obtained with the simple formula (6.35)

used is 3000. The calculations are performed without using the recalculation procedure.

After 8–10 iterations, the changes in the absolute value of the overlap between the controlled wavepacket and the target state become compatible with the error of the semiclassical wavepacket propagation method itself. Thus, we consider the results obtained after ten iterations to be the final ones. The final absolute values of the overlap between the controlled wave packet and the target state are 0.96 for the quantum and 0.91 for the semiclassical with correlation functions calculated by (6.34), and 0.83 for correlation functions calculated by the simple formula (6.35). Figure 6.4 presents the final wavepackets driven from the initial state by the optimal field calculated semiclassically and quantum mechanically together with the target state wavepacket. We can state that the last approximation also works well when evaluating the optimal field.

The controlling field and its spectra, calculated both semiclassically (thin and dash lines) and quantum mechanically (bold lines), are shown in Fig. 6.5. The frequencies of the main components of the optimal field spectra are the same for all three cases. However, the optimal field obtained quantum mechanically and semiclassically with formula (6.34) contains second harmonics. This means that additional quantum effects are taken into account by the correction from the dipole moment gradient included in (6.34).

b) Acceleration of the Ground-State Wavepacket of H_2O at the Same Position

The initial wavepacket is $|\phi(0)\rangle = |\Phi_i\rangle$. The target wavepacket is set to be a Gaussian wavepacket with the same central coordinate and width parame-
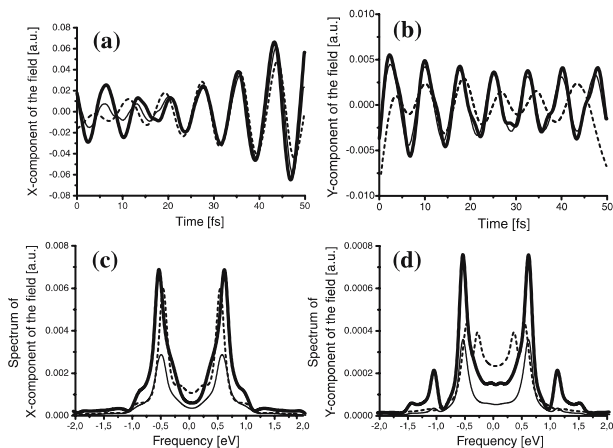
Fig. 6.5. Optimal field (**a–b**) and its spectra (**c–d**) calculated for an H_2O ground-state wavepacket shift. The *bold line* shows the exact quantum result. Semiclassical results: *thin line*: the correlation function obtained with (6.34); *dashed line*: the correlation function obtained with the simple formula (6.35)
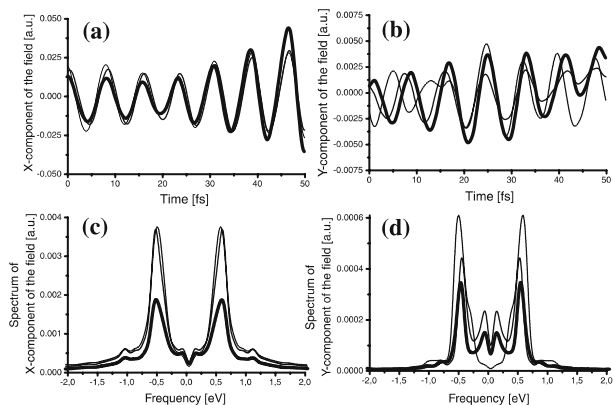
Fig. 6.6. Optimal field (**a–b**) and its spectra (**c–d**) calculated for H_2O ground-state wavepacket acceleration. The *bold line* shows the exact quantum result. Semiclassical results: *thin line*: the correlation function obtained with (6.34); *dashed line*: the correlation function obtained with the simple formula (6.35)

ters as those of the initial wavepacket. However, the central momentum is set to be 10.0 a.u. (kinetic energy is about 1 eV) along the R_1 axis. The optimization procedure runs for a duration of 50 fs with a zero initial guess field. The number of trajectories used is 3000. The calculations are performed without using the recalculation procedure.

Convergence is achieved after ten iterations of the algorithm. The absolute values of the overlap between the controlled wavepacket and the target

state are: 0.92 for quantum, 0.91 for semiclassical with correlation functions calculated by (6.34), and 0.89 for correlation functions calculated using the simple formula (6.35). Figure 6.6 presents the controlling field and its spectra calculated both semiclassically (thin and dash lines) and quantum mechanically (bold lines).

6.6.2 Control of reaction H + OD → HO + D

To illustrate the concept of guided optimal control, let us consider laser control of the reaction H + OD → HO + D. The initial and target wavepackets are set to be symmetric Gaussians with full widths at half maximum (FWHM) equal to 0.5 a.u. and zero central momenta. The central coordinates of the initial and target wavepackets are set to be $\mathbf{R}_i = (3.51, 1.81)^T$ and $\mathbf{R}_t = (1.81, 3.51)^T$, respectively, to represent reactant and product channels. The ground potential energy surface together with the initial and target wavepackets are presented in Fig. 6.7. For a reasonable duration of the process of 150 fs, the absolute value of the overlap between the initial wavepacket propagated with zero field and the target state wavepacket is 7.76×10^{-6}. If we run the optimization procedure straightforwardly, the maximal efficiency achieved will be only 17%. Thus, guided optimal control should be used to control the reaction.

The two intermediate target states are set to be symmetric Gaussians with the same width parameters as those of the initial and target states and zero central momenta. The central coordinates of the wavepackets are set to be: $\mathbf{R}_{its1} = (2.51, 1.81)^T$ and $\mathbf{R}_{its2} = (1.81, 2.51)^T$ (see Fig. 6.7). The initial guess field used to control the overall process is constructed by joining the optimal fields found for three intermediate steps: the control from the initial state to the first intermediate target state, the control from the first intermediate
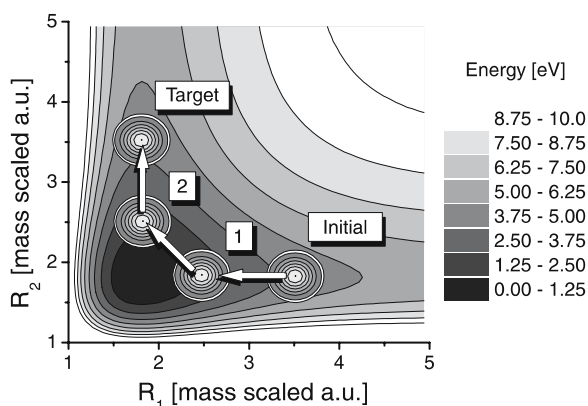
Fig. 6.7. Ground state of two-dimensional H_2O model system. The *white circles* contain the initial and target wavepackets and two intermediate target states
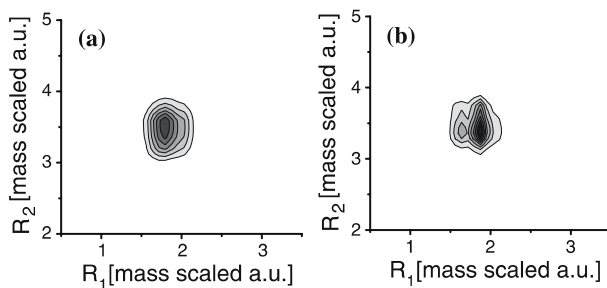
Fig. 6.8. Final wave packets driven by the optimal field, calculated both quantum mechanically and semilassically. **a** Quantum result. **b** Semiclassical result obtained with the simple formula (6.35)
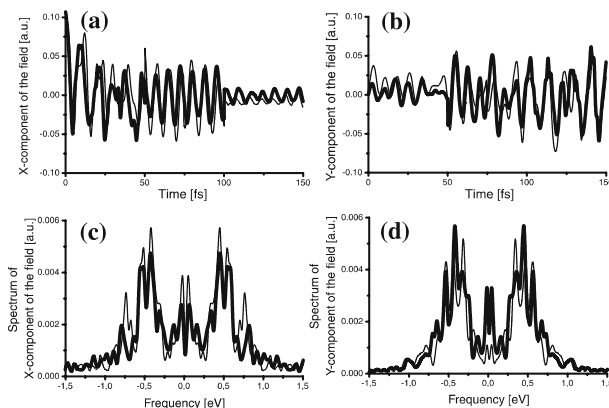
Fig. 6.9. Optimal field (**a–b**) and its spectra (**c–d**) calculated for the control of the H + OD → HO + D reaction. The *bold line* shows the exact quantum result. The *dashed line* shows the semiclassical result obtained with the simple formula (6.35) used for the correlation function

target state to the second intermediate target state, and the control from the second intermediate target state to the final target state. The durations of each process are set to be 50 fs, and zero initial guess fields are used. After this initial guess field is prepared, the final controlling field for the overall process is obtained using the same algorithm. The semiclassical correlation function is calculated by (6.35) using two coefficient recalculation steps.

Figure 6.8 presents the controlled wavepackets obtained both quantum mechanically and semiclassically. The controlling field and its spectra, calculated both semiclassically (dashed line) and quantum mechanically (bold line), are given in Fig. 6.9. The final absolute values for the overlap between the controlled wavepacket and the target state wavepacket are: 0.80 for the quantum calculations; 0.75 for the semiclassical calculations. The results demonstrate the high efficiency of the guided control.
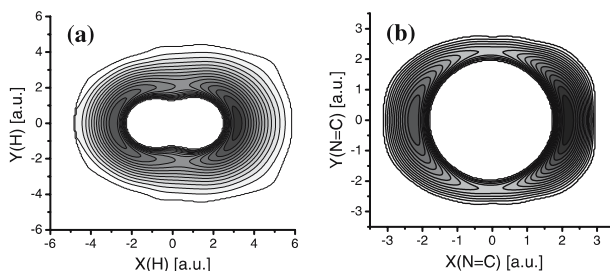
Fig. 6.10. Potential of the ground electronic state of HCN system as a function of: **a** the coordinates of the proton with the N=C bond fixed at its equilibrium position; **b** the coordinates of the N=C bond vector with the coordinates of the proton fixed at its equilibrium position

6.6.3 Control of the HCN–CNH Isomerization

In order to demonstrate the efficiency of the present theory for systems with many degrees of freedom, we have applied it to a 4-D model of HCN–CNH isomerization (i.e., isomerization in a plane). The system is described in terms of two vectors: $R_{N=C}$ for the vector from N to C, and R_H for the vector from the center of mass of the system to H. A fixed spatial Cartesian framework is used, with the x-axis set to be parallel to the initial direction of $R_{N=C}$, and the y- and z-axes perpendicular to it. The center of mass of NC is assumed to be the same as that of the whole system so that the kinetic part of the Hamiltonian is diagonal. The potential energy surface and the dipole moment are taken from [32].

Both the HCN and the CNH configurations are linear, so the molecule is initially axially symmetric. However, by applying an external field along the y-axis, the configuration is confined to a plane (i.e., to the xy-plane). The average value of the dipole moment along the z-axis is always zero so the nuclear motion can be controlled using only the x- and y-components of the laser field. The potential has a minimum along the z-axis, which prevents the wavepacket spreading along this direction. Due to all of these reasons, we can consider the vectors $R_{N=C}$ and R_H to be two-dimensional.

The ground-state wavepackets for the HCN and CNH configurations are approximated by Gaussian functions centered at $R_{N=C} = (2.1785, 0.0)^T$ a.u., $R_H = (3.1855, 0.0)^T$ a.u. and $R_{N=C} = (1.554, -1.554)^T$ a.u., $R_H = (-2.033, 2.033)^T$ a.u. (linear configuration rotated clockwise by $45°$), respectively. The width parameters are calculated to fit the principal modes of the potential wells.

Following the idea of guided control, the whole process is divided into three stages: (i) acceleration of the initial state wavepacket in the HCN configuration so that the energy exceeds the top of the interstate barrier; (ii) field-free propagation to the target (CNH) configuration region, and; (iii) deceleration so that the wavepacket stays in the target region.

The acceleration procedure is performed in three steps by introducing intermediate target states as Gaussian wavepackets with the same central coordinates and width parameters as those of the initial wavepacket. The central momenta are set to be $\boldsymbol{P}_{\mathrm{N=C}} = (0.0, -15.0)^T$ a.u. and $\boldsymbol{P}_{\mathrm{H}} = (0.0, 10.0)^T$ a.u. for the first step, $\boldsymbol{P}_{\mathrm{N=C}} = (0.0, -26.2)^T$ a.u. and $\boldsymbol{P}_{\mathrm{H}} = (0.0, 17.5)^T$ a.u. for the second and $\boldsymbol{P}_{\mathrm{N=C}} = (0.0, -30.0)^T$ a.u. and $\boldsymbol{P}_{\mathrm{H}} = (0.0, 20.0)^T$ a.u. for the third. The optimization procedure for the first step runs with a zero initial guess field. The field obtained as a result of the previous step is used as an initial guess field for the next. The acceleration is performed for 72 fs. The number of trajectories used at each control step is 100,000. Convergence is achieved in about ten iterations of the algorithm at each step. Figure 6.11 presents snapshots of the accelerated wavepacket at 72 fs in coordinate and momentum representations. The absolute value of the overlap between the controlled wavepacket and the third intermediate target state is 0.51.

The second control stage is a field-free propagation towards the target state potential well. Although the wavepacket reaches the CNH configuration in 30 fs (see Fig. 6.12), it stays there for only a short time because of the high momentum. Significant energy exchange between different molecular modes causes a fairly complicated combination of rotation and stretching of two bonds.

In order to decelerate the wavepacket so that it stays in the CNH configuration potential well, a three-step optimization procedure is used. The inter-
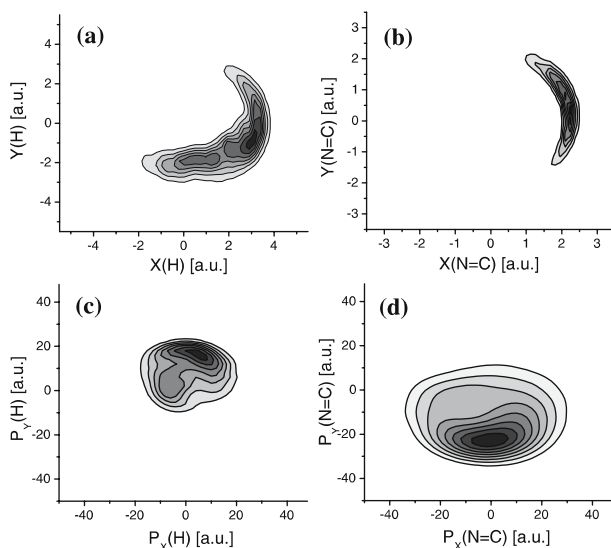
Fig. 6.11. Probability density of the accelerated wavepacket at 72 fs as a function of: **a** the coordinates of the proton; **b** the coordinates of the N=C bond vector; **c** the momentum of the proton; **d** the momentum of the N=C bond vector
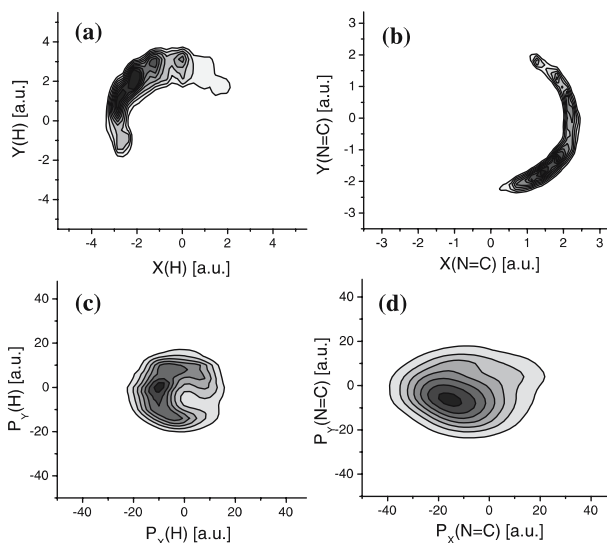
Fig. 6.12. Probability density of the wavepacket after 30 fs of field-free propagation of the wave packet shown in Fig. 6.1 as a function of: **a** the coordinates of the proton; **b** the coordinates of the N=C bond vector; **c** the momentum of the proton; (**d**) the momentum of the N=C bond vector
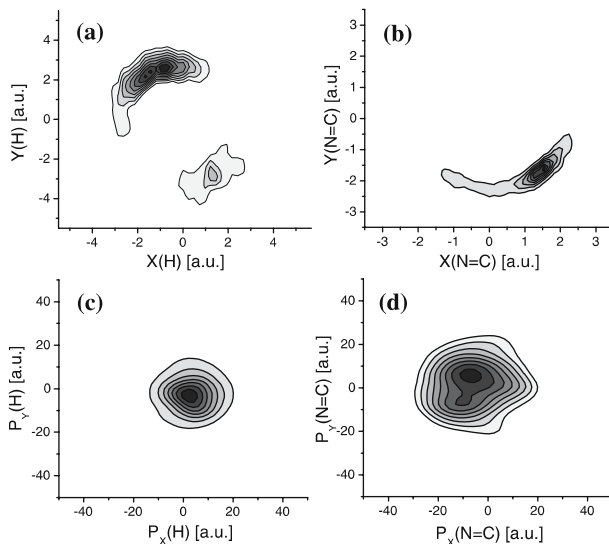
Fig. 6.13. Final wavepacket driven by the optimal field. Probability density is given as a function of: **a** the coordinates of the proton; **b** the coordinates of the N=C bond vector; **c** the momentum of the proton; **d** the momentum of the N=C bond vector

mediate target states for each step are set to be the ground state wavepacket in the potential well corresponding to CNH rotated clockwise by 45°. The optimization procedure runs for 15 fs with a zero initial guess field at each step, and the wavepacket obtained as a result of the previous step is set to be an initial state for the next. Although the absolute values for the overlap between the controlled wavepacket and the corresponding intermediate target state are not very large, the motion of the wavepacket is suppressed dramatically. The wavepacket obtained after deceleration is given in Fig. 6.13. This final result is found to be stable with respect to decay.

The final isomerization probability is calculated using the formula

$$P_{\mathrm{iso}}(t) = \langle \phi(t) |\, h\left(-\frac{\boldsymbol{R}_{\mathrm{N=C}} \boldsymbol{R}_{\mathrm{H}}}{R_{\mathrm{N=C}} R_{\mathrm{H}}} \right) |\phi(t)\rangle \ , \tag{6.36}$$
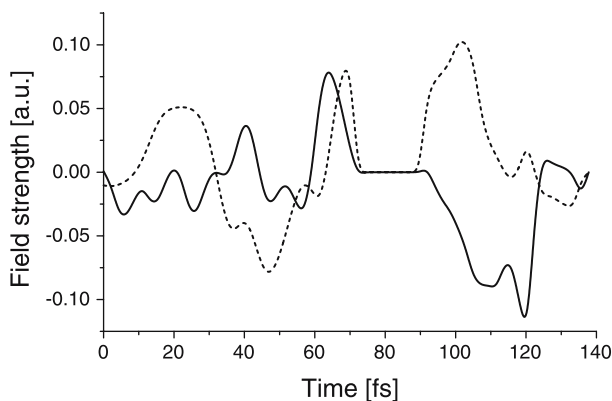
Fig. 6.14. Optimal field calculated for HCN–CNH isomerization control. *Solid line*: component along the x-axis; *dashed line*: component along the y-axis
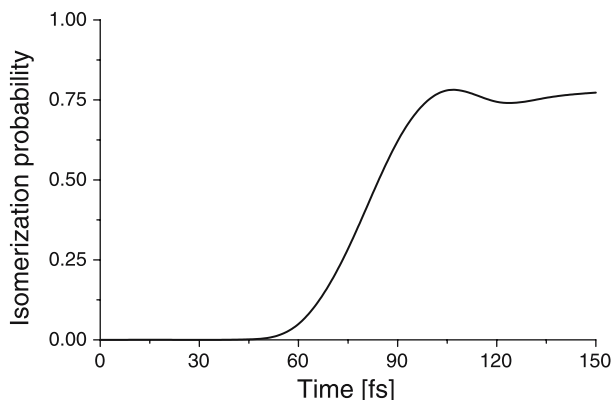
Fig. 6.15. Time variation for the probability of HCN–CNH isomerization

where $h(x) = 1$ for $x \geq 0$ and 0 for $x < 0$. The final efficiency achieved by the present control is 76%, even though the efficiency at intermediate stages is lower.

The controlling field obtained for the whole process is shown in Fig. 6.14. It consists of two intense low-frequency pulses that correspond to acceleration and deceleration of the proton. The isomerization probability is presented as a function of time in Fig. 6.15.

6.7 Future Perspectives

The control of wavepacket dynamics on a single adiabatic potential energy surface can be effectively performed using the semiclassical optimal control theory developed here. The approach is based on a particular semiclassical approach to wavepacket propagation and combines the advantages of the quantum and classical formulations of optimal control theory. This makes it possible to reproduce almost all quantum effects while ensuring that the computational costs do not grow rapidly as the dimensionality of the system increases (roughly as the square of the dimensionality). Another advantage of this method is that it can be used to control wavepacket broadening caused by energy exchange between different molecular modes. Numerical applications demonstrate that this theory can provide an efficient tool for manipulating molecular dynamics with many degrees of freedom using laser pulses.

One of the big defects of the optimal control theory is that in many cases the optimal field generated is difficult to realize experimentally. Also, if the initial guess field is not good enough, the optimization procedure can be very slow to converge and the final efficiency achieved is not satisfactory. Both of these defects can be avoided if control is based on intrinsic information about the molecular dynamics. This information can be included by guiding the control—by dividing the whole process into a sequence of steps and using appropriately chosen intermediate target states. Obviously this can also provide a natural way to combine the control of electronic transitions using quadratically chirped pulses with semiclassical optimal control on single adiabatic surface.

If the process to be controlled is simple enough, a sequence of intermediate target states can be introduced from intuitive physical considerations. However, if the system is large and the dynamics of the process are unclear, the choice of intermediate target states should be based on a particular variational principle. Intermediate target states should be placed along some curve in phase space that is calculated such that the power of the controlling laser pulse is minimized along it. This guided control path can be treated as a kind of reaction path on an effective potential surface. This will be investigated in future studies.

Finally, by combining the laser control of electronic transitions of wavepackets using quadratically chirped pulses [18,19] with semiclassical op-

timal control on a single adiabatic surface, we should be able to establish an effective methodology for controlling the dynamics of large-dimensional chemical and biological systems.

References

1. S.A. Rice and M. Zhao: *Optical Control of Molecular Dynamics* (Wiley, New York, 2000)
2. S.M. Hurley and A.W. Castleman, Science, **292**, 648 (2001)
3. A. Peirce, M. Dahleh and H. Rabitz, Phys. Rev. A **37**, 4950 (1988)
4. S. Shi, A. Woody and H. Rabitz, J. Chem. Phys. **88**, 6870 (1988)
5. C. Schwieters and H. Rabitz, Phys. Rev. A **44**, 5224 (1991); *ibid.* **48**, 2549 (1993)
6. J. Botina, H. Rabitz and N. Rahman, J. Chem. Phys. **102**, 226 (1995)
7. R. Kosloff, S. Rice, P. Gaspard, S. Tersigni and D. Tannor, Chem. Phys. **139**, 201 (1989)
8. J. Somlói, V. Kazakov and D. Tannor, Chem. Phys. **172**, 85 (1993)
9. M. Sugawara, Y. Fujimura, J. Chem. Phys. **100**, 5646 (1994)
10. Y. Ohtsuki, H. Kono, Y. Fujimura, J. Chem. Phys. **109**, 9318 (1998)
11. W. Zhu, J. Botina and H. Rabitz, J. Chem. Phys. **108**, 1953 (1998)
12. Y. Teranishi, K. Nagaya and H. Nakamura, *Advances in Multiphoton Processes and Spectroscopy*, Vol. 14. (World Scientific, Singapore, 2001)
13. Y. Teranishi and H. Nakamura, J. Chem. Phys. **109**, 1904 (1997)
14. Y. Teranishi and H. Nakamura, Phys. Rev. Lett. **81**, 2031 (1998)
15. Y. Teranishi and H. Nakamura, J. Chem. Phys. **111**, 1415 (1999)
16. K. Nagaya, Y. Teranishi and H. Nakamura, in: *Laser Control and Manipulation of Molecules*, edited by A.D. Bandrauk, R.J. Gordon and Y. Fujimura (American Chemical Society, Washington, DC, 2001)
17. K. Nagaya, Y. Teranishi and H. Nakamura, J. Chem. Phys. **117**, 9588 (2002)
18. S. Zou, A. Kondorskiy, G. Mil'nikov and H. Nakamura, J. Chem. Phys. **122**, 084112 (2005)
19. S. Zou, A. Kondorskiy, G. Mil'nikov and H. Nakamura, *Laser control of chemical dynamics. I. Control of electronic transitions by quadratic chirping.* In: *Progress in Ultrafast Intense Laser Science* (Springer, Berlin Heidelberg New York, 2005)
20. M. Herman and E. Kluk, Chem. Phys. **91**, 27 (1984)
21. E. Kluk, M. Herman and H. Davis, J. Chem. Phys. **84**, 326 (1986)
22. V.S. Batista and P. Brumer, Phys. Rev. Lett. **89**, 143201 (2002)
23. A. Kondorskiy and H. Nakamura, J. Theor. Comp. Chem. **4**, 72 (2005)
24. A. Kondorskiy, G. Mil'nikov and H. Nakamura, Phys. Rev. A **72**, 041401 (2005)
25. H. Wang, X. Sun and W.H. Miller, J. Chem. Phys. **108**, 9726 (1998)
26. X. Sun, H. Wang and W.H. Miller, J. Chem. Phys. **109**, 4190 (1998)
27. W.H. Miller, J. Phys. Chem. A **105**, 2942 (2001)
28. E. Heller, J. Chem. Phys. **94**, 2723 (1991)
29. A. Walton and D. Manolopoulos, Mol. Phys. **87**, 961 (1996)
30. S. Meyer and V. Engel, J. Phys. Chem. A **101**, 7749 (1997)
31. D.G. Imre and J. Zhang, Chem. Phys. **139**, 89 (1989)
32. T. van Mourik, G.J. Harris, O.L. Polyansky, J. Tennyson, A.G. Császár and P.J. Knowles, J. Chem. Phys. **115**, 3706 (2001)

7 Pulse Shaping Technology
of Intense Femtosecond Laser Pulses
for Molecule Control

F. Kannari[1], T. Tanabe[1], T. Okamoto[1], K. Ohno[1], H. Yazawa[1],
R. Itakura[2], and K. Yamanouchi[2]

[1] Department of Electronics and Electrical Engineering, Keio University,
    3-14-1 Hiysohi, Kohoku-ku, Yokohama, 223-8522, Japan
    e-mail: kannari@elec.keio.ac.jp
[2] Department of Chemistry, School of Science, The University of Tokyo,
    7-3-1 Hongo, Bunkyo-ku, Tokyo 113-0033, Japan

Summary. We demonstrated accurate pulse shaping of amplified femtosecond
laser pulses by modulating the amplitude and the phase prior to regenerative
chirped-pulse amplification. Based on a spectral interferometer, the pulse shaper
was adjusted to compensate for a transfer function of the amplifier consisting of
the gain narrowing and self-phase modulation. We performed experiments aim-
ing at selective bond breaking in such as a simple C–C–O structure by utilizing
the comprehensive pulse shaping technology, which can produce almost arbitrarily
shaped 800-nm laser pulses in the amplitude and the phase at peak intensities up
to $\sim 4 \times 10^{15}$ W/cm^2 range.

7.1 Introduction

One of the key technologies increasing the versatility of ultrashort laser pulse
is pulse shaping. When the optimum pulse shape in both the amplitude and
the phase can be theoretically predicted, such as those calculated by optimum
control theory in chemistry [1], the performance of coherent control depends
on the accuracy of pulse shaping. In high optical fields, the potential energy
surfaces of a molecule are modified to the extent that there is no longer a spec-
troscopic map to follow [2]. The electric field can exert a force directly on the
electrons, forcing them into high energy states or causing them to field ion-
ize. These high fields can also exert forces on the molecule and its constitute
atoms. Therefore, high-field control has the greatest possibility for manipu-
lating molecular structure and chemical transformations [3]. If the required
power of shaped laser pulses exceeds the PW/cm^2 regime, such as those used
in controlling the dissociative ionization of molecules, one need to precisely
shape ultrashort pulses amplified with a chirped pulse amplifier (CPA). When
a pulse shaper is placed after an entire laser amplifier system, one can obtain
arbitrarily shaped ultrashort laser pulses within the bandwidth of the laser
pulse and the spectral resolution of the pulse shaper. However, because of the
optical damage at the pulse shaper, the optical power density should be kept

lower than an average power of $500\,\mathrm{W/cm^2}$ at the conventional computer controlled liquid-crystal spatial light modulator (LC-SLM) [4]. Moreover, the transmission loss of pulse shapers significantly reduces the available laser pulse power at a light-matter interaction stage. An alternative method to overcome this optical damage and the power attenuation is to install a pulse shaper before an amplification stage [5–7]. This pre-shaping scheme can also reduce spatio-temporal coupling at the pulse shaper. Wefers and Nelson [8] theoretically showed that along with temporal shaping a 4-f pulse shaper also modulates the spatial profile of pulses. This is due to spatio-temporal coupling caused by diffraction at the shaping mask. Note that this coupling occurs no matter how perfectly a pulse shaper is aligned and it results in wave front chirping, which significantly varies light-matter interaction performance in intensity-sensitive experiments because the beam cannot be focused to the diffraction limit. For example, when a temporal laser pulse is shaped to a dual-peak pulse with 0-π phase shift at the center wavelength, the spatio-temporal coupling causes a dual-peak spatial pattern at the far-field [9]. Therefore, the laser power distribution in its far-field directly affects molecule control. Since a regenerative amplifier effectively incorporates spatial filtering defined by a pumping beam, the pre-shaping scheme can overcome this spatio-temporal coupling except for some spectral amplitude shaping caused by the spatial filtering. The only disadvantage of a pre-shaping scheme is that the spectral phase mask cannot easily be designed directly from the desired output pulse shape because the transfer function of a CPA system is often indescribable.

To overcome this, feedback schemes referring to output pulse shapes have been applied [5–7]. In this work, we used an acoustic optical phase-dispersion filter (AOPDF) [10] as a phase and amplitude modulator. To ensure a high accuracy of the shaped pulses, we used a temporal analysis by dispersing a pair of light e filed (TADPOLE) measurements [11] to characterize them. By sending an amplitude and phase correction signal to the pulse shaper, we experimentally demonstrated that a shaped pulse generated from the CPA is highly accurate to a target pulse. We, then, applied this pulse shaping system to ensure the effect of driving laser pulse shape on dissociative ionization of ethanol molecules. The open-loop molecule control experiment was also compared with the experimental results using a self-learning adaptive loop to shape the laser pulses.

7.2 Compensation for a Transfer Function of CPA to Generate Accurately Shaped Intense Ultrashort Laser Pulses

7.2.1 Experimental Setup [7]

Figure 7.1 shows a schematic of the experimental setup. An AOPDF is placed before the CPA, which operates at a repetition rate of $1\,\mathrm{kHz}$ and generates

Error calculation from the target
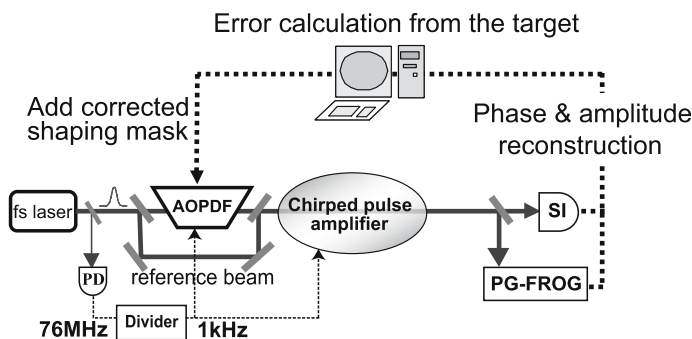
Fig. 7.1. Experimental setup of TADPOLE referring closed-loop pulse shape control [7]

$\sim$0.5 mJ output/pulse with the center wavelength of 800 nm. The bandwidth of Fourier transform limited output pulse is $\sim$30 nm (FWHM). The reference pulse detours around the AOPDF and enter the CPA to enable to generate spectral interference (SI) at the TADPOLE setup. The stretcher and the compressor of the CPA are aligned so that the reference pulse is almost limited by the Fourier transform after the CPA, where the reference pulse is characterized by a frequency-resolved optical gating (FROG) measurement [12].

The amplitude and phase corrections are calculated from the target pulse and the acquired pulse using a TADPOLE measurement, and the new amplitude and phase mask functions are simultaneously rewritten to the pulse shaper. The difference between the measured phase $\Phi_{\mathrm{acq}}(\omega)$ and the target phase $\Phi_{\mathrm{tar}}(\omega)$ is calculated and added to the current spectral phase mask of the AOPDF. For correction of the amplitude mask, $S_{\mathrm{tar}}(\omega)/(S_{\mathrm{acq}}(\omega) + \delta)$ is multiplied to the current mask, where $S_{\mathrm{tar}}(\omega)$ and $S_{\mathrm{acq}}(\omega)$ are the target and acquired spectrum amplitude, and δ is added to the background to prevent it from diverging to infinity at the edge of the spectrum, where $S_{\mathrm{acq}}(\omega)$ becomes zero.

In a CPA, because a large secondary dispersion is added to the stretcher, the spectrum is mapped to the temporal waveform in the amplifier. For that reason, the phase change added to the pulse shaper cannot cause a large change in the pulse shape in the CPA. Self-phase modulation depends on the temporal amplitude transition. Therefore, the phase perturbation can be regarded as almost linear in the amplifier. Thus, the inverse of the spectrum phase difference between the acquired and the target phase is added to the pulse shaper.

7.2.2 Experimental Results

We experimentally demonstrated double-pulse shaping by modulating both the amplitude and the phase. The shaped pulse shown in Fig. 7.2, which was obtained in two iterative correction loops, shows good agreement between the
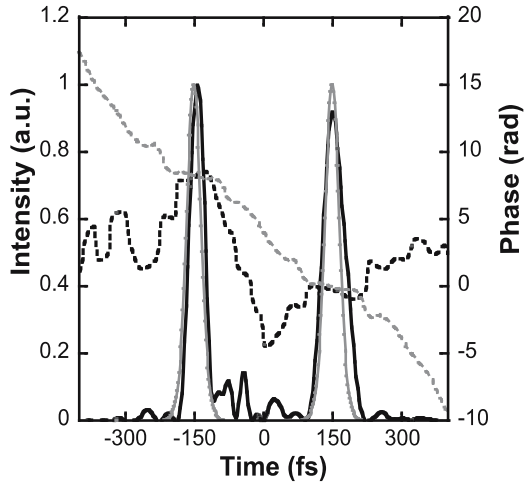
Fig. 7.2. Double pulse-shaping experiment by modulating both amplitude and phase at the pulse shaper. *Thin line* is the target pulse. *Thick line* is the shaped pulse. Pulses are corrected in two iterations [7]
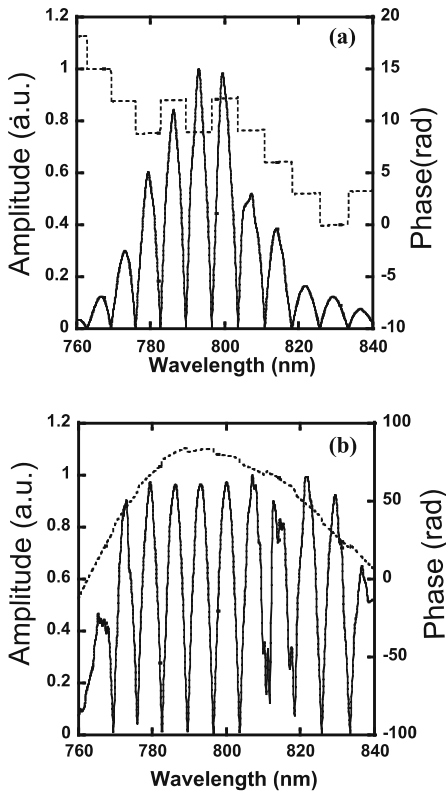
Fig. 7.3. a Target spectrum amplitude of a normal double pulse corresponding to Fig. 7.2, and **b** the mask function added to the AOPDF after two iterations [7]

shaped and the target waveform. The target spectrum and a mask function added to the AOPDF after two iterations are shown in Fig. 7.3. Even if we started with a non-transform limited 400-fs pulse, we also observed the same convergence performance.

Since we modulate both the amplitude and the phase of the ultrashort pulses, we can design more complex pulses. One example is pulse shaping that compensates for the gain narrowing effect of the CPA. We set a target pulse as two 30-fs pulses separated by 300-fs, of which bandwidth is broader than that obtained from the CPA in normal operation. Figure 7.4 shows the target spectrum and the corrected mask function after two iterations. This final spectral mask exhibits a low transmission at the edge of the spectrum. By adding such a mask function to the seed pulse, the gain narrowing effect of the CPA is automatically compensated for while the pulse is shaped into the desired pulse shape. This experiment shows that our automated iteration loop is applicable to simultaneous gain narrowing compensation and pulse shaping.
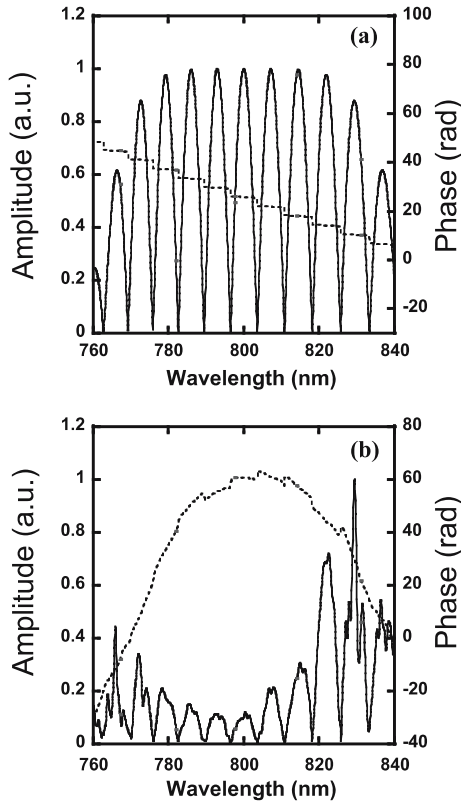
Fig. 7.4. a Target spectrum amplitude of a broader bandwidth double pulse, and **b** the mask function added to the AOPDF after two iterations [7]
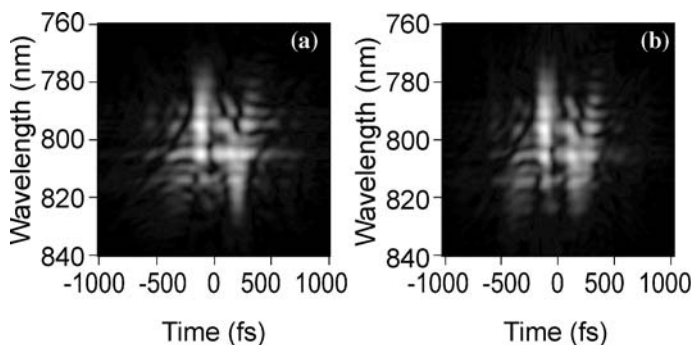
Fig. 7.5. a A spectrogram of the target complex pulse, and b a spectrogram of the shaped pulse obtained after two iterations [7]

We also demonstrated a more complex pulse shaping. The target pulse is designed to have a large time-bandwidth product. Such pulses are important in many coherent control studies. A pulse with multiple peaks in both the temporal and wavelength region is finely structured. The spectrogram of the target pulse is shown in Fig. 7.5a. Such pulses can be designed because we have full access to the phase and amplitude of the ultrashort optical pulses. The spectrogram of the shaped pulse shown in Fig. 7.5b exhibits an excellent agreement with the target spectrogram. Certainly, the multiple peaks and the fine structures are restored in the amplified laser pulse.

7.3 Dissociative Ionization of Ethanol with Shaped Intense Laser Pulses

7.3.1 Experimental Setup [13]

The femtosecond laser pulses shaped by the AOPDF are amplified by the CPA up to 0.5 mJ/pulse. Ethanol vapor is continuously flow into the vacuum chamber through a micro-syringe ($70 \, \mu m \phi$) with stagnation pressure of ~ 7 Torr at room temperature. The laser pulses are focused on a skimmed molecular beam of the ethanol vapor with an achromatic lens ($f = 145$ mm). The focal spot size of the laser beam is $20 \, \mu m \phi$. The peak intensity of the transform-limited laser pulse is calculated to 4×10^{15} W/cm^2. The fragment ions are mass-separated with Wiley-McLaren type time-of-flight (TOF) mass spectrometer, and are detected with a microchannel plate (MCP) detector.

7.3.2 Open-Loop Control Experiment

Prior to some adaptive close-loop control schemes, we revealed some key factors, which control molecule dissociative ionization by limiting the laser pulse

parameters varied, such as frequency chirp or intensity. By varying the frequency chirp rate from $-5.0 \times 10^{-2}\,ps^2$ to $+5.0 \times 10^{-2}\,ps^2$, we observed the differences in the photo dissociation ionization spectra of ethanol molecules (Fig. 7.6). In the recent studies of photochemical processes in an intense laser field, it was considered that the molecular energy levels are broadened by an AC Stark effect and the resonance condition with the light field is affected sensitively by the instantaneous frequency structure within an ultrashort pulse [14]. However, in our experiment, the relative yields of the fragment ions are not influenced by the sign of the chirp, indicating that the near infrared light could not cause an efficient resonance with electric transitions of ethanol. Since the temporal width of the ultrashort laser pulses increases as the linear chirp increases, the temporal width is considered to play a decisive role in determining the fragmentation processes. We also confirmed that the fragment ion yield ratios in the TOF spectra are less sensitive to the peak intensity in this $\sim 10^{15}\,W/cm^2$ regime. Rather, fragment yields formed from C–C bond breaking increase as the peak intensity of the transform-limited pulse is attenuated.
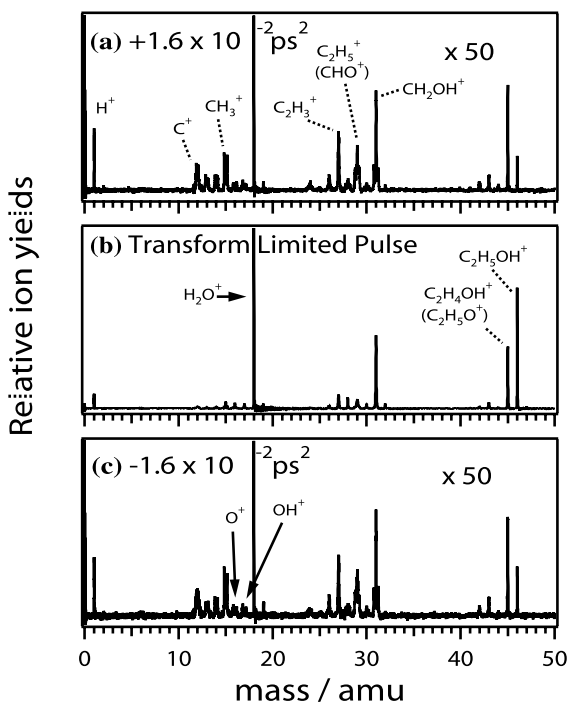
Fig. 7.6. The time-of-flight mass spectra of the ion species recorded when ethanol molecules are irradiated with intense laser pulses. The strong peak appearing at $m/q = 18$ is ascribed to the residual water molecules existing in the vacuum chamber. The linear chirp rates of the laser pulses are **a** $1.6 \times 10^{-2}\,ps^2$, **b** 0 (transform limit), and **c** $-1.6 \times 10^{-2}\,ps^2$ [13]

When the yield ratio $[C_2H_5^+]/[CH_2OH^+] = m_{29}/m_{31}$ is plotted along the frequency chirp level as shown in Fig. 7.7, the ratio increases sensitively as the absolute value of the chirp increases, indicating that the dissociative pathway of parent ions $CH_3CH_2OH^+$ for C–O bond breaking becomes preferred as the temporal pulse increases. The ratio of ~ 0.12 at the transform limited pulse indicates that the C–C bond breaking dominates over the C–O bond breaking, but as the light field duration increases the nuclear wave packet begins to flow more into the C–O bond. The increase in the ratio saturates to the value of ~ 0.45 when the pulse width reaches to 760 fs. Therefore, this pulse duration can be regarded as the characteristic holding time of the light-dressed potential energy surface to guide the wave packet into the C–O bond breaking.

The yield ratios with the fragment ions produced through the Coulomb explosion also exhibit significant pulse width dependence. As the pulse width increases, the yield ratio $[(CH_2OH^+)^*]/[CH_2OH^+]$ increases by a factor of 10. The characteristic holding time is estimated to 530 fs, which can be regarded as the holding time for the nuclear wave packet evolution to reach the critical distance where the enhanced ionization occurs to from secondary ions $C_2H_5OH^{2+}$. Similar observation was obtained for the Coulomb explosion at the C–O bond breaking.

Although we interpreted our experimental results with the motion of nuclear packets on the light-dressed ground state of the parent ions, a pump-probe scheme could also explain the pulse width dependence. When two successive pulses are interacted with molecules with a proper interval, the second pulse can be adjusted to achieve synchronicity with the motion of the nuclear wave packet of an excited state. This results in energy transitions to
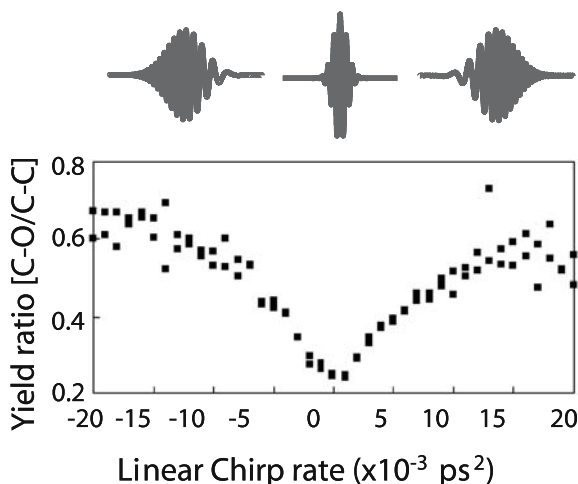
Fig. 7.7. The chirp dependence of the yield ratio of $[C_2H_5^+]/[CH_2OH^+] = m_{29}/m_{31}$. The ratio is normalized so that the ratio obtained with a transform limited pulse (0 chirp) is unity

the specific energy levels leading to dissociation. It has already been possible to control some molecule systems by such a pump-probe scheme. Therefore, we carried out an experiment to investigate the photo-induced dissociative ionization of ethanol excited by intense laser energy in various pulse trains. First, double pulses were generated before the amplifier system.

Changes in the ion ratio of m_{29}/m_{31} by the time interval between two pulses up to 3 ps are shown in Fig. 7.8. Changes in the fragment ion ratio of m_{29}/m_{31} shown in this figure are very small. The ion ratio gradually decreases as the temporal pulse separation increases. Such a finding reveals that the C–O bond breaking is not caused in the pump-probe schemes with two properly separated laser pulses. Since the ion ratios obtained at pulse intervals longer than 1.5 ps are the same as the fragment ratio generated by a single pulse, it can be concluded that two pulses with such long intervals have no dynamic accumulation effect on the nuclear wave packet.

However, would the record of latest excitation vanish once the electric field is shut off? The m_{29}/m_{31} ion ratios generated by two pulses with very short pulse intervals were larger than that obtained with a single pulse (at zero interval in Fig. 7.8, the peak intensity is the same as the dual pulses). Upon termination of the optical field, the movement of the nuclear packet cannot follow the rapid change in the electric field; consequently, the wave packet will be transmitted to an electric-field-free PES, maintaining the same nuclear distance through a non-adiabatic transition. Figure 7.8 clearly shows that very little change in the ion ratio is obtained with shorter pulse intervals. Therefore, if a pulse is irradiated again with sufficiently short intervals, it would not be possible for the wave packet to intermittently move again along the light-dressed potential energy surface (LD-PES).
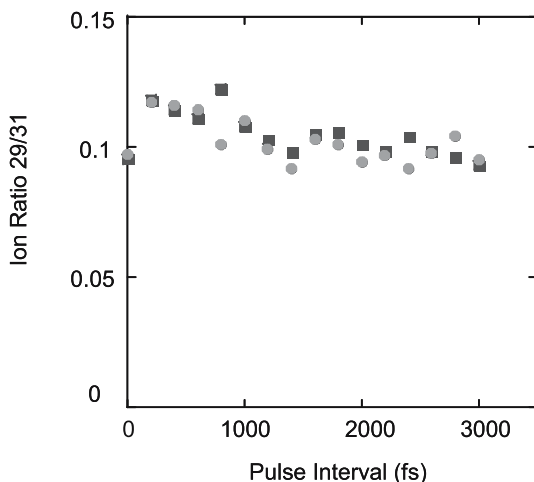
Fig. 7.8. Change in the fragment ion yield ratio of m_{29}/m_{31}. The pulse interval between two transform-limited pulses with the same energy is changed

To more clearly examine the effect of the interval time among successive pulses, we carried out a second experiment. Keeping the time period between the outermost pulses of pulse trains to 800 fs, we filled the space with light pulses of equal intensity. Thus, we have investigated the dependence of the ion ratio upon the number of pulses in pulse trains. The interval between each pulse in the pulse train is 400 fs in the three-pulse train, 276 fs in the four-pulse train, and 200 fs for the five-pulse train. The time period between the outermost pulses of the train was set to 800 fs, since the fragment ion ratio of m_{29}/m_{31} saturated with pulse lengths longer than 760 fs in our previous experiments done with linearly frequency-chirped laser pulses. When the accumulated excitation duration increases by boosting the number of pulses, the relative ion yields ratio linearly increases. The largest increase in the ion ratio of $\sim$2.5 times as large as that with a single Fourier-limited pulse was obtained with the five successive pulses. Therefore, when the field-free time period is sufficiently short, the wave packet can still intermittently move in the LD-PES, and thus the resultant fragment distribution reflects the accumulated effect. Because the increase in the relative C–O bond-breaking is linear to the number of pulses, the travel distance of the wave packet accumulates linearly when the interval is below 800 fs.
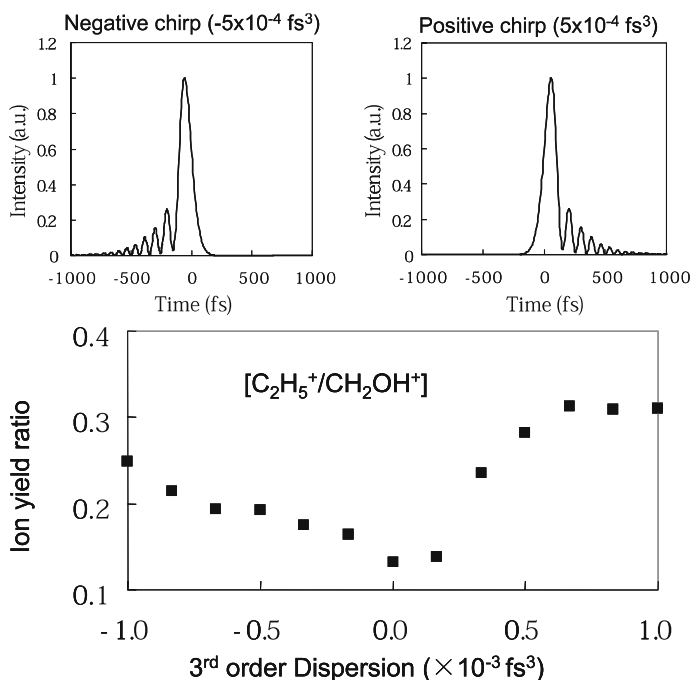
Fig. 7.9. Dependence of the fragment ion yield ratio of m_{29}/m_{31} on third-order dispersion coefficient

Figure 7.9 shows the dependence of the ion ratio of m_{29}/m_{31} up on third-order dispersion coefficient. Contrary to the experiment with various second-order dispersion coefficients, the ion ratio significantly varied by the sign of the third-order dispersion coefficient. At positive coefficients, since the center wavelength appears at the leading edge of a pulse, a steep leading edge is obtained. Therefore, parent ions generated at the leading edge of the pulse can hold enough long time to be dissociated at C–O bond. However, at negative coefficients, parent ions generated at the sharp end of the pulse cannot dissociate at C–O bond since no optical field follows. Therefore, the ion ratio of m_{29}/m_{31} rapidly increases only at the positive third-order dispersion coefficient.

7.3.3 Close-Loop Optimization Control Experiment

Next, we performed adaptive pulse shaping referring to the relative ratio of fragment ion yields. In the adaptive control we manipulated the spectral phase with 128 individual segments of the LC-SLM instead of the AOPDF. The spectral amplitude was left unchanged. The longest laser pulse duration was also limited by the spectral resolution of the pulse shape to $\sim 1.5\,\mathrm{ps}$ (FWHM) with our $4f$-pulse shaper setup. In our previous open-loop experiments with pulse trains or single pulses with various linear chirp rates, the fragment ion distribution was not sensitive to the temporal phase. Therefore, ignoring the temporal phase, in principle a wide range of pulse shapes can be shaped within the time window only by programming the spectral phase.

Experimental parameters used in the algorithm were: $T_{\mathrm{ini}} = 4 \times 10^{-1}$, and $\eta = 9.975 \times 10^{-1}$. The number of pixels changed in each iteration loop was locked at 16 and the maximum phase variation at one loop was set as $\Delta\phi_{\max} = 2\pi/16$. The minimum phase change was determined by the resolution of the voltage driver of the LC-SLM to be $2\pi/220$.

Figure 7.10 shows an evolution of optimization. In this run, because the initial mask was set to be a null mask, which generates a Fourier-limited pulse, the first iterations may not have acquired accurate ion ratios due to the limited dynamic range of our TOF signal-acquisition system. However, we separately confirmed that the change in the cost function during this early period does not influence the final experimental result. In this particular run, the increase of the cost function was relatively slow due to the small phase variation and the number of pixels changed in each iteration loop. Indeed, when the phase variation changed in each iteration was set to a larger value, the cost grew rapidly during the first few hundred iterations. To prevent the solution from being trapped into local minima, the mask was slowly changed. As a result of optimization, the ion ratio increased by a factor of approximately five times, which corresponds to about the same amount obtained by systematically changing the linear chirp rate. We have confirmed that when setting the cost function to an ion ratio m_{31}/m_{29} instead of m_{29}/m_{31},
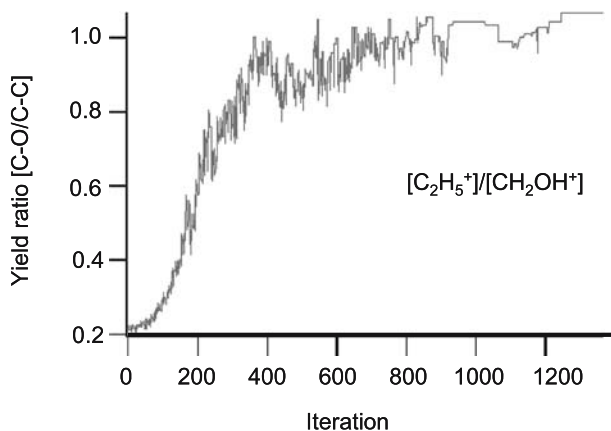
Fig. 7.10. Evolution of cost function during iterative control by manipulating individual 128 segments of the SLM. The optimized ion yield ratio is roughly as same as that obtained by varying the linear chirp rate

and starting the iterative control from a random phase mask, the optimized waveform converges to a transform-limited pulse.

We repeated the same optimization experiments and obtained the same maximum ion ratio of m_{29}/m_{31} at every run; the optimized waveforms, however, differed. Figure 7.11 shows the four pulses that produced the highest ion yield ratio of m_{29}/m_{31}. Figure 7.11a and b shows two sample waveforms acquired from the multi-parameter optimization experiments. The pulse shown in Fig. 7.11c is one shaped by adding second-order phase dispersion by the $4f$-pulse shaper to create a linear chirp pulse. With such a large second-order dispersion coefficient, the 128 pixels cannot provide a continuous function; therefore, a step-like phase change gives temporal amplitude modulation as shown. In Fig. 7.11d, an equivalent second-order dispersion was added by adjusting the pulse compressor of the CPA. The only similarity among these four pulses is that the pulse widths are $\sim$1–1.5 ps (FWHM). It is reasonable to suggest from our experimental results using pulse trains that high-frequency amplitude and phase modulation does not affect the movement of the wave packet, only the total pulse duration does. We also performed adaptive experiments by changing the optimization algorithm from SA to a genetic algorithm (GA). However, we obtained a similar conclusion with the SA.

To date, similar experiments on dissociative ionization of molecules by adaptively shaped ultrashort laser pulses have been reported, where specific ion ratios were targeted during iterative control using GA and SA [14, 15]. However, less detailed comparisons between adaptive control and open-loop control experiments regarding the laser pulse width, pulse train, and peak intensity exist. Moore et al. claimed that not only accelerated specific bond-breaking, but even new bond formation, can specified by adaptive pulse shape control [14]. Because ethanol molecules have a relatively simple main struc-
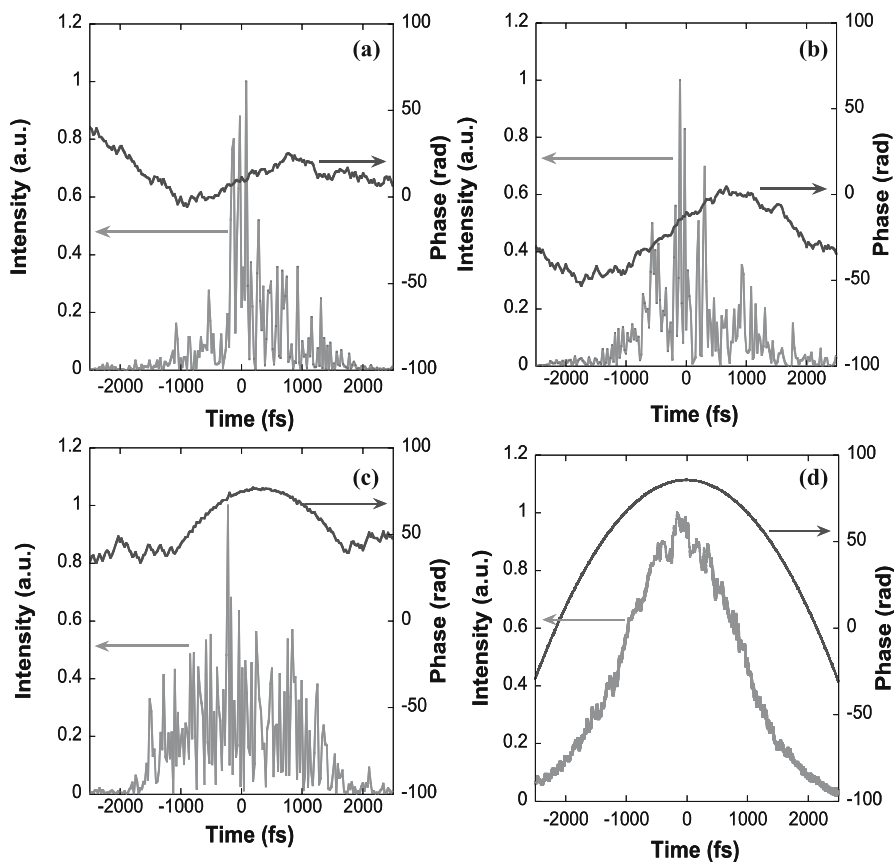
Fig. 7.11. Four excitation-pulse waveforms achieving the highest ion yield ratio of m_{29}/m_{31}. Waveforms in **a** and **b** were obtained by the self-learning adaptive pulse control. The waveform in **c** was obtained by applying a linear frequency chirp at $2.2 \times 10^{-2}\,\mathrm{ps}^2$ by the $4f$-pulse shaper. The waveform in **d** was obtained by applying a linear frequency chirp at $2.2 \times 10^{-2}\,\mathrm{ps}^2$ by adjusting the pulse compressor

ture compared with other molecules reported so far in adaptive control experiments, there might be only one path to enhance C–O bond breaking by maintaining nuclear wave packet flow toward the critical energy level crossing point. Another possibility is that because not many energy levels are near-resonantly involved during multi-photon excitation, there may be less freedom to control the LD-EPS by laser pulse shapes. In fact, we repeated fragmentation measurements for acetone, 1-propanol, 2-propanol, and acetonitrile by varying the linear chirp rate of excitation laser pulses. Relative ion yields by bond breakings which exhibit less at the shortest pulse increase by increasing the pulse duration. But, they do not depend on the sign of the frequency chirp as the case of ethanol, which suggests that the phase does

not influence the dissociative ionization of these molecules, too. Moreover, adaptive control experiments carried out on 1-propanol showed that C–O breakage in 1-propanol is enhanced by various long pulses, as in the case of ethanol; there is no specific optimal pulse shape for 1-propanol.

7.4 Conclusions

We demonstrated highly accurate pulse shaping for amplified pulses. By shaping pulses before amplification stage, we obtained pulses up to several PW/cm^2 focal intensities. Both the spectral amplitude and phase are modulated before the CPA and we used TADPOLE measurements to characterize the shaped pulse to iteratively correct the pulse shape at the pulse shaper. Although the pulse shaper-CPA system is not a perfectly linear system, where the FM to AM, or the AM to FM conversion takes place, altering the spectral phase more than twice can almost compensate for those errors, therefore the overall shaped pulse shows good agreement. This current iterative feedback scheme is more useful than our previous scheme of FROG referring adaptive shaping.

We applied this pulse shaping technology for controlling dissociative ionization of ethanol molecules, and revealed that the pulse width is the only parameter controlling the dissociative ionization of C–C and C–O bonds in ethanol molecules. Moreover, wave packets do not respond to the fast frequency and amplitude modulations around 10 THz in the laser field. The wave packet moves on the LD-PES defined by laser fields averaged over those modulations toward the critical energy-level crossing point, where the non-adiabatic transition to the repulsive energy level occurs. These results found for ethanol molecules contradict previous reports dealing with relatively large molecules for which efficient dissociation ionization was achieved through self-learning optimization control. If such an optimal pulse shape can lead to more selective dissociative ionizations than long, intense laser pulses, it will result in uniqueness of such particular molecules with respect to their LD-PES structure.

References

1. Peirce AP, Dahleh MA, Rabitz H (1988) Optimal-control of quantum-mechanical system-Existence, numerical approximation, and applications. Phys. Rev. A37:4950–4964

2. Yamanouchi K (2002) Ultrafast dynamics of molecules in intense laser-light fields: new research direction. In: Bandrauk AD, Fujimura Y, Gordon RJ (eds) Laser control and manipulation of molecules. American Chemical Soc., Washington DC, pp 251–266
3. Dantus M, Lozovoy VV (2004) Experimental coherent laser control of physicochemical processes. Chem. Rev. 104:1813–1859
4. Weiner AM (2000) Femtosecond pulse shaping using spatial light modulators. Rev. Sci. Instrum. 71:1929–2960
5. Ohno K, Tanabe T, Kannari F (2002) Adaptive pulse shaping of phase and amplitude of an amplified femtosecond pulse laser by direct reference to frequency-resolved optical gating traces. J. Opt. Soc. Amer. B19:2781–2790
6. Tanabe T, Ohno K, Okamoto T, Yamanaka M, Kannari F (2004) Feedback control for accurate shaping of ultrashort optical pulses prior to chirped pulse amplification. Jpn. J. Appl. Phys. 43:1366–1375
7. Tanabe T, Yamanaka M, Okamoto T, Kannari F (2004) Compensation for a transfer function of a regenerative amplifier to generate accurately shaped ultrashort pulses in both the amplitude and phase. IEEE J. Selected Topics in Quantum Electron. 10:221–228
8. Wefers MM, Nelson KA (1995) Analysis of programmable ultrashort waveform generation using liquid-crystal spatial modulators. J. Opt. Soc. Amer. 12:1343–1362
9. Tanabe T, Kannari F, Korte F, Koch J, Chichkov B (2005) Influence of spatiotemporal coupling induced by an ultrashort laser pulse shaper on a focused beam profile. Appl. Opt. 44:1092–1098
10. Verluise F, Laude V, Cheng Z, Spielman Ch, Tournois P (2000) Amplitude and phase control of ultrashort pulses by use of an acousto-optic programmable dispersive filter: pulse compression and shaping. Opt. Lett. 25:575–578
11. Fittinghoff DN, Bowie JL, Sweetser JN, Jennings RT, Krumbugel MA, De-Long KW, Trebino R, Walmsley IA (1996) Measurement of the intensity and phase of ultraweak, ultrashort laser pulses. Opt. Lett. 21:884–886
12. Trebino R, DeLong KW, Fittinghoff DN, Sweetser JN, Krumbugel MA, Richman BA, Kane DJ (1997) Measuring ultrashort laser pulses in the time-frequency domain using frequency-resolved optical gating. Rev. Sci. Instrum. 68:3277–3295
13. Itakura R, Yamanouchi K, Tanabe T, Okamoto T, Kannari F (2003) Dissociative ionization of ethanol in chirped intense laser fields. J. Chem. Phys. 119:4179–4186
14. Moore NP, Menkir GM, Markevitch AN, Graham P, Levis RJ (2002) In: Bandrauk AD, Fujimura Y, Gordon RJ (eds) Laser control and manipulation of molecules. American Chemical Soc., Washington DC, pp 207–220
15. Assion A, Baumert T, Bergt M, Brixner T, Kiefer B, Seyfried V, Strehle M, Gerber G (1998) Control of chemical reactions by feedback-optimized phase-shaped femtosecond laser pulses. Science 282:919–922

8 Control of High Harmonic Generation Processes Using Chirped and Self-Guided Femtosecond Laser Pulses

Chang Hee Nam, Hyung Taek Kim[1], and Valer Tosa[2]

Dept. of Phys. and Coherent X-ray Research Center,
Korea Advanced Institute of Science and Technology (KAIST), Yuseong-gu,
Daejeon 305-701, Korea
e-mail: Chnam55@kaist.ac.kr
[1] Current address: Femto Science Laboratory,
   Advanced Photonics Research Institute, GIST, Gwangju 500–712, Korea
[2] On leave from National Institute for R&D of Isotopic
   and Molecular Technologies, Cluj–Napoca, Rumania

Summary. High-order harmonic generation in a long gas jet is controlled in the space and time domains using chirped and self-guided femtosecond laser pulses. Since high-order harmonic generation is intrinsically connected to the ionization process of harmonic generation medium, ionization effects on high-order harmonic generation should be properly understood and taken into account. Here, we present a method to control high-order harmonic generation process by controlling the propagation mode of intense femtosecond laser pulses through the ionizing medium. Experimental results and theoretical analysis show that self-guided and chirped laser pulses can optimize high-order harmonics for achieving high brightness, low beam divergence, and narrow spectral bandwidth.

8.1 Introduction: High Harmonic Generation Processes

High harmonic generation (HHG) is a coherent interaction process between an intense laser field and atoms. An atom under intense laser field can be easily ionized by tunneling and the ionized electron moves in the intense laser electric field, gaining kinetic energy. As the sign of the laser electric field is reversed at every half-optical cycle, the electron returns and may recombine with the atom. The electron kinetic energy plus the binding energy is then released as radiation energy. During the next half cycle, this process is repeated in the opposite direction. As a result of the periodic repetition of this modulation of the atom, the harmonics of the driving laser frequency are emitted. As the induced polarization of the atom in a gaseous medium changes sign with the laser electric field, only odd harmonics are produced, of which order can be as high as several hundreds, reaching the extreme ultraviolet (EUV)/soft X-ray region. The high harmonics emitted by noble gases driven by intense femtosecond laser pulse posses unique features such as excellent coherence [1,2], ultrashort pulse duration [3], continuous wavelength

tuning capability [4], and tabletop scale; consequently, a high harmonic light source is very promising for ultrafast spectroscopy and interferometry in the EUV/soft X-ray region.

When atoms or molecules in a matter interact with a laser field, they may directly respond to the detailed structure of the laser electric field. It means that the interaction can be manipulated by controlling the temporal or spectral structure of the field; it is a coherently controllable process. This coherent control of the interaction process between the laser light and matter can be achieved by altering the temporal shape or spectral configuration of the interacting light. The coherent control process can be applied to HHG for the production of sharp and strong harmonics [5]. As the response of atoms to applied laser field determines high harmonic process, the temporal structure, i.e., amplitude and phase, of the laser field directly administers high harmonics emitted. For instance, rapidly increasing electric field in the rising edge of an ultrashort laser pulse can affect the phase of the electronic wave packet of a driven atom in such a way that a chirped structure is induced in high harmonics. Because atoms respond to the laser field at every optical cycle, this dynamically induced harmonic chirp can be coherently controlled by appropriately shaping the temporal structure of the laser field. In other words, the spectral structure of high harmonics can be controlled by applying properly shaped laser pulse.

For proper coherent control of HHG, the interaction between atoms and a driving laser pulse has to be treated comprehensively. The intensity and spectral width of each harmonic can be sensitive to the temporal profile of a driving laser pulse, especially the chirp condition. Chang et al. [6] showed that the spectral shape of the harmonics was asymmetric to the laser chirp direction and that a positively chirped laser pulse could compensate for a dynamically induced, negative harmonic chirp. Their experiment was carried out at relatively low intensities, where the effect of ionization on HHG was not significant. At strong laser intensity the ionization of atoms in the leading edge of the laser pulse is not negligible. The self-phase modulation (SPM) of the laser pulse propagating in an ionizing medium alters its spectral structure and temporal shape. In other words, atoms modify the chirp condition of the driving laser pulse, which will be directly transferred to the frequency chirp of harmonics [7]. Consequently, the coherent control to achieve sharp harmonics should treat the interaction between atoms and a laser pulse as an integral system. This is a new consideration required in the coherent control of HHG, compared to other coherent control processes that can be regarded just as an optical manipulation of atoms or molecules [5].

Strong HHG requires the application of intense femtosecond laser pulse to a high-density gas medium that is partially ionized during the harmonic generation process. The high harmonic generation process is diagrammatically represented in Fig. 8.1. If harmonics from individual atom are coherently added, high harmonics generated at different positions can be constructively added and the harmonic intensity is proportional to the square of the number
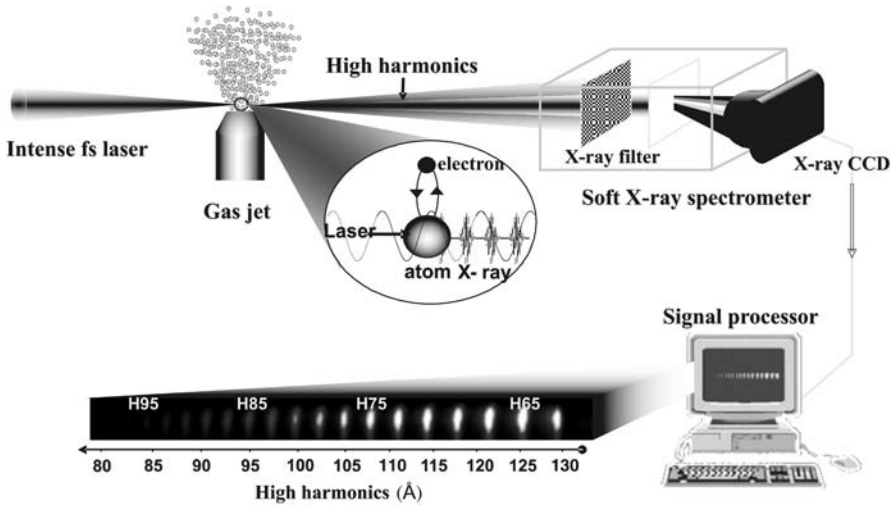
Fig. 8.1. Scheme of high harmonic generation

of atoms participating in the coherent addition of harmonics. The ionized gas medium, with higher electron density in the center than in the outer region, acts as a negative lens, leading to defocusing of the laser beam in a plasma. This plasma defocusing effect reduces laser intensity in the medium and also effective harmonic generation volume. In addition, the rapidly ionizing high-density gas medium modifies the temporal structure of the femtosecond laser pulse due to the self-phase modulation (SPM). Consequently, we have to optimize the harmonic generation conditions in both space and time domains in order to maximize the harmonic generation volume and to generate spectrally sharp harmonics, respectively.

Here we present theoretical and experimental works on strong HHG in a long gas jet achieved through the profile-flattening and chirp control of intense femtosecond laser pulses propagating through an ionizing gaseous medium [8]. We first look at the harmonic generation from a short medium to see the basic harmonic generation processes, and then analyze the conditions for bright harmonic generation from a long gas jet. The main advantages of harmonic generation in the long gas jet are the capability of coupling large laser energy into large interaction volume and the simplicity in target alignment. The plasma defocusing effect, however, should be overcome in order to fully utilize the long medium. The plasma defocusing can be compensated by tailoring the convergence of the laser beam entering the gas target. This results in profile flattening and self-guiding of intense femtosecond laser pulses, which efficiently increases effective harmonic generation volume. Simultaneously, the harmonic spectra are controlled by changing laser chirp while keeping guided laser propagation. Comprehensive theoretical analyses of the harmonic generation in the long gas jet are performed using a nona-

diabatic, three-dimensional propagation model both for laser field and harmonic field [9]. The spectral structures of laser pulses and harmonics are looked into by employing distribution functions in the time-frequency domain [10]. The simulations results agree remarkably well with experimental results, thus revealing detailed underlying physics of harmonic generation in the long gas jet.

8.2 High Harmonic Generation in an Ionizing Gaseous Medium

As high-power femtosecond lasers evolve into a high-intensity femtosecond regime, intense femtosecond laser pulses have been employed to obtain strong harmonics in high orders, and high harmonic emission then has exhibited complicated spectral features, such as spectral broadening, shifting and splitting [5–10]. These features do not appear in high harmonic spectra obtained using lasers with relatively weak intensity and pulse duration longer than one hundred femtosecond. The harmonics in this case show well-defined narrow harmonic peaks at odd multiples of the fundamental laser frequency. When intense laser pulses are utilized for harmonic generation for strong harmonic generation, the ionization of the medium is not negligible and affects the propagation of the laser pulse through the medium, which is usually overlooked. We first elucidate how the ionization effect modulates the femtosecond laser pulses propagating the ionizing medium, and discuss its subsequent influence on high harmonic spectrum. It is shown that the plasmas induce a positive frequency chirp on the leading edge of the laser pulse. Depending on the relative amount of the SPM-induced laser chirp, compared to the dynamic chirp, spectral broadening or narrowing can occur in high harmonic spectra [7].

For the generation of a proper harmonic spectrum required for specific applications, precise control of harmonic chirp is needed because the chirp can affect the spectral feature of generated harmonics. For instance, sharp and bright harmonic spectra are needed for X-ray spectroscopy or X-ray interferometry, for which harmonic chirp should be minimal. We observed two distinct regimes of driving laser intensity. At relatively low laser intensity the chirp of harmonics is dominated by dynamically induced negative chirp, but in a regime of high laser intensity the SPM-induced harmonic chirp may exceed the dynamically induced chirp [5]. Thus the effect of SPM-induced positive laser chirp on harmonic chirp is analyzed in the time-frequency domain, and we show that high harmonic generation can be coherently controlled using chirped femtosecond laser pulses.

We calculate the laser propagation along the propagation axis using a one-dimensional (1D) model and display the results using the time-frequency analysis. A distribution function in the time-frequency domain [11] is a powerful tool to analyze the chirp structure that cannot be revealed by a standard

Fourier analysis. Among several different kinds of time-frequency distributions, we employ the Wigner distribution function [12], defined as

$$W(t,\omega) = (1/\pi) \int E^*(t-t')E(t+t') \exp[-2i\omega t']dt' \, , \qquad (8.1)$$

where $E(t)$ is a time signal under inspection. One advantage of using the Wigner distribution function is its property that gives the exact time and frequency marginals. First, we examine the Wigner distribution function of the laser field after propagating through an ionizing medium to show the amount of the laser chirp induced by SPM. The time evolution of the laser field in the ionizing medium was obtained by numerically solving the one-dimensional (1D) wave equation,

$$\frac{\partial^2 E(x,t)}{\partial x^2} - \frac{1}{c}\frac{\partial^2 E(x,t)}{\partial t^2} = \frac{\omega_p^2(x,t)}{2c^2}E(x,t) \, , \qquad (8.2)$$

where $\omega_p(x,t) = \omega_0[N_e(x,t)/N_{cr}]^{1/2}$ is the local plasma frequency and ω_0 is the laser frequency. The critical plasma density N_{cr} is given in Gaussian units by $N_{cr} = m_e\omega_0^2/4\pi e^2$, where m_e is the electron mass and e is the electron charge. The electron density N_e is given by

$$N_e(x,t) = N_0 - N_0 \exp\left[-\int_{-\infty}^{t} w(x,t')dt'\right] \, , \qquad (8.3)$$

where N_0 is the initial gas density, and the ionization rate $w(x,t)$ is calculated from the Ammosov-Delone-Krainov model [13].

The propagation of 25-fs laser pulses through neon of density 2×10^{18} cm^{-3} is calculated. The time-frequency distributions of the laser pulses after propagation are displayed using the Wigner distribution. Figure 8.2 shows the results obtained with the laser intensities of 1×10^{15} W/cm^2 and 5×10^{15} W/cm^2. The dotted line connects the peak of the Wigner distribution for a given time. For the laser intensity of 1×10^{15} W/cm^2, the Wigner distribution of the laser pulse in Fig. 8.2a shows the chirp induced by SPM gas is not significant. At the higher laser intensity of 5×10^{15} W/cm^2, the SPM-induced laser chirp is significantly enhanced, and large positive chirp developed in the leading edge of the pulse is clearly seen in Fig. 8.2b. As the SPM-induced positive chirp of the laser pulse is transferred to the harmonic chirp, it should be properly taken into account in the analysis of chirp structure of high harmonics; the positive harmonic chirp due to the SPM effect may exceed the dynamically induced negative chirp.

Basic spectral features of high harmonics can be obtained from the HHG calculation of a single atom. Calculations of the time-dependent Schrödinger equation (TDSE) for a single atom may reveal the characteristic features of high harmonic generation, such as the plateau and cutoff in the high harmonic
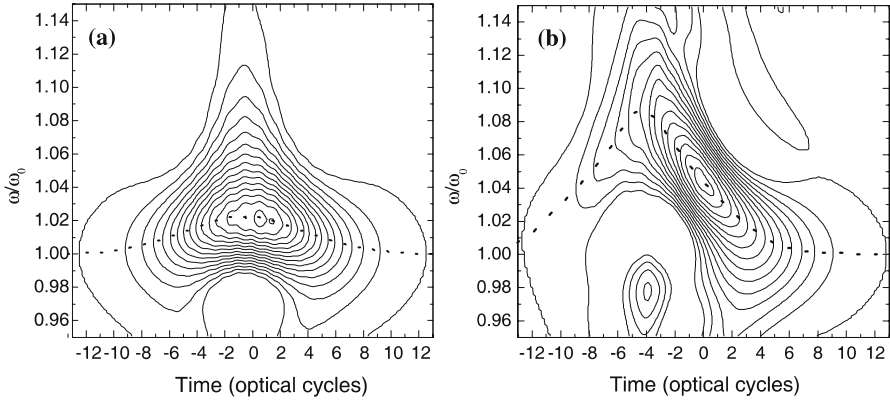
Fig. 8.2. Wigner distribution of the 25-fs, 825-nm laser pulse after propagating through a 0.7-mm long neon medium of density $2 \times 10^{18}\,\mathrm{cm}^{-3}$. The *dotted line* connects the peak points of the distribution at specific times. The laser intensity are **a** $I_0 = 1 \times 10^{15}\,\mathrm{W/cm}^2$, **b** $I_0 = 5 \times 10^{15}\,\mathrm{W/cm}^2$

spectra. However, they usually exhibit complicated harmonic structure in the plateau region when the pulse duration is reduced to a few tens of femtoseconds. The appearance of the intricate structure is due to the fact that many electron trajectories contributing to a given harmonic order cause the harmonic spectrum to split into several parts and as the width of the incident laser pulse decreases the split spectral lines begin to overlap and interfere with adjacent harmonic lines of different orders. To systematically investigate the high harmonics, in particular the location of harmonic components in the frequency domain, essentially required is thus the ability to differentiate the contributions from different trajectories. The dipole phase associated with each trajectory of an ionized electron has its own distinctive intensity dependence, and if dipole spectra at some different laser intensities are added, only the components corresponding to the trajectories whose dipole phases have less sensitive dependences on intensity will survive, while other components will be washed out due to destructive interference. This process usually occurs during the harmonic generation through a medium with finite length, over which laser intensity is slightly varying.

High harmonic generation in a medium is investigated using a 1-dimensional (1-D) propagation method [7]. The single-atom response is calculated by solving 1-D time-dependent Schrödinger equation. The propagation of harmonic field and laser pulse is considered to be along the propagation axis. In spite of its limitations, the 1-D model can provide a basic description on the chirp structure of harmonics. The HHG medium considered is a 0.7-mm long neon medium with density $2 \times 10^{18}\,\mathrm{W/cm}^2$. The Wigner distribution function of generated harmonics is used to see the spectral structure of harmonics in the time-frequency domain, which can be used to reveal the dependence of the harmonic chirp structure on the laser intensity and atomic species.

The Wigner distributions of harmonics obtained with laser intensity of 1×10^{15} W/cm^2 are shown in Fig. 8.3. In this case, the harmonics are negatively chirped at the leading edge of the chirp-free pulses as shown in Fig. 8.3a. So the positively chirped laser pulses can compensate for the negative harmonic chirp, as shown in Fig. 8.3b.

At the laser intensity of 5×10^{15} W/cm^2, the Wigner distribution of harmonics with chirp-free pulses became too complex to define frequencies at a given time as seen in Fig. 8.3c. This laser intensity is well above the OFI saturation intensity for neon. The laser pulse propagating through rapidly ionizing medium develops a large positive chirp due to the SPM at the beginning of the pulses as shown in Fig. 8.2b. In this case, negatively chirped pulses can compensate for the positive harmonic chirp. The complex spectral structure seen in the Wigner distribution becomes flattened in time with
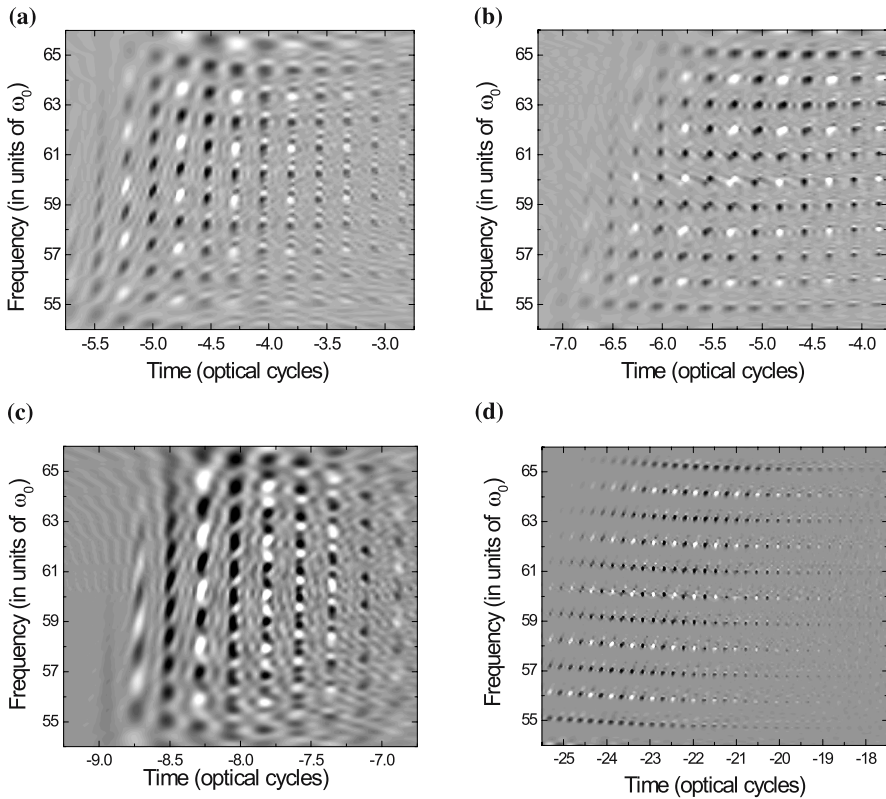
Fig. 8.3. Wigner distribution of harmonics after propagating through a 0.7-mm long neon medium of density 2×10^{18} cm^{-3}. Laser intensity applied is 5×10^{15} W/cm^2. The laser intensity and laser pulse duration used in four different cases are **a** 1×10^{15} W/cm^2, chirp-free 25 fs, **b** positively chirped 35 fs from **a**, **c** 5×10^{15} W/cm^2, chirp free 25 fs, and **d** negatively chirped 100 fs from **c**

a negatively chirped 100-fs pulse, as shown in Fig. 8.3d. These results clearly show that negatively chirped pulses must be applied to compensate for the harmonic chirp dominated by the SPM-induced positive chirp in the case of laser intensity well above the saturation intensity.

8.3 Characterization of Chirped Femtosecond Laser Pulses

For the experimental verification of harmonic chirp control, the temporal properties of chirped laser pulses need to be characterized. For harmonic generation experiments a chirped-pulse amplification (CPA) Ti:sapphire laser operating at 10-Hz repetition rate was employed as a driver. A long-wavelength injection method [14] was used to generate broad amplified spectrum, resulting in a bandwidth of 51 nm centered at 824 nm. The laser chirp was controlled by adjusting the separation of the grating pair in the pulse compressor [15] to observe the laser chirp effect on high harmonic generation. The pulse compressor of the CPA laser consists of two parallel gratings and a retro-reflector, and the zero grating detuning is set to the grating position that yields the shortest pulse duration. Grating positions with negative detuning correspond to positively chirped pulses, while those with positive detuning produce negatively chirped ones.

Temporal characterization of femtosecond laser pulses in terms of grating detuning is important for proper experimental control of harmonic generation. The intensity and phase profiles of chirped laser pulses were thus measured at various grating detuning using a single-shot second-harmonic generation frequency-resolved optical gating (FROG) technique. In order to minimize any artifacts in measurement we placed the FROG setup inside a vacuum chamber connected with the vacuum pulse compressor. The shortest pulse duration measured was 26 fs, while the transform-limited pulse duration, obtained from the inverse Fourier transform of the measured spectrum, is 24 fs.

The temporal characteristics of chirped laser pulses can be quantitatively analyzed in terms of linear chirp coefficient and pulse duration. The linear chirp coefficient, α, is defined as the second derivative of the temporal phase at time zero with minus sign, i.e., $-\mathrm{d}^2\phi/\mathrm{d}t^2\big|_{t=0}$, corresponding to the frequency variation in time at the pulse peak. The measured linear chirp coefficient versus the grating detuning is shown as squares in Fig. 8.4a, wherein the grating detuning, δZ, is scanned from $-350\,\mu\mathrm{m}$ to $350\,\mu\mathrm{m}$. The FROG measurement showed that the pulse shape at the zero detuning was nearly Gaussian. In the case of a Gaussian pulse, the linear chirp coefficient with regard to the grating detuning is given by

$$\alpha(\delta Z) = \frac{[(4\ln 2)^2 \cdot \beta(\delta Z)]}{T_0^4 + [4\ln 2 \cdot \beta(\delta Z)]^2} \,, \tag{8.4}$$
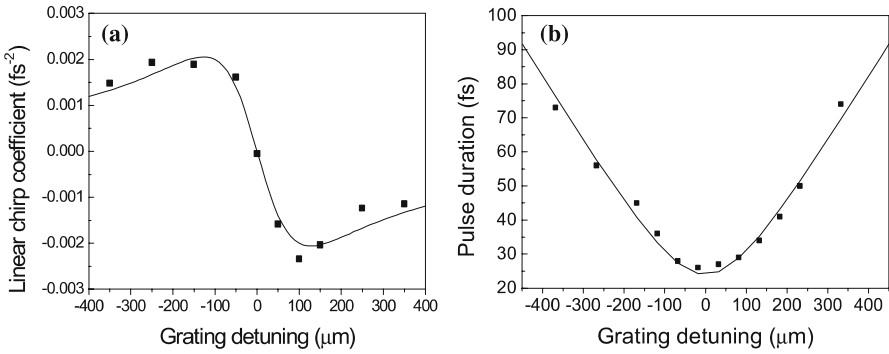
Fig. 8.4. a Linear chirp coefficient and **b** pulse duration of chirped laser pulses with respect to the grating detuning of a pulse compressor

where $\beta(\delta Z)$ is the group-delay dispersion (GDD) and T_0 is the transform-limited pulse duration. The fitting curve given by (8.4) with $T_0 = 24\,\text{fs}$ and $\beta = -1.7 \times \delta Z$ (fs^2) showed good agreement with the measured one as represented by a solid line and filled squares, respectively, in Fig. 8.4a. At first the linear chirp coefficient, the chirp parameter in time domain, increases with grating detuning and then it decreases, while GDD, chirp parameter in frequency domain, decreases linearly with grating detuning.

The pulse duration versus the grating detuning is shown as squares in Fig. 8.4b. The pulse duration with regard to the grating detuning for a Gaussian pulse may be written as

$$T_{\mathrm{p}}(\delta Z) = T_0 \sqrt{1 + \frac{[4\ln 2 \cdot \beta(\delta Z)]^2}{T_0^4}} \ . \qquad (8.5)$$

The fitting curve given by (8.5) well matches the measured one as represented by a solid line and the filled squares, respectively, in Fig. 8.4b. Figure 8.4a and b shows that the linear chirp rapidly varies around the zero detuning, whereas the pulse duration does not. Consequently, the laser chirp effect on the spectral structure of generated harmonics around zero detuning can appear more sensitively than that at larger grating detuning.

8.4 Strong Harmonic Generation Using Self-Guided Laser Pulses

For practical applications of harmonic light sources to interferometry and ultrafast spectroscopy, the generation of bright high harmonics is very essential [16–18]. Strong high harmonic generation requires the application of intense femtosecond laser pulse to a high-density gas medium that is partially ionized during the harmonic generation process. The ionized gas medium,

with higher electron density in the center than in the outer region, acts as a negative lens, leading to defocusing of the laser beam in a plasma and hence to a reduction in the effective harmonic generation volume [19]. In addition, the rapidly ionizing high-density gas medium modifies the temporal structure of the femtosecond laser pulse due to SPM that induces a positive chirp in the leading edge of the laser pulse [7]. Consequently, we have to optimize the harmonic generation conditions in both space and time domains in order to maximize the harmonic generation volume and to generate spectrally sharp harmonics, respectively. In this section we investigate the propagation condition of intense femtosecond laser pulses through a long gas medium and search for the conditions of guided propagation to maximize effective harmonic generation volume, realizing strong harmonic generation.

Spatial and temporal characteristics of a laser pulse propagating through an ionizing gas medium can be affected by the refractive index modulation that may vary in time and space. In the space domain, a Gaussian beam (or any peaked laser beam) produces a higher electron concentration in its central part than in the outer region, which results in the defocusing of the laser field [19]. On the other hand, the refractive index modulation induced by a variation of electron density in time induces SPM of the laser pulse [7]. Since these two effects can substantially modify the pulse characteristics, control of the ionization effects is an important issue in the investigation of the interactions between atoms and intense femtosecond laser pulses, such as high harmonics, self-channeling in air, and laser-assisted particle acceleration.

To investigate the laser pulse propagation in an ionizing medium, we performed three-dimensional (3-D) simulations of laser pulse propagation [9]. In an ionizing medium, the pulse propagation is affected by diffraction, refraction, nonlinear self-focusing, ionization, and plasma defocusing. The pulse evolutions in such media are described by the wave equation which can be written as

$$\nabla^2 E_1(r,z,t) - \frac{1}{c^2}\frac{\partial^2 E_1(r,z,t)}{\partial t^2} = \frac{\omega^2}{c^2}\left(1 - \eta_{\mathrm{eff}}^2\right) E_1(r,z,t) , \qquad (8.6)$$

where $E_1(r,z,t)$ is the transverse electric field of the laser with frequency ω. Since radial symmetry is assumed, cylindrical coordinates are used throughout the simulation. The effective refractive index of the medium can be written as $\eta_{\mathrm{eff}}(r,z,t) = \eta_0 + \eta_2 I(r,z,t) - \omega_{\mathrm{p}}^2(r,z,t)/2\omega^2$. The first linear term $\eta_0 = 1 + \delta_1 + i\beta_2$ accounts for the refraction (δ_1) and absorption (β_1), while the second term describes a $\chi^{(3)}$ process depending on laser intensity, which is well known as the optical Kerr effect. Finally, the third term reflects the generated electron effects on laser pulse propagation, which contains the plasma frequency $\omega_{\mathrm{p}} = (4\pi e^2 n_{\mathrm{e}}/m)^{1/2}$ and accounts for the presence of a density of electrons per unit volume. m and e are mass and charge of electron, respectively.

The spatial and temporal modifications of the laser profile during propagation are calculated for the case of a negatively chirped 42-fs pulse with 5-mJ energy. The gas medium is a 9-mm Ne gas jet with a density of 1.4×10^{18} cm^{-3}.

The reason for using a negatively chirped pulse is to control the SPM effect and will be discussed later in detail. Truncated Gaussian pulses, focused in a geometry of $f/85$, are used in the calculation to closely follow actual experimental conditions. The gas jet position is defined as $z = 0$, when the center of the gas jet is positioned at the laser focus. Figure 8.5 shows the evolution of laser beam profiles at the time of pulse peak along the laser propagation at the two gas jet positions of $z = 0$ and -18 mm. The negative sign means that the gas jet is located before the laser focus. In the case of $z = 0$ (Fig. 8.5a), the laser beam spreads quickly due to plasma defocusing. After the propagation, the laser intensity decreases to 3×10^{14} W/cm^2, while the initial intensity is more than 1×10^{15} W/cm^2. However, when the gas medium is placed 18mm before the laser focus, the laser beam forms a flattened profile with slightly reduced peak intensity.

The profile flattening and guiding of the laser pulse, when the gas jet is placed before the laser focus, arises due to the balance between plasma
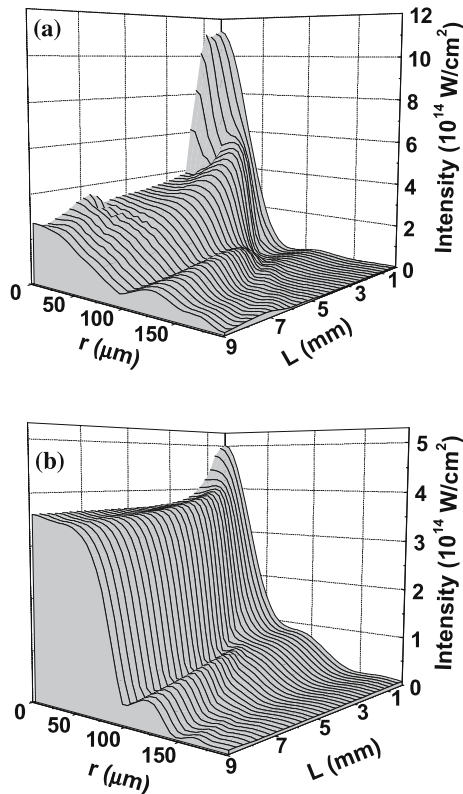
Fig. 8.5. Evolution of the laser beam profile in an ionizing medium calculated by 3D simulation. L is the propagation distance measured from the entrance plane of a 9-mm gas jet. The gas jet positions are **a** $z = 0$ and **b** $z = -18$ mm

defocusing and the convergence of the focused laser beam. When the gas jet is positioned before the laser focus, the central part of laser beam is refracted outward by the electron density gradient, while the less affected outer part continues to converge. This behavior of the laser pulse in the ionizing medium creates the flattened profile. After the formation of the flattened profile, the electron density is also flattened in the same region but rapidly drops at the boundary. This rapid change of the electron density results in a sharp refractive index change at the boundary and, thereby, a wave-guide structure is formed. Therefore, the profile flattening and self-guiding of laser pulses can be achieved by choosing a proper gas jet position [8].

To experimentally confirm the self-guided propagation and profile flattening of laser pulses, we captured visible plasma images along the propagation direction and radial profiles of the laser beam at the exit of the medium using charge-coupled device (CCD) detectors. The visible plasma images were captured from a transverse direction and the laser beam profile at the end of medium was obtained by imaging it on a CCD. The same conditions as those for the 3-D calculations were used in the experiments. The visible plasma image changed drastically with gas jet positions. At the gas jet position of $z = 0$ (Fig. 8.6a), the plasma image was bright only for the first 2-mm section of the medium. It is in good agreement with the 3-D calculation which showed the rapid decrease of laser intensity in the first 2 mm due to plasma defocusing. As the gas jet position moved away from the laser focus, the bright part of plasma image was extended and a nearly uniform plasma image over the entire gas jet was formed at $z = -18$ mm. This also matched the 3-D calculation result very well, which shows that self-guiding occurs for $z = -18$ mm, as shown in Fig. 8.5b.

The laser beam profile at the end of the medium can be direct evidence of the profile flattening. Figure 8.6b and c shows the laser profiles at the gas jet positions $z = 0$ and $z = -18$ mm. At $z = 0$, the laser profile was severely distorted and weakened after the propagation. On the other hand, at $z = -18$ mm, the laser beam formed a flattened profile with a radius of 60 μm, which closely matched the 3-D calculation. It is thus clear that a proper selection of the gas jet position is critical for the profile flattening and self-guiding of laser pulses.

We then investigated the spectral characteristics of high harmonics in the wavelength range of 120–180 Å. The harmonics generated from a long Ne gas jet were detected by a flat-field soft X-ray spectrometer [20] equipped with a back-illumination X-ray CCD with 400×1340 pixels (Princeton Instruments). Two Zr filters with a total thickness of 400 nm were installed in front of the CCD to block scattered laser light. Since the self-guiding condition of the laser pulse strongly depended on the gas jet position, the harmonic generation was also dramatically affected. We observed dramatic increase of harmonic signal as the gas jet was placed before the laser focus, as shown in Fig. 8.7. The 61st harmonic at 134 Å was the strongest among observed harmonics and at the gas jet position of $z = -18$ mm its spectral brightness

(a)

(z=0)

(z=-18 mm)

L (mm)

(b)

(c)
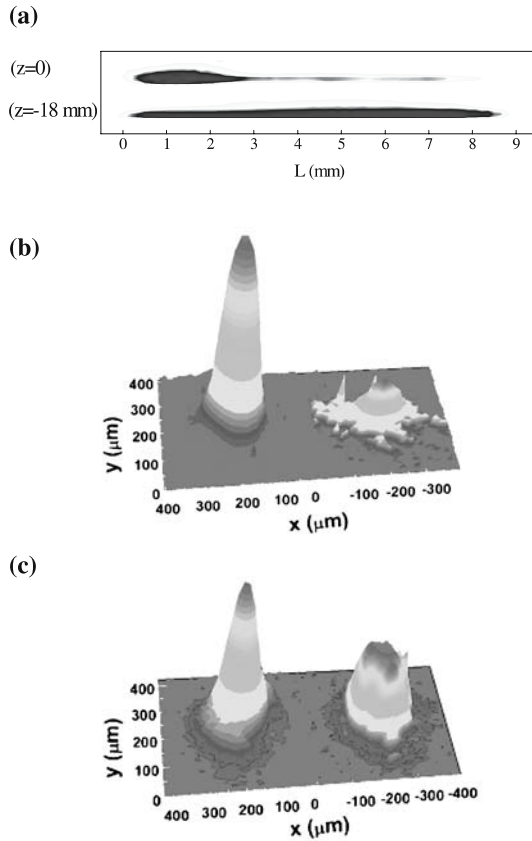
Fig. 8.6. a Visible images of Ne plasma obtained at two gas jet positions $z = 0$ and $z = -18$ mm. Laser beam profiles at the entrance (*left*) and exit (*right*) of the gas jet for the cases of **b** $z = 0$ and **c** $z = -18$ mm

was two orders of magnitude larger than that obtained at $z = 0$. At the optimum condition, the 61st harmonic was strong enough to saturate the X-ray CCD in a single shot of 5-mJ laser pulse. The beam divergence of the harmonics was measured by installing a cylindrical mirror in the soft X-ray spectrometer, instead of a toroidal mirror. The measured divergence of the 61st harmonic was 0.5 mrad (FWHM).

The self-guiding and profile flattening can provide a good phase matching between generated harmonics and a driving laser pulse. After the attainment of self-guided laser propagation, the geometric phase and the atomic phase do not affect the phase matching condition due to the collimated propagation and uniform intensity distribution of driving laser pulses. In this case the dispersion, contributed mainly by the neutral atoms and free electrons, determines the phase matching condition. The peak laser intensity estimated from the spatial profile shown in about Fig. 8.6 is 6×10^{14} W/cm^2. The
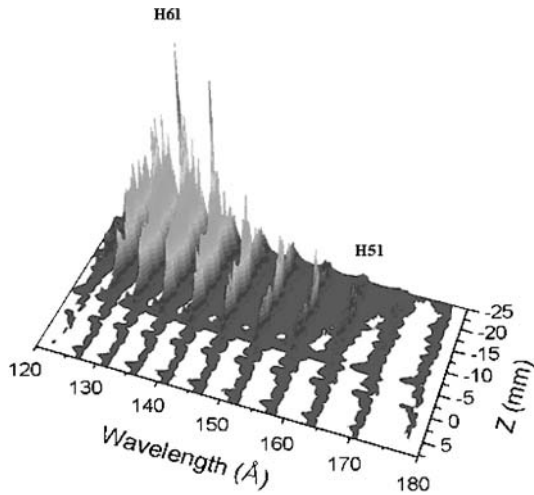
Fig. 8.7. Generation of bright harmonics from Ne by adjusting the target position along the laser propagation direction. Bright harmonics were obtained around the 61st order by placing the target at 18 mm before the laser focus. 'Hn' denotes the harmonic of order n

61st harmonic satisfies the phase-matching conditions at the ionization level of about 1%. The 3D simulation showed that this ionization level occurred at the leading edge of the laser pulse after the profile flattening was developed. The profile flattening automatically overcomes the problems associated with the variation of phase matching conditions along the radial direction, leading to a larger effective volume for harmonic generation. As the gas density and length corresponds to six times the absorption length in Ne, the generated harmonics are limited by the absorption in Ne. Consequently, the self-guiding and profile flattening provided an ideal condition for well phase-matched strong harmonic generation in a large volume. In addition, the use of profile-flattened laser pulses can be beneficial in resolving the spatial chirp problem [21] for the attosecond pulse generation because of the flattened laser intensity profile.

8.5 Chirp Control of High Harmonic Generation Performed with Self-Guided Laser Pulses

The self-guiding and profile-flattening of the laser pulses led to the maximization of effective harmonic generation volume, optimizing HHG in space. As intense laser pulses can acquire a positive chirp in the leading edge due to SPM in an ionizing medium, generated harmonics may inherit the laser chirp induced by SPM. When the harmonics are mainly generated in the leading edge, two different harmonic chirps, i.e., dynamically induced negative chirp

and SPM-induced positive chirp, compete and affect the spectral structure of high harmonics. Since chirped laser pulses can either compensate or enhance the harmonic chirp, the spectral structure of harmonics can be controlled by applying appropriately chirped laser pulses. Consequently, the spectral structure of high harmonics in the long gas jet needs to be inspected with regard to initial laser chirp, being an optimization process of harmonic generation in time.

The control of harmonic spectral structure by the adjustment of initial laser chirp was experimentally investigated after the self-guiding and profile-flattening conditions were formed. Even though the arrangement of the gas jet at 18 mm before the laser focus optimized the harmonic generation in the space domain, the harmonic spectrum can be broadened by the frequency chirp of harmonics. Figure 8.8 shows the chirp dependence of harmonic spectra with the Ne gas jet at $z = -18$ mm. The laser chirp was controlled by changing the grating separation in the pulse compressor while keeping the laser energy fixed. The negatively chirped 42-fs pulse generated the sharpest and brightest harmonics while the positively chirped 41-fs pulse produced a quasi-continuous harmonic spectrum. The laser propagation conditions did not depend sensitively on the sign of the laser chirp. The 3D simulation shows that the guided laser intensity was slightly higher in the case of the chirp-free 27-fs pulse than that in the case of negative 42-fs pulse. In the case of a rapidly ionizing high-density medium, the harmonic chirp is dominated by the SPM-induced positive chirp in the leading edge of the laser pulse [7]. As a result, a negatively chirped laser pulse can compensate the SPM-induced positive chirp and generate sharp and bright harmonics. With the negatively chirped 42-fs pulse, the bandwidth of the 61st harmonic was 0.7 Å and the spectral brightness was enhanced four times over that obtained from a chirp-free 27-fs pulse.
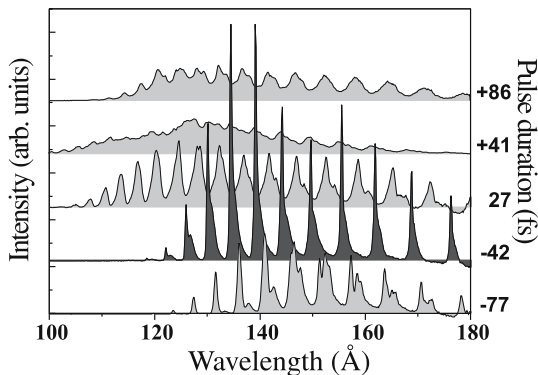
Fig. 8.8. Harmonic spectra from Ne driven by femtosecond laser pulses with different laser chirp at the gas jet position of $z = -18$ mm. The sign of the pulse duration refers to the sign of applied laser chirp

For detailed understanding of the spectral structure of harmonics observed in the experiments, a systematic analysis is performed through extensive numerical modeling. In order to look into the temporal behavior of harmonic generation by very short laser pulses, our approach uses a nonadiabatic 3-D model [9] for the propagation of both the driving field as well as the harmonic field. The results of our modeling are in good agreement with the experimental results and thus enable us to explain the observed features and to reveal the underlying physics. The spatial, spectral, and temporal modifications suffered by the laser pulse are used to explain observed harmonic characteristics. Furthermore, the phase matching between the laser pulse and generated harmonics also plays a role by selecting particular trajectories that survive and contribute to the final harmonic field.

The SPM effects on pulse propagation are analyzed using a time-frequency analysis based on the spectrogram method [11]. The temporal evolution of a laser field on axis is calculated by 3-D simulations with same parameters as used in Fig. 8.5b. Figure 8.9 shows the change of laser chirp structure during the pulse propagation. The solid circles show the contour of the spectrogram and the dotted lines indicate the mean frequency at a given time. It clearly shows the temporal modification of laser chirp structure caused by SPM. After 1-mm propagation, the initial negative chirp is modified by the SPM and laser pulses become nearly chirp-free in the leading edge, as shown in Fig. 8.9b. The positive chirp developed in the leading edge of the laser pulse increases with the propagation length and it overcomes the initial negative chirp after 4-mm propagation.

By controlling initial laser chirp the harmonic chirp can be managed. Since high harmonics are generated coherently by a driving field, the modulation of laser pulse due to the SPM of laser pulse during propagation directly affects the spectral structure of the harmonics. To generate sharp and bright harmonics, the initial chirp of laser pulses can be appropriately selected. In the case of chirp-free or positively chirped laser pulse, SPM-induced positive chirp in the leading edge of the laser pulse can be severe enough to broaden generated harmonic spectrum as the phase-matched harmonics are mainly generated in the leading edge. When we use negatively chirped pulses, the induced positive chirp in the leading edge can be reduced and matched dynamically induced negative chirp of harmonics, which results in sharp and bright harmonics.

In order to gain a realistic picture of the HHG process in the long gas jet by self-guided pulses, a series of simulations are carried out with laser chirp and energy as the main scan parameters. From the large amount of data obtained we focus our discussion on two specific cases, namely modeling HHG for positively chirped (PC) or negatively chirped (NC) 42-fs Gaussian pulses of same energy, all other conditions being those specified in Fig. 8.5b. The absolute value of the chirp is $8 \times 10^{-4}\,\text{fs}^{-2}$ for the two pulses, taken from experiments. The gas jet position is $z = -18\,\text{mm}$. The measured spectra, corresponding to these two cases are shown in Fig. 8.8. As is shown, the NC
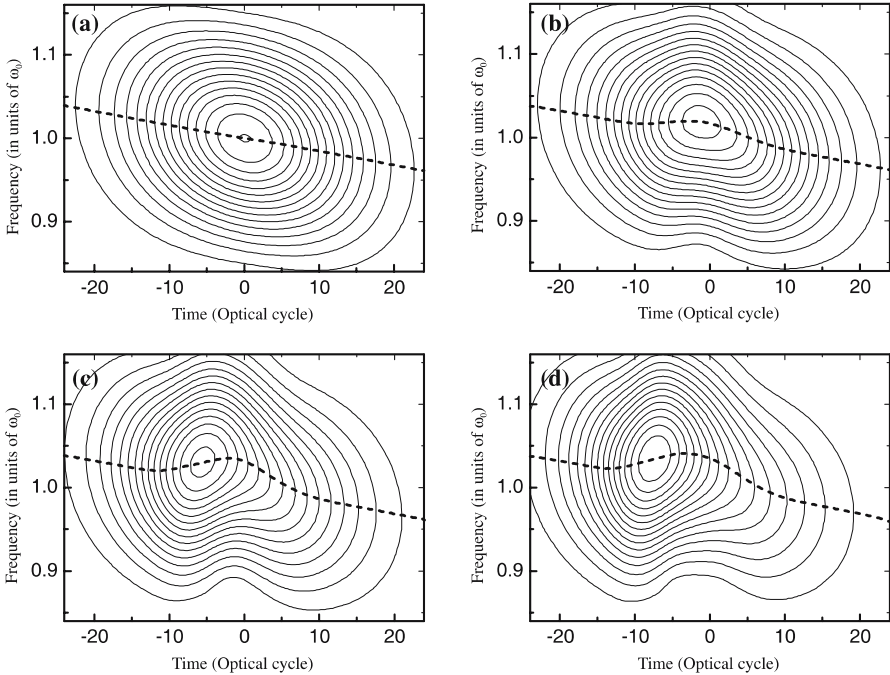
Fig. 8.9. Spectrograms of a laser pulse propagating through a 9-mm Ne medium with propagation length of **a** $L = 0$, **b** $L = 1\,\mathrm{mm}$, **c** $L = 4\,\mathrm{mm}$, and **d** $L = 9\,\mathrm{mm}$

42-fs pulse generates sharp and strong radiation around the 61st harmonic (H61), while the PC 41-fs pulses produces a quasi-continuous harmonic spectrum. Once the solution $E_1(r; z; t)$ for the propagating laser electric field is obtained, the single atom source, calculated at every grid point of the interaction region, is used to solve the propagation equation, (8.2), for the harmonic field. The solution, $E_h(r; z; \omega)$, allows a detailed characterization of the HHG mechanism, both in space and in time. In the following we analyze the harmonic field generated by PC and NC pulses which have the same spatial configuration of the driving field but opposite initial chirp values.

Solving the wave equation for the harmonic field, we obtain the harmonic field $E_h(r; z)$, calculated at every grid point over the interaction region. Shown in Fig. 8.10 are the time-frequency distributions of E_h at $z = 9\,\mathrm{mm}$ and $r = 0$, for PC a) and NC (b) cases respectively. We can see that the harmonic field, shown in the gray scale obtained after the propagation, and dipole distributions, shown as contour plots representing the single atom response at that position, do not completely overlap. In the NC case the cutoff trajectory component coincides with the portion of strong harmonic field. This beautifully shows the selection of specific trajectories as a result of harmonic field propagation. Some trajectories are enhanced even at low intensity dipole radiation, other trajectories, although strongly present in single atom response,
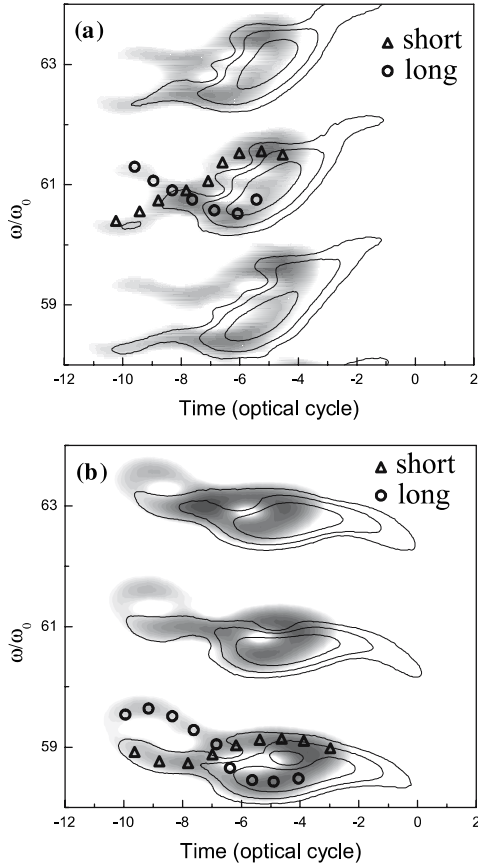
Fig. 8.10. Spectrograms of the atomic dipole (logarithmic scale, *white*:*gray* = 1:0) and harmonic field (contour plot, logarithmic scale 1:10) at $r = 0$ and $z = 9\,\mathrm{mm}$, as generated by the PC (**a**) and NC (**b**) pulses

does not survive in the propagation. Both fields have maximum intensity distributed mainly at the confluence between the long and the short trajectories, around $t = -4$ for NC and $t = -5$ for PC pulse. We note that the maximum H61 field is born at low intensity dipole radiation, at the minimum necessary laser intensity to generate the single dipole for H61; this clearly indicates that the strong harmonic generation is contributed from harmonics in the cut-off regime.

It is well known that for a harmonic in the plateau there are (within one optical cycle) two trajectories which yield the same kinetic energy, therefore contribute to the same harmonic. With increasing harmonic order, thus approaching the cut-off, the two trajectories become closer and, for the maximum achievable kinetic energy, they coincide. As shown in [22], the two trajectories do not contribute equally to the total emission; moreover, there

are more trajectories recombining after more than one optical cycle (with larger excursion times). These trajectories are not included in our modeling, as the integration time for the dipole moment was only 1.2 optical cycles. This is reasonable because the harmonics in study are very close to the cut-off.

Bearing in mind the above consideration we can now analyze the data in Fig. 8.10. One can see that the final harmonic field is built-up from the contributions of both short and long trajectories. However, in the NC case, the harmonic field builds-up mainly on the short trajectory component of the single atom response, despite the fact that SFA tends to overestimate [22] the long trajectory contribution. This results in a frequency profile even narrower than that of the corresponding single dipole. The emission spans in time over 10 optical cycles, but in a narrow frequency range, which gives a high spectral brightness. In the case of PC pulse, harmonics are also built from both short and long trajectories; however, the final field spans over two harmonic orders in frequency, which means overlapping between two adjacent orders, in full agreement with the experimental findings [8]. Consequently, the analysis of the harmonic field after propagation provides a detailed view in the temporal behavior of harmonic generation processes.

The analysis of the spatial distribution of high harmonics can provide detailed information on the spatial behavior of harmonics. The differences between the harmonic fields generated with PC and NC pulses of 42 fs can be seen in Fig. 8.11, where we have plotted the near field of the harmonics around H61 as a function of frequency and radial coordinate. The PC case (upper panel in Fig. 8.11) shows a diffuse spectral profile near the axis and a sharper one between $40\,\mu$m and $70\,\mu$m. On the contrary, the NC pulse produces a clean spectral profile in the compact central region extending up to about $40\,\mu$m. The present result demonstrates an optimization of the generation volume for our specific conditions of initial laser chirp.

The spectral features of the single atom response directly reflect those of the driving field distorted during propagation through a rapidly ionizing medium. For PC pulses, the resultant chirp of the driving field overcompensates the harmonic intrinsic chirp for $r \leq 30$–$40\,\mu$m and induces a broad dipole response that is also positively chirped. For larger r its chirp and spectral width of the single atom emission are reduced because the laser chirp decreases and can balance the dynamically induced harmonic chirp. For the conditions considered here this happens for $r > 40\,\mu$m, which explains the off-axis formation of a spectrally well-defined harmonic field. On the other hand, the NC pulses have, during dipole emission, a smaller resultant positive chirp that can balance the intrinsic harmonic chirp. This balance is maintained well in the central part of the self-guided region because of the small radial variation of the SPM, which provides the condition for homogeneous harmonic emission in the central region.

The behavior of harmonics generated by PC pulse has different spatial characteristics from that by NC pulse. For the case of PC pulse in Fig. 8.11, spectrally sharp field is generated around $40\,\mu$m s, though on-axis harmonic
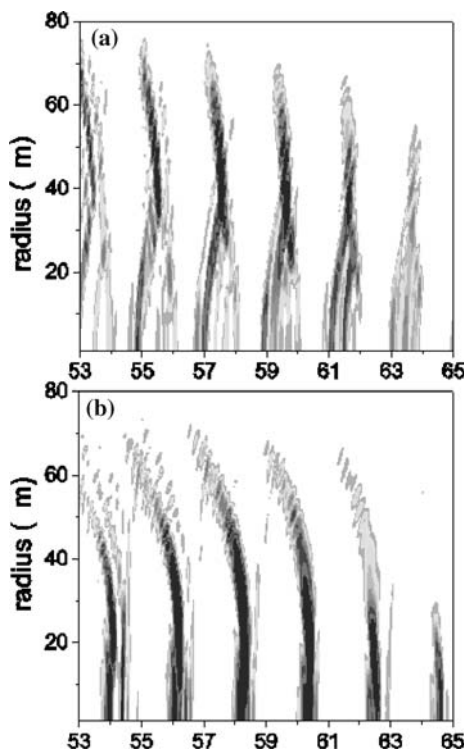
Fig. 8.11. Radial and frequency dependence of the harmonic field intensity at $z = 9$ mm, for 5-mJ **a** PC and **b** NC 42-fs pulses. Logarithmic scale, arbitrary units

field is broad. This indicates that the spectra generated in the far field could contain also well defined harmonic peaks. To clarify this point we also calculated the beam divergence of the harmonics at the exit of the interaction region, i.e.: at $z = 9$ mm. This was done by taking advantage of the fact that the final solution for the propagation equation is obtained in the spectral domain, which allows the calculation of the phase derivatives (wavevectors) both in radial $k_r = \partial\phi/\partial r$ and in axial $k_z = \partial\phi/\partial z$ directions. Therefore the component $E_h(\omega)$ of the field makes an angle α with the z axis, where $\tan(\alpha) = k_r/(k_z + \omega/c)$. The full emission angle (2α) calculated in this way is given in Fig. 8.12, for the harmonics plotted in Fig. 8.11. As one can see, on axis and for small radii, both PC and NC cases develops highly collimated harmonics, with a total divergence less than 0.5 mrad. This favors the NC case, as it allows the propagation of sharp harmonics near the axis with small divergence. For the PC case the spectrally broad field near the axis can propagate with low divergence, but spectrally well-defined harmonics at off axis propagate with large divergence, generating only weak signal. This is consistent with the experimentally observed harmonic spectrum of the PC laser pulse shown in Fig. 8.8.
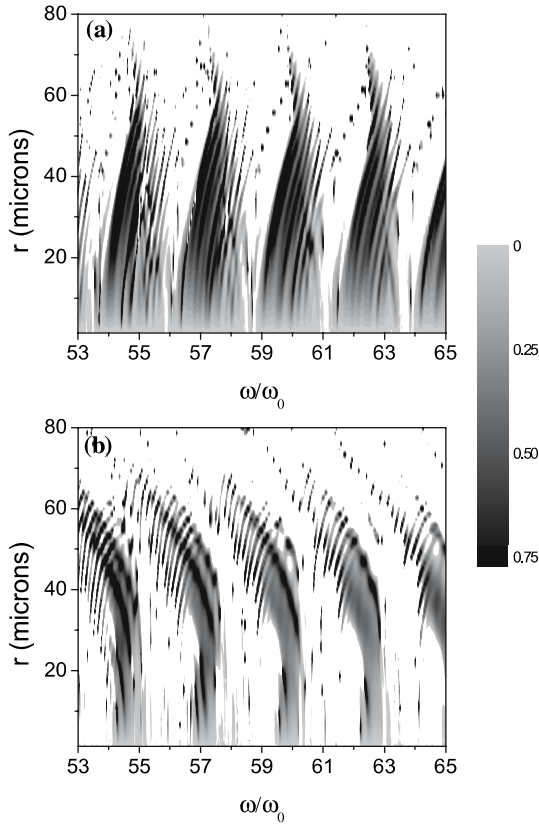
Fig. 8.12. Radial and frequency dependence of the harmonic field divergence (full angle) at $z = 9\,\mathrm{mm}$, for **a** PC and **b** NC 42-fs pulses. Linear scale from 0 to 0.75

The harmonic beam divergence at different laser chirp was calculated and compared with experimental measurements. From the far field profiles we measured the divergence of H61 for different chirp condition of the laser pulse, all other parameters being maintained constant and specified in Fig. 8.5b. The measured lowest beam divergence, 0.5 mrad, of the 61st harmonic was obtained in the case of 42-fs NC pulse, presented in Fig. 8.13 that shows the far field profile of harmonics captured on a back-illumination x-ray CCD. We note that this minimum divergence condition corresponds to that of the maximum harmonic brightness as a consequence of profile flattening and chirp compensation mechanism. From the modeling, a theoretical value of the H61 divergence was also obtained as a weighted average of the divergence angle presented in Fig. 8.12, within the frequency range of H61. The weighting factors are taken from the corresponding H61 intensities plotted in Fig. 8.11. The data on H61 divergence, presented in Fig. 8.14, clearly shows good agreement between the calculated and measured harmonic divergence. The good
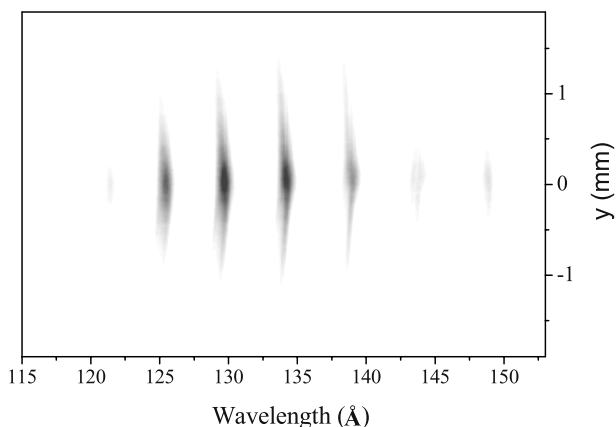
Fig. 8.13. Far field pattern of strong harmonics from 9-mm Ne gas jet measured at a distance of 1.2 m
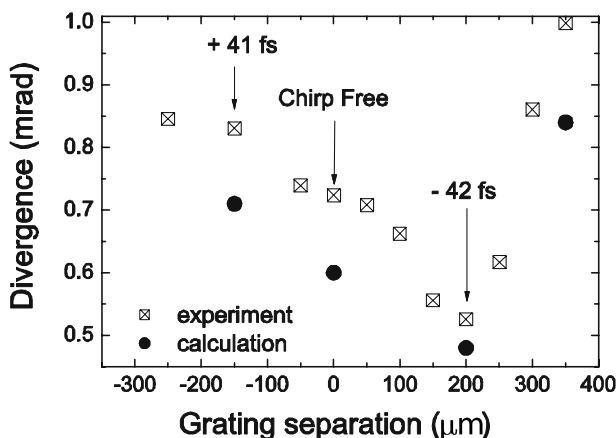
Fig. 8.14. Divergence measurement of H61 with respect to the grating separation obtained at the conditions of self-guided laser propagation

agreement between the calculated and observed harmonic divergences thus supports the current 3D calculation of laser propagation and high harmonic generation and propagation. Consequently, the experimental and simulation results show well the characteristics of the spectrally sharp, strong harmonics with low beam divergence and the underlying physics.

8.6 Conclusion

Experiments on bright harmonic generation using a long neon gas jet have been pursued and theoretical analysis has provided physical insights of de-

tailed harmonic generation processes. We found that the plasma defocusing effect severely limited the effective interaction length of harmonic generation and a proper selection of target position resulted in the self-guiding of profile-flattened laser pulse, and the laser chirp control led to the generation of bright harmonics with low beam divergence. The optimization in both space and time domains maximized the harmonic generation volume by inducing a profile-flattened, self-guided propagation of intense laser pulses, and allowed the generation of spectrally sharp harmonics by appropriately selecting initial laser chirp. The optimization of the harmonic emission volume was attained by placing the long gas jet about one Rayleigh length before the focus, while the brightness maximization was obtained by applying negatively chirped pulse. As a result, we have achieved the simultaneous optimization of bright harmonic generation in space and time using the self-guided and chirped femtosecond laser pulses. By the combination of self-guiding and laser chirp control, we generated bright 61st harmonic at 13 nm from a 9-mm Ne gas jet with narrow spectral bandwidth. Since high-reflectivity Mo:Si mirrors are available at this wavelength, this method can be applied to coherent EUV source development for at-wavelength EUV metrology [23].

References

1. D.G. Lee, J.J. Park, J.H. Sung, and C.H. Nam: Opt. Lett. **28**, 480 (2003).
2. R.A. Bartels, A. Paul, H. Green, H.C. Kapteyn, M.M. Murnane, S. Backus, I.P. Christov, Y. Liu, D. Attwood, and C. Jacobson: Science **297**, 376 (2002).
3. Y. Mairesse, A. de Bohan, L.J. Frasinski, H. Merdji, L.C. Dinu, P. Monchicourt, P. Breger, M. Kovaev, R. Taïeb, B. Carré, H.G. Muller, P. Agostini, P. Salières: Science **302**, 1540 (2003).
4. H.T. Kim, D.G. Lee, K.-H. Hong, J.-H. Kim, I.W. Choi, and C.H. Nam: Phys. Rev. A **67**, 051801 (R) (2003); H.J. Shin, D.G. Lee, K.-H. Hong, and C.H. Nam: Phys. Rev. Lett. **83**, 2544 (1999).
5. D.G. Lee, J.-H. Kim, K.-H. Hong, and C.H. Nam: Phys. Rev. Lett. **87**, 243902 (2001); H.T. Kim, I.J. Kim, K.-H. Hong, D.G. Lee, J.-H. Kim, and C.H. Nam: J. Phys. B: At. Mol. Opt. Phys. **37**, 1141 (2004).
6. Z. Chang, A. Rundquist, H. Wang, I. Christov, H.C. Kapteyn, and M.M. Murnane: Phys. Rev. A **58**, 30 (R) (1998).
7. J.-H. Kim and C.H. Nam: Phys. Rev. A **65**, 033801 (2002).
8. H.T. Kim, I.J. Kim, D.G. Lee, K.-H. Hong, Y.S. Lee, V. Tosa, and C.H. Nam: Phys. Rev. A **69**, 031805 (R) (2004).
9. V. Tosa, H.T. Kim, I.J. Kim, and C.H. Nam: Phys. Rev. A **71**, 063807 (2005).
10. V. Tosa, H.T. Kim, I.J. Kim, and C.H. Nam: Phys. Rev. A **71**, 063808 (2005).
11. L. Cohen: Proc. IEEE **77**, 941 (1989).
12. J.-H. Kim, D.G. Lee, H.J. Shin, and C.H. Nam: Phys. Rev. A **63**, 063403 (2001).

13. M.V. Ammosov, N.B. Delone, and V.P. Krainov: Sov. Phys. JEPT **64**, 1191 (1986).
14. Y.H. Cha, Y.I. Kang, and C.H. Nam: J. Opt. Soc. Am. B **16**, 1220 (1999).
15. K.-H. Hong, J.-H. Kim, Y.H. Kang, and C.H. Nam: Appl. Phys. B **74**, S231 (2002).
16. D.G. Lee, H.T. Kim, K.-H. Hong, and C.H. Nam: Appl. Phys. Lett. **81**, 3726 (2002).
17. I.J. Kim, C.M. Kim, H.T. Kim, G.H. Lee, Y.S. Lee, J.Y. Park, D.J. Cho, and C.H. Nam: Phys. Rev. Lett. **94**, 243901 (2005).
18. H.T. Kim, I.J. Kim, V. Tosa, Y.S. Lee, and C.H. Nam: Appl. Phys. B **78**, 863 (2004).
19. M. Bellini, C. Corsi, and M.C. Gambino: Phys. Rev. A **64**, 023411 (2001).
20. I.W. Choi, J.U. Lee, and C.H. Nam: Appl. Optics. **36**, 1457 (1997).
21. M.B. Gaarde and K.J. Schafer: Phys. Rev. Lett. **89**, 213901 (2002).
22. M.B. Gaarde and K.J. Schafer: Phys. Rev. A **65**, 031406 (R) (2002).
23. H.T. Kim, I.J. Kim, V. Tosa, C.M. Kim, J.J. Park, Y.S. Lee, A. Bartnik, H. Fiedorowicz, and C.H. Nam: IEEE Sel. Top. Quant. **10**, 1329 (2004).

9 Focusing Intense High-Order Harmonics to a Micron Spot Size

Akira Suda[1], Hiroki Mashiko[1,2], and Katsumi Midorikawa[1]

[1] RIKEN, 2-1 Hirosawa, Wako-shi, Saitama 351-0198, Japan
   e-mail: asuda@riken.jp
[2] Graduate School of Science and Engineering, Saitama University, 255 Okubo, Saitama-shi, Saitama 338-8570, Japan

Summary. The focusability of intense coherent radiation generated by high-order harmonic conversion is investigated. A variety of focusing mirrors are tested and used in the focusing experiments. We demonstrate the focusing of an extreme-ultraviolet/soft X-ray beam to a $1\,\mu m$ spot size with a peak intensity as high as $1 \times 10^{14}\,W/cm^2$, which is sufficient to stimulate nonlinear optical phenomena in the short wavelength region.

9.1 Introduction

The high-order harmonics of intense laser pulses are high-brightness coherent light sources in the extreme-ultraviolet (XUV) and soft X-ray (SXR) wavelength regions. These coherent sources of radiation have excellent spatial and spectral qualities together with wavelength tunability over a wide range of the spectrum [1–3]. The energy-scaling of high-order harmonics has been successfully demonstrated by recent efforts made to attain precise phase matching between the fundamental and harmonic waves [4–6]. Figure 9.1 summarizes the results of high-energy high-order harmonic generation in the spectral region from 10 nm to 80 nm that have been achieved at RIKEN. In argon, the intensity of the 27th harmonic (30 nm) of a femtosecond Ti:sapphire laser could be increased up to an absorption-limited value and an output energy of $0.3\,\mu J$ was obtained with an efficiency of 10^{-5} [4]. In xenon, the individual harmonic energies of the 11–15th orders (53–72 nm) exceeded $1\,\mu J$ with efficiencies as high as 10^{-4} [7]. In neon, harmonic energies as high as 20 nJ were obtained for the 27th to 67th harmonics (12–30 nm) [8]. Thus, these intense high-order harmonics cover the wavelengths between 10 nm and 80 nm.

The quality of optical elements in the XUV/SXR regime limits the availability of high-order harmonics in a variety of fields. In particular, the generation of nonlinear optical phenomena in the XUV/SXR regime requires mirrors with a reflectivity and surface accuracy that are sufficiently good to focus the beam. The surface roughness of mirror substrates has been considerably improved, and these now support relatively good mirror reflectivities when accompanied with the state-of-the-art multilayer-coating technology. Figure 9.2 shows the normal-incidence reflectivity for various XUV/SXR
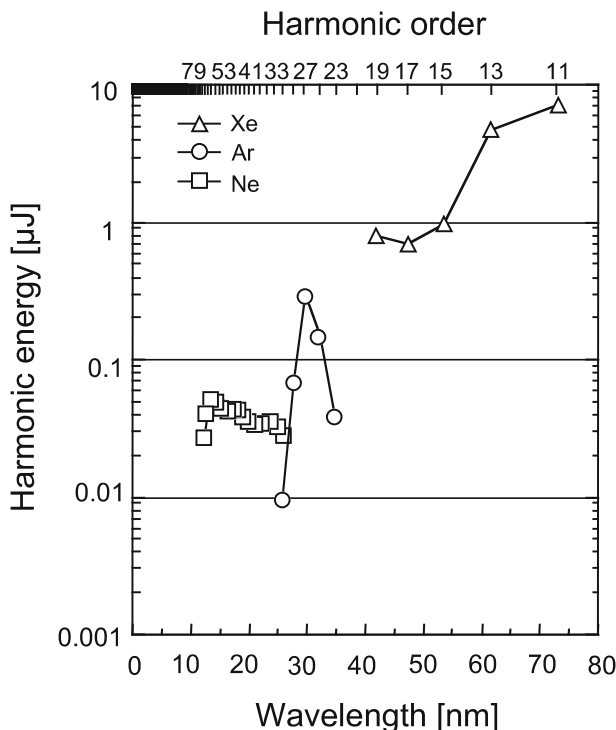
Fig. 9.1. Plots of measured energy of the high-order harmonics generated in xenon (*triangles*), argon (*circles*), and neon (*squares*)

mirrors that have been reported so far [9], where all of the mirrors (except the SiC mirror) are multilayer-coated. The solid lines show the theoretical values [10] and the plots are the measured data. We can see that a set of Mo/Si, SiC/Mg, Sc/Si and SiC mirrors covers the spectral region from 10 to 100 nm with reflectivities higher than 30%. The bandwidth of the multilayer-coated mirrors is typically 2–3 nm, which is narrow enough to select one of the discrete harmonic components, whereas thin metal-foil filters are required when using a SiC mirror in order to select the 9th (88 nm), 11th (72 nm), or 13th (61 nm) harmonics. Figure 9.3 shows an example of the reflectivity of a SiC/Mg multilayer-coated mirror [11]. A peak reflectivity in excess of 40% was obtained at 29.6 nm, which corresponds to the 27th harmonic wave.

There is also a great need for broadband reflection, i.e., the capability for a number of harmonic components to be reflected and/or focused all together. In particular, the XUV supercontinuum (25–40 nm) that has recently been demonstrated using a half-cycle polarization gating method requires broadband optics in its applications toward attosecond pulse char-
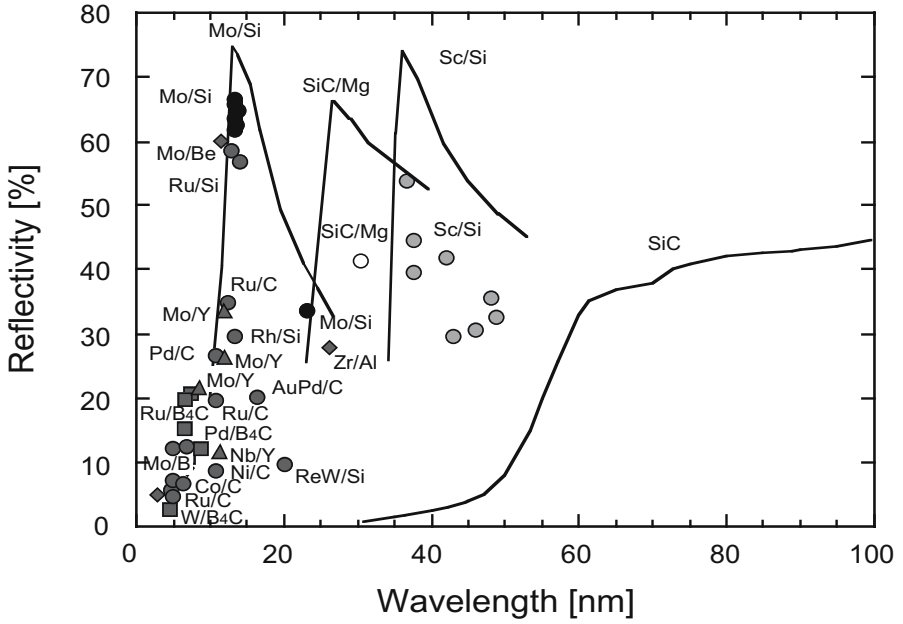
Fig. 9.2. Normal incidence reflectivity for various XUV/SXR mirrors. All of the mirrors, except the SiC mirror, are multilayer-coated. The *solid lines* show the theoretical values and the plots are measured data
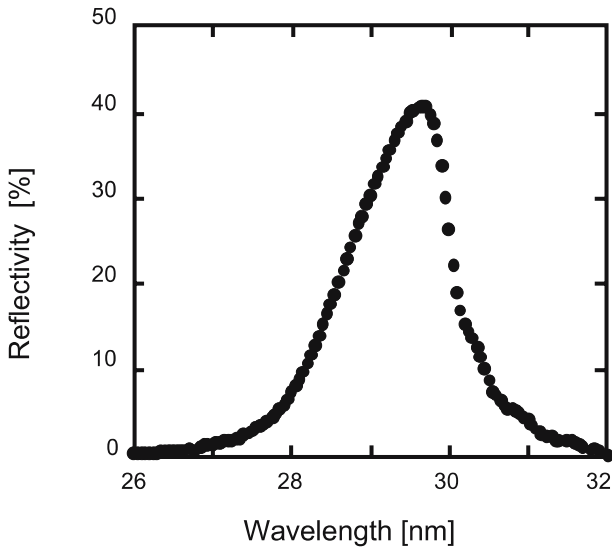
Fig. 9.3. Reflectivity of a SiC/Mg multilayer-coated mirror

acterization [12]. In such a case, the bandwidth of the multilayer-coated mirrors must be broadened at the expense of the reflectivity. An alternative method would be the use of metal-coated grazing-incidence mirrors [13]. The reflection characteristics in this case are simply determined by the complex refractive index of the metal element, which allows us to use these mirrors without necessitating the exact tuning of the wavelength.

The surface accuracy of commercial mirrors is typically $\lambda/5$–$\lambda/15$ at 633 nm, which corresponds to λ–3λ wavelengths in the XUV/SXR regime. Therefore, the focused intensity together with the focusability is limited by the quality of the curved mirrors. In spite of this situation high-order harmonics can be focused down to a micrometer spot size because of the good beam quality and spatial coherence [14–16].

We describe in the following sections how sub-μJ-level high-order harmonic beams can be well-focused to a micron spot size, resulting in intensities of 10^{13}–10^{14} W/cm^2. Various focusing mirrors, as shown in Table 9.1 are tested and used in the focusing experiment.

Table 9.1. Specifications of the focusing mirrors used in the experiment

Type of curves	Focal length	Substrate	Surface accuracy at 633 nm	Roughness (RMS)	Coating	Reflectivity
Spherical concave	50 mm	Fused silica	$\lambda/10$	0.4 nm	SiC/Mg multilayer	40% at 30 nm
Spherical concave	50 mm	Silicon carbide	$\lambda/10$	1.6 nm	None	30% at 61 nm
Off-axis parabolic	60 mm	Zerodur	$\lambda/8$	0.7 nm	SiC/Mg multilayer	40% at 30 nm
Ellipsoidal	107 mm	Stainless steel	$\lambda/10$	5.0 nm	Platinum	14% at 24–38 nm*

* for s-polarized light

9.2 Experimental Techniques

The high-order harmonics of a femtosecond Ti:sapphire laser at 800 nm were generated in argon or xenon. A Ti:sapphire laser system produces an output of 14 mJ, with a pulsewidth of 22 fs at a repetition rate of 10 Hz and a center wavelength of 785 nm. The output pulse was loosely focused using a $f = 4000$ mm plano-convex lens into an interaction cell filled with a gaseous medium to stimulate harmonic generation. Argon at 9-torr pressure was used to fill the cell to generate harmonics at around the 27th orders ($\sim$30 nm),

whereas 2.4-torr of xenon was used to generate harmonics at around the 13th orders ($\sim$61 nm). The $1/e^2$ diameter at the focus was approximately 300 μm, leading to an intensity of 1×10^{15} W/cm^2. The interaction cell has 1-mm diameter pinholes in both ends in order to isolate the vacuum and gas-filled sections by differential pumping. The generated harmonics were sent to a Si beam splitter with a reflectivity of approximately 50% and an extinction ratio of 10^{-4} to separate the harmonic wave from the fundamental wave [17]. A 200-nm-thick aluminum-foil filter (with a transmittance of 14% at 30 nm) that could be moved into the beam path, was used to block the residual fundamental beam and the 3rd to the 9th low-order harmonics. A 170-nm-thick tin-foil filter (with a transmittance of 11% at 61 nm) was used to select the 13th harmonic wave. The harmonic spectra were monitored using a grazing-incidence spectrometer with a micro-channel plate (MCP). A CCD camera detected the two-dimensional images of the spectrally-resolved far-field profiles of the harmonics on a phosphor screen placed behind the MCP. Figures 9.4 and 9.5 show typical spectra of the harmonics generated in argon and xenon, respectively. The absolute energy of the high-order harmonics was measured by positioning a calibrated silicon XUV photodiode (IRD Inc. AXUV-100) in front of the spectrometer. We have verified that the energy signal fell to zero when the argon gas was removed from the interaction cell. The 27th harmonic energy was derived from the relative strength of the spectrum and the total energy measured with the aluminum-foil filter. Consequently, the typical energies of the 27th harmonic with and without the aluminum-foil filter were 23 nJ and 160 nJ, respectively. After reflection by a SiC/Mg multilayer-coated mirror, the corresponding energies at the target were 9 nJ and 65 nJ, respectively. Similarly, the 13th harmonic energies with and without the tin-foil filter were 65 nJ and 600 nJ, respectively, and the corresponding energies after reflection by a SiC mirror were 20 nJ and 180 nJ.

We used an imaging system [18] as shown in Fig. 9.6 to measure the focal spot of the XUV/SXR beams. The harmonic wave was focused by the mirrors listed in Table 9.1. The diameter of the beam on the mirror surface was approximately 2 mm, which was estimated from the MCP spectrograph. In order to visualize the focal spot profile, the harmonic wave was converted to visible light at 550 nm using a 100-μm-thick Ce:YAG scintillator [13,18,19] placed at the focal point. A set of image relay optics were constructed with an objective lens ($NA = 0.65$, $f = 5$ mm) and a convex lens ($f = 500$ mm), which transferred the visible light image onto an image-intensified CCD camera installed outside the vacuum chamber. The scintillator and the objective lens were fixed on a single stage that could be translated along the beam axis to observe the variation of the beam profiles. The resolution of the imaging system was 0.5 μm, which was limited by the NA value of the objective lens. Data were taken from an accumulation of several successive shots, since the intensity of the high order harmonics was reduced by thin metal-foil filters to ensure the linearity of the scintillator.
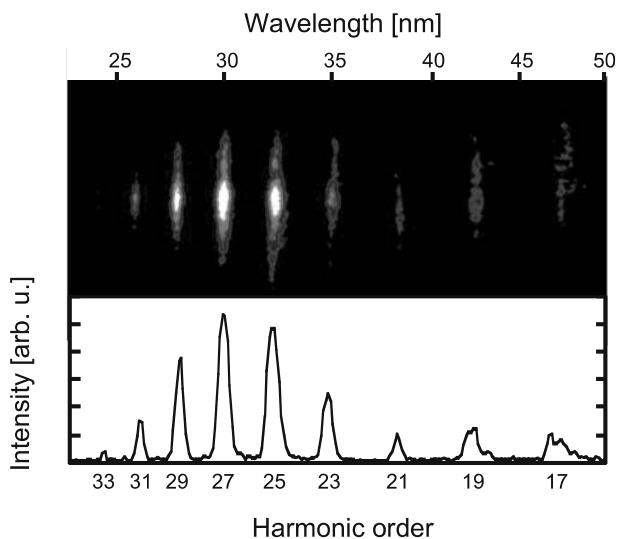
Fig. 9.4. Typical spectrograph (*upper*) and spectral intensity (*lower*) of the harmonic waves generated in argon
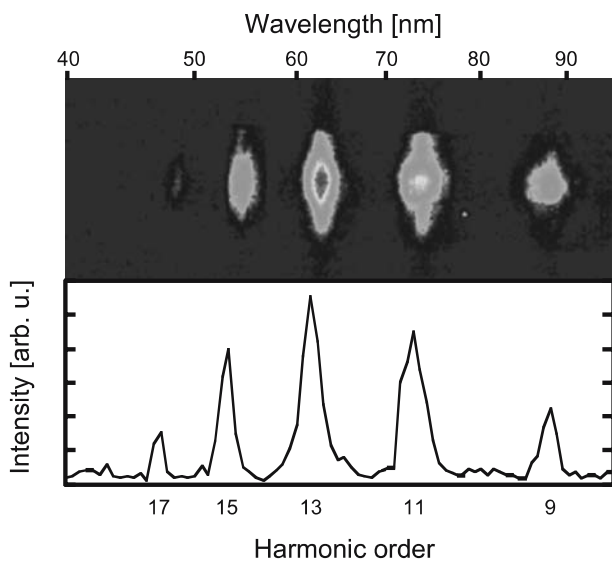
Fig. 9.5. Typical spectrograph (*upper*) and spectral intensity (*lower*) of the harmonic waves generated in xenon

9.3 Results and Discussions

9.3.1 Focusing the 27th Harmonic Beam
Using a SiC/Mg-coated Concave Mirror

Although concave mirrors with good surface accuracy can be obtained quite readily, astigmatism due to the tilted concave mirror makes it difficult to raise the focused intensity. In this experiment, the 27th harmonic beam at 30 nm was selected and focused by a SiC/Mg-coated concave mirror with a focal length of 50 mm, where the angle of incidence was set at 7 degrees. Figure 9.7 shows the $1/e^2$ beam spot size of the 27th beam as a function of distance from the concave mirror. The open circles and filled squares correspond to the horizontal and vertical directions, respectively. The difference between the horizontal and vertical spot sizes is caused by astigmatism. The solid lines are the best-fit curves based on the following equation [20],

$$\omega(z) = \omega_0 \sqrt{\left(1 - \frac{z}{R}\right)^2 + \left(\frac{M^2 \lambda z}{\pi \omega_0^2}\right)^2}, \qquad (9.1)$$

where ω_0 and $\omega(z)$ are the beam radii on the mirrors and at a distance z from the mirrors, respectively, λ is the wavelength and M^2 is the beam quality parameter. R is the wavefront curvature of the beam just after reflection. It is noted that the horizontal and vertical wavefront curvatures are given by $R/\cos\theta$ and $R\cos\theta$, respectively, where θ is the angle of incidence. Consequently, the M^2 values from the best-fit curves for the horizontal and vertical directions were 2.8 and 2.7, respectively. Figure 9.8 shows typical focused images taken at the beam waist in the horizontal and vertical directions marked by arrows in Fig. 9.7. The corresponding spot sizes are 1.6 μm and 1.4 μm, respectively, both of which are about 3 times the diffraction-limited value. This result might be reasonable because the surface accuracy of the concave mirror is $\lambda/10$ at 633 nm, which corresponds to 2.1λ at 30 nm.
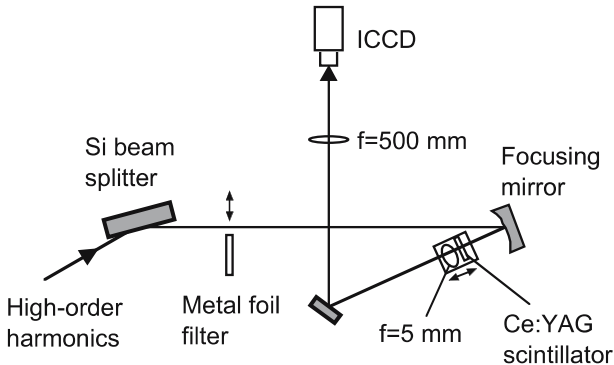
Fig. 9.6. Experimental setup for imaging the focused profiles of high-order harmonics
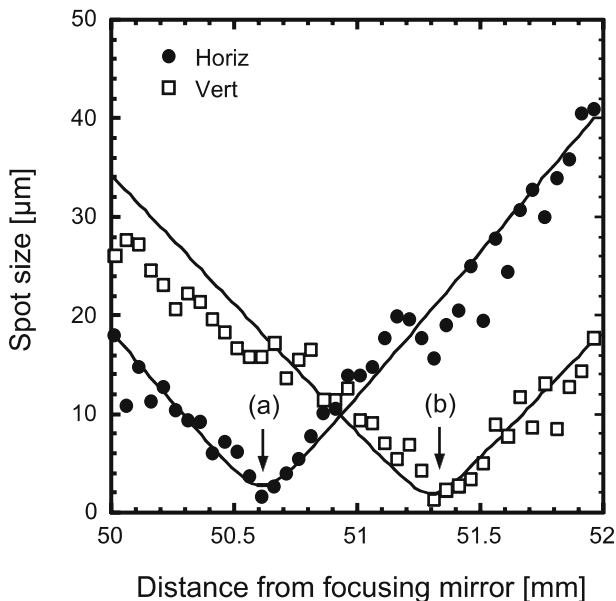
Fig. 9.7. Focused beam spot size of the 27th harmonic wave as a function of distance from the SiC/Mg multilayer coated concave mirror. The *open circles* and *filled squares* correspond to the horizontal and vertical directions respectively. The best-fit curves based on (9.1) are also shown by the *solid lines*
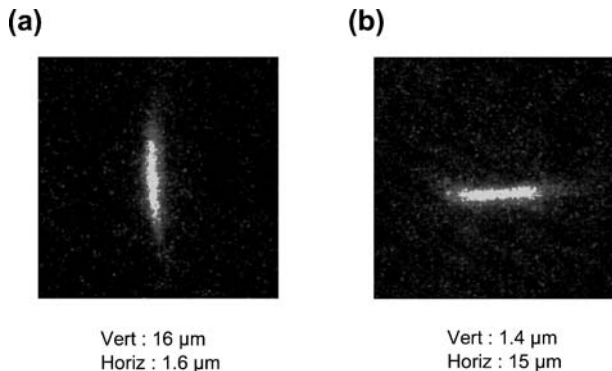
Fig. 9.8. Typical focal spot images taken at positions marked by *arrows* in Fig. 9.7

9.3.2 Focusing the 13th Harmonic Beam
Using a SiC Concave Mirror

In the same way, the 13th harmonic beam at 61 nm was selected by a tin-foil filter and focused by a SiC concave mirror with a focal length of 50 mm. The angle of incidence was set at 7 degrees. Figure 9.9 shows the $1/e^2$ beam spot size of the 13th beam as a function of distance from the concave mirror. The
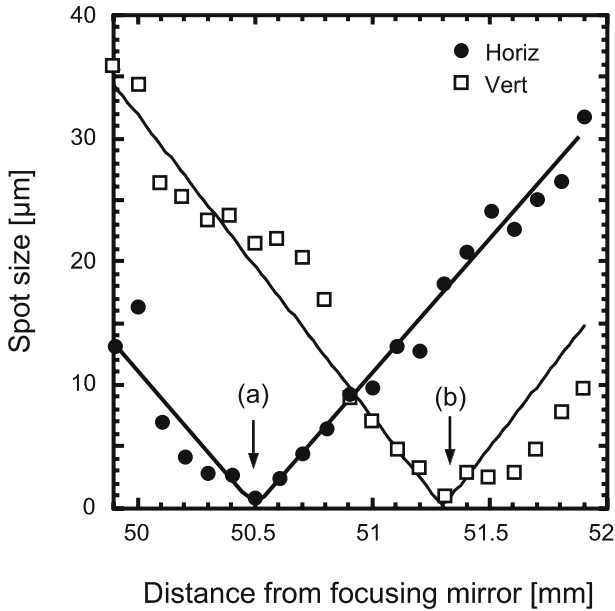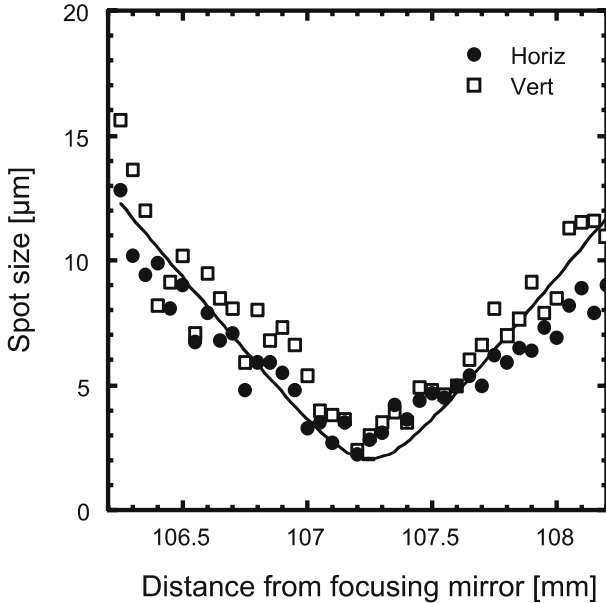

Fig. 9.9. Focused beam spot size of the 13th harmonic wave as a function of distance from the SiC concave mirror. The *open circles* and *filled squares* correspond to the horizontal and vertical directions respectively. The best-fit curves based on (9.1) are also shown by the *solid lines*
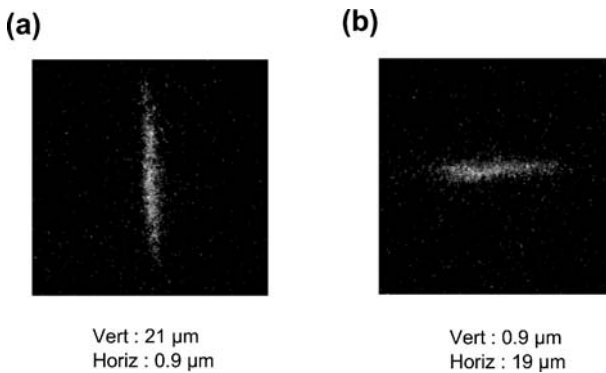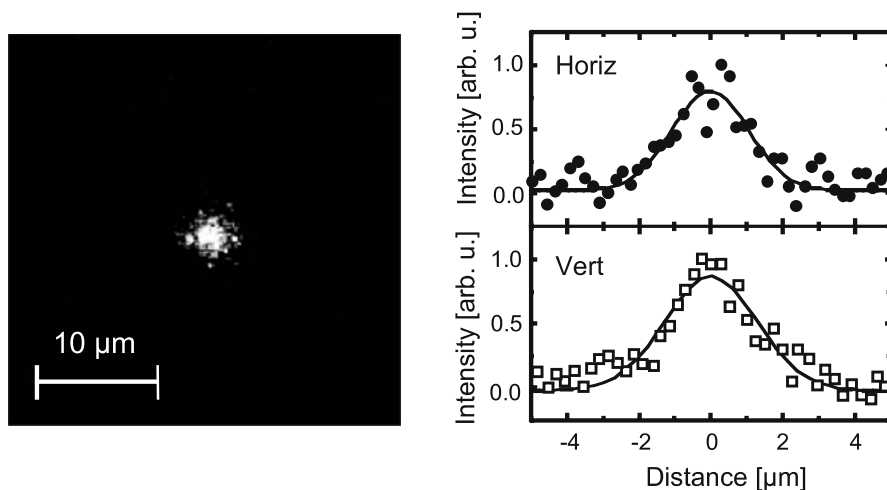

Fig. 9.10. Typical focal spot images taken at positions marked by *arrows* in Fig. 9.9

open circles and filled squares are the horizontal and vertical spot sizes, respectively. The best-fit curves shown by the solid lines provided M^2 values of 1.4. Figure 9.10 shows typical focused images taken at the beam waist in the horizontal and vertical directions marked by arrows in Fig. 9.9. The spot size is 0.9 μm in both directions, which is about 1.4 times the diffraction-limited value.

9.3.3 Focusing the 27th Harmonic Beam Using a SiC/Mg-Coated Off-Axis Parabolic Mirror

Among a variety of geometric forms that can be used as focusing mirrors, off-axis parabolic mirrors are basically free from spherical aberrations and astigmatism and are thus suitable for tightly-focusing XUV/SXR beams. Here, the 27th harmonic beam was selected and focused by a SiC/Mg-coated off-axis parabolic mirror with a focal length of 60 mm and an off-axis angle of 24 degrees. Figure 9.11 shows the $1/e^2$ beam spot size of the 27th harmonic beam as a function of distance from the off-axis parabolic mirror. The open circles and the filled squares are the horizontal and vertical spot sizes, respectively. There is little difference between the horizontal and vertical diameters, showing that circularity is maintained during focusing. The best-fit curve shown by the solid line provided an M^2 value of 1.4.
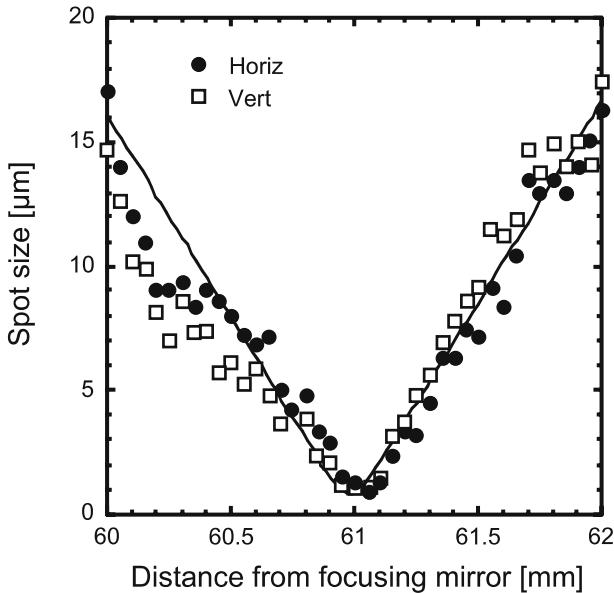
Fig. 9.11. Focused beam spot size of the 27th harmonic wave as a function of distance from the SiC/Mg multilayer coated off-axis parabolic mirror. The *open circles* and *filled squares* correspond to the horizontal and vertical directions respectively. The best-fit curve based on (9.1) is also shown by the *solid line*

Figure 9.12 shows a typical focused image taken in a single shot. The dimensions of the spot in the vertical and horizontal directions are 1.0 μm and 0.9 μm respectively, both of which are less than 1.7 times the diffraction-limited value. Because the high-order harmonics have excellent spatial coherence and beam quality, the focusability is dominated by the performance of the mirror. The peak-to-valley surface accuracy of the off-axis parabolic mirror over an area within a 1-inch diameter was 2.7λ at 29.6 nm. However, because the beam diameter is much smaller than the mirror size, the surface accuracy within a restricted small area would be good enough for a harmonic beam being focused to a nearly diffraction-limited spot size. It should be also noted that there was little scattered light observed in the surrounding area, showing that most of the energy was concentrated in the focal spot.

Figure 9.13 shows examples of ablation patterns taken in a single shot and observed by (a) an optical microscope and (b) an atomic force microscope (AFM). The diameter of the circular hole is approximately 2 μm, which agrees well with the Ce:YAG scintillator experiment.

We estimated the focused intensity of the 27th harmonic wave from the energy, the spot size, and the pulsewidth. Assuming that the pulsewidth of the 27th harmonic wave was the same as the fundamental pulse, i.e., 22 fs full-width at half maximum, the maximum focused intensities with and without the aluminum-foil filter were 1.4×10^{13} W/cm^2 and 1.0×10^{14} W/cm^2 respectively. If the pulse width is assumed to be approximately half the driving pulse based on the semi-classical theory for high-order harmonic generation [21], i.e., 11 fs full-width at half maximum, the corresponding intensities were 2.8×10^{13} W/cm^2 and 2.0×10^{14} W/cm^2, respectively.
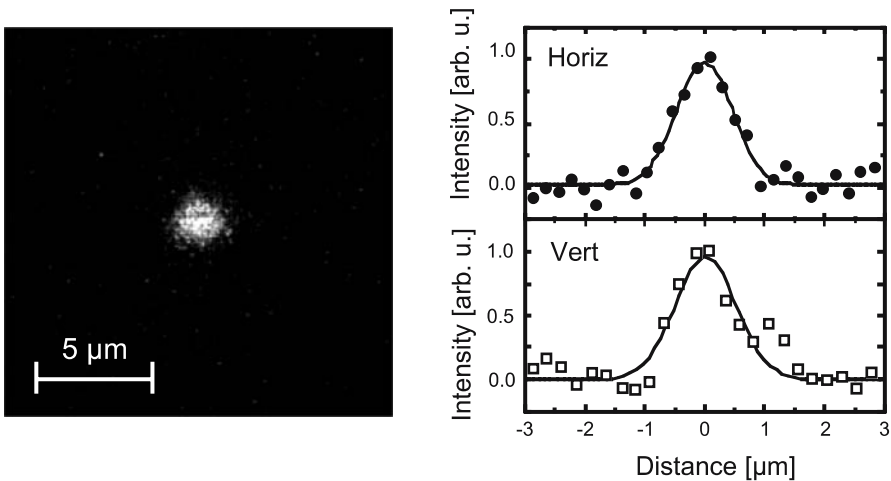
Fig. 9.12. Typical focal spot image for the 27th harmonic beam. The *horizontal* (*right upper*) and vertical (*right lower*) profiles are also shown

(a)   **(b)**
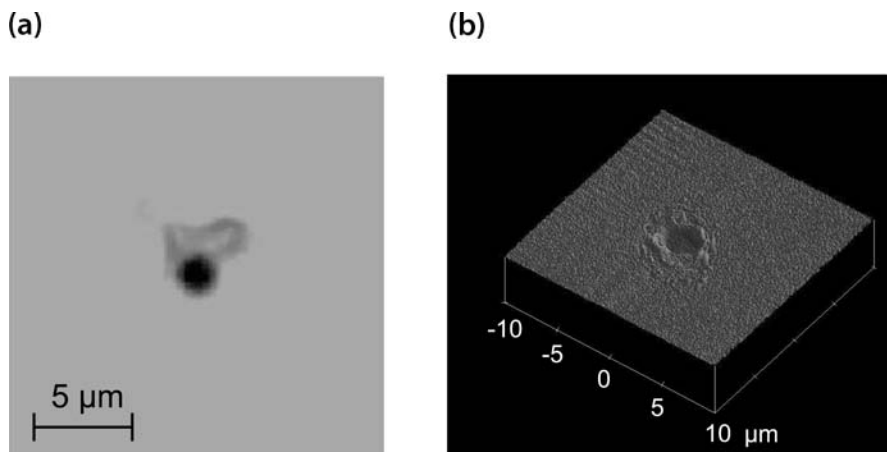
Fig. 9.13. Microscope and AFM images of an ablation pattern on an Au target

9.3.4 Focusing Multiple Harmonics (21st–33rd) Using a Grazing-Incidence Ellipsoidal Mirror

Ellipsoids are also free from spherical aberrations and astigmatism, and are therefore suitable for focusing at grazing incidence. The ellipsoidal mirror used in the experiment was fabricated by the Toshiba Corporate Manufacturing Engineering Center. The substrate was made of stainless steel that had been precisely cut by means of numerically-controled machining, which is a relatively simple and cost-effective method of fabricating such an aspheric geometry. The major and minor axes of the ellipsoid figure were chosen to be 800 mm and 200 mm, respectively. The mirror has dimensions of 40 mm × 20 mm and the angle of incidence is 60 degrees at the mirror center, as shown in Fig. 9.14. This is somewhat far away from conventional grazing incidence, but is not a serious concern for reflection at wavelengths longer than 25 nm, while still preserving the surface accuracy necessary for tight focusing (∼100 mm). After slight polishing of the surface, the mirror was coated with platinum.

We measured the surface accuracy by the Foucault method [22] using a HeNe laser at 633 nm. The reference wave was prepared by focusing the HeNe laser to a position that corresponded to the first focus of the ellipsoid. It was then incident on the mirror at an angle of incidence of 60 degrees. The reflected wave was partially cut by a knife-edge at the second focus of the ellipsoid, and thereafter, the Foucault image was monitored using a CCD camera with appropriate image relay optics. As a result, the wavefront distortion in the central area was found to be approximately $\lambda/10$ at 633 nm, which agreed with a contact probe experiment performed by the manufacturer. We also observed the surface condition using AFM and found that the rms surface roughness was 5 nm. The effective reflectivities over the 21st–

33rd harmonic components (24–38 nm) were measured to be 14% and 6% for s- and p-polarized light, respectively. The degradation of the reflectivity is mainly caused by the surface roughness.

We used an imaging system as shown in Fig. 9.6 to observe the focal spot of the harmonic beams. The harmonics were focused onto a Ce:YAG scintillator by the ellipsoidal mirror. Figure 9.15 shows the $1/e^2$ beam spot size
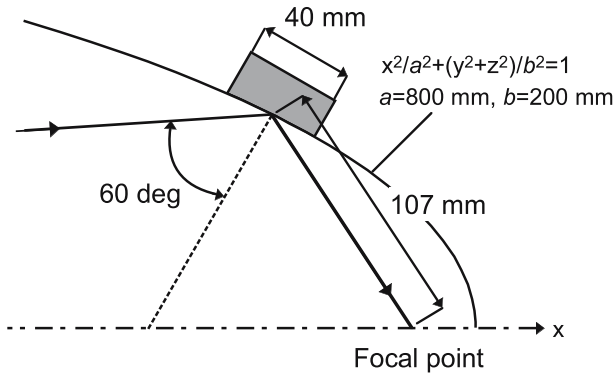
Fig. 9.14. A schematic of an ellipsoidal mirror used for focusing the harmonic beams

Fig. 9.15. Focused beam spot size of the harmonic waves as a function of distance from the ellipsoidal mirror. The *open circles* and *filled squares* correspond to the horizontal and vertical directions, respectively. The best-fit curve based on (9.1) is also shown by the *solid line*

Fig. 9.16. Typical focal spot image for the harmonic beams. The *horizontal* (*right upper*) and *vertical* (*right lower*) profiles are also shown

of the harmonic beams as a function of distance from the ellipsoidal mirror. The open circles and the filled squares are the horizontal and vertical spot sizes, respectively. There is little difference between the horizontal and vertical diameters, showing that circularity is maintained during focusing. The best-fit curve based on (9.1) provided a figure of $M^2 = 2.3$. Figure 9.16 shows a typical focused image taken in a single shot. The dimensions of the spot in the vertical and horizontal directions are $2.2\,\mu m$ and $2.4\,\mu m$ respectively, both of which are approximately 2.3 times the diffraction-limited value.

Finally, we estimated the focused intensity of the 21st–33rd harmonic waves from the total energy, the spot size, and the pulsewidth. Assuming that the pulsewidth of the harmonic waves were the same as the fundamental pulse, i.e., 22 fs full-width at half maximum, the maximum focused intensities without the aluminum filter for s- and p-polarized light were $2 \times 10^{13}\,W/cm^2$ and $9 \times 10^{12}\,W/cm^2$, respectively. If the spectral phase is constant over the entire bandwidth, the harmonics compose a train of attosecond pulses with a duration of approximately 200 as, leading to a peak intensity of $2 \times 10^{15}\,W/cm^2$. Of course, the characterization of such intense short pulses in the XUV/SXR regions is an objective that is still to be investigated.

9.4 Conclusions

The focusability of intense high-order harmonics was investigated using various XUV/SXR focusing mirrors. The 27th harmonic wave (30 nm), which has an energy in excess of $0.3\,\mu J$, was selected and focused using an off-axis parabolic mirror with an SiC/Mg multilayer coating. The focal spot images

observed after visualization with a Ce:YAG scintillator indicated a good beam profile with a nearly Gaussian distribution and an M^2 value as low as 1.4. The spot radius was less than $1\,\mu m$ at the focal position, resulting in a focused peak intensity of $1.0 \times 10^{14}\,\mathrm{W/cm^2}$. Similarly, the sub-$\mu J$ 13th harmonic wave (61 nm) could be focused to a spot size of less than $1\,\mu m$ using a concave SiC mirror. In order to focus multiple harmonic components we have designed and evaluated a platinum-coated ellipsoidal mirror. The surface accuracy measured by the Foucault method is $\lambda/10$ at 633 nm, corresponding to 2λ at the working wavelength. The ellipsoidal mirror was then used to reflect and focus intense coherent light in the spectral region from 25 nm to 40 nm. The focal spot images showed a good beam profile with a nearly Gaussian distribution and an M^2 value of 2.3. The spot radius was less than $2.5\,\mu m$ at the focal position, resulting in a focused peak intensity of $4.4 \times 10^{13}\,\mathrm{W/cm^2}$. Thus, high-order harmonics can be well focused to a micron spot size with focused intensities of 10^{13}–$10^{14}\,\mathrm{W/cm^2}$, owing to good beam quality and spatial coherence. These results should pave the way for further applications of ultrashort optical pulses and the observation of ultrafast nonlinear phenomena in the short wavelength regions.

References

1. A. McPherson, G. Gibson, H. Jara, U. Johann, T.S. Luk, I.A. McIntyre, K. Boyer, C.K. Rhodes: J. Opt. Soc. Am. B 4, 595 (1987)
2. J.J. Macklin, J.D. Kmetec, C.L. Gordon III: Phys. Rev. Lett. 70, 766 (1993)
3. Ch. Spielmann, N.H. Burnett, S. Sartania, R. Koppitsch, M. Schnürer, C. Kan, M. Lenzner, P. Wobrauschek, F. Krausz: Science 278, 661 (1997)
4. E. Takahashi, Y. Nabekawa, T. Otsuka, M. Obara, K. Midorikawa: Phys. Rev. A 66, 021802 (2002)
5. J.-F. Hergott, M. Kovacev, H. Merdji, C. Hubert, Y. Mairesse, E. Jean, P. Breger, P. Agostini, B. Carré, P. Saliéres: Phys. Rev. A 66, 021801 (2002)
6. D. Yoshitomi, T. Shimizu, T. Sekikawa, S. Watanabe: Opt. Lett. 27, 2170 (2002)
7. E. Takahashi, Y. Nabekawa, K. Midorikawa: Opt. Lett. 27, 1920 (2002)
8. E.J. Takahashi, Y. Nabekawa, K. Midorikawa: Appl. Phys. Lett. 84, 4 (2004)
9. M. Yamamoto, M. Yanagihara, H. Kimura, M. Watanabe: J. Jpn. Soc. Sync. Rad. Res. 9, 16 (1996)
10. The Center for X-Ray Optics at the Lawrence Berkeley National Laboratory, http://www-cxro.lbl.gov/optical_constants/multi2.html
11. S. Ichimaru, H. Takenaka, T. Ohchi, E.M. Gullikson: *Abstract of the 64th Autumn Meeting of the Japan Society of Applied Physics* (Japan Society of Applid Physics, Tokyo 2003) p. 615

12. B. Shan, S. Ghimire, Z. Chang: J. Mod. Opt. 52, 277 (2005)
13. C. Valentin, D. Douillet, S. Kazamias, Th. Lefrou, G. Grillon, F. Augé, G. Mullot, Ph. Balcou, P. Mercére, Ph. Zeitoun: Opt. Lett. 28, 1049 (2003)
14. Y. Tamaki, J. Itatani, M. Obara, K. Midorikawa: Jpn. J. Appl. Phys. 40, L1154 (2001)
15. R.A. Bartels, A. Paul, H. Green, H.C. Kapteyn, M.M. Murnane, S. Backus, I.P. Christov, Y. Liu, D. Attwood, C. Jacobsen: Science 297, 376 (2002)
16. D.G. Lee, J.J. Park, J.H. Sung, C.H. Nam: Opt. Lett. 28, 480 (2003)
17. E.J. Takahashi, H. Hasegawa, Y. Nabekawa, K. Midorikawa: Opt. Lett. 29, 507 (2004)
18. H. Mashiko, A. Suda, K. Midorikawa: Opt. Lett. 29, 1927 (2004)
19. M. Moszynski, T. Ludziejewski, D. Wolski, W. Klamra, L.O. Norlin: Nucl. Instrum. and Meth. A 345, 461 (1994)
20. A.E. Siegman, S.W. Townsend: IEEE J. Quantum Electron. 29, 1212 (1993)
21. M. Lewenstein, P. Balcou, M.Y. Ivanov, A. L'Huillier, P.B. Corkum: Phys. Rev. A 49, 2117 (1994)
22. J. Strong: *Procedures in experimental physics* (Prentice-Hall, New York 1938)

10 Application of X-Ray Spectroscopy to the Study of Energy Transport in Plasma Produced by an Ultrahigh-Intensity Laser

H. Nishimura[1], Y. Inubushi[1], S. Fujioka[1], T. Kawamura[2], S. Shimizu[3], M. Hashida[3], S. Sakabe[3], F. Koike[4], T. Johzaki[1], H. Nagatomo[1], and J. Mima[1]

[1] Institute of Laser Engineering, Osaka University, 2-6 Yamada-oka, Suita, Osaka 565-0871, Japan
e-mail: nishimu@ile.osaka-u.ac.jp
[2] Tokyo Institute of Technology, 4259 Nagatsuda-cho, Midori, Yokohama, Kanagawa 226-8502, Japan
[3] Institute for Chemical Research, Kyoto University, Gokasho Uji, Kyoto 611-0011, Japan
[4] Physics Laboratory, School of Medicine, Kitasato Unversity, Kitasato 1-15-1, Sagamihara, Kanagawa 228-8555, Japan

Summary. X-ray line emissions from ultrashort high-intensity laser-produced plasma were studied in order to clarify the physics of energy transport associated with the generation of ultrashort X-ray pulses for use in various applications. This article reviews two topics. The first is the application of Kα spectroscopy to the study of energy transport in laser-produced plasma. The second topic is the application of X-ray polarization spectroscopy to measurements of the anisotropy of hot electrons generated with ultrashort high-intensity laser pulses.

10.1 Introduction

The interaction of an ultrahigh-intensity laser with a dense plasma is of wide interest, as these lasers open up new horizons for research, such as fs X-ray radiation probing [1, 2], energetic particle acceleration [3], and inertial confinement fusion [4, 5]. A new spectroscopic method that provides the kind of time- and space-resolved information required to obtain a more quantitative understanding of energy deposition than that provided by particle measurements has been under development [5–8]. Because of the relatively low temperatures that can be accessed with current lasers, conventional K-shell line spectroscopy using near-fully ionized plasma is not suitable.

Much work has been performed to derive the fast electron spectrum and the energy transfer efficiency from observations of Kα lines from multilayer targets [9–12]. However, it has never been shown via spectroscopy that the region emitting the Kα lines is substantially heated by hot electrons. As

we will see in what follows, the observed Kα lines can consist of the primary Kα line from singly ionized ions and the energy-shifted components from partially ionized ions, but these cannot be distinguished due to the poor spectral resolution ($\sim$200 eV) obtained when a charged-coupled device is employed. Therefore, although CCD-based Kα line spectroscopy may be suited to observations of hot electron propagation, it is not suitable for energy deposition studies. In fact, X-ray spectra observed with a high-resolution spectrograph covering the spectral region from the Kα line to K-shell resonance lines have shown that the line intensities decrease dramatically as the over-layer thickness of the multilayer target increases [13–18]. This result indicates that the depth of the hot region is much less than those predicted from the fast electron temperatures measured or estimated from laser intensity scaling [19]. The inhibition of heat transport via hot electrons has been attributed to the space charge effect, which is strongly dependent on the electrical conductivity of the target material [20]. Therefore, in addition to conventional K-shell line spectroscopy, observation and analysis of the line radiation from inner shell transitions in partially ionized plasma are needed to improve our understanding of the energy transport and deposition mechanisms associated with the generation of X-rays from hot dense regions.

First, X-ray spectra ranging from Kα to Heα lines of chlorine or aluminum were observed by utilizing bilayered plastic or metallic targets, and the dependence of the emitted line intensities on the overcoat thickness was measured. The experimental results from the plastic targets were compared to an integrated analysis that attempted to simulate the observed spectrum. Thus, the ionization-shifted Kα lines were calculated in order to compare them to those obtained experimentally. The comparisons show a reasonable agreement with the experimental Cl Kα lines, but not with those from higher ionization stages such as the Heα line. Of particular importance is the dependence of heat transport on the initial target conductivity measured via high-resolution spectroscopy.

Second, the velocity distribution function (VDF) of hot electrons was directly measured to clarify the energy deposition process using X-ray line polarization spectroscopy. When the plasma has electromagnetic field anisotropy, polarized X-rays corresponding to the magnetic quantum number are emitted. In the case of polarization spectroscopy in an electron beam ion trap (EBIT) [21], the polarization degree P is generally defined by

$$P = \frac{I_\pi - I_\sigma}{I_\pi + I_\sigma} , \qquad (10.1)$$

where I_π is the intensity of the line X-ray whose electric field is parallel to the direction of the electron beam, and I_σ is that perpendicular to the beam. Hence, the VDF anisotropy of hot electrons can be derived by observing the degree of polarization P [22]. We will show that the diagnostic technique, i.e. polarized X-ray spectroscopy coupled with a multilayered target, can be used

to observe the change in the shape of the VDF with the depth of the target. In this study, the polarization of Cl–Heα line from a double-layered target irradiated with a 10 TW laser was observed.

10.2 Kα Line Spectroscopy

10.2.1 Experiments

Experiments were carried out using a Ti:sapphire laser system called T6 at the Institute of Laser Engineering, Osaka University [23]. This laser provides 100 mJ per pulse on the target for a duration of 132 fs at a wavelength of 800 nm at 10 Hz. The laser pulse is amplified by three stages of multipath amplification so that the overall amplified spontaneous emission (ASE) from the system on the target is well below detectable levels. The extinction ratio of the main pulse to a prepulse appearing 13 ns in advance of the main pulse is better than 10^{-6}. Figure 10.1 shows the experimental set-up and laser irradiation system. The P-polarized laser pulse was focused with an $f/3$ off-axis parabolic mirror onto a target at 45° from the target normal. The elliptical focal spot measured by an optical monitor was 15×21 μm, which included 70% of the incident energy, yielding an average laser intensity of 2×10^{17} W/cm^2. Two different types of target were used. One was a 200 μm-thick polyvinylchloride (C_2H_3Cl, density ρ_{CHCl} of 1.4 g/cm^3) sheet coated with a parylene layer (density ρ_{CH} of 1.0 g/cm^3) on which the overcoat thickness was varied from 0.0 to 2.1 μm. The second target was a 200 μm-thick Al (density ρ_{Al} of 2.69 g/cm^3) plate coated with a Mg layer (density ρ_{Mg} of 1.74 g/cm^3) on which the overcoat thickness was varied from 0.0 to 2.2 μm. Both targets were mounted on a rotating table to provide a fresh surface for every laser shot.

Time-integrated X-ray spectra from the plastic target were observed with a two-dimensionally curved crystal spectrograph. The bent quartz crystal,
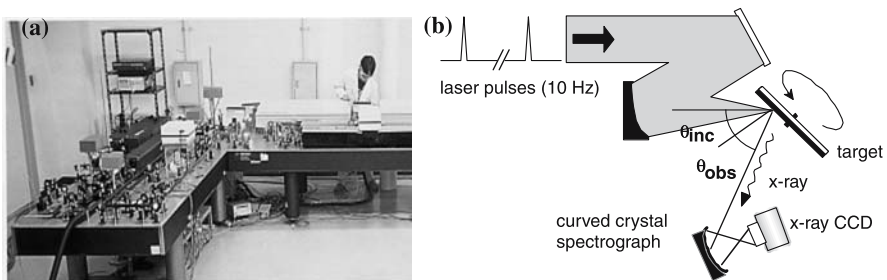
Fig. 10.1. a The T6 laser system used in this study. This provides a laser pulse of 100 mJ energy for a duration of 130 fs at 10 Hz repetition rate. **b** Experimental set-up

set 1162 mm away from the target, used (10-11) reflection with a meridional curvature radius of 200 mm and a sagital curvature radius of 178 mm. The meridional direction includes the dispersion plane. The image magnification of this spectrograph was 1/8. X-ray spectra ranging from 2.6 to 2.85 keV were recorded with a cooled, back-illuminated CCD detector. The spectral resolving power $\varepsilon/\delta\varepsilon$ where ε is the photon energy, was better than 10^4. Observations were made from the target normal.

Time-integrated spectra from the metallic target were observed with a Von Hamos crystal spectrograph. The crystal was made from pentaery-thritol (PET) and utilized (002) reflection with a bending radius of 100 mm. The spectra were recorded with an imaging plate [24] supplied by Fuji Film Co. The center of the PET crystal was set 130 mm away from the plasma and covered the spectral range from 1.48 to 1.62 keV. The spectral resolving power was better than 5000. The observation angle in this case was 45° from the target normal. To obtain clear signals on the detectors, several thousand laser shots were needed for both target types.

In addition to the spectroscopic measurements, the lateral size of the plasma was measured at the target normal by a knife-edge method. In this measurement the target was a 200-μm-thick Al plate irradiated on a single-shot basis to avoid errors arising from shot-to-shot variations. The image was recorded with a CCD detector with a 50-μm-thick Be filter. The image magnification was 100 yielding a spatial resolution of better than 1 μm. The energy range was $1.5 \sim 2.5$ keV, which was determined by the spectral sensitivities of the Be filter and the CCD detector. The width at the foot of the profile was 11 μm, which is somewhat smaller but close to that of the visible focal spot. Therefore, contributions due to weak X-ray emission from material surrounding the laser spot can be excluded [15].

Figure 10.2a shows a typical spectrum obtained from the plastic target. Between the Cl Kα and Cl Kβ lines, inner shell transition lines corresponding to Kα Cl^{9+} (O-like) to KαCl^{14+} (Li-like), the He-like $1s^2$–$1s2p$ (Heα) line and its unresolved Li-like satellite lines are seen. The Cl Kα line from Cl^{1+} appears to be broad partly because the signal is saturated on the CCD, and partly because it includes Kα Cl^{2+} to KαCl^{8+} lines on its blue wing. The shifted Kα lines are also broad, but this is due to the inclusion of sublevel transitions for a given ionization state. As the CH overcoat thickness is increased, all of the lines become monotonically weaker. Figure 10.2b plots the intensities of Kβ and Heα lines as a function of the product of density and thickness, $\rho_{CH}d$, of the overcoat. The Kβ line was chosen to represent the emission from the cold region and the Heα line to represent the hot region. Both lines decrease almost exponentially with respect to the overcoat $\rho_{CH}d$. In Fig. 10.2b, the solid lines are exponential fits to the data, i.e. $\exp(-\rho d/X)$, where X is a reduction factor corresponding to 8.6 cm^2/mg for Kβ and 9.4 cm^2/mg for Heα.

Figure 10.3a shows the intensities for the metallic target. Similarly, inner shell transition lines corresponding to Kα Al^{5+} (O-like) to Kα Al^{10+} (Li-like) are seen between Al Kα and He-like $1s^2$–$1s2p$ (Heα) lines. As the
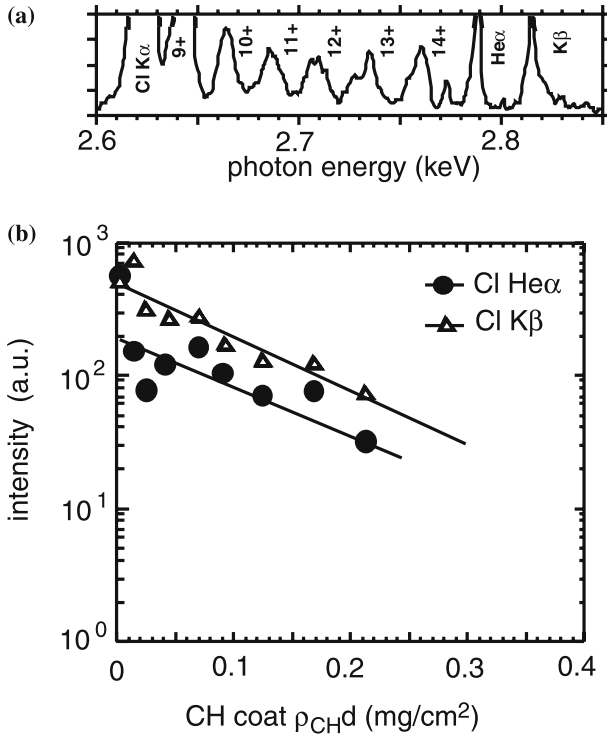
Fig. 10.2. a Typical X-ray spectrum from a CH/C_2H_3Cl target. **b** Dependence of Cl Heα and Kβ intensities on the product of the initial density and the thickness of the CH overcoat. Each *solid line* represents the fit to a single exponential

Mg overcoat thickness increases, all of the lines become weaker. Figure 10.3b shows the intensities of the Al Kα and Heα lines as a function of the product of density and thickness $\rho_{CH}d$ of the Mg overcoat. Both lines decrease almost exponentially with respect to the overcoat $\rho_{CH}d$, and, like the fits in Fig. 10.3b, reduction factors of $9.0\,cm^2/mg$ for Kα and $8.7\,cm^2/mg$ for He-α are found. Note here that these factors are very close to those obtained for the plastic targets and no significant difference was observed between the conductive and the nonconductive materials in terms of the depth of the hot region deduced from these reduction factors.

In a separate experiment performed under the same conditions, the spectra of an expanding cloud of hot electrons that are ejected from the rear side of the foil irradiated by the laser through a $2\,\mu m$-thick Mylar ($C_{10}H_8O_4$) foil were measured with an electron spectrometer [25]. The temperatures derived from the slopes of the electron spectra scale as $29(I_{17})^{0.74}\,keV$ with laser intensity for 800-nm laser light, where I_{17} is the laser intensity normalized to $1 \times 10^{17}\,W/cm^2$. Therefore, the hot electron temperature T_{hot} in the present experiment at $2 \times 10^{17}\,W/cm^2$ is estimated to be about $50\,keV$.
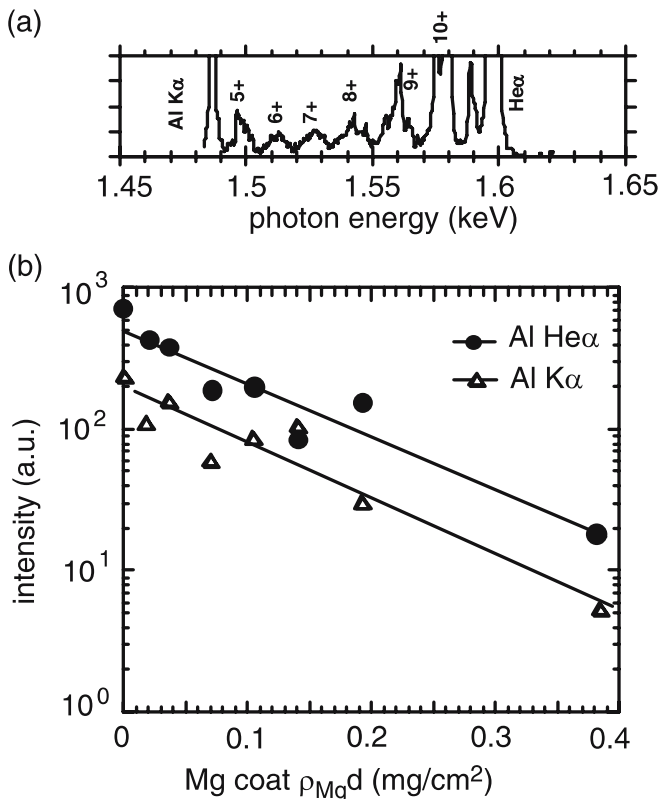
Fig. 10.3. a Typical X-ray spectrum from the Mg/Al target. **b** Dependence of Al Heα and Kα intensities on the product of the initial density and the thickness of the Mg overcoat. Each *solid line* represents the fit to a single exponential

10.2.2 Experimental Analysis

The experimental results were analyzed using an integrated approach. To obtain the temporal evolution of the temperature and the density profiles of the bulk plasma, the experimental hot-electron temperature was used as an initial condition for the 1D-FP code [26]. The number of hot electrons in the distribution function were adjusted according to the assumed laser absorption. The FP code is coupled to the 1-D radiation hydrodynamic simulation ILESTA [27]. The electron (or ion) heating rate from hot electrons is first calculated by the Fokker–Planck transport model and is then added to the energy equation for the electrons (or ions) in ILESTA-1D. Results were then used to drive an atomic kinetics package [28] to obtain the temporal evolution of the Kα lines from partially ionized Cl ions.

Fast Electron Transport and Energy Deposition

To evaluate the heating, a relativistic 1-D Fokker–Planck code was used. The configuration space is 1-D but the momentum space is 2-D, with axial symmetry. This code is coupled to a radiation–hydrodynamic simulation in order to include energy dissipation via ionization processes, hydrodynamic flow, the equation-of-state (EOS), and radiation transport. The loss of kinetic energy from hot electrons is treated through Coulomb and electromagnetic fields.

The radiation–hydrodynamic simulation includes the Quotidien EOS [29] and Ion EOS based on the Cowan model [30]. For the electron component, a set of fitting formulae derived from the numerical results from the Thomas–Fermi model and a semi-empirical bonding correction [31] are adopted. The effective Z-number of the partially ionized plasma is obtained from the average atom model. Radiation transport is treated by multigroup diffusion.

Atomic Kinetic Code

A population kinetics code was developed to treat the atomic processes associated with $1s$ inner-shell ionization and radiative transition from L-shell to K-shell orbits of Cl and Al atoms. Energy levels and radiative decay rates associated with the Kα emission were calculated using a multiconfiguration Dirac–Fock (MCDF) code called GRASP [32]. The Auger rates were calculated with an atomic code developed by Fritzsche et al. [33]. The free electron distribution $f(e)_{\mathrm{all}}$ was assumed to be a bi-Maxwellian distribution; one temperature is for the cold bulk component $f(e)_{\mathrm{bulk}}$ and the other is for the hot component $f(e)_{\mathrm{hot}}$; $f(e)_{\mathrm{all}} = (1-a)f(e)_{\mathrm{bulk}} + af(e)_{\mathrm{hot}}$, where a represents the fraction of fast electrons among all of the free electrons. In the same manner, effective rate coefficients, individually calculated for the two electron components, are determined in proportion to the fraction a except for the radiative and Auger decays as well as three-body recombination rates. Note that that the fraction of hot electrons is estimated to be a few % of all free electrons from the particle-in cell (PIC) simulation [34]. After solving the kinetics code for representative plasma parameters, the dependence of individual ionic states on cold and hot temperatures was investigated.

10.2.3 Experimental Analysis and Discussion

First, the experimental results were compared with atomic-code calculations that assume a steady state in order to derive time- and space-averaged electron temperatures of the bulk plasma. In this calculation, T_{hot} is assumed to be $50\,\mathrm{keV}$ and a to be 1%. C_2H_3Cl plasma with an ion density of $9\times10^{22}\,\mathrm{cm}^{-3}$ or Al plasma with a density of $6\times10^{22}/\mathrm{cm}^3$ was used. Results are shown in Fig. 10.4a for Cl. Due to difficulties with spectrally isolating the Cl^{9+} O-like Kα line from $Cl^+ \sim Cl^{8+}$ lines, the intensity ratios are taken with respect
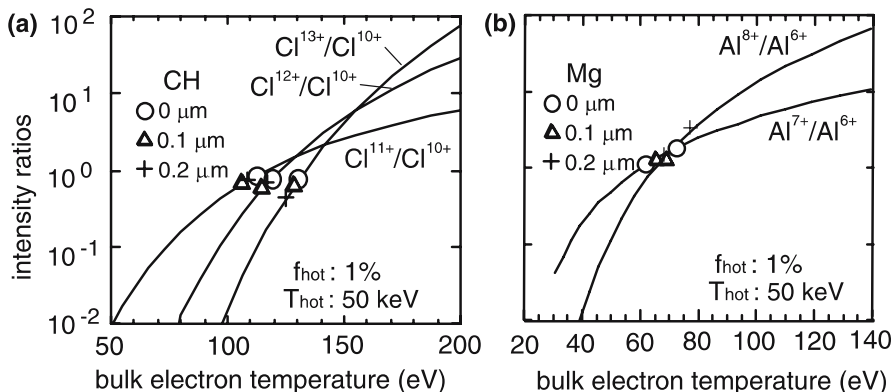
Fig. 10.4. Comparison of experimental results with steady state solutions from the atomic kinetics code for **a** C_2H_3Cl and **b** Al plasmas. Time- and space-averaged temperatures of 120 and 70 eV are obtained, respectively

to the Cl^{10+} N-like $K\alpha$-line. All data points are within a temperature range of 120 ± 10 eV. In the same manner, the temperature of Al was found to be 70 ± 20 eV, as shown in Fig. 10.4b.

The temporal evolution of the CHCl plasma calculated with the FP shows that the heat wave propagates deeper with time, but the typical depth obtained in these simulations is much deeper than that observed in the experiment. Furthermore, the typical temperature is lower than that found in the experiment, although 100% absorption is assumed. This disagreement can be resolved by noting that the inhibition of the heat transport in an overcritical region in 3-D Particle-in-Cell simulations [35]: the electric currents carried by hot electrons in the vacuum–plasma interface induce self-organized magnetic fields, but the current values are well above the Alfvén limit [36]. The magnetic fields induced bend the electron trajectories and prevent their penetration into the overdense region. Furthermore, the electrons in the return flow are scattered by the magnetic fields and their orbits become extremely diffusive. As a result, the plasma becomes resistive, longitudinal electric fields are created and these maintain the global current neutralization. In this way, anomalous damping of the heat transport may occur and bulk electrons may be heated in a very localized region in the vacuum–plasma interface.

To investigate the effect of transport inhibition on the temperature profile, the advection term involved in the FP equation was intentionally omitted. This treatment models a case where the absorbed energy is localized on the target surface and heat transport in the axial direction is inhibited. The result is shown in Fig. 10.5. In this calculation, 15% of the incident laser energy is deposited in the 2-µm-thick region at the target surface. Just after the end of the laser pulse, the number of hot electrons decreases with time and their energy is dissipated into bulk electrons. As a result, the temperature of bulk electrons rises gradually up to 140 eV after laser termination. Using
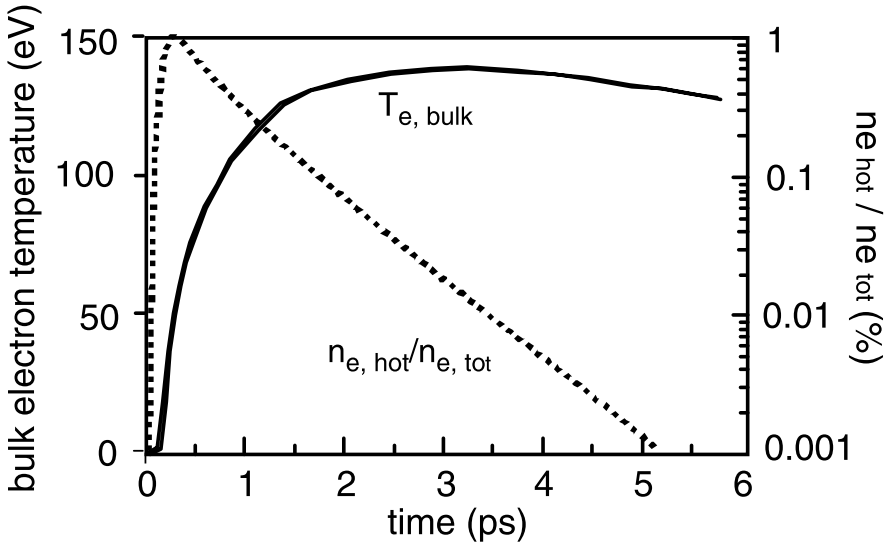
Fig. 10.5. Temporal variations in bulk electron temperature and fractional hot electrons calculated by the Fokker–Planck code

this result, the temporal evolutions of $K\alpha$ lines from partially ionized Cl ions were calculated and are shown in Fig. 10.6. Time-dependent emission from each line, corresponding to various ionization stages, is seen. Because of the time lag due to these ionization processes, emission from the higher ionization stages becomes much weaker than those from the lower ionization stages. After integrating the time-dependent emission intensities over time, we compared the calculated results with those from the experiment. In this comparison, the data obtained with no overcoat was used. The $K\alpha$ line from Cl^{9+} was chosen as the normalization standard. The results are shown in Fig. 10.7, where except for the $K\alpha$ lines from higher ionization stages, reasonable agreement between the calculation and experiment was obtained. The $K\alpha$ line from Cl^{14+} that was calculated may have been underestimated because only the $1s2s2p$ level is considered in the present calculation and the contributions from other levels such as $1s2p^2$ and $1s2p3l$ are excluded. In the same way, the treatment of the population calculation for He-like ions does not include the contribution from inner-shell ionization processes due to hot electrons, such as $1s^2nl + e^- - 1snl + 2e^-$. The effect of a lower energy component in the distribution on the energy deposition is important because lower energy electrons carry about half of the absorbed energy and are trapped in a self-generated electric field. However, the hot electron temperatures measured by the electron spectrometer are indicative of the higher energy component.

In summary, energy transport in ultrahigh-intensity laser-produced plasmas has been investigated via $K\alpha$ line spectroscopy. No significant differences were found between plastic (representing an insulator) and metallic (repre-
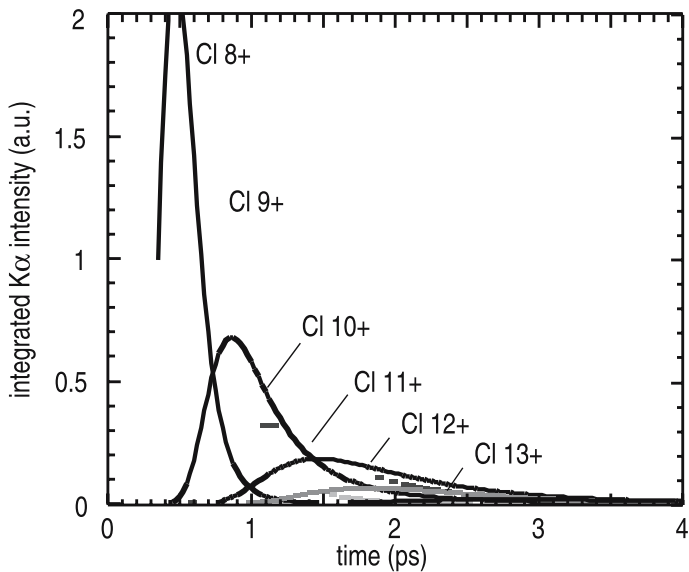
Fig. 10.6. Time dependences of Kα lines from partially ionized Cl ions, calculated by the atomic kinetics code. Temperature and density were given by the Fokker–Planck calculations shown in Fig. 10.5
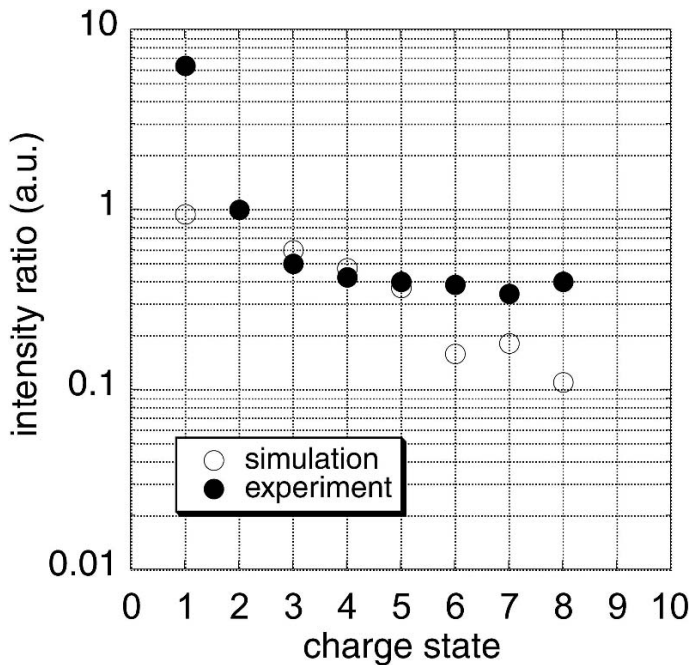
Fig. 10.7. Comparison of the time-integrated Cl Kα line intensities with the atomic kinetics code. Normalization was performed for the Kα Cl^{9+} line

senting an electric conductor) targets with respect to the dependence of the line emission intensity on the overcoat ρR values. Comparison of the results from the experiments with those from the Fokker–Planck simulation suggests the anomalous stopping of the heat wave carried by hot electrons. The temporal evolutions of the Kα lines were calculated for a practical case and a reasonable agreement was obtained with those obtained experimentally up to Cl^{+12}. This work represents the initial phase of benchmarking for an integrated computational method that will use time-resolved spectroscopic measurements to analyze energy transport and deposition in ultra-high intensity laser-produced plasmas.

10.3 X-Ray Line Polarization Spectroscopy

10.3.1 Experiments

Experiments were carried out using the same Ti:sapphire laser system used in the above experiment. The P-polarized pulse was focused with an $f/3$ off-axis parabolic mirror onto a target at 5° of incidence with respect to the target normal. The focal spot diameter was 15 μm and included 80% of the incident energy, yielding intensities ranging from 1.0×10^{17} to 1.5×10^{17} W/cm^2. Two different targets were used. One was a 200-μm C$_2$H$_3$Cl plate. The other had a 0.05-μm-thick CH overcoat on the same C$_2$H$_3$Cl plate. Line polarization was observed with a toroidally curved crystal spectrograph. The crystal was used in (10-11) reflection mode and set 1162 mm away from the target. The resulting image magnification was 1/8. Spectra discussed below were integrated over the whole plasma. Cl–Heα emission was observed at a Bragg angle 41.7°. Included orthogonal polarization components were corrected on the assumption of a perfect crystal. X-ray spectra from 2.5 to 2.9 keV were recorded with a cooled CCD camera. The spectral resolution $\varepsilon/\Delta\varepsilon$ (ε is the photon energy here), including source size effects, was better than 3000. The observation angle was 85° from the target normal. In order to obtain a clear signal on the CCD camera almost 3000 laser shots were needed. The orientation of the Bragg crystal was rotated by 90° around the line of sight to measure the degree of polarization of the Cl–Heα line emission for a different set of shots made under identical conditions. The case where the plane of dispersion is perpendicular to the target surface is called orientation H. The orthogonal case is called orientation V. Suppose that the VDF has a cigar-like shape, the axis of which is perpendicular to the target surface, and the intensity of the I_π component is more intense than that of the I_σ component. The I_σ component is detected for the orientation H and I_π for the orientation V. In order to confirm the stable creation of the plasma, X-ray spectra from the target were also observed with a flat crystal spectrograph at 40° from the target normal. The crystal used was RbAP in (100) reflection mode, set 250 mm away from the target. X-ray spectra from 2.6 to 3.3 keV were recorded with imaging plates [12].

10.4 Experimental Results and Discussion

Figure 10.8a and b shows the σ- and π-components for the case with an uncoated target, respectively. The σ-component appears to be slightly more intense than the π-component. I_σ and I_π are corrected using the following relations:

$$I_\sigma = \frac{I_H - I_V \cos 2\theta}{1 - \cos^2 2\theta} \ , \qquad I_\pi = \frac{I_V - I_H \cos 2\theta}{1 - \cos^2 2\theta} \ , \qquad (10.2)$$
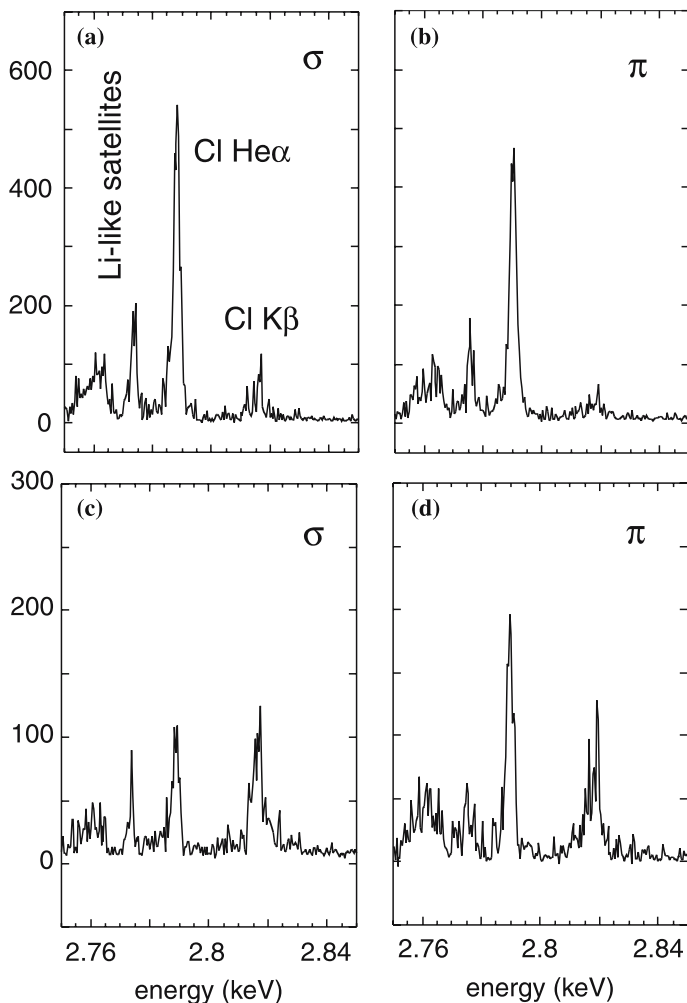
Fig. 10.8. Polarized X-ray spectra for the **a** σ component without overcoating, **b** π component without overcoating, **c** σ component with 0.05-μm-thick Ch over-coating, and **d** π component with 0.05-μm-thick CH overcoating

where I_H and I_V are the Heα line intensities measured in orientations H and V, and θ is the Bragg angle. The degree of polarization in the uncoated target is -0.08. Note that the spectral components emitted from the uncoated targets consist of emissions from both the surface and the inner deep region because of volume heating by hot electrons. Figure 10.8c and d shows the σ- and π-components for the case with the $0.05\,\mu$m-overcoated target, respectively. These spectra were clearly different from those for the uncoated targets. The intensity of the emitted π-component is higher than that of the σ-component. The degree of polarization in this case is 0.35. Under these experimental conditions, the laser-produced C_2H_3Cl plasma was optically thin for the Heα line [37], the spectra observed from the full C_2H_3Cl target is the sum of the spectra emitted from all regions of the target, while the spectrum emitted from the CH-coated target does not contain the spectrum emitted from the surface region. Therefore, the spectral component from the surface plasma alone is obtained by subtracting the spectra from the overcoated target. Furthermore, including Cl atoms from the laser–plasma interaction region had little effect on the hot electron spectrum. Consequently, P for the surface plasma corresponding to an initial thickness of $0.05\,\mu$m was -0.13. The measured VDF from hot electrons at the target surface region had a shape that was closer to that of the target surface, so it could be called a "pancake-like distribution", while that at the deeper region could be called a "cigar-like distribution". These VDFs were derived by comparing the experimentally obtained P with the result calculated by J.C. Kieffer [22], as shown in Fig. 9. At a laser intensity of $1.5 \times 10^{17}\,W/cm^2$, the quivering energy of the electrons under the laser field is nearly 30 keV, but that obtained by $J \times B$ acceleration is 120 eV [37]. Therefore, in the present study, resonance absorption dominates over the laser–plasma interaction and generates electrons whose VDF is anisotropic with respect to the target normal. This assumption is consistent with the experimental result of the cigar-like distribution in the deep plasma. The pancake-like distribution formed in the surface plasma might be due to the acceleration of electrons directly by the incident laser field. This is confirmed by preliminary calculations with a two-dimensional particle code. From these results, we can conclude that polarization spectroscopy coupled with a multilayered target is a useful diagnostic method for measuring the VDFs of hot electrons generated by ultra-high intense laser pulses [38].

References

1. Kieffer JC, Chaker M, Matte JP, Pépin H, Cotê CY, Beaudoin Y, Johnston TW, Chien CY, Coe S, Mourou G, Peyrusse O (1993) Ultrafast X-ray sources. Phys. Fluids B **5**:2676–2681

2. Rischel C, Rousse A, Uschmann I, Albouy P, Geindre J, Audebert P, Gauthier J, Foerster E, Martin J, Antonetti A (1997) Femtosecond time-resolved X-ray diffraction from laser-heated organic films. Nature **390**:490–491

3. Mackinnon AJ, Broghesi M, Hatchett S, Key MH, Patel PK, Campbell H, Schiavi A, Snavely R, Wilks SC, Willi O (2001) Effect of plasma scale length on multi-MeV proton production by intense laser pulses. Phys Rev Lett **86**:1769–1772

4. Tabak M, Hammer J, Glinsky ME, Kruer WL, Wilks SC, Woodworth J, Campbell EM, Perry MD, Mason RJ (1994) Ignition and high gain with ultrapowerful lasers. Phys Plasmas **1**:1626–1634

5. Kodama R, Norreys PA, Mima K, Dangor AE, Evans RG, Fujita H, Kitagawa Y, Krushelnick K, Miyakoshi T, Miyanaga N, Norimtsu T, Rose SJ, Shozaki T, Shigemori K, Sunahara A, Tampo M, Tanaka KA, Toyama Y, Yamanaka T, Zepf M (2001) Fast heating of ultrahigh-density plasma as a step towards laser fusion ignition. Nature **412**:798–802

6. Guethlein G, Food ME, Price D (1996) Electron temperature measurements of solid density plasmas produced by intense ultrashort laser pulses. Phys Rev Lett **77**:1055–1058

7. Disdier L, Garconnet J-P, Malka G, Miquel J-L (1999) Fast neutron emission from a high-energy ion beam produced by a high-intensity subpicosecond laser pulse. Phys Rev Lett **82**:1454–1458

8. Kitagawa Y, Sentoku Y, Akamatsu S, Mori M, Tohyama Y, Kodama R, Tanaka KA, Fuita H, Yoshida H, Matsuo S, Jitsuno T, Kawasaki T, Sakabe S, Nishimura H, Izawa Y, Mima K, Yamanaka T (2002) Progress of fast ignitor studies and petawatt laser construction at Osaka University. Phys Plasams **9**:2202–2207

9. Wharton KB, Hatchett SP, Wilks SC, Key MH, Moody JD, Yanovsky V, Offenberger AA, Hammel BA, Perry MD, Josi C (1998) Experimental measurements of hot electrons generated by ultraintense ($> 10^{19} \, \mathrm{W/cm}^2$) laser–plasma interactions on solid-density targets. Phys Rev Lett **81**:822–825

10. Hall TA, Ellwi S, Batani D, Bernardinello A, Masella A, Koenig M, Benuzzi A, Krishnan J, Pisani F, Djaoui A, Norreys P, Neely D, Rose S, Key M, Fews P (1998) Fast electron deposition in laser shock compressed plastic targets. Phys Rev Lett **81**:1003–1006

11. Pisani F, Bernardinello A, Batani D, Antonicci A, Martinolli E, Koenig M, Gremillet L, Amiranoff A, Baton S, Davies JR, Hall T, Scott D, Norreys P, Djaoui A, Rousssseaux C, Fews P, Bandulett H, Pepin H (2000) Experimental evidence of electric inhibition in fast electron penetration and of electric-field-limited fast electron transport in dense matter. Phys Rev E **62**:R5927–5930

12. Batani D, Davies JR, Bernardinello A, Pisani F, Koenig M, Hall TA, Ellwi S, Norreys P, Rose S, Djaoui A, Neely D (2000) Explanations for the observed increase in fast electron penetration in laser shock compressed materials. Phys Rev E **61**:5725–5733

13. Chen H, Soom B, Yaakobi B, Uchida S, Meyerhofer DD (1993) Hot-electron characterization from Kα measurements in high-contrast, p-polarized, picosecond laser-plasma interactions. Phys Rev Lett **70**:3431–3434

14. Jiang Z, Kieffer JC, Matte JP, Chaker M, Peyrusse O, Gilles D, Korn G, Maksimchuk A, Coe S, Mourou G (1995) X-ray spectroscopy of hot solid density plasmas produced by subpicosecond high contrast laser pulses at 10^{18}–$10^{19}\,\mathrm{W/cm^2}$. Phys Plasmas **2**:1702–1711

15. Teubner U, Uschmann I, Gibbon P, Altenbernd D, Förster E, Feurer T, Theobald W, Sauerbrey R, Hirst G, Key MH, Lister J, Neely D (1996) Absorption and hot electron production by high intensity femtosecond uv-laser pulses in solid targets. Phys Rev E **54**:4167–4177

16. Feurer T, Theobald W, Sauerbrey R, Uschmann I, Altenbernd D, Teubner U, Gibbon P, Föerster E, Milka G, Miquel JL (1997) Onset of diffuse reflectivity and fast electron flux inhibition in 528-nm-laser–solid interactions at ultrahigh intensity. Phys Rev E **56**:4608–4614

17. Rousse A, Audbert P, Geindre JP, Falliés F, Gauthier JC, Mysyrowicz A, Grillon G, Antonetti A (1994) Efficient Kα X-ray source from femtosecond laser-produced plasmas. Phys Rev E **50**:2200–2207

18. Koch JA, Key MH, Freeman RR, Hatchett SP, Lee RW, Pennington D, Stephens RB, Tabak M (2001) Experimental measurements of deep directional columnar heating by laser-generated relativistic electrons at near-solid density. Phys Rev E **65**:016410–1∼9

19. Wilks SC, Kruer WL (1997) Absorption of ultrashort, ultra-intense laser light by solid and overdense plasmas. IEEE J Quant Electron **33**:1954–1968, and references therein

20. Bell AR, Davies JR, Guerin S, Ruhl H (1997) Fast-electron transport in high-intensity short-pulse laser–solid experiments. Plasma Phys Control Fusion **39**:653–659

21. Beiersdorfer P, Slater M (2001) Measurement of the electron cyclotron energy component of the electron beam of an electron beam ion trap. Phys Rev E **64**:066408–1–6

22. Kieffer JC, Matte JP, Chaker, Beaudoin Y, Chien CY, Coe S, Mourou G, Dubau J, Inal MK (1993) X-ray-line polarization spectroscopy in laser-produced plasmas. Phys Rev E **48**:4648–4658

23. Sakabe S (1998) Fundamentals of lasers III: Ultra-short high-intesity lasers. Rev Laser Eng **26**:823–828 (in Japanese)

24. Amemiya Y (1995) Imaging plates for use with synchrotron radiation. J Synchrotron Rad **2**:13–21

25. Okihara S, Sentoku S, Sueda K, Shimizu S, Sato F, Miyanaga N, Mima K, Izawa Y, Iida T, Sakabe S (2002) Energetic proton generation in a thin plastic foil irradiated by intense femtosecond lasers. J Nucl Sci Technol **39**:1–5

26. Johzaki T et al. (2004) 2-D analysis of ignition and burn characteristics for fast ignition targets. In: Proc. 3rd Int. Conf. on Inertial Fusion Science and Applications (IFSA2003), Monterey CA, 2003, American Nuclear Society, La Grange Park IL, p 474

27. Takabe H, Ishii T (1993) Effect of nonuniform implosion on high-gain intertial confinement fusion targets. Jpn J Appl Phys **32**:5675–5680

28. Kawamura T, Nishimura H, Koike F, Ochi Y, Matsui R, Miao WY, Okihara S, Sakabe S, Uschmann I, Förster E, Mima K (2002) Population kinetics on K-alpha lines of partially ionized Cl atoms. Phys Rev E **66**:061401–1∼8

29. More RM, Warren KH, Young DA, Zimmerman GB (1988) A new quotidian equation of state (QEOS) for hot dense matter. Phys Fluids **31**:3059–3078
30. Cowan RD, Ashkin J (1957) Extension of the Thomas–Fermi–Dirac statistical theory of the atom to finite temperatures. Phys Rev **105**:144–157
31. Banes JF (1967) Statistical atom theory and the equation of state of solids. Phys Rev **153**:269–275
32. Dyall KG, Grant IP, Johnson CT, Parpia FA, Plummer EP (1989) GRASP: A general-purpose relativistic atomic structure program. Comput Phys Commun **55**:425–456
33. Fritzsche S, Fricke B (1992) Interchannel interactions and relaxation in the 2P auger spectra of Mg-like ions. Phys Scr **T41**:45–50
34. Sentoku Y, Mima K, Taguchi T, Miyamoto S, Kishimoto Y (2000) Particle simulation on X-ray emissions from ultra-intense laser produced plasmas. Phys Plasmas **5**:4366–4372
35. Sentoku Y, Mima K, Honda M, Sheng ZM, Kaw P, Nishihara K, Nishikawa K (2001) Anomalous resistivity resulting from MeV-electron transport in overdense plasma. Annu Prog Rep Inst Laser Eng, Osaka University, p 81–86, ISSN 1343–3857
36. Alfvén H (1939) On the motion of cosmic rays in interstellar space. Phys Rev **55**:425–430
37. Nishimura H, Kawamura, Matsui T, Ochi Y, Okihara S, Sakabe S, Koike F, Jhozaki T, Nagatomo H, Mima K, Uschmann I, Förster E (2003) Kα spectroscopy to study energy transport in ultrahigh-intensity laser-produced plasmas. J Quantit Spectrosc Ra **81**:327–337
38. Inubushi Y, Nishimura H, Ochiai M, Fujioka S, Izawa S (2004) X-ray polarization spectroscopy for measurement of anisotropy of hot electrons generated with ultraintense laser pulse. Rev Sci Instrum **75**:3699–3701

11 Collimated and Ultrafast X-Ray Beams from Laser–Plasma Interactions

Antoine Rousse, Kim Ta Phuoc, and Felicie Albert

Laboratoire d'Optique Appliquée (LOA) (ENSTA-CNRS-Ecole Polytechnique)
LOA-ENSTA, Chemin de la Hunière, 91761 Palaiseau cedex, France
e-mail: antoine.rousse@ensta.fr

Summary. We show that different schemes can be now followed to produce collimated X-ray radiation using laser systems. By focusing intense femtosecond laser light onto a gas jet, electrons of the plasma can be manipulated to generate ultrafast (femtosecond) X-ray radiation in the forward direction along the laser axis. In this chapter we discuss nonlinear Thomson scattering, betatron emission and Compton scattering. In years to come, the rapid development of laser technology will provide more intense laser systems. We can expect to see the creation of bright X-ray beams with a high degree of collimation ($< 1\,\mathrm{mrad}$ divergence), as well as even shorter pulse durations, down to attosecond time scales. Such sources will provide multidisciplinary scientific communities with unique tools to probe and excite matter.

11.1 Introduction

Aside from the first instant of the interaction of the laser with the matter, the X-ray radiation self-emitted from laser-produced plasmas provides an efficient diagnostic of processes that occur within such plasmas. Over the past ten years, the advent of short-duration laser systems and the progress made in the development of short-pulse X-ray sources have led to such systems being applied to multidisciplinary fields in order to probe matter.

Today, there is a strong need for increasingly short X-ray pulses that can be used to obtain ultrafast snapshots of the evolution of matter [1–4] and to study new states of matter that arise under intense X-ray irradiation. This has opened new areas of research and resulted in tremendous applications in various areas of science, including condensed matter physics, plasma physics, chemistry, biology, and engineering. Laser–plasma sources (atomic line emission) and accelerator-based technologies can now provide X-ray pulses of durations down to 100 fs, and a number of workshops, conferences and summer schools have been organized on these topics [5–9]. X-Ray Free-Electron Lasers (XFEL) at DESY (Hamburg, Germany) [1] and LCLS (Stanford, USA) [2], both of which will be capable of delivering short-pulse X-rays, are currently under development. In Japan, the Japan Science and Technology Agency has selected the field of ultrafast transitions as a priority program in condensed matter physics, and this program started in April 2004.

Laser-based X-ray sources have played a significant role in previous research in this field ever since the pioneering experiments conducted in 1997 using this technique [10]. This initial work was followed by extended experiments [11–17]. On the other hand, accelerator-based approaches have more recently provided the first results at the femtosecond time scale [18]. Despite this, their compactness and relatively inexpensive infrastructures as well as their perfect synchronization down to the femtosecond timescale with the process under study represent key advantages of the laser-based schemes.

However, their relatively small X-ray flux and/or spectral bandwidth severely hinders the efficient and broad experimental application of existing X-ray sources. In particular, few schemes that convert femtosecond visible laser light to femtosecond X-rays have been demonstrated. The principles of these sources were established more than ten years ago. Among them, the K_α X-ray source relies on inner shell electronic relaxation following excitation by electrons accelerated at moderate energies (a few tens of keV) during a laser–plasma experiment [19, 20]. Its principle is analogous to the standard "X-ray tube", with the difference that the duration of the electron bunch occurs on the femtosecond timescale thanks to the short duration of the laser pulse compared to thermionic emission (which occurs in the tube). This type of radiation has already shown its potential by enabling the first experiments in ultrafast X-ray science to be performed [10].

However, there are some important points that should be made about this existing source. First, the X-ray flux available for ultrafast experiments is severely limited due to the full divergence of the X-ray radiation [4]. This prevents the efficient development of applications. Second, the X-ray flux cannot be scaled-up due to the physics of the laser–matter interaction. Finally, the source is highly monochromatic and fairly tunable, which prevents any X-ray absorption applications.

Novel laser-based strategies must therefore be created to address these bottlenecks. The goal is to produce beams of X-ray radiation similar to the ones available at synchrotrons or the beams that the free-electron lasers will provide, but with the additional unique properties of the laser pulses being ultrafast (femtosecond time scale), and the laser system being more compact and cheaper in order to ensure high dissemination among the scientific community. In this article we will present three X-ray sources arising from the manipulation of electrons in laser-produced plasma electrostatic fields and in laser fields: nonlinear Thomson scattering, betatron radiation, and Compton scattering.

11.2 X-Rays from Nonlinear Thomson Scattering

11.2.1 Brief History

Among several schemes used to produce femtosecond or subfemtosecond pulses in the X-ray region (Fourier synthesis, the use of two short perpendicularly polarized pulses, high-order harmonics from a nonlinear medium

under an ultrafast intense laser, stimulated Raman scattering, and molecular coherence driven by electromagnetically induced transparency), nonlinear Thomson scattering [21–28] (or Larmor radiation) has the ability to generate attosecond pulses [28] and keV radiation. Such radiative emission was observed a few years ago by detecting the second and the third harmonics from a 1:053 μm laser system [27] and extending this to the thirtieth harmonic [29]. Soft X-ray emission (0.1 keV) was recently observed using intense and ultrafast laser fields [30], but the full X-ray region has not been accessed, and the expected femtosecond pulse duration has not been measured experimentally. The shortest pulses observed to date were obtained from high-order harmonics generation experiments performed in nonlinear media. Trains of 250 as pulses have been obtained in the extreme ultraviolet region that have photon energies of a few tens of eV, and 650 as Gaussian pulses have also been obtained at 90 eV photon energy [31].

11.2.2 Principle of the X-Ray Source

Thomson scattering radiation is produced as the electron oscillates in the laser field (we define the laser strength parameter as $a_0 = \frac{eE_0}{m\omega_0 c} = 0.85 \left(\frac{I_{\mathrm{W/cm^2}}}{10^{18}} \lambda_{\mathrm{\mu m}}^2\right)^{\frac{1}{2}}$). In the linear case, for $a_0 < 1$, the electron has a linear oscillating motion and radiates at the fundamental frequency (the laser frequency). Here we discuss the nonlinear case, where the motion of the electron, driven by a high-intensity laser field ($a_0 > 1$), becomes strongly nonlinear and relativistic.

The electron then radiates high-order harmonics, often called relativistic harmonics [27, 29, 30]. The radiation can be calculated from the trajectory of the electron using the formula for the radiation emitted by an accelerated charged particle [32]. This depends on the direction of observation, the position, the normalized velocity and the acceleration of the electron. The radiation is therefore anisotropic and strongly linked to the laser parameters. The angular distribution of the total power radiated by the electron, integrated over all frequencies, is displayed in Fig. 11.2. The radiation is emitted forward along two lobes centered on the directions of maximum momentum of the electron, corresponding to the angles $(\theta_{\mathrm{max}}, -\theta_{\mathrm{max}}) \sim \tan^{-1}(p_\perp/p_x)$. The divergence angle of each lobe is therefore given by $\theta_{\mathrm{max}} \sim 2/a_0$ and is directly related to the laser intensity. The spatial distribution of the radiation is broad and becomes more collimated as a_0 increases. For $a_0 = 4$ and $a_0 = 6$, the divergences are respectively $\theta = 34°$ and $\theta = 20°$. Figure 11.1 shows the spatial distribution for $a_0 = 0.1$ and $a_0 = 2$. For $a_0 = 0.1$ (nonrelativistic case), typical dipolar emission is observed, while two emission lobes are apparent for $a_0 = 2$.

The spatial distribution also strongly depends on the initial energy (longitudinal) of the electrons. If we consider that the electron has an initial energy, the component p_x of the momentum is increased, which directly results in more strongly collimated radiation. Numerical simulations show that elec-
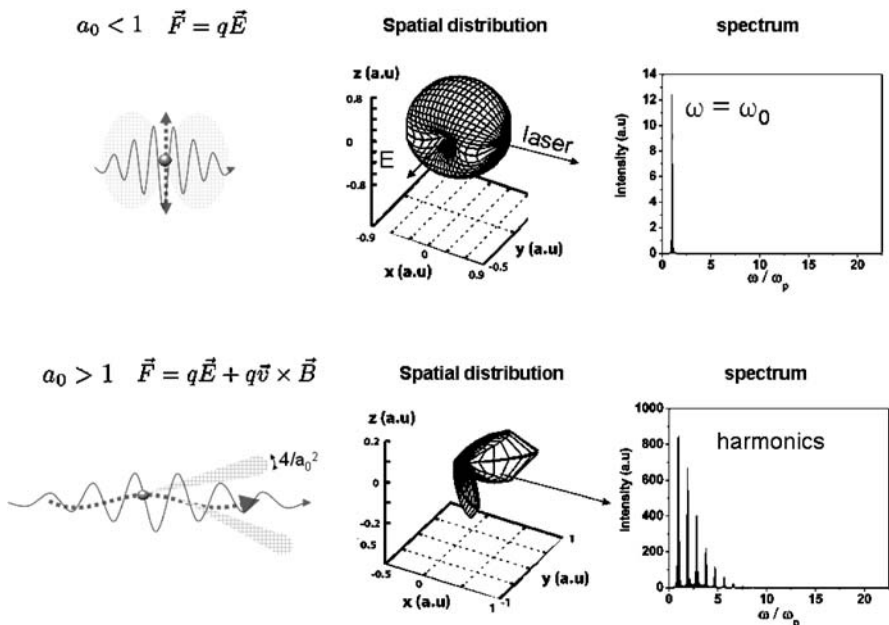
Fig. 11.1. Principle of the nonlinear Thomson scattering X-ray source. The non-linear motion of the free plasma electrons oscillating in the strong electromagnetic laser field (a_0) produces high harmonics of the fundamental laser light that can reach the X-ray spectral range. As a_0 is increased, the radiation becomes more collimated
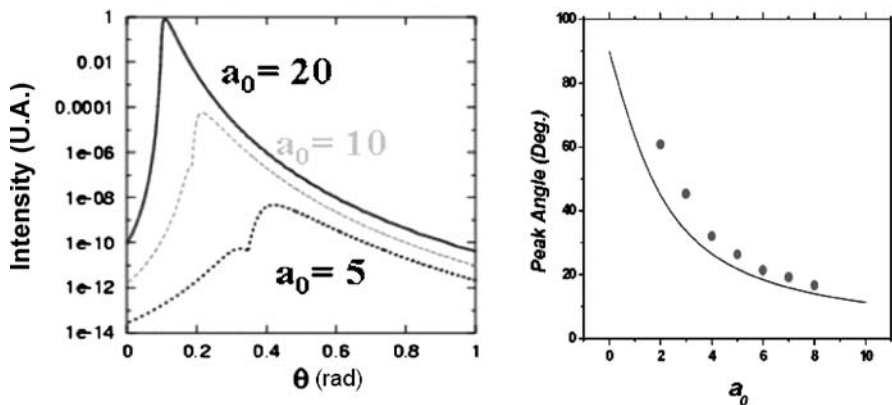
Fig. 11.2. Spatial distribution of the radiation as a function of the laser strength parameter a_0. The peak of each emission lobe depends on the backward contribution. The lobes are centered at an angle $\tan^{-1}(p_\perp/p_x) \sim 2/a_0$ in the plane of the polarization, with a width of $2/a_0^2$. $p_\perp$ and p_x are, respectively, the electron momentum perpendicular and parallel to the laser propagation axis. As a_0 is increased, the ponderomotive drift of the electron trajectory in the forward direction grows significantly, and the spatial distribution becomes more and more collimated

trons with an initial energy of 0.7 MeV produce emission centered at $\theta = 10°$ instead of 23° for the case of an electron initially at rest.

Radiation spectra calculated for different angles of emission are displayed in Fig. 11.3 for $a_0 = 4$. The spectra are broad, peaked, quasi-continuous and exhibit complex structures. They extend over several orders of magnitude of eV, and the more energetic X-rays are produced along the peak of each lobe, while the spectrum shifts to smaller energies for the other angles. The integrated (spatially) distribution function is displayed in Fig. 11.4 for two laser intensities, 10^{19} W/cm² and 10^{20} W/cm² ($a_0 = 10$). The position of the peak shifts to higher energies as a_0 increases. For lower $a_0 = 2$, 4 and 6, the peaks are respectively found at 10, 60, and 100 eV.

The shape of the spectrum significantly depends on the laser pulse duration. For an infinite plane wave, the spectrum consists of well-separated harmonics which are not at integral numbers of the laser wavelength. Their spectral separation depends on the observation angle, the laser intensity, and the initial energy of the electron. In the case of short laser pulses, the motion of the electron becomes strongly modulated in the laser pulse envelope and the consecutive harmonics overlap to form a continuous spectrum.
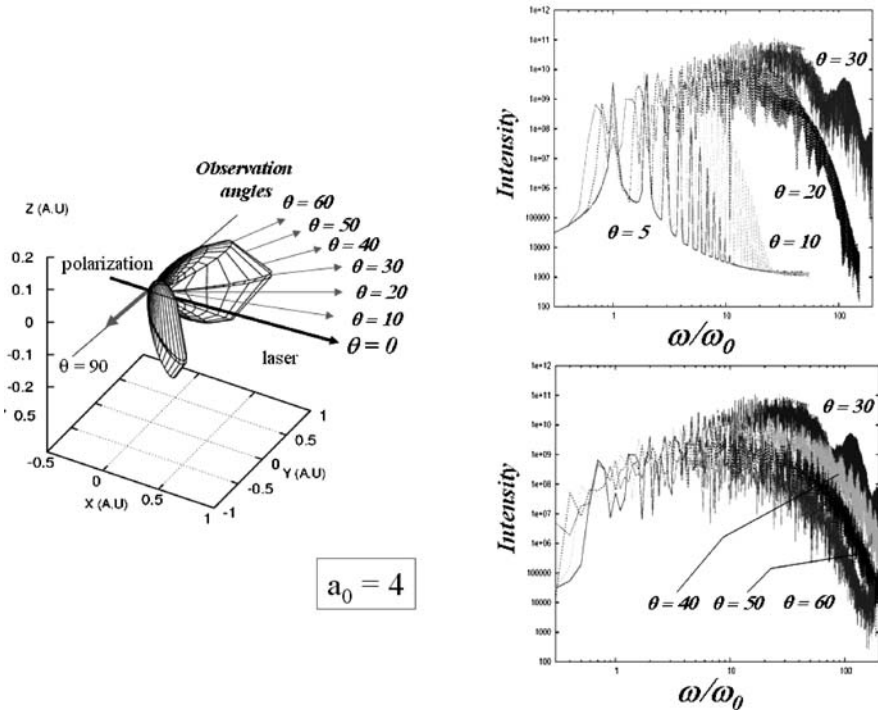
Fig. 11.3. Spectral distributions of the radiation as a function of the angle of emission for a laser strength parameter $a_0 = 4$. The more energetic X-rays are produced at the peak of each lobe of emission
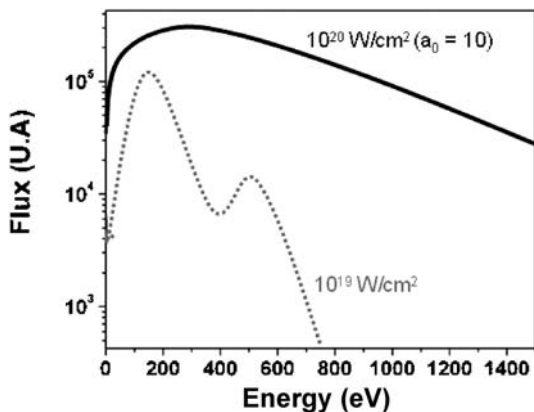
Fig. 11.4. Energy distribution functions of the radiation produced by nonlinear Thomson scattering in a laser field for two laser intensities. Radiation above $1\,\mathrm{keV}$ can be achieved for laser intensities larger than $10^{20}\,\mathrm{W/cm^2}$

11.2.3 Experiments

The experiment was performed at the Laboratoire d'Optique Appliquée (LOA) with the 30 fs and 1.5 J (50 TW) Ti:Sa laser system [33]. Laser intensities of up to $7 \times 10^{19}\,\mathrm{W/cm^2}$ were used in this particular experiment, which corresponds to a laser strength parameter $a_0 = 5.6$ for linear polarization.

The angular distribution of the X-ray radiation, integrated between 70 and 200 eV and measured in the plane of the laser polarization, is displayed in Fig. 11.5. It is found to be much broader than the theoretical width ($10°$) expected if the electron is considered to be initially at rest. It is also centered on the laser axis ($\theta = 0$) instead of $23°$ for $a_0 = 5.6$. Similar results were obtained at all the X-ray spectral bandwidths. However, as we have already discussed, the properties of the radiation produced depend on the parameters of the electrons [34]. The angular distribution is significantly modified,
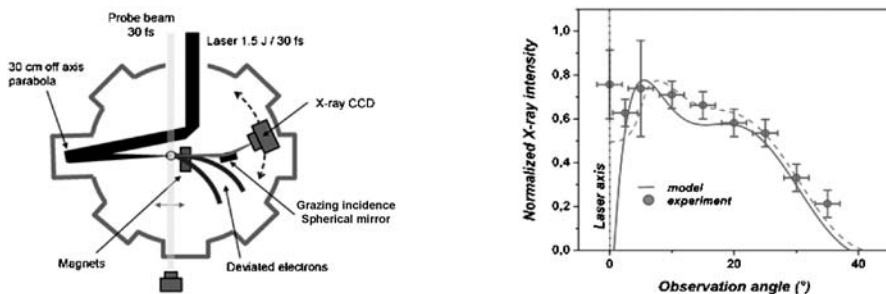
Fig. 11.5. Experimental setup (*left*) and spatial distribution function (*right*) of the radiation observed for a laser intensity $a_0 = 5.6$

broadened, and shifted toward the laser axis if the electrons experience an acceleration in addition to the laser field. This is the case in this experiment, where electrons accelerated in the forward direction have been clearly measured with radiochromic films covered by copper filters. Although the set of filters did not allow the distribution function to be characterized, the measurements indicate a strong population of electrons with energies between a few hundreds of keV and a few MeV. The fit in Fig. 11.5 takes into account an electron temperature of 0.9 MeV.

The spectrum of the radiation measured on the laser axis, at the maximum X-ray intensity and for $a_0 = 5.6$, is displayed in Fig. 11.6. A broad continuum extending from 20 to 400 eV is observed (the spectrometer did not allow characterization below 20 eV and above 400 eV). It is peaked at 100 eV, which is in close agreement with the numerical simulation done for $a_0 = 6$ and an electron energy of 1.5 MeV. The X-ray intensity then drops
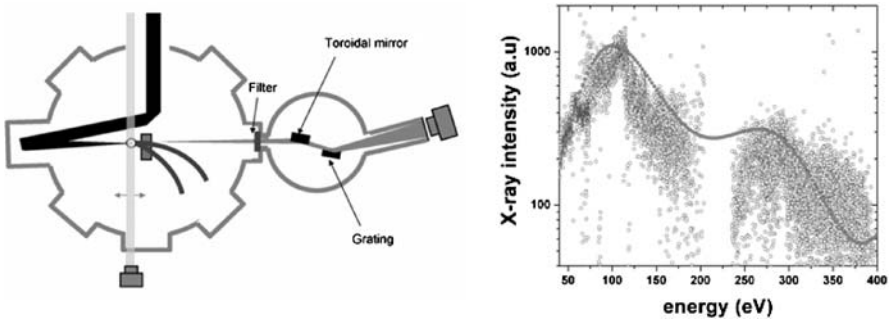
Fig. 11.6. Spectral distribution function of the radiation observed for laser intensity $a_0 = 5.6$
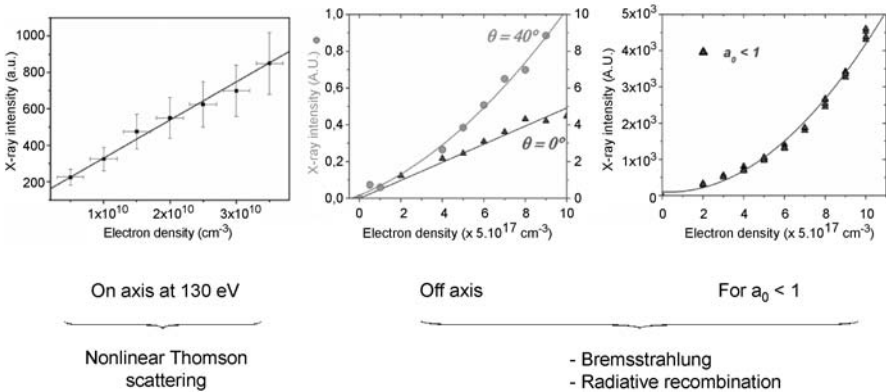
Fig. 11.7. X-ray intensity as a function of the electronic density of the plasma and the laser strength parameter. The process of nonlinear Thomson scattering for the production of X-ray emission can be observed for the highest laser intensities and along the laser axis ($a_0 = 5.6$ for the two first figures)

rapidly. The spectrum of the radiation also depends on the initial electron energy. However, in this co-propagative geometry (the laser and the electrons propagate in the same direction) this effect is weak because the Doppler shift of the laser frequency seen by the electron is counterbalanced by the Doppler shift of the emitted radiation.

Nonlinear Thomson scattering can only be observed for the highest laser intensities, as shown in Fig. 11.7. As expected from the theory, when $a_0 < 1$, the nonlinear Thomson scattering vanishes and the collisional radiative processes from the thermal plasma prevail (Bremsstrahlung and radiative recombination). For $a_0 > 1$, these latter processes are still effective, as shown by the quadratic dependency on the electronic density of the plasma observed for $\theta = 40°$. However, this isotropic thermal emission remains less intense than the collimated nonlinear Thomson scattering emission and becomes detectable only at a large angle of observation ($> 40°$).

11.3 Betatron X-Ray Radiation

11.3.1 Brief History

Laser-produced plasmas are efficient media for producing secondary radiative sources. It has been over a decade since they were first shown to produce ultrashort pulses in the X–UV or X-ray spectral regions. Nevertheless, up to now, beams of X-ray radiation have not been accessible. High-order harmonics of the fundamental laser light and the X–UV laser can generate collimated radiation with wavelengths of down to 10 nm [35–37]. On the other hand, the K_α X-ray source [4] provides subnanometer radiation, but is fully divergent. A fundamentally different approach must therefore be used to produce beams of radiation in the X-ray spectral region.

11.3.2 Principle of the X-Ray Source

In laser wakefield accelerators, the ponderomotive force of an intense femtosecond laser pulse generates, as it propagates through an underdense plasma, a large amplitude wakefield plasma wave (Fig. 11.8). This wake can break and trap plasma electrons, and then its large longitudinal electrostatic field can accelerate ultrashort pulse-duration electron beams to high energies (a few hundreds of MeV) over distances of millimeters [39]. A particularly efficient mechanism for wakefield generation occurs in the parameter regime corresponding to ultrashort laser pulses (30 fs), called the forced laser wakefield regime, which has been studied experimentally [40] as well as with 3-D particle-in-cell (PIC) simulations [40, 41]. In this regime, the wake has an electron-density depression right behind the laser pulse, leading to the formation of an ion column [41–43]. This charge displacement also results in a strong radial electrostatic field.

Longitudinal force: longitudinal acceleration

Transverse force: Transverse oscillations (Betatron)

$$\vec{F}_{res} = -m\omega_p^2 \vec{r}_\perp /2$$
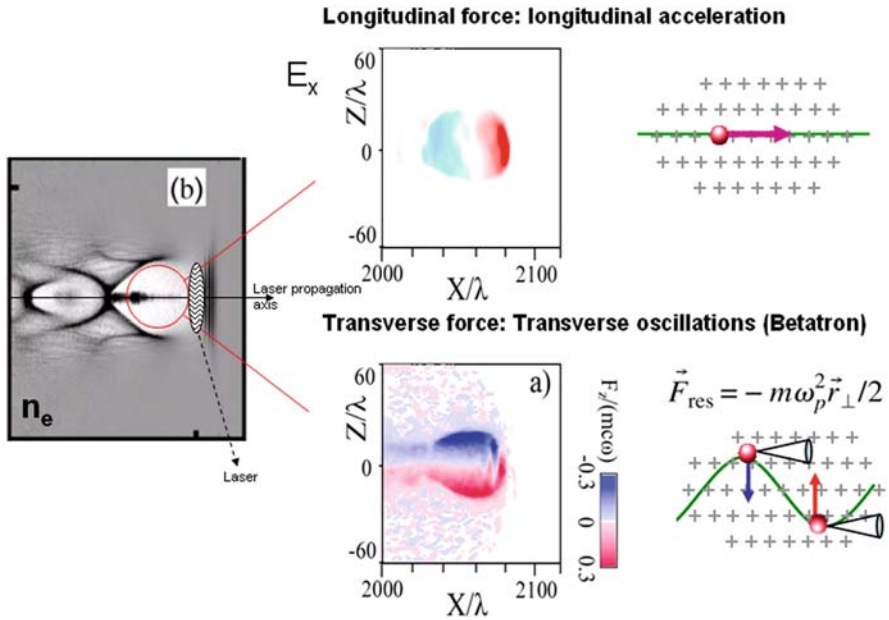
Fig. 11.8. Principle of the betatron X-ray source. As the laser beam propagates in the gas jet, the ponderomotive force in the front edge of the beam expels the electrons out of the laser axis, leaving an ion cavity in the wake of the laser. Some electrons are trapped in the back of the cavity and feel the strong electrostatic fields generated from the space charge separation (**b** shows an electronic density plot of the plasma produced by the laser; the ion cavity as well as the accelerated electron beam (encircled in *red*) can be seen in the wake of the laser propagating in the gas jet). They are longitudinally accelerated to energies of hundreds of MeV (*top right*). They also experience the transverse electrostatic field of the channel, prompting betatron oscillations which lead to the generation of a collimated beam of synchrotron radiation in the X-ray spectral domain (**a** shows a plot of the transverse force due to the space charge separation calculated from PIC simulations)

As the relativistic electrons propagate through these fields, they can undergo oscillations—called betatron oscillations—at a frequency given by $\omega_b = \omega_p/2\gamma$. Here ω_p is the plasma frequency and γ the relativistic factor of the electron. As in a conventional synchrotron, this oscillatory relativistic transverse motion produces a collimated X-ray beam [41,42,44,45]. However, because the wavelength of the wiggler can be much shorter in a laser–plasma interaction (microns) than in a synchrotron based on fixed magnets (centimeters), the distance required to produce a bright X-ray beam is much shorter (on the scale of millimeters, rather than 10 m); the required energy of the electron beam is also much lower (MeV, rather than GeV).

The oscillatory motion of the relativistic electron in the ion channel is comparable to that of an electron oscillating in an insertion device (an undulator or wiggler) of a synchrotron. Here, the ion channel acts as a wiggler

(Fig. 11.8)—or undulator—with a period λ_b and a strength parameter K given by $K = \gamma\theta = \gamma k_b r_0 = 1.33 \times 10^{-10} \, (\gamma n_e [\text{cm}^{-3}] \, r_0 [\mu\text{m}])^{0.5}$, where θ is the peak angular deflection of the electron trajectory. Consequently, as in a conventional insertion device, synchrotron radiation is emitted by the relativistic electron. The trajectory of the electron determines the divergence of the produced radiation. It consists of a narrow cone of divergence $\theta = K/\gamma$ in the forward direction. The radiation is emitted in regimes that are distinguished by the strength parameter K. For $K \ll 1$, the electron motion is near-axis and has a weak amplitude. The ion cavity then acts as an undulator and the radiation is primarily emitted at the fundamental frequency $\omega_f = \omega_b(2\gamma)^2 = 2^{0.5}\omega_p\gamma^{1.5}$, which corresponds to the betatron frequency Doppler-shifted in the laboratory reference frame. For $K > 1$, the amplitude of the electron motion is increased, the plasma acts as a wiggler, high harmonics are radiated, and broadband radiation is produced. In that case, the spectrum is described by the function $S(\omega/\omega_c)$ characteristic of the synchrotron radiation [32]. The spectral intensity increases to a frequency given by $\omega_c = (3/2)\gamma^3 c/R = (3/2)\gamma^3 cr_0 k_b^2$, where $R = 1/(r_0 k_b^2)$ is the effective radius of curvature of the electron path, and then exponentially decreases.

The average number of photons with mean energy $\hbar\omega_c$ emitted by one electron is given by [41], $N_x = 5.6 \times 10^{-3} N_0 K$, where N_0 is the number of betatron oscillations that the electron undergoes. For $\gamma = 60$, $n_e = 10^{19} \, \text{cm}^{-3}$, and an amplitude of oscillation $r_0 = 5 \, \mu\text{m}$ (obtained from PIC simulation), an X-ray beam providing 8×10^{-2} photons/electron/betatron oscillation centered at an energy of around $1 \, \text{keV}$ within a full divergence of $300 \, \text{mrad}$ can be produced. For properly chosen parameters, we therefore expect to generate an intense beam of keV radiation during the relativistic laser–plasma interaction.

11.3.3 Experiments

Betatron X-ray radiation has been observed at LOA [46, 47] using the same laser as used for the nonlinear Thomson scattering experiment described in the previous sections [33]. While the highest laser intensity on the target was necessary in that case, the betatron experiment requires rather smooth focusing (a one meter focal length parabola) to obtain the most efficient propagation of the laser into the gas jet, and allow time for the electron beam to be accelerated and wiggled. In the present case, imaging the plasma provides direct evidence of self-focusing over a few hundreds of microns.

By placing an X-ray CCD directly onto the laser axis, we have observed a beam of X-ray radiation (20 mrad divergence) in the spectral range of a few keV. The best shot is displayed in Fig. 11.9. Permanent magnets are used to deviate the energetic electrons accelerated in the plasma off-axis.

The properties of this X-ray beam are in a good agreement with the synchrotron radiation emitted by the trapped electrons undergoing betatron oscillations in an ion channel, as described by numerical simulations. The
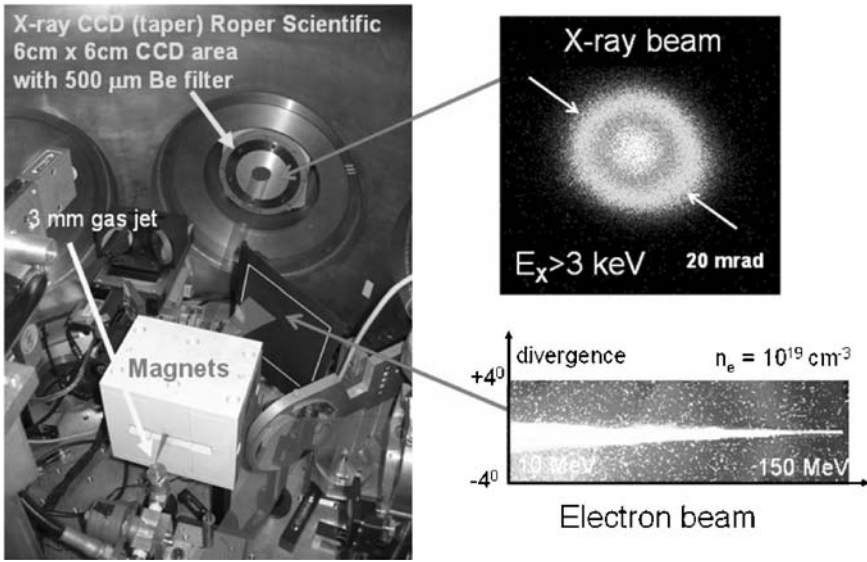
Fig. 11.9. Experimental setup used for the betatron experiment. Permanent magnets are used simultaneously to deviate the accelerated electron beam off-axis in order to make sure that the X-ray detection is unperturbed and to provide spectral information on the electron energy distribution. CCD pictures of the X-ray beam and the electron spectrum for a gas jet electronic density of $10^{19}\,\mathrm{cm}^{-3}$ are also shown

spectral distribution of the radiation was measured from 1 to 10 keV by placing a set of Be, Al, Sn, and Nb filters in front of the detector. The spectral resolution was limited by the bandwidths of the filters. The spectrum decreases exponentially from 1 to 10 keV. The total number of photons (integrated over the bandwidths of the filters and over the divergence of the X-ray beam) is found to be more than 10^8 photons (per shot/solid angle at 0.1% BW). The spectrum observed is in reasonable agreement with the test particle and PIC simulations [47], even if slight differences are observed in the shape and the total number of photons number. This is not surprising if we consider the large fluctuations of the electron spectrum and the dependence of the betatron X-ray radiation on the electron and plasma parameters.

Another unique feature of the betatron X-ray beam is its intensity as a function of the electron density of the plasma. It is found to be sharply peaked at $n_{\mathrm{e}} = 1.1 \times 10^{19}\,\mathrm{cm}^{-3}$, as shown in Fig. 11.10. Below this critical density, the X-ray signal rapidly vanishes, mainly because the number of trapped electrons is too low. This was confirmed by experiment: no electrons were detected by the spectrometer. At larger densities the X-ray signal drops and a plateau is reached. For these experimental conditions, the resulting amplitude of the plasma wave becomes too weak. The pulse must first be modulated and additional laser energy would be needed. As a result, the temperature of the electron beam decreases and its divergence increases. The PIC
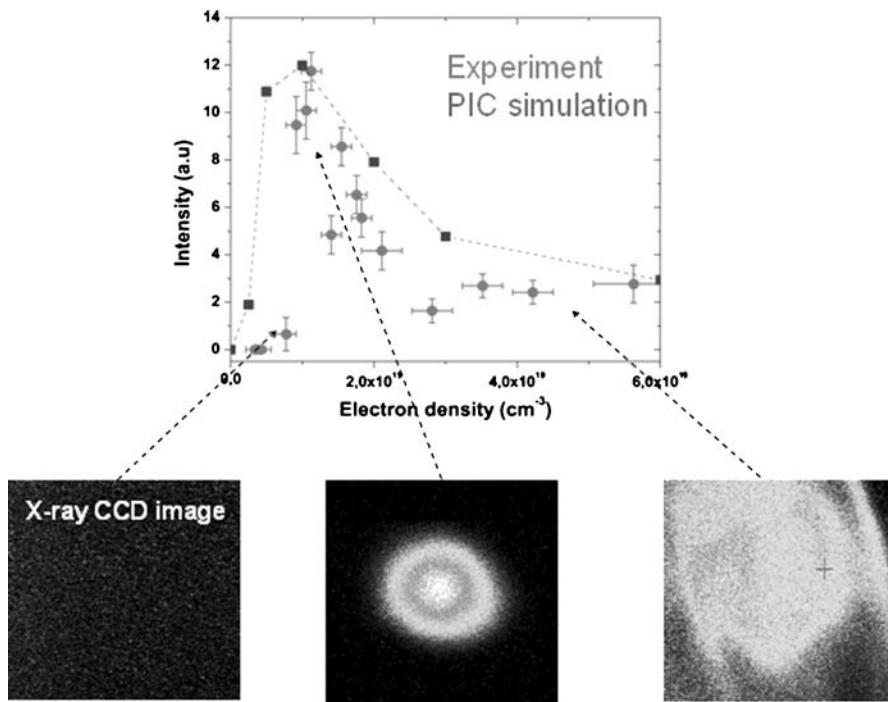
Fig. 11.10. Betatron X-ray intensity and spatial distribution in the beam as a function of the electronic density of the gas jet. Efficient X-ray beam generation is observed to occur within a sharp density range centered at $1 \times 10^{19}\,\mathrm{cm}^{-3}$

simulations clearly reproduce this experimental behavior: a sharp increase in the X-ray intensity is followed by a smoother decrease of the signal.

These results show that ultrashort-duration pulses of X-ray beams (of the same duration of the X-rays is close to the one of the laser and electron beam) can be produced by this synchrotron-like radiation mechanism in a compact device. 5×10^6 photons/pulse/s/0.1% BW were produced from these first experiments. The increase in the laser energy (i.e., the electron energy) as well as the propagation length of the laser (proportional to the number of betatron oscillations) results in a significant increase in the X-ray flux. The X-ray energy can also be extended to the harder spectral region by increasing the strength parameter K of the plasma wiggler.

11.4 Compton X-Ray Scattering

11.4.1 Brief History

The advent of relativistic electron beams generated from laser–plasma interactions opens the possibility of producing X-rays in the keV to 100 keV

range by Thomson scattering a second laser beam of lower intensity off the entire electron bunch [48]. The interaction between the electrons and the laser electromagnetic field can be described by an undulator model in which the radiation pattern is that of a relativistic oscillating dipole. The keV photon energy range is reached in the linear regime of Thomson scattering due to two large relativistic Doppler shifts: the first is on the laser frequency seen by the electron, the second is on the radiation emitted by the oscillating electrons and observed in the laboratory frame. This method has been already demonstrated using picosecond and femtosecond lasers synchronized to an RF linear accelerator (LINAC) [49–53]. Intense picosecond X-ray beams can be obtained in that case using head-on geometries. The duration of the X-ray pulse depends on the size of the interaction area, which fully depends on the sizes of the two beams as well as the angle of interaction. Different crossing techniques can then be used to keep the electron–photon superposition area small enough in the interaction region and produce subpicosecond X-ray pulses [54]. However, the X-ray flux becomes strongly attenuated, as the full population of the electron beam is not used. On the other hand, the all-optical scheme provides the unique possibility of producing perfectly synchronized (at the femtosecond time scale) and tunable femtosecond hard X-rays with laser beams used for pump–probe experiments in ultrafast X-ray science.

11.4.2 Principle of the X-Ray Source

The energy, E_{th}, of the X-rays produced depends on the interaction angle between the laser and the relativistic electron beam, φ, as well as on the angle of observation from the electron beam direction, θ. It is given by [18] as

$$E_{\mathrm{th}} = \frac{2\hbar\gamma\omega_0}{1+\gamma^2\varphi^2} \left[1 + \beta\cos\left(\theta\right)\right]$$

where ω_0 is the laser frequency, β the normalized electron velocity and γ is the relativistic Lorentz factor. The calculated spectrum of the expected X-ray pulse using a typical electron beam obtained in laser–plasma experiments [39] is displayed in Fig. 11.11. The number of few-keV X-ray photons reaches several 10^7 at a spectral bandwidth of 0.1%. The output radiation is not monochromatic due to the large broadening of the electron spectrum produced using the laser–plasma scheme. Recent results, however, show that quasi-monoenergetic electron beams with spectral widths from a few percent to 20% can now be obtained [55]. This will greatly improve the properties of the X-ray beam. In addition to its tabletop size, this source offers two principal advantages. First, it produces highly collimated hard femtosecond-pulse X-rays, and it does this over a spectral range that cannot be attained with the betatron method using laser intensities available at present.

Such ultrafast X-ray radiation is furthermore perfectly synchronized with the laser beam and could provide unique radiation properties for pump–
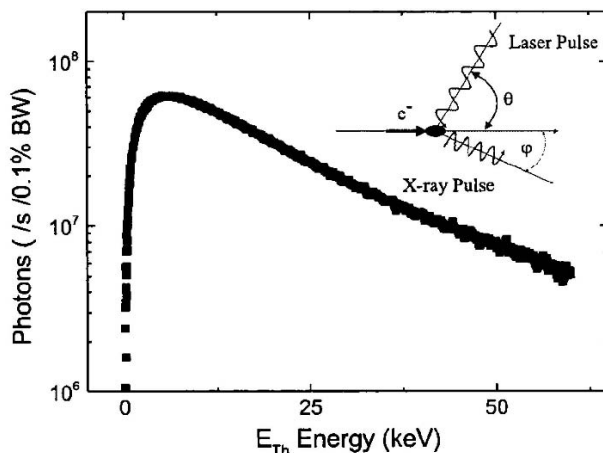
Fig. 11.11. Intensity of the X-ray radiation generated by all-optical Compton scattering using a 30 fs, 820 nm, 10 Hz and 1 J laser system

probe analysis of the ultrafast structural dynamics of matter. Second, as the period of the electromagnetic field is much shorter (micrometer scale) than a typical undulator with static magnets (centimeter scale), the electron energy required to produce hard X-rays is about a few hundred times less than in a synchrotron.

A few laboratories worldwide have started research programs aimed at experimentally demonstrating this new X-ray source. Despite several attempts, no successful or convincing experiments have been achieved to date. The advent of well-controlled (in terms of divergence, charge, energy) and stable electron beams shot-to-shot will be required to demonstrate this new scheme as well as to provide useful radiation for application experiments.

11.5 Conclusion

A new generation of laser-based X-ray sources (energy > keV) has arisen due to the advent of intense femtosecond laser systems capable of delivering intensities of $> 10^{18}$ W/cm^2 on the target. There are three main properties that have been enhanced compared to existing sources. First, collimated X-ray beams can now be produced. The betatron X-ray scheme provides 20 mrad radiation with current technology. A few mrad should be attainable in the near future using the few-hundred terawatt laser systems now under construction. A strong increase in the X-ray flux and X-ray energy is also expected in this case. 10^8 X-ray photons/shot/0.1% BW are attainable at photon energies of a few 10 keV. Second, tunability and polychromaticity are now available using the betatron source, which emulates the principle of a synchrotron. Finally, nonlinear Thomson scattering offers the unique possibility of reach-

ing attosecond pulse durations in the X-ray spectral range. This will greatly extend the range of applications of such systems, as the shortest X-ray pulse available to date is close to 100 fs.

References

1. G. Materlik, Th. Tschentscher (eds), The X-Ray Free Electron Laser (TESLA Technical Design Report). DESY, Hamburg/Zeuthen (see http://tesla.desy.de/ new_pages/TDR_CD/PartV/fel.html, last accessed 03 September 2006)
2. LCLS, Linac coherent light source website. LCLS, Menlo Park, CA (see http://www-ssrl.slac.stanford.edu/lcls/, last accessed 03 September 2006)
3. N. Bloembergen, Rev. Mod. Phys. **71**, S283 (1999)
4. A. Rousse et al., Rev. Mod. Phys. **73** (1), 17 (2001); Ch. Bressler et al., Chem. Rev. **104**, 1781 (2004)
5. ESG for ALS at Berkeley Lab, Workshop on new opportunities in ultra-fast science using X-rays, Napa, CA, USA, 2002 (see http://www-esg.lbl.gov/ Conferences%20&%20Meetings/ultrafast/index.html, last accessed 03 September 2006)
6. Hamburger Synchrotronstrahlungslabor, Winter School on ultrafast X-rays, Hamburg, Germany, 2002 (see http://www-hasylab.desy.de/conferences/ Xray-Course/, last accessed 03 September 2006)
7. Paul Scherrer Institut, Workshop on ultrafast science with electrons and X-rays, Montreux, Switzerland, 2003 (see http://sls.web.psi.ch/view.php/science/ events/uscience03, last accessed 03 September 2006)
8. Laboratoire d'Optique Appliquée, ENSTA, Summer school on ultrafast X-ray science with lasers and accelerator sources, Cargèse, France, 2003 (see http://loa.ensta.fr/ufx/, last accessed 03 September 2006)
9. Berkeley Lab, Workshop on ultrafast X-rays, San Diego, CA, USA, 2004 (see http://ultrafast2004.lbl.gov/, last accessed 03 September 2006)
10. C. Rischel et al., Nature **390**, 490 (1997)
11. C. Siders et al., Science **286**, 1340 (1999)
12. C. Rose-Petruck et al., Nature **398**, 310 (1999)
13. A. Rousse et al., Nature **410**, 65 (2001)
14. K. Sokolowski-Tinten et al., Phys. Rev. Lett. **87**, 225701 (2001)
15. A. Cavalleri et al., Phys. Rev. Lett. **87**, 237401 (2001)
16. Th. Feurer et al., Phys. Rev. E **65**, 016412 (2002)
17. K. Sokolowski-Tinten et al., Nature **422**, 287 (2003)
18. A. Lindenberg et al., Science **308**, 392 (2005)
19. A. Rousse et al., Phys. Rev. E **50** (3), 2200 (1994)
20. Ch. Reich et al., Phys. Rev. E **68**, 056408 (2003)
21. E. Esarey, S. K. Ride, and P. Sprangle, Phys. Rev. E **48**, 3003 (1993)
22. S.K. Ride et al., Phys. Rev. E **52**, 5425 (1995)
23. E.S. Sarachik and G.T. Shappert, Phys. Rev. D **1**, 2738 (1970)

24. B. Shen et al., Opt. Commun. **136**, 239 (1997)
25. Y. Ueshima et al., Laser Part. Beams **17**, 45 (1999)
26. K.J. Kim et al., Nucl. Instrum. Methods Phys. Res. A **341**, 351 (1994)
27. W.P. Leemans et al., IEEE J. Quantum Electron. **33**, 1925 (1997)
28. S.Y. Chen et al., Nature **396**, 653 (1998)
29. K. Lee et al., Phys. Rev. E **67**, 026502 (2003)
30. S. Banerjee et al., Phys. Plasmas **9**, 2393 (2002)
31. K. Ta Phuoc et al, Phys. Rev. Lett. **91**(19), 195001-1 (2003)
32. M. Hentschel et al., Nature **414**, 509 (2001)
33. J.D. Jackson, Classical Electrodynamics, 3rd ed. (Wiley, New York, 1998)
34. M. Pittman et al., Appl. Phys. B: Las. Opt. **74**, 529 (2002)
35. P. Tomassini et al., Phys. Plasmas **10**, 917 (2003)
36. Th. Brabec and F. Krausz, Rev. Mod. Phys. **72**, 545 (2000)
37. A. Tarasevitch et al., Phys. Rev. A **62**, 023816 (2000)
38. H. Daido, Rep. Prog. Phys. **65**, 1513 (2002)
39. D. Umstadter, J. Phys. D **36**, R151 (2003)
40. V. Malka et al., Science **298**, 1596 (2002)
41. A. Pukhov and J. Meyer ter Vehn, Appl. Phys. B **74**, 355 (2002)
42. I. Kostyukov, A. Pukhov, and S. Kiselev, Phys. Plasmas **10**, 4818 (2003)
43. E. Esarey et al., Phys. Rev. E **65**, 056505 (2002)
44. D. H.Whittum, Phys. Fluids B **4**, 730 (1992)
45. S. Wang et al., Phys. Rev. Lett. **88**, 135004-1 (2002)
46. C. Joshi et al., Phys. Plasmas **9**, 1845 (2002)
47. A. Rousse et al., Phys. Rev. Lett. (13) **93**, 135005-1 (2004)
48. K.Ta Phuoc et al., Phys. Plasmas **12**, 023101 (2005)
49. P. Catravas, E. Esarey, and W.P. Leemans, Meas. Sci. Technol. **12**, 1828 (2001)
50. S.C. Anderson et al., Appl. Phys. B **78**, 891 (2004)
51. A. Ting et al., Nucl. Instr. Methods Phys. Res. A **375** ABS68 (1996)
52. I.V. Pogorelsky et al., Phys. Rev. ST Accel. Beams **3**, 090702 (2000)
53. W.P. Leemans et al., Phys. Rev. Lett. **77**(20), 4182 (1996)
54. K. Chouffani et al., Nucl. Instr. Methods Phys. Res. A **495**, 95 (2002)
55. Y. Li et al., Phys. Rev. ST AB **5**, 0444701 (2002)
56. J. Faure et al., Nature **431**, 541 (2004)

12 Investigations of Relativistic Laser Plasma from Micron-Sized Ar Clusters

Yuji Fukuda and Koichi Yamakawa

Kansai Photon Science Institute (KPSI), Japan Atomic Energy Agency (JAEA),
8-1 Umemidai, Kizu-cho, Souraku-gun, Kyoto 615-0215, Japan
e-mail: fukuda.yuji@jaea.go.jp

Summary. Atomic clusters offer a unique area for studying high-intensity laser-matter interactions. When a high-intensity laser pulse interacts with a single cluster, the cluster absorbs most of the incident laser energy into its restricted small volume, producing a high-temperature "cluster plasma" which generates high-energy electrons and ions as well as bright X-rays. When a sufficiently short laser pulse is used, the laser energy is deposited before the cluster can expand, paving the way for developing laser-based debris-free ultrafast X-ray sources for time-resolved diffraction experiments. In this study, in order to understand a fundamental aspect of the laser-cluster interaction, we have carried out systematic investigations of the relativistic cluster plasmas, created by the action of superintense, ultrafast laser irradiation, by the simultaneous measurements of high-resolution X-ray emission spectra and ion energy spectra. It is found that hot electrons produced by a higher-contrast pulse shift the ion balance towards the higher charge states, which enhances both the X-ray line yield of the He-like argon ion and the ion kinetic energy.

12.1 Introduction

Recent developments in ultrashort, high-peak-power laser systems, based on the chirped pulse amplification (CPA) technique, have opened up a new regime of laser–matter interactions [1, 2]. The application of such laser pulses can currently yield laser peak intensities well above $10^{20}\,\mathrm{W\,cm^{-2}}$ at high repetition rates [3]. One of the important features of such interactions is that the duration of the laser pulse is much shorter than the typical time scale of hydrodynamic plasma expansion, which allows isochoric heating of matter, i.e., the generation of hot plasmas at near-solid density [4]. The heated region remains in this dense state for 1–2 ps before significant expansion occurs.

Recently, the development of laser-based radiation sources using cluster targets has attracted a lot of attention [5, 6]. This is because the clusters absorb most of the incident laser energy, and the absorbed energy cannot dissipate due to the finite system of clusters. This heats up the clusters significantly and leads to a number of characteristic phenomena such as enhanced emissions of X-rays in the kiloelectronvolt range [7], the generation of keV electrons [8], multiply charged ions with kinetic energies of up to 1 MeV [9], and nuclear fusion events using collisions of fast ions from deuterium clusters [10]. These sources are expected to be utilized as debris-free

X-ray sources for microscopy or lithography, electron or ion sources for table-top accelerators, and neutron sources for material damage studies.

The achievement of isochoric heating in cluster media is a promising way to develop laser-based debris-free ultrafast X-ray sources for time-resolved diffraction experiments. When a sufficiently short and intense laser pulse is used, the laser energy is deposited before the cluster can expand. A previous study predicts that X-ray emission from plasmas characterized by overcritical densities occur on time scales comparable to the laser pulse duration, whereas emission from plasmas at or below critical density may last longer than the laser pulse duration [11]. However, to establish isochoric heating in super-intense laser fields, we must avoid the formation of low-density preplasma created by a laser prepulse. The preplasma formation dramatically decreases X-ray emission yields. In order to suppress preplasma formation, we have used Pockel's cell switches to eliminate the prepulse. In addition, we have increased the cluster size using a specially designed conical nozzle, which is able to produce big clusters with an average diameter of 1.5 μm. Since the rate of cluster decay is primarily determined by the number of atoms in the cluster [12], the micron-sized clusters significantly reduce the cluster's sensitivity to the laser prepulse. These approaches guarantee direct interactions between the high-density cluster and the main fs pulse, and that isochoric heating is established.

In this study, in order to better understand the fundamentals of the laser–cluster interaction, we have carried out systematic investigations of the properties of X-ray radiation from high-density and high-temperature cluster plasma created by the action of superintense laser irradiation. The interrelationship between the X-ray radiation properties and ion kinetic energies has been examined for the first time via simultaneous measurements of X-ray radiation spectra and ion energy spectra. The time scale and mechanism of the X-ray emission process are discussed here based on a time-dependent plasma kinetics model. Moreover, in order to demonstrate the practical capabilities of the X-rays thus produced, pulse X-ray diffraction from an Si crystal using this source has been examined.

12.2 Experimental Procedure

The experiments were performed with the JAERI (Kyoto, Japan) 100 TW Ti:sapphire laser system, based on the technique of chirped pulse amplification, which was designed to generate 20-fs pulses centered at 800 nm at

Fig. 12.1. a Schematic diagram of the experimental setup: (*1*) the off-axis $f/3$ parabolic mirror, (*2*) the laser beam, (*3*) the specially designed pulsed conical nozzle, (*4*) the cluster gas jet, (*5*) the focusing spectrometer with the spherically bent mica crystal, (*6*) the vacuum-compatible X-ray CCD camera, (*7*) the ion detector for TOF measurements. **b** Typical X-ray CCD image measured at an intensity of 1.2×10^{19} W/cm^2, a pulse duration of 30 fs and a laser contrast of 5×10^{-6}. **c** Ion energy spectrum calculated from the ion TOF spectrum measured at an intensity of 3×10^{18} W/cm^2, a pulse duration of 30 fs and a laser contrast ratio of $C = 5 \times 10^{-6}$

(a)

(b)

(c)
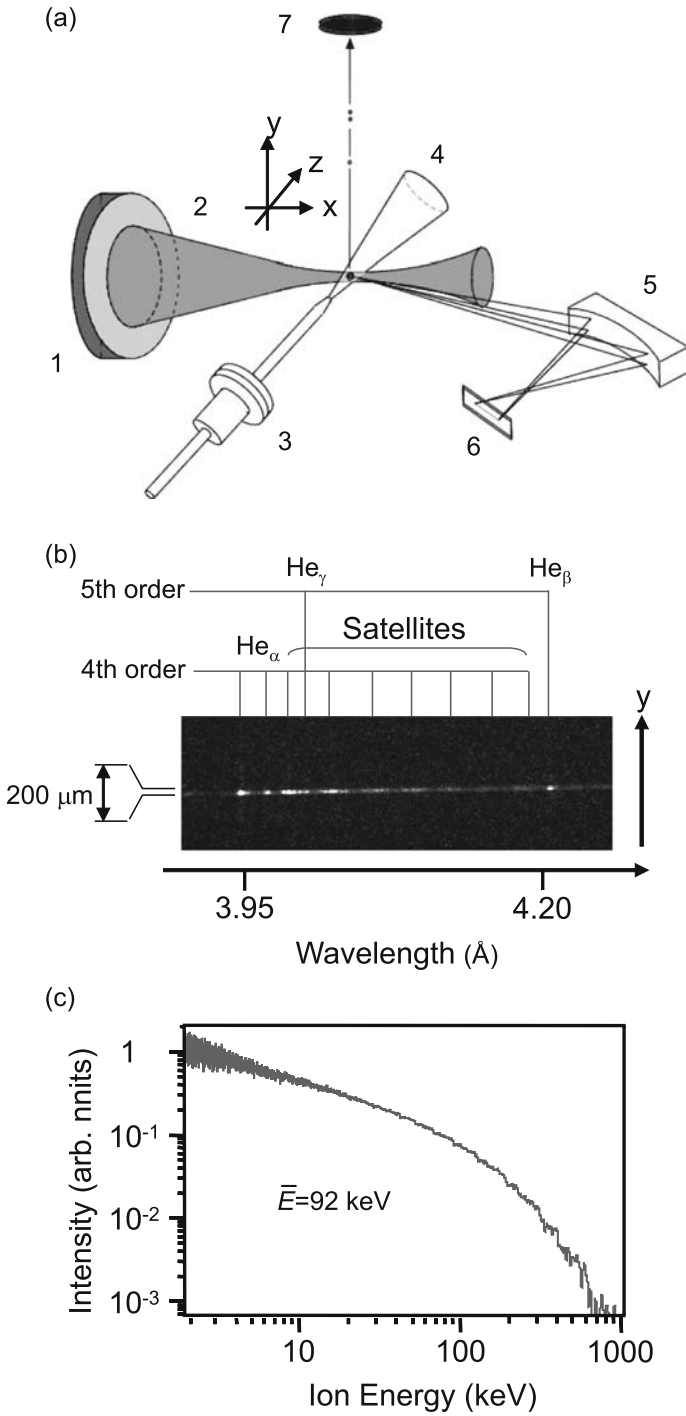
a repetition rate of 10 Hz and is capable of producing a focused intensity of up to 10^{20} W cm^{-2} [13]. The laser pulses centered at 800 nm were generated at 82.7 MHz by a Ti:sapphire laser oscillator (10-fs duration). The pulses from the oscillator were stretched to 1 ns, and amplified by a regenerative amplifier and two stage of a multipass amplifier. In this study, the amplified pulses were compressed to 30 fs by a vacuum pulse compressor yielding a pulse energy of 320 mJ. In this system, after the regenerative amplifier, the pulses go through two double Pockels cells to reduce the prepulse intensity. The contrast ratio, i.e., the ratio of the prepulse power to the laser power at the maximum of the main femtosecond pulse, was varied from $C = 2 \times 10^{-2}$ to 5×10^{-6}.

A schematic diagram of the experimental setup in JAERI is shown in Fig. 12.1a. The compressed pulses were introduced in a vacuum target chamber using a pair of Au-coated plane mirrors and focused using an $f/3$ Au-coated off-axis parabolic mirror. The measured spot size was 11 μm at $1/e^2$, which was 1.1 times as large as that of the diffraction limit. Approximately 64% of the laser energy was contained in an 11-μm Gaussian spot. These parameters give a focused laser peak intensity of 1.0×10^{19} W cm^{-2} with a pulse duration of 30 fs and a pulse energy of 200 mJ.

Ar clusters were produced by expanding a high-pressure ($p = 60$ bar) Ar gas into vacuum through the specially designed pulsed conical nozzle; the input and output diameters of the nozzle were 0.5 and 2.0 mm, respectively, and its length was 75 mm. The parameters of the nozzle were obtained from numerically modeling a cluster target using the code developed at the Institute of Mathematical Modeling of RAS [14]. Using this nozzle, Ar clusters with an average diameter of 1.5 μm could be produced without additional cooling of the nozzle [15]. Figure 12.2 shows some results from 2D-hydrodynamic calculations for the two-phase argon jet at different values of gas pressure at the cross-section positioned 1.5 mm downstream from the nozzle outlet. It shows that, at a gas pressure of 60 bar, the average diameter of the clusters increases rapidly to about 1.5 μm, and is almost constant in the cross-section of the gas jet. It is also seen that the cluster concentration and the gas-phase concentration do not change in the cross-sectional area near the axis.

The laser beam was focused 1.5 mm downstream from the nozzle. The spatially resolved X-ray spectra were measured using a focusing spectrometer with spatial resolution (FSSR-2D) [16]. This spectrometer was equipped with a spherically bent mica crystal ($R = 150$ mm) and a vacuum-compatible X-ray CCD camera (DX420-BN, Andor). The X-ray spectrum was recorded on the CCD camera through a 12-μm-thick mylar film and a 2-μm-thick polypropylene film coated with a 0.4-μm-thick aluminum layer (see Fig. 12.1b). The spherically bent mica crystal was placed 381.2 mm from the focusing point and was centered at $\lambda = 4.05$ Å, which corresponds to a Bragg angle of 54.3° for the fourth reflection order of the mica crystal. A pair of strong magnets were placed in front of the crystal to deflect the energetic electrons and ions. The reflection plane of the spectrometer was oriented along

(a)

n_{clust}, cm^{-3}

10^{10}
10^{9}
10^{8}
10^{7}
10^{6}

0.0   0.5   1.0   1.5   2.0

(b)

$n_{at}, 10^{19} cm^{-3}$

3.0
2.5
2.0
1.5
1.0
0.5
0.0

0.0   0.5   1.0   1.5   2.0

(c)

$\langle r \rangle$, μm

0.8
0.7
0.6
0.5
0.4
0.3
0.2
0.1

60 bar

40 bar

20 bar

0.0   0.5   1.0   1.5   2.0

X (mm)

(d)

$\langle d \rangle$, μm

20
16
12
8
4
0

0.0   0.5   1.0   1.5   2.0

X (mm)
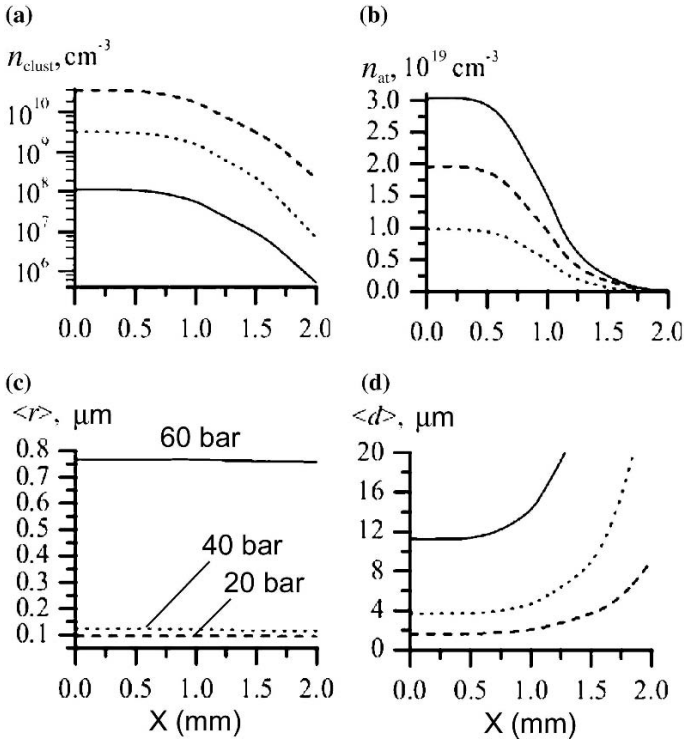
Fig. 12.2. 2-D calculations of axial radial profiles for the parameters of a two-phase Ar jet at the cross-section positioned 1.5-mm downstream from the nozzle outlet. The *solid*, *dotted*, and *broken lines* represent argon gas pressures of 60, 40, and 20 bar, respectively: **a** the mean cluster concentration, n_{clust}; **b** the gas-phase concentration n_{at}; **c** the mean cluster radius $\langle r \rangle$; **d** the mean distance between clusters $\langle d \rangle$

the direction of laser beam propagation to obtain spatial resolution in the transverse direction.

In this study, in parallel with the X-ray measurements, the kinetic energies of multiply-charged ions, Ar^{q+}, ejected from the laser–cluster interaction region were measured by a time-of-flight (TOF) method. The 737-mm-long flight tube was oriented perpendicularly to both the cluster beam and laser polarization axes (see Fig. 12.1a). The ions fly through the field-free region, and are detected by dual microchannel plates (MCP; F4655-12, Hamamatsu).

The measurements were carried out with various laser peak intensities, pulse durations and contrast ratios. We used a half-wave plate and two polarizers to change the laser energy. The original position of the grating, which gives a 30-fs pulse, was determined with high accuracy from ionization rates

for Xe atoms in a separate experiment; the signal intensities of Xe^{8+} and Xe^{9+} were measured as a function of the grating position using a TOF mass spectrometer [3].

12.3 K-Shell X-Ray Emission Spectra of Ar Clusters

Figure 12.3a shows the typical K-shell X-ray emission spectrum obtained from the CCD image measured at the highest peak intensity of $I = 1.3 \times 10^{19}\,\mathrm{W\,cm^{-2}}$ with a 30-fs pulse duration, and an Ar gas pressure of $p = 60\,\mathrm{bar}$. The spectrum was obtained by accumulating for 60 seconds (600 laser shots). To decrease the effect of the prepulse, a contrast ratio of $C = 5 \times 10^{-6}$ was achieved. Resonant ($He_{\alpha 1}$) and intercombination ($He_{\alpha 2}$) lines from the $1s2p$–$1s^2$ transition in He-like Ar ions (Ar^{16+}) were observed in the fourth reflection order as well as clearly resolved structure from collisional and dielectronic satellite lines from Li-like Ar ions (Ar^{15+}). The radiation lines from autoionizing states $1s2s^l2p^m$ of multiply charged Be- (Ar^{14+}) to F-like (Ar^{9+}) ions were also observed. Moreover, the Rydberg He-like lines from the $1snp$–$1s^2$ ($n = 3$–6) transition were observed in the fifth order in the same spectral record together with dielectronic satellites from the $1s3p$–$1s^2$ line. No emission from the $2p$–$1s$ line from H-like ions (Ar^{17+}) was observed. In contrast to the typical hard X-ray emissions from solid targets, only a small amount of K_α emission was observable, showing that almost all of the atoms that constituted the clusters were ionized to higher charge states at an early stage of the laser–cluster interaction.

The observation of intense satellite structures caused by transitions in multiply charged Ar ions (Be- to F-like) is a typical feature of femtosecond laser-produced plasma; nanosecond laser-produced plasma contains only strong He- and Li-like ions [17]. Moreover, as shown in Fig. 12.3b, the relative intensities of the collisional satellites q,r,a–d in Li-like satellites are much greater than those of the dielectric satellites k,j; in the case of nanosecond laser-produced plasma the intensities of collisional satellites are much less intense than those of dielectric satellites. According to kinetic calculations [18], the domination of q,r,a–d collisional satellites are due to enhanced excitation in the presence of hot electrons in the keV range, while in the absence of hot electrons the intensities of the k,j dielectric satellites are much greater than those of the collisional satellites. From the relative intensity of the $He_{\alpha 1}$ line and the $He_{\alpha 2}$ line, the plasma electron density was estimated as being $N_e \sim 2 \times 10^{22}\,\mathrm{cm^{-3}}$ [11]. It should be noted that this density

Fig. 12.3. a The time-integrated X-ray emission spectrum of laser-irradiated micron-sized Ar clusters measured at an intensity of $1.3 \times 10^{19}\,\mathrm{W/cm^2}$, a pulse duration of 30 fs, and a contrast ratio of $C = 5 \times 10^{-6}$. **b** Enlarged spectrum of **a** in the vicinity of the Li-like line structure

(a)

(b)
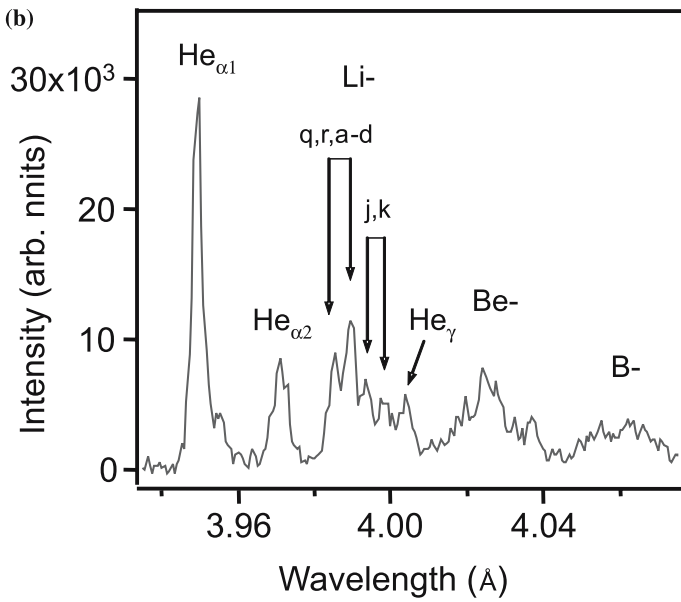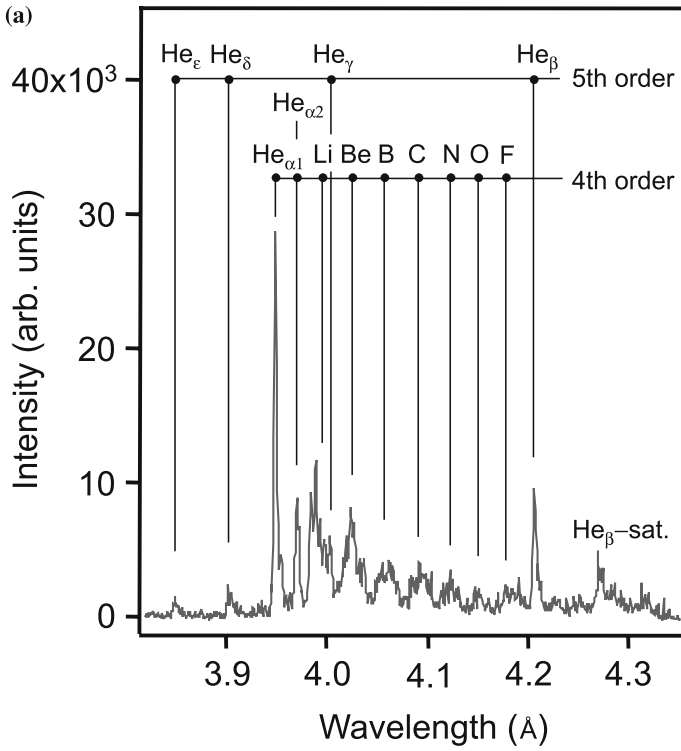
is about ten times greater than that of the critical density for Ti:sapphire lasers ($N_{crt} = 1.7 \times 10^{21}$ cm^{-3}). The X-ray radiation from such overcritically dense plasma is expected to be utilized as ultrafast (fs–ps) X-ray sources for time resolved X-ray diffraction measurements.

12.3.1 Size of X-Ray Emission Zone

The size of the emission zone for the He$_{\alpha 1}$ line was measured as $\sim$200 μm (see Fig. 12.1b). This dilation of the X-ray spot size relative to the laser focus spot size (11 μm at $1/e^2$) might be caused by laser beam deviation, cluster expansion due to the laser prepulse, or the caustic of the focusing system. Since the pointing stability of the focal spot of the laser at the laser–cluster interaction region is less than ± 5 μm, it would not severely contribute to increasing the X-ray emission zone. The influence of cluster expansion can be neglected due to the micron-sized cluster's insensitivity to the laser prepulse. At a prepulse intensity of about 10^{13} W cm^{-2}, ionization only occurs in a peripheral region and the cluster core can be treated as being frozen [19]. The factor most probably to blame is the caustic resulting from an off-axis parabolic mirror. Since the laser intensity inside a spot diameter of 200 μm is very high ($\sim 10^{17}$ W cm^{-2}), this laser intensity is strong enough to produce He-like Ar [18].

12.3.2 Laser Intensity Dependence of X-Ray Emission Spectra

Figure 12.4 shows the laser intensity dependence of X-ray emission spectra measured at a pulse duration of 30 fs with $C = 5 \times 10^{-6}$. As the laser intensity increased, the X-ray yields increased in proportion. The Rydberg He-like lines from the $1snp$–$1s^2$ ($n = 3$–6) transitions and the dielectronic satellites from the $1s3p$–$1s^2$ transition were especially enhanced, which shows that highly excited states of He-like Ar ions were produced due to intensive ion-election collisions.

12.3.3 Cluster Size Dependence of X-Ray Emission Spectra

Figure 12.5 shows the cluster size dependence of X-ray emission spectra. The top, middle, and bottom curves represent the spectra measured with a laser contrast of $C = 4 \times 10^{-4}$ at Ar gas pressures of 60, 50, and 40 bar, respectively. Note that no X-rays were observed at an Ar gas pressure of 40 bar. According to hydrodynamic calculations (see Fig. 12.2), at 40 bar, a cluster with an average diameter of 200 nm is one order of magnitude smaller than that with an average diameter of 1.5 μm at 60 bar. Thus, in the case of the 40-bar experiment, the clusters were almost completely destroyed by the prepulse. This result demonstrates the important role of big clusters, and the validity of the nozzle design.
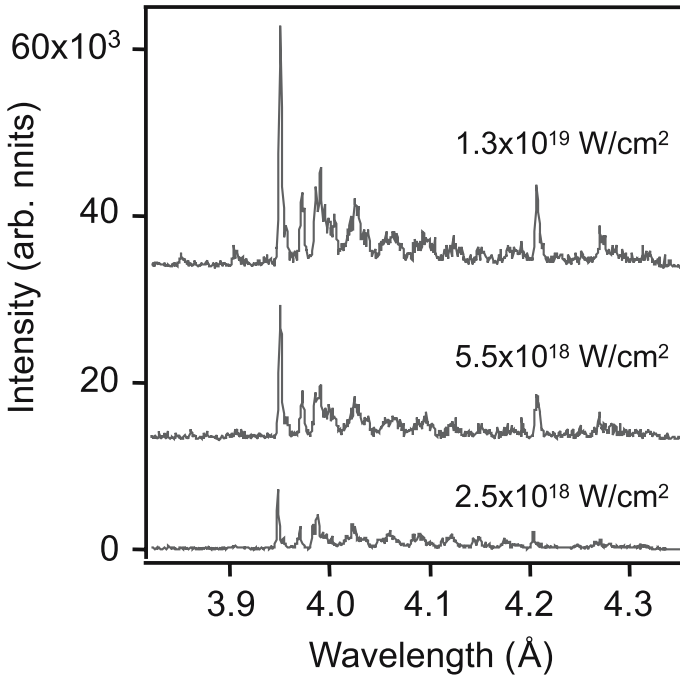
Fig. 12.4. The laser intensity dependence of X-ray emission spectra measured with a pulse duration of 30 fs and a contrast ratio of $C = 5 \times 10^{-6}$: $1.2 \times 10^{19}\,\mathrm{W/cm^2}$ (*top curve*); $6 \times 10^{18}\,\mathrm{W/cm^2}$ (*middle curve*); $3 \times 10^{18}\,\mathrm{W/cm^2}$ (*bottom curve*)

12.3.4 Estimation of X-Ray Flux

The absolute number of X-ray photons N_{phot} for the $\mathrm{He}_{\alpha 1}$ resonant line of Ar ($\lambda = 0.39491\,\mathrm{nm}$, $3.14\,\mathrm{keV}$) was estimated by considering isotropic emission over all of the solid angle 4π and using the relation

$$N_{\mathrm{phot}} = \frac{4\pi}{\Omega} \left(\frac{3.65}{3.14 \times 10^3} N \cdot g_{\mathrm{CCD}} \right) \left(t_{\mathrm{acq}} \cdot \tau_{\mathrm{filt}} \cdot \rho_{\mathrm{cryst}} \cdot \rho_{\mathrm{CCD}} \right)^{-1}, \quad (12.1)$$

where N is the number of CCD counts per pixel, g_{CCD} is the CCD gain, t_{acq} is the acquisition time, τ_{filt} is the filter transmission, ρ_{cryst} is the crystal reflectivity, ρ_{CCD} is the quantum efficiency of the CCD sensor, and $\Omega = \Delta x \Delta y / a^2$ is the solid angle from the target which contains X-ray radiation. Here, $\Delta x \Delta y$ is the size of the reflected zone on the crystal, while a is the distance between the target and crystal for the $\mathrm{He}_{\alpha 1}$ line. In our experiment, $\Delta x = 0.032\,\mathrm{mm}$, $\Delta y = 3.4\,\mathrm{mm}$, $a = 376\,\mathrm{mm}$, $N = 7040$ electrons per pixel, $g_{\mathrm{CCD}} =$ seven electrons per A/D, $t_{\mathrm{acq}} = 60\,\mathrm{s}$, $\tau_{\mathrm{filt}} = 0.8$, $\rho_{\mathrm{cryst}} = 0.01$, and $\rho_{\mathrm{CCD}} = 0.92$, so N_{phot} was estimated to be 2×10^9 photons $\mathrm{s^{-1}}$ $\mathrm{pixel^{-1}}$.
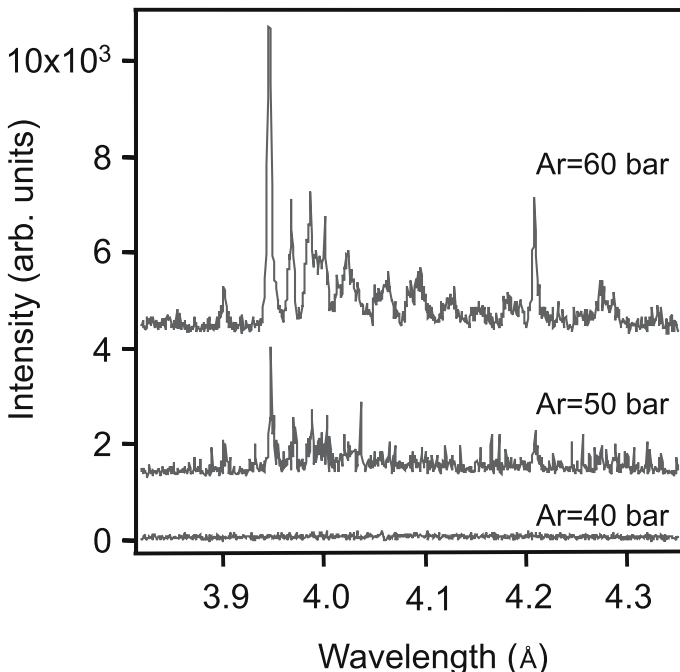
Fig. 12.5. The cluster size dependence of X-ray emission spectra measured at an intensity of $3 \times 10^{18}\,\mathrm{W/cm^2}$, a pulse duration of $30\,\mathrm{fs}$, and a laser contrast of 4×10^{-4}: Ar = 60 bar (*top curve*); Ar = 50 bar (*middle curve*); Ar = 40 bar (*bottom curve*)

12.4 Interrelationship Between X-Ray Emission Properties and Ion Kinetic Energies

12.4.1 Ion Energy Spectra of Laser-Irradiated Ar Clusters

In order to investigate the interrelationships between X-ray emission properties and the kinetic energy of the ions, in parallel with the X-ray measurements, the kinetic energies of the multiply charged ions (Ar^{q+}) emitted from the laser–cluster interaction region were measured using the TOF method [20]. The ion energy spectrum was obtained by translating the TOF spectrum into an energy distribution function for the ions using the relation,

$$f(E) = f(t)(\mathrm{d}E/\mathrm{d}t)^{-1} = f(t)m_\mathrm{i}^{-1}l^{-2}t^3 \ , \tag{12.2}$$

where E is the ion kinetic energy, m_i the ion mass, l the length of the flight tube, and t the flight time. The mean ion energy, $\bar{E}_\mathrm{ion}$, defined as,

$$\bar{E}_\mathrm{ion} = \int Ef(E)\mathrm{d}E / \int f(E)\mathrm{d}E \ , \tag{12.3}$$

was evaluated from the ion energy distribution. The uncertainty in the value of $\bar{E}_{\mathrm{ion}}$ thus obtained is estimated to be less than $\pm2\%$. Figure 12.1c shows the typical ion energy spectrum obtained at a laser intensity of $I = 3 \times 10^{18}\,\mathrm{W\,cm^{-2}}$, a pulse duration of 30 fs, and for a laser contrast of $C = 5 \times 10^{-6}$. The maximum ion energy observed is as high as $E_{\mathrm{max}} = 800\,\mathrm{keV}$, and the mean ion energy was calculated as $\bar{E}_{\mathrm{ion}} = 92\,\mathrm{keV}$. The number of ions produced in a $4\pi sr$ solid angle with kinetic energies of $100\pm1\,\mathrm{keV}$ is estimated as $\sim10^{9}$ per pulse by taking into account the quantum efficiency and gain of the MCP detector and assuming asymmetric emission of energetic ions. Similar ion energy spectra are measured with different laser contrasts and pulse durations.

12.4.2 Laser Contrast Dependence

The laser contrast dependences of the X-ray and ion energy spectra were investigated. Figure 12.6a shows the laser contrast dependence of the X-ray spectra. The upper curve is obtained at an intensity of $3 \times 10^{18}\,\mathrm{W\,cm^{-2}}$ and a laser contrast of $C = 5 \times 10^{-6}$. In this case, the intense resonance line $(\mathrm{He}_{\alpha1})$ of He-like argon ions is observed. However, as shown in the lower curve, the observed spectrum changes dramatically as the laser contrast is changed from 5×10^{-6} (smaller prepulse) to 2×10^{-2} (greater prepulse). The line yield of He-like argon ions decreases significantly and X-ray emission from Be-like argon ions is dominant. This can be explained by the important role of the laser prepulse. With the greater prepulse, the intensity of the prepulse is about $10^{16}\,\mathrm{W\,cm^{-2}}$. This is quite enough to ionize the clusters, and the main pulse interacts with a lower density preplasma. In this case, it is difficult to produce Ar ions with higher charge states by electron impact ionization.

On the other hand, the dependence of the laser contrast on the mean ion energy is shown in Fig. 12.6b. The mean ion energy increases slightly with the laser contrast. These results demonstrate that hot electrons produced by high-contrast pulses (smaller prepulses) shift the ion balance towards more highly charged states, which enhances both the X-ray yield of the He-like argon ion and the hydrodynamic/Coulombic pressure.

12.4.3 Pulse Duration Dependence

The pulse duration dependences of the X-ray and ion energy spectra were investigated at a fixed laser energy of 49 mJ, which corresponds to an intensity of $3\times10^{18}\,\mathrm{W\,cm^{-2}}$ at a pulse duration of 30 fs. As shown in Fig. 12.7, the mean ion energies for various pulse durations with positive and negative chirps do not change within the experimental uncertainty, although an increase in the pulse duration slightly increases the X-ray yield (see Fig. 12.8a). This result is in contrast to previous results for nanometer-sized clusters, where

(a)

(b)
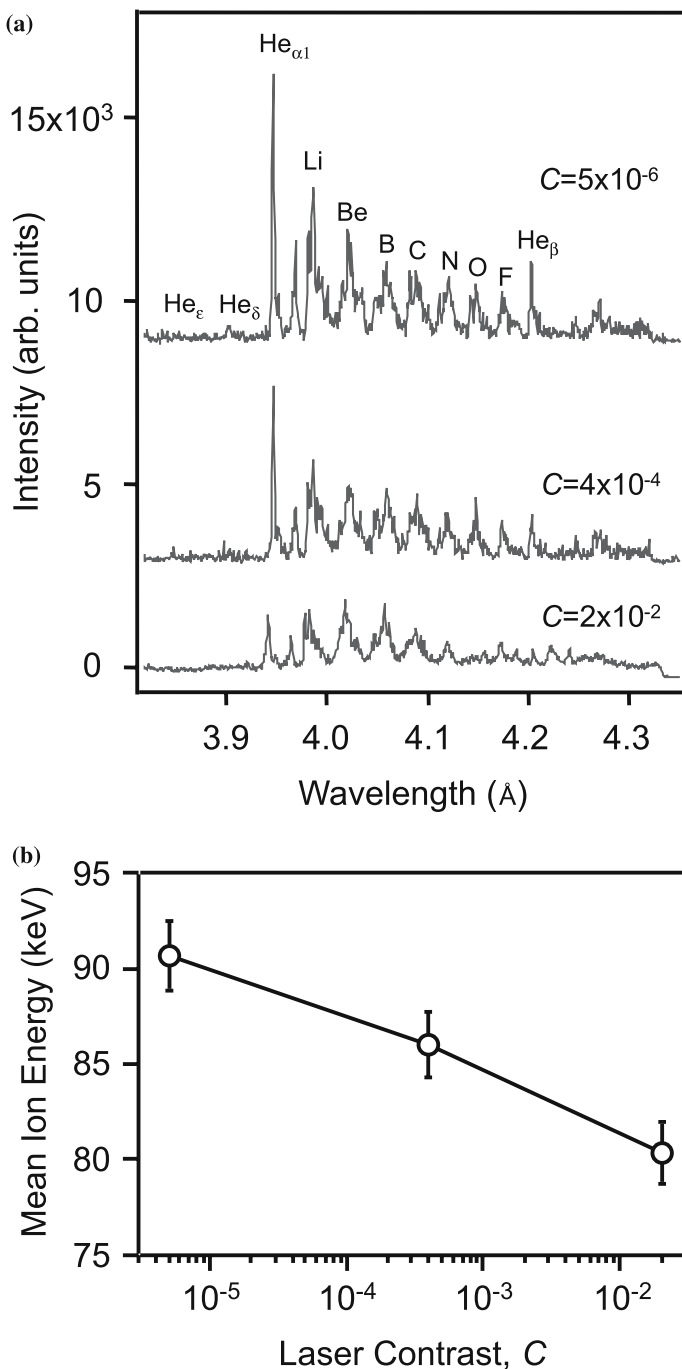
Fig. 12.6. The laser contrast dependence of **a** the X-ray spectrum and **b** the mean ion energy measured at an intensity of 3×10^{18} W/cm^2 and a pulse duration of 30 fs
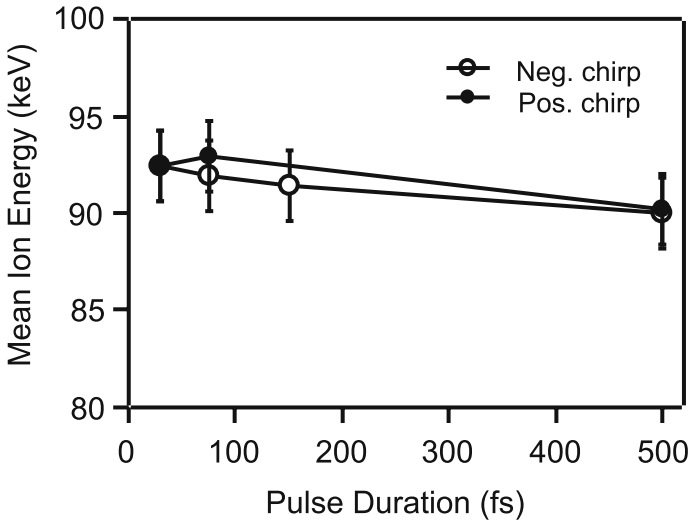
Fig. 12.7. The pulse duration dependence of the mean ion energy measured at a fixed laser energy of 49 mJ and a laser contrast of 5×10^{-6} with positive and negative chirps

it was shown that the influence of the pulse duration on the ion energy distribution and the X-ray yield is significant [21–23]. If we assume uniform, sonic expansion of the cluster plasma, the important role of the pulse duration in the laser–cluster interaction is interpreted in relation to the cluster lifetime,

$$\tau_{\text{ex}} \approx (N_{\text{e}}/N_{\text{crit}})^{1/3} R/C_{\text{s}} , \tag{12.4}$$

the time taken for clusters to expand to the surrounding ambient gas density, where R is the initial cluster radius, C_{s} is the plasma sound speed, N_{e} is the initial electron density of the cluster, and N_{crit} is the critical electron density [12]. For nanometer-sized clusters, a pulse duration of several hundred femtoseconds is well-suited to maximizing the resonant heating, where the electron temperature and the cluster expansion velocity increase dramatically. However, for micron-sized clusters with much longer lifetimes, it is obvious that the several hundred femtosecond time scale is too short to realize the resonant heating.

To further confirm this result, the kinetic energies of He-like argon ions were evaluated from the Doppler profile of the He$_{\alpha 1}$ line. Figure 12.8a shows how the He$_{\alpha 1}$ line shape changes with pulse duration for a fixed laser energy of 49 mJ. The solid, dotted and broken lines are Doppler profiles obtained by fitting the central parts of the lines to the experimental data. The corresponding values of line width are indicated on the plot. Figure 12.8b shows the difference in intensity between experimental data and calculations, which represents the contribution from fast ions to the line intensity in the blue

Fig. 12.8. a The pulse duration dependence of the He$_{\alpha 1}$ line shape for a fixed laser energy of 49 mJ. *Open circles*, *triangles*, and *squares* represent experimental data for pulse durations of 30, 500, and 1000 fs, respectively. The *solid*, *dotted*, and *dashed lines* represent Doppler profiles obtained by fitting the central part of the line to the experimental data. **b** The pulse duration dependence of the kinetic energies of He-like argon ions calculated from the Doppler shift

wing and thus relates to the fast ion energy distribution function. The values are normalized to the corresponding maximum intensity at the center of the He$_{\alpha 1}$ line. The ion energy was calculated from the Doppler shift by the relation

$$E = \frac{Mc^2}{2}\left(\frac{\lambda_0 - \lambda}{\lambda}\right)^2 , \qquad (12.5)$$

where M is the ion mass and λ_0 is the transition wavelength. The results show that as the pulse duration increases the relative contribution to the X-ray yield in the He$_{\alpha 1}$ line from fast ions decreases, although the mean and maximum energies of the fast ions do not change significantly. This result is consistent with the trends observed in direct ion energy measurements. Moreover, it is found that the bulk component of the fast ion energy is smaller than the mean ion energy of $\bar{E}_{\mathrm{ion}} = 92$ keV calculated from the direct ion energy measurement. This result indicates that, at the time of He$_{\alpha 1}$ line emission, most of the He-like argon ions are located in the high-density central part of cluster plasma. More elaborate examination of the electric field structures and the electron density structures is required to conclusively determine the time evolution of micron-sized clusters.

12.5 Time Scale and Mechanism of X-Ray Emission Process

X-ray emissions from highly ionized ions are expected to occur over a very short time, because fast electrons, which give rise to highly ionized ions, are only produced during the laser pulse, and because a recombination process could quickly quench the emission from a high charge state. The time scale for K-shell emission of the transient plasma has been estimated using a time-dependent plasma kinetics model [24]. In this model, the Boltzmann equation and a detailed collisional radiative model of the plasma with frozen ions are solved simultaneously as a function of time to model the time-integrated X-ray spectra of the transient plasma produced from laser-irradiated Ar clusters.

A time-varying electron energy distribution function (EEDF) was calculated from the Boltzmann equation. For convenience, all of the free electrons were placed near 5 keV to approximate an initial nonequilibrium EEDF. The population densities were given by the time-dependent solution to the rate

(a)

(b)
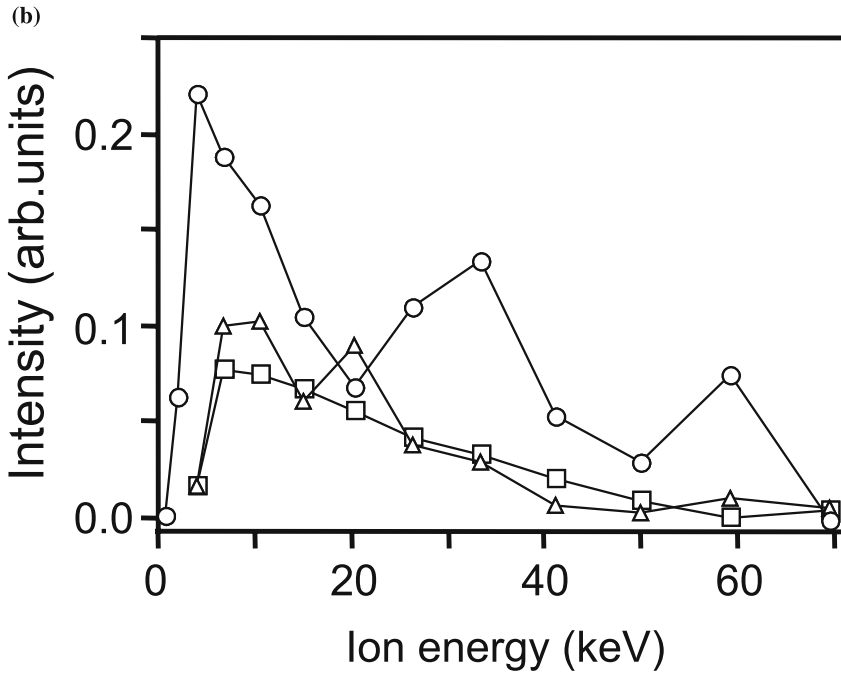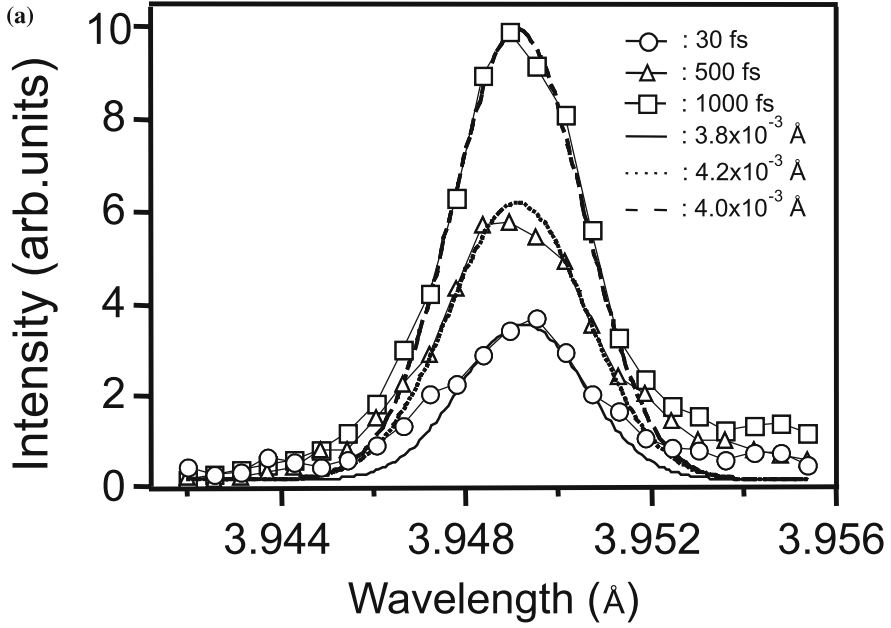
equations that were obtained by integrating the various cross-sections over the EEDF. The collisional radiative model included over 3000 levels in the Ne-like through H-like ion stages of argon. The atomic configurations were truncated at principle quantum number $n = 3$ to limit the number of levels produced. The atomic data also featured all possible $n = 1$ to $n = 2$ X-ray transitions within the $n = 3$ manifold for spectral comparison purposes. Specifically, for the model calculations considered here, it was assumed that all of the ions are initially in the ground state of the Ne-like ion (Ar^{8+}) due to the laser prepulse. The total ion density was assumed to be constant as a function of time. The atom number density was taken to be 6×10^{20} cm^{-3}. Thus, the initial electron density was 4.8×10^{21} cm^{-3}.

Figure 12.9 shows a comparison of calculated time-integrated spectra to 3 ps with experimental measurements. The experimental spectrum was obtained at a peak intensity of $I = 1.2 \times 10^{19}$ W cm^{-2}, a pulse duration of 30 fs and a contrast ratio of $C = 5 \times 10^{-6}$. The agreement with experiment for the He-like to Be-like emission is quite good. Note that the experimental spectral line that occurs near 4 Å is spurious and corresponds to He$_\gamma$ radiation from a different order of crystal reflection. Also note that for Li-like to B-like emission, the fine details of the calculated spectra, including component relative line positions and intensities, are in remarkable agreement with experiment.
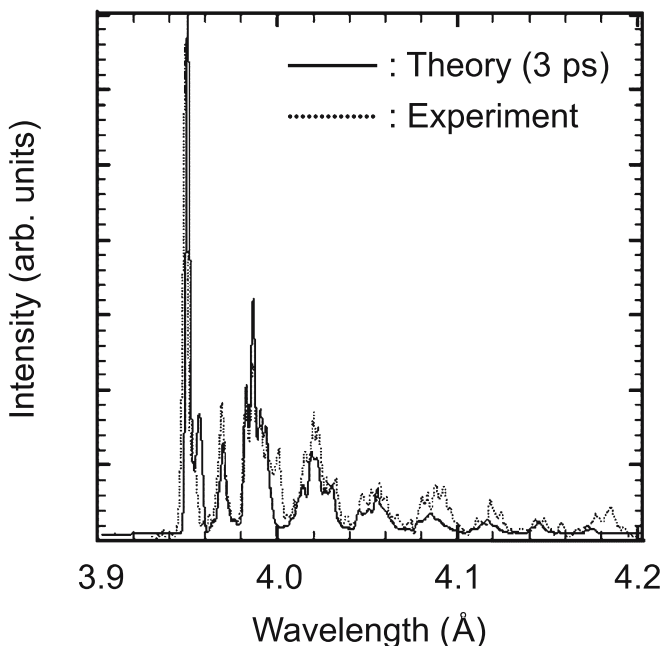
Fig. 12.9. Comparison of the calculated time-integrated He$_\alpha$ spectrum (*solid line*) with that obtained experimentally (*dotted line*) as a function of wavelength (Å)

The time scale for the decay of a cluster, that is expansion and cooling, under the current conditions, has been estimated to be in the range of 1–10 ps [25]. This fact suggests the following scenario for understanding the observed spectra. The laser energy of the main pulse is deposited into the clusters on a femtosecond timescale in the form of mostly hot electrons, creating a nonequilibrium plasma. The relaxation of the hot electrons in the presence of the ions causes excitation and ionization, and produces the spectrum discussed above. After a few ps, the ionization slows down as the plasma approaches the He-like ionization state and the electron energy distribution approaches Maxwellian. The expansion and cooling of the clusters then prevent further ionization.

12.6 X-Ray Diffraction From a Si(111) Crystal

Using laser-induced X-ray pulses from solid targets, ultrafast time-resolved X-ray diffraction experiments have been performed extensively and new phenomena such as ultrafast melting have been demonstrated [26, 27]. In the present study, in order to demonstrate the practical capabilities of the X-rays thus produced, the pulse X-ray diffraction obtained from a Si crystal with this source is examined [28].

Figure 12.10a shows a typical CCD image of the diffracted X-rays measured at the peak intensity of 6×10^{18} W/cm^2 with a pulse duration of 30 fs. This was obtained after 60 s of exposure, corresponding to an accumulation of 600 laser shots. Figure 12.10b shows the diffraction pattern obtained from this CCD image. The diffraction pattern consists of well-resolved K-shell emissions from highly ionized Ar ions, showing that the number of X-ray photons produced in the present study is much larger than the previous measurement [29]. Although the estimated number of photons (see Sect. 12.3.4) is smaller than that obtained from K_α emission from conventional solid targets [30–33], we have directly demonstrated that X-rays produced from the laser-irradiated clusters are strong enough to use as a debris-free light source for X-ray diffraction experiments.

12.7 Conclusions and Future Directions

Systematic investigations of the laser–cluster interaction were carried out by simultaneously measuring high-resolution X-ray emission spectra and ion energy spectra produced by the laser irradiation of micron-sized Ar clusters at laser intensities of 10^{18} to 10^{19} W/cm^2. To suppress the creation of preplasma, we designed a special conical nozzle and eliminated the laser prepulse. The results indicate that the explosion time scale for micron-sized clusters is much longer than that for nanometer-sized clusters. It is found that hot electrons produced by a higher contrast pulse (a smaller prepulse) allow the isochoric
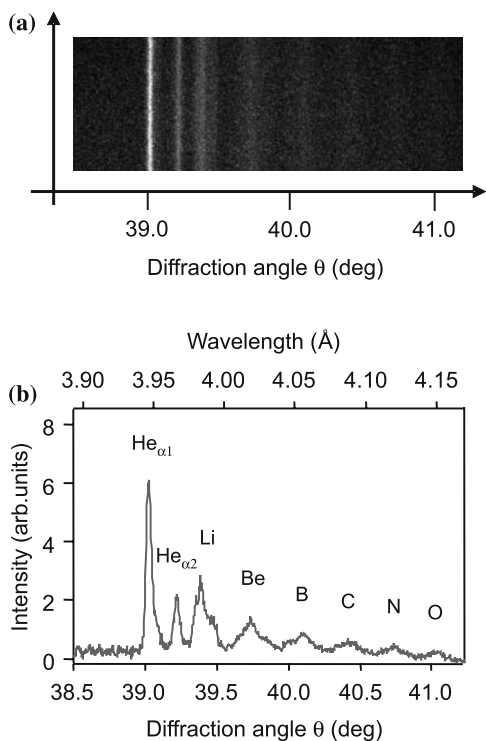
Fig. 12.10. a Typical CCD image of diffracted X-rays measured at a peak intensity of 6×10^{18} W/cm^2 with a pulse duration of 30 fs, and **b** the *rocking curve* obtained from the CCD image

heating of clusters and shift the ion balance towards higher charge states, which enhances both the X-ray line yield of the He-like argon ion and the kinetic energy of the ions.

The time-integrated spectrum calculated to 3 ps is in good agreement with that observed experimentally in the wavelength region near the He$_\alpha$ line. The Boltzmann model predicts the appearance of the He-like to F-like X-ray emission that is observed in the experiment. The calculated time scale for emission is also consistent with estimates of cluster decay times for these conditions. A recent spectral model that incorporates both time-dependent atomic kinetics and electron kinetics, where the initial non-Maxwellian electron energy distribution function (EEDF) for the Boltzmann solver is given by a particle-in-cell simulation, predicts that X-ray radiation can be generated over femtosecond time scales for atomic number densities above 10^{21} cm^{-3} [34]. Time-resolved X-ray diffraction using such X-rays will provide us directly with a detailed picture of the structural changes associated with ultrafast phenomena that are not governed by thermal processes.

We have also demonstrated that the photon flux of X-rays from highly ionized Ar ions in transient plasma are strong enough to enable X-ray diffraction experiments. Measurements of the emission time scales from different charge states using time-resolved X-ray diffraction is an interesting line of research for the future, since they could reveal the ever-changing environment associated with high-intensity, ultrafast laser–cluster interactions.

References

1. Mourou GA, Barty CPJ, Perry MD (1998) Ultrahigh-intensity-lasers: physics of the extreme on a table top. Physics Today **51**:22–28
2. Perry MD, Mourou GA (1994) Terawatt to petawatt subpicosecond lasers. Science **264**:917–924
3. Akahane Y, Ma J, Fukuda Y, Aoyama M, Kiriyama H, Sheldakova JV, Kudryashov AV, Yamakawa K (2006) Characterization of wavefront corrected 100-TW, 10-Hz laser pulses with peak intensities greater than $10^{20}\,\mathrm{W/cm^2}$. Rev. Sci. Instrum. **77**:0231021–0231027
4. Eidmann K, Andiel U, Pisani F, Hakel P, Mancini RC, Junkel-Vives GC, Abdallah Jr. J, Witte K (2003) K-shell spectra from hot dense aluminum layers buried in carbon and heated by ultrashort laser pulses. J. Quant. Spectrosc. Ra. **81**:133–146
5. Posthumus J (ed) (2001) Molecules and Clusters in Intense Laser Fields. Cambridge Univ. Press, Cambridge
6. Krainov VP, Smirnov MB (2002) Cluster beams in the super-intense femtosecond laser pulse. Phys. Rep. **370**:237–331
7. McPherson A, Thompson BD, Borisov AB, Boyer K, Rhodes CK (1994) Multiphoton-induced X-ray emission at 4–5 keV from Xe atoms with multiple core vacancies. Nature **370**:631–634
8. Ditmire T, Springate E, Tisch JWG, Shao YL, Mason MB, Hay N, Marangos JP, Hutchinson MHR (1998) Explosion of atomic clusters heated by high-intensity femtosecond laser pulses. Phys. Rev. A **57**:369–382
9. Ditmire T, Tisch JWG, Springate E, Mason MB, Hay N, Smith RA, Marangos J, Hutchinson MHR (1997) High-energy ions produced in explosions of superheated atomic clusters. Nature **386**:54–56
10. Ditmire T, Zweiback J, Yanovsky VP, Cowan TE, Hay G, Wharton KB (1999) Nuclear fusion from explosions of femtosecond laser-heated deuterium clusters. Nature **398**:489–492

11. Junkel-Vives GC, Abdallah Jr. J, Blasco F, Dorchies F, Caillaud T, Bonte C, Stenz C, Salin F, Faenov AYa, Magunov AI, Pikuz TA, Skobelev IYu (2002) Evidence of supercritical density in 45-fs-laser-irradiated Ar-cluster plasmas. Phys. Rev. A **66**:0332041–0332045

12. Ditmire T, Donnelly T, Rubenchik AM, Falcone RW, Perry MD (1996) Interaction of intense laser pulses with atomic clusters. Phys. Rev. A **53**:3379–3402

13. Yamakawa K, Aoyama M, Matsuoka S, Kase T, Akahane Y, Takuma H (1998) 100-TW sub-20-fs Ti:sapphire laser system operating at a 10-Hz repetition rate. Opt. Lett. **23**:1468–1470

14. Boldarev AS, Gasilov VA, Faenov AYa, Fukuda Y, Yamakawa K (2006) Gas-cluster targets for femtosecond laser interaction: Modelling and optimization. Rev. Sci. Instrum. **77**:0831121–08311210

15. Fukuda Y, Yamakawa K, Akahane Y, Aoyama M, Inoue N, Ueda H, Abdallah Jr. J, Csanak G, Faenov AYa, Magunov AI, Pikuz TA, Skobelev IYu, Boldarev AS, Gasilov VA (2003a) X-ray study of microdroplet plasma formation under the action of superintense laser radiation. JETP Lett. **78**:115–118

16. Blasco F, Stenz C, Salin F, Faenov AYa, Magunov AI, Pikutz TA, Skobelev IYu (2001) Portable, tunable, high-luminosity spherical crystal spectrometer with an X-ray charge coupled device, for high-resolution X-ray spectroscopy of clusters heated by femtosecond laser pulses. Rev. Sci. Instrum. **72**:1956–1962

17. Dyakin VM, Skobelev IYu, Faenov AYa, Bartnik A, Fiedorowicz H, Szczurek M, Osterheld A, Nilsen J (1997) Precision measurements of the wavelengths of spectral lines of multiply charged krypton and argon ions formed in a gas target heated by laser radiation. Quantum Electron. **27**:691–695

18. Abdallah Jr. J, Faenov AYa, Skobelev IYu, Magunov AI, Pikuz TA, Auguste T, D'Oliveira P, Hulin S, Monot P (2001) Hot-electron influence on the X-ray emission spectra of Ar clusters heated by a high-intensity 60-fs laser pulse. Phys. Rev A **63**:0327061–0327068

19. Smirnov MB, Skobelev IYu, Magunov AI, Faenov AYa, Pikuz TA, Fukuda Y, Yamakawa K, Akahane Y, Aoyama M, Inoue N, Ueda H (2004) Microdroplet evolution induced by a laser pulse. JETP **98**:1123–1132

20. Fukuda Y, Akahane Y, Aoyama M, Inoue N, Ueda H, Kishimoto Y, Yamakawa K, Faenov AYa, Magunov AI, Pikuz TA, Skobelev IYu, Boldarev AS, Abdallah Jr. J, Csanak G, Boldarev AS, Gasilov VA (2004a) Generation of X rays and energetic ions from super intense laser irradiation of micron-sized Ar clusters. Laser Part. Beams **22**:215–220

21. Parra E, Alexeev I, Fan J, Kim KY, McNaught SJ, Milchberg HM (2000) X-ray and extreme ultraviolet emission induced by variable pulse-width irradiation of Ar and Kr clusters and droplets. Phys. Rev. E **62**:R5931–R5934

22. Magunov AI, Pikuz TA, Skobelev IYu, Faenov AYa, Blasco F, Dorchies F, Caillaud T, Bonte C, Salin F, Stenz C, Loboda PA, Litvinenko IA, Popova VV, Baidin GV, Junkel-Vives GC, Abdallah Jr. J (2001) Influence of ultrashort laser pulse duration on the X-ray emission spectrum of plasma produced in cluster target. JETP Lett. **74**:375–379

23. Fukuda Y, Yamakawa K, Akahane Y, Aoyama M, Inoue N, Ueda H, Kishimoto Y (2003b) Optimized energetic particle emissions from Xe clusters in intense laser fields. Phys. Rev. A **67**:0612011–0612014

24. Abdallah Jr. J, Csanak G, Fukuda Y, Yamakawa K, Akahane Y, Aoyama M, Inoue N, Ueda H, Faenov AYa, Magunov AI, Pikuz TA, Skobelev IYu (2003) Time-dependent Boltzmann kinetic model of X-rays produced by ultrashort-pulse laser irradiation of argon clusters. Phys. Rev. A **68**:0632011–0632018
25. Auguste T, D'Oliveira P, Hulin S, Monot P, Abdallah Jr. J, Faenov AYa, Skobelev IYu, Magunov AI, Pikuz TA (2000) The role of the prepulse in cluster heating by a high-power femtosecond laser pulse. JETP Lett. **72**:38–41
26. Siders CW, Cavalleri A, Sokolowski-Tinten K, Tóth Cs, Guo T, Kammler M, Horn von Hoegen M, Wilson KR, von der Linde D, Barty CPJ (1999) Detection of nonthermal melting by ultrafast X-ray diffraction. Science **286**:1340–1342
27. Sokolowski-Tinten K, Blome C, Dietrich C, Tarasevitch A, Morn von Hoegen M, von der Linde D, Cavalleri A, Squier J, Kammler M (2001) Femtosecond X-ray measurement of ultrafast melting and large acoustic transients. Phys. Rev. Lett. **87**:2257011–2257014
28. Fukuda Y, Akahane Y, Aoyama M, Inoue N, Ueda H, Nakai Y, Tsuji K, Yamakawa K, Hironaka Y, Kishimura H, Morishita H, Kondo K, Nakamura KG (2004b) Relativistic laser plasma from micron-sized argon clusters as a debris-free X-ray source for pulse X-ray diffraction. Appl. Phys. Lett. **85**:5099–5101
29. Larsson J, Sjögren A (1999) Evaluation of laser-irradiated Ar clusters as a source for time-resolved X-ray studies. Rev. Sci. Instrum. **70**:2253–2256
30. Rousse A, Audebert P, Geindre JP, Fallès F, Gauthier JC, Mysyrowicz M, Grillon G, Antoneti A (1994) Efficient K_α X-ray source from femtosecond laser-produced plasmas. Phys. Rev. E **50**:2200–2207
31. Yoshida M, Fujimoto Y, Hironaka Y, Nakamura KG, Kondo K, Ohtani M, Tsunemi H (1998) Generation of picosecond hard x rays by terawatt laser focusing on a copper target. Appl. Phys. Lett. **73**:2393–2395
32. Feurer T, Morak A, Uschmann I, Ziener Ch, Schwoerer H, Reich Ch, Gibbon P, Förster E, Sauerbrey R, Ortner K, Becker CR (2001) Femtosecond silicon Ka pulses from laser. Phys. Rev. E **65**:0164121–0164124
33. Guo T, Spielmann Ch, Walker BC, Barty CPJ (2001) Generation of hard X-rays by ultrafast terawatt lasers. Rev. Sci. Instrum. **72**:41–47
34. Sherrill ME, Abdallah Jr. J, Csanak G, Dodd ES, Fukuda Y, Akahane Y, Aoyama M, Inoue N, Ueda H, Yamakawa K, Faenov AYa, Magunov AI, Pikuz TA, Skobelev IYu (2006) Spectroscopic characterization of an ultrashort laser driven Ar cluster target incorporating both Boltzmann and particle-in-cell models. Phys. Rev. E **73**:0664041–0664046

13 Full Vectorial, Intense Ultrashort Pulse Propagators: Derivation and Applications

J.V. Moloney and M. Kolesik

Arizona Center for Mathematical Sciences and Optical Sciences Center,
University of Arizona, Tucson AZ 85721
jml@acms.arizona.edu

Summary. Rapid progress in recent years in the development of high power ultra-short pulse laser systems has opened up a whole new vista of applications and computational challenges. New experimental developments in the field of extreme nonlinear optics will require more rigorous electromagnetic propagation models beyond those existing in the current literature. In this chapter, we derive a 3D time domain unidirectional vector Maxwell propagator that resolves the underlying optical carrier wave while allowing propagation over macroscopic many-meter distances. Our model allows for extreme focusing conditions down to the order of the wavelength in the material. A novel aspect of our approach is that the pulse propagator is designed to faithfully capture the light-material interaction over the broad spectral landscape of relevance to the interaction. Moreover the model provides a seamless and physically self-consistent means of deriving the many ultra-short pulse propagation equations presented in the literature. Amongst current applications that are most challenging from a computational point of view are those involving critical self-focusing with concomitant explosive growth in the generated light spectrum. Specific application areas chosen for illustration include multiple filament formation during propagation of ultra-intense femtosecond laser pulses in air and nonlinear self-trapping in condensed media. These examples exhibit rather different aspects of intense femtosecond pulse propagation and demonstrate the robustness and flexibility of our recently formulated unidirectional Maxwell propagator. A clear message to emerge from our study is the inadequacy of spectrally local light-material interaction models when nonlinear coupling exists over many hundreds of nanometer frequency bandwidths. More sophisticated, computationally feasible, models of nonlinear dispersion are needed.

13.1 Introduction

Rapid progress in recent years in the development of high power ultra-short pulse laser systems has opened up a whole new vista of applications and computational challenges. Amongst those applications that are most challenging from a computational point of view are those involving explosive critical self-focusing with concomitant explosive growth in the generated light spectrum. Moreover, new experimental developments in the field of extreme nonlinear optics will require more rigorous propagation models beyond those existing in the current literature. Specific aplications areas chosen for illustration in this chapter include atmospheric light string

propagation and nonlinear self-trapping in condensed media. These examples exhibit rather different aspects of intense femtosecond pulse propagation and demonstrate the robustness and flexibility of the unidirectional Maxwell propagator. A novel aspect of our approach is that the pulse propagator is designed to faithfully capture the light-material interaction over the broad spectral landscape of relevance to the interaction. Moreover the model provides a seamless and physically self-consistent means of deriving the many ultrashort pulse propagation equations presented in the literature.

13.2 Derivation of Unidirectional Pulse Propagation Equations

In this Section we expand the discussion presented in [1]. We outline the key steps in deriving a physically self-consistent and robust ultrashort pulse propagator that resolves the underlying optical carrier wave while enabling propagation over many meter propagation lengths. Our goal is to retain the full rigor of Maxwell's equations while reducing the problem complexity by constraining the model to unidirectional propagation. As our immediate interest is in very short intense pulse propagation with potentially large induced nonlinear polarization, we will need to accurately capture the very broad spectral landscape that the pulse experiences during its interaction with a host dielectric material. In many cases, spectral superbroadening is such that the generated bandwidth far exceeds in magnitude the underlying carrier frequency i.e. $\Delta\omega/\omega_0 \gg 1$. In this limit, we expect the Nonlinear Schrödinger Equation (NLSE) to fail. Many attempts have been made to derive nonlinear envelope models that go beyond NLSE and we will discuss most of these below when we show explicitly how each can be seamlessly derived from our unidirectional pulse propagation equation (UPPE).

13.2.1 Time-Propagated and Space-Propagated Equations

Most of the pulse propagation problems in nonlinear optics are solved in one of two formulations: Either one has an initial condition (electric and magnetic fields) specified in all space, and the evolution is calculated along the time axis, or the initial condition is given as a function of local pulse time and transverse (w.r.t. propagation direction) coordinates, and the numerical evolution proceeds along the propagation axis. We refer to these cases as time- and z-propagated equations.

The z-propagated approach is much more common in nonlinear optics simulations based on envelope equations, often related to NLS. The time-propagated approach is on the other hand common for solvers based on direct integration of Maxwell's equations.

Due to space limitations, we focus in this chapter on the z-UPPE. As discussed in [1] in more detail, the time-propagated versions of UPPE are more suitable for tight-focusing scenarios when non-paraxial effects start to play a role. The z-propagated equations are easier to use in situations that allow to neglect the longitudinal field components as sources of nonlinear material responses.

The z-propagated approach is more common in nonlinear optics and we start by deriving it explicitly, then discuss briefly its numerical implementation, relation to other envelope models and provide some illustrative examples of its implementation. We refer the reader to [1] for details concerning the details of numerical treatment of the nonlinear material response in both t-UPPE and z-UPPE cases.

13.2.2 Starting Point: Maxwell Equations

As a first step in derivation of various versions of UPPE, we derive an exact coupled-modes system of equations. This is a well-known textbook formula that can be found in the literature in several different forms. To keep our derivation self-contained, we re-derive the starting formula using a standard approach based on orthogonality relations for modes of an electromagnetic field.

Electromagnetic fields of a light pulse propagating along the z axis can be expanded into modal contributions that reflect the geometry of the waveguide (we consider homogeneous medium a special case of the latter).

$$\boldsymbol{E}(x,y,z,t) = \sum_{m,\omega} A_m(\omega,z)\boldsymbol{\mathcal{E}}_m(\omega,x,y)\mathrm{e}^{\mathrm{i}\beta_m(\omega)z - \mathrm{i}\omega t}$$

$$\boldsymbol{H}(x,y,z,t) = \sum_{m,\omega} A_m(\omega,z)\boldsymbol{\mathcal{H}}_m(\omega,x,y)\mathrm{e}^{\mathrm{i}\beta_m(\omega)z - \mathrm{i}\omega t} . \qquad (13.1)$$

Here, m labels all transverse modes, and an initial condition $A_m(\omega, z = 0)$ is supposed to be given or calculated from the field values at $z = 0$. Note that the above expansion is valid for the transverse components only.

To save space, the following short-hand notation will be used below

$$\boldsymbol{\mathcal{E}}_m \equiv \boldsymbol{\mathcal{E}}_m(\omega,x,y)\mathrm{e}^{\mathrm{i}\beta_m(\omega)z - \mathrm{i}\omega t}$$

$$\boldsymbol{\mathcal{H}}_m \equiv \boldsymbol{\mathcal{H}}_m(\omega,x,y)\mathrm{e}^{\mathrm{i}\beta_m(\omega)z - \mathrm{i}\omega t} . \qquad (13.2)$$

The starting point is Maxwell's equations. We consider a non-magnetic medium ($\mu = \mu_0$) with a linear permittivity $\epsilon(\omega, x, y)$ that doesn't depend on the propagation coordinate z.

$$\boldsymbol{j} + \partial_t \boldsymbol{P} + \epsilon_0 \partial_t \epsilon * \boldsymbol{E} = \nabla \times \boldsymbol{H}$$

$$-\mu_0 \partial_t \boldsymbol{H} = \nabla \times \boldsymbol{E} , \qquad (13.3)$$

where the star represents a convolution.

First, we scalar-multiply the Maxwell's equations by the complex conjugate modal fields

$$\mathcal{E}_m^*.(j + \partial_t P) + \epsilon_0 \mathcal{E}_m^*.\partial_t \epsilon * E = \mathcal{E}_m^*.\nabla \times H$$
$$-\mu_0 \mathcal{H}_m^*.\partial_t H = \mathcal{H}_m^*.\nabla \times E \ . \tag{13.4}$$

Using the formula $b.(\nabla \times a) = \nabla.(a \times b) + a.(\nabla \times b)$, we transform both RHS to obtain

$$\mathcal{E}_m^*.(j + \partial_t P) + \epsilon_0 \mathcal{E}_m^*.\partial_t \epsilon * E = \nabla.[H \times \mathcal{E}_m^*] + H.[\nabla \times \mathcal{E}_m^*]$$
$$-\mu_0 \mathcal{H}_m^*.\partial_t H = \nabla.[E \times \mathcal{H}_m^*] + E.[\nabla \times \mathcal{H}_m^*] \ . \tag{13.5}$$

Since modal fields themselves satisfy the Maxwell's equations

$$\nabla \times \mathcal{E}_m^* = -\mu_0 \partial_t \mathcal{H}_m^*$$
$$\nabla \times \mathcal{H}_m^* = \epsilon_0 \partial_t \epsilon * \mathcal{E}_m^* \ , \tag{13.6}$$

the above equations can be written as

$$\mathcal{E}_m^*.(j + \partial_t P) + \epsilon_0 \mathcal{E}_m^*.\partial_t \epsilon * E = \nabla.[H \times \mathcal{E}_m^*] - \mu_0 H.\partial_t \mathcal{H}_m^*$$
$$-\mu_0 \mathcal{H}_m^*.\partial_t H = \nabla.[E \times \mathcal{H}_m^*] + \epsilon_0 E.\partial_t \epsilon * \mathcal{E}_m^* \ . \tag{13.7}$$

We subtract the two equations and collect terms that constitute full time derivatives

$$\mathcal{E}_m^*.(j + \partial_t P) + \partial_t [\epsilon_0 \mathcal{E}_m^*.\epsilon * E]$$
$$= \nabla.[H \times \mathcal{E}_m^*] - \partial_t [\mu_0 \mathcal{H}_m^*.H] - \nabla.[E \times \mathcal{H}_m^*] \ . \tag{13.8}$$

Now integrate over the whole xyt domain. Note that all terms except the first and the ∂_z (implicit in $\nabla.$) are derivatives that give rise to "surface terms" after integration over x, y, t. Since we consider spatially and temporally localized pulse-like solutions, these terms vanish. The only surviving derivative will be ∂_z from $\nabla.$:

$$\int \mathcal{E}_m^*.(j + \partial_t P) \mathrm{d}x \mathrm{d}y \mathrm{d}t = \partial_z \int z.[H \times \mathcal{E}_m^*] \mathrm{d}x \mathrm{d}y \mathrm{d}t$$
$$- \partial_z \int z.[E \times \mathcal{H}_m^*] \mathrm{d}x \mathrm{d}y \mathrm{d}t \ . \tag{13.9}$$

Here and in what follows, t integrations are understood like this: $\int \mathrm{d}t \equiv \frac{1}{T} \int_{-T/2}^{+T/2} \mathrm{d}t$ where T is a large normalization "volume", and integrals over x, y are understood in a similar way. Because only transverse field components enter above equation, we can use our modal expansion here:

$$\int \boldsymbol{\mathcal{E}}_m^* \cdot (\boldsymbol{j} + \partial_t \boldsymbol{P}) \mathrm{d}x \mathrm{d}y \mathrm{d}t =$$

$$\partial_z \int \boldsymbol{z}. \left[\sum_{n,\Omega} A_n(\Omega, z) \boldsymbol{\mathcal{H}}_n(\Omega) \times \boldsymbol{\mathcal{E}}_m^*(\omega) \right] \mathrm{e}^{\mathrm{i}\beta_n(\Omega)z - \mathrm{i}\Omega t} \mathrm{e}^{-\mathrm{i}\beta_m(\omega)z + \mathrm{i}\omega t} \mathrm{d}x \mathrm{d}y \mathrm{d}t$$

$$- \partial_z \int \boldsymbol{z}. \left[\sum_{n,\Omega} A_n(\Omega, z) \boldsymbol{\mathcal{E}}_n(\Omega) \times \boldsymbol{\mathcal{H}}_m^*(\omega) \right] \mathrm{e}^{\mathrm{i}\beta_n(\Omega)z - \mathrm{i}\Omega t} \mathrm{e}^{-\mathrm{i}\beta_m(\omega)z + \mathrm{i}\omega t} \mathrm{d}x \mathrm{d}y \mathrm{d}t .$$

$$(13.10)$$

Integration over time gives a Kronecker delta between angular frequencies, $\delta_{\Omega\omega}$, which in turn reduces the sum over Ω:

$$\int \boldsymbol{\mathcal{E}}_m^* \cdot (\boldsymbol{j} + \partial_t \boldsymbol{P}) \mathrm{d}x \mathrm{d}y \mathrm{d}t =$$

$$\partial_z \int \boldsymbol{z}. \left[\sum_n A_n(\omega, z) \boldsymbol{\mathcal{H}}_n(\omega, x, y) \times \boldsymbol{\mathcal{E}}_m^*(\omega, x, y) \right] \mathrm{e}^{\mathrm{i}\beta_n(\omega)z} \mathrm{e}^{-\mathrm{i}\beta_m(\omega)z} \mathrm{d}x \mathrm{d}y$$

$$- \partial_z \int \boldsymbol{z}. \left[\sum_n A_n(\omega, z) \boldsymbol{\mathcal{E}}_n(\omega, x, y) \times \boldsymbol{\mathcal{H}}_m^*(\omega, x, y) \right] \mathrm{e}^{\mathrm{i}\beta_n(\omega)z} \mathrm{e}^{-\mathrm{i}\beta_m(\omega)z} \mathrm{d}x \mathrm{d}y .$$

$$(13.11)$$

Collecting like terms results in an equation

$$\int \boldsymbol{\mathcal{E}}_m^* \cdot (\boldsymbol{j} + \partial_t \boldsymbol{P}) \mathrm{d}x \mathrm{d}y \mathrm{d}t = \partial_z \sum_n A_n(\omega, z) \mathrm{e}^{\mathrm{i}\beta_n(\omega)z} \mathrm{e}^{-\mathrm{i}\beta_m(\omega)z}$$

$$\times \int \boldsymbol{z}. \left[\boldsymbol{\mathcal{H}}_n(\omega, x, y) \times \boldsymbol{\mathcal{E}}_m^*(\omega, x, y) - \boldsymbol{\mathcal{E}}_n(\omega, x, y) \times \boldsymbol{\mathcal{H}}_m^*(\omega, x, y) \right] \mathrm{d}x \mathrm{d}y ,$$

$$(13.12)$$

where the general orthogonality relation

$$\int \boldsymbol{z}. \left[\boldsymbol{\mathcal{E}}_m \times \boldsymbol{\mathcal{H}}_n^* - \boldsymbol{\mathcal{H}}_m \times \boldsymbol{\mathcal{E}}_n^* \right] \mathrm{d}x \mathrm{d}y = 2\delta_{m,n} N_m(\omega) \qquad (13.13)$$

can be used to reduce the sum over modes

$$\int \boldsymbol{\mathcal{E}}_m^* \cdot (\boldsymbol{j} + \partial_t \boldsymbol{P}) \mathrm{d}x \mathrm{d}y \mathrm{d}t = -\partial_z \sum_n A_n(\omega, z) \mathrm{e}^{\mathrm{i}\beta_n(\omega)z} \mathrm{e}^{-\mathrm{i}\beta_m(\omega)z} 2\delta_{m,n} N_m(\omega) ,$$

$$(13.14)$$

and finally obtain the evolution equation for the expansion coefficients:

$$\partial_z A_m(\omega, z) = -\frac{1}{2N_m(\omega)XYT} \int_{-T/2}^{+T/2} \mathrm{d}t \int_{-Y/2}^{+Y/2} \mathrm{d}y \int_{-X/2}^{+X/2} \mathrm{d}x \times$$

$$\mathrm{e}^{-\mathrm{i}\beta_m(\omega)z + \mathrm{i}\omega t} \boldsymbol{\mathcal{E}}_m^*(\omega, x, y) . [\boldsymbol{j}(x, y, t) + \partial_t \boldsymbol{P}(x, y, t)] . \quad (13.15)$$

This is the starting point for the z-propagated unidirectional equations.

13.2.3 Z-propagator UPPE for Homogeneous Medium

In the following, (13.15) is specialized for the case of a homogeneous medium. Field modes are plane waves labeled by transverse wavenumbers k_x, k_y, a polarization index $s = 1, 2$, and a $\pm$ sign depending on the direction of propagation along z:

$$m \equiv k_x, k_y, s, \pm . \tag{13.16}$$

The frequency and wavenumber dependent propagation "constant" is

$$\beta_{k_x,k_y,s,\pm}(\omega) \equiv k_z(\omega, k_x, k_y) = \sqrt{\omega^2 \epsilon(\omega)/c^2 - k_x^2 - k_y^2} \, , \tag{13.17}$$

and the modal field amplitudes are

$$\boldsymbol{\mathcal{E}}_{k_x,k_y,s,\pm} = \boldsymbol{e}_s \exp\left[\mathrm{i}k_x x + \mathrm{i}k_y y \pm \mathrm{i}k_z(\omega, k_x, k_y)\right] \tag{13.18}$$

$$\boldsymbol{\mathcal{H}}_{k_x,k_y,s,\pm} = \frac{1}{\mu_0 \omega} \boldsymbol{k} \times \boldsymbol{\mathcal{E}}_{k_x,k_y,\omega,s,\pm} \, . \tag{13.19}$$

Here, $\boldsymbol{e}_{s=1,2}$ are unit polarization vectors normal to the wave-vector

$$\boldsymbol{k} = \left\{ k_x, k_y, k_z \equiv \sqrt{\omega^2 \epsilon(\omega)/c^2 - k_x^2 - k_y^2} \right\} \, . \tag{13.20}$$

From these formulas, it is straightforward to calculate the modal normalization constant

$$2N_{k_x,k_y,s,\pm}(\omega) = \int \boldsymbol{z}.[\boldsymbol{\mathcal{E}}_m \times \boldsymbol{\mathcal{H}}_m^* - \boldsymbol{\mathcal{H}}_m \times \boldsymbol{\mathcal{E}}_m^*] \mathrm{d}x \mathrm{d}y$$

$$= 2\boldsymbol{z}.[\boldsymbol{e}_s \times (\boldsymbol{k} \times \boldsymbol{e}_s)] \frac{1}{\mu_0 \omega} = \pm 2k_z(\omega, k_x, k_z) \frac{1}{\mu_0 \omega} \tag{13.21}$$

$$N_{k_x,k_y,s,\pm}(\omega) = \pm \frac{k_z(\omega, k_x, k_z)}{\mu_0 \omega} \, . \tag{13.22}$$

Now we can insert expressions for the modal fields and normalization constant into coupled mode equation (13.15)

$$\partial_z A_{k_x,k_y,s,+}(\omega, z) = -\frac{\omega \mu_0}{2k_z} \mathrm{e}^{-\mathrm{i}k_z z} \int \frac{\mathrm{d}x\mathrm{d}y\mathrm{d}t}{L_x L_y T} \mathrm{e}^{\mathrm{i}(\omega t - k_x x - k_y y)}$$

$$\times \boldsymbol{e}_s.[\boldsymbol{j}(x, y, z, t) + \partial_t \boldsymbol{P}(x, y, z, t)] \, . \tag{13.23}$$

The above integral is nothing but spatial and temporal Fourier transform, so one can write it in the spectral domain as

$$\partial_z A_{k_x,k_y,s,+}(\omega, z) = \frac{\omega}{2\epsilon_0 c^2 k_z} \mathrm{e}^{-\mathrm{i}k_z z} \boldsymbol{e}_s. \left[\mathrm{i}\omega \boldsymbol{P}_{k_x,k_y}(\omega, z) - \boldsymbol{j}_{k_x,k_y}(\omega, z)\right] \, . \tag{13.24}$$

This is the propagation equation that is actually solved numerically, but let us express it in terms of field rather than in terms of modal expansion coefficients. From a modal expansion, the transverse part of the electric field is

$$\boldsymbol{E}^{\perp}_{k_x,k_y,+}(\omega,z) = \sum_{s=1,2} \boldsymbol{e}^{\perp}_s \boldsymbol{A}_{k_x,k_y,s,+}(\omega,z)\mathrm{e}^{\mathrm{i}k_z(k_x,k_y,\omega)z} \ , \qquad (13.25)$$

and its z derivative reads

$$\partial_z \boldsymbol{E}^{\perp}_{k_x,k_y,+}(\omega,z) = \mathrm{i}k_z(k_x,k_y,\omega)\boldsymbol{E}^{\perp}_{k_x,k_y,+}(\omega,z)$$
$$+ \sum_{s=1,2} \boldsymbol{e}^{\perp}_s \partial_z \boldsymbol{A}_{k_x,k_y,s,+}(\omega,z)\mathrm{e}^{\mathrm{i}k_z(k_x,k_y,\omega)z} \ . \qquad (13.26)$$

Using (13.24) we obtain the homogeneous medium full-vectorial UPPE

$$\partial_z \boldsymbol{E}^{\perp}_{k_x,k_y,+}(\omega,z) = \mathrm{i}k_z \boldsymbol{E}^{\perp}_{k_x,k_y,+}(\omega,z)$$
$$+ \sum_{s=1,2} \boldsymbol{e}^{\perp}_s \boldsymbol{e}_s \cdot \left[\frac{\mathrm{i}\omega^2}{2\epsilon_0 c^2 k_z} \boldsymbol{P}_{k_x,k_y}(\omega,z) - \frac{\omega}{2\epsilon_0 c^2 k_z}\boldsymbol{j}_{k_x,k_y}(\omega,z) \right].$$
$$(13.27)$$

This is an exact system of equations that describes the evolution of modal amplitudes along the z-axis for the forward propagating field. A similar equation holds for the backward propagating component, of course.

Because the nonlinear polarization in this equation results as a response to the *complete* field, this equation can't be used to calculate the forward field only. The equation becomes "unidirectional" only after resorting to the following approximation

$$\boldsymbol{P}(\boldsymbol{E}), \boldsymbol{j}(\boldsymbol{E}) \rightarrow \boldsymbol{P}(\boldsymbol{E}_f), \boldsymbol{j}(\boldsymbol{E}_f) \qquad (13.28)$$

In other words, to obtain a closed system to solve numerically, we must require that the nonlinear polarization is well approximated by the nonlinear polarization calculated only from the forward propagating field. This means that the equation is only applicable when the back-reflected portion of the field is so small that its contribution to the nonlinearity can be neglected.

13.2.4 *Z*-propagated UPPE, Simplified, Most Practical Version

Equation (13.27), with nonlinear polarization approximated by (13.28) can easily become a rather large system to solve numerically for typical problems encountered in the femtosecond pulse propagation area. Fortunately, in most cases the transverse dimensions of the resulting field remain relatively large compare to the wavelength, and further approximations are possible. Concretely, one can neglect the z components of the field and polarization vectors.

In such a situation the sum over polarization vectors reduces approximately to unity

$$\sum_{s=1,2} e_s^{\perp} e_s \approx 1 \; , \tag{13.29}$$

and the full UPPE simplifies into an equation for the transverse component(s) of the field

$$\partial_z E_{k_x,k_y}(\omega, z) = \mathrm{i} k_z E_{k_x,k_y}(\omega, z) + \frac{\mathrm{i}\omega^2}{2\epsilon_0 c^2 k_z} P_{k_x,k_y}(\omega, z)$$
$$- \frac{\omega}{2\epsilon_0 c^2 k_z} j_{k_x,k_y}(\omega, z) \; ,$$
$$k_z = \sqrt{\omega^2 \epsilon(\omega)/c^2 - k_x^2 - k_y^2} \; . \tag{13.30}$$

This is the most useful form for practical calculation, and is therefore called simply UPPE in the following.

13.2.5 Nonlinear Material Response

In most cases, the propagation equations discussed in this chapter do not require a specific form of material response. However, for the sake of concreteness, as well as for discussion of numerical methods, we want to describe a generic model of nonlinear material response. We consider a nonmagnetic, dispersive medium with relative permittivity ϵ that is a function of the transverse coordinates x, y and of the angular frequency ω

$$\epsilon = \epsilon(\omega, x, y) \; , \quad \mu = \mu_0 \; . \tag{13.31}$$

This medium specification includes any dispersive homogeneous medium such as air or water as well as structured fiber-like media such as photonic, microstructured and tapered optical fibers.

Nonlinear effects are usually described in terms of polarization P through the material constitutive relation:

$$\boldsymbol{D} = \epsilon_0 \epsilon * \boldsymbol{E} + \boldsymbol{P} \; . \tag{13.32}$$

The star in this formula represents a convolution integral with ϵ being the linear response function corresponding to the frequency dependent $\epsilon(\omega, x, y)$. The non-linear polarization is an "arbitrary" function of the electric field $\boldsymbol{P} = \boldsymbol{P}(\boldsymbol{E})$. We will also include a current density that is driven by the optical field

$$\boldsymbol{j} = \boldsymbol{j}(\boldsymbol{E}) \tag{13.33}$$

to describe interactions with plasma generated by the high-intensity optical pulse.

The main physical effects that influence propagation of ultrashort, high-power light pulses in nonlinear dispersive media include the optical Kerr and stimulated Raman effects, free-electron generation, defocusing by the generated plasma and losses caused by avalanche and multiphoton ionization (MPI). With minor modifications, models including these effects can be used for description of ultra-short optical pulses propagation in gases [2–18], condensed bulk media [19–23] and in conventional, microstructured, and tapered fibers [24–26] as well as in ultra-thin silica "wires" [27].

The optical Kerr and stimulated Raman effects cause a local modification of the optical susceptibility

$$\boldsymbol{P} = \epsilon_0 \Delta\chi \boldsymbol{E} \tag{13.34}$$

that responds to the history of the light intensity I:

$$\Delta\chi = 2n_{\mathrm{b}}n_2 \left[(1-f)I + f \int_0^\infty \mathcal{R}(\tau)I(t-\tau)\mathrm{d}\tau \right] . \tag{13.35}$$

Here, f is the fraction of the delayed nonlinear response, and $\mathcal{R}$ is the memory function of the stimulated Raman effect. Parameterization by $\mathcal{R}(\tau) \sim \sin(\Omega\tau)\mathrm{e}^{-\Gamma\tau}$ is often sufficient for ultrashort pulses [7]. This simple formula has the advantage of easy implementation that avoids explicit calculation of the convolution integral. Often, an even simpler, exponential memory function is used, $\mathcal{R}(\tau) \sim \mathrm{e}^{-\Gamma\tau}$ in simulations (see e.g. [28]). If the real memory function is sufficiently complex, a numerical convolution approach must be used to calculate the convolution. This is e.g. the case in silica [29].

Because of the potentially high intensities occuring in femtosecond pulses, free electrons are generated by MPI and avalanche mechanisms. Then it is necessary to account for the response of the optical field to the presence of a dilute plasma. Since the relevant times scales are so short, plasma diffusion and ion motion are neglected, and the free-electron density ρ is usually obtained as a solution to an equation of the following form [7,12,13]

$$\partial_t \rho = a\, I\rho + b(I) - c\rho^2 . \tag{13.36}$$

Here, I is the light intensity, a parameterizes the avalanche free-electron generation, and $b(I)$ represents the Multi Photon Ionization (MPI) rate that is a highly nonlinear function of the intensity. The last term describes plasma recombination.

We assume that the collective electron velocity $\boldsymbol{v}$ responds to the optical field and the total current density is governed by the following simple equation (see e.g. [30])

$$\frac{\mathrm{d}}{\mathrm{d}t}\boldsymbol{j}(t) = \frac{e^2}{m_{\mathrm{e}}}\rho(t)\boldsymbol{E}(t) - \boldsymbol{j}(t)/\tau_{\mathrm{c}} , \tag{13.37}$$

where τ_{c} is the mean time between collisions experienced by electrons. This equation is solved together with (13.36) to capture effects of the plasma on

the propagation of the optical field, namely defocusing due to plasma and plasma induced losses.

Losses caused by multiphoton ionization are usually incorporated as either an equivalent current (see e.g. [30, 31]) or an imaginary susceptibility contribution that extracts from the field the energy needed for the free-electron generation.

13.2.6 Numerical Algorithms

The general structure of both t- and z-UPPE propagation equations is quite similar. A UPPE equation actually comprises a large system of ordinary differential equation with a free propagation part, and a nonlinear coupling.

An important feature that affects the numerical solution strategy is that these equations are written in the spectral space, either in the three dimensional space of wave-vectors (t-propagated UPPE) or in a two-dimensional space of transverse wave-vectors plus a one dimensional angular-frequency space (z-propagated UPPE). At the same time, the nonlinear material response must be calculated in the real-space representation. Consequently, a good implementation of Fast Fourier Transform is essential for a UPPE solver.

Due to the nature of FFT, or spectral transforms in general, parallelization of the solver is more suited to a shared memory architecture than to the Message Passing Interface approach. Further, since the most time-consuming portion of the code deals with calculating the RHS of the equation, we choose to apply a single threaded library for ODE solvers (gsl in our case) and only parallelize the calculation of derivatives needed in the ODE solver.

For concreteness, we describe solution of the z-propagated UPPE equation:

$$\partial_z E_{k_x,k_y}(\omega, z) = \mathrm{i} k_z E_{k_x,k_y}(\omega, z) + \frac{\mathrm{i}\omega^2}{2\epsilon_0 c^2 k_z} P_{k_x,k_y}(\omega, z)$$

$$- \frac{\omega}{2\epsilon_0 c^2 k_z} j_{k_x,k_y}(\omega, z) ,$$

$$k_z = \sqrt{\omega^2 \epsilon(\omega)/c^2 - k_x^2 - k_y^2} . \tag{13.38}$$

Suppose we have a solution at $z = 0$, and want to propagate it over a distance corresponding to an integration step Δz. Although we wrote the equation in terms of field, it is more natural to solve numerically for the modal expansion coefficients to eliminate fast oscillatory terms. We therefore express the field through the expansion coefficients A which are actually the "native solver variables":

$$E_{k_x,k_y}(\omega, z) = A_{k_x,k_y}(\omega, z) \mathrm{e}^{\mathrm{i} k_z(\omega, k_x, k_y) z} \tag{13.39}$$

to transform the equation into

$$\partial_z A_{k_x,k_y}(\omega,z) = e^{-ik_z z} \left[\frac{i\omega^2}{2\epsilon_0 c^2 k_z} P_{k_x,k_y}(\omega,z) - \frac{\omega}{2\epsilon_0 c^2 k_z} j_{k_x,k_y}(\omega,z) \right].$$
(13.40)

Depending on the concrete ODE scheme one chooses to use, the ODE solver may require one to calculate the derivative (RHS) at various values of z. Nonlinear polarization and current are of course functions of the electric field which in turn is calculated for any given z from (13.39). That is nothing but applying a linear propagator (in the spectral representation) to a given field. Thus, to evaluate the RHS in (13.40) given $A_{k_x,k_y}(\omega,z)$, one first applies (13.39) to obtain electric field in the spectral-space representation. Subsequently, a real-space representation is obtained by Fourier transform. (Note that this is a "global" operation which forces each parallel execution thread to access large amount of data "owned" by all other threads. This is the main reason why the UPPE solvers are easier to implement on a shared memory machine.) Having the electric field in real space, one calculates the material response using the model described in the previous Section. This is done by integrating the material equations along the time dimension independently for each point in the transverse x,y plane. Consequently, this portion of the code is straightforward to parallelize. As a result, one obtains the nonlinear polarization and current in the real-space representation. This is then Fourier transformed back into spectral space to finally evaluate the RHS in the propagation equation (13.40). An ODE solver calls this procedure as many times as it needs to perform a single integration step and thus calculates $A_{k_x,k_y}(\omega,z+\Delta z)$.

A final operation that finishes one solver step is to calculate the field in the frame moving with a an appropriate group velocity so that the pulse is kept in the center of the computational domain. This is achieved by applying a modified linear propagator

$$A_{k_x,k_y}(\omega,z+\Delta z) \rightarrow A_{k_x,k_y}(\omega,z+\Delta z) \exp\left\{ i\left[k_z(\omega,k_x,k_y) - \frac{\omega-\omega_R}{v_g} \right]\Delta z \right\}.$$
(13.41)

The group velocity that enters above is usually calculated from the linear dispersion relation

$$\frac{1}{v_g} = \partial_\omega k_z(\omega,k_x=0,k_y=0)|_{\omega=\omega_R}$$
(13.42)

at the frequency that corresponds to the maximum of the pulse spectral power (pulse center frequency). Let us emphasize that this last operation is just a change of coordinates, so the introduction of the reference frequency at this point doesn't change the light propagation in any way. However, it is

important to include the moving frame, because it makes it easier and more efficient to apply absorbing boundary layers in the computational domain. Without a moving window, the computational domain would we periodically wrapped into itself in the time direction. In order to apply artificial absorption at the boundary and also for integrating the material equations, the latter would need to be identified at each step.

Thus, since the UPPE is actually a big ODE system, the solver implementation is simple in principle, though it involves significant "auxiliary" calculations described above to supply the ODE solver with the routine to calculate the derivatives.

A final remark in this Section concerns axially symmetric problems. We usually treat these in radial coordinates and apply a numerical Hankel transform instead of the Fourier transform. This is a "slow" transform with a dense matrix, but due to the relatively small computational domain radially symmetric problems require, this is not a big problem. Alternatively, one could treat such situations by finite differencing in the radial dimension, but it would mean accepting additional (paraxial) approximation, and would introduce artificial numerical dispersion into the algorithm.

13.3 General Method for Derivation of Various Propagation Equations from UPPE

Several types of unidirectional propagation equations are widely used in the nonlinear optics literature. The most important examples are Non-Linear Schrödinger (NLS) equation [32], Nonlinear Envelope Equation [33] (NEE), the First-Order Propagation equation [31] (FOP), Forward Maxwell's equation [34] (FME), and several other equations that are closely related to these. The derivations found in the literature differ from equation to equation, and in some cases the physical meaning of the required approximations may not be readily evident due to a number of neglected terms.

In this section, we provide a unified approach that will subsequently be used to derive several of the light-pulse propagation equations found in the literature. The main benefit of re-deriving known equations from a common starting point, namely UPPE, using the same method, is that it allows us to compare the physical assumptions and approximation underlying different equations. It also reveals relations between the equation which may not be obvious either because of their apparently different form, or because of different methods used in the original derivations.

It is instructive to break the derivation procedure into several steps. As a first step, we adopt a scalar, one component approximation and write the UPPE in the following form:

$$\partial_z E_{k_x,k_y}(\omega, z) = \mathrm{i}K E_{k_x,k_y}(\omega, z) + \mathrm{i}Q P_{k_x,k_y}(\omega, z) \,, \tag{13.43}$$

where

$$K(k_x, k_y, \omega) = \sqrt{\omega^2 \epsilon(\omega)/c^2 - k_x^2 - k_y^2} \qquad (13.44)$$

is the linear field propagator in the spectral representation, and

$$Q(k_x, k_y, \omega) = \frac{\omega^2}{2\epsilon_0 c^2 \sqrt{\omega^2 \epsilon(\omega)/c^2 - k_x^2 - k_y^2}} \qquad (13.45)$$

will be called nonlinear coupling term.

In the second step, we replace K and Q by suitable approximations. In most cases they are nothing but Taylor expansions in frequency and in transverse wavenumbers.

To obtain envelope equations, one expresses the field in terms of an envelope by factoring out the carrier wave at a chosen reference angular frequency ω_R with the corresponding wave-vector $k_R = K(0, 0, \omega_R)$:

$$E(x, y, z, t) = \mathcal{A}(x, y, z, t) e^{i(k_R z - \omega_R t)} \qquad (13.46)$$

A similar factorization is of course introduced for the nonlinear polarization $P(x, y, z, t)$ as well.

Step three consist in transforming the equation from the spectral- to the real-space representation. Mathematically, this is nothing but a Fourier transform that results in the following standard rules for differential operators:

$$(\omega - \omega_R) \to i\partial_t \quad ik_x \to \partial_x \quad ik_y \to \partial_y \quad \partial_z \to ik(\omega_R) + \partial_z . \qquad (13.47)$$

Finally, in most cases we also transform to a frame moving with a suitable group velocity such that the pulse remains close to the center of the computational domain.

13.3.1 Derivation of Non-Linear Schrödinger Equation from UPPE

The Nonlinear Schrödinger Equation (see [32] for applications in optics) (NLS) is a prototype propagation equation in nonlinear optics. This is also the simplest case suitable to illustrate the general procedure outlined above. One characteristic feature of NLS and of other envelope type equations is the presence of a reference frequency. Usually, one chooses the reference angular frequency ω_R as the central frequency of the initial pulse, but this is not necessary. Actually it is useful to keep in mind that ω_R is to a certain extent a free parameter, and that the obtained results must be almost independent of its concrete choice. If a numerical simulation turns out to be sensitive to the choice of ω_R, it means that an envelope equation is being used outside of its region of validity.

Following the general procedure, we replace the K and Q "coefficients" with appropriate approximations. We denote by $k_R = k(\omega_R)$ the reference wavenumber corresponding to the chosen reference frequency ω_R, and take

$$K(k_x, k_y, \omega) = \sqrt{\omega^2 \epsilon(\omega)/c^2 - k_x^2 - k_y^2}$$
$$\approx k_R + v_g^{-1}(\omega - \omega_R) + \frac{k''}{2}(\omega - \omega_R)^2 - \frac{1}{2k_R}\left(k_x^2 + k_y^2\right) . \tag{13.48}$$

This is a second-order Taylor expansion in $\omega - \omega_R$ and in k_x, k_y.

In the nonlinear coupling coefficient, we neglect all variable dependencies and take its value at the reference frequency and zero transverse wavenumbers:

$$Q(k_x, k_y, \omega) = \frac{\omega^2}{2\epsilon_0 c^2 \sqrt{\omega^2 \epsilon(\omega)/c^2 - k_x^2 - k_y^2}} \approx \frac{\omega_R}{2\epsilon_0 n(\omega_R)c} . \tag{13.49}$$

For simplicity, in NLS we only account for the instantaneous optical Kerr effect, and write the nonlinear polarization envelope as

$$\mathcal{P} = 2\epsilon_0 n(\omega_R) n_2 I \mathcal{A} . \tag{13.50}$$

Inserting the above expressions into (13.43), (13.46) we obtain

$$\partial_z \mathcal{A} = +iv_g^{-1}(\omega - \omega_R)\mathcal{A} + \frac{ik''}{2}(\omega - \omega_R)^2\mathcal{A} - \frac{i}{2k_R}\left(k_x^2 + k_y^2\right)\mathcal{A} + \frac{i\omega_R}{c}n_2 I \mathcal{A} . \tag{13.51}$$

It is customary to normalize the envelope amplitude such that $|\mathcal{A}|^2 = I$. Using rules (13.47) we finally obtain the NLS equation:

$$\left(\partial_z + v_g^{-1}\partial_t\right)\mathcal{A} = \frac{i}{2k_R}\Delta_\perp \mathcal{A} - \frac{ik''}{2}\partial_{tt}\mathcal{A} + \frac{i\omega_R}{c}n_2|\mathcal{A}|^2\mathcal{A} . \tag{13.52}$$

The above derivation shows explicitly what approximations need to be adopted to obtain NLS: Approximating K to second order in frequency and transverse wavenumber amounts to the paraxial, and quasi-monochromatic approximations for the linear wave propagation. The approximation in the nonlinear coupling Q also requires a narrow spectrum in order to be able to represent Q by a constant.

13.3.2 Nonlinear Envelope Equation

The Nonlinear Envelope Equation [33] is a paraxial equation with some additional approximations related to chromatic dispersion. This equation appears to be extremely close to the paraxial version of UPPE.

Once again we follow the general procedure and approximate the linear propagator by its paraxial version:

$$K(k_x, k_y, \omega) = \sqrt{\omega^2 \epsilon(\omega)/c^2 - k_x^2 - k_y^2} \approx +k(\omega) - \frac{c}{2\omega n_{\mathrm{b}}(\omega_{\mathrm{R}})} \left(k_x^2 + k_y^2\right) \ .$$
(13.53)

This is essentially the second-order (paraxial) Taylor expansion in transverse wavenumbers with only minor additional approximation. Namely, we replaced $n_{\mathrm{b}}(\omega) \to n_{\mathrm{b}}(\omega_{\mathrm{R}})$ in the denominator of the diffraction term, and thus partly neglected the chromatic dispersion.

Further, the first term in the above approximation, which is an exact propagation constant for a plane wave propagating along the z-axis, is re-expressed as a sum of its two lowest-order Taylor expansion terms plus the rest:

$$k(\omega) = k(\omega_{\mathrm{R}}) + v_{\mathrm{g}}^{-1}(\omega - \omega_{\mathrm{R}}) + D(\omega - \omega_{\mathrm{R}}) \ ,$$
(13.54)

where

$$D(\omega - \omega_{\mathrm{R}}) = \sum_{n=2}^{\infty} \left(\frac{\partial^n k}{\partial \omega^n}\right)_{\omega = \omega_{\mathrm{R}}} \frac{(\omega - \omega_{\mathrm{R}})^n}{n!} \ .$$
(13.55)

This is formally exact and can be practically implemented in the spectral domain without further approximations, but sometimes a finite number of series expansion terms is used to fit the linear chromatic dispersion of a medium or of a waveguide. What we understand under NEE in the following assumes an exact treatment of the dispersion operator.

Next, we approximate the nonlinear coupling term. Unlike in NLS, we preserve the frequency dependence exactly, but neglect the transverse wavenumber dependence:

$$Q(k_x, k_y, \omega) \equiv \frac{\omega^2}{2\epsilon_0 c^2 \sqrt{\omega^2 \epsilon(\omega)/c^2 - k_x^2 - k_y^2}} \approx \frac{(\omega - \omega_{\mathrm{R}}) + \omega_{\mathrm{R}}}{2\epsilon_0 c n(\omega_{\mathrm{R}})} \ .$$
(13.56)

Here, as in the free propagation term, we neglect the chromatic dispersion of the background index of refraction.

After putting the above approximations for K and Q into the original UPPE, we obtain

$$\partial_z \mathcal{A} = \mathrm{i} v_{\mathrm{g}}^{-1}(\omega - \omega_{\mathrm{R}}) \mathcal{A} + \mathrm{i} D(\omega - \omega_{\mathrm{R}}) \mathcal{A}$$
$$- \frac{\mathrm{i} c}{2\omega_{\mathrm{R}} n(\omega_{\mathrm{R}})} \left(1 + \frac{\omega - \omega_{\mathrm{R}}}{\omega_{\mathrm{R}}}\right)^{-1} \left(k_x^2 + k_y^2\right) \mathcal{A}$$
$$+ \frac{\mathrm{i} \omega_{\mathrm{R}}}{2\epsilon_0 c n(\omega_{\mathrm{R}})} \left(1 + \frac{\omega - \omega_{\mathrm{R}}}{\omega_{\mathrm{R}}}\right) \mathcal{P} \ .$$
(13.57)

Finally, transforming into the real-space representation, we arrive at NEE

$$\partial_z \mathcal{A} + v_g^{-1} \partial_t \mathcal{A} = iD(i\partial_t)\mathcal{A} + \frac{i}{2k_R}\left(1 + \frac{i}{\omega_R}\partial_t\right)^{-1} \Delta_\perp \mathcal{A}$$
$$+ \frac{ik_R}{2\epsilon_0 n_b^2(\omega_R)}\left(1 + \frac{i}{\omega_R}\partial_t\right)\mathcal{P}. \qquad (13.58)$$

Thus, the additional approximations underlying the NEE are paraxiality both in the free propagator and in the nonlinear coupling, and a small error in the chromatic dispersion introduced when the background index of refraction is replaced by a constant, frequency independent value in both the spatio-temporal correction term and in the nonlinear coupling term. Note that the latter approximations are usually not serious at all.

As in all envelope equations a reference frequency and a reference wavenumber appear in the NEE. They are chosen equal to the central frequency and wave-number of the input pulse in practical calculation, but one has to keep in mind that these quantities are artificial and to a certain degree arbitrary "gauge" parameters that, of course, do not appear in the Maxwell's equations. Consequently, numerical solutions should not depend on how the reference is chosen. In other words a propagation equations should be "reference-frequency-invariant". While NLS is manifestly dependent on the reference choice, NEE is nearly invariant although ω_R appears in it several times. For example, the spatio-temporal focusing correction term (operator) $\omega_R^{-1}(1 + \frac{1}{\omega_R}\partial_t)^{-1}$ that appears in the NEE equation and modifies the diffraction term seems to depend on the reference ω_R, but it is in fact proportional to ω^{-1} as long as it is implemented in the spectral domain that allows to include all orders of the series expansion. It is to be stressed that this (approximate) invariance is only achieved in the infinite order. Truncating the operators that appear in the NEE to finite number of series expansion terms breaks the invariance and brings about undesirable artifacts as we point out in the following example.

We consider a 25-femtosecond (0.1 mm waist) pulse with a carrier wavelength of 775 nm and power of 8 GW propagating in air. The pulse duration is chosen very short to highlight propagation effects that are absent in the NLS approach, namely space-time focusing and the frequency dependent nonlinear response (shock formation). We compare supercontinuum generation using UPPE with full chromatic dispersion of dry air taken into account in the wavelength region from 1200 to 200 nm [35] and the NEE equation with the dispersion operator $\mathcal{D} = \sum_{k=2}^{L} \beta^{(k)}/k!(i\partial_t)^k$ (13.58) is expanded up to the second ($L = 2$) and/or third ($L = 3$) order with $\beta^{(k)}$ being purely real in this case. We term the latter approximations ad2NEE and ad3NEE, respectively (standing for NEE with approximate dispersion). In all cases we assume an instantaneous optical Kerr effect with $n_2 = 5 \times 10^{-23}\,\mathrm{m}^2/\mathrm{W}$, and plasma generation by multiphoton ionization. The reader is referred to [7] for a physical description of the model.
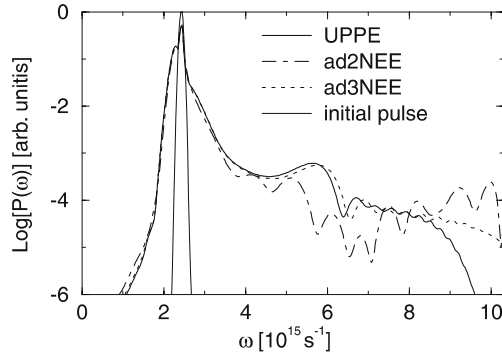
Fig. 13.1. Supercontinuum generated in a femtosecond pulse propagating in air. *Full curve* was obtained from the full UPPE simulation while the *other curves* correspond to NEE equation simulated with two and three terms included in the dispersion operator

Figure 13.1 shows the pulse spectrum after the self-focusing collapse is arrested by plasma generation. In all cases, a broad high-frequency component is generated on the steepened trailing edge of the pulse as described previously in [36]. However the details of the spectra are rather different. Here, the UPPE solution describes the correct propagation properties of all wavelengths that contribute to the spectral range shown. The difference between the UPPE and ad2(3)NEE solutions can be traced to difference in the susceptibility they model. It happens that the GVD is rather small around 800 nm and the approximated susceptibility rapidly deviates from the actual susceptibility at higher frequencies. Including the third-order dispersion substantially improves the agreement with the UPPE solution. The remaining discrepancy is then restricted to the high-frequency range in which the supercontinuum spectral intensity falls-off. This demonstrates that in the NEE the dispersion operator should be treated exactly in the spectral domain or care should be exercised in approximating chromatic dispersion by an expansion. When the dispersion is handled properly, NEE is an excellent approximation. It can be shown that the error it introduces is of fourth order in the transverse wave-number.

13.3.3 Partially Corrected NLS

The Partially Corrected NLS (PC-NLS) equation can be viewed as a "simplification" of NEE. It is derived from the UPPE in the same way, with one additional step. Namely, the following first order series expansion is applied in the correction term of the free propagator in (13.57):

$$\left(1 + \frac{\omega - \omega_R}{\omega_R}\right)^{-1} \approx \left(1 - \frac{\omega - \omega_R}{\omega_R}\right) \ . \tag{13.59}$$

This step is meant to make it easy to implement a numerical solver in the real space, as it results in the equation that only contains "simple" differential operators in the real-space representation:

$$\partial_z \mathcal{A} + v_{\mathrm{g}}^{-1}\partial_t \mathcal{A} = \mathrm{i}D(\mathrm{i}\partial_t)\mathcal{A} + \frac{\mathrm{i}}{2k_{\mathrm{R}}}\left(1 - \frac{\mathrm{i}}{\omega_{\mathrm{R}}}\partial_t\right)\Delta_\perp \mathcal{A}$$

$$+ \frac{\mathrm{i}k_{\mathrm{R}}}{2\epsilon_0 n_{\mathrm{b}}^2(\omega_{\mathrm{R}})}\left(1 + \frac{\mathrm{i}}{\omega_{\mathrm{R}}}\partial_t\right)\mathcal{P}\,. \tag{13.60}$$

While it may seem that the Partially Corrected NLS is essentially NEE with a "little more" approximation, this equation is not to be recommended. Because of the arbitrary truncation of an infinite series, the dispersion properties of the linear part of this equation are unphysical. While the PC-NLS provides better-than-NLS approximation around the reference frequency ω_{R}, its dispersion properties become rather pathological around $\omega \approx 2\omega_{\mathrm{R}}$ where its diffraction term changes sign as a consequence of the truncated correction factor. Artifacts in the angular distribution of the spectrum can be observed at high frequencies beyond $\omega \approx 2\omega_{\mathrm{R}}$. This is illustrated in Fig. 13.2. Consequently, this equation is only applicable in the same regime as the NLS, namely when the spectrum of the pulse remains relatively narrow.
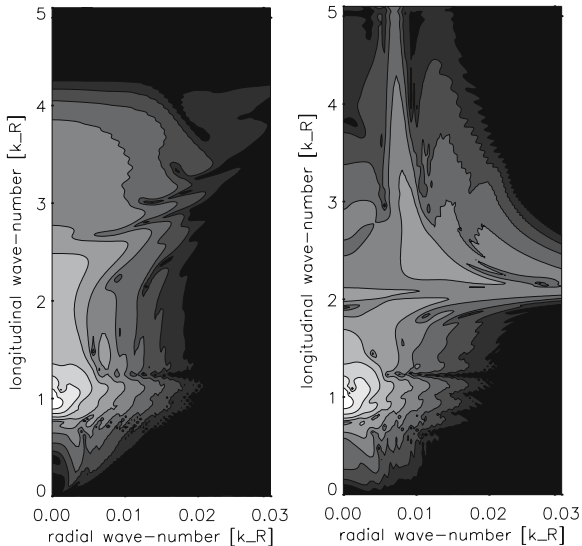
Fig. 13.2. Spatial spectra of a supercontinuum generated in air. *Left panel* represents a solution obtained from UPPE, the *right panels* is a corresponding spectrum obtained from PCNLS. Artifacts in the spectrum around the wavenumbers that correspond to the twice the reference frequency are clearly visible

13.4 Applications of UPPE Simulators

This section provides three illustrative applications of the z-UPPE model. The first is the computationally more challenging as it involves a full 3D + time simulation of the propagation of a wide pancake shaped pulse in air.The second provides a nice illustration of the need to go beyond the paraxial approximation for nonlinear X-wave generation in condensed media and the last illustrates the subtle interplay between plasma generation and chromatic dispersion in limiting the extent of the supercontinuum spectrum.

13.4.1 Femtosecond Atmospheric Light Strings

Multiple Filament Formation

This application of the z-UPPE simulator illustrates break-up of a high-power, wide femtosecond pulse into chaotically interacting light filaments. Beams that carry power exceeding the critical self-focusing power many times usually break transversally into multiple filaments. To capture such dynamics, a fully spatially resolved simulator is needed that doesn't impose axial symmetry.

Below, we illustrate how such multiple filaments are concurrently created at different transverse and longitudinal locations, and how they interact with the low-intensity background. It was first proposed in [15] that such an interaction is crucial for long distance propagation of high-power femtosecond pulses in air. The basic idea is that of dynamic exchange of energy between multiple, essentially unsynchronized and spatially sharply localized filament cores and the low-intensity, spatially wide pedestal of the beam.

In this wide-beam simulation, the initial condition is a Gaussian pulse with a phase perturbation. The waist of the initially collimated Gaussian was chosen to be 5 mm, the pulse duration is 500 fs, $\lambda = 248$ nm, and the maximal intensity is $2 \times 10^{14}\,\mathrm{W\,m^{-2}}$. The total pulse energy is approximately 9 mJ. A random phase perturbation is imposed on the pulse to initiate the transverse break-up of the pulse into multiple filaments (see Fig 13.3). We adjusted the amplitude of the perturbation such that it results in the filamentation onset after a few meters of propagation.

The first stage of nonlinear self-focusing is driven by the smooth, large-scale profile of the pulse. After a few meters, local perturbations develop into hot spots which grow into high-intensity filaments. The first panel shows the overall scale of the input pulse with the high-intensity regions forming from the low-intensity background. There is practically no plasma formation at this propagation distance.

The initial perturbations grow rapidly and reach intensities high enough to ionize air (second panel). Collapse of a filament is eventually regularized by plasma induced defocusing. That causes decay of the filament and returns
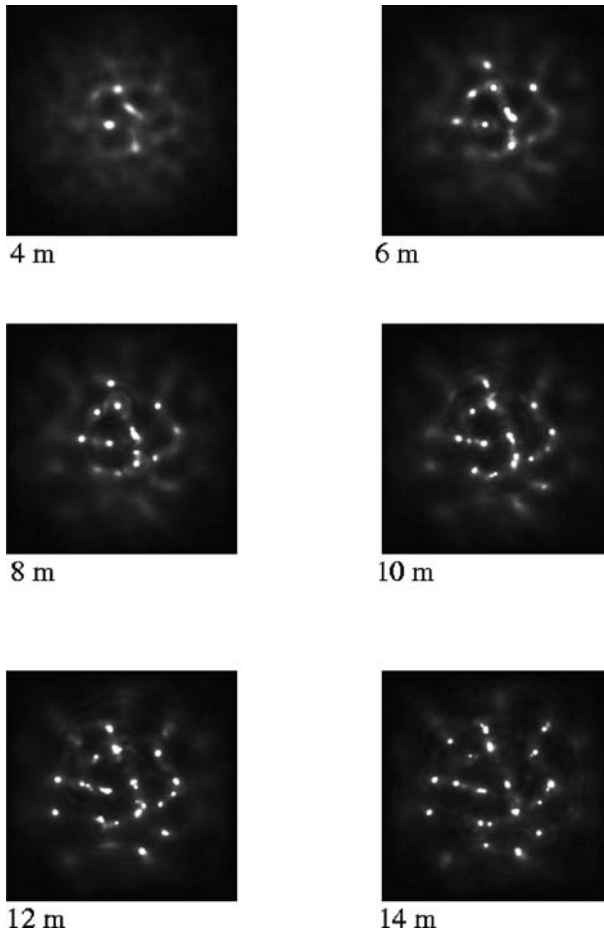
Fig. 13.3. Transverse profile of the fluence (time-integrated intensity) "measured" at several propagation distances. The color scheme was chosen such that one can see the structure of the low-intensity background. On the other hand, it makes it difficult to compare filament intensities. The size of the depicted domain in all panels is $1\,\mathrm{cm} \times 1\,\mathrm{cm}$

most of its energy into the low-intensity background. From there, new filaments grow and these replenishment cycles repeat with relatively modest energy losses to plasma generation (subsequent panels).

Later in the propagation, filaments start to appear in the peripheral regions further from the center. This is due to less overall intensity and therefore slower self-focusing and growth of perturbations. Though it is not evident on these fluence pictures, later-stage filaments tend to generate less plasma than the ones that appear at the very beginning of the filamentation onset. This is the stage when the single-filament dynamic spatial replenishment scenario
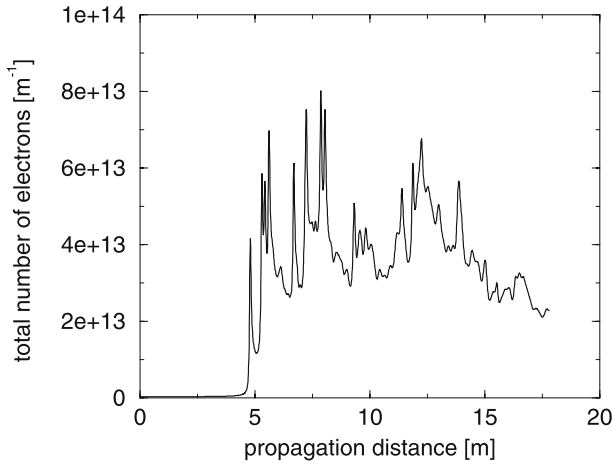
Fig. 13.4. Total number of free electrons generated as a function of propagation distance

crosses over to a regime where replenishment energy originates in "neighboring" filaments rather than from the same one.

This gradual change in the dynamics is reflected also in the plasma generation as shown in Fig. 13.4. Initial sharp spikes in the total number of generated electrons, associated with the onset of individual filaments, decay with distance. We expect the shot-to-shot fluctuation to smooth-out the sharp features of this curve due to randomization of the filament formation. With the propagation distance, the spatial coherence of the beam deteriorates, and the late-stage filaments are less "organized" than those created just after the self-focusing onset. Consequently, it takes less of the plasma generation to arrest their collapse because the typical filament temporal duration is shorter. One can say that the increasing "disorder" or the partial loss of spatial coherence in the developing composite pulse makes the collapse arrest due to plasma more efficient and thus contributes to the ability of the pulse to propagate over long distances. One can speculate, and recent experiments [37] as well as theoretic studies [38] indicate that a regime can be eventually reached where the plasma generation is almost negligible.

13.4.2 Nonlinear X-Waves in Condensed Media

In this Section, we present an example of simulation of an ultrashort pulse in water. This particular example requires that the solver captures correctly the linear dispersion in a broad range of frequencies and propagation angles, and is thus an ideal candidate for UPPE application. Full details can be found in an earlier publication [39].

We consider a loosely focused femtosecond pulse centered around the 520 nm wavelength, propagating in a water sample. An appropriate combi-

nation of focusing and pulse intensity and duration results in a long filament (compared to the Rayleigh range corresponding to the transverse size of the beam at the water-cell entrance).

Figure 13.5 shows the resulting filament transverse dimension (size) for several pulse energies as a function of the propagation distance in water (left). The right panel illustrates that supercontinuum is easily generated at these energies. We thus deal with a highly non-NLS regime.

The question we want to shed light on in this numerical experiment is what mechanism is responsible for creation of that seemingly several centimeters long filament. Further, we want to know if the mechanism is universal in any way.

First, it is important to note that what is actually observed, in experiment and in simulation alike, is not a "steady-state" self-guided filament. Rather, we deal with a series of pulse splitting events akin to the scenario of spatial dynamical replenishment [7]. In this case, however, the role of plasma as the arrestor of the self-focusing collapse is less pronounced compared to propagation in air.

Figure 13.6 shows a series of snapshots that depict the temporal profile of on-axis intensity of the now quite complicated "pulse". One observes several cycles consisting of formation and subseqent splitting of a sub-pulse in the center of the time domain. The "daughter" sub-pulses resulting from each pulse-split event play an important role in the formation of the spatial and temporal spectrum. Namely they are still intense enough to induce localized changes to the material susceptibility that in turn follow these split-off pulses and thus propagate with different "group" velocities. These material waves then act as scatterers in a three-wave mixing process that transforms the input optical waves into scattered ones. Linear propagation dispersion properties together with the propagation velocity of the material wave then
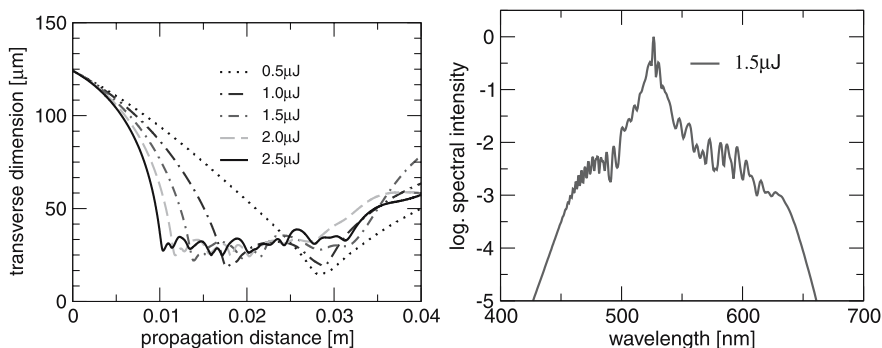
Fig. 13.5. Femtosecond pulse loosely focused into water creates a long filament with a nearly constant diameter that extends over many Rayleigh ranges (*left*), and generates a broad supercontinuum spectrum (*right*). This seemingly stationary filament is created by a series of very dynamic multiple pulse splittings illustrated in the following
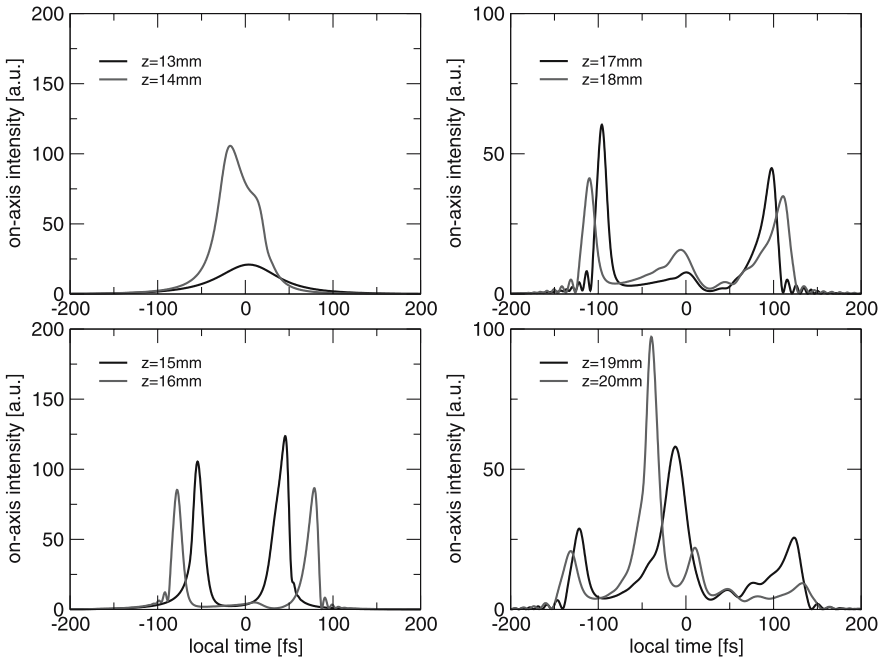
Fig. 13.6. Pulse splitting cycle: Single central pulse undergoes splitting. The split-off-pulses act a "scatterers", which concentrate most of the energy in the spatio-temporal spectrum around loci that support "diffractionless" wave-forms. This provides the energy for a new central pulse, and the cycle repeats ...
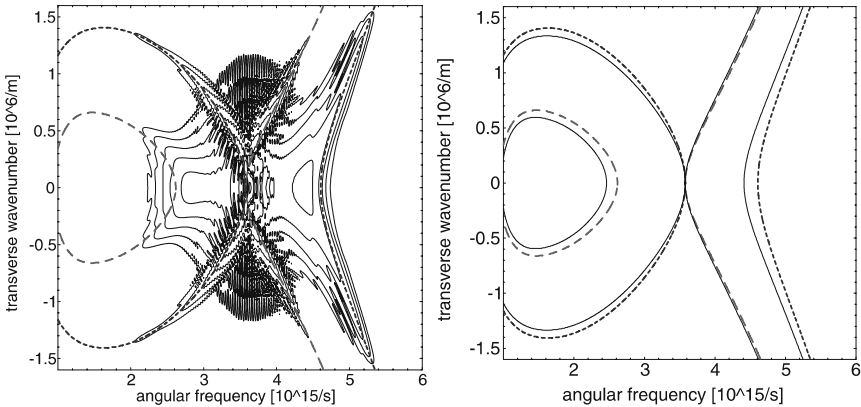
Fig. 13.7. Angle-resolved spectrum of an ultrashort pulse propagating in water (*left panel*). The *dashed lines* represent the loci of spectral energy concentration predicted from an effective three-wave mixing argument. The *right panel* compares these loci to the manifold that supports the spectrum of z-invariant X-wave solutions that propagate without distortions

determine where in the spectral space will the scattered energy accummu-
late.

The resulting spatio-temporal spectrum of a loosely focused ultrashort
pulse after propagation in water is shown in Fig. 13.7 on left. The dashed
lines (in both, left and right panels) represent the loci where energy con-
centrates due to the non-linear interactions irrespectively of the details
of the underlying dynamics. The resulting central X-shaped feature is al-
ways close to the manifold (shown in full line, right panel) that supports
the z-invariant X-waves that propagate long distances without changing
their spatio-temporal shapes. In any normal-GVD medium, the "theoreti-
cal X-wave" spectrum and the "real-pulse" spectral concentration will be
close to each other because of the simple landscape of chromatic dispersion
in the space of frequency and transverse wavenumber. Thus, even highly non-
stationary pulses inherit their tendency for long-distance propagation form
the nonlinear X-waves.

13.4.3 Supercontinuum Generation in Bulk Media

In this Section, we describe comparative simulations that provided further
insight into how supercontinuum is generated by powerful femtosecond pulses
propagating in bulk medium. Readers interested in more details can found
those in [22] and in [21].

The SC generation requires high intensities that are initiated by self-
focusing collapse in the medium. The mechanism that arrests the collapse
is supplied by multi-photon ionization (MPI) which produces both a di-
rect energy loss for the collapsing field and an electron–ion plasma, which
subsequently absorbs, defocuses, and spectrally blue-shifts the optical field.
The combined effects of MPI and plasma defocusing provide a mechanism
for the arrest of self-focusing collapse, which clamps the maximum inten-
sity $I_{\max}$ reached by the collapsing pulse, and also limits the maximum
rate of plasma generation $\partial_t \rho \propto I_{\max}^K$, with ρ the plasma density and K
the order of the MPI. The standard scenario [23, 40–43] maintains that the
dominant contribution to spectral broadening comes from the spectral blue-
shifting due to the plasma [42, 44], with the maximum blue-side frequency
shift $\Delta\omega_{\max} \propto \partial_t \rho \propto I_{\max}^K$. Thus, according to the standard scenario, limiting
of the maximum intensity $I_{\max}$ as self-focusing is arrested is the dominant
factor that determines the spectral extent $\Delta\omega_{\max}$ of SC generation.

In order to put the standard SC generation scenario to a test, we com-
pare the water SC generation simulations with analogous simulations per-
formed using an artificial medium which is the same as the "original" but
with a modified linear dispersion. The later is "constructed" such that the
artificial medium exhibits self-focusing and plasma dynamics that are almost
identical to those of the real medium model.

Frequency mapping $\omega \rightarrow \Omega(\omega)$ that is used to construct the artificial
water susceptibility is shown in long-dashed line in Fig. 13.8 (the dotted

line shows identity function for comparison). The artificial and water susceptibility functions are depicted in dashed and full lines, respectively in Fig. 13.8. The arrow illustrates the susceptibility transformation. Susceptibility is preserved around the pulse carrier frequency, in order to preserve all the quantities that control the SC generation under the standard scenario, such as the highest light intensities and plasma density. Consequently, according to the standard scenario, the two media should generate the same SC spectra. Numerical simulations are used to check if this is the case.

To show that both model media should indeed provide essentially the same SC spectrum in our simulations, provided the standard SC scenario is correct, we present a comparison of the nonlinear response for water and
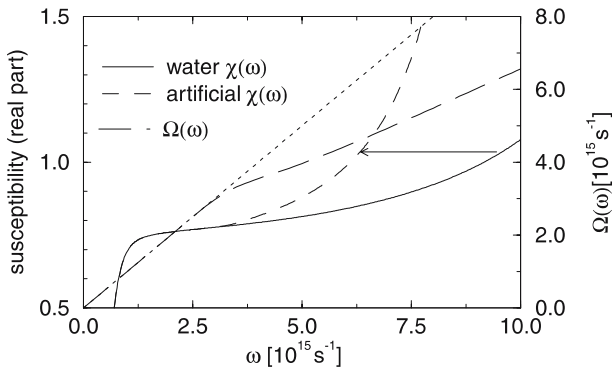
Fig. 13.8. "Artificial" vs "real" water susceptibility used in comparative simulations designed to test the standard supercontinuum generation scenario for bulk media
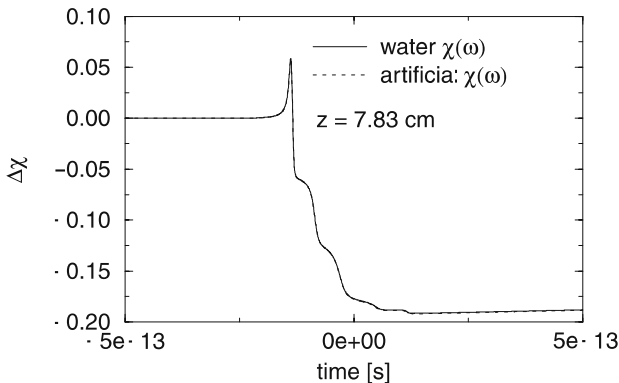
Fig. 13.9. Local susceptibility variation induced by the nonlinear effects in the femtosecond pulse. Water and the comparative artificial medium exhibit very similar responses

the artificial medium in Fig. 13.9. The nonlinear response consist in a local change $\Delta\chi$ of the medium susceptibility. As a function of the "local time" at pulse location, it first increases due to the increasing intensity created by the selffocusing. Then the susceptibility change decrease into negative values because of the de-focusing caused by the plasma generated in the high-intensity light pulse. The picture shows, that the nonlinear response of the artificial medium is extremely close to that of the water. This indicates that if the standard model of SC generation is complete, the almost same response dynamics implies closely similar SC spectra.

The comparison of the SC spectra obtained using the realistic and artificial water susceptibilities is shown in Fig. 13.10. The original and artificial medium spectra agree quite well in the vicinity of the excitation wavelength. However, at high frequencies the two materials produce drastically different continua. The long-dashed line shows the SC spectrum transformed by the same transformation that produced the artificial medium susceptibility from the water susceptibility. This appears to be very close to the artificial medium spectrum. This indicates that the extent of the spectrum is actually determined mostly by the linear dispersion properties of the medium.

Thus, we arrive at the conclusion that the standard scenario for supercontinuum generation in bulk media *is incomplete*. Although it correctly identifies the key quantities (peak intensity, plasma density generation rate) and processes (collapse arrest, MPI), our numerical experiments demonstrate that it doesn't explain the supercontinuum spectral properties.

It should be noted that Gaeta pointed out the importance of self-steepening terms (which are, of course, fully captured by the UPPE solver used in our simulations) for the high-frequency component of the supercon-
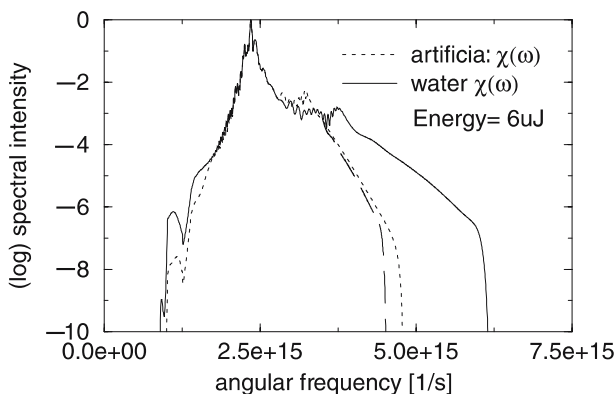
Fig. 13.10. Supercontinuum spectra generated in water (*solid line*) and in the artificial medium (*dotted line*). The *long-dashed line* represents the spectrum edge obtained from the real water spectrum the same way as the artificial susceptibility was obtained from the original water susceptibility. The standard SC scenario predicts the same spectra for both models

tinuum was pointed in [36], and thus partly corrected the standard scenario. However, to complete the supercontinuum generation picture for bulk media, the medium's frequency-dependent linear susceptibility must be taken into account as a key factor that determines the maximal attainable width of the white light spectrum.

Further simulations (not shown) also showed that the so-called super-continuum band-gap dependence is due to stronger chromatic dispersion at higher frequencies. Namely, increasing the excitation frequency has a similar effect on the SC spectrum as the artificial modification of the susceptibility we used in our simulations; the curvature of the dispersion function is stronger closer to the band-gap and reduces the spectral broadening due to the larger phase-mismatch in the underlying wave mixing processes.

13.5 Future Work and Perspectives

This chapter has focused on procedures for deriving ultra short propagation pulse propagation models starting from Maxwell's equations. The uni-directional pulse propagation equation(UPPE) possesses all of the essential ingredients for current and future studies in the emerging field of extreme nonlinear optics. We have shown that the latter provides a unifying theoretical framework from which the many propagation equations in the literature can be seamlessly derived. Moreover, the physical approximations made in these models are clearly exposed and their interrelationships stressed.

References

 1. M. Kolesik and J. V. Moloney, Phys. Rev. E **70**, 036604 (2004).
 2. A. Braun et al., Opt. Lett. **20**, 73 (1995).
 3. A. Brodeur et al., Opt. Lett. **22**, 304 (1997).
 4. H. R. Lange et al., Opt. Lett. **23**, 120 (1998).
 5. E. T. J. Nibbering et al., Opt. Lett. **21**, 62 (1996).
 6. O. G. Kosareva et al., Opt. Lett. **22**, 1332 (1997).
 7. M. Mlejnek, E. M. Wright, and J. V. Moloney, Opt. Lett. **23**, 382 (1998).
 8. B. La Fontaine et al., Phys. of Plasmas **6**, 1615 (1999).
 9. M. Mlejnek, E. M. Wright, and J. V. Moloney, Phys. Rev. E **58**, 4903 (1998).
10. J. Schwartz et al., Opt. Commun. **180**, 383 (2000).

11. A. Chiron et al., Eur. Phys. J. D **6**, 383 (1999).
12. A. Couairon and L. Bergé, Phys. of Plasmas **7**, 193 (2000).
13. L. Bergé and A. Couairon, Phys. of Plasmas **7**, 210 (2000).
14. S. Petit, A. Talebpour, A. Proulx, and S. L. Chin, Opt. Commun. **175**, 323 (2000).
15. M. Mlejnek, M. Kolesik, J. V. Moloney, and E. M. Wright, Phys. Rev. Lett. **83**, 2938 (1999).
16. A. Talebpour, S. Petit, and S. L. Chin, Opt. Commun. **171**, 285 (1999).
17. J. V. Moloney, M. Kolesik, M. Mlejnek, and E. M. Wright, Chaos **10**, 559 (2000).
18. N. Aközbek, C. M. Bowden, A. Talebpour, and S. L. Chin, Phys. Rev. E **61**, 4540 (2000).
19. J. Noack and A. Vogel, IEEE J. Quantum Electron. **35**, 1156 (1999).
20. S. Tzortzakis et al., Phys. Rev. Lett. **87**, 213902 (2001).
21. M. Kolesik, G. Katona, J. V. Moloney, and E. M. Wright, Phys. Rev. Lett. **91**, 043905 (2003).
22. M. Kolesik, G. Katona, J. V. Moloney, and E. M. Wright, Appl. Phys. B **77**, 185 (2003).
23. W. Liu et al., Opt. Commun. **202**, 189 (2002).
24. J. M. Dudley and S. Coen, Opt. Lett. **27**, 1180 (2002).
25. J. M. Dudley et al., J. Opt. Soc. Am. B **19**, 765 (2002).
26. A. L. Gaeta, Opt. Lett. **27**, 924 (2002).
27. L. Tong et al., Nature **426**, 816 (2003).
28. A. Couairon and L. Bergé, Phys. Rev. Lett. **88**, 135003 (2002).
29. D. Hollenbeck and C. D. Cantrell, J. Opt. Soc. Am. B **19**, 2886 (2002).
30. V. P. Kandidov et al., Appl. Phys. B **77**, 149 (2003).
31. M. Geissler et al., Phys. Rev. Lett. **83**, 2930 (1999).
32. A. C. Newell and J. V. Moloney, *Nonlinear optics* (Addison-Wesley, Redwood City, CA, 1992).
33. T. Brabec and F. Krausz, Phys. Rev. Lett. **78**, 3282 (1997).
34. A. V. Husakou and J. Herrmann, Phys. Rev. Lett. **87**, 203901 (2001).
35. E. R. Peck and K. Reeder, J. Opt. Soc. Am. **62**, 958 (1972).
36. A. L. Gaeta, Phys. Rev. Lett. **84**, 3582 (2000).
37. G. Méchain et al., Appl. Phys. B **79**, 379 (2004).
38. S. Champeaux and L. Bergé, Phys. Rev. E **71**, 046604 (2005).
39. M. Kolesik, E. M. Wright, and J. V. Moloney, Phys. Rev. Lett. **92**, 253901 (2004).
40. W. Lee Smith, P. Liu, and N. Bloembergen, Phys. Rev. A **15**, 2396 (1977).
41. A. Brodeur and S. L. Chin, Phys. Rev. Lett. **80**, 4406 (1998).
42. A. Brodeur and S. L. Chin, J. Opt. Soc. Am. B **16**, 637 (1999).
43. C. Nagura et al., Appl. Opt. **41**, 3735 (2002).
44. Y.-D. Qin, D.-L. Wang, S.-F. Wang, and Q.-H. Gong, Chin. Phys. Lett. **18**, 390 (2001).

14 Some Properties
of Femtosecond Laser Filamentation
Relevant to Atmospheric Applications
Part I. The Robustness of Filamentation

Jérôme Kasparian

Teramobile, Laboratoire de Spectrométrie Ionique et Moléculaire,
UMR CNRS 5579, Bâtiment Kastler, Université Claude Bernard Lyon 1,
43 bd du 11 novembre, F69622 Villeurbanne Cedex France
e-mail: jkaspari@lasim.univ-lyon1.fr

Summary. When ultrashort (fs), high-power laser pulses propagate through the atmosphere, extended plasma filaments form and emit white light in a spectral range spanning from the ultraviolet (230 nm) to the infrared (4.5 µm). This strongly non-linear optical phenomenon results from a dynamical balance between respectively focusing and defocusing Kerr- and plasma-lenses, which are formed by a non-uniform, intensity-dependent refractive index across the laser beam profile. This non-linear propagation regime opens the way to various applications in atmospheric sciences, such as white-light Lidar relying on the white light continuum, which can be observed up to high altitudes and allows multicomponent remote sensing. Other applications rely on the ability of the filaments to deliver high-intensities and induce non-linear optical effects at remote locations, e.g. bioaerosols remote sensing or solid target analysis. Furthermore, the ionization of the fs-laser-induced filaments permits to control high-voltage discharges, opening the way to laser lightning rods.

This chapter shall review the basic properties of filamentation, with a particular emphasis on one spectacular feature: Their ability to propagate unperturbed across clouds and fogs.

14.1 Introduction

In the recent years, atmospheric applications of ultrashort, ultra-intense laser pulses have emerged. The most promising include non-linear Lidar [1–3], remote laser-induced breakdown spectroscopy (LIBS) [4] and the control of high-voltage discharges [5–11]. The interest for these perspectives has been strongly enhanced when the groups of L. Wöste and R. Sauerbrey, who tried to generate an atmospheric plasma "white lamp" using slightly focused 100 fs laser pulses with 3 TW peak power, observed a long white-light filament in the atmosphere. The beam, similar to observations at shorter scale on the laboratory [12], was clearly visible with bare eye (Fig. 14.1) [1,13], although the laser wavelength was in the infrared, around 800 nm. This white-light filament was visible even when the laser was emitted collimated. The backscattered signal in the blue-green spectral region could be detected from altitudes above

Fig. 14.1. White-light filament generated in the atmosphere by infrared femtosecond-terawatt laser pulses. (Photo C. Wedekind)

10 km. This experiment constituted the first observation of filamentation on an atmospheric scale.

Atmospheric applications in turn require a good characterization of the non-linear propagation of ultrashort laser pulses over long distance up to the multi-kilometre range, raising the need for field experiments. In that purpose, the first mobile femtosecond-terawatt laser system, *Teramobile* [14], was set-up and constructed by a French-German consortium. For the first time, the *Teramobile* allows this class of lasers to get out of the laboratory and work under hard conditions, including temperature fluctuations, humidity, dust, etc. Using this system, the *Teramobile* team characterized many properties of filamentation relevant for long-distance propagation of ultrashort laser pulses and their applications in the atmosphere.

After recalling the basics of filamentation, this chapter will briefly present the *Teramobile* laser system, and discuss the transmission of filaments through atmospheres perturbed by fog and clouds.

14.2 The Physics of Filamentation in the Atmosphere

The formation of self-guided filaments in the air at the laboratory scale has been known for almost ten years [12, 15–17]. Filamentation occurs when high-power laser pulses propagate in a highly non-linear way in transparent media (Fig. 14.2). This high non-linearity induces a self-action, which

Kerr effect focuses: Δn =n $_2$*I   Plasma defocuses: Δn = - N(I) / 2N$_{crit}$
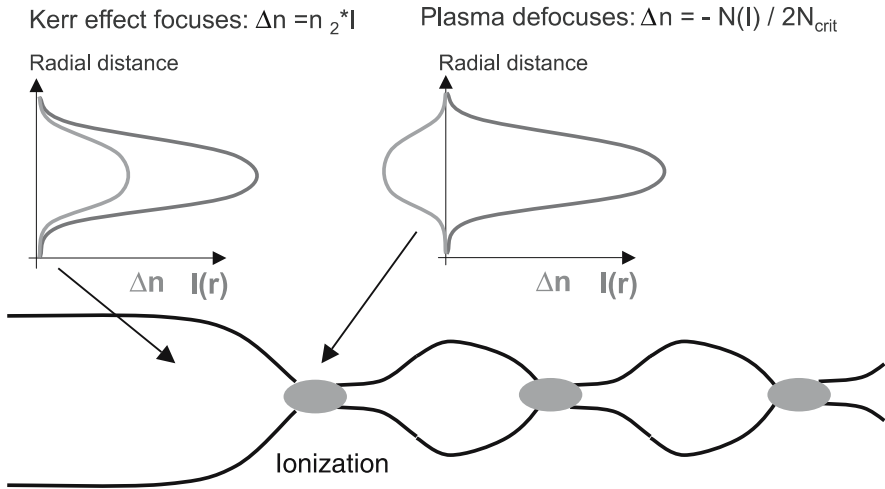
Fig. 14.2. Principle of filamentation. The beam first self-focuses and collapses due to the Kerr effect. Ionization at the non-linear focus then defocuses the beam. A dynamical balance establishes between both processes over distances much over the Rayleigh length

strongly modifies the pulses spatially (self-focusing [18], self-guiding [12], self-reflection [19]), spectrally (four-wave mixing [20], self-phase modulation [21–23]) as well as in the temporal domain (self steepening [24–26], pulses splitting [27]). Moreover, the propagation medium is strongly affected by multiphoton ionization, which generates a plasma [28–32].

Those phenomena have been investigated both theoretically and experimentally since the 1970's in condensed media. The advent of the chirped pulse amplification (CPA) technique [33, 34] in 1985 allowed the generation and the amplification of ultrashort laser pulses, reaching very high intensities (up to 10^{21} W/cm^2) at which those non-linear processes can be observed even in atmospheric pressure gases in spite of their low non-linearity. In the following, we shall focus on the non-linear propagation of ultrashort laser pulses in the air and the processes leading to filamentation and the generation of a broad white-light supercontinuum.

14.2.1 Kerr-Lens Self-Focusing

The first non-linear effect at play in the propagation of high-power laser pulses is Kerr self-focusing [35, 36]. For high fluences, the refractive index of air depends on the incident intensity:

$$n(I) = n_0 + n_2 \cdot I \, , \tag{14.1}$$

where $n_2 \approx 3 \times 10^{-19}$ cm^2/W [37] is the non-linear refractive index of air. Since the intensity profile of the beam is not flat, the Kerr effect generates

a refractive index profile (Fig. 14.2, left), which acts as a convergent lens or "Kerr lens", which focal length depends on the intensity. The more the beam is focused by the Kerr lens, the higher the intensity, so that the focusing gets stronger and stronger until the beam collapses. Therefore, the Kerr effect alone would prevent high power laser pulses to propagate over long distances in the air. For the self-focusing to effectively occur, the Kerr lens term of the propagation equation has to overcome the diffraction, i.e. $k^2 \cdot n_2 \cdot I - 1/w^2 > 0$, where w is the beam diameter, $1/w^2$ is the diffraction term in the propagation equation, and k is the wave number [24]. Therefore, self-focusing happens if the beam power exceeds a *critical power*:

$$P_{\text{crit}} = I \cdot \pi \cdot w^2 = \frac{\pi}{k^2 \cdot n_2} = \frac{\lambda^2}{4\pi \cdot n_2} \ . \tag{14.2}$$

For a titanium:sapphire ($\lambda = 800\,\text{nm}$) in the air, $P_{\text{crit}} \sim 3\,\text{GW}$.

Although the Kerr effect involves the intensity, the occurrence of self-focusing is determined by the beam *power* rather than the beam *intensity*. However, once the self-focusing occurs, the beam diameter, and hence its intensity, determines the non-linear focal length, i.e. the point where the beam will collapse. The location z_{f} of the non-linear focus for a power P is given by the empirical Marburger formula [38]:

$$\frac{1}{z_{\text{f}}(P)} = -\frac{1}{R} \pm \frac{\sqrt{\left(\sqrt{P/P_{\text{crit}}} - 0.852\right)^2 - 0.0219}}{0.367 \cdot k \cdot a^2} \ , \tag{14.3}$$

where R is the initial curvature of the wavefront, k is the wavenumber and a the beam radius at $1/e$.

14.2.2 Ionization and Plasma Generation

The strong focusing of a high-power laser beam results in a high local intensity. When this intensity reaches 10^{13} to $10^{14}\,\text{W/cm}^2$, higher-order non-linear processes come into play, such as ionization. The main process at the root of ionization by near-infrared, ultrashort laser pulses is mainly tunnel ionization [39] (MPI). At 800 nm, 8 to 10 photons are required to ionize nitrogen and oxygen molecules and produce a plasma [40]. Contrary to longer pulses, ultrashort pulses combine a high intensity resulting in efficient ionization, and moderate energy so that the average generated electron densities (10^{15}–$10^{17}\,\text{cm}^{-3}$) are well below saturation [41]. Moreover, losses by inverse Bremsstrahlung are negligible because the laser pulses are much shorter than the typical mean free time of an electron in air (1 ps). These weak losses allow long-distance propagation. However, the electron density ρ has a negative contribution to the refractive index. Due to the radial intensity profile of the laser, this contribution results in a negative refractive index gradient which behaves like a diverging lens and defocuses the beam, as shown in the right panel of Fig. 14.2.

14.2.3 Filamentation of High-Power Laser Pulses

Considered alone, both the beam collapse due to the Kerr effect and the defocusing induced by the plasma would prevent long-distance propagation of high-power laser pulses in the air. However, both effects can dynamically balance each other and give rise to a self-guided, quasi-solitonic propagation regime [42]. The laser beam first self-focuses by Kerr effect. When a sufficient intensity is reached, a plasma is generated and defocuses the beam until the intensity is reduced and ionization stops, so that the Kerr effect dominates again. This *dynamical balance* between the Kerr effect and ionization leads to the formation of stable structures, or *filaments* (Fig. 14.2). Filaments have been observed already in 1995 by par A. Braun et al. [12], who discovered that mirrors could be damaged by ultrashort laser pulses even at large distances from the laser source. The intensity in the filaments is almost constant (typically $10^{14}\,\mathrm{W/cm^2}$) [43], as are the energy that they can transport (several mJ), their diameter (typically $100\,\mu\mathrm{m}$) and their electron density (typically $10^{16}\,\mathrm{cm^{-3}}$) [41]. The dynamic balance can guide light in the filaments over distances much exceeding the Rayleigh length for the initial beam, up to many tens or meters. Guiding over several hundreds of meters was even observed, although the process balancing the Kerr effect is probably not ionization in this case [44–46].

14.2.4 Modelling of Filamentation

Many groups have devoted efforts to model the non-linear propagation of high-power, ultrashort laser pulses, in the single filament regime at moderate energy [see e.g. [17, 47–53]] as well as in the multiple-filament regime at high energy [46, 54–59]. The details of such modelling are beyond the scope of this chapter. However, the principle is based on considering the propagation of laser pulses as governed by the Maxwell equations:

$$\nabla^2 E - \frac{1}{c^2} \cdot \frac{\partial^2 E}{\partial t^2} = \mu_0 \cdot \sigma \cdot \frac{\partial E}{\partial t} + \mu_0 \cdot \frac{\partial^2 P}{\partial t^2} \; , \qquad (14.4)$$

where σ is the conductivity and accounts for losses, and P is the medium polarization. Contrary to the linear case, P includes a non-linear term accounting for the Kerr effect and plasma generation:

$$P = P_\mathrm{L} + P_\mathrm{NL} = \varepsilon_0 \cdot (\chi_\mathrm{L} + \chi_\mathrm{NL}) \cdot E \; , \qquad (14.5)$$

where χ_L and χ_NL are the linear and non-linear susceptibilities, respectively. Considering a pulse with radial symmetry propagating along the z axis in a referential propagating at the group velocity v_g, and considering only dominating terms into account yields the Non-linear Schrödinger equation (NLSE) [60]:

$$\nabla_\perp^2 \varepsilon + 2\mathrm{i} \left(k \frac{\partial \varepsilon}{\partial z} \right) + 2k^2 n_2 \cdot |\varepsilon|^2 \cdot \varepsilon - k^2 \frac{\rho}{\rho_\mathrm{c}} \cdot \varepsilon = 0 \; , \qquad (14.6)$$

where $\varepsilon = \varepsilon(r, z, t)$ is the envelope of the electrical field and ρ_c is the critical electron density (1.8×10^{21} cm^{-3} at 800 nm [42]). ε is supposed to vary slowly in both time (compared to the optical frequency) and in space (compared to the beam diameter). At the first order, group velocity dispersion (GVD), self-steepening, retarded Kerr effect and Raman effect are neglected, as well as the losses through ionization and plasma absorption ($\sigma = 0$). In (14.6), the Laplacian accounts for the diffraction in the transverse direction, while the last two terms correspond to the two opposite non-linear contributions to propagation: Kerr self-focusing and defocusing on the plasma. The electron density $\rho(r, z, t)$ is calculated from a kinetic equation (14.7), in a self-consistent scheme with Equation (14.6):

$$\frac{\partial \rho}{\partial t} - \gamma \, |\varepsilon|^{2\alpha} \, (\rho_n - \rho) = 0 \ . \tag{14.7}$$

In this equation, ρ_c is the concentration of molecules in the air, γ the efficiency of MPI and α the photon number required to ionize air molecules, i.e. typically 8 to 10 [40]. Numerically integrating the NLSE yields the evolution of the pulse intensity $I = |\varepsilon|^2$ as a function of the propagation distance, as shown in Fig. 14.3. The initial Kerr self-focusing as well as the MPI-generated plasma are well reproduced by such simulation. Here, the filament propagation is simulated over 60 m, limited by the computer capacity.
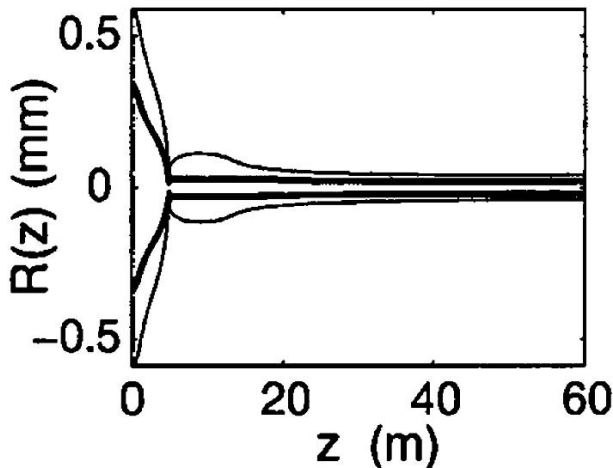
Fig. 14.3. Numerical simulation of filamentation [50]

14.2.5 Self-Phase Modulation and White-Light Generation

The high intensity within the filaments (4 to 6×10^{13} W/cm^2) [43] generates an efficient self-phase modulation (Fig. 14.4), resulting in the emission of

a white-light supercontinuum. This is due to a temporal counterpart of the Kerr effect. Since the intensity $I(t)$ is time dependent within the pulse, so is the refractive index, as described by (14.1), which can be rewritten in the time domain:

$$n(t) = n_0 + n_2 \cdot I(t) \ . \tag{14.8}$$

This effect induces a time-dependent dephasing, and hence shifts the frequency $\omega(t)$:

$$\omega(t) = \frac{\mathrm{d}\Phi(t)}{\mathrm{d}t} = \omega_0 - \frac{n_2 \omega_0}{c} z \frac{\mathrm{d}I(t)}{\mathrm{d}t} \ , \tag{14.9}$$
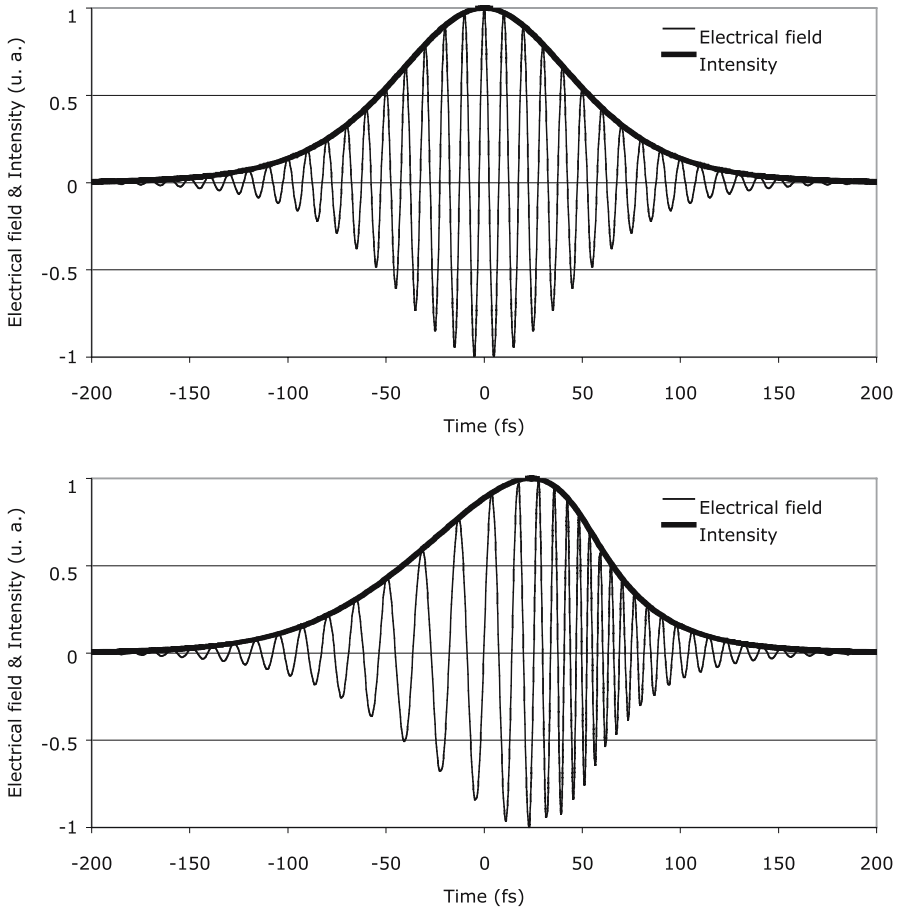
Fig. 14.4. Effect of self-phase modulation. The initial pulse (*top*) is deformed along the propagation. The centre of the beam, which is more intense, is retarded relative to its head and trail by the non-linear refractive index. The resulting change in the envelope generates low frequencies on the rising front and high frequencies on the trailing front

where $\Phi(t)$ is the phase at time t, c is the speed of light, z the propagation distance and ω_0 is the initial laser frequency. The slowly varying envelope model yields a strong spectral broadening around ω_0. Due to this mechanism, the generated white-light is coherent. It is mainly emitted forward, with one part emitted collinear with the filament as a "white-light laser" [61], and the other part as *conical emission* [15,62,63] forming coloured rings with an angle function of the wavelength, ordered reversely to diffraction (Fig. 14.5a). The interpretation of this conical emission is not fully clear to date. Some authors attribute it to Cerenkov emission [15], while other ones attribute it to the refraction of the white-light emitted at the trail of the pulse, by the plasma generated at the front of the same pulse [62].

It has also been shown that a significant part of the white-light is emitted in the backward direction [64]. At 179°, the relative backscattered intensity is one order of magnitude higher than in the linear Rayleigh backscattering. An even stronger effect is expected at 180°, although the experimental setup cannot cover that angle. This backward enhanced emission can be interpreted as due to the partial reflection of the white-light on the longitudinal refractive index gradients produced by the fluctuations in the plasma density. Raman coupling could also be involved in the process. Such a self-reflection, combined with the self-guiding which strongly reduces the beam divergence, is a great advantage for Lidar: Contrary to what happens with classical white-light sources with a low luminance, such as flashlamps, an important part of the white-light generated at a given distance can be collected by the Lidar detector located near to the laser source.
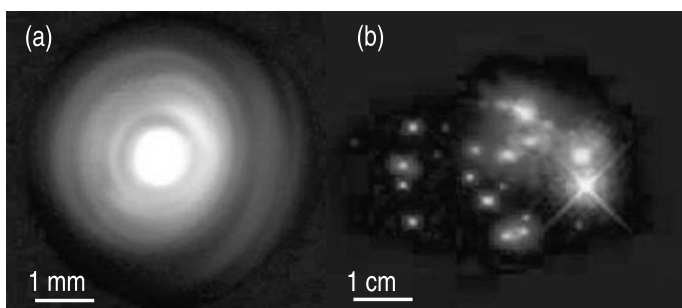
Fig. 14.5. a Conical emission observed on a screen; **b** Multifilament pattern on a screen

14.2.6 Propagation at Higher Energy

At an even higher power ($P \gg P_{\text{crit}}$), the beam profile divides itself into several localized filaments. The intensity within each filament is limited to about 10^{14} W/cm^2, corresponding to an energy of several mJ. Hence, increasing the

peak power of the pulses increases the filament number without notably influencing neither their individual intensity nor energy. Figure 14.5 displays the profile of filamenting laser beams, at moderate (Fig. 14.5a, 5 mJ) and high energy (Fig. 14.5b, 400 mJ), respectively leading to single and multiple filamentation.

Filamentation makes Femtosecond-terawatt lasers good candidates for the development of atmospheric applications to remote sensing, lightning control or remote analysis of surfaces. It provides a unique source of coherent white-light ("white-light laser" [61]) with enhanced backscattering, very suitable for multispectral Lidars capable of multipollutant remote sensing and mapping [3,65]. Also, the generation of ionized filaments over long distances opens the way to the control of high-voltage discharges [5–11], or even lightning. Finally, the ability of the filaments to deliver high intensities at distances without diffraction limitation can be applied to remote surface analysis by LIBS [4]. Such applications [2] have motivated a wide spectrum of experiments regarding the propagation of ultrashort laser pulses and filamentation in the atmosphere, under realistic conditions. Propagation properties related to these applications are detailed below, after a short description of the *Teramobile* laser, which made most of them possible by offering for the first time the opportunity to perform field measurements with a femtosecond-terawatt laser.

14.3 The *Teramobile* Laser [14]

Field experiments require mobility to perform investigations at adequate locations. Studies of high-power femtosecond laser beam propagation over kilometre-range distances can only be performed realistically in outdoor experiments. The fs-Lidar measurements have to be performed where relevant gaseous or aerosol pollutants occur, e.g. in urban areas or at industrial sites. Laser-lightning studies require spots where the lightning probability is high, as well as test experiments at high voltage facilities. These considerations clearly define the need for a mobile fs-TW laser system, embedded in a standard freight container-integrated laboratory equipped with the necessary Lidar detection, power and cooling supplies, temperature stabilization, vibration control, and an additional standard Lidar system to assure eye safety.

This was first achieved by the *Teramobile* system [14]. The laser itself is based on the chirped pulse amplification (CPA) technique [33, 34], with a Ti:Sapphire oscillator and a Nd:YAG pumped Ti:Sapphire amplification chain. It provides 350 mJ pulses with 70 fs duration resulting in a peak power of 5 TW at a wavelength around 800 nm, with a repetition rate of 10 Hz. Its integration in the reduced space of the mobile laboratory required a particularly compact design (Fig. 14.6). The classical compressor set-up has been improved into a chirp generator to pre-compensate the group velocity dispersion (GVD) in air. Combined with an adjustable focus, this permits to
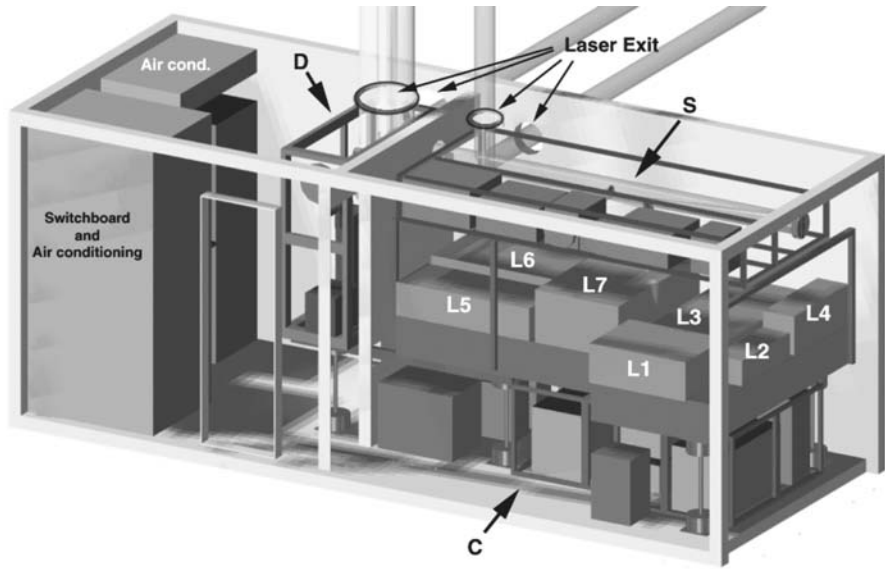
Fig. 14.6. Three-dimensional view of the Teramobile. (L): Laser system: Ti:Sa oscillator and its Nd:YAG pump laser ($L1$), stretcher ($L2$), regenerative amplifier, multipass preamplifier ($L3$) and their Nd:YAG pump laser ($L4$); Multipass main amplifier ($L5$) pumped by two Nd:YAG units ($L6$); Compressor ($L7$). (S), Beam expanding system; (C), Power supplies (D), Lidar detection system [14]

control the distance of the onset of filamentation and its length. Particular care was taken to the control of the mechanical and thermal stability of the mobile laboratory, so that the Teramobile can be transported to virtually any place in the world, and operated even under adverse weather conditions.

The *Teramobile* container also includes a Lidar detection chain based on a 40 cm receiving telescope, a high-resolution spectrometer equipped with a set of gratings and detectors allowing simultaneous temporal and spectral analysis of the return signal in a wavelength range between 190 nm and 2.5 μm.

14.4 Filament Transmission Through Clouds

Since it allows field experiments, the *Teramobile* opens the way to atmospheric applications of ultrashort, high-power lasers. Such applications also require a comprehensive knowledge about the atmospheric propagation of fs-TW laser pulses in the atmospheres, under realistic conditions. This implies experiments over long propagation distances, up to the kilometre range, as well as the transmission through temperature or pressure gradients or through perturbed atmospheres, e.g. rain or fog. The transmission of a laser beam across the atmosphere, and especially through clouds, is a key question

for free space communication, Lidar remote sensing [1–3], telemetry, active imaging, lightning discharge control [5–11], or even to test general relativity effects in the earth gravitational field [66]. Filaments are promising candidates to overcome the limitation of the optical transmission through the atmosphere (turbulence, group velocity dispersion, scattering), since they propagate as quasi-solitons [42], which generate localized structures in the beam, with a typical diameter of 100 μm. The high intensity ($\sim 10^{14}$ W/cm^2) [67] and the electron density ($\sim 10^{15}$ to 10^{17} cm^{-3}) [41] within the filaments, as well as the changes induced on the propagation medium, could lead to a lower sensitivity to local fluctuations in the propagation medium. For example, the non-linear contribution of the Kerr effect to the index of refraction ($\Delta n \sim 10^{-5}$) is much larger than that produced by thermal fluctuations in the atmosphere.

However, the thermal fluctuations are not the only process that could perturb the propagation of ultrashort laser pulses through the atmosphere. Aerosol particles, like water droplets or dust, can have dimensions of several tens of microns, comparable with the filament diameter: they could seriously harm the delicate dynamical balance required to propagate filaments.

14.4.1 Filament Interaction with an Isolated Droplet [68]

Experiments dedicated to the interaction of a single filament with a single droplet at the laboratory scale have been performed with 7 mJ laser pulses of 120 fs pulse duration at 810 nm. The filament formation was forced by a slight focusing ($f = 5$ m). The filaments propagated over more than 3 m, i.e. 30 times the Rayleigh length. For a given laser power, the onset of filamentation is stable within a few centimetres: This point has been taken as the origin for the propagation distance d.

At $d = 1$ m, the filament interacted with a calibrated micrometric droplet, produced by a piezoelectric nozzle. The droplet diameter was varied between 30 and 100 μm, typical of the largest atmospheric aerosols. The filament contains only a fraction of the beam energy, while the rest propagates around it as a "photon bath" of typically 2 mm diameter. After 1 m propagation, the filament bears typically one third of the total beam energy, and this proportion falls to 13% after 1 more meter propagation. The rest of the energy propagates as a "photon bath" parallel to the filament, within 2 mm around it. This "photon bath" has been demonstrated to behave as an "energy reservoir" [17] dynamically exchanging energy with the filament. The energy encompassed within the filament decreases from 2.7 mJ at $d = 1$ m, to 0.25 mJ at $d = 3$ m.

If a 50 μm droplet is inserted in the centre of the filament at $d = 1$ m after the filament onset, the filament appears unperturbed, although the dynamical balance between Kerr self-focusing and defocusing on the plasma plays a critical role due to the strong non-linearity of the filamentation process. Moreover, the filament length is not affected by the interaction with the droplet. Comparing the filament energy with and without droplet shows very limited losses. Shortly after the interaction with the droplet, the loss is only

$130\pm40\,\mu$J, but the dynamical balance is immediately restored. Furthermore, during its subsequent propagation, the filament seems to regain energy, since the difference with the unperturbed filament decreases, reaching $40\pm3\,\mu$J at the filament end. Similar results were obtained with bigger droplets (up to $95\,\mu$m diameter, intercepting most of the filament energy) as well as opaque particles.

This result confirms that the filaments receive energy from the photon bath. Theoretical predictions [69, 70] as well as numerical simulations reproducing the experimental results [71, 72], show that the "photon bath" exchanges energy with the filament and gives it the required energy for further propagation. This interpretation was further demonstrated by symmetrical observations showing that the filamentation is blocked by a diaphragm which of about $300\,\mu$m diamter, which is larger than the filament diameter but blocks the photon bath [73,74]. More precisely, recent simulations by L. Bergé et al. [72] showed that the region of the photon bath efficiently contributing to the filament feeding has a typical diameter of $350\,\mu$m. Associated with the filament core with a typical diameter of $100\,\mu$m, this bath constitutes a stable system. This description provides an interface between the dynamical instability model, in which the filament exchanges energy with the surrounding beam, and the description of filamentation in terms of quasi-solitons.

14.4.2 Filament Transmission Through a Cloud [68]

The above results show that the possibility to transmit filaments through a cloud is governed by the transmission of the photon bath through the cloud to re-feed the filament after its collision with an obscurant. Experiments have been performed in an open cloud chamber of 35 cm length, containing a fog of water droplets with an average diameter of $4\,\mu$m. The filament can propagate in a cloud with an optical thickness up to 3.2, corresponding to a droplet concentration of $4 \times 10^5\,\mathrm{cm}^{-3}$. However, the filament propagation beyond such a dense cloud is limited to a few centimetres: The losses to the photon bath, due to multiple scattering, prevent it from further feeding the filament, since the transmitted power of 2.3 GW is below the critical power P_{crit} required for filamentation. However, the filament appears unaffected after propagating through a cloud with an optical thickness as high as 1.2 ($10^5\,\mathrm{droplets/cm}^3$). The energy losses in the photon bath were checked to depend exponentially with the droplet concentration in the cloud, showing that linear extinction (Mie scattering and multiple scattering) is the main limiting factor for filament transmission through clouds and fogs.

14.4.3 Multiple Filamentation Through Clouds [75]

The optical thickness of the fog used in the above-described laboratory experiments is typical for clouds like cumulus or stratocumulus [76]. To extend those results to atmospheric scales, experiments have been performed with

the *Teramobile* in the multiple filamentation regime. The *Teramobile* beam propagated freely over 40 m, and interacted then with an open cloud chamber over 10 m (Fig. 14.7) [3]. The fog was approximately homogeneous. Its droplet size distribution was centred around 1 μm, much smaller than the filament diameter. The laser beam was launched collimated, with an initial diameter of 3 cm, and its chirp was adjusted so that the filamentation began shortly before the fog. The initial pulse duration was 600 fs, i.e. 0.3 TW for 220 mJ. The propagation of the beam through the fog was characterized by imaging beam profiles on a screen with a digital camera recording one single shot per image in the infrared spectral region: this technique provides a good measurement of the laser beam profile itself [57].

Filaments were visible in the beam profile at the exit of the fog as soon as the transmitted pulse energy was greater than 25 mJ (45 GW), corresponding to 15% transmission (extinction coefficient $0.2\,\mathrm{m}^{-1}$). Hence, filamentation can be transmitted in a fog over a distance comparable with the visibility. In this configuration the particle density was $8.6 \times 10^4\,\mathrm{cm}^{-3}$, so that the mean free path for a 100 μm filament was 0.5 mm: Each single filament hits on average 2000 droplets per meter propagation. However, since the droplet radius is about 100 times smaller than the filament diameter, the filaments them-

Fig. 14.7. Open cloud chamber. The generated cloud spans over 10 m (Photo Université Lyon 3/DAVM/A. Gratié)

selves are not perturbed significantly. The influence of fog on filamentation is essentially due to the losses induced to the "photon bath".

This influence can be further demonstrated by comparing the beam profiles at the exit of the cloud chamber for two incident energies, both with and without fog. As shown in Fig. 14.8, the transmitted energy determines the filamentation pattern, and in particular the number of filaments. Beam profiles, and in particular the filament patterns, for similar transmitted energy, are comparable. Hence, the cloud plays the role of an attenuator affecting the propagation through linear extinction of the photon bath. This is further confirmed by the dependence of the filament number as a function of the transmitted power. It is well known that pulses well above the critical power divide themselves into cells, each of them containing a few critical powers and generating one filament. In the experimental conditions of Fig. 14.8, one filament is generated for each 15 GW transmitted power, i.e. 5 critical powers. This quantity is independent on the presence of the cloud. Therefore, the cloud affects the propagation by reducing the peak power of the pulses through linear extinction.
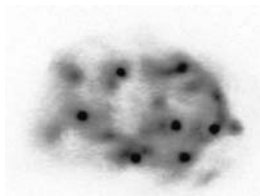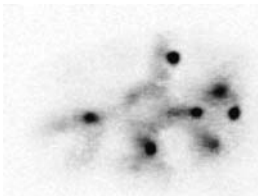
Initial pulse enrgy	Free propagation	Fog, 50 % transmission
220 mJ	(a) E_T = 220 mJ	(b) E_T = 110 mJ
90 mJ	(c) E_T = 90 mJ	(d) E_T = 45 mJ

Fig. 14.8. Beam profile at the exit of the cloud chamber, for free propagation (**a,b**) and through fog (50% transmission, i.e. $0.07\,\mathrm{m}^{-1}$, and $3.2 \times 10^4\,\mathrm{droplets\,cm}^{-3}$) (**b,d**) [75]

As a summary, the filaments generated by ultrashort laser pulses can survive their interaction with a droplet of diameter as large as that of the filaments themselves. Moreover, filaments can be transmitted through a dense fog, on the laboratory scale as well as in the multiple filamentation regime over tens of meters. In the latter case, the propagation distance of the filaments is comparable with the visibility within the cloud. This survival is related to the capacity of the filaments to regenerate after they have met an obscurant, from energy fed by the photon bath surrounding them.

14.5 Conclusion

Filamentation in the atmosphere is now a well-characterized phenomenon. It stems from a dynamical balance between Kerr self-focusing and defocusing on plasma generated in the air by the laser pulse itself. It has been found to be a surprisingly robust process, capable of propagating almost unperturbed through clouds or fogs. There results are particularly promising for atmospheric applications of laser pulses, such as lightning protection, where rain has to be taken into account [11]. Also, applications that use filaments to deliver high intensities on remote samples, like non-linear Lidar for aerosol remote sensing [3], or remote LIBS (R-FIBS) [4], could be used even within or beyond clouds.

However, the ability to use filaments over large scale in the atmosphere requires to propagate them over long distances, and to characterize carefully their geometry and spectral contents: This will be the purpose of the second part of this contribution [77].

References

1. P. Rairoux, H. Schillinger, S. Niedermeier, M. Rodriguez, F. Ronneberger, R. Sauerbrey, B. Stein, D. Waite, C. Wedekind, H. Wille, L. Wöste, *Remote sensing of the atmosphere using ultrashort laser pulses*, Applied Physics B **71**, 573–580 (2000)
2. J. Kasparian, M. Rodriguez, G. Méjean, J. Yu, E. Salmon, H. Wille, R. Bourayou, S. Frey, Y.-B. André, A. Mysyrowicz, R. Sauerbrey, J.-P. Wolf, L. Wöste, *White-light filaments for atmospheric analysis*, Science **301**, 61 (2003)
3. G. Méjean, J. Kasparian, J. Yu, S. Frey, E. Salmon, J.-P. Wolf, *Remote Detection and Identification of Biological Aerosols using a Femtosecond Terawatt Lidar System*, Applied Physics B **78**, 535 (2004)
4. K. Stelmaszczyk, P. Rohwetter, G. Méjean, J. Yu, E. Salmon, J. Kasparian, R. Ackermann, J.-P. Wolf, L. Wöste, *Long-distance remote laser-induced breakdown spectroscopy using filamentation in air*, Applied Physics Letters **85**, 3977 (2004)
5. H. Pépin, D. Comtois, F. Vidal, C. Y. Chien, A. Desparois, T. W. Johnston, J. C. Kieffer, B. L. Fontaine, F. Martin, F. A. M. Rizk, C. Potvin, P. Couture, H. P. Mercure, A. Bondiou-Clergerie, P. Lalande, I. Gallimberti, *Triggering and guiding high-voltage large-scale leader discharges with sub-joule ultrashort laser pulses*, Physics of Plasmas **8**, 2532 (2001)
6. D. Comtois, C. Y. Chien, A. Desparois, F. Gérin, G. Jarry, T. W. Johnston, J. C. Kieffer, B. L. Fontaine, F. Martin, R. Mawassi, H. Pépin, F. A. M. Rizk, F. Vidal, P. Couture, H. P. Mercure, C. Potvin, A. Bondiou-Clergerie, I. Gallimberti, *Triggering and guiding leader discharges using a plasma channel created by an ultrashort laser*, Applied Physics Letters **76**, 819 (2000).
7. D. Comtois, H. Pépin, F. Vidal, F. A. M. Risk, C.-Y. Chien, T. W. Johnston, J.-C. Kieffer, B. La Fontaine, F. Martin, C. Potvin, P. Couture, H. P. Mercure, A. Bondiou-Clergerie, P. Lalande, I. Gallimberti, *Triggering and guiding of an upward positive leader from ground rod with an ultrashort laser pulse-I: Experimental results*, IEEE transactions on plasma science **31**, 377 (2003)
8. D. Comtois, H. Pépin, F. Vidal, F. A. M. Risk, C.-Y. Chien, T. W. Johnston, J.-C. Kieffer, B. La Fontaine, F. Martin, C. Potvin, P. Couture, H. P. Mercure, A. Bondiou-Clergerie, P. Lalande, I. Gallimberti, *Triggering and guiding of an upward positive leader from ground rod with an ultrashort laser pulse-II: Modeling*, IEEE transactions on plasma science **31**, 387 (2003)
9. B. La Fontaine, D. Comtois, C. Y. Chien, A. Desparois, F. Gérin, G. Jarry, T. W. Johnston, J. C. Kieffer, F. Martin, R. Mawassi, H. Pépin, F. A. M. Rizk, F. Vidal, C. Potvin, P. Couture, H. P. Mercure, *Guiding large-scale spark discharges with ultrashort pulse laser filaments*, Journal of Applied Physics **88**, 610 (2000).
10. M. Rodriguez, R. Sauerbrey, H. Wille, L. Wöste, T. Fujii, Y.-B. André, A. Mysyrowicz, L. Klingbeil, K. Rethmeier, W. Kalkner, J. Kasparian, E. Salmon, J. Yu, J.-P. Wolf, *Megavolt discharges triggered and guided with laser filaments*, Optics Letters **27**, 772 (2002)
11. R. Ackermann, K. Stelmaszczyk, P. Rohwetter, G. Méjean, E. Salmon, J. Yu, J. Kasparian, G. Méchain, V. Bergmann, S. Schaper, B. Weise, T. Kumm, K. Rethmeier, W. Kalkner, J. P. Wolf, L. Wöste, *Triggering and guiding of megavolt discharges by laser-induced filaments under rain conditions*, Applied Physics Letters **85**, 5781 (2004)

12. A. Braun, G. Korn, X. Liu, D. Du, J. Squier, G. Mourou, *Self-channeling of high-peak-power femtosecond laser pulses in air*, Optics Letters **20**, 73–75 (1995)

13. L. Wöste, C. Wedekind, H. Wille, P. Rairoux, B. Stein, S. Nikolov, C. Werner, S. Niedermeier, F. Ronnenberger, H. Schillinger, R. Sauerbrey, *Femtosecond atmospheric lamp*, Laser und Optoelektronik **29**, 51 (1997)

14. H. Wille, M. Rodriguez, J. Kasparian, D. Mondelain, J. Yu, A. Mysyrow-icz, R. Sauerbrey, J. P. Wolf, L. Woeste, *Teramobile: a mobile femtosecond-terawatt laser and detection system*, European Physical J. Applied Physics **20**, 183 (2002)

15. E. T. J. Nibbering, P. F. Curley, G. Grillon, B. S. Prade, M. A. Franco, F. Salin, A. Mysyrowicz, *Conical emission from self-guided femtosecond pulses in air*, Optics Letters **21**, 62 (1996).

16. A. Brodeur, C. Y. Chien, F. A. Ilkov, S. L. Chin, O. G. Kosareva, V. P. Kandidov, *Moving focus in the propagation of ultrashort laser pulses in air*, Optics Letters **22**, 304 (1997)

17. M. Mlejnek, E. M. Wright, J. V. Moloney, *Dynamic spatial replenishment of femtosecond pulses propagating in air* Optics Letters **23**, 382 (1998)

18. D. Strickland, P. B. Corkum, *Resistance of short pulses to self-focusing*, Journal of the Optical Society of America B **11**, 492 (1994)

19. L. Roso-Franco, Self-Reflected Wave inside a Very Dense Saturable Absorber, Physical Review Letters **55**, 2149 (1995)

20. R. R. Alfano, S. L. Shapiro, *Emission in the region 4000 to 7000 Å via four-photon coupling in glass,* Physical Review Letters **24**, 584 (1970)

21. R. R. Alfano, S. L. Shapiro, *Observation of Self-Phase Modulation and Small-Scale Filaments in Crystals and Glasses*, Physical Review Letters **24**, 592 (1970)

22. R. R. Alfano, S. L. Shapiro, *Direct distortion of electric clouds of rare-gas atoms in intense electric fields,* Physical Review Letters **24**, 1217 (1970)

23. A. Brodeur, S. L. Chin, *Ultrafast white-light continuum generation and self-focusing in transparent condensed media,* Journal of the Optical Society of America B **16**, 637 (1999)

24. Y. R. Shen, *The principles of nonlinear optics*, John Wiley & Sons, New York (1984)

25. G. Yang, Y. Shen, *Spectral broadening of ultrashort pulses in a nonlinear medium,* Optics Letters **9**, 510 (1984)

26. A. Gaeta, *Catastrophic collapse of ultrashort pulses,* Physical Review Letters **84**, 3582 (2000)

27. J. K. Ranka, R. W. Schirmer, A. L. Gaeta, *Observation of pulse splitting in nonlinear dispersive media*, Physical Review Letters **77**, 3783 (1996)

28. A. Proulx, A. Talebpour, S. Petit, S. L. Chin, *Fast pulsed electric field created from the self-generated filament of a femtosecond Ti:Sapphire laser pulse in air*, Optics Communications **174**, 305 (2000)

29. S. Tzortzakis, M. A. Franco, Y.-B. André, A. Chiron, B. Lamouroux, B. S. Prade, A. Mysyrowicz, *Formation of a conducting channel in air by self-guided femtosecond laser pulses*, Physical Review E **60**, R3505–R3507 (1999)

30. S. Tzortzakis, B. Prade, M. Franco, A. Mysyrowicz, *Time evolution of the plasma channel at the trail of a self-guided IR femtosecond laser pulse in air*, Optics Commun. **181**, 123 (2000)

31. H. Schillinger, R. Sauerbrey, *Electrical conductivity of long plasma channels in air generated by self-guided femtosecond laser pulses*, Applied Physics B **68**, 753 (1999)

32. J. Schwarz, P. Rambo, J. C. Diels, *Measurements of multiphoton ionization coefficients with ultrashort ultraviolet pulses*, Applied Physics B **72**, 343-347 (2001)

33. D. Strickland, G. Mourou, *Compression of amplified chirped optical pulses*, Optics Communications **56**, 219 (1985)

34. P. Maine, D. Strickland, P. Bado, M. Pessot, G. Mourou, *Tabletop terawatt laser by chirped pulse amplification*, IEEE Journal of Quantum Electronics **24**, 398 (1988)

35. P. L. Kelley, *Self-focusing of optical beams*, Physical Review Letters **15**, 1005 (1965); P. L. Kelley, *Erratum: Self-focusing of optical beams*, Physical Review Letters **16**, 384 (1965)

36. G. A. Ashkaryan, *The self-focusing effect*, Sov. Phys. J. **16**, 680 (1974)

37. X. M. Zhao, P. Rambo, J.-C. Diels, *Effect of oxygen on the laser triggering of lightning*, QELS'95 **16**, 178 (1995)

38. J. H. Marburger, E. L. Dawes, *Dynamical formation of a small-scale filament*, Physical Review Letters **21**, 556 (1968). Note that the radius considered in the classical writing of the Marburger formula is the half width at $e^{-1/2}$, not at $1/e$ or $1/e^2$ as usual.

39. S. L. Chin, *From Multiphoton to Tunnel Ionization*, in *Advances in Multiphoton Processes and Spectroscopy*, eds. S. H. Lin, A. A. Villaeys and Y. Fujimura, World Scientific, Singapore, 16, 249–272 (2004)

40. A. Talebpour, J. Yang, S.L. Chin, *Semi-empirical model for the rate of tunnel ionization of N_2 and O_2 molecules in an intense Ti:Sapphire laser pulse*, Optics Communications **163**, 29 (1999)

41. J. Kasparian, R. Sauerbrey, S. L. Chin, *The critical laser intensity of self-guided light filaments in air*, Applied Physics B **71**, 877 (2000)

42. L. Bergé, A. Couairon, *Gas-induced solitons*, Physical Review Letters **86**, 1003 (2001)

43. A. Becker, N. Aközbek, K. Vijayalakshmi, E. Oral, C. M. Bowden, S. L. Chin, *Intensity clamping and re-focusing of intense femtosecond laser pulses in nitrogen molecular gas*, Applied Physics B **73**, 287 (2001).

44. B. La Fontaine, F. Vidal, Z. Jiang, C. Y. Chien, D. Comtois, A. Desparois, T. W. Johnston, J.-C. Kieffer, H. Pépin, H. P. Mercure, *Filamentation of ultrashort pulse laser beams resulting from their propagation over long distances in air*, Physics of Plasmas **6**, 1615 (1999).

45. M. Rodriguez, R. Bourayou, G. Méjean, J. Kasparian, J. Yu, E. Salmon, A. Scholz, B. Stecklum, J. Eislöffel, U. Laux, A. P. Hatzes, R. Sauerbrey, L. Wöste, J.-P. Wolf, *Kilometer-range non-linear propagation of femtosecond laser pulses*, Physical Review E **69**, 036607 (2004)

46. G. Méchain, A. Couairon, Y.-B. André, C. D'amico, M. Franco, B. Prade, S. Tzortzakis, A. Mysyrowicz, R. Sauerbrey, *Long-range self-channeling of infrared laser pulses in air: a new propagation regime without ionization*, Applied Physics B **79**, 379 (2004)

47. W. G. Wagner, H. A. Haus, J. H. Marburger, *Large-scale self-trapping of optical beams in the paraxial ray approximation*, Physical Review **175**, 256 (1968); W. G. Wagner, H. A. Haus, J. H. Marburger, *Erratum: Large-scale self-trapping of optical beams in the paraxial ray approximation*, Physical Review A **3**, 2150 (1971)

48. P. M. Goorjian, A. Taflove, R. M. Joseph, S. C. Hagness, IEEE Journal of Quantum electronics **28**, 2416 (1992)

49. J. K. Ranka, A. L. Gaeta, *Breakdown of the slowly varying enveloppe approximation in the self-focusing of ultrashort pulses*, Optics Letters **23**, 534 (1998).

50. A. Chiron, B. Lamouroux, R. Lange, J.-F. Ripoche, M. Franco, B. Prade, G. Bonnaud, G. Riazuelo, A. Mysyrowicz, *Numerical simulations of the nonlinear propagation of femtosecond optical pulses in gases*, The European Physical Journal D **6**, 383 (1999)

51. N. Aközbek, C. M. Bowden, A. Talepbour, S. L. Chin, *Femtosecond pulse propagation in air: variational analysis*, Physical Review E **61**, 4540 (2000)

52. D. L. Hovhannisyan, *Analytic solution of the wave equation describing dispersion-free propagation of a femtosecond laser pulse in a medium with cubic and fifth-order nonlinearity*, Optics Commun. **196**, 103 (2001)

53. P. Sprangle, J. R. Peñano and B. Hafizi, *Propagation of intense short laser pulses in the atmosphere*, Physical Review E **66**, 046418 (2002).

54. M. Mlejnek, M. Kolesik, J. V. Moloney, E. M. Wright, *Optically turbulent femtosecond light guide in air*, Physical Review Letters **83**, 2938 (1999)

55. C. Ren, R. G. Hemker, R. A. Fonseca, B. J. Duda, W. B. Mori, *Mutual attraction of laser beams in plasmas: braided light*, Physical Review Letters **85**, 2124 (2000).

56. G. Fibich, B. Ilan, *Deterministic vectorial effect lead to multiple filamentation*, Optics Letters **26**, 840 (2001)

57. L. Bergé, S. Skupin, F. Lederer, G. Méjean, J. Yu, J. Kasparian, E. Salmon, J. P. Wolf, M. Rodriguez, L. Wöste, R. Bourayou, R. Sauerbrey, *Multiple filamentation of TW laser pulses in air*, Physical Review Letters **92**, 225002 (2004)

58. S. A. Hosseini, Q. Luo, B. Ferland, W. Liu, S. L. Chin, O. G. Kosareva, N. A. Panov, N. Aközbek, V. P. Kandidov, *Competition of multiple filaments during the propagation of intense femtosecond laser pulses*, Physical Review A **70**, 033802 (2004)

59. V. P. Kandidov, N. Akozbek, M. Scalora, O. G. Kosareva, A. V. Nyakk, Q. Luo, S. A. Hosseini, S. L. Chin, *Towards a control of multiple filamentation by spatial regularization of a high-power femtosecond laser pulse*, Applied Physics B **80**, 267-275 (2005)

60. L. V. Keldysh, Sov. Phys. JETP **20**, 1307 (1965)

61. S. L. Chin, S. Petit, F. Borne, K. Miyazaki, *The white light supercontinuum is indeed an ultrafast white light laser*, Japanese Journal of Applied Physics **38**, L126 (1999)

62. O. G. Kosareva, V. P. Kandidov, A. Brodeur, C. Y. Chen, S. L. Chin, *Conical emission from laser-plasma interactions in the filamentation of powerful ultrashort laser pulses in air*, Optics Letters **22**, 1332 (1997).

63. J. Zhang, H. Yang, J. Zhang, X. Lu, Y. Li, Y. Li, H. Teng, Z. Chen, Z. Wei, Z. Sheng, 286th Heraeus Seminar on Optical methods in atmospheric analysis, Bad Honnef, Germany, 14–18 October 2002.

64. J. Yu, D. Mondelain, G. Ange, R. Volk, S. Niedermeier, J.-P. Wolf, J. Kasparian, R. Sauerbrey, *Backward supercontinuum emission from a filament generated by ultrashort laser pulses in air*, Optics Letters **26**, 533-535 (2001)

65. R. Bourayou, G. Méjean, J. Kasparian, M. Rodriguez, E. Salmon, J. Yu, H. Lehmann, B. Stecklum, U. Laux, J. Eislöffel, A. Scholz, A. P. Hatzes, R. Sauerbrey, L. Wöste, J.-P. Wolf, *White-light filaments for multiparameter analysis of cloud microphysics*, Journal of the Optical Society of America **22**, 369 (2005)

66. L. Iorio, *Classical and Quantum Gravity* **19**, 175 (2002)
67. W. Liu, S. Petit, A. Becker, N. Aközbek, C. M. Bowden, S. L. Chin, *Intensity clamping of a femtosecond laser pulse in condensed matter*, Optics Communications **202**, 189-197 (2002)
68. F. Courvoisier, V. Boutou, J. Kasparian, E. Salmon, G. Méjean, J. Yu, J. P. Wolf, *Light filaments transmitted through clouds*, Applied Physics Letters **83**, 213 (2003)
69. S. Skupin, L. Bergé, U. Peschel, F. Lederer, G. Méjean, J. Yu, J. Kasparian, E. Salmon, J. P. Wolf, M. Rodriguez, L. Wöste, R. Bourayou, R. Sauerbrey, *Filamentation of femtosecond light pulses in the air: Turbulent cells versus long-range clusters*, Physical Review E **70**, 046602 (2004)
70. M. Mlejnek, E. M. Wright, J. V. Moloney, Optics Express **4**, 223-228 (1999).
71. M. Kolesik, J. V. Moloney, *Self-healing femtosecond light filaments*, Optics Letters **29**, 590 (2004)
72. S. Skupin, L. Bergé, U. Peschel, F. Luderer, *Interaction of femtosecond light filaments with obscurants in aerosols*, Physical Review Letters **93**, 023901 (2004)
73. S. L. Chin, A. Brodeur, S. Petit, O. G. Kosareva, V. P. Kandidov, *Filamentation and supercontinuum generation during the propagation of powerful ultrashort laser pulses in optical media (white light laser),* Journal of Nonlinear Optical Physics and Materials **8**, 121 (1999)
74. W. Liu, J.F. Gravel, F. Théberge, A. Becker, S.L. Chin, *Background reservoir: its crucial role for long-distance propagation of femtosecond laser pulses in air*, Applied Physics B **80**, 857 (2005)
75. G. Méjean, J. Kasparian, J. Yu, E. Salmon, S. Frey, J.-P. Wolf, S. Skupin, A. Vinçotte, R. Nuter, S. Champeaux, L. Bergé, *Multifilamentation transmission through fog*, Physical Review E **72**, 026611 (2005)
76. Classification of the *World Climate Research Program* (WCRP). See e.g.: http://isccp.giss.nasa.gov/cloudtypes.html
77. J. Kasparian, Chapter 15 in this volume

15 Some Properties of Femtosecond Laser Filamentation Relevant to Atmospheric Applications
Part II. Large-Scale Filamentation

Jérôme Kasparian

Teramobile, Laboratoire de Spectrométrie Ionique et Moléculaire, UMR CNRS 5579, Bâtiment Kastler, Université Claude Bernard Lyon 1, 43 bd du 11 novembre, F69622 Villeurbanne Cedex France
e-mail: jkaspari@lasim.univ-lyon1.fr

Summary. Filamentation is a non-linear propagation regime of ultrashort, high-power laser pulses, in which a dynamic balance is established between Kerr self-focusing and defocusing on the air ionized by the laser pulse itself. It opens the way to various applications in atmospheric sciences, such as white-light Lidar relying on the white light continuum, which can be observed up to high altitudes and allows multicomponent remote sensing. Other applications rely on the ability of the filaments to deliver high intensities and induce non-linear optical effects at remote locations, e.g. the remote sensing of aerosols or the analysis of solid targets. Furthermore, the ionization of the fs-laser-induced filaments permits to control high-voltage discharges, opening the way to laser lightning rods. These applications require a good characterization of filamentation over long distances in the atmosphere.This chapter reviews experimental results about long-range filamentation, the build-up of the white-light continuum and the beam geometry. Emphasis is put on results directly relevant for atmospheric applications.

15.1 Introduction

In the recent years, atmospheric applications of ultrashort, ultra-intense laser pulses have emerged. The most popular include non-linear Lidar [1–3], remote laser-induced breakdown spectroscopy (LIBS) [4] and the control of high-voltage discharges [5–11]. Most of them rely on filamentation [12], a non-linear propagation regime where a dynamical balance is established between the Kerr self-focusing and the defocusing by the plasma generated by the pulse. The previous chapter [13] focused on the basic physical processes at the root of filamentation, and on the capacity of filaments to survive their interaction with aerosol particles, fog and clouds. The *Teramobile* system [14] has also been presented. As the first mobile femtosecond-terawatt laser, it allows field experiments, opening the way to atmospheric applications of ultrashort, high-power lasers. Such applications also require a comprehensive knowledge about the atmospheric propagation of fs-TW laser pulses in the atmosphere, under realistic conditions. This implies experiments over

long propagation distances, up to the kilometre range, as well as the build-up of the white-light supercontinuum: The present chapter focuses on these issues.

15.2 Propagation of fs-TW Pulses in the Multiple Filamentation Regime [15, 16]

To characterize multiple filamentation, it is necessary to follow a high power (several TW) beam over a distance of many tens of meters. This was made possible by the *Teramobile*, which allowed open-field outdoor experiments. At high powers much above the 3 GW critical power in air, the beam does not self-focus as a whole, but breaks up into many cells encompassing several critical powers, each of which gives rise to one filament. Once one cell has dissipated too much energy to maintain a filament, this filament gives its energy back to the "photon bath" around it. Cells can then rearrange to create new structures [17], so that filamentation goes on in a dynamical process called modulational instability [18]. According to this model based on short-distance numerical simulations, filamentation is a dynamical process in which local cells in the transverse beam profile generate filaments, which propagate over short distances and then vanish and "give back" their energy to the "photon bath" of the overall beam. Then, this energy is available for the generation of new filaments in newly arranged cells. In this description, the macroscopic filamentation length is independent on the length of individual filaments.

Modelling such a process requires to implement high energies, large beam diameters and long propagation distances, with a very high resolution, both transverse (several microns, to resolve the filaments) and longitudinal (e.g., because of the catastrophic character of the Kerr effect). The corresponding computing resources are prohibitive for atmospheric relevant distances [18–21], which prevents a theoretical description based on numerical simulations, and raises the need for long-distance experimental measurements. Long distance experiments are therefore required to test new simulation schemes for long-distance propagation. Fully resolved (3D + 1) numerical simulations, which model the propagation of a laser pulses and resolve the three spatial dimensions and time, are prohibitive over distances and beam diameters relevant for atmospheric experiments. Therefore, the group of L. Bergé proposed to reduce the problem by averaging out the beam along the z axis, resulting in a 2D + 1 description of propagation. Under this condition, it is possible to use a sufficiently high resolution on the remaining dimensions, and especially a 10 µm transverse resolution required to resolve the filaments, on a 1000×1000 cells grid which is necessary to encompass the whole beam. However, considering the complexity of the process at play also in the temporal dimension, this averaging out is a strong assumption, which requires experimental validation.

To provide this validation, the *Teramobile* team has followed the evolution of the beam profile of their laser along its propagation over 50 m. The beam profile was observed on a screen, which was moved along the beam, and recorded using a CCD camera equipped with a filter to block the white-light and measure only the beam profile at the fundamental wavelength. The camera was synchronized with the laser so as to record one single laser shot on each image. Comparing two successive images at a given distance shows that, although the position of individual filaments varies from shot to shot, their overall pattern remains unchanged.

Figure 15.1 displays two examples of such profiles compared with the corresponding simulations obtained with the 2D + 1 model, using the initial experimental beam profile ($z = 1$ m) as initial conditions. Since the measurements at each distance can not be performed on the same shot, the fluctuations of both the laser and the atmosphere prevent exact agreement between the simulations and the measurements. However, the qualitative agreement is excellent, since the simulations reproduce the patterns of the experimental profile, in particular the filament density and the local patterns within the profile. Such patterns include the nucleation of the first filaments on a ring on the outer part of the beam profile, where the gradient of the intensity, and hence of the non-linear refractive index, are stronger. This agreement validates the assumptions at the basis of the 2D + 1 simulation code, allowing its use in other situations, such as the studies of the ultraviolet part of the
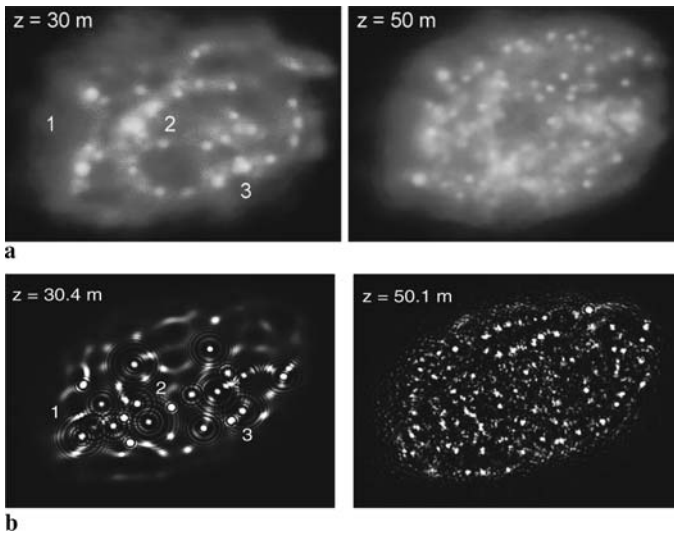
Fig. 15.1. Measured (*top*) and simulated (*bottom*) beam profile of laser pulses with $700\,P_{\mathrm{Crit}}$ for two propagation distances. The regions labelled 1 to 3 denote qualitative similarities within the filamentation pattern. The beam diameter is 5 cm. (Adapted from [15])

supercontinuum (see Sect. 15.4.1) and the propagation of filaments through fog and clouds [22, 23].

However, observing the beam profile on a screen does not provide information about the validity of the modulational instability model, since it does not grant access to the length of the individual filaments observed at a given distance. Measuring the individual filament length requires to observe the filament as a whole for a single shot. This was achieved by propagating the beam over more than 10 m through a "fog" of adequate density to scatter a slight fraction of the light without affecting the beam propagation. The "fog" was produced by an aerosol generator. The scattered light from individual shots was observed from downstream, with a small parallax (see top panel of Fig. 15.2). The result is displayed in the bottom panel of Fig. 15.2 in the case of a slightly focused beam ($f \sim 40$ m). Three filamentary structures clearly appear over 8 m. Numerical simulations show that, while the modulational instability is observed in the "free" regime before the focus,
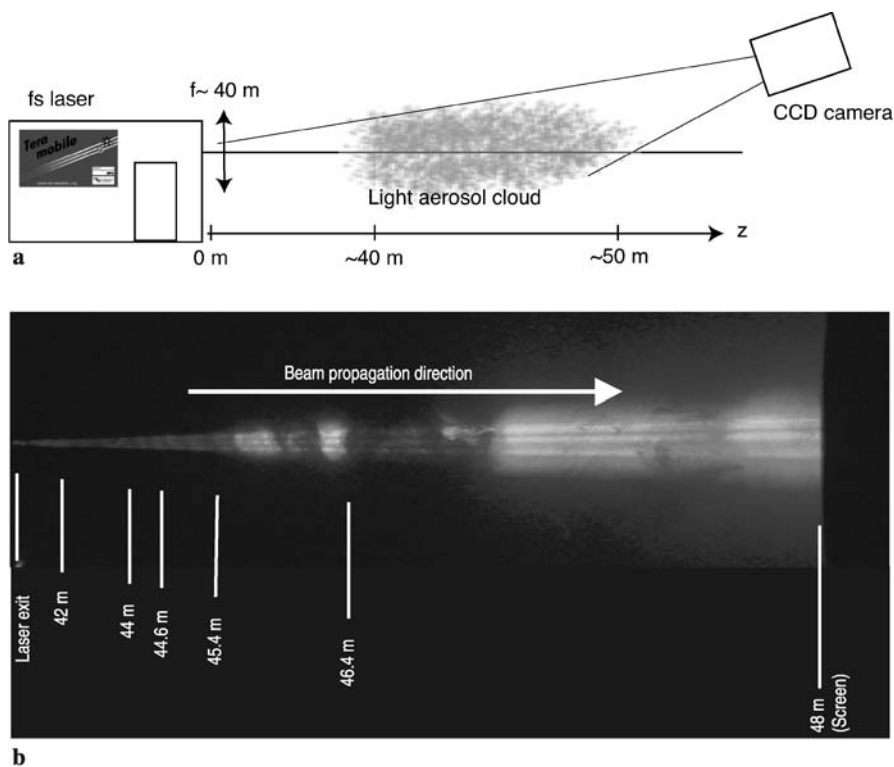
Fig. 15.2. *Top*: Experimental setup. *Bottom*: Optical pillars generated beyond the focus by the propagation of slightly focused ($f \sim 40$ m) fs-TW laser pulses carrying 760 critical powers. The discontinuities in the optical pillars are due to inhomogeneities in the fog scattering them. The non-linear distance scale (from the laser output port) is due to the parallax [16]

the latter forces the filaments together and reorganizes the beam into three optical pillars which propagate stable over several meters [16].

This experiment illustrates the capability of a mobile fs-TW laser system like the *Teramobile*. Although simple in principle, such an experiment is impossible without an ultrashort laser system allowing field experiments. Now, this experiment allowed to validate a new class of propagation codes capable of simulating the propagation of ultrashort laser pulses over atmospheric scales. This simple experiment also permitted us to characterize the modulational instability as well as its end generated by a slight focusing, resulting in a new propagation regime where optical pillars are formed from the photon bath.

15.3 Long Distance Vertical Filamentation [24]

Vertical propagation of fs-TW laser pulses is essential in view of atmospheric applications, since most of them require to launch the beam vertically. Moreover, vertical experiments permit to study how temperature and pressure variations along the beam affect the non-linear propagation [25]. In spite of the difficulty to perform calculations at this distance scale, numerical calculations conducted by Sprangle et al. predicted a collapse of the beam at 20 km altitude for well-chosen laser parameters [19]. But this calculation is based on a highly simplified variational approach, which calls for an experimental check. Finally, turbulence plays little role in vertical propagation experiments, contrary to horizontal propagation where turbulence near the ground is more important.

However, characterizing the filaments at high altitude is a technical challenge. The usual filament characterization techniques are based on nitrogen fluorescence [26–28], or local techniques like the filament conductivity [29–31], sonometry [32] or terahertz radiation [33], which are unpractical for very-long distance measurements, especially in the vertical direction. Therefore, the *Teramobile* team acquired spectral as well as geometrical data using a large-scale (2 m) imaging telescope to fully characterize the beam geometry, showing the first evidence of anomalous beam propagation on km-scales. These measurements constituted the first data set for non-linear propagation in a gaseous medium with (known) decreasing pressure and temperature gradients. Moreover, the white-light generation at high altitudes was investigated as a function of the laser parameters, especially chirp and initial focusing. These data are useful for the optimization of white-light Lidar configurations.

15.3.1 High-Resolution, Long-Distance Imaging of the Non-Linear Propagation of Terawatt Laser Pulses

The experiments have been conducted by installing the *Teramobile* laser near to the 2-m diameter telescope [34] of the *Thüringer Landessternwarte*

(Thuringian State Observatory/TLS) in Tautenburg (Germany), used in its Schmidt (imaging) configuration. The imaging device was a CCD providing an angular resolution of 6 μrad/pixel, with a sensitivity range from 350 to 1000 nm. In most of the experiments, the laser beam was emitted vertically as a parallel beam with a typical diameter of 3 cm. However, in some of the experiments, an off-axis sending telescope with a tuneable focal length was used to expand the beam diameter by a factor of 3. Besides focusing and initial diameter, the initial laser chirp was varied during the experiments by moving a grating in the compressor. Three chirp values have been used: short pulse with slight GVD precompensation (150 fs pulse duration), as well as long pulses with strong GVD precompensation (negative chirp) and anti-compensation (positive chirp), both with 600 fs pulse duration.
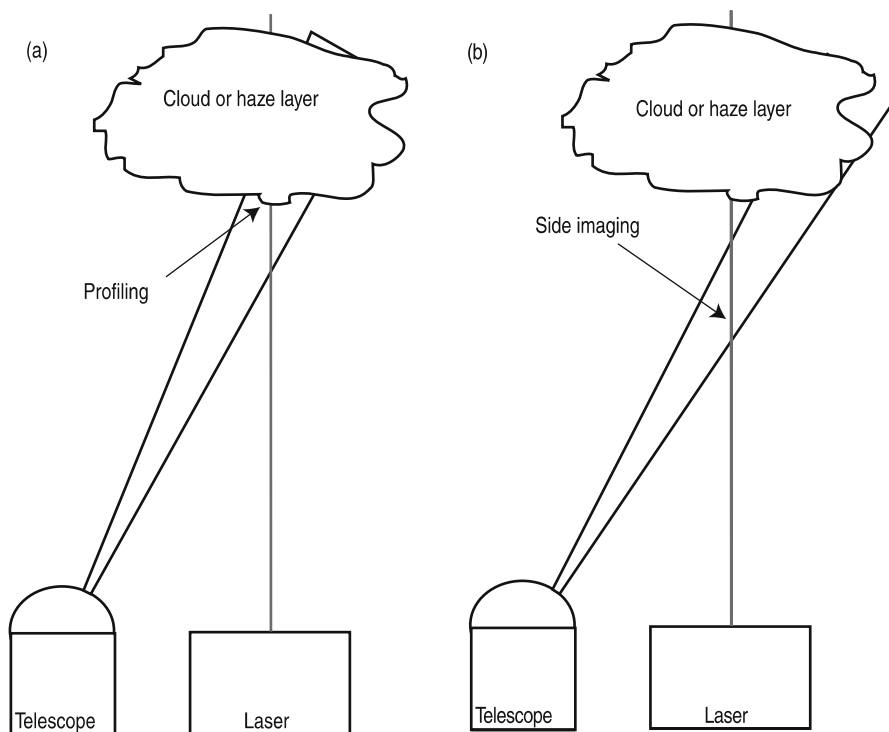
Fig. 15.3. Principle of beam imaging. **a** Beam profiling on a cloud or haze layer; **b** Side imaging of the beam with Rayleigh scattering. In real pictures (see also Fig. 15.4), a combination of both components are recorded together [24]

Fig. 15.4. Typical fs beam image of the *Teramobile* laser beam from Tautenburg observatory. **a** fundamental wavelength, 1 s exposure time, **b** in the blue-green band of the continuum, 180 s. The horizontal strips across the pictures are stars passing through the telescope field of view. Note the strongly non-linear altitude scale due to triangulation [24]
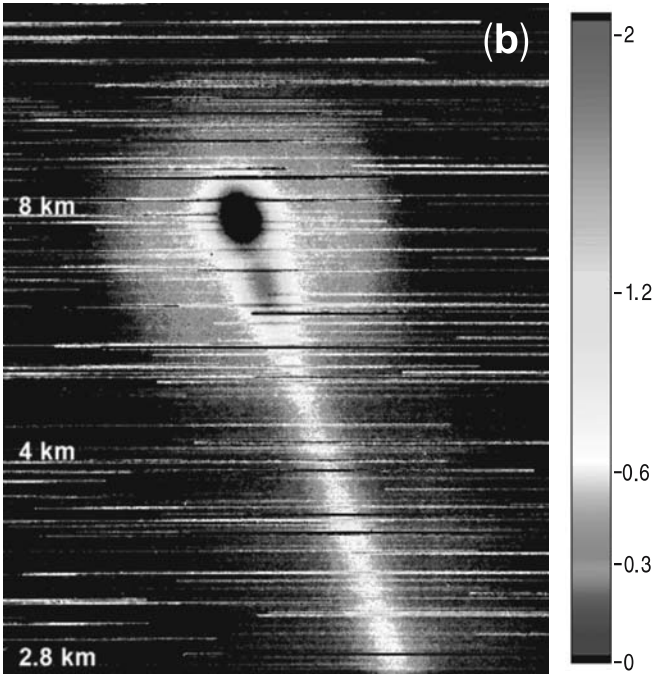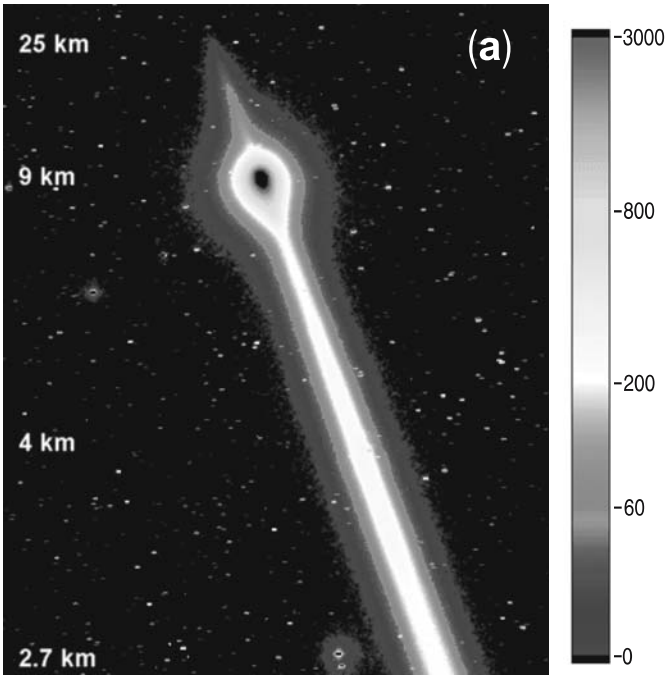
The slightly off-axis position of the *Teramobile* allowed both (i) cross-section images of the beam on the bottom of clouds or haze layers acting as screens, and (ii) side imaging of the Rayleigh-scattered light from the beam over large altitude ranges (Fig. 15.3). In the latter case, the altitude was retrieved using triangulation and crosschecked by classical Lidar measurements. Real images are a combination of both the cross section and side imaging components (see Fig. 15.4). Images have been acquired with several glass filter sets, covering the visible and infrared sides of the white-light continuum, as well as the fundamental wavelength.

Figure 15.4a displays a typical image in the fundamental wavelength channel of the fs-TW laser beam. Elastic scattering was detected from the ground to an altitude of at least 25 km. Similar measurements in the white-light band (Fig. 15.4b) demonstrated efficient supercontinuum generation by SPM: Under haze-free conditions, white-light signals in the blue region have been detected from altitudes beyond 18 km.

15.3.2 High Altitude Filamentation

Two key parameters were used to control the non-linear propagation and filamentation processes: temporal focusing (impinging an initial chirp to the pulse) and spatial focusing using the variable focal length sending telescope. Beam profile images have been taken on a cloud at 6 km altitude in the white-light band. When the beam is sent collimated with a slight GVD pre-compensation (slightly negative chirp), the beam profile images on the cloud exhibit a ring structure around the laser beam (see Fig. 15.5a). This ring corresponds to the projection of a cone, i.e. the conical emission from the filaments formed at lower altitudes (see Fig. 15.5b). The ring diameter corresponds to the projection of conical emission with an half angle of about 2.7 mrad [12,35,36], emitted near to the ground: It is the signature of filamentation generated (and ending) close to the ground level (Fig. 15.5b). Moreover, integrating the beam profile showed for the first time that the conical emission accounts for 65% of the overall white-light energy in this band. This measurement is impossible in laboratory-scale experiments where the angular separation of the main beam and the conical emission is not sufficient, and the filament intensity would destroy detectors inserted into the beam.

With a stronger initial negative chirp, therefore compensating GVD on longer distances, the ring disappears (Fig. 15.5c). A careful analysis of the pictures shows that the ring still exists, but has merged with the central beam, forming a pedestal. Since the angle of conical emission is fixed for a given wavelength, this reduced ring radius is the signature for an emission occurring nearer to the cloud, i.e., at a higher altitude of 2 km (Fig. 15.5d). The observation of remote filamentation at the kilometre-scale was subsequently confirmed in horizontal propagation [37]. These measurements provide the first evidence that the filaments can be generated remotely on the kilometre-scale.
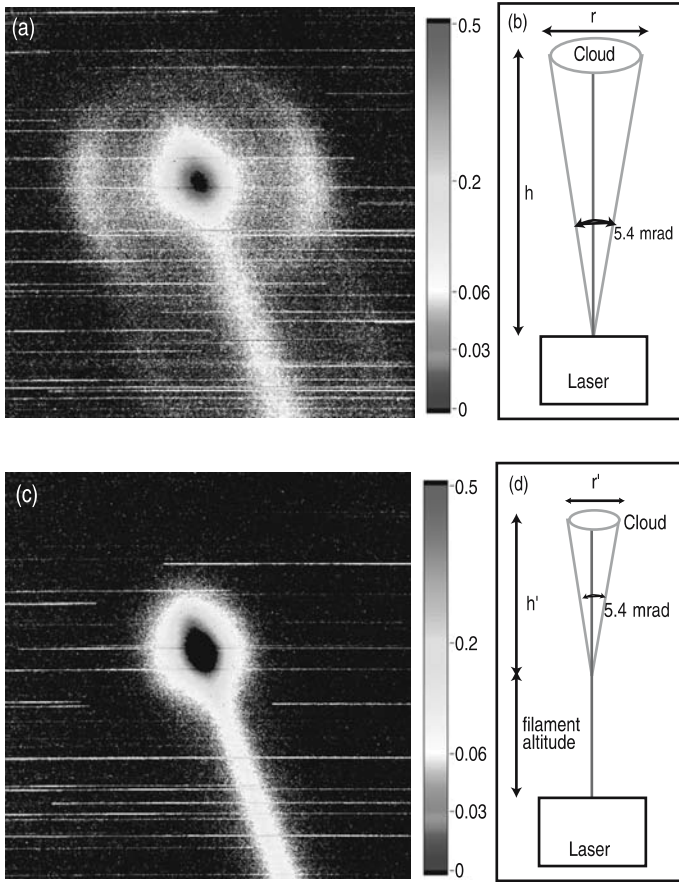
Fig. 15.5. a Beam impact on a haze layer in the blue band of the white light, with slight GVD precompensation. A conical emission ring is clearly visible. **b** Schematic of the ring emitted from low-altitude filaments imaged on high-altitude clouds. **c,d** Same as **a** and **b** for a stronger GVD precompensation, pushing the filamentation to higher altitudes, and reducing the apparent diameter of the imaged conical emission ring [24]

15.3.3 Beam Divergence and Spatial Focusing Effects

Outside the aerosol layers, Rayleigh scattering provides a side image of the beam. Measuring the beam diameter as a function of altitude yields the divergence of the beam. At the fundamental wavelength, for a collimated beam, the beam divergence is almost constant and amounts to 0.16 mrad half angle, i.e. three times the initial beam divergence. This divergence is independent on the chirp. On the opposite, the observed divergence of an initially focused beam is smaller than expected from geometrical optics, with a difference of about 0.6 mrad. In other words, the beam refocuses near to

the geometrical focus, which means that the non-linear propagation does not only concern filaments, but also the beam as a whole near to the geometrical focus, as predicted by Mlejnek et al. [18]. However, no non-linear propagation at high altitude is observed, in contradiction with the model of Sprangle et al. [19], which predicted a beam collapse around 20 km altitude.

Divergence measurements of the white-light supercontinuum generated by SPM were also performed. When the beam is sent parallel, the white light is significantly more divergent than the fundamental, e.g. 0.7 mrad in the 400–500 nm band instead of 0.16 mrad. This value is larger than a diffraction-limited behaviour of the whole 3 cm beam, but still much smaller than would be expected from diffraction at the exit of a 100 μm filament. This suggests that the filament vanish gradually, with their diameter increasing up to about 300 μm near their end, where the white light is released. Note that such a large diameter was observed by Lange et al. in a gas cell [38]. The small divergence of the white light might also be related to a recollimation by residual Kerr effect after the filament, or to multiple filaments acting as several individual "white light lasers" [39] behaving as in-phase point sources interfering to generate a narrow emission lobe. Anyway, this small divergence of the white light is favourable in view of Lidar applications, since the 0.7 mrad (half angle) value is in the same range or smaller than the field of view of typical Lidar receivers.

When the beam is focused, the white-light is still more divergent than the fundamental. More precisely, the divergence of the white light amounts to the convolution of the beam divergence at the fundamental wavelength with the angle of the conical emission from a single filament [35]. This suggests the picture of filaments evenly spread across the beam, forming a bundle which divergence is that of the beam. Inside the bundle, the conical emission is the same as that of an isolated filament (Fig. 15.6).
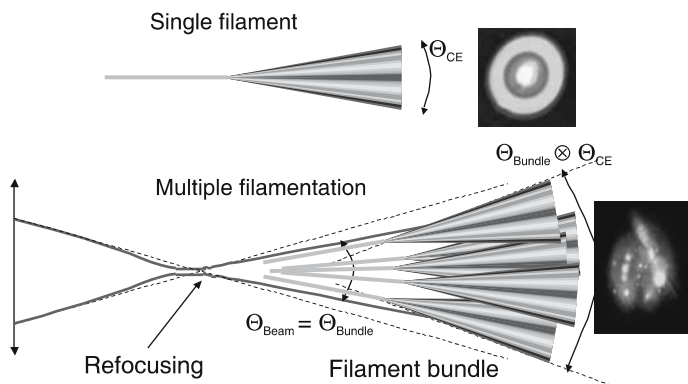
Fig. 15.6. Structure of a multifilamenting, high-power ultrashort laser beam

In summary, from the direct observation of the vertical propagation of femtosecond-terawatt laser pulses in the atmosphere, it is demonstrated that not only the filaments, but also the whole beam, have a non-linear behaviour [18]. The overall beam is partially recollimated near to the non-linear focus. Also, filamentation can occur at 2 km altitude, which is essential for remote atmospheric applications of filamentation.

15.4 The White-Light Supercontinuum

15.4.1 Spectral Contents of the White-Light Continuum

The spectrum of the white-light continuum has raised interest since it was discovered in the 1970s [40–42], first in condensed matter, and then in atmospheric pressure gases after the advent of the CPA technique. Higher harmonics generation up to 150 nm has been observed in rare gases at high pressure [43]. In this section, we present results about the spectrum of the white-light continuum generated in the air at atmospheric pressure. Such measurements are essential for Lidar, since they allow to characterize the light source used in multipollutant remote sensing. The white-light continuum generated in the atmosphere by ultrashort, ultraintense lasers has been progressively characterized over the last years, with progressively extending bandwidths.

A first set of measurements has been performed in the visible and near-infrared region, up to 4.5 μm [44] (Fig. 15.8). This region covers in particular the absorption band of volatile organic compounds (VOCs) between 3 and 3.5 μm. These species constitute a family of organic compounds with strongly overlapping absorption spectra, which prevents any measurement by DIAL Lidar [45]. Hence, the extension of the white-light continuum in this region opens the way to their remote sensing by multicomponent white-light Lidar. Experiments have been conducted with slightly focused pulses of 60 mJ energy in 35 fs pulse duration (i.e. 2 TW). The pulses were propagated over a few tens of meters in the laboratory atmosphere. Measurements have been performed in several bands with adequate spectrometers and detectors, with sufficient overlap to allow the connection of the spectra.

Since many atmospheric pollutants such as ozone have absorption bands in the ultraviolet, measurements have also been performed in this spectral region. Recently, it was shown that phase locking within the filaments results in enhanced third harmonic generation [46]. Then, the build-up of the ultraviolet supercontinuum was characterized over both the laboratory and the atmospheric scales. The UV-visible part of the continuum measured in the laboratory with a single filament is presented in Fig. 15.7. At the beginning of filamentation, a third harmonic band with 20 nm bandwidth is generated around 270 nm. Two meters further, the intensity of the third harmonic is reduced and a plateau appears in the UV-Visible region be-
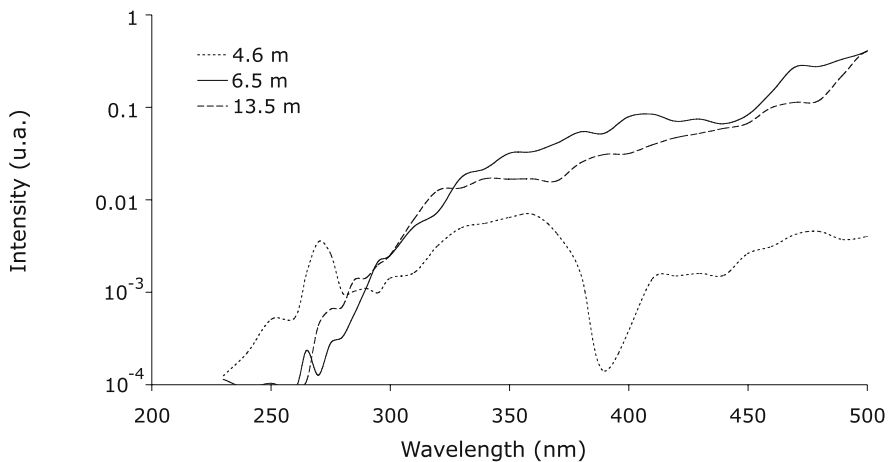
Fig. 15.7. Evolution of the white-light continuum in the UV-visible spectral region. Filaments begin after $3.3\,\mathrm{m}$ propagation [50]
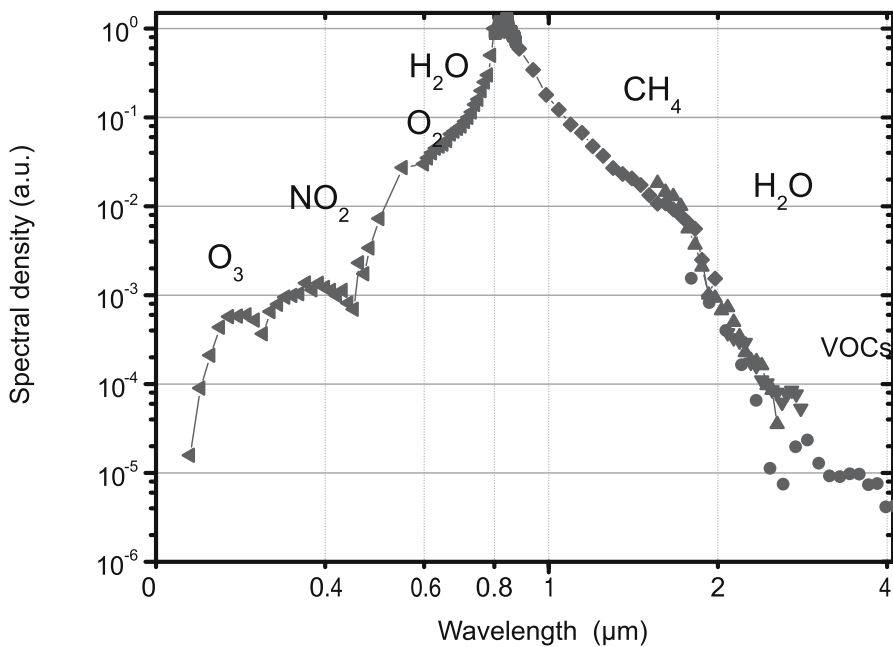
Fig. 15.8. Spectrum of the white light continuum assembled from 5 spectral regions. *Symbols above the curve* indicate the main atmospheric absorption bands

tween 300 and 500 nm. This plateau remains stable along further propagation, even after the end of the filament. Such behaviour shows that the third harmonic once generated interacts with the fundamental wavelength through four-wave mixing, resulting in the third harmonic depletion and the transfer of its energy towards the UV-visible plateau. The same process was observed independently by Théberge et al. [47, 48], who varied the pulse energy instead of the propagation distance. This process has also been well reproduced by numerical simulations, which showed that the third harmonic generation acts like a loss-free 5th order saturation process, which contributes to the robustness of filamentation over long distances. Similar results were obtained in a Lidar configuration over several hundreds of meters, showing that the supercontinuum generation in multifilamentation is a cumulative process [49, 50].

The resulting continuum is very broad, since it could be measured from 230 nm in the ultraviolet to 4.5 µm in the mid-infrared. The combined spectrum is shown in Fig. 15.8. The fast decrease of the spectrum up to 2.5 µm (4 orders of magnitude between 800 nm and 2.5 µm) slows down beyond 2.5 µm, with only one order of magnitude drop between 2.5 and 4.5 µm. On the spectrum, the absorption band of water between 1.8 and 2.5 µm is clearly visible, showing the potential of the white-light for optical remote sensing in the atmosphere.

15.4.2 White-Light Generation Efficiency

Besides its spectral contents, the white-light generation efficiency is a key parameter in view of Lidar applications. Measurements have been performed at the TLS in the 400–500 nm band at 4750 m altitude as a function of the initial beam focus [24]. A strong focusing yields more efficient white-light generation, up to a factor of 50 compared to a collimated beam. The intensity at the focus is therefore a key parameter for an efficient self-phase modulation. As expected, the chirp strongly influences the efficiency conversion. In the 400–600 nm band, pulses with the same initial pulse duration of 600 fs and opposite chirps yield conversion efficiencies 6 times higher in favour of the negative chirp compared to positive chirp.

Those results show that adjusting the chirp and the focus of the laser allows to control the non-linear processes so as to optimize the white-light generation. However, the brightness of the white-light source, expressed in W/sr/nm, is a combination of the emitted intensity and the beam divergence. A tighter focusing is therefore not always the optimum configuration for Lidar. However, it is possible to strongly improve the white-light generation efficiency while keeping the beam divergence below the field of view of a typical Lidar receiver. Then, the whole generated white-light can be collected.

15.5 Conclusion and Outlook

In the last years, great progresses have been made in the understanding of the non-linear propagation of high-power laser pulses over long distances in the atmosphere. Especially, the *Teramobile* permitted to demonstrate that filamentation can be initiated at kilometre-scale distances, even through clouds. Filaments can therefore be used to remotely deliver high intensities sufficient to generate non-linear effects in-situ. The spectrum of the white-light continuum is much broader than expected a few years ago, especially in the ultraviolet where the mixing between the fundamental wavelength and the third harmonic gives rise to a plateau extending down to 230 nm, most probably limited by the atmospheric transmission window.

These progresses now open the way to atmospheric applications, such as remote sensing of gaseous pollutants and aerosols by Lidar, remote analysis of solid samples by LIBS, or the control of high-voltage electrical discharges, or even lightning. Due to its mobility, the *Teramobile* allowed to demonstrate the feasibility of many of such techniques. These applications will probably be pushed forward in the future by improvements coming in the technology of ultrashort laser pulses: more reliable and more compact systems, diode pumping, as well as spatial and temporal pulse shaping. New active media, such as Ytterbium doping [51, 52] or OPCPA [53, 54] also open the way to new spectral regions, especially the infrared. This spectral region, where the eye-safety issues are easier to address, is nearer to the absorption region of many pollutants, such as VOCs. These more flexible systems will be easier to operate, opening the way to more routine use for implementing the applications currently under development, beyond the feasibility demonstration up to the precision and reliability of actual atmospheric measurements, for the routine production of relevant data.

References

1. P. Rairoux, H. Schillinger, S. Niedermeier, M. Rodriguez, F. Ronneberger, R. Sauerbrey, B. Stein, D. Waite, C. Wedekind, H. Wille, L. Wöste, *Remote sensing of the atmosphere using ultrashort laser pulses*, Applied Physics B **71**, 573–580 (2000)
2. J. Kasparian, M. Rodriguez, G. Méjean, J. Yu, E. Salmon, H. Wille, R. Bourayou, S. Frey, Y.-B. André, A. Mysyrowicz, R. Sauerbrey, J.-P. Wolf, L. Wöste, *White-light filaments for atmospheric analysis*, Science **301**, 61 (2003)
3. G. Méjean, J. Kasparian, J. Yu, S. Frey, E. Salmon, J.-P. Wolf, *Remote Detection and Identification of Biological Aerosols using a Femtosecond Terawatt Lidar System*, Applied Physics B **78**, 535 (2004)
4. K. Stelmaszczyk, P. Rohwetter, G. Méjean, J. Yu, E. Salmon, J. Kasparian, R. Ackermann, J.-P. Wolf, L. Wöste, *Long-distance remote laser-induced breakdown spectroscopy using filamentation in air*, Applied Physics Letters **85**, 3977 (2004)
5. H. Pépin, D. Comtois, F. Vidal, C. Y. Chien, A. Desparois, T. W. Johnston, J. C. Kieffer, B. L. Fontaine, F. Martin, F. A. M. Rizk, C. Potvin, P. Couture, H. P. Mercure, A. Bondiou-Clergerie, P. Lalande, I. Gallimberti, *Triggering and guiding high-voltage large-scale leader discharges with sub-joule ultrashort laser pulses*, Physics of Plasmas **8**, 2532 (2001)
6. D. Comtois, C. Y. Chien, A. Desparois, F. Gérin, G. Jarry, T. W. Johnston, J. C. Kieffer, B. L. Fontaine, F. Martin, R. Mawassi, H. Pépin, F. A. M. Rizk, F. Vidal, P. Couture, H. P. Mercure, C. Potvin, A. Bondiou-Clergerie, I. Gallimberti, *Triggering and guiding leader discharges using a plasma channel created by an ultrashort laser*, Applied Physics Letters **76**, 819 (2000).
7. D. Comtois, H. Pépin, F. Vidal, F. A. M. Risk, C.-Y. Chien, T. W. Johnston, J.-C. Kieffer, B. La Fontaine, F. Martin, C. Potvin, P. Couture, H. P. Mercure, A. Bondiou-Clergerie, P. Lalande, I. Gallimberti, *Triggering and guiding of an upward positive leader from ground rod with an ultrashort laser pulse-I: Experimental results*, IEEE transactions on plasma science **31**, 377 (2003)
8. D. Comtois, H. Pépin, F. Vidal, F. A. M. Risk, C.-Y. Chien, T. W. Johnston, J.-C. Kieffer, B. La Fontaine, F. Martin, C. Potvin, P. Couture, H. P. Mercure, A. Bondiou-Clergerie, P. Lalande, I. Gallimberti, *Triggering and guiding of an upward positive leader from ground rod with an ultrashort laser pulse-II: Modeling*, IEEE transactions on plasma science **31**, 387 (2003)
9. B. La Fontaine, D. Comtois, C. Y. Chien, A. Desparois, F. Gérin, G. Jarry, T. W. Johnston, J. C. Kieffer, F. Martin, R. Mawassi, H. Pépin, F. A. M. Rizk, F. Vidal, C. Potvin, P. Couture, H. P. Mercure, *Guiding large-scale spark discharges with ultrashort pulse laser filaments*, Journal of Applied Physics **88**, 610 (2000)
10. M. Rodriguez, R. Sauerbrey, H. Wille, L. Wöste, T. Fujii, Y.-B. André, A. Mysyrowicz, L. Klingbeil, K. Rethmeier, W. Kalkner, J. Kasparian, E. Salmon, J. Yu, J.-P. Wolf, *Megavolt discharges triggered and guided with laser filaments*, Optics Letters **27**, 772 (2002)
11. R. Ackermann, K. Stelmaszczyk, P. Rohwetter, G. Méjean, E. Salmon, J. Yu, J. Kasparian, G. Méchain, V. Bergmann, S. Schaper, B. Weise, T. Kumm, K. Rethmeier, W. Kalkner, J. P. Wolf, L. Wöste, *Triggering and guiding of megavolt discharges by laser-induced filaments under rain conditions*, Applied Physics Letters **85**, 5781 (2004)

12. A. Braun, G. Korn, X. Liu, D. Du, J. Squier, G. Mourou, *Self-channeling of high-peak-power femtosecond laser pulses in air*, Optics Letters **20**, 73–75 (1995)
13. J. Kasparian, Chapter 14 in this volume
14. H. Wille, M. Rodriguez, J. Kasparian, D. Mondelain, J. Yu, A. Mysyrowicz, R. Sauerbrey, J. P. Wolf, L. Woeste, *Teramobile: a mobile femtosecond-terawatt laser and detection system*, European Physical J. Applied Physics **20**, 183 (2002)
15. L. Bergé, S. Skupin, F. Lederer, G. Méjean, J. Yu, J. Kasparian, E. Salmon, J. P. Wolf, M. Rodriguez, L. Wöste, R. Bourayou, R. Sauerbrey, *Multiple filamentation of TW laser pulses in air*, Physical Review Letters **92**, 225002 (2004)
16. S. Skupin, L. Bergé, U. Peschel, F. Lederer, G. Méjean, J. Yu, J. Kasparian, E. Salmon, J. P. Wolf, M. Rodriguez, L. Wöste, R. Bourayou, R. Sauerbrey, *Filamentation of femtosecond light pulses in the air: Turbulent cells versus long-range clusters*, Physical Review E **70**, 046602 (2004)
17. M. Mlejnek, E. M. Wright, J. V. Moloney, *Dynamic spatial replenishment of femtosecond pulses propagating in air* Optics Letters **23**, 382 (1998)
18. M. Mlejnek, M. Kolesik, J. V. Moloney, E. M. Wright, *Optically turbulent femtosecond light guide in air*, Physical Review Letters **83**, 2938 (1999)
19. P. Sprangle, J. R. Peñano, B. Hafizi, *Propagation of intense short laser pulses in the atmosphere*, Physical Review E **66**, 046418 (2002)
20. A. Couairon, L. Bergé, *Light filaments in air for ultraviolet and infrared wavelengths*, Physical Review Letters **88**, 135003 (2002)
21. M. Mlejnek, E. M. Wright, J. V. Moloney, *Power dependence of dynamic spatial replenishment of femtosecond pulses propagating in air*, Optics Express **4**, 223 (1999)
22. F. Courvoisier, V. Boutou, J. Kasparian, E. Salmon, G. Méjean, J. Yu, J. P. Wolf, *Light filaments transmitted through clouds*, Applied Physics Letters **83**, 213 (2003)
23. G. Méjean, J. Kasparian, J. Yu, E. Salmon, S. Frey, J.-P. Wolf, S. Skupin, A. Vinçotte, R. Nuter, S. Champeaux, L. Bergé, *Multifilamentation transmission through fog*, Physical Review E **72**, 026611 (2005)
24. M. Rodriguez, R. Bourayou, G. Méjean, J. Kasparian, J. Yu, E. Salmon, A. Scholz, B. Stecklum, J. Eislöffel, U. Laux, A. P. Hatzes, R. Sauerbrey, L. Wöste, J.-P. Wolf, *Kilometer-range non-linear propagation of femtosecond laser pulses*, Physical Review E **69**, 036607 (2004)
25. M. Mlejnek, E. M. Wright, J. V. Moloney, *Femtosecond pulse propagation in argon: A pressure dependence study*, Physical Review E **58**, 4903 (1998)
26. A. Talebpour, S. Petit, S. L. Chin, *Re-focusing during the propagation of a focused femtosecond Ti:Sapphire laser pulse in air*, Optics Communications **171,** 285 (1999)
27. A. Iwasaki, N. Aközbek, B. Ferland, Q. Luo, G. Roy, C.M. Bowden, S.L. Chin, *A Lidar technique to measure the filament length generated by a high-peak power femtosecond laser pulse in air*, Applied Physics B **76**, 231 (2003)
28. S. A. Hosseini, Q. Luo, B. Ferland, W. Liu, S.L. Chin, O.G. Kosareva, N.A. Panov, N. Aközbek, V.P. Kandidov, *Competition of multiple filaments during the propagation of intense femtosecond laser pulses*, Physical review A **70**, 033802 (2004)

29. A. Proulx, A. Talebpour, S. Petit, S.L. Chin, *Fast pulsed electric field created from the self-generated filament of a femtosecond Ti:Sapphire laser pulse in air*, Optics Communications **174**, 305 (2000).

30. S. Tzortzakis, M. A. Franco, Y.-B. André, A. Chiron, B. Lamouroux, B. S. Prade, A. Mysyrowicz, *Formation of a conducting channel in air by self-guided femtosecond laser pulses*, Physical Review E **60**, R3505–R3507 (1999)

31. H. Schillinger, R. Sauerbrey, *Electrical conductivity of long plasma channels in air generated by self-guided femtosecond laser pulses*, Applied Physics B **68**, 753 (1999)

32. J. Yu, D. Mondelain, J. Kasparian, E. Salmon, S. Geffroy, C. Favre, V. Boutou, J. P. Wolf, *Sonographic probing of laser filaments in air*, Applied Optics **42**, 7117 (2003)

33. S. Tzortzakis, G. Méchain, G. Pantalano, Y.-B. André, B. Prade, M. Franco, A. Mysyrowicz, J.-M. Munier, M. Gheudin, G. Beaudin, P. Encrenaz, *Coherent subterahertz radiation from femtosecond infrared filaments in air*, Optics Letters **27**, 1944 (2002)

34. H. Lehmann, http://www.tls-tautenburg.de/telesc.html (2002).

35. O. G. Kosareva, V. P. Kandidov, A. Brodeur, C. Y. Chen, S. L. Chin, *Conical emission from laser-plasma interactions in the filamentation of powerful ultrashort laser pulses in air*, Optics Letters **22**, 1332 (1997).

36. J. Zhang, H. Yang, J. Zhang, X. Lu, Y. Li, Y. Li, H. Teng, Z. Chen, Z. Wei, Z. Sheng, 286th Heraeus Seminar on Optical methods in atmospheric analysis, Bad Honnef, Germany, 14–18 October 2002.

37. G. Méchain, A. Couairon, Y.-B. André, C. D'amico, M. Franco, B. Prade, S. Tzortzakis, A. Mysyrowicz, R. Sauerbrey, *Long-range self-channeling of infrared laser pulses in air: a new propagation regime without ionization*, Applied Physics B **79**, 379 (2004)

38. H. R. Lange, G. Grillon, J.-F. Ripoche, M. A. Franco, B. Lamouroux, B. S. Prade, A. Mysyrowicz, E. T. J. Nibbering, A. Chiron, *Anomalous long-range propagation of femtosecond laser pulses through air: moving focus of pulse self-guiding ?*, Optics Letters **23**, 120 (1998)

39. S. L. Chin, S. Petit, F. Borne, K. Miyazaki, *The white light supercontinuum is indeed an ultrafast white light laser*, Japanese Journal of Applied Physics **38**, L126 (1999)

40. R. R. Alfano, S. L. Shapiro, *Emission in the region 4000 to 7000 Å via four-photon coupling in glass,* Physical Review Letters **24**, 584 (1970)

41. W. Yu, R. R. Alfano, C. L. Sam, R. J. Seymour, *Spectral broadening of picosecond 1.06 μ pulse in KBr*, Optics Communications **14**, 344 (1975)

42. P. B. Corkum, P. P. Ho, R. R. Alfano, J. T. Manassah, *Generation of infrared supercontinuum covering 3-14 μm in dielectrics and semiconductors*, Optics Letters **10**, 624 (1985)

43. H. Nishioka, W. Odajima, K. Ueda, H. Takuma, *Ultrabroadband flat continuum generation in multichannel propagation of terawatt Ti:sapphire laser pulses*, Optics Letters **20**, 2505 (1995)

44. J. Kasparian, R. Sauerbrey, D. Mondelain, S. Niedermeier, J. Yu, J.-P. Wolf, Y.-B. André, M. Franco, B. Prade, A. Mysyrowicz, S. Tzortzakis, M. Rodriguez, H. Wille, L. Wöste, *Infrared extension of the supercontinuum generated by fs-TW-laser pulses propagating in the atmosphere*, Optics Letters **25**, 1397–1399 (2000)

45. J.P. Wolf, *UV-DIAL-Lidar Techniques for Air Pollution Monitoring*, in "Encyclopedia of Analytical Chemistry", Ed. R.A. Meyers, Vol 3, pp 2226–2247, J. Wiley & Sons, New-York (2000)

46. N. Aközbek, A. Iwasaki, A. Becker, M. Scalora, S. L. Chin, C. M. Bowden, *Third-harmonic generation and self-channeling in air using high-power femtosecond laser pulses*, Physical Review Letters **89**, 143901 (2002)

47. F. Théberge, W. Liu, Q. Luo, S. L. Chin, *Ultrabroadband continuum generated in air (down to 230 nm) using ultrashort and intense laser pulses*, Applied Physics B **80**, 221 (2005)

48. F. Théberge, Q. Luo, W. Liu, S.A. Hosseini, M. Sharifi, S.L. Chin, *Long-range third-harmonic generation in air using ultrashort intense laser pulses*, Applied Physics Letters **87**, 081108 (2005)

49. L. Bergé, S. Skupin, G. Méjean, J. Kasparian, J. Yu, S. Frey, E. Salmon, J. P. Wolf, *Supercontinuum emission and enhanced self-guiding of infrared femtosecond filaments sustained by third-harmonic generation in air*, Physical Review E **71**, 016602 (2005)

50. G. Méjean, J. Kasparian, J. Yu, S. Frey, E. Salmon, J. P. Wolf, L. Bergé, S. Skupin, *UV-Supercontinuum generated by long-range filamentation in air*, submitted to Physical Review E

51. C. Hönninger, R. Paschotta, M. Graf, F. Morier-Genoud, G. Zhang, M. Moser, S. Biswal, J. Nees, A. Braun, G.A. Mourou, I. Johannsen, A. Giesen, W. Seeber, U. Keller, *Ultrafast ytterbium-doped bulk lasers and laser amplifiers*, Applied Physics B **69**, 3 (1999).

52. A. A. Lagatsky, C. T. A. Brown, W. Sibbett, *Highly efficient and low threshold diode-pumped Kerr-lens mode-locked Yb:KYW laser*, Optics Express **12**, 3928 (2004)

53. A. Dubietis, G. Jonusauskas, A. Piskarskas, *Powerful femtosecond pulse generation by chirped and stretched pulse parametric amplification in BBO crystal*, Optics Communications **88**, 437 (1992)

54. M. J. Guardalben, J. Keegan, L. J. Waxer, V. Bagnoud, I. A. Begishev, J. Puth, J. D. Zuegel, *Design of a highly stable, high-conversion-efficiency, optical parametric chirped-pulse amplification system with good beam quality*, Optics Express **11**, 2511 (2003)

16 Fast Electrons in High-Intensity Laser Interactions with Plasmas

J. Zhang, Y.T. Li, Z.M. Sheng, Z.Y. Wei, Q.L. Dong, and X. Lu

Laboratory of Optical Physics, Institute of Physics, Chinese Academy of Sciences, Beijing 100080, China
e-mail: jzhang@aphy.iphy.ac.cn

Summary. Fast electrons are generated in the interaction between intense ultrashort laser pulses and the target. This interaction depends on the laser's intensity, polarization, incident angle, the scale length of the plasma, and the target material. In this review, recent studies carried out at our laboratory on the dependence of the fast electrons on the experimental conditions of the laser and plasma as well as ways to control the fast electrons are presented.

16.1 Introduction

One of the most remarkable advances in laser technology was the development of the chirped pulse amplification (CPA) technique in the mid-1980s [1], which led to the rapid development of a new class of compact femtosecond and picosecond laser systems, operating at powers ranging from terawatts to petawatts. When such a laser pulse is focused onto a solid target with a focal spot a few micrometers in diameter, the laser intensity on the target surface is extremely high (currently as high as 10^{21} W/cm^2). Under such intense laser irradiation, the target matter is highly ionized, forming a relativistic plasma. During the interaction, electrons can be accelerated to very high energies (up to $\sim$100 MeV) by some processes, resulting in fast electron emission. For example, fast electrons can be generated by $\boldsymbol{J} \times \boldsymbol{B}$ heating [2] and vacuum heating [3] in a plasma with steep electron density gradients, or by stochastic heating [4], inverse free-electron laser acceleration (or direct laser acceleration) [5], ponderomotive force acceleration [6], and various parametric instabilities [7] when a preplasma is formed in advance of the peak of the laser pulse. Studies on laser-produced fast electrons have attracted great interest worldwide due to their potential applications in science and industry, such as point-size hard X-ray/γ-ray sources, laser acceleration, nuclear phenomena, laser fusion, and so on. One of their most important applications is in the fast ignition scheme for inertial confinement fusion (ICF), as proposed in 1994 by Tabak et al. [8]. In their proposal, the fast ignition scheme consists of three phases. First, the capsule is imploded to assemble a high-density fuel configuration, as in the conventional approach to inertial confinement fusion. The second phase consists of boring a hole through the corona and pushing

the critical density surface close to the compressed core, so that in the third phase the interacting high-intensity laser pulse can pass through the hole without energy loss and hit the high density capsule core to produce the fast electrons that trigger the ignition. In this fast ignition scheme, one of the most important issues is the production of directional fast electron beams with suitable energies and the deposition of their energy in the high-density fuel region with high efficiency.

To address the physics of fast electron generation in high intensity laser interactions with plasmas, we have carried out a series of experiments, mainly at the Laboratory of Optical Physics of the Institute of Physics, CAS. In this review we will concentrate on our investigation of the interactions of high intensity lasers with plasmas formed from planar solid targets. The article is organized as follows. In Sect. 16.2, we describe our homemade 20 TW laser system, eXtreme Light (XL-II), and the main experimental diagnostic instruments used. In Sect. 16.3, we discuss experimental and theoretical results on the effects of the laser's polarization, intensity, incident angle, and of the plasma density scale length on the fast electron emission. Studies on the propagation of fast electrons in solid and foam targets are presented in Sect. 16.4. A summary of the review is given in Sect. 16.5.

16.2 The 20 TW Ti:sapphire Femtosecond Laser System and Experimental Diagnostics

In order to obtain an experimental platform for high-field physics research, a 20 TW Ti:sapphire femtosecond (fs) laser system (XL-II) incorporating recently improved techniques was constructed, which is capable of delivering energies of up to 640 mJ within a pulse duration of 30 fs. In the XL-II laser system, an adaptive optics system is used to correct the wavefront distortion of the compressed laser pulses. This deformable mirror system enables $1.5\times$ diffraction-limited beam quality to be attained when focused by an off-axis parabola, providing a focused power density of 10^{19} W/cm^2 on the target. The seeding pulse is injected by a Kerr-lens modelocking (KLM) Ti:sapphire laser with a pulse duration of 20 fs used as the oscillator. After applying a Martinez telescope stretcher, 300 ps chirped pulses are amplified up to 640 mJ by a regenerative amplifier and a multipass amplifier. The compressor in the vacuum then compresses the pulse into 30 fs. Home-built laser diagnostic instruments such as SPIDER, FROG and single-shot autocorrelators are used to monitor each laser pulse on the target.

The experimental setup is illustrated in Fig. 16.1. The 30 fs laser pulses can be split into successive pulses separated by a variable time period that act as prepulses and interacting pulses, respectively. Circularly and linearly (s- and p-) polarized incident laser pulses can be obtained using wave plates. Using an off-axis $f/3$ paraboloid mirror, up to 75% of the 650 mJ laser energy can be collected into a focal spot with a diameter of less than 10 μm,
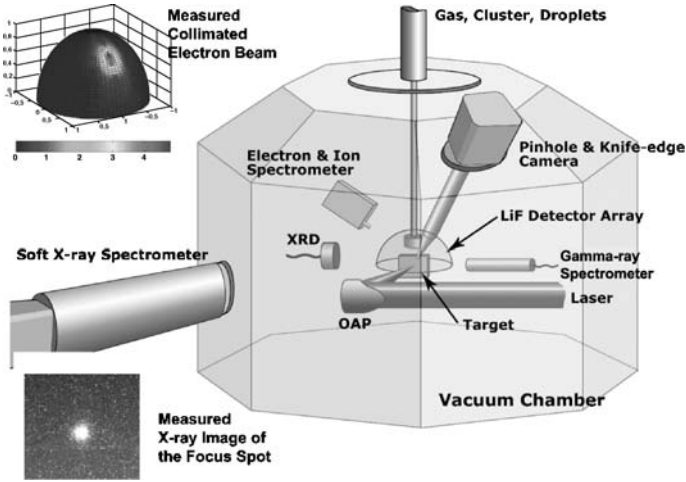
Fig. 16.1. Experimental setup. The focal spot X-ray image is also shown as an *inset*, as well as the well-collimated fast electron beams measured to have energies greater than 250 keV arising from ultrashort laser interactions with the plasma at an intensity of $1 \times 10^{16}\,\mathrm{W/cm^2}$

providing an intensity higher than $10^{19}\,\mathrm{W/cm^2}$. We monitored the focal spot with a pinhole camera. A typical hard X-ray image is shown in Fig. 16.1 as an inset. We typically used planar solid targets in experiments. The laser–plasma interactions for clusters, microliquid droplets and foam targets were also used in some special experiments. Devices were built to produce clusters of various sizes. The same device can also be used to produce water or ethanol microdroplets.

In the experiments, we controlled the density profiles by introducing pre-pulses in advance of the interacting pulse. Shadowgraphy and interferometry techniques were applied to measure the plasma density profile.

The diagnostic techniques used included γ-ray spectrometers to measure radiations of up to a few hundred keV. The spectrometer consisted of a NaI detector, a photomultiplier, an amplifier and a multichannel energy analyzer. In order to eliminate the noise level caused by the random γ-ray scattering and to enhance the signal-to-noise ratio, this assembly was fully enclosed in a Pb cylinder with a 10-mm-diameter hole in the 50-mm-thick cross-surface close to the rear of the target, between which an electronic pulsed gate was installed in front of the detector and synchronized with the main laser pulse, as shown in Fig. 16.1. The spectrometers were calibrated using a γ-ray source ^{22}Na ($\sim$511 and 1270 keV). To avoid any overlap of photons in the detectors, the distances between the detectors and the plasma and the diameter of the hole in the lead block in front of the detectors were adjusted so that the probability of detecting a γ-ray photon for each shot was less than 0.2.

Magnetic spectrometers with 380 G, 1000 G, 2000 G and 5000 G permanent magnets were used to measure the electron energy distributions, covering an energy range from 0.01 to 100 MeV. The energy spectra were also recorded by the calibrated imaging plates (IP) or by LiF thermoluminescent dosimeter (TLDs) detectors.

Fast electron angular distributions are measured via a detecting sphere consisting of hundreds of TLDs, radiochromic film pieces or IP stacks arranged around the target. The expected electron energy range was selected via a composite filter assembly in front of the detectors. The filter assembly consisted of aluminum foils of different thicknesses. These detectors are sensitive to ions, X-ray photons, and electrons. However, the thick aluminum filters in front of the detectors can block the ions generated in the experiments. By comparing the signal intensity in the detectors with and without a 1500 G magnetic field we found that the contribution from X-rays was $< 5\%$. Thus, the signal recorded by the detectors was mainly from fast electrons. Some of the measurements obtained are presented in Fig. 16.1 as an inset, which shows one collimated electron beam with a divergence angle of less than 15° [9].

We determined the absorption of the laser pulse by recording the scattered and specularly reflected laser light with 4π-arranged calorimeters. In front of the calorimeters, a 2-mm thick quartz plate was installed to block charged particles and X-rays. In some experiments, low-order harmonics of the laser beam were analyzed using a monochromatic meter. Crystal spectrometers were used to record the plasma self-emission of X-rays, from which the ionization states of the target materials were obtained.

16.3 Fast Electrons from Ultrashort Laser Interaction with Solid Targets

In this section, we discuss the effects of laser polarization, intensity, preplasma, and incident angle on the fast electrons produced by the interactions of ultrashort laser pulses with solid targets.

16.3.1 Dependence on Laser Polarization

With moderately intense laser pulses, the electric field dominates the interaction process. Experiments were carried out to study the polarization effects of the interactions of laser pulses with plasmas with steep or exponential density profiles.

Figure 16.2a shows the angular distribution of fast electrons generated from plasma with an exponential density profile by p-polarized laser light at an intensity of 2×10^{16} W/cm^2 [10]. Almost all of the outgoing fast electrons were emitted in the normal direction. The emission direction of the fast electrons basically obeys the law of momentum conservation [11]. However, when
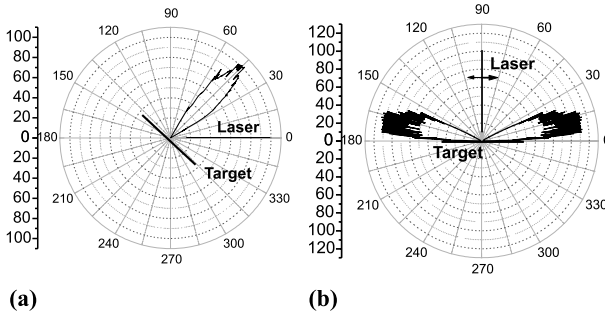
Fig. 16.2. a,b. The angular distributions of outgoing fast electrons with energies over 50 keV in the incident plane for a p-polarized laser (**a**) and in the plane perpendicular to the incident plane for an s-polarized laser (**b**) when the laser intensity is about 2×10^{16} W/cm^2

the solid target was irradiated by an s-polarized laser pulse, the behavior of the fast electrons was much different to that produced by p-polarized laser pulses. As Fig. 16.2b shows, the outgoing fast electrons were found to be collimated along the laser polarization direction in a plane perpendicular to the incident plane. In the incident plane, no fast electrons were measured. It was also found that fast electrons with higher energies have narrower angular divergences. When there was a coronal preplasma in front of the target, a very small percentage of the outgoing fast electrons were found in the incident plane. This suggests that the outgoing fast electrons were mainly accelerated by the electric field of the s-polarized laser pulses. When there is a coronal preplasma in front of the overdense plasma, the potential modulation of the critical surface of the preplasma will steer a very small percentage of the fast electrons away from the direction of polarization. This phenomenon seems to be similar to the results from a laser accelerator injector based on laser ionization and the ponderomotive acceleration of electrons in gas, where electrons are accelerated in the direction of polarization [12], but the heating mechanism is obviously different in the two cases.

If the laser intensity is increased a relativistic level ($a_0 > 1$), the effects of the laser polarization on the fast electron emission are not as important as they are for lower intensities, especially when a large-scale preplasma is formed before the main pulse. Figure 16.3a shows the angular distributions of the forward fast electrons behind the target for p-polarized and s-polarized laser pulses [13]. Here $0°$ corresponds to the laser propagation direction. In the experiment, a 0.6–1 ps, 1.053 μm linearly polarized laser pulse with an energy of up to 10 J, output by the GEKKO Module II (GM-II) laser facility at the Institute of Laser Engineering, Osaka University, was focused onto a 5 μm-thick aluminum foil target at an incident angle of 45°. The diameter of the focus was about 30 μm. The laser intensity on the target was adjustable in the range of $(2$–$4) \times 10^{17}$ W/cm^2. A prepulse with an energy of about 3×10^{-3} of the main pulse, originating from the regenerative amplifier, starts from 700 ps
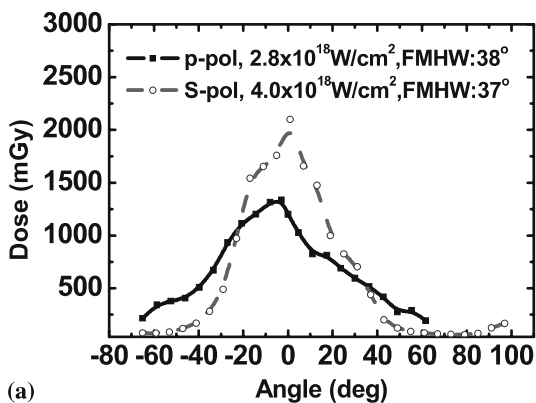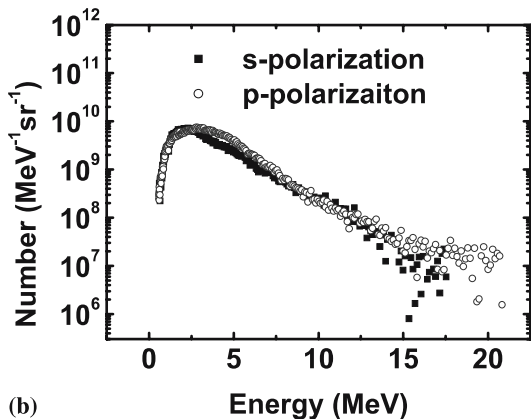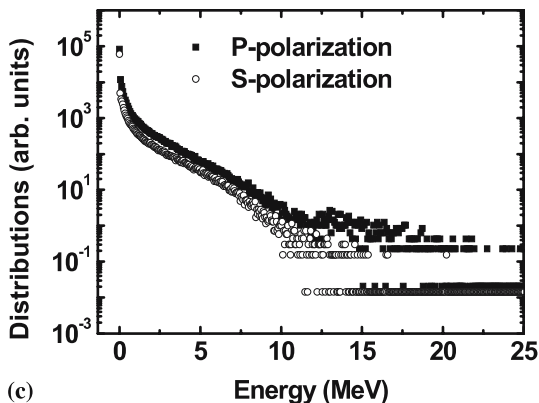
Fig. 16.3. a,b. The measured angular distributions (**a**), energy spectra (**b**), and PIC-simulated spectra (**c**) of fast electrons at a laser intensity of 3–4×10^{18} W/cm^2 for both *p*-polarized and *s*-polarized laser pulses

ahead of the main pulse peak. Therefore, the main laser pulse interacted with a preplasma. The forward fast electrons ware measured behind the target by LiF (Mg, Cu, P) thermoluminescence dosimeters (TLD). The emission directions and the cone angles of the fast electrons measured for both polarizations

are very similar. Figure 16.3b and c shows the measured energy spectra and the theoretical spectra obtained from 1-D PIC simulations for relativistic laser intensities, for both p-polarized and s-polarized laser light. One can see that the energy spectra of the fast electrons measured for both polarizations are also very similar. Both simulation and experiment show that the laser polarization has little effect on the electron energy distribution and emission direction at the relativistic laser intensity when a large-scale preplasma occurs. This is very different to the interaction with a short density gradient scale at low laser intensity. The phenomena are mainly due to the following two reasons. The first is that the forward acceleration due to the laser's magnetic field dominates for $a_0 > 1$. This acceleration is less dependent on the polarization of the laser. The other reason is that the critical surface of the plasma becomes curved due to the high laser pressure. This leads to the formation of a p-polarized component of the laser electric field.

16.3.2 Dependence on Plasma Density

When a long laser pulse of ns/ps duration interacts with a plasma, it is well-known that the plasma density profile will evolve with time. The evolution includes coronal plasma expansion and ponderomotive steepening near the critical surface [6, 7]. However, when an *ultrashort* laser pulse interacts with a solid target, the very short duration does not allow significant evolution of the plasma. There has been a great deal of recent interest in laser absorption and X-ray emission from solid targets irradiated by ultrashort laser pulses [14], where the plasma density scale length can be much less than the laser wavelength λ_0. Similarly, if such an ultrashort laser pulse interacts with a solid target with a preformed plasma in front of it, the interaction will depend to a large extent on the properties of the preformed plasma, particularly its scale length. By using a carefully controlled prepulse, one can create any desired plasma density scale length by controlling the time interval between the prepulse and the main pulse. Therefore, an ultrashort laser pulse allows for "clean" interaction with a preformed plasma without any significant dynamic evolution of the latter, providing a unique opportunity to identify the various interaction processes that depend strongly on the plasma density scale length.

   Here we investigate the effects of the plasma density scale length on laser absorption, X-ray emission, and fast electron temperature by varying the time gap between the main pulse and the prepulse over a very wide range, from 0 to 275 ps. This corresponds to varying the density scale length from 0 to about 11 μm in our prepulse parameters. In experiments, p-polarized short laser pulses at a moderate intensity of around $2 \times 10^{16} \, \mathrm{W/cm^2}$ were used, while results from s-polarized laser pulses are also invoked for comparison. We demonstrate the existence of clearly defined multiple absorption peaks and the corresponding peaks in X-ray production and fast electron temperature. The multiple absorption peaks are identified as originating from the transi-

tion between principal absorption mechanisms as the density scale length is increased, namely from vacuum heating/resonance absorption to parametric instabilities. To compare, only one absorption peak is observed over the same range at a relatively large scale-length for s-polarized irradiation.

Figure 16.4 shows the measured absorption of laser energy as a function of the scale length L of the plasma. For p-polarized irradiation, three local peaks of absorption at around $0.2\lambda_0$, $2.8\lambda_0$, and $5.5\lambda_0$ were found. Note that there is considerable absorption even without a prepulse. This is apparently due to vacuum heating and collisional absorption, resulting in absorption even at very small L (corresponding to a step-like density profile). The absorption decreases significantly when the main pulse immediately follows the prepulse. As L is increased, an absorption peak appears at $0.2\lambda_0$. This can be attributed to resonance absorption at $L = 0.2\lambda_0$. When the scale length is increased to more than $2\lambda_0$, other peaks appear. To our knowledge, this is the first time that additional absorption peaks have been observed at large scale lengths. There are also three main peaks that correspond to the absorption peaks in the Bremsstrahlung X-ray emission (Fig. 16.5). On the other hand, for s-polarized incidence there is only one absorption peak at $L = 5.8\lambda_0$, and only one main peak (at relatively large L) in both of the Bremsstrahlung X-ray emission distributions shown.

Angular distribution measurements showed the collimated jet emission of fast electrons at different scale lengths. We found that the direction of fast electron emission changed dramatically as the plasma scale length L increased from zero. Interaction between an ultrashort laser pulse and a plasma with a steep density profile ($L = 0$) produced a very collimated jet in the specular reflection direction, similar to that observed in Fig. 16.2. As L is increased, emission in the specular direction decreases abruptly and a sharp collimated jet of fast electrons appears in the normal direction. The angular divergence of the fast electrons also decreases with increasing fast electron energy. As the absorption reaches the local peaks at $L = 0.2\lambda_0$, $2.8\lambda_0$, $5.5\lambda_0$,
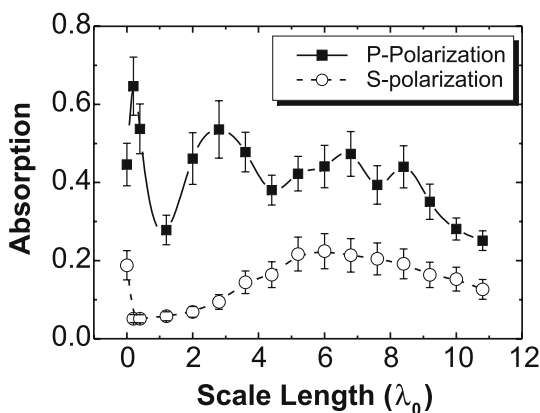
Fig. 16.4. The absorption of laser energy as a function of scale length L (in λ_0) for p-polarized irradiation (*solid squares*) and s-polarized irradiation (*shallow circles*) with an incident angle of $45°$
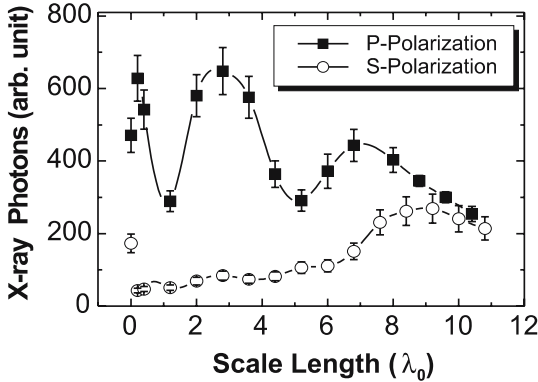
Fig. 16.5. The X-ray emission counts as a function of scale length L (in λ_0) for both p- (*solid squares*) and s-polarized (*shallow circles*) irradiation with an incident angle of $45°$

corresponding local minima can be observed in the angular divergence of fast electron emission for p-polarized irradiation.

The increased absorption as well as X-ray production for large scale lengths ($L > 2\lambda_0$) implies the presence of different absorption mechanisms, which predominate in the preformed plasma with large density scale lengths. Among the possible mechanisms, linear vacuum heating and nonlinear $\boldsymbol{J} \times \boldsymbol{B}$ type mechanisms can be ruled out, since they usually appear only for plasmas with scale lengths of less than one laser wavelength. On the other hand, stimulated Raman scattering (SRS) and two-plasmon decay (TPD) instabilities, together with inverse Bremsstrahlung absorption, can dominate for both p- and s-polarized irradiation. Indeed, the correlation between the fast electron generation/Bremsstrahlung X-ray emission and TPD/SRS was evident in our experiments, where clear TPD/SRS spectroscopic signatures at $3\omega_0/2$ and $\omega_0/2$ were observed for larger scale lengths in the specular and backward directions.

16.3.3 Dependence on Laser Intensity

The generation mechanisms of fast electrons depend closely on the laser intensity. For a single electron, its behavior and trajectory are determined by the intensity, temporal profile, and polarization state of the laser pulse. For a subrelativistic laser intensity of $I\lambda^2 < 1.37 \times 10^{18}\,\mathrm{W/cm^2}$ ($a_0 \ll 1$), where I is the laser intensity in $\mathrm{W/cm^2}$, and λ is the laser wavelength in $\mu\mathrm{m}$, the electron mainly responds to the electric component of the laser pulse. For the s-polarized laser field, electrons are mainly dominated by transverse acceleration, while for the p-polarized laser field, processes such as resonance absorption and vacuum heating will accelerate electrons in the target normal direction. The emission direction of the fast electrons obeys the momentum conservation law [11]. In general, the beam quality is good with a divergent angle of less than $30°$, while the conversion efficiency is less than 10%. The magnetic component plays a more and more impor-

tant role as the intensity of the laser increases. When $a \sim 1$, electric and magnetic components exert forces of the same order of magnitude on the electron and push it along the gradient direction of the laser intensity as the electron quivers in the polarization plane [15]. However, with plasma targets, the behavior of electrons in laser fields is determined by the combined effects of the laser field and collective plasma functions. The production mechanisms of fast electrons are rather difficult to identify. For example, the component of the nonrelativistic laser electric field along the plasma density gradient can resonantly drive the plasma wave to break, producing large numbers of fast electrons with an effective temperature greater than $T_{\mathrm{H}} \sim 6 \times 10^{-5} (I\lambda)^{0.33}$eV [16], deduced for long pulse interactions. For a relativistic laser intensity of $I\lambda^2 > 1.37 \times 10^{18}$ W/cm^2 ($a > 1$), the laser ponderomotive force or $\boldsymbol{V} \times \boldsymbol{B}$ force dominates the interaction mechanism for a solid-density plasma. This interaction produces fast electrons with a Maxwellian distribution characterized by an effective temperature that is the same as the laser ponderomotive potential $T_{\mathrm{H}} \sim 0.511 \times (\sqrt{1 + a^2/2} - 1)$MeV [17]. Electrons are mainly accelerated in the longitudinal direction. If a large scale length preplasma is formed before the main pulse arrives, the interaction process can be much more complicated. Various parametric instabilities as well as other mechanisms such as stochastic heating [18] and plasma wake waves may also accelerate electrons, as discussed above for underdense plasmas [19]. Each interaction mechanism has its own characteristics that manifest themselves in the fast electron emissions.

16.3.4 Dependence on Incident Angle

After the fast electrons gain enough energy, a proportion of them will be ejected backward into the vacuum from the underdense plasma in front of the target. The others move forward into the overdense plasma region and propagate inside the cold target region. About 20–40% of the laser energy can be converted to fast electrons at intensities of $\sim 10^{19}$ W cm^{-2}. This forms a highly directional fast electron beam with a current that can reach as high as MA (or even GA) [20, 21]. This will induce huge electrostatic fields and magnetic fields inside the plasma or target bulk. The bulk fields, in turn, will affect the fast electron transport. The feedback processes between the fast electrons and the bulk fields can lead to the self-organized propagation of fast electrons. Firstly, the electrostatic fields will lead to an effective energy loss of the fast electrons and inhibit the electron penetration (self-inhibition) [22,23]. Secondly the fast electron beam will be collimated by the static magnetic fields (self-pinch) [24–27]. Finally, the fast electron beam may be broken up into filaments due to two-stream instability and Weibel instability [28]. The current filaments evolve to a self-organized state in which the net current of each filament is less than the Alfven limit [29].

Self-organization processes can also occur at the target surface when the incident angle of a laser pulse is large. Recently, a theory proposed by Naka-

mura et al. [30] and a particle in cell (PIC) simulation done by Sentoku et al. [31]) have predicted that a fast electron current layer along the target surface can be generated due to the reflection of surface magnetic fields. These theoretical findings have been used to explain the enhanced neutron yield in fast ignition experiments with a cone target [32,33]. However, no direct experimental observation of the surface electron emission has been reported so far.

In this section, we present experimental evidence of the self-organized motion of fast electrons at the front target surface in the interaction of a femtosecond laser pulse with a metallic foil by directly detecting the fast electrons for different laser incident angles and electron density scale lengths. Our measurements show that a novel fast electron beam emitted along the target surface is generated when the electron density gradient is steep. Moreover, this beam becomes stronger and stronger as the angle of incidence of the laser increases. The signal from the fast electrons behind the foil decreases almost to noise levels when the incident angle is increased to 70°. However, for long density scale lengths, the surface fast electron beam disappears. Our two-dimensional PIC simulations clearly show that the surface fast electrons are guided along the target surface due to static electric fields and surface magnetic fields induced by the fast electrons themselves.

Figure 16.6a–c shows the angular distributions of fast electrons in the polarization plane for laser incident angles of 22.5°, 45°, 70°, respectively. The fast electrons were produced in the interaction of a p-polarized laser pulse with a 30 μm thick aluminum foil at a subrelativistic laser intensity of 5–7×10^{17} W/cm^2. Each data point in the polar diagrams was obtained by integrating the signal intensities on the IP. All data have been normalized to 100. The fast electrons were measured by a stack array of imaging plates.

The most striking aspect of our measurements is the presence of fast electrons ejected along the front target surface, marked as "surface electrons" in the figures [in Fig. 16.6 an inset with an enlarged scale is used to show them clearly]. In particular, the number of surface fast electrons increases with the laser incident angle. The emission peak along the target surface is fivefold more intense than those close to the target normal for the case with an incident angle of 70°. Moreover, in this case the surface electron jet is also well-collimated, with a cone angle of less than 15° (FWHM).

Table 16.1. The fractions of the electrons along the front surface (f_{se}) and the fractions of the transmitted electrons in the π solid angle behind the target (f_{te}) to the total electrons of 2π in the incident plane. The uncertainty comes from the shot-to-shot fluctuations from 3–5 shots. The ratio of the front-surface electrons increases with the incidence angle, while the transmitted fraction is on the contrary

Incident angle	f_{se}	f_{te}
22.5°	2–6%	20–28%
45°	17–28%	8–16%
70°	50–65%	1–5%
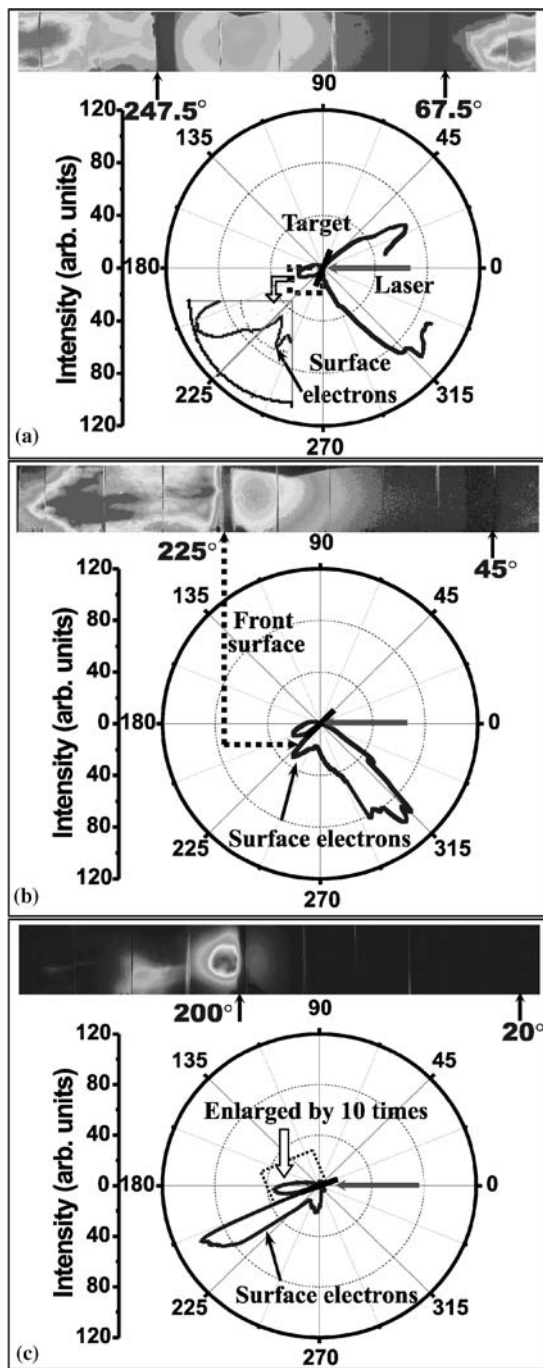
Fig. 16.6. a–c. The IP images and the corresponding angular distributions of fast electrons with energies greater than 300 keV in the laser incident plane for a p-polarized laser pulse at an intensity of 1–2×10^{18} W/cm^2 for three different incidence angles of $22.5°$ (a), $45°$ (b), and $70°$ (c), where $0°$ corresponds to the incident laser direction. The positions of the front and rear target surfaces are marked on each image by *two arrows*. A novel fast electron jet emitted along the front target surface is observed

Table 16.1 shows the ratios of the surface electrons and the transmitted electrons to the total electrons, respectively. One can see that the fraction of front-surface electrons increases with the incidence angle, while the transmitted electrons decrease with the laser incidence angle. For the case with an angle of incidence of 70°, the fraction of surface electron jet to the total is larger than 50%, and the number of transmitted electrons drops to almost noise levels. Note that the fast electrons observed behind the target have to overcome the sheath electrostatic field at the rear surface in order to be ejected into the vacuum [34–37]. Therefore, the fractions of transmitted electrons are generally low, for example only 20–30% at an angle of incidence of 20°, though the surface magnetic field is small for such a small angle of incidence.

In order to deduce the experimental conditions for the surface electron jet, s-polarized and circularly-polarized laser pulses were also used to irradiate the 30 μm-thick Al targets and CH target at different laser incident angles. The results were similar to those for the p-polarized laser. However, when a prepulse was introduced, the surface of the surface electron jet disappeared. To check the role of the electron density scale length, a 200 ps laser beam, split from the laser beam before the compressor, was used to create a preplasma 0.5 ns before the main pulse arrived. The prepulse intensity on the target surface was about 3.5×10^{13} W/cm^2. The result for the preplasma case is shown in Fig. 16.7, where the main laser intensity was set to be 2×10^{18} W/cm^2, similar to that in Fig. 16.6b. No surface electrons are produced when the preplasma occurs. This suggests that the confinement of both the surface magnetic field and the sheath electrostatic field in front of the target is essential to the formation of surface electron beams. A preplasma with a large density scale will destroy the sheath field and lead to the disappearance of the surface electron beam.

In order to understand the characteristics of the surface fast electrons, a 2-D fully relativistic PIC code has been used to simulate the generation of the surface electromagnetic fields and the fast electrons in the interactions.
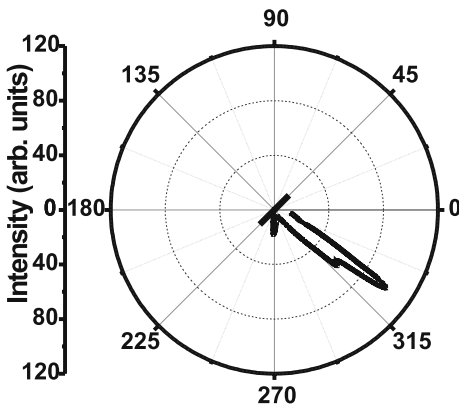
Fig. 16.7. The angular distribution of the fast electrons produced at a laser intensity of 2×10^{18} W/cm^2, but with an intended large-scale preplasma that was created by a 200 ps laser beam with a separation time 0.5 ns in advance of the main pulse

In the PIC simulations, a p-polarized laser pulse with an irradiance of 2–5×10^{18} W/cm^2 is incident at $70°$ onto an $8n_c$, $4\lambda_0$ thick plasma slab with a sharp boundary, where n_c and λ_0 are the critical density and the laser wavelength respectively. The diameter of the laser focus is $10\lambda_0$. The laser electric field is in the Y-direction. Figure 16.8a shows typical trajectories of fast electrons at the front target surface. One can see that some fast electrons in the focus move along the target surface in an oscillating form, instead of ejecting into the target region. After running away from the focus, they have deviated from the initial direction and been redirected to the target surface direction, resulting in a surface fast electron jet.

This novel phenomenon is due to the self-organization of the fast electrons. When the fast electrons from a solid target with a steep density gradient are accelerated into the target bulk, due to either $\boldsymbol{J} \times \boldsymbol{B}$ heating or vacuum heating, quasi-static magnetic fields will be induced by the fast electron current itself around the front surface. A quasi-static electrostatic field perpendicular to the target surface will form as well due to charge separation. Figure 16.8b shows the spatial distributions of the magnetic field B_z and the electrostatic field E_x. The fields are normalized by $m\omega_0 c/e$. Both the magnetic and elec-

(a)

(b)
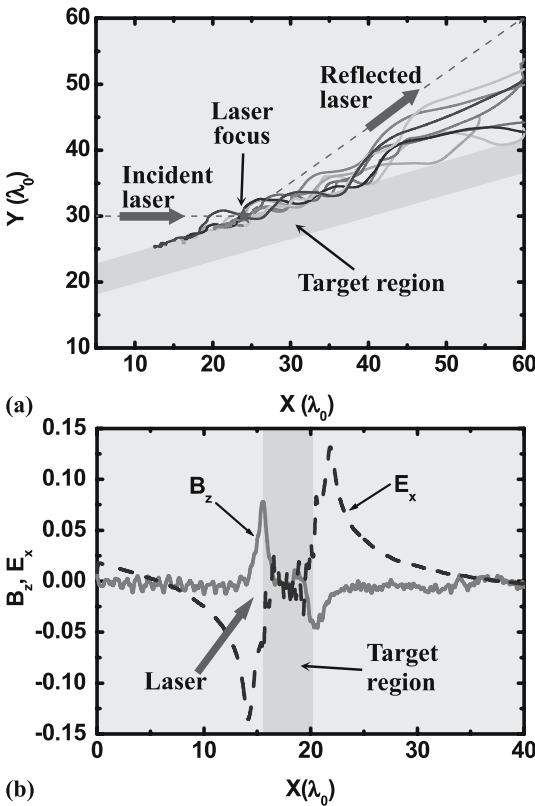
Fig. 16.8. a,b. The typical simulated fast electron trajectories at the front target surface (**a**), and the electrostatic field (E_x) and magnetic field (B_z) profiles obtained from 2-D PIC simulations (**b**)

tric fields are located in the skin layers near the surface. Some of the fast electrons generated in the interaction region are reflected to the vacuum side by B_z. However, the negative sheath field E_x, whose peak position slightly shifts to the vacuum relative to that of the B_z, will push them back towards the target again. This push–pull process will lead to the enhancement of the surface electron current and the magnetic field. Therefore, a drift of the fast electrons along the target surface in an oscillating form will be produced self-consistently. Thus, a fast electron jet along the target surface will be generated after they propagate away from the focus.

In the PIC simulations no surface fast electrons are observed when a pre-plasma is added in front of the sharp-boundary plasma slab. This agrees with experimental measurements for the larger density scale case.

16.4 Transport of Fast Electrons Through Solid and Foam Targets

16.4.1 Transport of Fast Electrons in Solids

The propagation of fast electrons in plasmas is very important to the fast ignition concept. However, it is impossible to directly investigate the behavior of the ingoing fast electrons in plasmas. The propagation characteristics can only be found from fast electrons penetrating through plasmas and measured behind the target. Experiments on this subject have been conducted in our laboratory and the results are discussed below. We have used two kinds of targets. One is 1 μm aluminum film deposited on flat fused glass substrates by a laser–plasma deposit technique. The other is simply a 5 μm aluminum film stuck in parallel onto fused glass substrates, with a gap of 20 μm between each. P-polarized laser pulses are incident on the target at $10°$. The fast electrons produced can pass through the plasma and the remains of the target, then penetrate into the fused glass and ionize it, leaving a plasma channel (path) in the substrate, which is monitored by the time-resolved shadowgraphy technique. To realize this, a well-synchronized laser pulse of duration 30 fs and wavelength 400 nm acts as the probe beam, which is injected perpendicular to the plasma channel.

Figure 16.9a shows a typical shadowgram for the 1 μm Al-coated fused glass slide at different time delays after the interaction [38]. In order to enhance the contrast of this particular image, we have subtracted the image of the unperturbed glass substrate in the presence of the probe beam. The dark region in the image corresponds to a plasma density greater than the critical density of 400-nm light, $6.9 \times 10^{21}/\mathrm{cm}^3$. Besides the plasmas before the Al film, there is an almost isotropic dark region behind the Al film. According to the calculated velocity of its expansion edge into the glass (2×10^8 cm/s), this dark region may be attributed to radiation-driven thermal transport ionization waves. What interested us is the narrow dark jet within the ionization
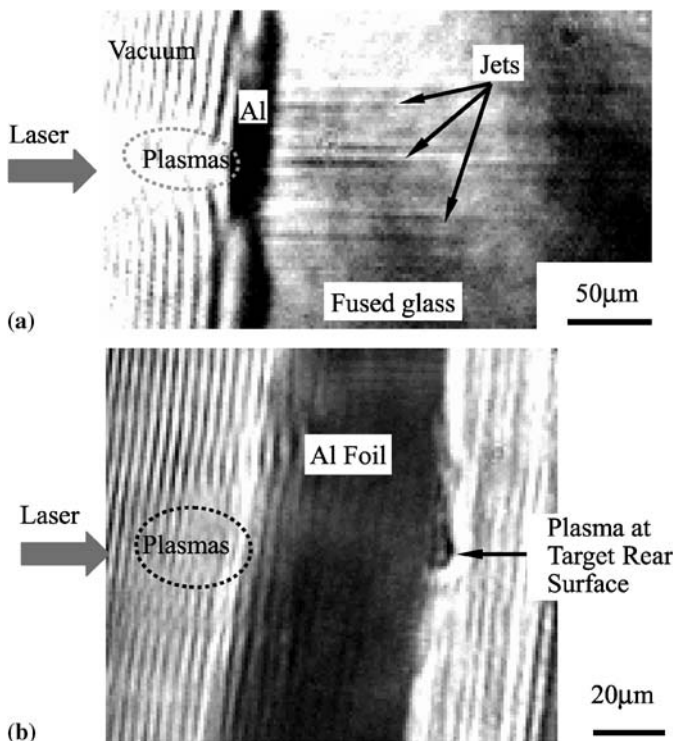
Fig. 16.9. a,b Typical shadowgraphs of the plasma channels ionized by fast electrons from the Al film (**a**) and the mushroom-like plasma at the rear of the target (**b**)

wave, which originates from the interaction region and extends far into the glass.

The self-focused laser light, hard X-rays, and fast electrons can all induce the plasma tracks in the glass. However, the 1 μm Al coating on the glass can block the incident laser during the interaction period. The contrast ratio of the laser pulse is 10^{-5} at 1 ps, as measured by a third-order autocorrelator. Numerical simulation suggests that the laser pedestal does not ablate the 1 μm Al film. The shockwave was found to propagate through the 1 μm Al 100 ps later, which is long after the interaction and the fast electron's arrival at the end of its journey in the substrate. The presence of laser light filaments in the glass can therefore be ruled out. Strong X-ray emission is another candidate that could cause ionized tracks. A composite target consisting of a 5 μm Al foil stick on the fused glass was used to investigate this possibility. The basic idea to use the space–charge field in the rear plasma interface with the vacuum to reduce the energies of fast electrons. The space–charge field is estimated to be 7.6×10^{11} V/m, which induces ionization of the material at the rear surface of the foil, forming the mushroom-like plasma shown in Fig. 16.9b [39]. Plasma tracks formed in the glass with these composite targets

are much shorter than those obtained with the deposited Al film target, excluding the possibility of X-rays ionizing plasma channels, since they are not susceptible to changes in the space–charge field.

It is interesting to note that in Fig. 16.9a there are two jets at the center of the focal spot, and several jets parallel to but away from the axis of the laser beam. This phenomenon is possibly due to two reasons. The first originates from the process of fast electron production. The focal spot is measured to have a full width at half maximum of 10–20 μm. When the energy is increased, the laser beam quality is strongly modulated by thermal effects and the inhomogeneity of the dopant concentration in the Ti:sapphire crystal. Thus, hot spots exist in the laser beam. When the beam is focused, the hot spots will become many small local high-intensity spots around the focus, which have intensities sufficiently high to produce fast electrons that induce ionization plasma channels in the fused silica. The second cause is Weibel instability, which takes place during the propagation of fast electrons in plasmas. Filaments can occur when the fast electron beam splits. Some filaments are diffused outward from the center of the focal spot and produce the plasma channel away from the axis of the laser.

16.4.2 Transport of Fast Electrons in Foams

The experiments were carried out using the laser system Gekko Modulate II (GMII) at the Institute of Laser Engineering, Osaka University. It delivers laser pulses of 0.6 ps and wavelength 1.053 μm and with energies of up to 10 J, which were focused by an $f/3.8$ off-axis parabolic mirror onto the target. The laser pulses were p-polarized with an incident angle of 20°. The diameter of the focus on the target was also about 30 μm. A prepulse with an energy of about 3×10^{-3} of the main pulse, originating from the regenerative amplifier, starts from 700 ps ahead of the main pulse peak.

Low-density deuterated foams and solids were used as targets. The target material was deuterated polystyrene $[(C_2D_3)_n$, with a D enrichment greater than 98%]. The foams were prepared by the sol gel–aerosol method. Two different foams with average densities of 50 mg/cm^3 and 160 mg/cm^3 were used.

In order to understand the electron transport inside the targets, the forward fast electrons ejected from the rear target surface were measured by a stack of layers of radiochromic films (RCF) in 40×40 mm, CR39 plastic nuclear track detectors, as well as imaging plates (IP). The stacks were set parallel to the target surface at a distance of 5 cm from the target. A magnetic spectrometer with 2500-Gauss permanent magnets was aligned in the laser propagation direction to measure the electron energy distribution. The acceptance angle of the spectrometer was 10^{-5} rad. The electron energy spectrum was recorded by calibrated imaging plates.

Figure 16.10a and b shows the spatial distributions of the fast electrons with different energy ranges for the solid and 50 mg/cc foam targets, respec-
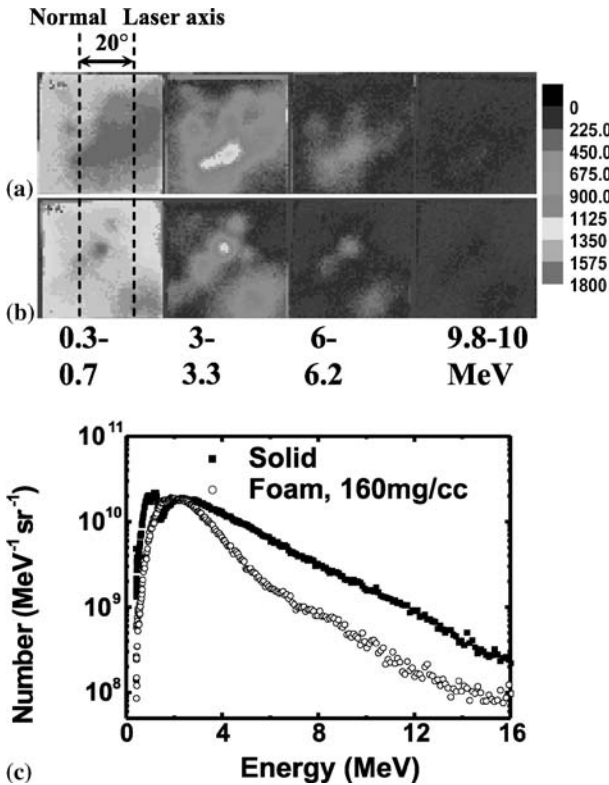
Fig. 16.10. a–c. Spatial distributions of hot electrons for a 0.25 mm-thick solid (**a**) and a 0.25 mm-thick 50 mg/cc foam (**b**), as well as typical energy spectra for a 0.25 mm-thick solid and a 1.7 mm-thick 160 mg/cc foam (**c**). The *dashed lines* in **a** and **b** indicate the rear target normal and the forward laser axis directions

tively, measured behind the targets. The directions of the rear target normal and the forward laser axis are marked by the dashed lines. The laser energies on the targets were 10.7 J and 10.3 J, respectively. The electron beam patterns for both the solid and foam targets appear to be broken-up. This is more obvious for the foam case, where the whole electron beam is even split into two parts in addition to the embodied fine filaments. Note that the filamentation of fast electron beams inside a foam plasma has also been observed very recently [40]. More interestingly, after integrating the counts over the whole area of each imaging plate layer (each layer corresponds to a different energy range), we find that the total signal counts for the foam are much lower than that for the solid. This suggests that the transport of fast electrons is seriously suppressed inside the foams. This suppression can also be seen in Fig. 16.10c, which shows typical electron spectra for the 0.25 mm-thick solid and 1.6 mm-thick, 160 mg/cc foam target.

The inhibition of the fast electron transport in foams can be explained by the following scenario. The current of the fast electron beam produced in the experiments is greater than the Alfvén limit, the maximum current that can be propagated by an electron beam in vacuum [41]. For currents exceeding the limit, the intense self-consistent magnetic field associated with the beam will

deflect the electron trajectories back and prevent their forward movement. However, such a huge fast electron current can propagate in solid targets because the background cold electron current can neutralize the space charge of the beam and slow down the fast electrons. Therefore, the fast electron transport strongly depends on the conductivity [42] and the density of the target material. Studies have shown that their transport in dielectric targets [43] and low-density gas targets [44, 45] is inhibited more significantly than it is in metal targets. For foam targets, on the one hand the return current is weaker than it is in solids since there are fewer cold background electrons due to their low average density. On the other hand, there will be multipeak electric fields induced around the lamellar layers inside the foams when fast electrons transport to the region (see simulation results in the following). As a result, significant inhibition of the fast electron beam is generated inside the foam, as observed in the experiments. A similar inhibition of fast electrons in plastic foams has also been observed by K_α spectroscopy [46].

In order to clarify the physical processes that occur in the foams, one-dimensional fully relativistic PIC simulations have been conducted. In the simulations, the electron density in the underdense plasma increases from $0.01n_c$ to n_c exponentially in a scale length of $40\lambda_0$, where n_c is the critical density and is λ_0 the laser wavelength, respectively [see Fig. 16.11a]. The high-density region consists of 40 thin layers of overdense plasma at a density of $9n_c$ in the x direction to imitate the foam structure. The thickness of each layer is $0.1\lambda_0$ and the separation between neighboring layers is λ_0. Although this is much simplified from the real foam structure, such a model can be helpful for deducing the main physical processes that occur along a given direction. The target consists of fully ionized deuterons (ion mass is $3680m_e$), D^+, and carbon ions ionized four times, C^{4+}. The incident laser intensity is $4.0 \times 10^{18}\,\mathrm{W/cm^2}$. Figure 16.11b shows the induced longitudinal electric
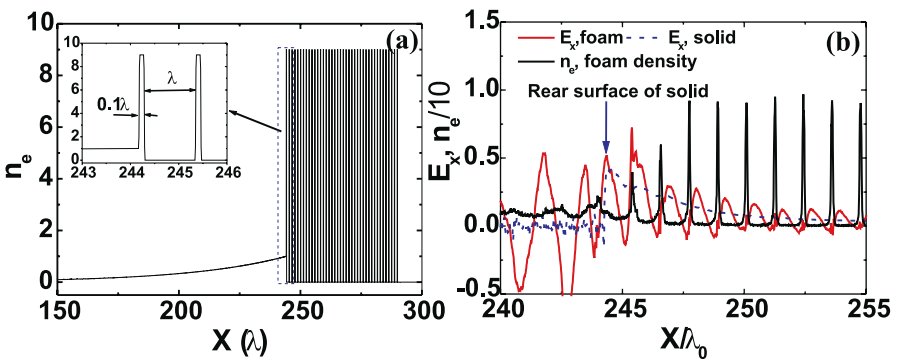
Fig. 16.11. a Initial electron density distribution used in the 1-D PIC simulations; **b** electric fields inside the foam (*red solid line*) and the fields behind the rear surface of solid target (*blue dashed line*) at $t = 400$ laser cycles. The electron density at the same time (divided by a factor of 10) is also shown (*black solid line*)

fields for the foam and solid targets, as well as the electron density for the foam target at $t = 400$ laser cycles. In the case with the solid foil, when the fast electrons produced in the laser–plasma interaction pass through the rear target surface, an electrostatic field builds up behind, which decays with the distance from the rear surface. One can see that an electrostatic field with multiple peaks is built up around each lamellar layer inside the bulk foam when fast electrons move inside it, as shown in Fig. 16.11b. This ambipolar field structure, partially caused by the return electron current around individual overdense lamellar layers, leads to the inhibition of the transport of fast electrons in a foam.

16.5 Summary

To summarize this topical review, we would like to mention an encouraging experiment related to the fast ignition scheme, efficiency was increased by about 50% above normal [31, 47]. Experiments were carried out at the Institute of Laser Engineering, Osaka University, Japan, where a large laser facility capable of producing energies of several kJ was used to achieve a highly compressed fuel core, while a 60 J, 100 TW laser delivered igniting pulses. However, it should be pointed out that it is expected that it will still be quite some time before the ICF project is realized. Such a project is among the most expensive in the world and only a few huge laser facilities could be constructed for experimental tests. On the other hand, many physical processes associated with ICF can now be studied with university-level laser systems via the CPA technique, making ICF research more accessible to those interested and thus boosting participation in this field. In addition, the relativistic laser–plasma interactions associated with small laser systems could well yield a variety of novel tabeltop particle and radiation sources, such as monoenergetic femosecond electron bunches, ultrashort hard X-ray pulses, attosecond radiation pulses, etc., which may breed countless applications in different research fields in the future.

References

1. D. Strickland and G. Mourou, Opt. Commun. **56**, 219 (1985).
2. W.L. Kruer and K. Estabrook, Phys. Fluids **28**, 430 (1985).

3. F. Brunel, Phys. Rev. Lett. **59**, 52 (1987).
4. Z.-M. Sheng et al., Phys. Rev. Lett. **88**, 055004 (2002).
5. A. Pukhov, Z.-M. Sheng, and J. Meyer-ter-Vehn, Phys. Plasmas **6**, 2847 (1999).
6. S.C. Wilks et al., Phys. Plasmas **2**, 274 (1995).
7. W.L. Kruer, *The Physics of Laser Plasma Interaction* (Addison-Wesley, New York, 1988).
8. M. Tabak et al., Phys. Plasmas **1**, 1626 (1994).
9. J. Zhang, Z.L. Chen, H. Teng et al., Invited talk on CLEO/Pacific Rim 2001, July 15–19, 2001, Chiba, Japan.
10. L. M. Chen, J. Zhang et al., Phys. Rev. Lett. **87**, 225001 (2001).
11. Z.-M. Sheng et al., Phys. Rev. Lett. **85**, 5340 (2000); Y. Sentoku et al., Phys. Plasmas **6**, 2855 (1999).
12. C. I. Moore et al., Phys. Rev. Lett. **82**, 1688 (1999); D. Pesme et al., Phys. Rev. Lett. **84**, 278 (2000).
13. Y. T. Li et al., Phys. Rev. E **69**, 036405 (2004).
14. H. M. Milchberg et al., Phys. Rev. Lett. **61**, 2364 (1988); J. C. Kieffer et al., *ibid.* **62**, 760 (1989); M. M. Murnane et al., *ibid.* **62**, 155 (1989); R. Fedosejevs et al., *ibid.* **64**, 1250 (1990); D. F. Price et al., Phys. Rev. Lett. **75**, 252 (1995); U. Teubner et al., *ibid.* **70**, 794 (1993); A. Ng et al., *ibid.* **72**, 3351 (1994); Q.L. Dong et al., Phys. Rev. E **64**, 26411 (2001).
15. Y. Cang et al., Chin. Phys. Lett. **21**, 2414 (2004).
16. D. W. Forslund, J. M. Kindel, and K. Lee, Phys. Rev. Lett. **39**, 284 (1977).
17. T. E. Cowan, A.W. Hunt, T.W. Phillips et al., Phys. Rev. Lett. **84**, 903 (2000).
18. Z.-M. Sheng et al., Phys. Rev. Lett. **88**, 055004 (2002)
19. M. J. Everett, A. Lal, D. Gordon et al., Phys. Rev. Lett. **74**, 1355 (1995).
20. M. H. Key et al., Phys. Plasmas **5**, 1966 (1998).
21. R. Kodama et al., Phys. Plasmas **8**, 2268 (2001).
22. J. R. Davis et al., Phys. Rev. E **56**, 7193 (1997).
23. Y. Sentoku et al., Phys. Rev. Lett. **90**, 155001 (2003).
24. A. R. Bell et al., Phys. Rev. Lett. **91**, 035003 (2003).
25. M. Tatarakis et al., Phys. Rev. Lett. **81**, 999 (1998).
26. M. Borghesi et al., Phys. Rev. Lett. **83**, 4309 (1999).
27. L. Gremillet et al., Phys. Rev. Lett. **83**, 5015 (1999).
28. M. S. Wei et al., Phys. Rev. E **70**, 056412 (2004) and references therein.
29. M. Honda, J. Meyer-ter-Vehn, and A. Pukhov, Phys. Plasmas **7**, 1302 (2000).
30. T. Nakamura et al., Phys. Rev. Lett. **93**, 265002 (2004).
31. Y. Sentoku et al. Phys. Plasmas **11**, 3083 (2004).
32. R. Kodama et al., Nature (London) **412**, 798 (2001).
33. P A Norreys et al., Phys. Plasmas **11**, 2746 (2004).
34. S. Wilks et al., Phys. Plasmas **8**, 542 (2001).
35. S. Hatchett et al., Phys. Plasmas **7**, 2076 (2000).
36. M. Allen et al., Phys. Rev. Lett. **93**, 265004 (2004).
37. J. Fuchs et al., Phys. Rev. Lett. **94,** 045004 (2005) and references therein.
38. H. Teng, J. Zhang et al., Phys. Rev. E **67**, 026408 (2003)
39. H. Teng, J. Zhang et al., Appl. Phys. B **76**, 687 (2003).
40. R. Jung et al., Phys. Rev. Lett. **94**, 195001 (2005).
41. H. Alfvén, Phys. Rev. **55**, 425 (1939).
42. A. R. Bell et al., Plasma Phys. Control. Fus. **39**, 653 (1997).
43. F. Pisani et al., Phys. Rev. E **62**, R5927 (2000).

44. D. Batani et al., Phys. Rev. Lett. **94,** 055004 (2005).
45. M. Tatarakis et al., Phys. Rev. Lett. **90**, 175001 (2003).
46. D. Batani et al., Phys. Rev. E **65**, 066409 (2002).
47. R. Kodama et al., Nature **418**, 933 (2002).

17 Ultraintense Electromagnetic Radiation in Plasmas: Part II. Relativistic Electromagnetic Solitons and Laser-Driven Ion Acceleration

M. Lontano[1] and M. Passoni[1,2]

[1] Plasma Physics Institute "P. Caldirola", C.N.R., Milan, Italy
   lontano@ifp.cnr.it
[2] Nuclear Engineering Dept., Polytechnic of Milan, Milan, Italy
   matteo.passoni@polimi.it

Summary. Two laser-plasma processes among several others, namely the formation of relativistic electromagnetic solitons in warm plasmas and the ion acceleration driven by the interaction of ultraintense and ultrafast laser pulses with thin solid targets, have attracted great scientific interest in the last few years, both from a fundamental point of view and also in the light of the expected future technological applications. In this chapter, these two physical phenomena are presented and discussed, and the currently available theoretical descriptions are reviewed. Particular attention is paid to the analytical approaches, which allow to model the underlying physics in a transparent way and to give scaling laws with the laser and the plasma parameters. Emphasis is given to the discussion of the possible different regimes, which can characterize these processes, and to the identification of the most suitable theoretical treatments in the various cases.

17.1 Introduction

In Part I, in PUILS I [1], various fundamental plasma processes characteristic of ultraintense laser–plasma interactions were discussed. Moreover, we presented the theoretical fluid and kinetic models that can be used to describe the response of the plasma to a relativistically intense electromagnetic (EM) field, which depends on the interaction regime. In order to illustrate how the interaction of ultraintense EM radiation with a pre-existing plasma is treated in typical situations, in this chapter we will consider two laser–plasma processes which have attracted the attention of both theoreticians and experimentalists in the last few years: EM equilibria corresponding to so-called relativistic EM solitons (Sect. 17.2) in a warm plasma, and proton acceleration driven by the interaction of an ultraintense and ultrashort laser pulse with a thin solid target (Sect. 17.3). Concluding remarks are given in Sect. 17.4.

17.2 Relativistic Electromagnetic Solitons in Plasmas

Relativistic electromagnetic solitons (RES) play an important role in the strongly nonlinear interaction between EM radiation and plasma [2]. They

are localized distributions of the EM field, characterized by a normalized value of the transverse electric field $a = eE_\perp/mc\omega \geq 1$. RES are long-living EM structures trapped within a quasi-stationary electron density dip. They can manifest a finite drift velocity, or can be nondrifting. In a cold plasma they result from the equilibrium between the ponderomotive force, which originates from a nonuniform EM energy distribution, and the electrostatic (ES) force, which is associated with charge separation. Several particle-in-cell (PIC) numerical simulations show that RES are easily generated behind an ultrashort relativistically intense laser pulse propagating through an underdense plasma. The mechanism of formation is as follows. The laser pulse/plasma system develops a Raman backscattering instability, which leads to dramatic changes in the pulse shape, frequency and intensity distribution. In particular, part of the EM radiation of the pulse is subject to a frequency downshift, which causes its group velocity to slow down. At the same time, the electron density develops a cavity where the low-frequency EM radiation becomes trapped at zero group velocity [3]. A stationary RES is then formed. EM solitary waves are also important in astrophysics and cosmology. Indeed, it is believed that spatial density fluctuations in the early Universe (between 10^{-2} and $1\,\mathrm{s}$ after the Big Bang) provided the seeds for the formation of galaxies and clusters of galaxies [4]. Moreover, spatial nonuniformities in the temperature of the primordial hot plasma would have caused the observed inhomogeneities in the distribution of the cosmic microwave background radiation. Therefore, interest in the physics of RES extends well beyond laboratory applications and such physics deserves accurate theoretical investigations.

17.2.1 RES in Numerical Simulations

Since the early investigations into the relativistic regimes of laser–plasma interactions [5], it has been observed that the frequency and the amplitude of the laser pulse change during propagation such that the following quantity is conserved:

$$N(t) = \int \frac{|E|^2}{\omega} \mathrm{d}V = \mathrm{const} . \tag{17.1}$$

This can be interpreted as the number of photons, since it is the volume integral of the ratio between the EM energy density and the radiation frequency. The laser pulse is strongly depleted by both the ES and the magnetostatic wakefield excitation (magnetic vortex formation was studied in [6]; for a relativistic hydrodynamic study of wakefield excitation, see also [7]) and by the stimulated backward Raman scattering; its amplitude decreases and, due to the adiabatic invariance of the total number of photons, its frequency and its group velocity should also decrease. A characteristic propagation length for the nonlinear depletion can be estimated as $\ell_{\mathrm{depl}} \approx ct_{\mathrm{depl}} \approx \ell(\omega/\omega_{\mathrm{pe}})^2$, for a short laser pulse, and $\ell_{\mathrm{depl}} \approx a^{-1}\ell(\omega/\omega_{\mathrm{pe}})^2$ in the case of a long laser

beam [3,8], where ℓ is the pulse length. Therefore, portions (up to 20%) of the initially propagating radiation ($\omega > \omega_{\mathrm{pe}}$) slow down and become trapped ($\omega < \omega_{\mathrm{pe}}$) inside localized density hollows, drifting with a group velocity much smaller than that of the pulse. The fundamental role played by the laser frequency variations during soliton formation is supported by the strong spectral broadening [3] and frequency down-shifting (up to a factor of 0.25 of the laser frequency) [9] that characterizes the EM radiation in regions containing solitons.

PIC simulations have shown that RES are produced over a broad range of physical conditions for the laser–plasma interaction: for linearly and circularly polarized lasers, for both s- and p-polarized pulses, for background plasma densities comprised between 0.04 and $2n_{\mathrm{c}}$, and for pulse amplitudes of $1 < a < 10$. It has also been shown that up to ∼20% of the laser energy is trapped in the plasma in the form of RES and does not contribute to the wakefield acceleration process. The RES observed in the simulations are sub-cycle solitary waves, containing half a wavelength of the EM field. As a consequence, they cannot be described in the framework of the envelope approximation; the full field structure should be considered in theoretical models. Once RES have been formed, they appear to be long-living EM/plasma structures. Indeed, numerical simulations of a plasma with mobile electrons and fixed ions show that a single soliton can achieve an almost stationary state within a few hundred laser cycles. In a uniform plasma, two- and three-dimensional RES are generated with almost zero group velocity. If two RES of opposite phases are produced sufficiently close to each other, their fields tend to oscillate closer in phase with time until the two solitons merge into a single solitary wave which preserves the total EM energy [2,10]. A relativistic electromagnetic soliton produced in a nonuniform plasma is accelerated in the opposite direction with respect to the density gradient [9]. In a weakly nonhomogeneous dispersive plasma the soliton moves according to the equations of geometric optics: $\mathrm{d}\boldsymbol{r}/\mathrm{d}t = \partial H/\partial \boldsymbol{k}$, $\mathrm{d}\boldsymbol{k}/\mathrm{d}t = -\partial H/\partial \boldsymbol{r}$, where the Hamiltonian is the wave frequency $H(\boldsymbol{r}, \boldsymbol{k}) = [k^2 c^2 + \omega_{\mathrm{pe}}^2(\boldsymbol{r})]^{1/2}$. Then, if a soliton is generated in a plasma which extends over a limited region with its density decreasing towards the boundaries, the solitary wave eventually escapes from the plasma and, once at the edge, it leaves the plasma emitting its EM energy in the form of a burst of radiation. The spectrum of the radiation exhibits a wide peak well below (a few tenths of) the laser frequency. Experimental observation of the frequency spectra from the radiation emitted from a plasma used as a target for ultrastrong laser pulses revealed the onset of physical processes leading to a frequency down-shift [11]. This could provide indirect proof that solitons have been generated.

For large laser intensities (i.e., $a > 1$) or for simulation times longer than $(M/m)^{1/2}$ times the radiation period, the ion dynamics plays an important role in the strong laser–plasma interaction and specifically for the evolution of RES. Indeed, the ES field associated with the charge separation acts in order to redistribute the ion density. Two-dimensional [12, 13] and three-

dimensional [14] PIC simulations with mobile electrons and ions show that asymptotic soliton dynamics are rich with new physical phenomena. The formation of RES, accompanied by a radiation frequency down-shift, takes place over time scale shorter than the ion response time ($\sim 2\pi(M/m)^{1/2}\omega_{pe}^{-1}$). Later on, the Coulomb repulsion in the electrically non-neutral ion core pushes the ions away, in a process which is analogous to the so-called "Coulomb explosion" [15–18], resulting in the ions being accelerated to energies of the order of $mc^2 a_{max}$, where a_{max} is the maximum absolute value of the normalized vector potential [13]. The plasma cavity goes on expanding slowly (on the electron timescale) in the radial direction. In the two-dimensional case, the expansion can be modeled with the "snow plow" approximation [19], which, for $t \to \infty$, gives $R \propto t^{1/3}$. The characteristic time scale of the cavity expansion is $\tau = (6\pi R_0^2 n_0 M/\langle E_0^2\rangle)^{1/2}$, where $R_0 \approx c/\omega_{pe}$ is the soliton radius [12]. The total energy trapped in the cavity remains constant, so the field amplitude and frequency decrease as $E \propto t^{4/5}$ and $\omega \propto t^{-2/5}$, respectively. This EM structure, which behaves as a soliton in the early part of its evolution (until it is dominated by the electron dynamics), has been called a "post-soliton" in the ion-dominated phase, since it is no longer in a stationary state.

The formation of RES and their evolution into post-solitons have been observed in three-dimensional simulations as well [14]. The EM structure of the three-dimensional soliton is such that the electric field is poloidal and the magnetic field is toroidal. Therefore it is named a "TM-soliton." The soliton core is characterized by an overall positive charge, resulting in its Coulomb explosion and in the acceleration of the ion. On the long time-scale, the quasi-neutral plasma cavity is subject to a slow continuous radial expansion, while the soliton amplitude decreases and the ion temperature increases.

Recent one-dimensional particle-in-cell (PIC) simulations of the stimulated Brillouin back-scattering (SBBS) of EM radiation [20, 21] have shown that, even at subrelativistic intensities ($I\lambda^2 = 10^{16}\,\mathrm{W\,\mu m^2/cm^2}$), nondrifting solitary waves are easily produced and remain almost unchanged throughout the whole simulation, typically $\approx 2.5 \times 10^4\,\omega^{-1}$, where ω is the laser angular frequency [22, 23]. The associated formation of deep cavities in the density disrupts the resonant SBBS amplification and leads to strong electron and ion heating of the background plasma. Notice that, during the early phase of formation of the soliton, its intensity becomes on the order of I_{rel} locally, the relativistic limit given in (10.4) in Part I, even though the laser intensity is below I_{rel}. We will not go into the details of this study. We only wish to mention that the solitons formed are half-cycle, quasi-neutral, down-shifted in frequency to 0.25ω, but their typical spatial extension is at least an order of magnitude larger than the skin depth c/ω_{pe}, and they are formed in a plasma in which electrons are heated during the laser interaction up to $50\,\mathrm{keV}$. We shall come back to this point in the next section, when we will be discussing theoretical models of RES.

17.2.2 Theory of RES

Modeling EM solitary waves in a plasma is quite a challenging problem
due to the intrinsic nonlinearity of these objects. Most of the theories have
been developed for one-dimensional quasi-stationary EM energy distribu-
tions, which represent the asymptotic equilibrium states that are achieved
by the radiation–plasma system after long interaction times. The analyti-
cal modeling of the phase of formation of an EM soliton, which we qual-
itatively described in the previous section, is still an open problem. What
are usually called solitons are asymptotic quasi-stationary solutions of the
Maxwell equations; that is, the amplitude of the associated vector potential
is either an harmonic function of time (for example, for linear polarization)
or it is a constant (circular polarization). Let's briefly review the theory of
one-dimensional RES.

Equations (10.14), (10.20) and (10.21) in Part I can be reduced in the
one-dimensional case, where it is assumed that all physical quantities depend
on the propagation direction of the laser pulse (say x) but are independent
of the transverse coordinates y and z. In this case, $A_x = 0$ and $P_y = P_z = 0$.
The relevant equations, if the ion dynamics are neglected at first for the sake
of simplicity, take the form

$$\frac{\partial^2 \boldsymbol{A}_\perp}{\partial x^2} - \frac{1}{c^2}\frac{\partial^2 \boldsymbol{A}_\perp}{\partial t^2} - \frac{4\pi e^2 n}{mc^2\gamma}\boldsymbol{A}_\perp = 0 \, , \qquad \frac{\partial^2 \phi}{\partial x^2} = 4\pi e\,(n - n_0) \qquad (17.2)$$

$$\frac{\partial p_x}{\partial t} - \frac{\partial}{\partial x}\left(e\phi - mc^2\gamma\right) = 0 \, , \qquad \frac{\partial n}{\partial t} + \frac{\partial}{\partial x}\left(\frac{np_x}{m\gamma}\right) = 0 \, , \qquad (17.3)$$

where $\gamma = \left[1 + (e\boldsymbol{A}/mc^2)^2 + (p_x/mc)^2\right]^{1/2}$.

Let's assume that the background plasma is homogeneous and that the
EM waves propagate at a constant velocity, V_φ. Then, we introduce the new
independent variables $\xi = x - V_\varphi\tau$ and $\tau = t$ and look for solutions of the
form

$$\boldsymbol{A}(\xi, \tau) = \frac{(\hat{\boldsymbol{e}}_y + i\hat{\boldsymbol{e}}_z)}{\sqrt{2}} A(\xi) \exp\left[i\omega\left(\frac{\tau}{\gamma_\varphi^2} - \frac{\beta_\varphi}{c}\xi\right)\right] + \text{c.c.} \, , \qquad (17.4)$$

which correspond to a nonuniform distribution for propagating, circularly po-
larized EM radiation. Correspondingly, $\gamma = \left[1 + (e\boldsymbol{A}/mc^2)^2 + (p_x/mc)^2\right]^{1/2}$
does not depend on time and we can look for stationary $p_x(\xi)$, $n(\xi)$, $\phi(\xi)$.
Equation (17.3) can be integrated, giving

$$p_x = mc\beta_\varphi\gamma_\varphi^2\left(1 + \frac{e\phi}{mc^2}\right) - mc\gamma_\varphi^2\left[\left(1 + \frac{e\phi}{mc^2}\right)^2 - \frac{\gamma_\perp^2}{\gamma_\varphi^2}\right]^{1/2} \, , \qquad (17.5)$$

$$n = -n_0\beta_\varphi^2\gamma_\varphi^2 + n_0\beta_\varphi\gamma_\varphi^2\frac{1 + \frac{e\phi}{mc^2}}{\left[\left(1 + \frac{e\phi}{mc^2}\right)^2 - \frac{\gamma_\perp^2}{\gamma_\varphi^2}\right]^{1/2}} \, , \qquad (17.6)$$

where $\phi(\xi)$ and $A(\xi)$ only appear in the r.h.s. of the equation. Equations (17.2) become respectively

$$\frac{\partial^2 A}{\partial \xi^2} + \frac{\omega^2}{c^2} A - k_p^2 \frac{\beta_\varphi \gamma_\varphi^2}{\beta_\varphi \gamma - p_x/mc} A = 0 \,, \tag{17.7}$$

$$\frac{\partial^2 \phi}{\partial \xi^2} = k_p^2 \frac{c p_x}{e(\beta_\varphi \gamma - p_x/mc)} \,, \tag{17.8}$$

where we have defined the constant parameters $\beta_\varphi = V_\varphi/c$, $\gamma_\varphi = (1-\beta_\varphi^2)^{-1/2}$, $\omega_{\mathrm{pe}} = (4\pi n_0 e^2/m)^{1/2}$, and $k_p = \omega_{\mathrm{pe}}/c$. Equations (17.7), (17.8) are exact for fixed ions and are the starting point for the cold analysis of a relativistic electron plasma in the presence of intense circularly polarized EM radiation. It is worth mentioning that, starting from (17.8) with $\boldsymbol{A}_\perp = 0$, the maximum value of the longitudinal electric field in a periodic plasma wave has been calculated by Akhiezer and Polovin [24] (see Sect. 17.2.2).

Equations (17.7) and (17.8) can be derived from the following Hamiltonian (which is therefore conserved during the evolution of the system):

$$H\left(A, \phi, \frac{\mathrm{d}A}{\mathrm{d}\xi}, \frac{\mathrm{d}\phi}{\mathrm{d}\xi}\right) = \frac{e^2}{m^2 c^4}\left[\frac{1}{2\gamma_\varphi^2}\left(\frac{\mathrm{d}A}{\mathrm{d}\xi}\right)^2 - \frac{1}{2}\left(\frac{\mathrm{d}\phi}{\mathrm{d}\xi}\right)^2\right] + V\left(A, \phi\right) \,; \tag{17.9}$$

H is the Hamiltonian for the motion of a pseudo-particle in the potential field $V\left(\xi; A, \phi\right)$ in the two-dimensional space with coordinates A, ϕ, which reads

$$V\left(A, \phi\right) = \frac{e^2}{m^2 c^4} \frac{1}{2\gamma_\varphi^2} \frac{\omega^2}{c^2} A^2$$
$$- k_p^2 \gamma_\varphi^2 \left\{ 1 + \frac{e\phi}{mc^2} - \beta_\varphi \left[\left(1 + \frac{e\phi}{mc^2}\right)^2 - \frac{\gamma_\perp^2}{\gamma_\varphi^2}\right]^{1/2}\right\} \,, \tag{17.10}$$

with $\gamma_\perp = \left[1 + (eA/mc^2)^2\right]^{1/2}$. Notice that the two terms forming the "kinetic energy" in the r.h.s. of (17.9) have opposite signs. In the quasi-neutral approximation (i.e., for $|n - n_0|/n_0 \ll 1$), the l.h.s. of (17.8) can be placed equal to zero. The r.h.s. then gives a relationship between ϕ and A which can be inserted into (17.7) to obtain a single nonlinear equation for $A(\xi)$. The resulting equation can be expanded for $(eA/mc^2)^2 \ll 1$, since quasi-neutrality in drifting solitons is only allowed for small amplitude fields. The solitary wave solution is found in the form

$$\boldsymbol{A}(\xi, \tau) = \frac{mc^2}{e} \frac{(\hat{\boldsymbol{e}}_y + i\hat{\boldsymbol{e}}_z)}{\sqrt{2}} \frac{2\left(1 - \frac{\omega^2}{\gamma_\varphi^2 \omega_{\mathrm{pe}}^2}\right)^{1/2} \exp\left[i\omega\left(\frac{\tau}{\gamma_\varphi^2} - \frac{\beta_\varphi}{c}\xi\right)\right]}{\cosh\left[\xi k_p \left(1 - \frac{\omega^2}{\gamma_\varphi^2 \omega_{\mathrm{pe}}^2}\right)^{1/2}\right]} + \mathrm{c.c.} \,. \tag{17.11}$$

where the maximum amplitude is $A_0 = \left(2mc^2/e\gamma_\varphi\right)\left(\gamma_\varphi^2 - \omega^2/\omega_{\mathrm{pe}}^2\right)^{1/2}$, the soliton width $\Delta\xi \approx 1/k_p\left[\gamma_\varphi - (\omega/\omega_{\mathrm{pe}})^2\right]^{1/2}$, and its frequency $\omega \approx \omega_{\mathrm{pe}}\gamma_\varphi\left[1 - (eA_0/2\sqrt{2}mc^2)^2\right]$.

The extension of (17.7) and (17.8) to moving ions has been used to describe drifting one-dimensional relativistic EM solitary waves [25]. Localized solutions in the form of one-dimensional RES, accompanied by an electron density depletion and by an ion density compression, in both underdense and overdense plasmas, have been obtained by numerical integration of the two relevant second-order differential equations for the vector and scalar potentials, obtained from (10.14), (10.20) and (10.21) in Part I. Multi-humped concentrations of EM energy (with either even or odd numbers of nodes) inside electron density cavities bounded by density "walls" were described in [25, 26] (ions are held fixed in the latter paper). An EM solitary wave is always accompanied by a plasma perturbation and by a charge imbalance due to the ponderomotive force, which acts primarily on light electrons. In the case of a drifting soliton, the equilibrium between the ponderomotive force and the restoring ES force permits the existence of a localized field. This equilibrium can also be interpreted as a trapping of the propagating light pulse inside a self-generated ES wave, which is excited at the front of the moving soliton and absorbed at its rear, in such a way that the plasma perturbation remains localized at the pulse position. In [25] it was shown that circularly polarized one-dimensional solitons only exist in a cold plasma if their drift velocity is larger than $c(m/M)^{1/2}$, where M is the ion rest mass. The problem of the transition from swift solitons to slowly drifting or standing solitary waves was later investigated in [27–29]. In these papers it was shown that at low drift velocity the ion dynamics plays a crucial role in defining the existence field of RES. Moreover, upon lowering the soliton velocity a lower limit is found, corresponding to a bifurcation in the parameter space, where RES with very steep field and density profiles can be found. Another interesting result derived in [25] is that for drifting solitary waves the quasineutral approximation only holds for small amplitude solitons. This point will be commented on later when standing solitons in a warm plasma are considered. RES propagating at a speed close to c were investigated in [26, 30], with the aim of exploiting the potential to accelerate charged particles to relativistic velocities. In particular, the possibility of using so-called "triplesolitons" (a combination of two EM waves and one ES wave in beat-wave resonance), propagating in a plasma channel, has been investigated [30]. The main advantage of using a swift soliton instead of a laser pulse as a driver for accelerating particles is that it does not produce any wakefield behind itself, thus overcoming the problem of pump depletion, which is so severe in the classical laser-driven accelerator concept [31].

As mentioned in the previous section, PIC simulations show that mostly standing, or very slowly drifting, RES are produced during the intense laser–plasma interaction. Equations (17.2) can be solved using the transformation

given in (17.4) for $V_\varphi = 0$. The first equation of (17.3) gives $e\phi = mc^2(\gamma - 1)$, which can be used in the second equation of (17.2) to get

$$n = n_0 \left(1 + \frac{1}{k_p^2} \frac{\mathrm{d}^2\gamma}{\mathrm{d}\xi^2} \right) , \qquad (17.12)$$

where $\gamma = \gamma_\perp$. Substituting for n into the first equation of (17.2), we obtain a single equation for the scalar amplitude of the vector potential [32]

$$\frac{\mathrm{d}^2 A}{\mathrm{d}\xi^2} + k_p^2 \left[\frac{\omega^2}{\omega_{\mathrm{pe}}^2} - \frac{1}{\gamma} \left(1 + \frac{\mathrm{d}^2\gamma}{\mathrm{d}\xi^2} \frac{1}{k_p^2} \right) \right] A = 0 . \qquad (17.13)$$

Equation (17.13) can be solved with boundary conditions suitable for a localized EM field distribution, and (17.4) becomes

$$A(\xi, \tau) = \frac{mc^2}{e} \frac{(\hat{e}_y + \mathrm{i}\hat{e}_z)}{\sqrt{2}} \frac{2 \left(1 - \frac{\omega^2}{\omega_{\mathrm{pe}}^2} \right)^{1/2} \cosh \left[\xi k_{\mathrm{p}} \left(1 - \frac{\omega^2}{\omega_{\mathrm{pe}}^2} \right)^{1/2} \right] \mathrm{e}^{\mathrm{i}\omega\tau}}{\cosh^2 \left[\xi k_{\mathrm{p}} \left(1 - \frac{\omega^2}{\omega_{\mathrm{pe}}^2} \right)^{1/2} \right] + \frac{\omega^2}{\omega_{\mathrm{pe}}^2} - 1} + \mathrm{c.c.}$$

$$(17.14)$$

The solution in (17.14) is exact and is only real in the frequency range $(2/3)\omega_{\mathrm{pe}} < \omega < \omega_{\mathrm{pe}}$. The maximum amplitude is $A(\xi = 0) = (mc^2/e)2\omega_{\mathrm{pe}} \left(\omega_{\mathrm{pe}}^2 - \omega^2 \right)^{1/2}/\omega^2$, the minimum electron density in the cavity formed by the EM field is $n(\xi = 0) = n_0 \left[1 - 4(\omega_{\mathrm{pe}}^2 - \omega^2)^2/\omega^4 \right]$, and the soliton scale-length is $\Delta\xi = c/\sqrt{\omega_{\mathrm{pe}}^2 - \omega^2}$. If we try to lower the frequency below $(2/3)\omega_{\mathrm{pe}}$, the electron density becomes negative and (17.14) is no longer valid. This unphysical behavior is a consequence of achieving zero electron density at $\xi = 0$, which becomes possible in a cold fluid since there is no thermal motion opposing the total expulsion of particles. In order to avoid negative densities, one should solve the field equations piece-wise, in the plasma region and in vacuum region separately, and then match the solutions at the boundaries properly [33–35]. This procedure provides consistent density profiles with discontinuous derivatives and spiky spatial distributions, which can give rise to stability problems. At this point we should mention that the extension of the cold one-dimensional RES to the case of a uniformly magnetized plasma has been discussed in [36], and the two-dimensional case has been considered in [10, 37].

The introduction of a finite particle temperature changes the structure of the longitudinal (in the direction of wave propagation) component of the momentum equation for the electrons, leading to a definite non-negative electron density, as for example, in the case of a Boltzmann electron distribution [38]; that is:

$$n(\xi) = n_0 \exp \left[\frac{e\phi - mc^2(\gamma - 1)}{T_{\mathrm{e}}} \right] . \qquad (17.15)$$

A hot fluid model would be highly desirable for applications in astrophysics. As we have already mentioned, the formation of RES in the primordial plasma could be an important source of large-scale nonuniformities in density and temperature, which seeded the formation of galaxies and clusters of galaxies [4]. In particular, it is conjectured that in the early universe matter was present in the form of a mixture of electrons, positrons and photons in thermal equilibrium at a temperature above mc^2. It is evident that the propagation of relativistic EM waves in such peculiar environment should be addressed in the framework of a hot-plasma model.

Following the same procedure outlined for the cold plasma, we can specialize the system of (10.17) and (10.18) in Part I to the one-dimensional case with circular polarization and zero group velocity. The explicit forms of the relevant equations are given in [39], where RES in an electron–positron plasma were studied. Since the two species have equal masses and absolute values of charge, the plasma does not develop any charge separation for $T_e = T_p = T_0$ and so $\phi = 0$. A single second-order nonlinear differential equation for the normalized vector potential, $a(\xi)$, is left, and this can be reduced to quadrature and solved numerically [39]. Here, we wish to comment on the behavior of the plasma density, which takes the form

$$n(\xi) = \frac{n_0 R_0}{(R_0^2 - a^2)^{\frac{1}{2}}} \left\{ \frac{1}{\alpha\lambda} \left[(R_0^2 - a^2)^{\frac{1}{2}} - 1 \right] \right\}^{\frac{1}{\Gamma - 1}}, \qquad (17.16)$$

where $R_0 = 1 + \alpha\lambda$, $\lambda = T/mc^2$ and $a = eA/mc^2$. From inspecting (17.16), it is clear that $n(\xi)$ is non-negative provided that $\gamma - 1 < \alpha\lambda$; that is, that the equilibrium kinetic pressure is high enough to balance the ponderomotive pressure. The conditions required for the existence of RES have been studied for different frequencies ω and equilibrium temperatures T_0. In the plane $(\omega/\omega_{pe}, \lambda)$, RES exist for $\lambda < (2\omega_{pe}^2/\omega^2 - 1)/\alpha$, in a narrow region of width $\Delta\lambda \approx 2(\alpha - 2)/\alpha^2\omega^2$ for $\lambda > 1$, and for any values of λ for $\lambda < 1$. In a strongly overdense plasma ($\omega^2 \ll \omega_{pe}^2$), the ultrarelativistic kinetic pressure and the ponderomotive pressure balance each other, giving rise to solitons with extremely large amplitudes. For example, for $\lambda = 30$ we get $a(0) \approx 110$, with $\omega = 0.1\omega_{pe}$. Correspondingly, the typical scale length of the soliton is a few ten times the classical skin depth, c/ω_{pe}, and 20% of the plasma density is left at $\xi = 0$, the position of the maximum field amplitude. At low temperature ($\lambda = 10^{-4}$), even a low-amplitude soliton field ($a(0) \approx 0.02$) is able to dig a deep plasma hole down to the full density expulsion, over a few skin depths. EM solitons in an electron–positron(–ion) plasma have also been investigated in [40–43].

A kinetic approach to the study of one-dimensional RES in a hot plasma was developed in [44] and applied to RES in an electron–positron plasma [44], electron–ion plasma [45], and electron–positron–ion plasma [46]. A highly anisotropic particle distribution function for each plasma species j (where $j = e$ for electrons and $j = i$ for ions) was considered, with a finite constant

parallel temperature T_j and a transverse thermal spread, which was assumed to be negligible compared with the kinetic energy associated with the ordered particle motion in the EM wave field, $\boldsymbol{p}_j = q_j \boldsymbol{A}_\perp/c$; that is

$$f_j(W_j, \boldsymbol{P}_{j\perp}) = \frac{N_{0j}}{2m_j c K_1\left(\beta_j^{-1}\right)} \delta(\boldsymbol{P}_{j\perp}) \exp\left(-\frac{W_j}{T_j}\right) , \qquad (17.17)$$

where $W_j(\boldsymbol{r}, t) = m_j c^2 \gamma_j + q_j \phi(\boldsymbol{r}, t)$ is the total particle energy,

$$\boldsymbol{P}_j(\boldsymbol{r}, t) = \boldsymbol{p}_j + q_j \boldsymbol{A}(\boldsymbol{r}, t)/c$$

is the transverse component of the canonical momentum, and $\beta_j = T_j/m_j c^2$ is the ratio of the thermal energy to the rest energy of the j-species. *Parallel* and *transverse* refer to the direction of propagation of the EM waves under consideration. $K_1(\zeta)$ is the modified first-order Bessel function with argument ζ. Other notations are consistent with previous definitions. Equation (17.17) is an exact solution for the relativistic Vlasov equations (10.15) in Part I, reduced to a stationary one-dimensional system, and in the presence of circularly polarized EM fields. It can be used to calculate its lowest order moments, like the particle density

$$n_j(\boldsymbol{r}, t) = \int f_j(W_j, \boldsymbol{P}_{j\perp}) \mathrm{d}^3\boldsymbol{p}_j = n_{0j} \frac{K_1\left(\gamma_{\perp j}\beta_j^{-1}\right)}{K_1\left(\beta_j^{-1}\right)} \gamma_{\perp s} \exp\left(-\frac{q_j\phi_j}{T_j}\right) ,$$
$$(17.18)$$

and the transverse component of the current density

$$\boldsymbol{j}_{j\perp}(\boldsymbol{r}, t) = q_j \int \boldsymbol{v}_\perp f_j(W_j, \boldsymbol{P}_{s\perp}) \mathrm{d}^3\boldsymbol{p}_j$$
$$= -\frac{q_j^2}{m_j c} n_{0j} \frac{K_0\left(\gamma_{\perp j}\beta_j^{-1}\right)}{K_1\left(\beta_j^{-1}\right)} \boldsymbol{A}_\perp \exp\left(-\frac{q_j\phi_j}{T_j}\right) \qquad (17.19)$$

originating from the j-species. Equation (17.18) clearly shows that the particle density is strictly non-negative for any value of the EM radiation intensity. Once more, the EM field in (10.14) in Part I is reduced to a couple of nonlinear, second-order, ordinary differential equations for $A(\xi)$ and $\phi(\xi)$, which again permits a Hamiltonian formulation. We leave the details of the analysis of the corresponding equations to [44, 45]; we only make only few remarks here. Generally speaking, in the isothermal description, standing RES can exist in a hot plasma over a much wider region of the parameter plane $(\omega/\omega_{\mathrm{pe}}, \lambda)$ than in the adiabatic case. For a given frequency ω, no lower limit in temperature is found, while the upper limit, related to the linear cut-off, is given by

$$\omega^2 < \frac{K_0\left(\lambda_e^{-1}\right)}{K_1\left(\lambda_e^{-1}\right)} + \rho Z \frac{K_0[(\nu\lambda_i)^{-1}]}{K_1[(\nu\lambda_i)^{-1}]} , \qquad (17.20)$$

where $\nu = m/M$. In an electron–positron plasma, ultrarelativistic temperatures allow the trapping of ultraintense EM radiation with partial density cavitation, in a very similar way to that predicted by the adiabatic model. The main difference between the two models (adiabatic and isothermal) is that in a low-temperature isothermal plasma ($\lambda \ll 1$), where it is "easy" to dig a hole in the plasma density, a "wide" cavity (tens of c/ω_{pe}) can be produced which has an exponentially vanishing density. These characteristics also pertain to RES in an electron–ion plasma. EM solitary waves have been studied at both ultrarelativistic and low temperatures under the quasi-neutral approximation. In particular, it has been found that the conditions of exponential cavitation are met for $\lambda \ll 1$, i.e.,

$$n_{\mathrm{e}}(\xi) \approx n_{0\mathrm{e}}\sqrt{\gamma_\perp}\exp\left[-\frac{mc^2\,(\gamma_\perp - 1) - e\phi}{T_{\mathrm{e}}}\right]\,, \qquad (17.21)$$

so that the vacuum solution to the equation for $A(\xi)$ can be constructed:

$$\boldsymbol{A}(\xi,\tau) = \frac{(\hat{\boldsymbol{e}}_y + \mathrm{i}\hat{\boldsymbol{e}}_z)}{\sqrt{2}}\sigma^{\frac{1}{2}}\cos\left(\frac{\omega\xi}{c}\right)\mathrm{e}^{\mathrm{i}\omega\tau} + \mathrm{c.c.}\,, \qquad (17.22)$$

where $\sigma = \left[8\pi n_0\left(ZT_{\mathrm{e}} + T_{\mathrm{i}}\right)/Z\omega^2\right]$. In (17.21), the normalized amplitude $a(\xi)$ can be of the order of unity, provided $\omega \ll \omega_{\mathrm{pe}}$. The ponderomotive force associated with the EM radiation acts primarily on plasma electrons, a charge imbalance appears, and ion density is also redistributed, over typical ion time-scales in a way that mimics the electron density. Therefore, the asymptotic status of the system becomes quasi-neutral. However, a residual charge separation remains, which produces a quasi-static longitudinal electric field $\boldsymbol{E}_\ell$. In the presence of strong density cavitation, this electric field takes the form of

$$\boldsymbol{E}_\ell(\xi) = \hat{\boldsymbol{e}}_x\frac{\omega_{\mathrm{pe}}^2}{eZc\omega}\left[\frac{T_{\mathrm{i}}}{\sqrt{1 + \sigma\cos^2\left(\frac{\omega\xi}{c}\right)}} - \nu Z^2 T_{\mathrm{e}}\right]\sin\left(\frac{2\omega\xi}{c}\right)\,. \qquad (17.23)$$

It is found that $\boldsymbol{E}_\ell(\xi)$ has a dipolar structure, and for $T_{\mathrm{e}} \approx T_{\mathrm{i}}$ it is pointing outward, the ion temperature playing a major role in determining its amplitude. If, however, the ions remain cold and electrons are strongly heated during the formation of the soliton in such a way that $T_{\mathrm{i}} \ll \nu ZT_{\mathrm{e}}$, $E_\ell(\xi)$ becomes very small and inward-pointing.

We can summarize the main results from the previous investigations in the following points: (i) soliton solutions have been found under general conditions for an electron–positron plasma and by assuming quasi-neutrality in an electron–ion plasma; (ii) sub-cycle nondrifting solitary waves represent an equilibrium in a multicomponent warm plasma; that is, half-wavelengths of the EM radiation can be trapped inside a plasma density well; (iii) the

corresponding plasma depletion can be appreciable and, for $T \ll mc^2$, an exponentially small plasma density remains where the soliton is located; (iv) the frequency of the trapped EM radiation is appreciably smaller than the unperturbed plasma frequency; if the surrounding plasma is strongly overdense, the soliton has a typical spatial scale that is much larger than the classical skin depth; (v) a strong quasi-static electric field develops inside the soliton, which can be responsible for charge acceleration; (vi) many of the above characteristics also manifest themselves at nonrelativistic amplitudes. Generally speaking, the results from the studies related to warm RES are in good agreement with the standing RES observed in PIC simulations [47], as described in Sect. 17.2.1. In particular, as it has already been anticipated, in recent one-dimensional PIC simulations [20,21] of the SBBS of EM radiation at subrelativistic intensities, a series of nondrifting EM solitons have been produced that manifest all of the abovementioned peculiarities. The trapped radiation amplitude increases to $a \approx 1$, while 5% of the unperturbed quasi-neutral plasma is left in the trapping region. Correspondingly, the soliton frequency is down-shifted to a quarter of the laser frequency during soliton formation. The model (17.21), (17.22), (17.23) has been able to reproduce the numerical results to within a factor of the order of unity, provided that the strong plasma heating (T_e has been observed to reach $50\,\mathrm{keV}$ in the runs) is taken into account [22,23].

We conclude this section by mentioning the first experimental evidence of long-living macroscopic bubble-like structures that accompany the intense laser–solid interaction [48]. They have been observed by measuring the deflection of a proton beam (proton imaging) due to the presence of a localized quasi-static electric field associated with the charge imbalance inherent to the bubbles [49]. The region over which the electric field is concentrated has a typical spatial scale of $50\,\mu\mathrm{m}$, which corresponds to a hundred times the skin depth, evaluated at a peak plasma density of $\approx 0.1 n_c$. The lifetime of a bubble is $\approx 50\,\mathrm{ps}$, corresponding to $10^4 \tau_L$, where $\tau_L = 2\pi/\omega$, at $\lambda = 1\,\mu\mathrm{m}$. From a single particle model, the quasi-static electric field producing the proton deflection is estimated to be on the order of $40\,\mathrm{MV/cm}$. It is worth noticing that such numerical values are in reasonable agreement with the predictions from the kinetic model [45,47].

17.3 Ion Acceleration Driven by Ultrastrong Laser Pulses in Thin Solid Targets

Ultrahigh intensity lasers have been shown to be particularly suitable for accelerating ions to energies of hundreds of keV or more, even up to the multi-MeV range, when they are directed onto high-density targets. Since the late 1990s, many experimental results have been reported that demonstrate the effectiveness of laser-driven acceleration processes [50–67]. In Sect. 17.3.1, we will review general concepts associated with laser-driven ion accelera-

tion, while one-dimensional analytical models for describing the hot electron cloud that produces the accelerating electric field will be discussed in Sect. 17.3.2.

17.3.1 Ion Acceleration Processes in Laser–Solid Interactions

Ions can be accelerated due to a variety of physical processes that take place in different regions of the target. At least two physical mechanisms, possibly acting simultaneously, may explain the acceleration of ions from the front surface of a solid target [62]: the ponderomotive acceleration of the ions at the vacuum–solid interface [68], and the space charge acceleration that occurs at the critical surface when an underdense preplasma is formed [69]. Ion acceleration can occur inside the target volume due to the potential onset of the large electric field associated with the propagation of relativistic electrons through the solid target and with the establishment of the relevant return currents [70–73]. However, the most effective acceleration mechanism is believed to take place at the rear side of the target, leading to ions being accelerated to energies much higher than the laser ponderomotive energy (for $I = 10^{20}\,\mathrm{W/cm^2}$, $\Phi_{\mathrm{pm}} = 6\,\mathrm{MeV}$). The acceleration process at the rear side is a result of the huge charge separation induced in matter when acted upon by a laser field. This gives rise to the so-called target normal sheath acceleration (TNSA) process [74]. When a relativistic laser pulse is focused onto a thin solid target, the laser energy is converted (through the mechanisms briefly described in Sect. 17.2.2) with high efficiency (around 20 or 30%) at the front side of the target into the kinetic energy of a population of relativistically hot ($T_{\mathrm{h}} \approx$ few MeV) collisionless electrons. These electrons move through the solid target and appear at its rear side, where a cloud of relativistic electrons is formed, extending out of the target for several Debye lengths, and giving rise to an extremely intense longitudinal electric field, which is responsible for the efficient ion acceleration [50, 51]. By looking at the physical phenomena which lead to the final ion acceleration process in more detail, we can identify the existence of at least two qualitatively different electron populations. The first is the hot electron component, directly created by the laser pulse in the plasma plume at the front surface of the target. These electrons form a beam propagating normally to the target surface, with a divergence of between 3 and 15°. The density of this electron population is on the order of the critical density (10^{20}–$10^{21}\,\mathrm{cm^{-3}}$), and its temperature is on the order of the laser ponderomotive potential ($\sim$MeV for the relativistically intense pulses). The free motion of this hot electron beam through the target requires the presence of a return current which locally compensates for the flow of the hot (and fast) electron component. The return current in metallic targets is provided by a second electron species, the conduction electrons, which are propelled by the electric field generated by the fast electrons. In insulators, the background free electron population is created by field and thermal ionization. Since in both cases the density of

the background electron population is on the order of the solid density, in other words it is much bigger than the fast electron density, the velocity required for current neutralization is small and their temperature is much lower than that of the hot electrons. However, this cold and dense electron population can be ohmically heated by the return currents. To summarize, the electric field generated on the rear side of the solid target depends on the physical parameters of these two electron populations, which are related to the laser–solid interaction on the front surface, the transport of the hot component through the target and the heating of the background electrons. The acceleration is most effective on protons, which are usually present on the rear surface in the form of contaminants like hydrocarbons and water, or can be present among the constituents of the solid target (e.g., in plastic targets). The heaviest ion population of the target (which may consist of several ion species) provides a positive charge which offers much more inertia and causes the charge separation that is responsible for the huge accelerating field. Part of this heavy population may also be accelerated, on a longer time scale, if there are not enough protons to acquire most of the energy contained in the electric field, or if protons are removed before the arrival of the laser pulse, for example upon heating the target. In the following section these considerations will be used to formulate a theoretical model of TNSA ion acceleration. Before concluding this section, let us very briefly mention the results from PIC calculations performed to simulate the process [16, 18, 74–80]. It is important to note that there are particular difficulties involved in performing these kind of simulations compared with those mentioned in Sect. 17.2.1. These difficulties arise from the huge range of values seen for experimental parameters, ranging from almost solid density and low energy for the solid system to the low density and very high energy of the relativistic electron population. This issue prevents current supercomputers from being able to provide a fully realistic description of the system, and consequently the results obtained from them can suffer from significant limitations.

17.3.2 Theory for the Rear Side Acceleration Mechanism

Based on the above discussion, the physics of the ion acceleration process can be theoretically modeled under the following assumptions, leading to the formulation of a relatively simple system of equations which can be investigated analytically and numerically. First of all, let us restrict our analysis to a one-dimensional geometry. The electron population can be described as a two-temperature Boltzmann distribution, where the subscripts c and h refer to the *cold* and *hot* electron components, respectively,

$$n_e = n_{0h} e^{e\phi/T_h} + n_{0c} e^{e\phi/T_c} . \tag{17.24}$$

In addition, we consider the existence of two different ion species, a light (L) and a heavy (H) population: in this way it is possible to model the accel-

eration of light species present on the rear side of a solid target made from
heavy ions. The equations defining the one-dimensional model for the ion ac-
celeration process following from the above assumptions are then the Poisson
equation which, using (17.24), takes the form

$$\frac{\partial^2 \phi}{\partial x^2} = 4\pi e \left(n_{0\mathrm{h}} e^{e\phi/T_\mathrm{h}} + n_{0\mathrm{c}} e^{e\phi/T_\mathrm{c}} - Z_\mathrm{L} n_\mathrm{L} - Z_\mathrm{H} n_\mathrm{H} \right) \tag{17.25}$$

and the equations governing the ion dynamics. If the ions are described kin-
etically, the 1-D Vlasov equation is obtained from (10.15) in Part I in the
nonrelativistic limit and assuming 1-D geometry:

$$\frac{\partial f_j}{\partial t} + v \frac{\partial f_j}{\partial x} + \frac{Z_j e}{m_j} \frac{\partial \phi}{\partial x} \frac{\partial f_j}{\partial v} = 0 \qquad n_j = \int f_j \mathrm{d}v \qquad j = L, H \ . \tag{17.26}$$

In a fluid description, the ions are described by the 1-D, nonrelativistic, cold
versions of (10.17) and (10.18) in Part I:

$$\frac{\partial u_j}{\partial t} + u_j \frac{\partial u_j}{\partial x} = -\frac{Z_j e}{m_j} \frac{\partial \phi}{\partial x} \qquad j = L, H \tag{17.27}$$

$$\frac{\partial n_j}{\partial t} + \frac{\partial}{\partial x} (n_j u_j) = 0 \ . \tag{17.28}$$

The system based on (17.25) and (17.26) (or (17.25), (17.27) and (17.28))
can be treated analytically by introducing different approximations; their
limits of applicability establish the physical regimes where the corresponding
solutions hold. By invoking quasi-neutrality, assuming a single temperature
electron population and a single ion population, (17.25) can be replaced by
the simpler condition $n_\mathrm{e} = Z_i n_i$. The fluid system based on (17.25), (17.27)
and (17.28) permits the application of the classical self-similar solution first
found by Gurevich et al. [81]; that is, $n_i = n_0 \exp[-(1 + \xi/c_\mathrm{s})]$, $u_i = c_\mathrm{s} + \xi$,
$E = T_\mathrm{e}/ec_\mathrm{s}t$, where $\xi = x/t$ is the self-similar variable, and c_s is the sound
velocity. An analytical solution can also be found, with the quasi-neutral
approximation, for the kinetic system based on (17.25) and (17.26) [82, 83]
by using a renormalized group theoretical approach. By assuming plasma
quasi-neutrality, two-temperature electron distributions have also been con-
sidered [83–87]. In general, all of these solutions can describe the physical
behavior of the system on a time scale longer than the typical ion accelera-
tion time, $\tau \approx L/c_\mathrm{s}$, which for a $L = 100\,\mu\mathrm{m}$ foil and $T_\mathrm{e} = 100\,\mathrm{eV}$ may span
from tens of picoseconds to nanoseconds.

However in the subpicosecond regime, the ion inertia is important and
the assumption of quasi-neutrality must be abandoned in order to get a bet-
ter description of the process. A completely different set of approximations
can then be used in order to find analytical solutions suitable for describing
a physical regime closer to that which produces the most energetic ions in
ultraintense laser–solid target experiments, and to investigate the effect of
the strong charge separation which can develop on the rear side of the solid
target. The heavy ions are assumed to be immobile over the time scale of

interest, while the light ions are considered to be sufficiently rare that their effect on the evolution of the electrostatic potential, which in this limit is given by

$$\frac{\partial^2 \phi}{\partial x^2} = 4\pi e(n_{0h} e^{e\phi/T_h} + n_{0c} e^{e\phi/T_c} - Z_L n_{0L}) , \qquad (17.29)$$

can be neglected.

The solution for (17.29) in a semi-infinite plasma region $x > 0$, assuming for the sake of simplicity that only fast electrons are present (i.e., $n_{0c} = 0$), is [88]

$$\phi(x) = -\frac{2T}{e} \ln\left(1 + \frac{x}{\sqrt{2e}\lambda_{de}}\right) - 1 \qquad (17.30)$$

from which the corresponding electron density and electric field can be immediately calculated. Here, $T_h \to T$ and $n_h \to n$ refer to the hot electron population. The conservative nature of the system leads to an infinite acceleration of a test proton which is initially at zero energy in $x = 0$. Since the experiments show accelerated ion energy spectra with a sharp upper cutoff, it is necessary to include a truncation mechanism in the acceleration process. By assuming that the hot electron population occupies only a finite region of width h, the solution for (17.29) and the electron density in vacuum, $0 < x < h$, take the form [89]

$$\phi(x) = \frac{T}{e} \ln\left[1 + \tan^2\left(\frac{h-x}{\sqrt{2}\lambda_{eh}}\right)\right] \quad n_e(x) = n_{eh}\left[1 + \tan^2\left(\frac{h-x}{\sqrt{2}\lambda_{eh}}\right)\right] . \qquad (17.31)$$

Accordingly, the electric field is

$$E(x) = \sqrt{2}\frac{T}{e\lambda_{eh}} \tan\left(\frac{h-x}{\sqrt{2}\lambda_{eh}}\right) = \sqrt{2}\frac{T}{e}\sqrt{\frac{1}{\lambda_e^2(x)} - \frac{1}{\lambda_{eh}^2}} . \qquad (17.32)$$

In the above equations, the "local" electron Debye length $\lambda_e(x) = [T/4\pi e^2 n_e(x)]^{1/2}$ and $\lambda_{eh} \equiv \lambda_e(h)$ are defined. The length h is still undetermined. A very rough estimate of the extension of the electron cloud can be given by the following energetic argument: the kinetic energy acquired by a test electron from the laser pulse should be equal to the work done by the electron to cover the distance h in the presence of the spatial distribution of the other fast electrons [90]. The resulting expression reads

$$h = \sqrt{\frac{\gamma_e - 1}{\pi r_c n_{av}}} , \qquad (17.33)$$

where $r_c = e^2/mc^2$ is the classical electron radius, γ_e is the relativistic factor of the test electron, $n_{av} = N_e/V$ the average density of the hot electrons,

N_e the total number of fast electrons produced by the laser, and $V = \pi R_e^2 L$ the volume they occupy. Finally, R_e and L are the radius and the depth, respectively, of the region inside the target from which the hot electrons are emitted [56]. This approach is not self-consistent, since the length h occurs in the determination of the length λ_e. Moreover, (17.31) and (17.32) represent a nonstationary solution, due to the discontinuity of $n_e(x)$ at $x = h$. However, they give simple analytical expressions for the hot electron density and for the accelerating field distributions, as functions of the interaction parameters. Equation (17.32) can be used to calculate the quasi-static electron distribution of a given temperature at a sharp solid–vacuum interface. Recently, in order to overcome the issue of the discontinuity in the electron density spatial distribution, the Poisson equation has been solved by assuming that a quasi-stationary state is established where only those electrons (*trapped electrons*) with negative total (potential plus kinetic) energy are retained, while those with positive total energy are lost from the system [91]. Accordingly, the trapped electron density can be written as

$$n_e^{\mathrm{tr}}(x) = n_0 \Phi \left(\sqrt{e\phi/T_h} \right) \exp \left(e\phi/T_h \right) \qquad (17.34)$$

and

$$n_e^{\mathrm{tr}}(r) = n_0 \Phi \left(\sqrt{e\phi/T_h} \right) \exp \left(e\phi/T_h \right) - \left(2/\sqrt{\pi} \right) \sqrt{e\phi/T_h} \qquad (17.35)$$

in the one-dimensional and in the spherically symmetric three-dimensional cases, respectively; here, Φ is the error function. It can easily be checked that both distributions behave regularly, as they tend to zero for $\phi \to 0$. Specifically, the analytical solution to the one-dimensional Poisson equation in the limit $|e\phi/T_h| \ll 1$ gives $\phi(x) \propto 1/(x_f - x)^4$; that is, the ES potential, the ES field and the electron density distributions go to zero at the finite position x_f. On the other hand, in the three-dimensional case, $\phi(r) \propto 1/r^4$, the hot electron cloud extends up to infinity. As a result, as long as multidimensional effects can be neglected, the limited extension of the planar distribution of hot electrons can be confirmed using a consistent treatment of hot electrons. It is worth noting here that recent experiments (see [92] and S.V. Bulanov, 2005, private communication) show that the accelerating electric field at the rear side of a planar target appears to become negligible at a finite distance from the target, in agreement with the results from the models discussed above.

Quasi-stationary models assume that, besides their spatial distribution, the temperature of the fast electrons also does not evolve during the ion acceleration process. These issues do not seem to provide a major problem when determining the maximum ion energy, since the acceleration of these ions (which will be the most energetic) takes place over a time scale over which the temperature and the entire distribution do not vary appreciably [93].

It turns out that the spatial profiles present very steep gradients, especially close to the rear target surface; in particular the values exhibited by

the accelerating electric field around $x = 0$ can be very large and, correspondingly, the electrostatic potential decreases by 50% in the first μms, depending on the particular values of the parameters. Therefore estimates of the maximum ion energies based on "average" values of such quantities can give unrealistic results, while these simple models provide a reliable method for estimating the maximum energy achievable by a test light ion in the calculated electron distribution, and the relevant energy spectrum, for specific experimental conditions. As far as the ion acceleration is concerned, a fairly good agreement between prediction and experimental results has been shown in the parameter regime for which this model can be applied. Further details about the limits of applicability and a discussion of the results can be found in [89, 91].

If both electron populations are considered, it is possible to find an implicit analytical solution to (17.29), inside ($x < 0$) and outside ($x > 0$) the target, by imposing the continuity of the potential and the electric field at the solid–vacuum interface, $x = 0$. In the region $x < 0$, the solution reads [94]

$$\int_{\varphi(0)}^{\varphi(x)} \frac{\mathrm{d}\varphi}{[\exp\varphi + ab\exp(\varphi/b) - (1 + ab) - (1 + a)\varphi]^{1/2}} = -\sqrt{2}\frac{x}{\lambda_{\mathrm{dh}}} \quad (17.36)$$

while for $x > 0$

$$\int_{\varphi(0)}^{\varphi(x)} \frac{\mathrm{d}\varphi}{[\exp\varphi + ab\exp(\varphi/b)]^{1/2}} = -\sqrt{2}\frac{x}{\lambda_{\mathrm{dh}}} \; . \quad (17.37)$$

In these equations, the parameters $a \equiv n_{0c}/n_{0h}$ and $b \equiv T_c/T_h$ have been defined. The important result here is that the spatial profile of the electrons depends strongly on the cold electron population. In particular, it determines the spatial penetration of the electric field inside the solid target, since the field drops, almost exponentially, inside the target from its maximum value to zero over a few cold electron Debye lengths. The maximum field value can be affected by the cold electrons too. From these considerations, it is evident that, in order to study the effect of the two populations on the resulting accelerating electric field, an estimate of the cold temperature of the background electron population is required. T_c can increase with respect to the room temperature because of the ohmic heating provided by the return current and the finite resistivity of the solid target. A simple analytical model of the process has been proposed [94, 95], to which we refer the reader for further details and results.

Self-consistent analysis of the 1-D fluid and kinetic models presented here can be developed through numerical simulations, where (17.30) and (17.32) or (17.36) and (17.37) can be used to define the initial conditions for the electric field at time $t = 0$, when the ion acceleration process begins. Results from these studies that use the fluid and the kinetic descriptions can be found in the literature, where either a single electron population [88, 96–99]

or the two electron component case have been considered [93, 100–102]. By describing the electron population as a fluid initially accelerated at relativistic velocities and freely expanding in vacuum, the maximum ion energy gain in the corresponding electron cloud has been calculated [103], and this was found to be substantially larger than the electron energy.

In order to be able to consider the ion motion during the acceleration process as being one-dimensional, the electron cloud should be spatially uniform in the plane normal to the ion motion. One way to impose this condition is to require that $h/2R_e < 1$. This condition translates into preferences for the laser energy and intensity: for a given final ion energy, low intensity and high energy are preferable to high intensity and low energy. Furthermore, the ion acceleration is expected to be planar if the transverse extension of the ion-enriched layer (the portion of the rear surface where the light ions to be accelerated are concentrated), $2R_i$, is smaller than that of the electron cloud; that is, $R_i/R_e < 1$.

The models described above are definitely stationary, while the electron cloud formation is not. It is assumed that the electron cloud does not evolve during the acceleration process and is not affected by the ions flowing through it. The latter condition requires that the number of the ions that are accelerated is much smaller than the number of hot electrons, $N_i \ll N_e$.

Concerning the electron energy distribution, it has been assumed that the electron temperature does not evolve with time, although it is expected that the energy of the hot electrons will decay over time due to their expansion and to collisional and radiative losses. Therefore, a better characterization of the ion acceleration process would incorporate the temporal evolution of the electron temperature, which could compete with the effect of a finite acceleration length in the determination of the maximum energy gain. Indeed, electron cooling has been considered in a few recent papers [93, 101].

Ultimately, several spurious mechanisms, not considered here, will inevitably tend to broaden the final ion energy spectra.

17.4 Concluding Remarks

In this chapter we have reported on theoretical investigations of two different regimes of interaction between ultraintense EM radiation and plasmas, as examples of the application of the theoretical models developed in a previous chapter. First, we have studied the existence of localized spatial distributions of EM radiation, which appear in numerical simulations as a result of the injection of an ultrashort and intense laser pulse into an underdense plasma. Such solitonic structures originating from the equilibrium between the EM radiation pressure, the plasma pressure and the ambipolar field associated with the space charge have been described in the framework of both a relativistic kinetic model and a relativistic fluid approach. It has also been shown that

the RES predicted by large-scale PIC simulations are satisfactorily reproduced by the kinetic model developed by the authors. As a second example, the ion acceleration arising from the interaction between an ultrashort and intense laser pulse and a thin solid target was considered. The most significant analytical approaches for the theoretical investigation of this process were presented. In particular, the quasi-stationary ES spatial distribution at the sharp boundary between a planar plasma and vacuum in the presence of a hot electron population has been consistently calculated by solving the Poisson equation where the source term contains the contribution from hot electrons trapped in the positive potential well produced by the target ions before they start moving. As far as two-dimensional effects can be considered negligible, it has been shown that the hot electron population is distributed over a finite spatial interval and does not extend to infinity. This peculiarity seems to be in agreement with recent experimental observations. The calculated electric field spatial distribution has been used to calculate the maximum energy achieved by a test ion and this result compared favorably with experimental measurements.

References

1. M. Lontano, M. Passoni: Chapter 10 in *Progress in Ultrafast Laserscience I*
2. S.V. Bulanov, F. Califano, G.I. Dudnikova et al.: Relativistic interaction of laser pulses with plasmas. In: *Reviews of Plasma Physics*, edited by V.D. Shafranov (Kluwer Academic/Consultants Bureau, New York 2001), vol. 22, pp 227–335
3. S.V. Bulanov, I.N. Inovenkov, V.I. Kirsanov et al.: Phys. Fluids B **4**, 1935 (1992)
4. T. Tajima, T. Taniuti: Phys. Rev. A **42**, 3587 (1990)
5. S.V. Bulanov, V.I. Kirsanov, A.S. Sakharov: Sov. J. Plasma Phys. **16**, 543 (1990)
6. S.V. Bulanov, M. Lontano, T.Zh. Esirkepov et al.: Phys. Rev. Lett. **76**, 3562 (1996)
7. D. Farina, M. Lontano, I.G. Murusidze, S.V. Mikeladze: Phys. Rev. E **63**, 056409 (2001)
8. S.V. Bulanov, I.N. Inovenkov, V.I. Kirsanov et al.: Physica Scripta **47**, 209 (1993)
9. Y. Sentoku, T.Zh. Esirkepov, K. Mima et al.: Phys. Rev. Lett. **83**, 3434 (1999)
10. S.V. Bulanov, T.Zh. Esirkepov, N.N. Naumova et al.: Phys. Rev. Lett. **82**, 3440 (1999)
11. C.A. Coverdale, C.B. Darrow, C.D. Decker et al.: Plasma Phys. Rep. **22**, 617 (1996)
12. N.M. Naumova, S.V. Bulanov, T.Zh. Esirkepov et al.: Phys. Rev. Lett. **87**, 185004 (2001)
13. G. Mourou, Z. Chang, A. Maksimchuk et al.: Plasma Phys. Rep. **28**, 12 (2002)
14. T. Esirkepov, K. Nishihara, S.V. Bulanov, F. Pegoraro: Phys. Rev. Lett. **89**, 275002 (2002)

15. G.S. Sarkisov, V.Yu. Bychenkov, V.N. Novikov et al.: Phys. Rev. E **59**, 7042 (1999)
16. T.Zh. Esirkepov, Y. Sentoku, K. Mima et al.: JETP Lett. **70**, 82 (1999)
17. S.V. Bulanov, T.Zh. Esirkepov, F. Califano et al.: JETP Lett. **71**, 407 (2000)
18. Y. Sentoku, T.V. Liseikina, T.Zh. Esirkepov: Phys. Rev. E **62**, 7271 (2000)
19. Ya.B. Zel'dovich, Yu.P. Raizer: *Physics of Shock Waves and High-Temperature Hydrodynamic Phenomena*, (Academic, New York 1967)
20. S. Weber, C. Riconda, V.T. Tikhonchuk: Phys. Rev. Lett. **94**, 055005 (2005)
21. S. Weber, C. Riconda, V.T. Tikhonchuk: Phys. Plasmas **12**, 043101 (2005)
22. S. Weber, M. Lontano, M. Passoni et al.: Phys. Plasmas **12**, 112107 (2005)
23. M. Lontano, M. Passoni C. Riconda et al.: Laser Part. Beams **24**, 125 (2006)
24. A.I. Akhiezer, R.V. Polovin: Sov. Phys. JETP **30**, 915 (1956)
25. V.A. Kozlov, A.G. Litvak, E.V. Suvorov: Sov. Phys. JETP **49**, 76 (1979)
26. P.K. Kaw, A. Sen, T. Katsouleas: Phys. Rev. Lett. **68**, 3172 (1992)
27. D. Farina, S.V. Bulanov: Plasma Phys. Rep. **27**, 641 (2001)
28. D. Farina, S.V. Bulanov: Phys. Rev. Lett. **86**, 5289 (2001)
29. D. Farina, S.V. Bulanov: Plasma Phys. Contr. Fus. **47**, A 73 (2005)
30. K. Mima, T. Ohsuga, H. Takabe et al.: Phys. Rev. Lett. **57**, 1421 (1986)
31. T. Tajima, J.M. Dawson: Phys. Rev. Lett. **43**, 267 (1979)
32. T.Zh. Esirkepov, F.F. Kamenets, S.V. Bulanov, N.M. Naumova: JETP Lett. **68**, 36 (1998)
33. F. Cattani, A. Kim, D. Anderson, M. Lisak: Phys. Rev. E **62**, 1234 (2000)
34. A. Kim, F. Cattani, D. Anderson, M. Lisak: JETP Lett. **72**, 241 (2000)
35. F. Cattani, A. Kim, D. Anderson, M. Lisak: Phys. Rev. E **64**, 016412 (2001)
36. D. Farina, M. Lontano, S.V. Bulanov: Phys. Rev. E **62**, 4146 (2000)
37. F. Pegoraro, S.V. Bulanov, F. Califano et al.: Physica Scripta **T84**, 89 (2000)
38. M.D. Feit, A.M. Komashko, S.L. Musher et al.: Phys. Rev. E **57**, 7122 (1998)
39. M. Lontano, S.V. Bulanov, J. Koga: Phys. Plasmas **8**, 5113 (2001)
40. L.N. Tsintsadze: Physica Scripta **50**, 413 (1994)
41. V.I. Berezhiani, S.M. Mahajan: Phys. Rev. E **52**, 1968 (1995)
42. S. Kartal, L.N. Tsintsadze, V.I. Berezhiani: Phys. Rev. E **53**, 4225 (1996)
43. T. Tatsuno, V.I. Berezhiani, S.M. Mahajan: Phys. Rev. E **63**, 046403 (2001)
44. M. Lontano, S.V. Bulanov, J. Koga et al.: Phys. Plasmas **9**, 2562 (2002)
45. M. Lontano, M. Passoni, S.V. Bulanov: Phys. Plasmas **10**, 639 (2003)
46. J.B. Kim, S.V. Bulanov, H. Suk, I.S. Ko: Phys. Lett. A **329**, 464 (2004)
47. M. Lontano, M. Borghesi, S.V. Bulanov et al.: Laser Part. Beams **21**, 541 (2003)
48. M. Borghesi, S.V. Bulanov, D.H. Campbell et al.: Phys. Rev. Lett. **88**, 135002 (2002)
49. M. Borghesi, D.H. Campbell, A. Schiavi et al.: Phys. Plasmas **9**, 2214 (2002)
50. E.L. Clark, K. Krushelnick, J.R. Davies et al.: Phys. Rev. Lett. **84**, 670 (2000)
51. R.A. Snavely, M.H. Key, S.P. Hatchett et al.: Phys. Rev. Lett. **85**, 2945 (2000)
52. A.P. Fews, P.A. Norreys, F.N. Beg et al.: Phys. Rev. Lett. **73**, 1801 (1994)
53. F.N. Beg, A.R. Bell, A.E. Dangor et al.: Phys. Plasmas **4**, 447 (1997)
54. J. Badziak, E. Woryna, P. Parys et al.: Phys. Rev. Lett. **87**, 215001 (2001)
55. J. Badziak, E. Woryna, P. Parys et al.: Nucl. Instr. Methods in Phys. Res. A **498**, 503 (2003)
56. S.P. Hatchett, C.G. Brown, T.E. Cowan et al.: Phys. Plasmas **7**, 2076 (2000)
57. A. Maksimchuk, S. Gu, K. Flippo et al.: Phys. Rev. Lett. **84**, 4108 (2000)

58. K. Krushelnick, E.L. Clark, M. Zepf et al.: Phys. Plasmas **7**, 2055 (2000)
59. Y. Murakami, Y. Kitagawa, Y. Sentoku et al.: Phys. Plasmas **8**, 4138 (2001)
60. A.J. Mackninnon, M. Borghesi, S. Hatchett et al.: Phys. Rev. Lett. **86**, 1769 (2001)
61. A.J. Mackinnon, Y. Sentoku, P.K. Patel et al.: Phys. Rev. Lett. **88**, 215006 (2002)
62. M. Zepf, E.L. Clark, K. Krushelnick et al.: Phys. Plasmas **8**, 2323 (2001)
63. E.L. Clark, K. Krushelnick, M. Zepf et al.: Phys. Rev. Lett. **85**, 1654 (2000)
64. M. Hegelich, S. Karsch, G. Pretzler et al.: Phys. Rev. Lett. **89**, 085002 (2002)
65. M. Zepf, E.L. Clark, F.N. Beg et al.: Phys. Rev. Lett. **90**, 064801 (2003)
66. M. Roth, T.E. Cowan, C. Brown et al.: Nucl. Instr. Meth. Plasma Res. A **464**, 201 (2001)
67. M. Roth, A. Blazevic, M. Geissel et al.: Phys. Rev. Spec. Top.: Accel. Beams **5**, 061301 (2002)
68. M. Zepf, M. Castro-Colin, D.M. Chambers et al.: Phys. Plasmas **3**, 3242 (1996)
69. W. Yu, V. Bychenkov, Y. Sentoku et al.: Phys. Rev. Lett. **85**, 570 (2000)
70. J.R. Davies, A.R. Bell, M. Tatarakis: Phys. Rev. E **59**, 6032 (1999)
71. J.R. Davies: Laser Part. Beams **20**, 243 (2002)
72. J. Sakai, S. Saito, H. Mae et al.: Phys. Plasmas **9**, 2959 (2002)
73. M. Allen, Y. Sentoku, P. Audebert et al.: Phys. Plasmas **10**, 3283 (2003)
74. S.C. Wilks, A.B. Langdon, T.E. Cowan et al.: Phys. Plasmas **8**, 542 (2001)
75. H. Ruhl, S.V. Bulanov, T.E. Cowan et al.: Plasma Phys. Rep. **27**, 363 (2001)
76. A. Pukhov: Phys. Rev. Lett. **86**, 3562 (2001)
77. T. Nakamura, S. Kawata: Phys. Rev. E **67**, 026403 (2003)
78. T. Esirkepov, M. Borghesi, S.V. Bulanov et al.: Phys. Rev. Lett. **92**, 175003 (2004)
79. E. d'Humieres, E. Lefebvre, L. Gremillet: Phys. Plasmas **12**, 062704 (2005)
80. E. Fourkal, I. Velchev, C.-M. Ma: Phys. Rev. E **71**, 036412 (2005)
81. A.V. Gurevich, L.V. Pariiskaya, L.P. Pitaevskii: Soviet Phys. JETP **22**, 449 (1966)
82. D.S. Dorozhkina, V.E. Semenov: Phys. Rev. Lett. **81**, 2691 (1999)
83. V.F. Kovalev, V.Yu. Bychenkov, V.T. Tikhonchuk: J. Exp. Theor. Phys. **95**, 226 (2002)
84. L.M. Wickens, J.E. Allen, P.T. Rumsby: Phys. Rev. Lett. **41**, 243 (1978)
85. L.M. Wickens, J.E. Allen: J. Plasma Phys. **22**, 167 (1979)
86. A.V. Gurevich, D. Anderson, H. Wilhelmsson: Phys. Rev. Lett. **42**, 769 (1979)
87. M.A. True, J.R. Albritton, E.A. Williams: Phys. Fluids. **24**, 1885 (1981)
88. J.E. Crow, P.L. Auer, J.E. Allen: J. Plasma Phys. **14**, 65 (1975)
89. M. Passoni, M. Lontano: Laser Part. Beams **22**, 163 (2004)
90. V.T. Tikhonchuk: Phys. Plasmas **9**, 1416 (2002)
91. M. Lontano, M. Passoni: Phys. Plasmas **13**, 042102 (2006)
92. L. Romagnani, J. Fuchs, M. Borghesi et al.: Phys. Rev. Lett. **95**, 195001 (2005).
93. P. Mora: Phys. Rev. E **72**, 056401 (2005)
94. M. Passoni, V.T. Tikhonchuk, M. Lontano et al.: Phys. Rev. E **69**, 026411 (2004)
95. J. R. Davies: Phys. Rev. E **68**, 056404 (2003)
96. M. Widner, I. Alexeef, W.D. Jones: Phys. Fluids **14**, 795 (1971)
97. J.S. Pearlman, R.L. Morse: Phys. Rev. Lett. **40**, 1652 (1978)

98. J. Denavit: Phys. Fluids **22**, 1384 (1979)
99. P. Mora: Phys. Rev. Lett. **90**, 185002 (2003)
100. V.Yu. Bychenkov, V.N. Novikov, D. Batani et al.: Phys. Plasmas **11**, 3242 (2004)
101. S. Betti, F. Ceccherini, F. Cornolti, F. Pegoraro: Plasma Phys. Contr. Fus. **47**, 521 (2005)
102. V.T. Tikhonchuk, A.A. Andreev, S.G. Bochkarev, V.Yu. Bychenkov: Plasma Phys. Contr. Fus. **47**, B869 (2005)
103. S.V. Bulanov, T.Zh. Esirkepov, J. Koga et al.: Plasma Phys. Rep. **30**, 18 (2004)

Index